

Towards a neutron multiplicity  
measurement with the  
Accelerator Neutrino Neutron  
Interaction Experiment

Dissertation

zur Erlangung des Grades  
*Doktor der Naturwissenschaften*

am Fachbereich  
Physik, Mathematik und Informatik  
der Johannes Gutenberg-Universität in Mainz

Michael Thomas Nieslony

---

Mainz, den 18. Mai 2022



Supervisor: Prof. Dr. Michael Wurm  
Reviewer: Prof. Dr. Martin Fertl  
Date of disputation: 25.11.2022

*Für meine Eltern.*



# Abstract

---

The Accelerator Neutrino Neutron Interaction Experiment (ANNIE) is a 26 ton Gadolinium (Gd)-loaded water Cherenkov detector located on the Booster Neutrino Beam line at Fermilab. Its main goals are the measurement of the neutron multiplicity in neutrino-nucleus interactions as well as the cross-section of Charged Current Quasi-Elastic (CCQE) neutrino interactions on water. Besides the physics goals, the experiment also aims to be a testbed for new technologies such as Large Area Picosecond Photodetectors (LAPPDs) and Water-based Liquid Scintillators (WbLS).

This thesis presents a preliminary measurement of the neutron multiplicity with ANNIE, using an analysis conducted on a fraction of the 2021 beam year. As preparatory measures, the efficiency of ANNIE's Front Muon Veto (FMV) was determined to be  $\bar{\epsilon}_{\text{FMV}} = (95.6 \pm 1.6)\%$  while the average efficiency for active scintillator paddles in the Muon Range Detector (MRD) was found to be  $\bar{\epsilon}_{\text{MRD}} = (92.1 \pm 7.9)\%$ . Furthermore, the simulation framework used for ANNIE was validated and adapted to reproduce the experimental data by comparing the detector response for samples of Michel electrons, Americium Beryllium neutrons, and through-going muons.

The analysis finds average neutron yields of  $\bar{n}_{\text{data}}(\text{beam}) = (0.272 \pm 0.010_{\text{stat}})$  for an inclusive set of all identified muon neutrino candidates and  $\bar{n}_{\text{data}}(\text{beam, FV}) = (0.287 \pm 0.044_{\text{stat}})$  for interactions which happened inside of the Fiducial Volume of ANNIE, which was optimized to increase the neutron detection acceptance. The presented neutron multiplicity values represent the number of detected neutrons after all event selection cuts and are not yet corrected for the neutron detection efficiency. An equivalent analysis on a simulated beam sample predicts neutron yields of  $\bar{n}_{\text{MC}}(\text{beam}) = (0.515 \pm 0.007_{\text{stat}})$  and  $\bar{n}_{\text{MC}}(\text{beam, FV}) = (0.627 \pm 0.031_{\text{stat}})$ , indicating that the models tend to overpredict the number of neutrons produced in such interactions. Systematic errors have been briefly considered to contribute  $\sigma_{\text{sys,FMV}} \sim 0.01$  neutrons/ $\nu$ -interaction due to the slight FMV inefficiency and  $\sigma_{\text{sys,n}} \sim 0.05$  neutrons/ $\nu$ -interaction due to the neutron detection efficiency.

Simulation studies further highlighted the importance of neutron detection in Diffuse Supernova Background (DSNB) searches. A combination of neutron tagging and Convolutional Neural Networks was found to reduce the most relevant Neutral Current Quasi-Elastic (NCQE) interaction background below the signal level, achieving a Signal-to-Background ratio of 4:1. In a further study, we investigated the positive impact of a deployment of a WbLS target on the energy reconstruction in ANNIE. WbLS provides a scintillation signal from hadronic recoils in addition to the charged lepton that can be included in neutrino energy reconstruction. It was found that a deployed WbLS volume in ANNIE improves the neutrino energy reconstruction from 14% to 12%, with the potential of going beyond this if more sophisticated reconstruction algorithms are developed in the future.



# Contents

---

ABSTRACT	v
CONTENTS	x
<b>I PROLOGUE</b>	<b>1</b>
1 INTRODUCTION	3
2 NEUTRINO PHYSICS	7
2.1 The Standard Model of Particle Physics . . . . .	8
2.2 Neutrino physics . . . . .	11
2.2.1 Detection mechanisms for neutrinos . . . . .	12
2.2.2 A historic perspective: The solar neutrino problem . . . . .	16
2.2.3 Neutrino oscillations . . . . .	20
2.2.4 Different regimes of neutrino oscillations . . . . .	22
2.2.5 Neutrino flavor conversions in matter . . . . .	27
2.2.6 Global best fit parameters . . . . .	33
2.2.7 Open questions in neutrino physics . . . . .	34
2.3 GeV-scale neutrino interactions . . . . .	41
2.3.1 Overview of interaction channels . . . . .	41
2.3.2 Cross-section measurements . . . . .	48
2.3.3 Neutrino event generators . . . . .	51
2.3.4 Neutron multiplicity measurements . . . . .	52
<b>II THE ACCELERATOR NEUTRINO NEUTRON INTERACTION EXPERIMENT</b>	<b>61</b>
3 THE ACCELERATOR NEUTRINO NEUTRON INTERACTION EXPERIMENT (ANNIE)	63
3.1 The Fermi National Accelerator Laboratory . . . . .	64
3.1.1 Accelerator complex overview . . . . .	64
3.1.2 The Booster Neutrino Beam (BNB) . . . . .	67
3.1.3 Accelerator clock signals . . . . .	73
3.2 The ANNIE detector . . . . .	74
3.2.1 The Water Tank . . . . .	75
3.2.2 The Muon Range Detector (MRD) . . . . .	77
3.2.3 The Front Muon Veto (FMV) . . . . .	80
3.2.4 Large Area Picosecond Photodetectors (LAPPDs) . . . . .	81
3.2.5 Gd-loading and Water filtration . . . . .	88
3.3 Physics analysis goals of ANNIE . . . . .	91

3.3.1	Neutron multiplicity measurement . . . . .	92
3.3.2	Neutrino cross-section on water . . . . .	94
3.3.3	Phases of ANNIE . . . . .	96
3.4	Data taking in ANNIE . . . . .	99
3.4.1	Data Acquisition (DAQ) . . . . .	100
3.4.2	Trigger schemes in ANNIE . . . . .	104
3.4.3	Event Building . . . . .	107
3.4.4	Online monitoring . . . . .	110
4	MUON RANGE DETECTOR AND FRONT MUON VETO EFFICIENCIES . . . . .	117
4.1	Muon Range Detector Paddle Efficiencies . . . . .	117
4.1.1	Muon track fit procedure . . . . .	118
4.1.2	Efficiency determination method . . . . .	119
4.1.3	Monte Carlo efficiency study . . . . .	120
4.1.4	Current Muon Range Detector efficiencies . . . . .	123
4.2	Front Muon Veto Paddle Efficiencies . . . . .	126
4.2.1	Efficiency determination method . . . . .	127
4.2.2	Monte Carlo efficiency study . . . . .	130
4.2.3	Laboratory measurements & Phase I efficiencies . . . . .	130
4.2.4	Current Front Muon Veto efficiencies . . . . .	132
4.3	Impact of efficiencies on track reconstruction performance . . . . .	136
<b>III TOWARDS A NEUTRON MULTIPLICITY MEASUREMENT WITH ANNIE</b>		<b>139</b>
5	VALIDATION & TUNING OF THE MONTE CARLO SIMULATION . . . . .	141
5.1	ANNIE Monte Carlo simulation . . . . .	142
5.1.1	Simulation of neutrino interactions . . . . .	143
5.1.2	Physics & Detector simulation . . . . .	145
5.2	Commissioning data: Differences between data & simulation . . . . .	146
5.3	Modifications to the simulation . . . . .	149
5.3.1	General properties of the simulation . . . . .	150
5.3.2	PMT positions from laser scan file . . . . .	154
5.3.3	Addition of PMT holders to the simulation . . . . .	157
5.3.4	Implementation of custom PMT charge response functions . . . . .	158
5.4	Tuning of parameters . . . . .	163
5.4.1	Tuning of overall light yield: Michel electrons . . . . .	163
5.4.2	Tuning of material reflectivity values: Through-going muons . . . . .	168
5.4.3	Am-Be neutron calibration . . . . .	175
5.4.4	Validation of tuning campaign . . . . .	182
5.5	Validation of the MRD implementation . . . . .	185
6	ANNIE PHASE II NEUTRON MULTIPLICITY ANALYSIS . . . . .	187
6.1	Commissioning of the detector . . . . .	188
6.1.1	Detecting the beam spill window with ANNIE . . . . .	188

6.1.2	Subsystem timing alignment . . . . .	189
6.1.3	Event Displays of different event types . . . . .	191
6.2	Data taking overview . . . . .	195
6.2.1	Data taking period . . . . .	195
6.2.2	Trigger rates & event type fractions . . . . .	196
6.3	Prompt event analysis - muon classification . . . . .	201
6.3.1	Neutrino event candidate selection . . . . .	201
6.3.2	Characterization of muon neutrino candidates in data . . . . .	204
6.4	Delayed event analysis - neutron counting . . . . .	211
6.4.1	Expected neutron yield . . . . .	212
6.4.2	Selection cuts for neutron candidates . . . . .	213
6.4.3	Properties of selected neutron candidates . . . . .	215
6.4.4	Integrated neutron multiplicity . . . . .	217
6.5	Combined analysis - Neutron multiplicity as a function of muon kinematics . . . . .	219
6.5.1	Combining the prompt and delayed event analysis . . . . .	220
6.5.2	Comparison with neutron multiplicity in simulation . . . . .	222
6.6	Brief outlook on systematic uncertainties . . . . .	224
<b>IV FUTURE APPLICATIONS</b>		<b>229</b>
7	DETECTING THE DIFFUSE SUPERNOVA BACKGROUND IN NEXT-GENERATION NEUTRINO EXPERIMENTS	231
7.1	The Diffuse Supernova Background (DSNB) . . . . .	232
7.2	Backgrounds for the DSNB search . . . . .	235
7.2.1	Atmospheric neutrinos . . . . .	235
7.2.2	Atmospheric NCQE background . . . . .	236
7.2.3	Atmospheric NC- $n\pi$ background . . . . .	242
7.2.4	Invisible muons . . . . .	242
7.3	Simulation of the DSNB and Atmospheric NCQE background signals . . . . .	243
7.3.1	Detector configuration and simulation framework . . . . .	243
7.3.2	Simulation of DSNB sample . . . . .	243
7.3.3	Simulation of Atmospheric NCQE sample . . . . .	244
7.3.4	Event selection & normalization . . . . .	244
7.4	DSNB/NCQE event discrimination with Convolutional Neural Networks . . . . .	247
7.4.1	Network architecture & performance . . . . .	248
7.4.2	Results of DSNB/NCQE classification . . . . .	254
7.5	Future NCQE measurement with ANNIE . . . . .	256
7.5.1	Neutral Current trigger setup . . . . .	256
7.5.2	NC Event Selection steps . . . . .	256
8	FUTURE ENDEAVORS: WATER-BASED LIQUID SCINTILLATORS	259
8.1	The novel detection medium Water-based Liquid Scintillator (WbLS) . . . . .	260
8.1.1	The best of both worlds: Scintillation & Cherenkov light . . . . .	261
8.1.2	Chemical structure and production of WbLS . . . . .	262

8.1.3	Characterization of WbLS . . . . .	263
8.2	WbLS in ANNIE . . . . .	267
8.2.1	Phase II Upgrade: Deploying the SANDI volume . . . . .	268
8.2.2	Simulation of SANDI in ANNIE . . . . .	269
8.2.3	Investigation of neutrino interactions in SANDI . . . . .	271
8.2.4	Muon & recoil light contributions . . . . .	275
8.2.5	Improved neutrino energy reconstruction . . . . .	280
8.2.5.1	Simple formula-based reconstruction . . . . .	281
8.2.5.2	Random Forest . . . . .	284
8.3	WbLS in future neutrino experiments . . . . .	288
9	CONCLUSION & OUTLOOK . . . . .	291
	BIBLIOGRAPHY . . . . .	295
	APPENDIX . . . . .	317
A	Data structures in ANNIE . . . . .	317
B	Additional information on FMV efficiencies . . . . .	321
C	Complementary AmBe calibration plots . . . . .	323
	ACKNOWLEDGEMENTS . . . . .	325

Part I

PROLOGUE



# 1

## Introduction

---

*“The thing that is important is the thing that is not seen.”*

—Antoine de Saint-Exupéry

Since its postulation, the neutrino has managed to fascinate and captivate physicists all around the world with its unique and – at times – surprising properties. While at first the whole idea of such a barely interacting particle may have seemed like a desperate attempt to save the laws of energy conservation [1], the neutrino has been studied in more and more detail ever since and inspired the generation of an entire subfield of particle physics. Many of its properties have been uncovered and measured since then, most notably the mechanism of neutrino oscillations [2] in which neutrinos can change their flavor during propagation, directly implying that at least two neutrino mass eigenstates must have a non-zero mass. However, many things are also still currently unknown: For instance, neutrinos could be their own antiparticles when considering them to be Majorana particles. Similarly, the ordering of the mass eigenstates and the value for the leptonic CP-phase  $\delta_{\text{CP}}$  are currently not known.

Future large-scale neutrino experiments aim to shed light on these matters, for example by investigating the oscillation signature in dedicated appearance channels in long baseline environments [3]. However, an accurate knowledge of the cross-sections and interaction channels is needed to minimize systematic uncertainties and biases in these analyses. Particularly the neutron yield in neutrino interactions can help to identify more complicated interaction topologies and in turn improve the neutrino energy resolution or reduce backgrounds in rare signal studies like proton decay searches [4]. However, the corresponding models for neutron generation currently feature rather large uncertainties, both regarding the primary neutrino interaction as well as secondary hadronic interactions in the target medium [5]. While some measurements of the neutron multiplicity already exist for atmospheric neutrino samples [6, 7], further experimental data is vital to test the existing models more rigorously in this regard.

The Accelerator Neutrino Neutron Interaction Experiment (ANNIE) is a 26 ton Gadolinium (Gd)-loaded water Cherenkov detector located on the Booster Neutrino Beam (BNB) at

Fermi National Accelerator Laboratory (Fermilab) [8]. One of the main goals of ANNIE is measuring the neutron yield in neutrino interactions in an accelerator neutrino environment. Compared to atmospheric neutrinos, the more controlled beam sample of almost purely muon neutrinos allows the reconstruction of the interaction angle in addition to the muon energy due to the known direction of the neutrino beam. The neutron multiplicity can hence be probed as a function of a larger number of kinematic variables, allowing for a more detailed test of the model predictions. This thesis will present a first measurement of the neutron multiplicity with ANNIE, featuring an analysis of a fraction of the data collected during the 2021 beam year. The findings will be compared with current model expectations based on state of the art neutrino interaction generators and hadronic scattering models.

This work will start with a summary of the current status of neutrino physics in chapter 2. The history of neutrino oscillations will be outlined briefly before both the current global picture of best fit parameters and remaining open questions are highlighted. A particular focus at the end of the chapter will be put on the status of neutrino event generators and the modeling of neutron multiplicities in neutrino interactions.

In chapter 3, the ANNIE experiment will be described in more detail. The accelerator environment, the experimental setup as well as the data taking process and triggering scheme will be presented comprehensively in preparation for the neutron multiplicity analysis following in a later chapter. In addition, ANNIE's additional role as testbed for new technologies will be highlighted by presenting the planned utilizations of Large Area Picosecond Photodetectors (LAPPDs), Gd-loaded water and Water-based Liquid Scintillators (WbLS) within ANNIE.

Inefficiencies in the various subsystems of ANNIE will have an influence on the neutron multiplicity measurement as systematic uncertainties. In this context, chapter 4 will highlight an investigation of the scintillator paddle efficiencies of the Front Muon Veto (FMV) and the Muon Range Detector (MRD) and their impact on the neutron yield characterization.

Furthermore, the development of reconstruction algorithms as well as a reasonable comparison with model predictions necessitates the presence of a simulation framework which has been validated to reproduce reality as closely as possible. The required adaptations of the simulation environment of ANNIE as well as detailed comparison of equivalent event samples were both carried out as a part of this work and will be presented in chapter 5.

Chapter 6 then highlights the preliminary neutron multiplicity measurement which has been conducted on a subset of the 2021 beam year recorded with ANNIE. After presenting some general properties of the event sample and their stability, the chapter will continue with a characterization of muon neutrino and neutron candidates within that sample. The section closes with the presentation of averaged and energy-dependent multiplicity distributions and a brief consideration of systematic uncertainties related to the measurement.

The understanding of neutron yields will also be of vital importance for future measurements like the search for the Diffuse Supernova Background (DSNB) signal. Due to higher expected neutron multiplicities in background reactions, a combination of neutron count-

ing and the application of a Convolutional Neural Network (CNN) represents a promising avenue in reducing background levels and detecting the DSNB. Chapter 7 will present the results of a simulation study that investigates the benefits of such a discrimination technique for a Super-Kamiokande-like detector geometry.

The last chapter 8 highlights another future application of neutron tagging for neutrino detectors filled with WbLS as their target material. This novel detection medium allows a simultaneous detection of both scintillation and Cherenkov light and therefore opens up the possibility to detect lower-energetic hadrons in addition to the directional reconstruction of primarily leptonic signals in conventional Cherenkov detectors. The proton-induced scintillation light can, on the one hand, be used as an additional input variable for the determination of differential cross-sections in water. On the other hand, the application of correction factors based on the amount of observed scintillation light provides the opportunity to minimize biases in the neutrino energy reconstruction, when additionally identifying inelastic interactions via neutron tagging. In this context, the benefits of a proposed upgrade of the ANNIE experimental configuration featuring a small WbLS-filled vessel inside of the water tank are investigated in the scope of a first simulation study.



# 2

## Neutrino physics

---

*“Neutrinos win the minimalist contest:  
zero charge, zero radius, and very possibly zero mass.”*

—Leon Lederman

Back when the beta decay process puzzled the entire physics community, the idea of a massless and only weakly interacting particle – later known as the neutrino – emerged as a last resort by Pauli to save the fundamental law of energy conservation in 1930 [1]. By postulating the presence of an additional particle and hence making the process a three-body decay, the observed continuous electron energy spectrum could be explained. The concept of the neutrino was soon adopted and refined in Fermi’s theory of weak decays in 1934 [9], which was able to describe the observed properties remarkably well. While the neutrino was initially believed to be undetectable due to its low interaction probability, Cowan and Reines proved this to be a misconception in the fifties when they managed to detect neutrinos from a nuclear power plant [10]. Since then, a whole field of neutrino physics has emerged, and is currently studying their properties with ever growing accuracy and larger and larger detectors.

The current chapter will provide a brief overview of neutrinos and their properties, particularly in the context of higher-energetic neutrino interactions which will be of relevance for the Accelerator Neutrino Neutron Interaction Experiment (ANNIE) [8]. Firstly, an overview of the Standard Model of particle physics is presented in section 2.1, before moving on to a more detailed description of neutrino physics in section 2.2. Within the neutrino physics section, their fundamental interaction channels will be presented alongside an extended discussion of the concept of neutrino oscillations. Furthermore, currently unknown properties of neutrinos will be highlighted at the end of the section. The chapter closes in section 2.3 with an overview of high-energetic neutrino interactions, including the relevance of neutron multiplicity measurements for interesting experimental investigations such as search for the Diffuse Supernova Background (DSNB) or proton decay.

## 2.1 THE STANDARD MODEL OF PARTICLE PHYSICS

The Standard Model is the main theoretical framework of particle physics which can be utilized to describe all elementary particles and their interactions with each other. Within the Standard Model, three main particle types exist: The so-called fermions (spin-1/2 particles) which make up ordinary matter, the gauge bosons (spin-1 particles) which are responsible for mediating the interactions between the particles, and the scalar (spin-0) Higgs boson responsible for the mass generation mechanism of fermions. While the presence of the Higgs boson has been postulated for a long time, it has only relatively recently been discovered in a joint effort of the CMS and ATLAS detectors at the LHC in 2012 [11, 12]. Since the different interaction types are typically referred to as forces, the gauge bosons are also called *force carriers* in this context. The four types of interactions are called the strong, electromagnetic, weak, and gravitational force. They are mediated by gluons, photons,  $W/Z$  bosons, and gravitons, respectively. While the Standard Model does not include gravity in its current state, it is believed that a more general theory would be able to accommodate the graviton as an additional gauge boson, with the Standard Model then being an effective version of this more general theory at lower energies [13, 14]. Depending on the intrinsic properties of the particles, only a certain subset of interactions can take place. For instance, only particles with non-zero electromagnetic charge will take part in the electromagnetic interaction. Similarly, so-called color charge is needed for participation in the strong interaction.

The Standard Model is a gauge theory with the local symmetry group [15]

$$SU(3)_C \times SU(2)_L \times U(1)_Y. \quad (2.1)$$

The group  $SU(3)_C$  represents the strong interaction, related to the color charge  $C$ . This group can be described by eight generators, corresponding to the eight massless gluons which represent the gauge bosons of the strong force. The group  $SU(2)_L$  describes interactions related to left-handed chiral fields in the context of the electroweak interaction, with the three bosons ( $W^1, W^2, W^3$ ) as generators. The last group  $U(1)_Y$  represents the hypercharge and is associated to the boson  $B$  as its generator. The  $SU(2)_L$  and  $U(1)_Y$  groups transform into the  $SU(2)_{\text{weak}}$  and  $U(1)_{\text{E\&M}}$  groups in the process of electroweak symmetry breaking. These groups are represented by the more well known gauge bosons  $W^{+/-}$ ,  $Z$ , and  $\gamma$ . The corresponding fields are related to the  $W^i$  and  $B$  boson fields via

$$W_\mu^{+/-} = \frac{1}{\sqrt{2}} (W_\mu^1 \mp iW_\mu^2) \quad (2.2)$$

$$A_\mu = B_\mu \cos \theta_W + W_\mu^3 \sin \theta_W \quad (2.3)$$

$$Z_\mu = -B_\mu \sin \theta_W + W_\mu^3 \cos \theta_W, \quad (2.4)$$

where  $A_\mu$  denotes the electromagnetic field which describes the photon. The Weinberg angle  $\theta_W$  describes the relation between the electromagnetic and weak interactions in the context of electroweak unification, with  $\sin^2 \theta_W \approx (0.23146 \pm 0.00012)$  being the mean value of different experiments and analyses [16].

There are two different kinds of fermions, leptons and quarks. The main difference between the two types is the fact that quarks carry color charge and hence take part

in the strong interaction while leptons do not. Both quarks and leptons come in three generations corresponding to different mass scales. For each generation, two leptons are present in the form of a charged heavy lepton  $l$  and a corresponding uncharged massless neutrino  $\nu$ . The charged leptons in the different generations are called the electron, the muon and the tau, also referred to as the lepton flavors. Correspondingly, the neutrinos are labeled electron-neutrino, muon-neutrino, and tau-neutrino.

Similarly to the leptons, each quark generation consists of two quarks  $u$  and  $d$  with differing charges of  $2/3e$  and  $-1/3e$ . The quarks are called *up/down* in the first generation, *charm/strange* in the second generation, and *top/bottom* in the third generation. While the quark masses in the first generation are still rather light (e.g.  $m_{\text{up}} \approx 2.2 \text{ MeV}$  [17]), the quarks in the second and third generation are significantly more heavy, with the top mass even reaching a value of  $m_{\text{top}} \approx 173 \text{ GeV}$  [17]. Due to the confinement principle, quarks only occur in combined states for which the total color vanishes. As a consequence, properties of individual quarks can only be observed in high-energy collisions of particles.

Figure 2.1 provides an overview of all currently included elementary particles in the Standard Model. Different particle types are represented in different colors, with leptons shown in green, quarks in purple, gauge bosons in red, and scalar bosons in yellow. For each particle, intrinsic properties such as their mass, charge and spin are highlighted. In addition, faint bubbles indicate which fermions are able to interact with which gauge bosons. As pointed out above, all fermions interact with the W and Z bosons, while only quarks and charged leptons are able to interact with the photon, and only quarks are affected by the strong interaction mediated by the gluons.

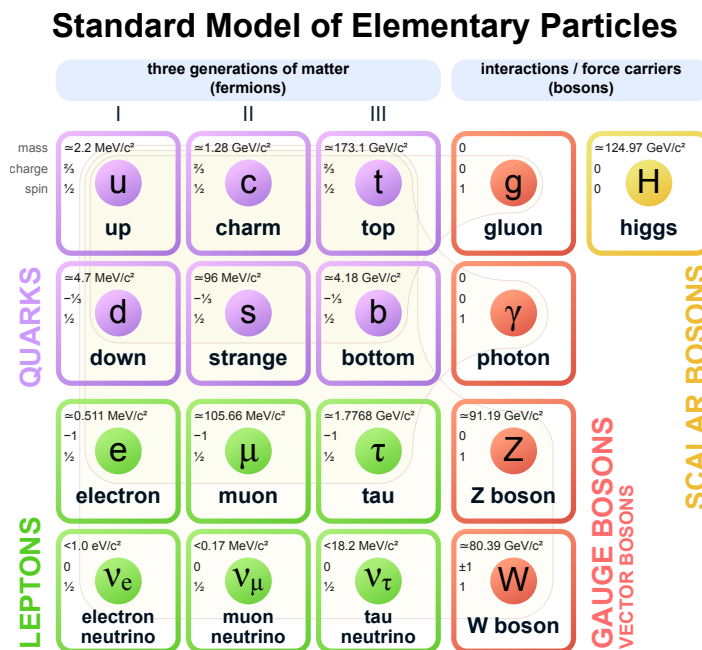


**Figure 2.1:** The constituent particles of the Standard Model, divided into quarks (purple), leptons (green), gauge bosons (red), and scalar bosons (yellow). While the gauge bosons mediate the different interactions, the scalar Higgs boson is responsible for the generation of fermion masses. Figure taken from [18].

Fermions can be grouped in doublets and singlets of the weak isospin  $I$ , with the doublets (singlets) corresponding to an isospin of  $I = 1/2$  ( $0$ ). For each of the three generations, the lepton doublets  $L_L$  combine neutrinos and charged leptons, while quark doublets  $Q_L$  combine up and down quarks:

$$L_L = \begin{pmatrix} \nu_{eL} \\ e_L \end{pmatrix} \quad Q_L = \begin{pmatrix} u_L \\ d_L \end{pmatrix} \quad (2.5)$$

In addition to the doublets, singlet states with  $I = 0$  also exist. They result in the additional states of  $e_R$ ,  $u_R$ , and  $d_R$ . Since neutrinos are assumed to be massless in the Standard Model, no singlet state  $\nu_{eR}$  is present.

The subscripts  $L$  refer to the left-handed chirality of the particles in the doublets, while the subscript  $R$  refers to right-handed chiral particles. Chirality is a property which defines the eigenvalues and eigenstates of the gamma matrix  $\gamma^5$ . The two eigenstates  $\psi_R$  and  $\psi_L$  of  $\gamma^5$  correspond to the eigenvalues  $+1$  and  $-1$ . Each spinor field  $\psi$  can be composed into a right-chiral and a left-chiral component,  $\psi = \psi_L + \psi_R$ . The chiral projection operators  $P_{L/R}$

$$P_R = \frac{1 + \gamma^5}{2} \quad P_L = \frac{1 - \gamma^5}{2} \quad (2.6)$$

are then able to single out the left-handed and right-handed chirality component of any field  $\psi$ :

$$P_R \psi = \psi_R \quad P_L \psi = \psi_L. \quad (2.7)$$

In the context of the V-A theory [19] which was developed as a response to the observed effect of parity violation in weak interactions [20], charged weak currents are only observed for left-handed chiral particles. As a consequence, charged-current weak interactions only take place for the fermion doublets and not the singlets. Neutral Current interactions mediated by the  $Z$  boson, however, do additionally couple to right-handed chiral particles to some extent. However, the coupling to right-handed particles is smaller than for left-handed chiral particles, and is directly proportional to the charge  $Q_f$  of the respective fermion. The corresponding  $Z$ -related coupling factors  $c_L$  and  $c_R$  are given by [15]

$$c_L = I_3 - Q_f \sin^2 \theta_W \quad c_R = -Q_f \sin^2 \theta_W \quad (2.8)$$

with  $Q_f$  being the charge of the fermion. As a consequence, the  $Z$  boson couples to right-handed charged leptons and quarks, but not to right-handed neutrinos.

Table 2.1 provides an overview of the isospin, charge, and hypercharge values of the lepton and quark singlet and doublet states. The hypercharge  $Y$  and the isospin  $z$ -component  $I_3$  are related via the Gell-Mann-Nishijima relation [21, 22]

$$Q = I_3 + \frac{Y}{2}. \quad (2.9)$$

As visible in the table, each singlet or doublet state is characterized by a unique hypercharge value. In addition, leptons are attributed integer charge and hypercharge values, while the quark-related equivalents are given by non-integer fractional values.

Description	Variable	I	$I_3$	Y	Q
Lepton doublet	$L_L = \begin{pmatrix} \nu_{eL} \\ e_L \end{pmatrix}$	1/2	$\begin{matrix} +1/2 \\ -1/2 \end{matrix}$	-1	$\begin{matrix} 0 \\ -1 \end{matrix}$
Lepton singlet	$e_R$	0	0	-2	-1
Quark doublet	$Q_L = \begin{pmatrix} u_L \\ d_L \end{pmatrix}$	1/2	$\begin{matrix} +1/2 \\ -1/2 \end{matrix}$	1/3	$\begin{matrix} +2/3 \\ -1/3 \end{matrix}$
Quark singlets	$\begin{matrix} u \\ d \end{matrix}$	0	0	$\begin{matrix} +4/3 \\ -2/3 \end{matrix}$	$\begin{matrix} 2/3 \\ -1/3 \end{matrix}$

**Table 2.1:** Isospin ( $I$  and  $I_3$ ), hypercharge ( $Y$ ) and charge ( $Q$ ) values for the lepton and quark singlet and doublet configurations. While the values are shown for one generation only, all displayed properties are also equally valid for the other generations.

While neutrinos are assumed to be massless in the context of the Standard Model, experimental evidence ultimately showed that neutrinos must have non-zero mass, as discussed in more detail in the subsequent section 2.2. So-called physics beyond the Standard Model (BSM) is hence required to explain neutrino masses and all associated phenomena, such as neutrino oscillations.

## 2.2 NEUTRINO PHYSICS

Neutrinos provide a unique window to the Universe due to their weakly interacting nature and near-zero masses. Since their postulation by Wolfgang Pauli as a mere placeholder to solve the kinematics of the beta decay, they have come a long way in being studied by a multitude of experiments. Many of their properties have been unveiled since then, including some surprising features like their oscillating nature during propagation, which ultimately lead to the discovery that at least two neutrino mass eigenstates must have a non-zero mass. The current and next generation of experiments are closing in on a lot of features such as more detailed measurements of the oscillation parameters, the absolute masses of neutrinos as well as the neutrino mass ordering. Another interesting problem revolves around the question whether CP violation also occurs in the leptonic sector, which would manifest itself in a slight alteration of the neutrino oscillation process. While the value of this CP-violating phase is currently still not well known, next-generation neutrino experiments like Hyper-Kamiokande [23] and DUNE [24] will be able to shed some light on the (in-)existence of leptonic CP-violation.

The current chapter will first explore the detection mechanisms for neutrinos in section 2.2.1 and in this scope present the most common target materials used in neutrino experiments. Afterwards, the solar neutrino problem is briefly discussed in section 2.2.2 to provide some context on how the process of neutrino oscillations was discovered. A basic theoretical derivation of the oscillation mechanism is then presented in section 2.2.3, with special experimental regimes presented in section 2.2.4 and deviations in the case of matter highlighted in section 2.2.5. The chapter continues with an overview of the current global status of neutrino oscillation parameters in section 2.2.6 before closing with a brief overview of current open questions in section 2.2.7. The derivations and theoretical considerations that are presented in this chapter closely follow the textbooks *Fundamentals of Neutrino Physics and Astrophysics* by Carlo Giunti and Chung W. Kim [15]

and *Modern Particle Physics* by Mark Thomson [16], with additional references being cited explicitly.

### 2.2.1 DETECTION MECHANISMS FOR NEUTRINOS

Due to their weakly interacting nature, the detection of neutrinos proves to be rather difficult, requiring large experimental apparatuses and long exposure times. In fact, only the interaction products of the neutrinos can be detected and not the neutrino itself. As a consequence, neutrino experiments are usually optimized to identify the charged lepton partners and characterize them in terms of their energy, vertex and directional information in order to gain information about the underlying neutrino event characteristics.

In order to reduce background levels, the exposure to undesired particle sources is usually kept to a minimum level. This is either achieved by placing experiments deep underground and use the overburden rock to shield the apparatus from the flux of cosmic rays, or by using stringent timing requirements on the neutrino signal such as in the case of bunched particle beams in accelerator-based neutrino experiments.

Neutrinos will interact weakly with matter in the scope of the Charged Current (CC) and Neutral Current (NC) channels via the exchange of a  $W$  or  $Z$  boson. Figure 2.2 depicts some Feynman diagrams of these scattering processes for the cases of electron and nucleon scattering. All neutrino flavors  $\alpha$  participate in the NC interactions and CC nucleon interactions, while mainly electron neutrinos participate in the CC electron scattering reaction.

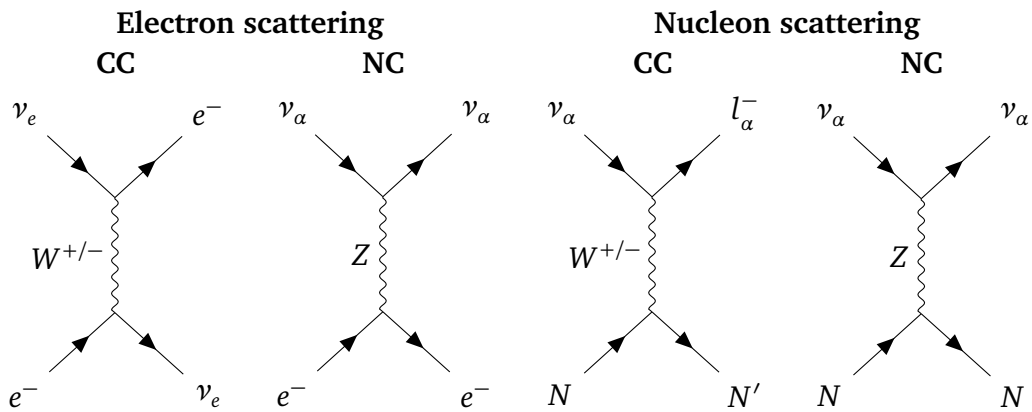


**Figure 2.2:** Feynman diagram for neutrino scattering off electrons and nucleons. Both channels are further divided into Charged Current (CC) and Neutral Current (NC) processes. The Feynman graphs were created with the tikz-feynman package [25].

Typically, the most interesting channels in the context of neutrino detectors are the CC processes, for which the resulting charged leptons can be easily identified and characterized. NC interactions, on the other hand, are more difficult to utilize in an experimental setup. Since the outgoing neutrino cannot be detected, such interactions are usually only detectable in case of neutrino-nucleus interactions for which the residual nucleus ends up in an excited state and can be identified by an associated de-excitation gamma.

In addition to scattering on electrons and nucleons, higher-energetic neutrinos will also interact with whole nuclei. In such interactions, different channels are present, namely Quasi-Elastic interactions, resonant particle production or Deep Inelastic Scattering. These processes and their characteristics will be highlighted in more detail in section 2.3 which is covering GeV-scale neutrino interactions.

When constructing a neutrino detector, the main considerations from an experimental perspective revolve around the detection efficiency, energy threshold and scalability of a particular detection medium. Furthermore, event-by-event characterization possibilities in terms of deposited energy and particle direction are extremely desirable. Due to the extremely low interaction cross sections, massive detectors and large target volumes are necessary, imposing additional constraints on the price of the respective material. Two target materials that are particularly suited in these regards and were often used in the past are liquid scintillators and water. While liquid scintillators have a larger light yield and lower energy threshold, water Cherenkov detectors can reconstruct additional directional information from each event, as opposed to isotropic light emission in the case of a liquid scintillator detector. In addition to liquid scintillator and water Cherenkov detectors, liquid argon detectors have recently also become a very prominent technique in the context of detecting neutrino interactions. Due to the time projection technique employed in such detectors, detailed images of the interacting particles can be reconstructed. They are hence very promising detectors, particularly in the context of differentiating various exclusive interaction channels in the context of beam neutrino events. The following paragraphs will briefly highlight the concepts of water Cherenkov and liquid scintillators detectors due to their relevance for ANNIE in its current and future phases.

### Water Cherenkov detectors

Electrically charged particles traversing a dielectric medium with a velocity greater than the phase velocity of photons will lead to the emission of light in form of so-called Cherenkov photons, originally discovered in 1934 [26]. The primary particle will polarize the atoms of the medium, forming a time-dependent dipole field which is emitting dipole radiation. In case of small velocities  $v < c/n$ , the dipoles are arranged symmetrically and no net dipole radiation is observed. For the relevant case of velocities  $v > c/n$ , the arrangement of dipoles is asymmetric, in turn leading to an observable radiation in form of so-called Cherenkov photons [16, 27]. Cherenkov light is emitted at a specific angle  $\theta_C$  which depends on the velocity  $\beta$  of the particle and the refractive index  $n$  of the corresponding medium. The angle is defined as

$$\theta_C = \arccos \frac{1}{n\beta}. \quad (2.10)$$

Figure 2.3 depicts the geometric aspects of the Cherenkov emission process, with the primary particle shown in red, and the Cherenkov light front shown in blue. The cone-like structure of the emitted light front is apparent. The depicted light cone describes the situation for which the particle has propagated exactly up until the rightmost edge of the cone.

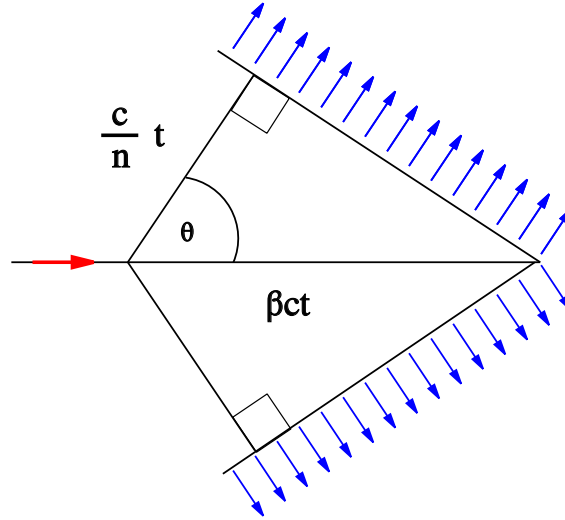


**Figure 2.3:** Principle of Cherenkov light emission. A particle crossing a medium with a velocity  $v$  greater than the phase velocity  $v_p = c/n$  will lead to the emission of Cherenkov light (blue) under an angle  $\theta$ , forming a cone of outgoing light. Figure taken from [28].

The emission spectrum of Cherenkov photons was theoretically derived by I. Frank and I. Tamm [29] in 1937 and can be described by the following formula [30]

$$\frac{d^2N}{dx d\lambda} = \frac{2\pi\alpha}{\lambda^2} \left( 1 - \frac{1}{\beta^2 \cdot n^2(\lambda)} \right). \quad (2.11)$$

The  $\lambda^{-2}$ -dependence in (2.11) indicates that most Cherenkov photons will be emitted in the ultraviolet region, invisible to the human eye and conventional single photon counting devices in neutrino experiments. However, the tail of the spectrum at higher wavelengths is visible and for instance leads to the characteristic blue glow in the water pool of nuclear reactors.

Water Cherenkov detectors in neutrino physics are usually constructed as a large water-filled target volume with arrays of photomultipliers covering the inner surfaces of the detector. Charged leptons are produced in CC interactions of neutrinos in the water volume and in turn emit Cherenkov light in the form of a cone. The intersection of the light cone with the photomultiplier-covered surface results in the detection of so-called Cherenkov rings. The exact geometry and hit time residuals of the observed rings can be used to infer the direction and interaction vertex of the charged lepton, which in turn enables to infer some properties of the initial neutrino.

Due to the minimum velocity  $v_{\min} = \frac{1}{n\beta}$ , particles need a minimum total energy  $E_{\text{tot,thr}}$  (rest mass + kinetic energy) of

$$E_{\text{tot,thr}} = mc^2 \sqrt{\frac{1}{1 - \frac{1}{n^2}}} \quad (2.12)$$

in order to emit Cherenkov radiation. Since the threshold is directly related to the mass of the particles, it is particularly hard to observe heavier hadronic particles such as protons in a water Cherenkov detector ( $E_{\text{thr}}(p) \approx 1.4 \text{ GeV}$ ), while it is considerably easier to observe

light leptons ( $E_{\text{thr}}(e) \approx 0.8 \text{ MeV}$ ,  $E_{\text{thr}}(\mu) \approx 160 \text{ MeV}$ ). As a consequence, only leptons, gammas and light charged mesons are typically observable as interaction products of neutrino interactions in Cherenkov detectors. Neutrons as uncharged particles do not emit Cherenkov light, but can be tagged by identifying gammas from the neutron capture processes on target nuclei.

### Liquid Scintillator detectors

Scintillators are materials capable of emitting light after being excited by ionizing radiation. Liquid scintillators can be sorted into the category of organic scintillators which emit light as a consequence of transitions of free valence electrons between molecular  $\pi$ -orbitals [31]. Figure 2.4 schematically depicts the different energy levels of electrons within such a liquid scintillator. Ionizing radiation can either result in an excited singlet ( $S_1$ ,  $S_2$ ) or triplet ( $T_1$ ,  $T_2$ ) state with successive relaxation into the ground state  $S_0$  via fluorescence (phosphorescence) in the case of excited singlet (triplet) states. While fluorescence is a rather fast process that occurs on the timescale of nanoseconds, phosphorescence can be delayed by a time frame of milliseconds or longer [31].

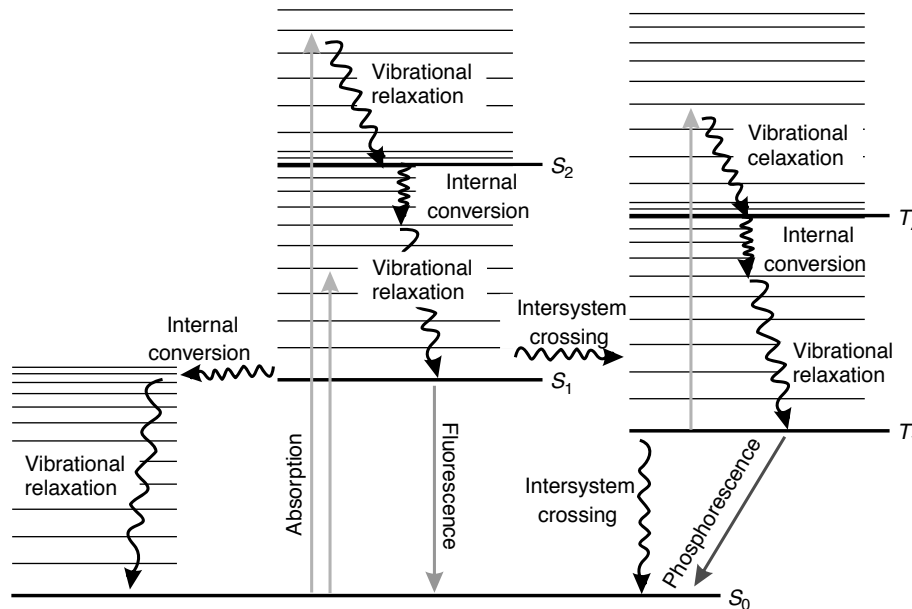


**Figure 2.4:** Schematic depiction of excitation levels of a typical organic scintillator. Fluorescence describes the de-excitation process from an excited singlet state ( $S_1$ ) to the ground state ( $S_0$ ) and happens on the order of nanoseconds, while phosphorescence describes the transition from an excited triplet state ( $T_1$ ) and rather happens on time scales of milliseconds or longer. Figure taken from [32].

In contrast to water Cherenkov detectors, liquid scintillator experiments have a much lower energy threshold and are sensitive to sub-MeV neutrino energies, as demonstrated by Borexino with an effective threshold of 50 keV in its solar neutrino analysis [33]. The light output per unit length of scintillating materials is given by the empirical Birks' formula [34]

$$\frac{dL}{dx} = \frac{S \cdot \frac{dE}{dx}}{1 + kB \frac{dE}{dx}} \quad (2.13)$$

which includes the absolute scintillation yield  $S$ , the Birks' constant  $kB$  and the energy loss per unit length  $\frac{dE}{dx}$ . The dependence on the stopping power  $\frac{dE}{dx}$  results in so-called

quenching effects for ions and heavier particles with low energy loss values such that the observed light level is significantly reduced for such particles. While lighter particles will observe scintillation yields of  $L_{\text{light}} = S \cdot E$ , ion-like particles will instead create a reduced amount of  $L_{\text{ion}} = \frac{S \cdot E}{k_B}$ .

The typical emission wavelengths of organic scintillators are located in the ultraviolet region of the emission spectrum for which conventional photomultiplier tubes are not sensitive. The main scintillator component is therefore often mixed with a so-called fluor that serves as a wavelength-shifter and increases the wavelengths of the photons in the scope of absorption and re-emission processes. As a consequence, the scintillation time emission profile usually needs to be described as a combination of multiple exponentials with different weights  $w_i$  and decay times  $\tau_i$ :

$$N(t) = \sum_{i=1}^N w_i \cdot \exp(-t/\tau_i). \quad (2.14)$$

In contrast to Cherenkov light, the scintillation light emission does not happen instantaneously but is instead characterized by a small delay on the order of nanoseconds. Target materials that feature both scintillation and Cherenkov light emission can hence potentially separate the two contributions based on the relative timing of photon hits on the photodetectors.

### 2.2.2 A HISTORIC PERSPECTIVE: THE SOLAR NEUTRINO PROBLEM

Whilst neutrinos were originally deemed undetectable at the time of their postulation by Wolfgang Pauli [1, 35], he was later proven wrong when Cowan and Reines managed to record neutrino-induced signals with two separate experimental setups near reactor complexes in the years 1953 to 1956 [10]. The key ingredient for successfully detecting neutrinos consisted of using rather large detector volumes to compensate for the extremely low cross-sections of neutrino interactions. In their main experiment located in close proximity to the Savannah Power Plant reactor core, their neutrino detector therefore consisted of two Cadmium-loaded water tanks with a total capacity of roughly 200 liters as the target material. The experimental design of the detector featured a sandwich structure with three scintillator layers in between the main water tanks which were used to detect the gammas produced in the interactions. The reactor antineutrinos were detected via the Inverse Beta Decay process, resulting in a positron and neutron as final state detectable particles. Both the annihilation gammas and neutron capture gammas were produced in the water volume and then detected in the scintillator layers, with background reduction achieved via the coincidence requirement of a prompt positron and a delayed neutron signal.

Historically, the next promising neutrino signal after the first detection of neutrinos was the search for solar neutrinos due to their large predicted flux of  $\phi_{\text{solar}} \approx 6 \cdot 10^{10} \frac{1}{\text{cm}^2\text{s}}$  and their potential insight into verifying the predictions of the Standard Solar Model (SSM), particularly with respect to the fusion processes happening in stars. The SSM was initially developed by John Bahcall in 1962 and aims to provide a coherent model which predicts the properties of neutrinos emitted in the fusion processes of the Sun [36]. According

to the theoretical considerations in the SSM, two main hydrogen fusion processes are present in stars: the *pp*-chain and the *CNO*-cycle. Both of these chains of reactions convert hydrogen into helium via the overall reaction



While the *pp*-chain directly combines protons to form helium over multiple steps, the *CNO*-cycle requires the presence of carbon, nitrogen and oxygen nuclei as catalysts to form helium. As a consequence, the *CNO* chain will dominate the fusion processes for larger stars while the *pp*-cycle will be the main process for smaller stars. In the case of our sun, the *CNO* fusion is expected to contribute only a fraction of  $\approx 1\%$  of the total energy output [37].

Neutrinos are emitted at different times within the fusion process, and will have different energetic profiles depending on their exact creation process. For instance, neutrinos associated with the  ${}^7\text{Be}$ -reaction



will have two separate discrete energy values due to the nature of the electron capture process (0.39 MeV and 0.86 MeV), while neutrinos from the initial *pp*-fusion reaction



with three final state particles will be produced over a large range of energies (0 - 0.42 MeV). Figure 2.5 provides an overview of the different reactions within the *pp*-chain of the Sun, alongside the predicted fluxes and the relevant neutrino species produced along the way. Most of the flux is provided by *pp*-neutrinos, followed by  ${}^7\text{Be}$ -neutrinos, *pep*-neutrinos and  ${}^8\text{B}$ -neutrinos. The energy spectra of the different branches of the *pp*-chain were extensively measured by the Borexino collaboration [38], which also provided the first evidence for the existence of the *CNO* cycle in our sun [39].

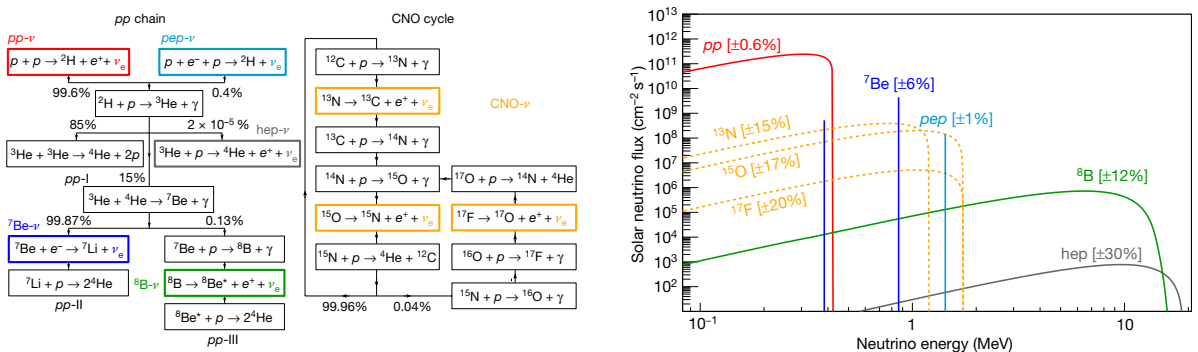


**Figure 2.5:** Left: The different processes making up the *pp*- and *CNO*-fusion cycles of the Sun. Reactions that are associated with the emission of neutrinos are highlighted in colored boxes, with the conventional solar neutrino naming schemes put next to them. Right: Flux spectra of the different solar neutrino species. Figures taken from [38], with fluxes originally obtained from [40].

Solar neutrinos were first successfully discovered in the radiochemical Homestake experiment [41], which utilized the neutrino capture process on chlorine to detect neutrinos above the reaction threshold of 0.814 MeV (*i.e.* primarily  ${}^7\text{Be}$ -neutrinos, *pep*-neutrinos, and  ${}^8\text{B}$ -neutrinos) via the process



The argon atoms produced in the neutrino capture process were extracted from the tank filled with 615 tons of tetrachloroethylene ( $\text{C}_2\text{Cl}_4$ ) via chemical methods and subsequently counted by identifying Auger electrons from electron capture processes on the Argon atoms. The solar neutrino rate in Homestake was determined to be  $R_{\text{Homestake}} = (2.56 \pm 0.16 \pm 0.16)$  SNU [42], with one *Solar Neutrino Unit* being defined as  $10^{-36}$  events/atom/s. Compared to the theoretical value of  $R_{\text{theo,Cl}} = (7.6_{-1.1}^{+1.3})$  SNU as predicted by a common SSM by Bahcall *et. al* [43], the experimental value was hence smaller by a factor of roughly 3.

Further experimental efforts concentrated on the verification of the solar neutrino deficit measured by the Homestake experiment. In order to be sensitive to a larger range of solar neutrino species, multiple experiments were constructed with Gallium as target material, detecting neutrinos via the reaction



Due to the much smaller energy threshold of  $E_{\text{thr,Ga}} = 0.233$  MeV, those experiments were able to detect contributions of neutrinos from all reactions of the *pp*-chain. The GALLium EXperiment (GALLEX [44], later renamed Gallium Neutrino Observatory (GNO) [45]) was a detector at the Laboratori Nazionali del Gran Sasso (LNGS) underground laboratory which contained 101 tons of gallium chloride solution as its target material. GALLEX/GNO performed its solar neutrino measurement from 1991 to 2003 and measured a solar neutrino rate of [46]

$$R_{\text{GALLEX/GNO}} = (69.3 \pm 4.1 \pm 3.6) \text{ SNU}, \quad (2.20)$$

which was smaller than the predicted rate  $R_{\text{theo,Ga}} = (127_{-7}^{+9})$  SNU by roughly a factor of two. An independent Gallium-based neutrino observatory called *Soviet-American Gallium Experiment* (SAGE) [47] positioned at the Baksan neutrino observatory in Russia confirmed the results of GALLEX/GNO by measuring a rate of [48]

$$R_{\text{SAGE}} = (65.4_{-3.0}^{+3.1}(\text{stat})_{-2.8}^{+2.6}(\text{syst})) \text{ SNU} \quad (2.21)$$

in their overall measurement interval of 1990 to 2007.

All radiochemical solar neutrino experiments (independently of using chlorine or gallium as target material) hence observed a deficit of solar neutrinos with respect to the predictions of the solar models. The water Cherenkov detectors *Kamioka Nucleon Decay Experiment* (Kamiokande) [49] and its successor Super-Kamiokande [50] made equivalent observations for the  ${}^8\text{B}$ -neutrino flux, with initial results of

$$\phi_{\text{sB,Kam}} = (2.80 \pm 0.38) \cdot 10^6 \text{ cm}^{-2}\text{s}^{-1} \quad \phi_{\text{sB,SK-I}} = (2.35 \pm 0.08) \cdot 10^6 \text{ cm}^{-2}\text{s}^{-1} \quad (2.22)$$

for Kamiokande (1987 - 1995) [51] and the first phase of Super-K (1996-2001) [52]. Compared to the prediction of the boron-neutrino flux

$$\phi_{\text{B,theo}} = 5.05 \left(1.00^{+0.20}_{-0.16}\right) \cdot 10^6 \text{ cm}^{-2}\text{s}^{-1} \quad (2.23)$$

based on the calculations in the solar model by Bahcall *et. al* considered earlier [43], the measured rate showed a deficit of a factor of 2 or more. All experimentally collected data hence lead to the conclusion that a deficit of solar neutrinos was observed, commonly referred to as the *solar neutrino problem*.

Initial theories about the lack of neutrinos suspected flaws in the modeling of the interior properties in stars, *i.e.* problems with the solar models themselves (e.g. [53]). A different theory emerged roughly at the same time which hypothesized that the solar model was actually correct and the lack of electron neutrinos on Earth was due to conversion processes which transformed the flavor of neutrinos on their way from the Sun to Earth [54, 55, 56]. The deficit in observed solar neutrinos would in this case be explained by missing sensitivity of the experiments to muon and tau flavored neutrinos.

The Sudbury Neutrino Observatory (SNO) [57] tested the latter hypothesis by constructing a water Cherenkov detector out of heavy water (D<sub>2</sub>O) and measuring different channels of neutrino interactions within their detector [58]:

$$\text{CC : } \quad \nu_e + d \rightarrow p + p + e^- \quad (2.24)$$

$$\text{NC : } \quad \nu_\alpha + d \rightarrow p + n + \nu_\alpha \quad (2.25)$$

$$\text{ES : } \quad \nu_\alpha + e^- \rightarrow \nu_\alpha + e^- \quad (2.26)$$

Both the Neutral Current (NC) and Elastic Scattering (ES) processes are sensitive to all neutrino flavors ( $e, \mu, \tau$ ) and therefore enable the verification of the neutrino conversion hypothesis. Events associated to the NC reaction channel were identified by looking for neutron capture signals in the heavy water, leading to the emission of a 6.25 MeV gamma-ray particle. In order to increase the sensitivity and detection efficiency of such neutron capture events, a dedicated *salt phase* of the experiment was initiated. Within this phase, NaCl was dissolved in the detector to improve the neutron capture cross-section from 0.5 mb to 44 b and additionally increase the total neutron capture gamma ray energy to 8.6 MeV. A significantly larger flux was observed for the NC reaction channel compared to the CC channel [58]:

$$\phi_{\text{CC,SNO}} = \left(1.68 \pm 0.06^{+0.08}_{-0.09}\right) \cdot 10^6 \text{ cm}^{-2}\text{s}^{-1} \quad (2.27)$$

$$\phi_{\text{NC,SNO}} = \left(4.94 \pm 0.21^{+0.38}_{-0.34}\right) \cdot 10^6 \text{ cm}^{-2}\text{s}^{-1}, \quad (2.28)$$

providing unambiguous evidence that the overall predicted solar neutrino flux is indeed correct (as shown by the measured NC solar neutrino rate), but arrives in a mixed form of electron, muon and tau neutrinos at Earth. The observation of this neutrino conversion mechanism was further confirmed by the Super-Kamiokande experiment in an independent measurement of atmospheric neutrinos. The comparison of upward and downward going atmospheric neutrinos revealed that less upward-going neutrinos were detected in contrast

to the expected uniform distribution [59]. This observation was in agreement with the so-called neutrino oscillation mechanism which would result in a transformation of muon neutrinos to tau neutrinos over longer propagation lengths such as the path of upward-going neutrinos through the Earth.

Both the neutrino flavor transformations in the scope of solar neutrinos and in the case of atmospheric neutrinos require neutrinos to have a non-zero mass, contrary to the original expectations within the Standard Model. The following section will highlight how these neutrino masses lead to oscillatory flavor conversion processes in case the flavor eigenstates are not the mass eigenstates via the neutrino oscillation mechanism. In addition, resonant flavor conversion processes in matter with varying density will be highlighted separately.

### 2.2.3 NEUTRINO OSCILLATIONS

The experimental detection of neutrino flavor conversions in the context of the solar neutrino problem and the atmospheric neutrino data necessitated that the flavor eigenstates of neutrinos are not identical to their mass eigenstates. The neutrino mass eigenstates ( $\nu_1$ ,  $\nu_2$ , and  $\nu_3$ ) represent the stationary eigenstates of the Hamiltonian and are related to the flavor eigenstates ( $\nu_e$ ,  $\nu_\mu$ , and  $\nu_\tau$ ) via the unitary *Pontecorvo-Maki-Nakagawa-Sakata* (PMNS) matrix  $U_{\text{PMNS}}$ :

$$\begin{pmatrix} \nu_e \\ \nu_\mu \\ \nu_\tau \end{pmatrix} = \underbrace{\begin{pmatrix} U_{e1} & U_{e2} & U_{e3} \\ U_{\mu1} & U_{\mu2} & U_{\mu3} \\ U_{\tau1} & U_{\tau2} & U_{\tau3} \end{pmatrix}}_{U_{\text{PMNS}}} \cdot \begin{pmatrix} \nu_1 \\ \nu_2 \\ \nu_3 \end{pmatrix} \quad (2.29)$$

While neutrinos are produced and detected as a specific flavor eigenstate, their subsequent behavior during propagation is more easily described by the time evolution of the different mass eigenstates. If one considers a neutrino of flavor  $\alpha$  (with  $\alpha \in \{e, \mu, \tau\}$ ), the state at production  $|\Psi(\vec{x}, t = 0)\rangle$  can be described as a superposition of the three mass eigenstates:

$$|\Psi(\vec{x}, t = 0)\rangle = |\nu_\alpha\rangle = U_{\alpha 1}^* |\nu_1\rangle + U_{\alpha 2}^* |\nu_2\rangle + U_{\alpha 3}^* |\nu_3\rangle = \sum_{i=1}^3 U_{\alpha i}^* |\nu_i\rangle \quad (2.30)$$

In order to derive the time dependence of the considered particle state  $|\Psi\rangle$ , the dependencies of the single involved mass eigenstates need to be understood. The time evolution of each mass eigenstate can be described by the time evolution operator  $U(t)$ :

$$|\nu_i(t)\rangle = U(t) |\nu_i\rangle = e^{-iE_i t} |\nu_i\rangle, \quad (2.31)$$

The composition of the state  $\Psi$  at a certain time  $t$  is hence given by

$$|\Psi(\vec{x}, t)\rangle = \sum_{i=1}^3 U_{\alpha i}^* e^{-iE_i t} |\nu_i\rangle \quad (2.32)$$

In case the various mass eigenstates have differing non-zero masses, they will propagate dissimilarly and the flavor composition of the particle state  $|\Psi\rangle$  will change with time. This results in a non-zero probability that a neutrino which was created with a specific flavor  $\alpha$  is subsequently detected as a different flavor  $\beta$  after propagation. The probability for the conversion from flavor  $\alpha$  to  $\beta$  is given by

$$P(\nu_\alpha \rightarrow \nu_\beta) = \left| \langle \nu_\beta | \Psi(\vec{x}, t) \rangle \right|^2 = \left| \langle \nu_\beta | \sum_{i=1}^3 U_{\alpha i}^* | \nu_i \rangle \right|^2 \quad (2.33)$$

The expression can most easily be evaluated by decomposing the mass eigenstates  $\nu_i$  into superpositions of flavor eigenstates,  $\nu_i = \sum_{\alpha'} U_{\alpha' i} \nu_{\alpha'}$ . Inserting into (2.33) yields

$$P(\nu_\alpha \rightarrow \nu_\beta) = \left| \langle \nu_\beta | \sum_i U_{\alpha i}^* e^{-ip_i \cdot x} \sum_{\alpha'} U_{\alpha' i} | \nu_{\alpha'} \rangle \right|^2 = \left| \sum_i U_{\alpha i}^* e^{-ip_i \cdot x} \sum_{\alpha'} U_{\alpha' i} \underbrace{\langle \nu_\beta | \nu_{\alpha'} \rangle}_{\delta_{\alpha' \beta}} \right|^2 \quad (2.34)$$

This eventually results in the following formula:

$$P(\nu_\alpha \rightarrow \nu_\beta) = \left| \sum_{i=1}^3 U_{\alpha i}^* U_{\beta i} e^{-iE_i t} \right|^2 = \sum_{i,j=1}^3 U_{\alpha i}^* U_{\beta i} U_{\alpha j} U_{\beta j}^* e^{-(E_i - E_j)t} \quad (2.35)$$

The phase difference  $\Delta\phi_{ij} = (E_i - E_j)t$  appearing in the exponential can be simplified by assuming that the three-vector momenta of the mass eigenstates  $i$  and  $j$  are identical due to the ultrarelativistic nature of neutrinos, such that  $|\vec{p}_i| \approx |\vec{p}_j| \approx E$ . In this case, the energies  $E_i$  of a single mass state can be approximated as

$$E_i = \sqrt{|\vec{p}_i|^2 + m_i^2} = |\vec{p}_i| \cdot \sqrt{1 + \frac{m_i^2}{p_i^2}} \stackrel{p_i \approx E}{\approx} E \cdot \sqrt{1 + \frac{m_i^2}{E^2}} \stackrel{\text{Taylor}}{\approx} E \cdot \left(1 + \frac{m_i^2}{2E^2}\right). \quad (2.36)$$

The phase difference  $\Delta\phi_{ij}$  is then given by

$$\Delta\phi_{ij} = (E_i - E_j) \cdot t = \left( \frac{m_i^2 - m_j^2}{2E} \right) \cdot t = \frac{\Delta m_{ij}^2}{2E} \quad (2.37)$$

The oscillation probability  $P(\nu_\alpha \rightarrow \nu_\beta)$  then becomes (with  $t = L$ ):

$$P(\nu_\alpha \rightarrow \nu_\beta) = \sum_{i,j=1}^3 U_{\alpha i}^* U_{\beta i} U_{\alpha j} U_{\beta j}^* \exp\left(-\frac{\Delta m_{ij}^2}{2E} L\right) \quad (2.38)$$

Equation (2.35) can also be parameterized in terms of its real and imaginary components as

$$P(\nu_\alpha \rightarrow \nu_\beta) = \delta_{\alpha\beta} - 4 \sum_{i>j} \text{Re}\left(U_{\alpha i}^* U_{\beta i} U_{\alpha j} U_{\beta j}^*\right) \sin^2\left(\frac{\Delta m_{ij}^2 L}{4E}\right) + 2 \sum_{i>j} \text{Im}\left(U_{\alpha i}^* U_{\beta i} U_{\alpha j} U_{\beta j}^*\right) \sin\left(\frac{\Delta m_{ij}^2 L}{2E}\right) \quad (2.39)$$

The PMNS matrix is commonly defined in terms of three real-numbered angles ( $\theta_{12}$ ,  $\theta_{13}$ ,  $\theta_{23}$ ) and one complex phase  $\delta_{\text{CP}}$ . Based on the dimensionality of the matrix, a total of six complex phases would be expected for a general description of a unitary matrix. However, five of these phases can be absorbed into the phases of the interacting particles and are therefore not relevant from a physics perspective. A useful parameterization is the following three-matrix combination:

$$U_{\text{PMNS}} = \underbrace{\begin{pmatrix} 1 & 0 & 0 \\ 0 & c_{23} & s_{23} \\ 0 & -s_{23} & c_{23} \end{pmatrix}}_{\text{atmospheric}} \cdot \underbrace{\begin{pmatrix} c_{13} & 0 & s_{13}e^{-i\delta} \\ 0 & 1 & 0 \\ -s_{13}e^{i\delta} & 0 & c_{13} \end{pmatrix}}_{\text{reactor}} \cdot \underbrace{\begin{pmatrix} c_{12} & s_{12} & 0 \\ -s_{12} & c_{12} & 0 \\ 0 & 0 & 1 \end{pmatrix}}_{\text{solar}}, \quad (2.40)$$

with the abbreviations  $s_{ij} = \sin(\theta_{ij})$  and  $c_{ij} = \cos(\theta_{ij})$ . The separation in three distinct matrices highlights the experimental regimes in which the different angles are dominant based on typical length scales and energies. For instance, oscillations of solar neutrinos are mainly governed by the mixing angle  $\theta_{12}$ , while reactor neutrino oscillations are described by  $\theta_{13}$  and the propagation of atmospheric neutrinos is parameterized by  $\theta_{23}$ .

In case neutrinos are Majorana particles, meaning they are their own anti-particle, two additional phases  $\alpha_{21}$  and  $\alpha_{31}$  are needed to characterize the leptonic mixing:

$$U_{\text{PMNS, Majorana}} = U_{\text{PMNS}} \cdot \begin{pmatrix} 1 & 0 & 0 \\ 0 & \frac{\alpha_{21}}{2} & 0 \\ 0 & 0 & \frac{\alpha_{31}}{2} \end{pmatrix} \quad (2.41)$$

The quartic product  $U_{\alpha i}^* U_{\beta i} U_{\alpha j} U_{\beta j}^*$  remains invariant under transformations of the form

$$U_{\alpha i} \rightarrow e^{i\Psi_\alpha} \cdot U_{\alpha i} \cdot e^{i\phi_i}. \quad (2.42)$$

Since the additional Majorana phase correspond to such a transformation to the unitary mixing matrix, the Majorana angles do not influence the quartic product and hence do not alter the oscillation probabilities. They can therefore not be detected in neutrino oscillation experiments, but must be probed in other experimental settings such as neutrinoless double beta decay searches.

## 2.2.4 DIFFERENT REGIMES OF NEUTRINO OSCILLATIONS

The dependence of the oscillation probabilities on the ratio  $L/E$  allows to probe specific parameters of the PMNS-matrix with experiments that cover different regions of the  $L/E$  parameter space. Various limits of the formula can be derived for different regimes, with the most important applications being the simplified assumption of 2-flavor oscillations, and the oscillation probabilities in the case of reactor neutrinos and long-baseline neutrino experiments. These specialized cases will be presented briefly in the current subsection alongside some visual representations of the oscillation in the various scenarios.

### Two-flavor case

In cases where the oscillation behavior is dominated by one of the angles, it is sometimes sufficient to only consider two neutrino flavors for the description of the conversion and survival probabilities. In such a case, the PMNS-matrix simplifies and takes on the following form with one real-numbered parameter  $\theta$  and no imaginary phase:

$$\begin{pmatrix} \nu_\alpha \\ \nu_\beta \end{pmatrix} = \begin{pmatrix} U_{\alpha 1} & U_{\alpha 2} \\ U_{\beta 1} & U_{\beta 2} \end{pmatrix} \cdot \begin{pmatrix} \nu_1 \\ \nu_2 \end{pmatrix} = \begin{pmatrix} \cos(\theta) & \sin(\theta) \\ -\sin(\theta) & \cos(\theta) \end{pmatrix} \cdot \begin{pmatrix} \nu_1 \\ \nu_2 \end{pmatrix} \quad (2.43)$$

The neutrino conversion probability  $P(\nu_\alpha \rightarrow \nu_\beta)$  introduced in (2.38) then becomes

$$P(\nu_\alpha \rightarrow \nu_\beta) = \sin^2(2\theta) \sin^2\left(\frac{\Delta m_{12}^2 L}{4E}\right). \quad (2.44)$$

Equivalently, the survival probability for  $\nu_\alpha$  is given by

$$P(\nu_\alpha \rightarrow \nu_\alpha) = 1 - \sin^2(2\theta) \sin^2\left(\frac{\Delta m_{12}^2 L}{4E}\right). \quad (2.45)$$

For frequently used units of meters and MeV, the formula becomes

$$P(\nu_\alpha \rightarrow \nu_\alpha) = 1 - \sin^2(2\theta) \sin^2\left(1.27 \frac{\Delta m_{12}^2 [\text{eV}^2] L [\text{m}]}{E [\text{MeV}]}\right). \quad (2.46)$$

The oscillation length  $L_{\text{osc}}$  is an interesting property with regards to experimental efforts since it defines the length scale of maximal disappearance for a specific set of mixing parameters. It is realized if the argument of the second sine becomes  $\pi$ :

$$L_{\text{osc}} = \frac{\pi \cdot E [\text{MeV}]}{1.27 \cdot \Delta m_{12}^2 [\text{eV}^2] \cdot L [\text{m}]} = \frac{2.47 \cdot E [\text{MeV}]}{\Delta m_{12}^2 [\text{eV}^2] \cdot L [\text{m}]}. \quad (2.47)$$

### Typical baselines and sensitivities

The oscillation probability for the two-flavor case given in (2.46) highlights the fact that experiments will be very sensitive to regions of the parameter space for which the argument of the sine is roughly equal to 1. In such cases, the effect of oscillations is maximal and the corresponding mixing parameters can be detected with a high significance. In the case that the argument of the sine is very small ( $\Delta m^2 L/E \ll 1$ ), no oscillations will be detectable. Similarly, for the case of very large arguments ( $\Delta m^2 L/E \gg 1$ ), the oscillation pattern will be washed out and only an averaged effect will be observable, as explained in more detail in the subsequent paragraph. Depending on the energies and typical baselines for a particular neutrino species, the  $L/E$  combinations result in a specific sensitive region of the  $\Delta m^2$  parameter. In this context, table 2.2 summarizes the squared mass difference sensitivities of solar, atmospheric, reactor, and accelerator neutrino experiments.

Due to the extremely long baseline between the Sun and Earth, solar vacuum oscillations are sensitive to extremely small  $\Delta m^2$ -values on the order of  $10^{-10} \text{ eV}^2$ . However, as will

be pointed out in the later section 2.2.5, the solar neutrino detection probabilities are primarily influenced by the matter-related MSW effect in addition to averaged vacuum oscillations by a larger squared mass difference.

Atmospheric neutrinos span a wide range of energies and baselines, resulting in a fairly spread out range of accessible mass difference values in the range  $10^{-4} \text{ eV}^2 < \Delta m^2 < 10^{-1} \text{ eV}^2$ .

Both the baselines of reactor and accelerator neutrino experiments can be optimized in order to access different ranges of  $\Delta m^2$ : The different scenarios are called Short Baseline (SBL) and Long Baseline (LBL) in both instances. In the case of reactor neutrino experiments, short baselines refer to order of kilometers and are sensitive to the angle  $\theta_{13}$  and the squared mass difference  $\Delta m_{13}^2$ , while long baselines correspond to length scales of tens or hundreds of kilometers and are useful for measurements of  $\theta_{12}$  and  $\Delta m_{12}$ . Regarding accelerator neutrino experiments, short baselines refer to distances of hundreds of meters and are only sensitive to very heavy neutrino mass differences. As a consequence, those experiments are currently primarily used to search for sterile neutrino oscillations on the eV-scale. LBL accelerator experiments, on the other hand, are sensitive to smaller  $\Delta m^2$  values in the range  $10^{-3} \text{ eV}^2 < \Delta m^2 < 10^{-2} \text{ eV}^2$ . In addition, they are also useful in the context of the CP-phase  $\delta_{\text{CP}}$ , which will be highlighted in some more detail in the corresponding paragraph.

Neutrino type	Typical baseline (m)	Energy range (MeV)	$\Delta m^2$ sensitivity ( $\text{eV}^2$ )
Solar	$10^{10}$	1	$10^{-10}$
Atmospheric	$10^4 - 10^7$	$10^2 - 10^5$	$10^{-1} - 10^{-4}$
Reactor (SBL)	$10^2 - 10^3$	1	$10^{-2} - 10^{-3}$
Reactor (LBL)	$10^4 - 10^5$	1	$10^{-4} - 10^{-5}$
Accelerator (SBL)	$10^2$	$10^3 - 10^4$	$> 0.1$
Accelerator (LBL)	$10^5 - 10^6$	$10^3 - 10^4$	$10^{-2} - 10^{-3}$

**Table 2.2:** Typical baselines, energy ranges, and  $\Delta m^2$  sensitivity regions of different neutrino species. Both reactor and accelerator neutrino experiments are divided into Short Baseline and Long Baseline variants. Table taken from reference [17].

### Averaged neutrino oscillations

The measurement of neutrino oscillation probabilities would ideally be performed for an exact  $L/E$  value in order to get a highly resolved comparison with respect to the theoretical expectations. However, in reality experiments are limited by a finite resolution both in the energy ( $\sigma_E$ ) and the distance ( $\sigma_L$ ). These individual uncertainties propagate to a global uncertainty on  $L/E$ , which in turn results in experiments observing a certain region of  $L/E$ -values and as a consequence smearing out the detected oscillation probability. Due to this effect, certain oscillation effects can only be observed in an averaged manner.

If the  $L/E$  uncertainty  $\sigma_{L/E}$  is assumed to be of Gaussian nature with a mean value of  $\langle L/E \rangle$ , the  $\phi\left(\frac{L}{E}\right)$  distribution can be written as

$$\phi\left(\frac{L}{E}\right) = \frac{1}{\sqrt{2\pi\sigma_{L/E}^2}} \exp\left(-\frac{(L/E - \langle L/E \rangle)^2}{2\sigma_{L/E}^2}\right). \quad (2.48)$$

The detected oscillation probability then represents some integrated region of the  $L/E$  parameter space instead of a discrete value:

$$P(\nu_\alpha \rightarrow \nu_\beta) = \frac{1}{2} \sin^2 2\theta \left( 1 - \int \cos\left(\frac{\Delta m^2 L}{2E}\right) \phi\left(\frac{L}{E}\right) d\frac{L}{E} \right). \quad (2.49)$$

For the case of the Gaussian uncertainty presented in (2.48), the appearance probability becomes [15]

$$P(\nu_\alpha \rightarrow \nu_\beta) = \frac{1}{2} \sin^2 2\theta \left[ 1 - \cos\left(\frac{\Delta m^2}{2} \left\langle \frac{L}{E} \right\rangle\right) \exp\left(-\frac{1}{2} \left(\frac{\Delta m^2}{2} \sigma_{L/E}\right)^2\right) \right] \quad (2.50)$$

Figure 2.6 presents the implications of this smearing effect on the detected oscillation probabilities, assuming a detector resolution of  $\sigma_{E/L} = 0.2 \langle E/L \rangle$  and maximum mixing ( $\sin^2(2\theta) = 1$ ). While the first oscillation peak is only a little suppressed, especially the oscillation patterns in the parameter region

$$\left\langle \frac{L}{E} \right\rangle \Delta m^2 > 20 \text{ m} \cdot \text{eV}^2/\text{MeV}$$

cannot be resolved anymore. In this region, an averaged appearance probability of  $\frac{1}{2} \sin^2 2\theta = \frac{1}{2}$  is observed independently of the  $L/E$ -value. Due to these detector resolution effects, it is customary for experiments to choose distance/energy combinations that result in a positioning within the first oscillation peak, for which the oscillation effects can still be resolved very well and are not averaged out.

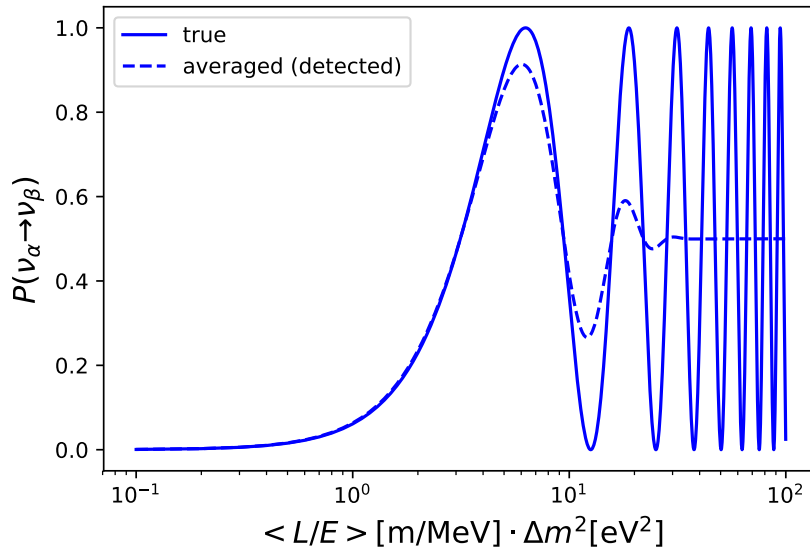


**Figure 2.6:** The true (solid line) and averaged (dashed line) 2-flavor appearance oscillation pattern for a mixing angle of  $\sin^2(2\theta) = 1$ . The detection resolution is assumed to be  $\sigma_{E/L} = 0.2 \langle E/L \rangle$ .

### Reactor neutrino regime

For reactor neutrinos, the antineutrino survival probability is given by [16]

$$P(\bar{\nu}_e \rightarrow \bar{\nu}_e) = 1 - \cos^4(\theta_{13}) \sin^2(2\theta_{12}) \sin^2\left(\frac{\Delta m_{21}^2 L}{4E}\right) - \sin^2(2\theta_{13}) \sin^2\left(\frac{\Delta m_{32}^2 L}{4E}\right). \quad (2.51)$$

The associated oscillation curve is shown in figure 2.7 and features both a low frequency and a higher frequency component. The parameters  $\theta_{13}$  and  $\Delta m_{31}^2$  are responsible for the smaller and faster oscillation pattern occurring on distance scales of  $\mathcal{O}(1 \text{ km})$ . This smaller oscillation curve is embedded into a larger mixing pattern induced by  $\theta_{12}$  and  $\Delta m_{12}^2$  which is characterized by a wavelength of  $\lambda_{12} = \mathcal{O}(100 \text{ km})$  and has a much larger amplitude.

Depending on the parameters of interest, different baselines need to be considered. The rather small mixing angle  $\theta_{13}$  is most accessible at medium baselines on the kilometer scale and was precisely characterized by the Daya Bay [60], RENO [61] and Double Chooz [62] experiments, all situated at baselines of 1-2 km. The parameters related to the larger-scale oscillation pattern ( $\theta_{12}$ ,  $\Delta m_{12}^2$ ) can most easily be probed on longer scales on the order of hundreds of kilometers. They were e.g. investigated by the KamLAND experiment [63], situated roughly 180 km away from a nuclear power plant. The right side of figure 2.7 highlights the sensitivities of the various experiments with their different baselines to different aspects of the oscillation patterns. KamLAND is able to resolve the multiple oscillation peaks in its sensitive region by making use of the energy information of individual neutrino events. Similarly, the short-baseline reactor experiments also utilize the energetic information for a more accurate analysis.

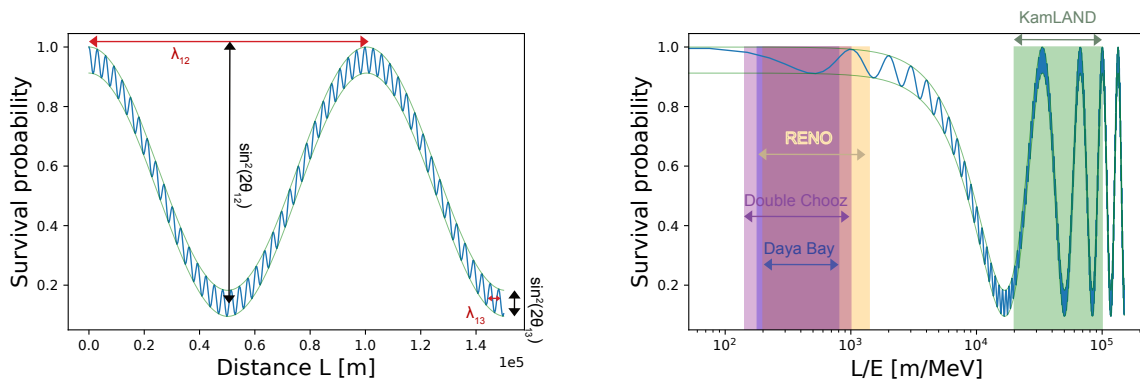


**Figure 2.7:** **Left:** Survival probability of reactor antineutrinos with an energy of  $E_{\bar{\nu}_e} = 3 \text{ MeV}$ . The faster oscillation pattern mediated through the mixing angle  $\theta_{13}$  and the mass difference  $\Delta m_{13}^2$  is embedded in the long-distance oscillation pattern induced by  $\theta_{12}$  and  $\Delta m_{12}^2$ . **Right:** Reactor survival probability as a function of  $L/E$  with indicated sensitivity regions of the RENO, Double Chooz, Daya Bay and KamLAND experiments.

Global fits of the oscillation parameters usually combine the solar and KamLAND reactor data to obtain the most precise estimates for  $\Delta m_{12}^2$  and  $\theta_{12}$ . In this context, KamLAND provides the better sensitivity to the squared mass difference, while the solar experiments

can pin down the angle  $\theta_{12}$  with greater accuracy [17]. Regarding the angle  $\theta_{13}$ , the main sensitivity is provided by the medium-baseline reactor experiments presented in the section above. However, a precise knowledge of this mixing angle is also very important for a variety of other applications such as long-baseline neutrino experiments which are briefly presented in the next paragraph. In these cases, the determined value of  $\theta_{13}$  from the reactor experiments is needed to evaluate the observed oscillation probabilities, especially in the case of the electron appearance channel.

### Long-baseline neutrino regime

For long-baseline neutrino experiments, the muon survival probability primarily depends on the mass squared difference  $\Delta m_{32}^2$  and the mixing angle  $\theta_{23}$  [64, 65]:

$$P(\nu_\mu \rightarrow \nu_\mu) \approx 1 - \cos^2 \theta_{13} \sin^2(2\theta_{23}) \sin^2 \frac{\Delta m_{32}^2 L}{4E} \quad (2.52)$$

The electron appearance probability, on the other hand, includes additional dependences on matter-related properties and the CP phase  $\delta_{\text{CP}}$  [66, 67, 68]:

$$\begin{aligned} P(\nu_\mu \rightarrow \nu_e) \approx & \frac{4}{(1-A)^2} \sin^2 \theta_{13} \sin^2 \theta_{23} \sin^2 \left( \frac{\Delta m_{31}^2 L}{4E} \right) \\ & + \frac{\alpha^2}{A^2} \sin^2 2\theta_{12} \cos^2 \theta_{23} \sin^2 \left( \frac{A\Delta m_{31}^2 L}{4E} \right) \\ & + 8\alpha J_{\text{CP}}^{\text{max}} \cos \left( \frac{\Delta m_{31}^2 L}{4E} \pm \delta_{\text{CP}} \right) \frac{\sin \Delta A \sin \Delta(1-A)}{A(1-A)}, \end{aligned} \quad (2.53)$$

with

$$\begin{aligned} \alpha &= \Delta m_{21}^2 / \Delta m_{31}^2, \quad \Delta = \frac{\Delta m_{31}^2 L}{4E}, \quad A = \frac{2EV}{\Delta m_{31}^2} \\ J_{\text{CP}}^{\text{max}} &= \cos \theta_{12} \sin \theta_{12} \cos \theta_{23} \sin \theta_{23} \cos^2 \theta_{13} \sin \theta_{13}. \end{aligned}$$

The last term directly depends on the CP-phase  $\delta_{\text{CP}}$  and hence provides a direct handle on CP-violation in the leptonic sector for the electron neutrino appearance channel in long-baseline experiments.

## 2.2.5 NEUTRINO FLAVOR CONVERSIONS IN MATTER

The previous two sections introduced the concept of neutrino oscillations in vacuum. When moving to neutrino propagation in matter, the situation looks slightly different: In this case, the Hamiltonian describing the system needs to take into account the effect of elastic forward scattering on electrons in the environment. Depending on whether the density distribution within matter is constant or variable, either modified oscillations

or resonant flavor conversions can occur. Both of these mechanisms will be highlighted shortly in what follows.

### Modified oscillations in matter

Since the presence of matter introduces an effective potential

$$V_\alpha = V_{\text{CC}}\delta_{\alpha e} + V_{\text{NC}} = \sqrt{2}G_{\text{F}}\left(N_e\delta_{\alpha e} - \frac{1}{2}N_n\right) \quad (2.54)$$

for a given neutrino flavor  $\alpha$ , the Hamiltonian  $H_{\text{matter}}$  describing the time evolution of eigenstates needs to be modified as follows:

$$i\frac{d}{dt}|\nu_\alpha(t)\rangle = H_{\text{matter}}|\nu_\alpha(t)\rangle = (H_{\text{vacuum}} + V_\alpha)|\nu_\alpha(t)\rangle. \quad (2.55)$$

The amplitudes of flavor transitions  $\psi_{\alpha\beta}(t) = \langle\nu_\beta|\nu_\alpha(t)\rangle$  in this case still depend on the mass square differences and the density of electrons, in the form

$$i\frac{d}{dx}\Psi_\alpha = H_{\text{F}}\Psi_\alpha, \quad (2.56)$$

with

$$H_{\text{F}} = \frac{1}{2E}(U\mathbb{M}^2U^\dagger + \mathbb{A}) \quad (2.57)$$

and

$$\Psi_\alpha = \begin{pmatrix} \psi_{\alpha e} \\ \psi_{\alpha\mu} \\ \psi_{\alpha\tau} \end{pmatrix}, \quad \mathbb{M}^2 = \begin{pmatrix} 0 & 0 & 0 \\ 0 & \Delta m_{21}^2 & 0 \\ 0 & 0 & \Delta m_{31}^2 \end{pmatrix}, \quad \mathbb{A} = \begin{pmatrix} 2\sqrt{2}EG_{\text{F}}N_e & 0 & 0 \\ 0 & 0 & 0 \\ 0 & 0 & 0 \end{pmatrix}. \quad (2.58)$$

The modified Hamiltonian leads to the fact that the propagation of neutrinos is described by modified matter eigenstates  $|\nu_{\text{M},i}\rangle$  instead of the vacuum mass eigenstates  $|\nu_i\rangle$ . Similarly, the relation between the flavor and mass eigenstates is described by modified matter mixing angles  $\theta_{\text{M},ij}$ . For illustrative purposes, it is advisable to consider the simplest case of 2-flavor mixing in matter. In this case, there is only one angle  $\theta_{\text{M}}$  that fully characterizes the mixing between the flavor and mass eigenstates in matter. It relates to the vacuum mixing angle  $\theta$  via

$$\tan 2\theta_{\text{M}} = \frac{\tan 2\theta}{1 - \frac{2\sqrt{2}EG_{\text{F}}N_e}{\Delta m^2 \cos 2\theta}}. \quad (2.59)$$

Similarly, the effective mass square difference of the matter mass eigenstates can be expressed via

$$\Delta m_{\text{M}}^2 = \sqrt{(\Delta m^2 \cos 2\theta - 2\sqrt{2}EG_{\text{F}}N_e)^2 + (\Delta m^2 \sin 2\theta)^2}. \quad (2.60)$$

In the case that the electron density  $N_e$  is constant for a given material, neutrino oscillations in matter are created by a comparable mechanism as in vacuum. The conversions between

the different flavors are created by phase differences of the matter mass eigenstates in an oscillatory manner. As a consequence, the muon neutrino appearance probability in matter can be expressed as

$$P(\nu_e \rightarrow \nu_\mu)(x) = \sin^2 2\theta_M \sin^2 \left( \frac{\Delta m_M^2 x}{4E} \right). \quad (2.61)$$

When considering the case of a varying electron density  $N_e$ , the situation looks a little different: In this instance, the flavor composition of the matter eigenstates  $\nu_{M,i}$  changes during propagation. As a consequence, neutrino flavor transformations are not described by an oscillatory behavior, but are rather characterized by a density-driven change in the flavor composition. This effect can even become resonant for certain electron density values, as described in more detail in the following paragraph.

### Resonant flavor conversion: the MSW effect

The *Mikheyev-Smirnov-Wolfenstein* (MSW) effect was envisioned in 1985 [69, 56] and describes the resonant flavor conversion of neutrinos in matter for the case that a critical electron density  $N_{e,\text{crit}}$  is crossed in the considered medium. Maximum mixing is achieved in case the matter angle  $\theta_M$  takes on a value of  $\pi/4$ . Based on the previously presented formula (2.59), this happens in case the electron density is equal to the critical value

$$N_{e,\text{crit}} = \frac{\Delta m^2 \cos 2\theta}{2\sqrt{2}EG_F}. \quad (2.62)$$

If one considers media where the density change occurs rather slowly in an *adiabatic* fashion, one can assume that the neutrino stays in the same matter mass eigenstate  $\nu_{M,i}$  despite of the density-induced change in flavor composition during propagation. As a consequence, an electron neutrino which is produced in a region of very high density  $N_e \gg N_{e,\text{crit}}$  will initially be an almost pure  $\nu_{M,2}$  mass eigenstate, and will remain the same mass eigenstate during propagation even if the density falls below the resonance density value. However, due to the simultaneous change of the matter mixing angle  $\theta_M$ , the same matter mass eigenstate will almost purely correspond to a muon neutrino flavor eigenstate as soon as the density falls much below the resonance value,  $N_e \ll N_{e,\text{crit}}$ . In such a way, the MSW effect can lead to an almost complete flavor conversion in case the vacuum mixing angle is sufficiently small.

This effect of enhanced flavor conversion processes is visualized in figure 2.8 in terms of the dependence of the matter mixing angle as a function of the electron density  $N_e$ . Two different scenarios are considered, a very small vacuum mixing angle of  $\theta_{\text{small}} = 0.9^\circ$  alongside a squared mass difference of  $\Delta m_{\text{small}}^2 = 7 \cdot 10^{-6} \text{ eV}^2$  as well as solar-neutrino like mixing parameters ( $\theta_{\text{solar}} = 31.6^\circ$ ,  $\Delta m_{12}^2 = 7.39 \cdot 10^{-5} \text{ eV}^2$ ). For the small mixing angle scenario (shown in *blue*), the electron neutrino can be considered a pure  $\nu_{M2}$  state in the core region of the Sun ( $N_e/N_A \approx 100 \text{ cm}^{-3}$ ). During propagation from the central region to the outer layers of the Sun, the electron density decreases and leads to a complete flavor swap around the resonance electron density. While the neutrino will still correspond to a  $\nu_{M2}$  mass eigenstate under adiabatic conditions, this will now correspond to a muon neutrino flavor state in the less dense region of the star. When comparing the cases of

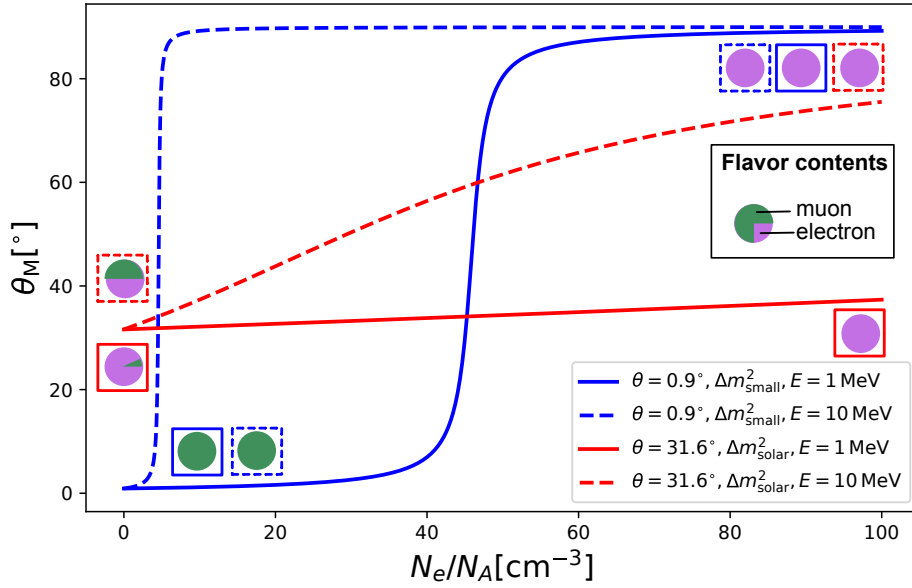


**Figure 2.8:** The dependence of the leptonic mixing angle in matter of the electron density  $N_e$ . Two different vacuum mixing angles are considered: The behavior for a very small mixing angle of  $\theta = 0.9^\circ$  is shown in blue, while the behavior for the solar neutrino mixing angle  $\theta_{12} \approx 31.6^\circ$  is shown in red. Two different neutrino energies are considered in each case, with the solid lines depicting the case of  $E = 1$  MeV and the dashed lines representing a larger energy of  $E = 10$  MeV.

different neutrino energies, a distinct shift to lower resonance density values is visible for higher neutrino energies.

In the case of solar neutrino mixing parameters (shown in *red*), the enhanced flavor conversion is less prominent. Especially for the case of lower-energetic neutrinos with  $E = 1$  MeV, the flavor composition of the matter mass eigenstates almost remains the same over the whole range of electron densities in the Sun. In this regime, basically no MSW-induced neutrino flavor transformation takes place. For higher energies ( $E = 10$  MeV), at least some amount of conversion occurs. One can hence expect a larger suppression of the flux of higher-energetic solar electron neutrinos based on the MSW effect.

It is also instrumental to consider the behavior of the effective squared masses  $m_{Mi}^2$  as a function of the electron density. They are defined as

$$m_{M2,1}^2 = \frac{1}{2} (m_1^2 + m_2^2 + 2\sqrt{2}EG_F N_e \pm \Delta m_M^2). \quad (2.63)$$

Figure 2.9 shows these effective squared masses as a function of the electron matter density for the case of neutrinos with energies of  $E = 1$  MeV (*blue*) and  $E = 10$  MeV (*red*). The upper curve represents the matter mass eigenstate  $\nu_{M,2}$  while the lower curve represents the other eigenstate  $\nu_{M,1}$ . The encountered densities in the Sun are highlighted by the grey area. Electron neutrinos are produced in the central region of the Sun, corresponding to densities of  $N_e/N_A \approx 100 \text{ cm}^{-3}$  as a  $\nu_{M2}$  mass eigenstate. During their path in the Sun, they travel towards regions with lower densities, moving leftwards on the plot. For the

example of higher-energetic neutrinos, the resonance region (indicated by the dotted line) is crossed, while the initial density is lower than the resonance density in the case of the lower-energetic neutrinos. At the resonance density, the difference between the effective squared masses is minimal, and eigenstate hopping of the form  $\nu_{M,1} \rightarrow \nu_{M,2}$  becomes most likely. The probability for a conversion of the matter mass eigenstates at that particular density is given by the so-called crossing probability  $P_C$  which depends on the energy and the effective squared mass difference.

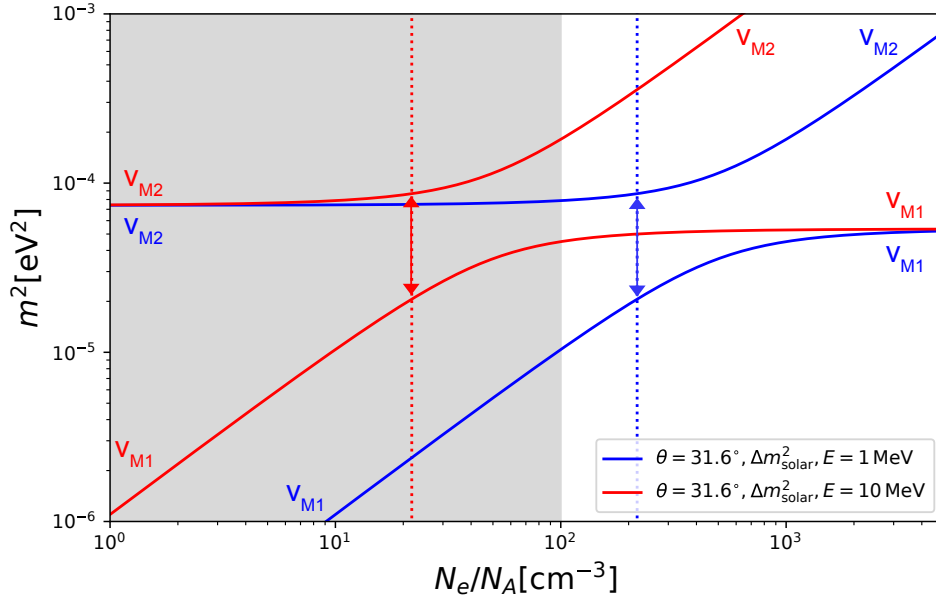


**Figure 2.9:** Effective neutrino masses as a function of the electron density  $N_e/N_A$  for the best fit solar oscillation parameters for  $\theta_{12}$  and  $\Delta m_{12}^2$ . Two different energies are considered, with the blue curve depicting the behavior for  $E = 1$  MeV and the red curve highlighting the behavior for  $E = 10$  MeV. Resonance density values are highlighted as dotted lines in both cases. For the Large Mixing Angle (LMA) parameters considered here, the probability for resonance level crossing is basically zero. The grey region roughly represents the range of density values which are encountered in the Sun.

The average survival probability including the crossing probability  $P_C$  is given by the Parke formula [70]

$$\bar{P}(\nu_e \rightarrow \nu_e) = \frac{1}{2} + \left( \frac{1}{2} - P_C \right) \cos 2\theta_M^{(i)} \cos 2\theta, \quad (2.64)$$

where  $\theta_M^{(i)}$  denotes the initial matter mixing angle.

In the case of adiabatic conditions, the probability for mass eigenstate crossing is zero and the average survival probability becomes

$$\bar{P}_{\text{adiabatic}}(\nu_e \rightarrow \nu_e) = \frac{1}{2} + \frac{1}{2} \cos 2\theta_M^{(i)} \cos 2\theta. \quad (2.65)$$

If the resonance region is not crossed, the survival probability is roughly equal to the one in vacuum:

$$\bar{P}_{\text{no-res}}(\nu_e \rightarrow \nu_e) \approx \bar{P}_{\text{vacuum}}(\nu_e \rightarrow \nu_e) = 1 - \frac{1}{2} \sin^2 2\theta. \quad (2.66)$$

### MSW solution for the solar neutrino problem

Two main oscillation parameter regions were considered as solutions to the solar neutrino problem: The *Small Mixing Angle* (SMA) and the *Large Mixing Angle* (LMA) solution. While the SMA scenario corresponds to very small values of the vacuum mixing angle and would lead to a strong enhancement of flavor conversions in the Sun by means of the MSW effect, the LMA scenario would result in less severe matter effects.

In particular, different energy dependences are expected. For the SMA parameter region, low-energy neutrinos ( $E < 0.3 \text{ MeV}$ ) feature a critical density which is larger than the one encountered in the center of the Sun. They hence would not cross the resonance region on their way through the Sun and their survival probability can be approximated by the vacuum oscillation formula. Due to the very small vacuum mixing angle, this would lead to no conversions of electron neutrinos in this energy regime, corresponding to a survival probability of 100%. For neutrinos in the energy region  $0.3 \text{ MeV} < E < 1 \text{ MeV}$ , the solar neutrinos would cross the resonance region adiabatically, leading to a complete disappearance of the electron neutrino flux. For the highest energy region ( $E > 1 \text{ MeV}$ ), the crossing probability would become larger with energy due to very small effective squared mass splittings. As a consequence, the resonance crossing would become non-adiabatic and less electron neutrinos would be converted into muon neutrinos.

The LMA solution exhibits different properties in terms of the expected neutrino survival probability values. Lower-energetic neutrinos below 1 MeV are almost not affected by MSW-enhanced neutrino conversion processes since the neutrinos do not cross the resonance electron density in this case. As a consequence, the survival probability is given by the vacuum solution. For energies above 1-2 MeV, the neutrinos cross the resonance region and electron neutrinos are transformed adiabatically, leading to a decreased survival probability according to equation (2.65).

When comparing experimental results of the survival probabilities with the theoretical models as presented in figure 2.10, it becomes clear that the MSW-LMA solution is in good agreement with the observed survival probability values. The MSW-SMA or the vacuum-LMA solution, on the other hand, are not able to describe the observed distribution in any way. After many years of uncertainty, the solar neutrino problem was therefore finally resolved by a combination of the Super-Kamiokande and SNO experiments, and further confirmed by measurements of the Borexino experiment. While the verification of the standard solar models was a great success, the enhanced knowledge about the properties of neutrinos was even more exciting. Particularly the discovery of their oscillatory behavior was so fundamental that it led to the Nobel Prize in 2015 for Takaaki Kajita and Arthur McDonald in their function as spokespersons of the Super-Kamiokande and SNO experiments and their role in the discovery of neutrino oscillations [71]. The discovery also shaped the way for a whole generation of new neutrino experiments, designed to measure the oscillation parameters with far greater accuracy and delve into the current unknowns such as the question of CP violation, the neutrino mass ordering or provide clarity on the Dirac/Majorana nature of neutrinos.

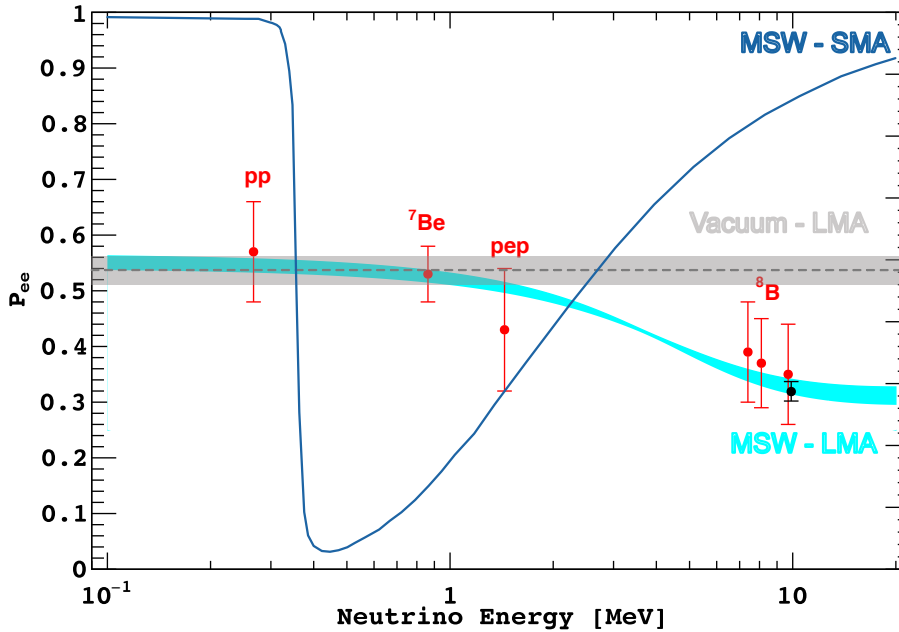


**Figure 2.10:** The observed survival probabilities of the different solar neutrino species by Borexino [38] (red data points) and SNO/Super-Kamiokande (black data point) alongside the predictions by the different theoretical parameter spaces. The MSW-induced survival probability values are depicted in light (dark) blue for the LMA (SMA) solution, while the vacuum LMA theory is shown in grey for comparison purposes. The figure was taken from references [17, 38], with the MSW-SMA curve added from reference [72].

## 2.2.6 GLOBAL BEST FIT PARAMETERS

The data from all available neutrino experiments is combined in so-called *global fits* to determine the best fit values for all oscillation parameters in the  $3\nu$ -scenario. The sensitivities of different neutrino species and detectors to the various parameters depends on the considered energies and baselines, as discussed briefly in section 2.2.4. Table 2.3 presents the current global fit results of the NuFIT group [73]. While most parameters are already well constrained, some open questions remain.

For instance, the octant of the mixing angle  $\theta_{23}$  is still not known, with the scenario of maximum mixing ( $\theta_{23} = 45^\circ$ ) still being allowed within the fitted  $3\sigma$  range. Some discrepancies in the best fit regions of the two leading accelerator neutrino experiments T2K and NovA surfaced in 2017, with T2K favoring a region around  $\sin^2 \theta_{23} \approx 0.51$  [74] and NovA excluding that very same region [75]. Currently, both experiments favor a very similar parameter region again after increasing their statistics to include the latest data [76, 77]. Additional data from next-generation experiments will be needed to reduce the current uncertainties on this parameter and close in more precisely on the octant of  $\theta_{23}$ .

A further parameter of interest is the CP-phase  $\delta_{\text{CP}}$  which is currently still very unconstrained. Currently, the two competitors T2K and NovA favor slightly different parameter regions. While NovA prefers a value of  $\delta_{\text{CP}} = 0.82^{+0.27}_{-0.87}$  for the normal mass ordering scenario [77], T2K published a best-fit value of  $\delta_{\text{CP}} = 1.25^{+0.70}_{-0.58}$  [78]. This discrepancy is visualized in figure 2.11 in the  $\delta_{\text{CP}}$ - $\sin^2 \theta_{23}$  parameter plane. Particularly when considering

Parameter	NO	NO (3 sigma)	IO	IO (3 sigma)
$\theta_{12}/^\circ$	$33.82^{+0.78}_{-0.76}$	$31.61 \rightarrow 36.27$	$33.82^{+0.78}_{-0.76}$	$31.62 \rightarrow 36.27$
$\theta_{23}/^\circ$	$48.6^{+1.0}_{-1.4}$	$41.1 \rightarrow 51.3$	$48.8^{+1.0}_{-1.2}$	$41.4 \rightarrow 51.3$
$\theta_{13}/^\circ$	$8.60^{+0.13}_{-0.13}$	$8.22 \rightarrow 8.98$	$8.64^{+0.12}_{-0.13}$	$8.26 \rightarrow 9.02$
$\delta_{CP}/^\circ$	$221^{+39}_{-28}$	$144 \rightarrow 357$	$282^{+23}_{-25}$	$205 \rightarrow 348$
$\Delta m_{21}^2/10^{-5} \text{ eV}^2$	$7.39^{+0.21}_{-0.20}$	$6.79 \rightarrow 8.01$	$7.39^{+0.21}_{-0.20}$	$6.79 \rightarrow 8.01$
$\Delta m_{32}^2/10^{-3} \text{ eV}^2$	$2.454^{+0.029}_{-0.031}$	$2.362 \rightarrow 2.544$	$-2.510^{+0.030}_{-0.031}$	$-2.601 \rightarrow -2.419$

**Table 2.3:** Current status of the global best fit parameters, combining most of the available neutrino oscillation data from solar, reactor, atmospheric, and beam neutrino experiments. Values taken from the 2020 PDG neutrino summary [17].

the full  $3\sigma$  allowed parameter region, a wide range of values is still available, including CP-conserving and CP-violating options. Also in this case, next-generation neutrino experiments like Hyper-Kamiokande, DUNE, and JUNO are expected to provide more clarity on the matter.

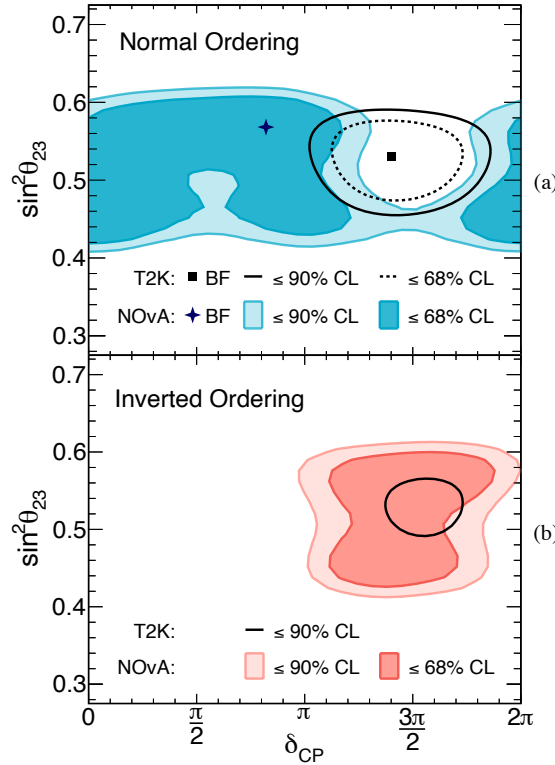


**Figure 2.11:** Best fit regions of T2K (black lines) and NOvA (colored regions) in the  $\delta_{CP}$ - $\sin^2 \theta_{23}$  plane. While consistent results are observed for  $\delta_{CP}$  in the case of an inverted mass ordering, discrepancies are observed for the preferred  $\delta_{CP}$  value for the normal ordering. Figure taken from [77].

### 2.2.7 OPEN QUESTIONS IN NEUTRINO PHYSICS

While a lot of neutrino properties have been uncovered since their first detection, some mysteries still remain to this day. For instance, the missing sensitivity of oscillation

experiments to the sign of the mass squared difference leads to the problem that the ordering of the neutrino mass eigenstates is not fully known, currently still allowing two possible scenarios. Furthermore, it is also unclear whether neutrinos are of Dirac or Majorana nature and whether CP-violating effects occur in the leptonic sector. Lastly, it remains to be probed whether so-called sterile neutrinos exist which would participate in the oscillation mechanism but would not interact weakly with matter. The current chapter will briefly highlight each of these issues and present possible avenues for exploring them in the future.

### Neutrino mass ordering

The missing sensitivity of vacuum neutrino oscillation processes to the sign of the mass squared difference leads to an ambiguity in the way the neutrino masses are arranged, the so-called neutrino mass ordering problem. While it is known that  $\nu_2$  is heavier than  $\nu_1$  as a consequence of the MSW effect in the Sun, the sign of  $\Delta m_{31}^2$  is still unknown, allowing  $m_3$  to be either heavier or lighter than the other two neutrino mass eigenstates. The former scenario is called *Normal Ordering (NO)* whereas the latter is referred to as *Inverted Ordering (IO)*. Figure 2.12 provides a visual representation of the two mass ordering schemes, with the different mass eigenstates shown in different colors. Due to the larger mass splitting  $\Delta m_{31}^2$ , the Inverted Ordering scenario generally leads to a larger total neutrino sum  $m_{\text{total}} = \sum_i m_i$  compared to the Normal Ordering case.

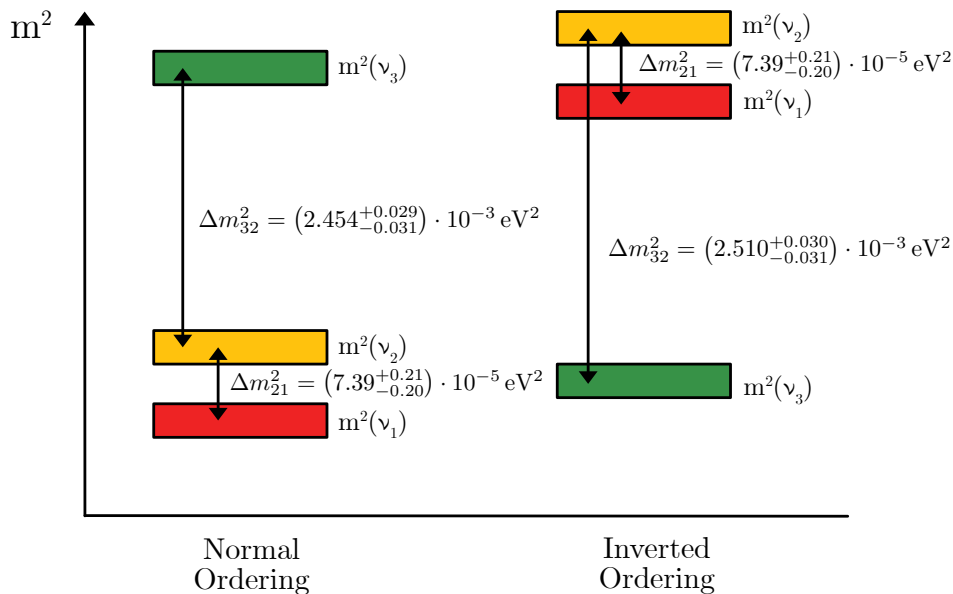


**Figure 2.12:** The two currently allowed ordering scenarios of neutrino masses, namely the Normal Ordering (NO) and Inverted Ordering (IO). While it is known that the second mass eigenstate  $\nu_2$  is heavier than the first one ( $\nu_1$ ), the third eigenstate  $\nu_3$  can either be the lightest or the heaviest of the neutrino masses. The values for the squared mass differences are taken from the PDG neutrino summary [17].

Experimental efforts to resolve the neutrino mass ordering problem typically make use of deviations in the oscillations probabilities induced by matter effects, such as in the case of Long Baseline accelerator or atmospheric neutrino experiments. The key contributing

detectors in these areas in the upcoming years will be DUNE [24] and T2HK [79] for the case of Long Baseline experiments and Hyper-Kamiokande [23], ORCA [80], and PINGU [81] for atmospheric neutrinos. Expected sensitivities range from at least  $5\sigma$  in the case of DUNE (7 years) to  $3\sigma$  discrimination capabilities in the cases of T2HK (5 years), ORCA (3 years), and PINGU (3 years).

Another promising technique focuses around differences in the survival probability and hence subtle deviations in the observed energy spectrum of reactor neutrinos at medium baselines of around 50 km, as for instance pursued by the JUNO experiment. With an excellent energy resolution of  $\Delta E \sim 3\%/\sqrt{E(\text{MeV})}$ , JUNO is expected to be able to determine the mass ordering with a significance of  $3\text{--}4\sigma$  after taking data for 6 years [82]. In a combined analysis with PINGU, the sensitivity of JUNO would increase to a value of  $5\sigma$  for a measurement time frame of 1.5 years (3 years) if the Normal (Inverted) Ordering holds true [83].

Complementary approaches in the future could furthermore make use of direct neutrino mass measurements with  $\beta$ -sources, neutrinoless double beta decay searches, and cosmological observations to help determine the mass ordering [84].

### Neutrino: Dirac or Majorana?

The smallness of neutrino masses ( $m_\nu < 1\text{ eV}$ ) with respect to all other fermions in the Standard Model ( $m_{\text{other-fermions}} \in [511\text{ keV}, 1.78\text{ GeV}]$ ) raises the question whether their internal properties are fundamentally different in some sense. While it is in principle possible to construct equivalent Dirac mass terms for neutrinos similarly to the other particles, another interesting scenario would entail neutrinos to be Majorana-type particles. In this case, neutrinos would be their own antiparticles such that  $\nu^c = \nu$ . This paragraph closely follows the discussion in André de Gouvêa's summary *Neutrino Mass Models* [85] and describes how neutrinos acquire mass in the different scenarios.

The neutrino mass terms in the Lagrangian are constructed differently depending on the Dirac or Majorana nature of neutrinos. In the case of Dirac neutrinos, the mass term would look like

$$\mathcal{L}_{\text{Dirac}} = y^{ai} L_\alpha n_i^c H + \text{h.c.}, \quad (2.67)$$

where  $y^{ai}$  denotes the Yukawa coupling strengths,  $L_\alpha$  describes the lepton doublets (with  $\alpha = e, \mu, \tau$ ),  $n_i^c$  are additional left-handed singlet fields which are introduced, and  $H$  represents the Higgs boson. The newly added  $n_i^c$  fields and the left-handed neutrino fields  $\nu_\alpha$  in  $L_\alpha$  form massive Dirac neutrino states  $\nu_D$  in the context of electroweak symmetry breaking. These Dirac neutrinos would then be associated to the Dirac mass elements  $(m_D)_{ai} = y_{ai} v$ , with  $v$  being the vacuum expectation value of the Higgs boson  $H$ . The experimentally observed smallness of the neutrino masses then requires very small Yukawa couplings on the order of  $y \sim 10^{-12}$ . This coupling is much smaller than for all other fermions which is often considered unsatisfactory from a theoretical model building perspective.

A more natural way of explaining the smallness of neutrino masses seems to be possible in the case of Majorana neutrinos. Majorana mass terms result from introducing an additional

non-renormalizable operator (often called the *Weinberg operator*) of the form

$$\mathcal{L}_{\text{Weinberg}} = -\frac{\lambda^{\alpha\beta}}{2\Lambda} (L_\alpha H)(L_\beta H) + \text{h.c.} \quad (2.68)$$

to the Lagrangian with dimensionless coefficients  $\lambda^{\alpha\beta}$  and an effective new physics scale  $\Lambda$  representing the high-energy region responsible for the presence of Majorana masses. The introduction of such a term results in the following mass term after spontaneous symmetry breaking:

$$\mathcal{L}_{\text{Majorana}} = -\frac{m_{\alpha\beta}}{2} \nu^\alpha \nu^\beta + \text{h.c.} \quad (2.69)$$

Majorana mass terms are typically realized in one of the so-called Seesaw mechanisms, which occur in three different forms:

$$\begin{aligned} \mathcal{L}_{\text{SeesawI}} &= y^{\alpha i} L_\alpha n_i^c H - \frac{M^{ij}}{2} n_i^c n_j^c + \text{h.c.} \\ \mathcal{L}_{\text{SeesawII}} &= \frac{f_{\alpha\beta}}{2} L^\alpha L^\beta \xi + \text{h.c.} \\ \mathcal{L}_{\text{SeesawIII}} &= y^{\alpha i} L_\alpha T_i H - \frac{M^{ij}}{2} T_i T_j + \text{h.c.} \end{aligned}$$

In the first and third realization of the Seesaw mechanism, both a Yukawa coupling term and a Majorana-associated mass term are present. The difference between the two types I and III solely depends on the singlet ( $n_i$ ) or triplet ( $T$ ) nature of the  $N_n$  newly introduced SU(2)-lepton particles. Both type I and III lead to a  $(n + N_n) \times (n + N_n)$  mass matrix of the form

$$m_\nu = \begin{pmatrix} 0 & m_D \\ m_D^T & M \end{pmatrix}. \quad (2.70)$$

The neutrino masses then inversely depend on the right-handed neutrino masses  $M$  like  $m_\nu \sim m_D \frac{1}{M} m_D^T$ . The smallness of the neutrino masses could in this scenario naturally be explained by very large right-handed neutrino masses  $1 \text{ eV} < M < 10^{16} \text{ GeV}$  [86], also leading to the name of the *Seesaw* mechanism [87]. However, also very small right-handed neutrino masses  $M < 10^{-9} \text{ eV}$  are theoretically still allowed in the so-called Pseudo-Dirac regime [88].

For the case of the type II-Seesaw mechanism, a new scalar SU(2)-particle  $\xi$  with hypercharge -1 (often referred to as Higgs triplet) is added to the Lagrangian. The neutrino mass terms then take the form [89]

$$m_{\nu, \text{SeesawII}} = \frac{\lambda v^2}{M_\xi} y^{\alpha\beta}. \quad (2.71)$$

The main experimental efforts to resolve the question of the Dirac or Majorana nature of neutrinos focus on the search for the process of neutrinoless double beta decay. Within

this particular decay mode, the neutrinos annihilate and lead to a discrete narrow peak at the high-energy end of the electron spectrum, violating lepton number by 2 units. The process is hence only allowed if neutrinos are Majorana particles and provides a unique test of this intrinsic property. So far, only lower limits have been obtained for the neutrinoless double beta decay times of various isotopes, for instance in the scope of the GERDA [90], CUORE [91], and KamLAND-Zen [92] experiments regarding the isotopes Germanium ( $^{76}\text{Ge}$ ), Tellurium ( $^{130}\text{Te}$ ), and Xenon ( $^{136}\text{Xe}$ ). At present, best lower limits for the neutrinoless double beta decay times are on the order of  $T_{1/2}^{0\nu} \approx 10^{23}$  y in the case of Tellurium and  $T_{1/2}^{0\nu} \approx 10^{26}$  y for Xenon and Germanium as target materials [93]. Future experimental efforts like the LEGEND experiment [94] will aim for decay time sensitivities on the order of  $T_{1/2}^{0\nu} \approx 10^{28}$  y and will possibly be able to shed more light on the potential Majorana nature of neutrinos.

### Absolute neutrino masses

Another open question related to neutrino masses emerges when considering the absolute scale of neutrino masses. Neutrino oscillation experiments are only sensitive to the differences of neutrino masses but not directly to the masses themselves. The absolute neutrino masses are therefore a very intriguing field on their own and are currently under investigation by a variety of approaches and experiments. One possibility of investigating neutrino masses makes use of the distortion of the electron energy spectrum in beta decays. The presence of non-zero neutrino masses will lead to a minor shift in the measured endpoint of the spectrum which is directly related to the electron-neutrino mass

$$m_{\beta} = \sqrt{\sum_{i=1}^3 |U_{ei}|^2 m_i^2}$$

The current best limit of neutrino masses with this particular method is  $m_{\beta} < 0.8$  eV (90% CL), as obtained by the KATRIN experiment [95].

A further – more indirect – approach makes use of the study of large-scale structures within cosmological observations. Phenomena such as Baryonic Acoustic Oscillations (BAO) or the multipole spectrum of the Cosmic Background Radiation (CMB) will have different properties depending on the considered neutrino masses. While this approach depends on cosmological models, it is currently able to place the best limits on the total mass of all neutrinos with observations by the Planck collaboration [96] leading to the limit

$$m_{\text{total}} = \sum_{i=1}^3 m_i < 0.12 \text{ eV (90\%CL)}.$$

Lastly, neutrinoless double beta decay experiments are also sensitive to neutrino masses, specifically the effective mass term [93]

$$\langle m_{\beta\beta} \rangle = |U_{ei}^2 m_i|.$$

Due to the presence of the Majorana phases  $\alpha_i$  in  $m_{\beta\beta}$ , partial cancellations of individual mass contributions  $m_i$  can occur. As a consequence, the significance of the mass term

$\langle m_{\beta\beta} \rangle$  needs to be treated with some caution with respect to the individual contributions  $m_i$ . Current best limits are on the order of  $\langle m_{\beta\beta} \rangle \lesssim 0.2 \text{ eV}$  [93].

### The leptonic CP-phase $\delta_{\text{CP}}$

One of the three Sakharov criteria [97] which are aiming to describe the observed matter-antimatter asymmetry in the Universe requires the violation of the CP symmetry in the Standard Model of particle physics. While such CP-violating effects were already observed in the baryonic sector in the scope of  $K$  and  $B$  meson systems [98, 99], it is currently unclear whether CP violating effects also occur in leptonic processes. Neutrino experiments will play a fundamental role in establishing the presence or absence of such processes.

As presented in equation (2.53), the oscillation probability for long baseline experiments depends on the leptonic CP phase  $\delta_{\text{CP}}$  in case of a non-zero mixing angle  $\theta_{13}$ . Future LBL experiments like DUNE and Hyper-Kamiokande are promising candidates for determining this phase with good accuracy. Some degeneracies are present with respect to the mass ordering and the angle  $\theta_{23}$  and need to be fit simultaneously or measured with independent experiments. Expected sensitivities for DUNE are on the order of  $5\sigma$  after a run time of 7 years for  $\delta_{\text{CP}}$ -values sufficiently different from the CP-conserving cases of 0 or  $\pm\pi$  [3], with similar sensitivities expected for the Hyper-Kamiokande experiment [23]. If leptonic CP violation is realized in nature, these two experiments will hence possess the capabilities to confirm this scenario during their time of operation.

### Sterile neutrinos

The number of light active neutrinos can be determined in a variety of ways, such as by investigating the width of the  $Z$  boson decay or more indirectly by investigating the number of effective neutrinos  $N_{\text{eff}}$  in the scope of cosmological investigations of the Cosmic Microwave Background (CMB) multipole spectrum. Both the measurements of the  $Z$  boson decay width ( $N_\nu = 2.9840 \pm 0.0082$  [100]) and the effective number of neutrinos from the CMB spectrum (e.g.  $N_{\text{eff}} = 3.13 \pm 0.32$  [101]) agree rather well on a total number of 3 light active neutrinos, rendering a fourth generation of active neutrinos unlikely.

However, there is still room for so-called *sterile* neutrinos in the current experimental landscape of the Standard Model. Such neutrinos would not participate in the weak interaction but would only be observable indirectly through their effects on neutrino oscillations. The simplest scenario consists of adding one additional sterile neutrino state and is conventionally referred to as the (3+1)-model. The PMNS matrix would in this case grow to a size of  $(4 \times 4)$  and an additional flavor state  $\nu_s$  and mass state  $\nu_4$  would need to be introduced such that the mixing process is described by

$$\begin{pmatrix} \nu_e \\ \nu_\mu \\ \nu_\tau \\ \nu_s \end{pmatrix} = U_{\text{PMNS},4 \times 4} \cdot \begin{pmatrix} \nu_1 \\ \nu_2 \\ \nu_3 \\ \nu_4 \end{pmatrix}. \quad (2.72)$$

The idea of sterile neutrinos gained attraction after some anomalous results were reported by the LSND experiment [102] in 1998 and later the MiniBooNE experiment [103]. Both the excess of electron anti-neutrino events in LSND and the excess of low-energetic neutrino

events in MiniBooNE could in principle be explained by the existence of a sterile state in the eV mass range. Furthermore, additional anomalies were observed in reactor neutrino experiments for which the measured antineutrino rate was observed to be lower than expected after recomputing the reactor fluxes [104], and Gallium source experiments such as SAGE which observed a lower electron neutrino flux than expected [105]. Both the reactor and Gallium rate deficiencies could also be explained in such an eV-scale (3+1)-sterile neutrino scenario.

However, the reported anomalies never provided conclusive results and merely hinted at the possible existence of a sterile neutrino. In order to resolve this ambiguous situation, a lot of effort has been spent on building additional *Very Short Baseline (VSBL)* Experiments aimed at verifying or disproving this hypothesis. In this context, several reactor neutrino experiments (e.g. PROSPECT [106], STEREO [107], DANSS [108], NEOS [109], Neutrino-4 [110]) were designed and have been taking data in the recent years. While PROSPECT, STEREO, and DANSS observe no hints for oscillations into a sterile state [111, 112, 113], the analysis of the NEOS data allows a 68% best fit region around the mixing parameters  $|\Delta m_{41}^2| = 2.41 \pm 0.03 \text{ eV}^2$  and  $\sin^2 2\theta_{14} = 0.08 \pm 0.03$  [114] and the Neutrino-4 data seems to favor the oscillation parameter region  $|\Delta m_{41}^2| = (7.3 \pm 1.17) \text{ eV}^2$  and  $\sin^2 2\theta = (0.36 \pm 0.12)$  at a significance of  $2.9\sigma$  [115]. More data from all of these experiments will be required before more definitive conclusions can be drawn on the existence and properties of a potential sterile state.

It should be noted that the significance of the original Reactor Antineutrino Anomaly (RAA) might have already been lowered recently due to a reevaluation of the reactor antineutrino spectra with updated measurements of the Uranium and Plutonium  $\beta$ -spectra, revealing a lower expected rate for these two isotopes which would be consistent with the measured rates at the reactor neutrino experiments [116]. If this finding proves to be true and is verified by further independent measurements, the RAA would basically cease to exist and only leave the originally observed low-energy excess and the Gallium anomaly as potential hints for sterile neutrinos.

In addition to the reactor neutrino experiments, the Short-Baseline Neutrino Program at Fermilab [117] aims to combine the data from a variety of detectors in the Booster Neutrino Beam line to investigate potential short baseline oscillations into sterile neutrino states in an accelerator environment. In this context, so far only data from the MicroBooNE experiment is available, which shows no evidence of the low-energy excess previously seen by the MiniBooNE experiment [118]. Since MicroBooNE possesses much better event identification capabilities and is situated in the same beam line, the new results call into question the original low-energy excess, potentially lowering the probability for a sterile neutrino as the main hypothesis. However, they do not cover the whole available parameter space and do not provide a fully model-independent test of the original MiniBooNE excess, still leaving room for a sterile neutrino to exist [119].

## 2.3 GEV-SCALE NEUTRINO INTERACTIONS

The general properties of neutrino interactions have been introduced in section 2.2.1, mainly covering the case of interactions with individual electrons or nucleons in matter. While for instance electron scattering is a very dominant and important process for lower-energetic neutrino sources in the MeV energy regime (such as solar neutrinos), it becomes less relevant for higher neutrino energies on the GeV scale. In this case, the neutrinos will mainly interact with the nuclei of the target material in a variety of channels. The complexity of nuclear structure makes such interactions much more difficult to model, and as a consequence has generated a whole research field of developing so-called neutrino event generators. The current section will first introduce the different neutrino-nucleus interaction channels in section 2.3.1 before providing an overview on the current status of the corresponding cross-section measurements in section 2.3.2. The last section will eventually cover the aspect of the number of neutrons produced in neutrino interactions, the so-called neutron yield or neutron multiplicity. This property will be measured by the ANNIE experiment, as discussed in more detail in chapter 3. The usefulness of such a neutron multiplicity measurement with respect to a series of interesting signals such as the Diffuse Supernova Background or proton decay searches will be discussed while furthermore presenting the current status and open questions.

### 2.3.1 OVERVIEW OF INTERACTION CHANNELS

When considering interactions of neutrinos with bound nucleons for a given target material, one needs to take into account the nuclear environment: On the one hand, this includes the fact that nucleons are not stationary, but rather move around the nucleus with momenta on the order of 100-200 MeV in the scope of the so-called *Fermi motion*. On the other hand, the interaction partners of the neutrino cannot be considered as free particles but rather undergo additional interactions in the nucleus before being able to leave. These *Final State Interactions* (FSIs) modify the list of particles that eventually result from the neutrino interaction and are therefore also an important aspect of neutrino nucleus interactions.

Figure 2.13 schematically presents the series of steps that are usually encountered in a typical neutrino-nucleus interaction. First of all, the initial conditions in the nucleus need to be modeled. In this context, nucleons are assumed to be bound in different nuclear shells and are modeled to move around the nucleus with momenta up until the Fermi momentum  $p_F$ . Different models can be considered for this initial configuration, e.g. the Relativistic Fermi Gas (RFG), the Local Fermi Gas (LFG), or the Spectral Function (SF) model. The properties and differences between these models will be briefly highlighted in the upcoming paragraph on initial nuclear states.

The incoming neutrino then interacts with one of the moving nucleons where three main interaction channels are encountered: the Quasi-Elastic (QE) interaction for which a neutron (proton) is converted into a proton (neutron) via the exchange of a  $W$ -boson, the Resonant Meson production (RES) for which a Delta resonance with subsequent decay into a pion is encountered, and the Deep Inelastic Scattering (DIS) channel which describes the scattering off individual quarks within the nucleon. In all CC interaction channels, the neutrino is converted into its charged leptonic counterpart in the scope of the  $W$ -

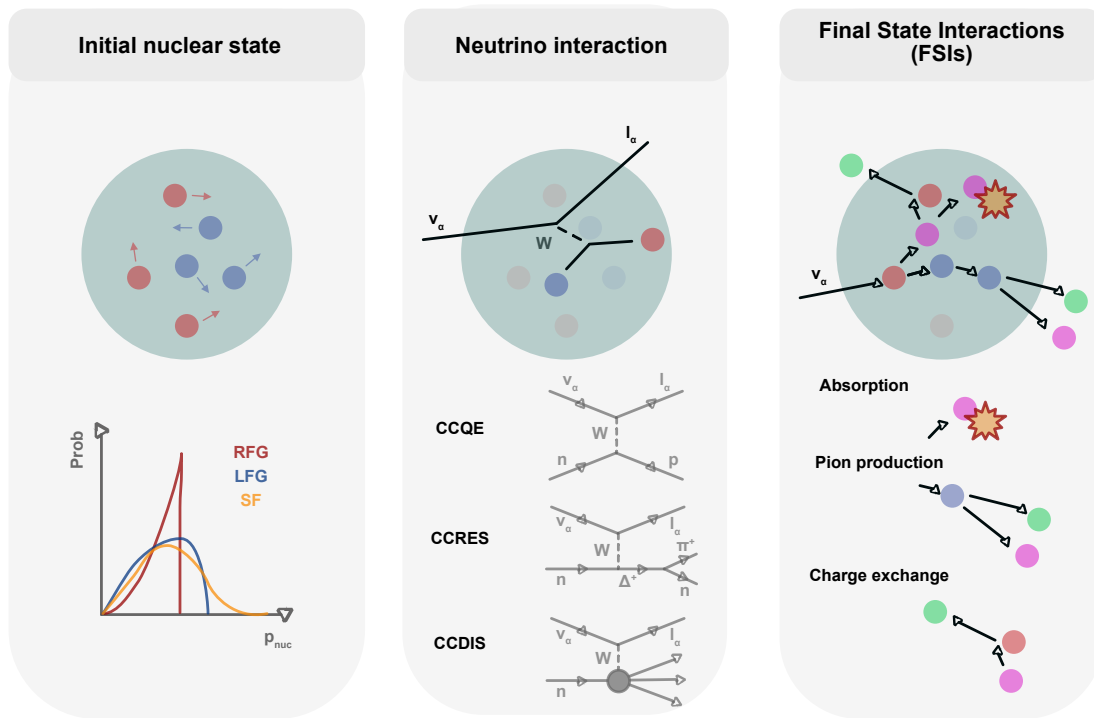


**Figure 2.13:** Overview of the different steps in neutrino nucleus interactions. The nucleons in the nuclei are usually modeled to move around the nucleus with a given momentum in the scope of a nuclear model (*left*). The neutrino interacts with those nucleons within the nucleus via one of three main interaction channels (*center*). The struck nucleon then further interacts in so-called Final State Interactions (FSIs) such as absorption or pion production (*right*).

boson exchange. For instance, muon neutrinos as encountered in an accelerator neutrino environment will be converted into a muon which then produces a distinct signature in the detector. In addition to the presented Charged Current variants, equivalent interaction channels also exist for the Neutral Current case. Furthermore, neutrinos will sometimes interact with a correlated pair of nucleons instead of single nucleons in so-called  $2p2h$  interactions (*two particle – two hole*) for which two nucleons are ejected from the nucleus, in contrast to the aforementioned  $1p1h$  channels.

After the neutrino-nucleon interaction took place, the charged lepton will leave the nucleus unimpeded while the hadronic component will potentially undergo further interactions within the nucleus in the scope of FSIs. These FSIs comprise for instance processes such as elastic scattering, absorption, pion production, and charge exchange processes. Many of those processes will alter the set of particles that are produced in the primary neutrino interaction alongside their properties. For example, additional pions can be produced in nuclear interactions after a CC-QE neutrino interaction, making it look like a Resonant Meson Production channel instead. This complication prompted the distinction between the nomenclature of theory-driven interaction channels and experiment-driven event topologies, which is presented in some more detail in the paragraph about Final State Interactions.

## Initial nuclear states

The initial nuclear configuration and the properties of nucleons within the nuclei can be approximated in a variety of models, with the main options being the Relativistic Fermi Gas (RFG), the Local Fermi Gas (LFG), and the Spectral Function (SF) model. The differences and peculiarities of each of the options will be briefly highlighted in the current paragraph. From a neutrino interaction perspective, the main observables of interest are the momenta and the binding energies of the nucleons.

The RFG model [120] assumes that the interior of the nucleus can be described as a so-called Fermi gas in which the nucleons fill up nuclear shells and move around the nucleus with increasing momenta up until the Fermi momentum  $p_F$ . As shown on the left in figure 2.14, more deeply bound nucleons will be associated with a lower momentum while the least bound states will move around with the highest achievable momentum  $p_F$ . The resulting momentum distribution is shown on the right hand side of figure 2.14 and features a rising slope for increasing momenta  $p$ , followed by a sharp edge at  $p = p_F$ .

While the RFG model is widely used, it is known to have some deficiencies as an accurate depiction of reality. The LFG model [121] aims to improve on that by assuming the same overall Fermi gas ansatz, but additionally introducing a spatial component which takes into account the distance from the nuclear center when determining the most likely nucleon momentum. As a consequence, the momentum distribution is more smeared out compared to the RFG case.

The SF approximation is a semi-empirical model that utilizes electron scattering data to construct a two-dimensional parameter space of nucleon momenta and their corresponding binding energies.

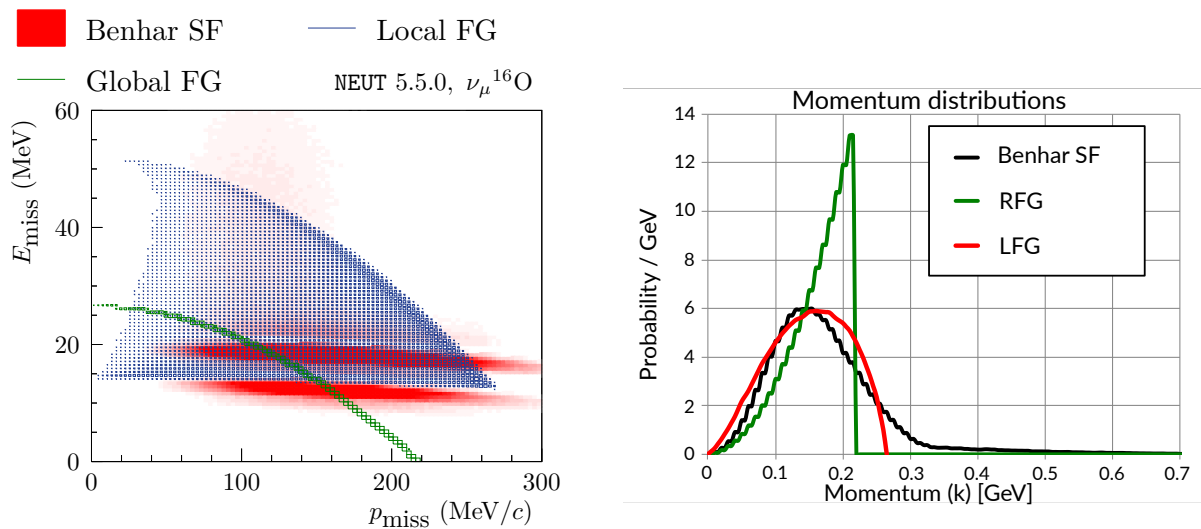


**Figure 2.14:** **Left:** Correlation of nucleon removal energy  $E_{\text{miss}}$  and the momentum of nucleons  $p_{\text{miss}}$  for different nuclear ground state models. The Global (Relativistic) Fermi Gas (RFG, *green*), Local Fermi Gas (LFG, *blue*), and the Benhar Spectral Function (SF, *red*) models are contrasted in the scope of their implementation in the NEUT neutrino generator framework. Figure taken from [122]. **Right:** Momentum distribution of nucleons in nuclei, as modeled by the different nuclear initial state models RFG, LFG and SF. Figure adapted from [123].

The Benhar SF model [124, 125, 126] shown in the above figure is a rather popular version of this approach and is for instance used in the neutrino event generator NEUT. The data-driven approach of Spectral Functions is assumed to be rather realistic due to being constructed based on direct experimental input. On the flip side, the SF models cannot predict the nucleon properties based on first theoretical principles but rather have to rely on the underlying data instead, making them less theoretically contained.

**Neutrino-nucleon interaction channels**

Within the context of Charged Current interactions, there are three main interaction channels that are of interest in neutrino-nucleus interactions, namely the Quasi-Elastic (QE), Resonant Meson Production (RES) and Deep Inelastic Scattering (DIS) channels. All three interactions are mediated by the  $W$ -boson such that the neutrino  $\nu_\alpha$  will be converted into its charged lepton counter particle  $l_\alpha$ . On the nuclear side of things, neutrons or individual quarks will participate in the interaction and are converted into a variety of other particles in the process.

The Feynman diagrams for the different processes are shown in figure 2.15. In the case of a CC-QE interaction, the neutrino is modeled to interact with the nucleon as a free target and converts the affected neutron into a proton. Kinematically, this process is the easiest to model and allows a reconstruction of the neutrino energy solely based on the reconstructed charged lepton energy  $E_\mu$  and the angle  $\theta_\mu$  of the same particle with respect to the primary neutrino direction (which is known in an accelerator neutrino environment). The neutrino energy is then given by [127, 128]

$$E_\nu = \frac{m_p^2 - (m_n - E_b)^2 - m_\mu^2 + 2(m_n - E_b)E_\mu}{2(m_n - E_b - E_\mu + p_\mu \cos \theta_\mu)}. \tag{2.73}$$

In addition to the charged lepton energy and direction variables, constant terms are present in the form of the proton mass  $m_p$ , the neutron mass  $m_n$ , the muon mass  $m_\mu$ , and the binding energy  $E_b$ . While formula (2.73) will provide a rather good approximation of the neutrino energy in CC-QE interactions, nuclear effects such as the Fermi motion of the nucleons and the recoil energy of the residual nucleus will introduce some biases and smearing to the reconstructed energy distribution.

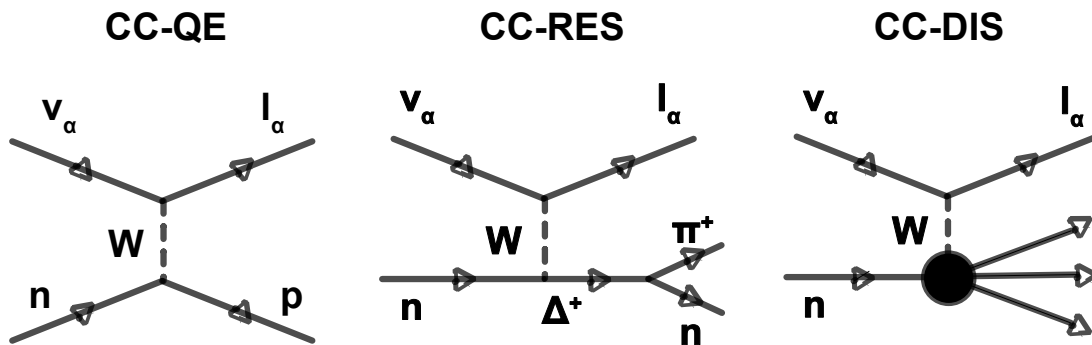


**Figure 2.15:** Feynman diagrams for CC neutrino-nucleon scattering channels. The Quasi-Elastic (QE), Resonant Meson Production (RES) and Deep Inelastic Scattering (DIS) channels dominate the cross section for regions of increasing energy transfer.

The second interaction channel CC-RES involves the production of a resonance particle (usually a  $\Delta$  particle) which then further decays into a pion/nucleon pair. The Feynman graph in figure 2.15 exemplarily shows the channel  $\Delta^+ \rightarrow \pi^+ + n$ , but other channels such as  $\Delta^+ \rightarrow \pi^0 + p$  or  $\Delta^{++} \rightarrow \pi^+ + p$  are also relevant. As a consequence, the CC-RES interaction channel is almost always accompanied by the presence of a pion. Due to the variety of involved particles, this interaction is already much harder to model than the CC-QE one, which in turn increases the uncertainty in the reconstructed neutrino energy and the cross-section of the process.

The last neutrino-nucleus interaction channel of interest is CC-DIS. In this case, the neutrino has enough energy to interact with individual quarks within the nucleon. The cross-section of this channel is relatively easy to model for very high energy transfers but gets harder to approximate for lower energies, especially in the transition region to CC-RES interactions. More information on the theoretical and experimental status of the cross-sections for the different interaction channels is presented in the upcoming section 2.3.2.

Figure 2.16 shows the qualitative behavior of the cross-section of the three presented interactions as a function of the neutrino energy transfer  $\omega$ . CC-QE interactions are dominant for the lowest energies around  $\omega \approx \frac{Q^2}{2M}$  while CC-RES interactions are present for higher values of  $\omega$  and DIS processes primarily occur in the region of highest energy transfers [129]. Transition regions for which two processes are equally important are present both at the CC-QE/CC-RES and at the CC-RES/CC-DIS borders and further complicate the modeling of neutrino-nucleus interactions.

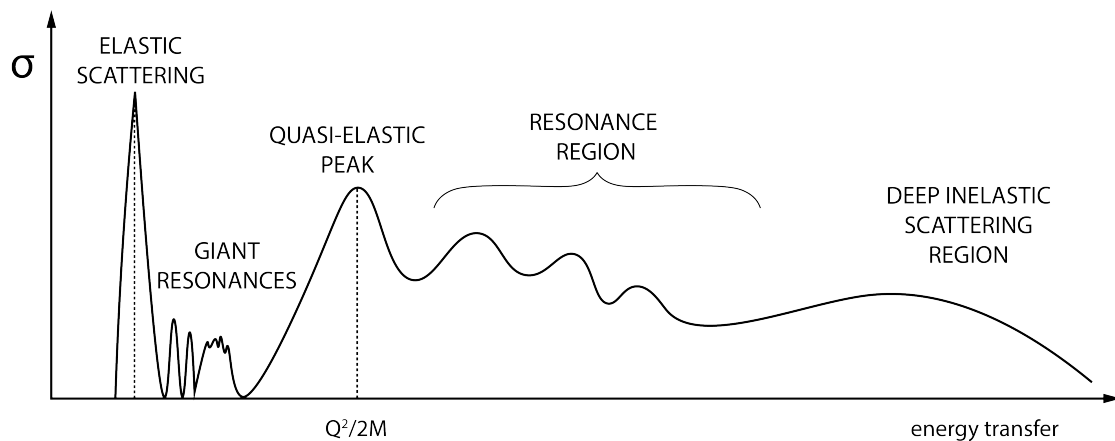


**Figure 2.16:** Illustrative depiction of the dependence of the cross-section of the energy transfer in neutrino-nucleus interactions. Distinct regions with prominent features are visible for the Elastic Scattering, Giant Resonances, Quasi-Elastic, Resonance, and Deep Inelastic Scattering processes (in terms of increasing energy transfer). Figure taken from [129].

### Final State Interactions (FSIs)

After the initial neutrino-nucleon interaction, the involved nucleon will have to traverse the nuclear medium before being able to leave the nucleus. During this propagation through the nucleus, the properties of the nucleon can change significantly by scattering and absorption processes with other nucleons. Figure 2.17 exemplarily shows some of these so-called Final State Interactions (FSIs) following a neutrino interaction.

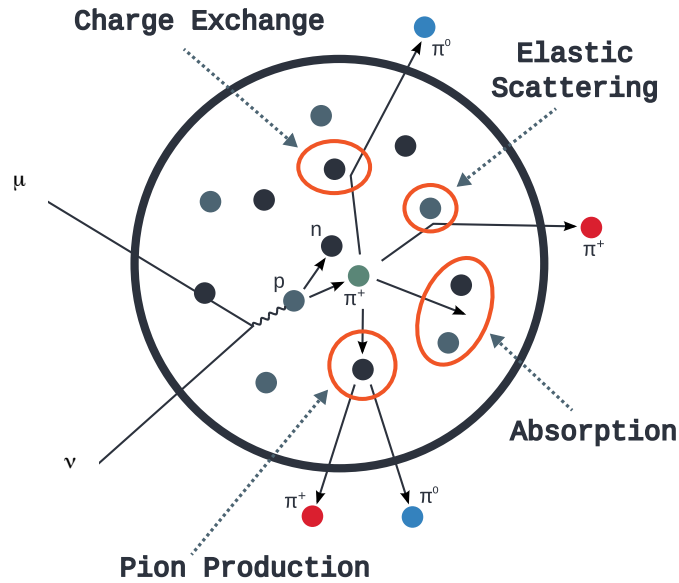


**Figure 2.17:** Schematic overview of different Final State Interactions within a nucleus. Absorption, elastic scattering, pion production, and charge exchange processes can alter the composition and properties of Final State particles. Figure taken from [5].

One possible FSI involves the production of additional pions while another scenario involves the absorption of produced particles. FSIs can therefore both increase and decrease the number of observed pions in an event. Further FSIs comprise elastic scattering processes which will only change the momentum of the involved particle or charge exchange processes in which e.g. a positively charged pion is converted into a neutral pion. FSIs therefore have a significant influence on the set of final state particles and their properties [5].

As a consequence of FSIs, the original interaction channel is not always determinable in an experimental setting. For instance, a CC-QE interaction with additional pion production processes in the nucleus will more likely look like a CC-RES interaction from an experimental point of view. Similarly, a CC-RES interaction with subsequent pion absorption in the nucleus will rather look like a CC-QE event in the detector. This difficulty in identifying the correct interactions prompted the separation of theoretically motivated interaction channels and experimentally oriented event topologies, as visualized in figure 2.18.

Event topologies are characterized by the observed final state particles within an event and are not directly related to any of the theoretical interaction channels. One prominent event signature is the CC- $0\pi$  one, which requires no observed pion and the flavor-corresponding charged lepton of the neutrino in the final state. This event topology mainly consists of CC-QE events, but has further contributions from CC-RES, CC-DIS, or CC-2p2h interactions with additional FSIs. Similarly, CC- $1\pi$  interactions consist of events that feature the charged lepton partner of the neutrino and one observed pion. This event category mainly consists of CC-RES interactions, but additionally also includes other interactions such as CC-QE ones with further pion production processes in the nucleus. Since the interaction channels are not directly accessible in experiments, it makes more sense to compare the

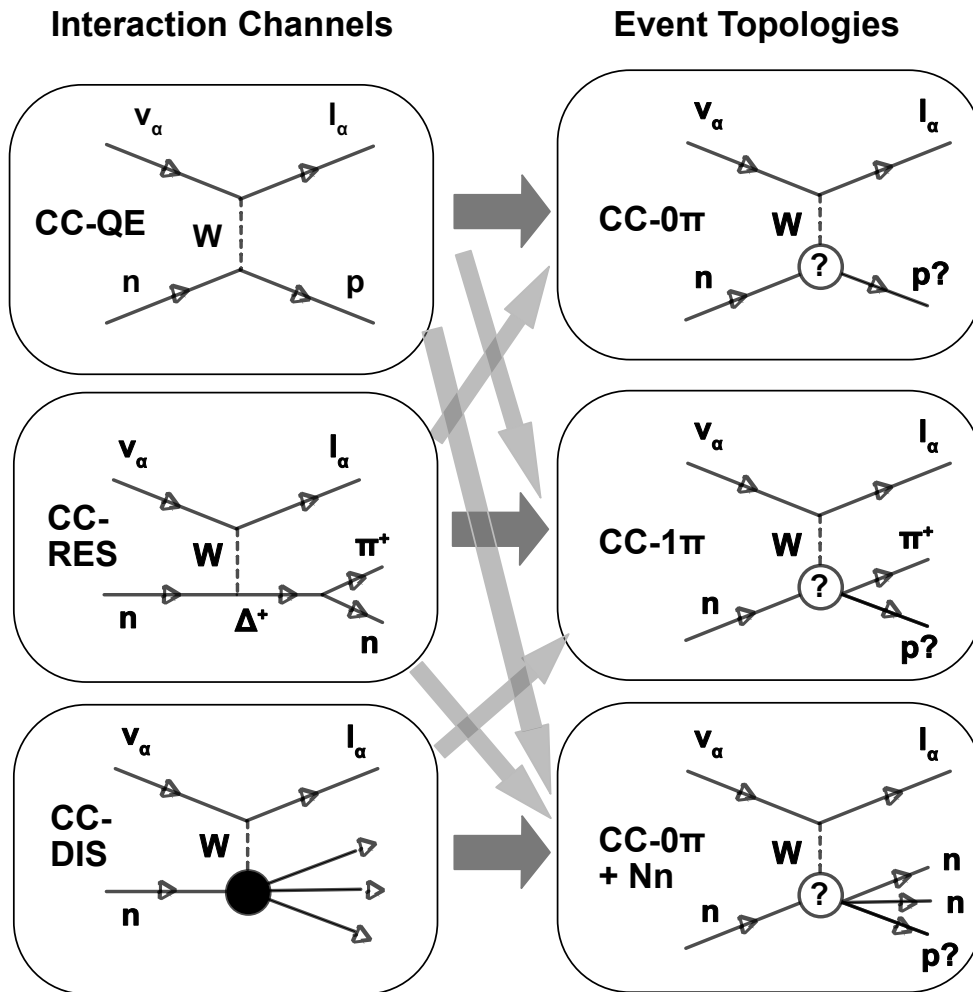


**Figure 2.18:** Overview of the relation between theoretical neutrino interaction channels and event topologies as observed by experiments. While a strong correlation will be present between e.g. the CC-QE channel and the CC-0 $\pi$  event topology, Final State Interactions and other effects will for instance also lead to cases where additional pions are produced in CC-QE interactions, leading to an observed CC-1 $\pi$  event signature instead. Similar cross-correlation effects are present for the other channels such as CC-RES and CC-DIS interactions. Figure inspired by [128].

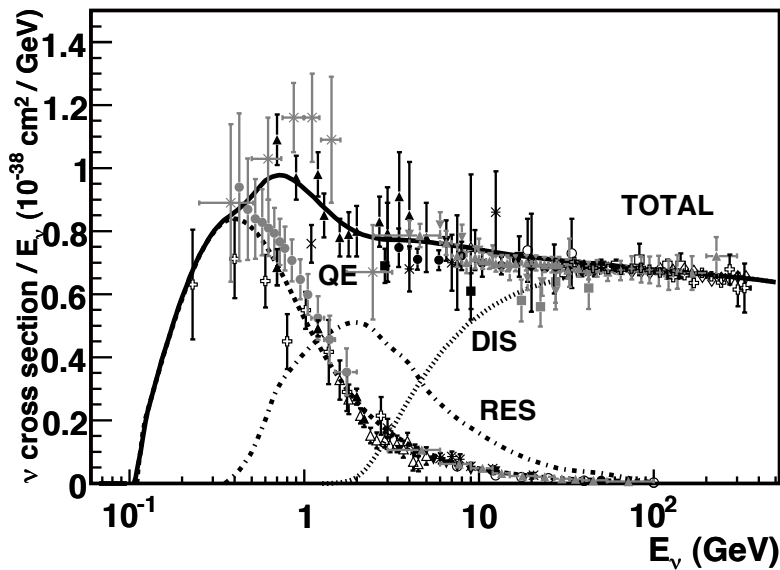
predicted and observed properties (e.g. cross-sections) in terms of the respective event topologies instead.

In addition to the inclusive channels of CC-0 $\pi$  and CC-1 $\pi$  which are integrated over all possible hadronic states, more exclusive interaction channels can be constructed by additionally taking into account the number of observed neutrons or protons. Depending on the employed detector technology, usually only either protons or neutrons can be identified and counted within one experiment. In the case of ANNIE (see the upcoming chapter 3 for details), the Gadolinium-loaded water target material allows excellent neutron tagging capabilities and therefore enables more exclusive Nn channels such as for instance CC-0 $\pi$ -1n. These topologies again correspond to a variety of interaction channels, especially since the number of neutrons is similarly influenced by Final State Interactions. Additionally, secondary interactions of particles with other nuclei in the target volume can lead to the production of further neutrons in the scope of inelastic scattering processes.

### 2.3.2 CROSS-SECTION MEASUREMENTS

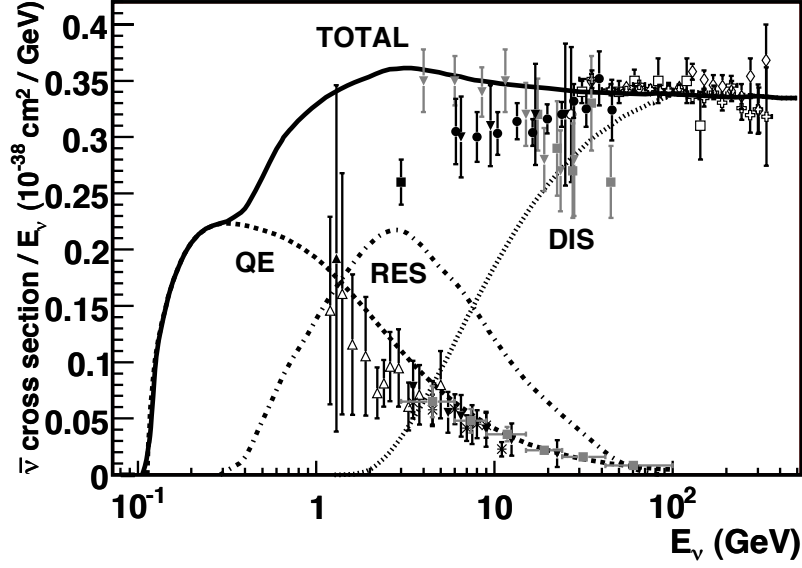
Cross-sections of neutrino interactions are important input parameters for neutrino oscillation analyses, and as such need special consideration and precise measurements for a variety of target materials. The current section will briefly present the theoretical and experimental status of inclusive cross-sections for the QE, RES, and DIS interaction channels. Exclusive cross-section models including the hadronic dynamics are much harder to calculate and are hence omitted in this brief overview.

Figure 2.19 presents the cross-sections per nucleon for neutrino-nucleus scattering as a function of the neutrino energy, measured by a multitude of experiments (data points with errors, different shades indicate different experiments). Most of the data which is presented in the plot was collected in bubble chamber or spark chamber experiments back in the 1970s and 1980s and used target materials with few nucleons (such as deuterium) [130]. As a consequence, these measurements are ideally suited to evaluate the interactions with individual nucleons. The expected theoretical cross-sections are depicted as lines in the same plot, and are shown both separated by interaction channel (dashed/dotted lines) and in form of the combined cross-section of all interaction channels (solid line). Reasonable agreement is observed between the experimental data and the theoretical predictions in terms of these inclusive cross-sections.



**Figure 2.19:** Theoretical predictions and measurements of cross-sections per nucleon for different neutrino-nucleus interaction types, specifically the processes Quasi-Elastic (QE), Deep Inelastic Scattering (DIS), and Resonance (RES). Figure taken from [130].

Similarly, the cross-sections for antineutrino-nucleus scattering are shown in figure 2.20. Compared to the neutrino case, fewer measurements and less statistics are present. Furthermore, no measurements below a neutrino energy of 1 GeV are available and the agreement between the data and the theoretical models is worse than for the neutrino case. The issue of larger error bars can be traced back to less beam time in antineutrino mode for most experiments as well as larger background contaminations when measuring the antineutrino cross-sections [130].



**Figure 2.20:** Theoretical predictions and measurements of cross-sections per nucleon for different antineutrino-nucleus interaction types, specifically the processes Quasi-Elastic (QE), Deep Inelastic Scattering (DIS), and Resonance (RES). Figure taken from [130].

The inclusive cross-section for the CC-QE process can be parameterized by a formula first developed by Llewellyn-Smith in 1972 [131]:

$$\frac{d\sigma}{dQ^2} = \frac{G_F^2 M^2 |V_{ud}|^2}{8\pi E_\nu^2} \left[ A \pm \frac{(s-u)}{M^2} B + \frac{(s-u)^2}{M^4} C \right]. \quad (2.74)$$

Within the formula,  $Q^2$  refers to the squared four-momentum transfer,  $G_F$  is the Fermi coupling constant,  $E_\nu$  denotes the initial neutrino energy,  $M$  ( $m$ ) is the nucleon (lepton) mass, and the  $+$  ( $-$ ) sign applies in the case of neutrino (antineutrino) scattering. Furthermore, the combination of Mandelstam variables can also be expressed as  $(s-u) = 4ME_\nu - Q^2 - m^2$  while the factors  $A$ ,  $B$ , and  $C$  depend on the various form factors  $F_i$  as [130]

$$\begin{aligned} A &= \frac{m^2 + Q^2}{M^2} [(1 + \eta) F_A^2 - (1 - \eta) F_1^2 + \eta(1 - \eta) F_2^2 + 4\eta F_1 F_2 \\ &\quad - \frac{m^2}{4M^2} \left( (F_1 + F_2)^2 + (F_A + 2F_p)^2 - \left( \frac{Q^2}{M^2} + 4 \right) F_p^2 \right)], \\ B &= \frac{Q^2}{M^2} F_A (F_1 + F_2), \\ C &= \frac{1}{4} (F_A^2 + F_1^2 + \eta F_2^2). \end{aligned}$$

While the vector form factors  $F_1$  and  $F_2$  can be obtained from electron scattering data, the axial vector form factor  $F_A$  is only accessible in neutrino data and is usually parameterized as a dipole term

$$F_A(Q^2) = \frac{g_A}{\left(1 + \frac{Q^2}{M_A^2}\right)^2}. \quad (2.75)$$

This form factor depends on  $g_A = F_A(0) = 1.2694 \pm 0.0028$  [132] and an "axial mass" term of  $m_A \sim 1.0 \text{ GeV}$  [133]. Out of the two, the first one can be obtained in nuclear beta decay experiments, while  $M_A$  is only accessible in neutrino scattering experiments. The pseudoscalar form factor  $F_p$  is typically not of high relevance due to its suppression by the factor of  $\frac{m^2}{M^2}$ .

Neutrino interactions involving the production of a resonance particle – i.e. the CC-RES channel – are harder to model than CC-QE interactions. Typically, models and generators rely on the considerations and calculations by Rein and Sehgal [134] to predict the cross-section for this channel.

The cross-section for DIS neutrino interactions can be described in terms of the Bjorken scaling variable  $x$  and the inelasticity  $y$  which describe the fraction of momentum carried by the individual quark and the amount of energy which is transferred into the hadronic system. They are defined as

$$x = \frac{Q^2}{2ME_\nu y} \quad (2.76)$$

$$y = E_{\text{had}}/E_\nu. \quad (2.77)$$

The DIS cross-section can then be described by [130]

$$\begin{aligned} \frac{d^2\sigma}{dx dy} = \frac{G_F^2 M E_\nu}{\pi (1 + Q^2/M_{W,Z}^2)^2} & \left[ \frac{y^2}{2} 2xF_1(x, Q^2) + \left(1 - y - \frac{Mxy}{2E}\right) F_2(x, Q^2) \right. \\ & \left. \pm y \left(1 - \frac{y}{2}\right) xF_3(x, Q^2) \right]. \end{aligned} \quad (2.78)$$

The  $+(-)$  sign in equation (2.78) refers to the case of neutrino (antineutrino) scattering while  $M_{W,Z}$  denotes the mass of the  $W$  or  $Z$  boson. The  $F_i(x, Q^2)$  terms are nuclear structure functions that encompass the sum of parton distribution functions which represent the quark and gluon structure of nucleons. The first two structure functions  $F_1$  and  $F_2$  represent the vector contribution and can also be accessed in electron scattering experiments, while  $F_3$  represents the  $V - A$  interference term and can only be probed in neutrino interactions.  $F_2$  and  $F_3$  are given by [130]

$$F_2(x, Q^2) = 2 \sum_{i=u,d,\dots} (xq(x, Q^2) + x\bar{q}(x, Q^2)) \quad (2.79)$$

$$xF_3(x, Q^2) = 2 \sum_{i=u,d,\dots} (xq(x, Q^2) - x\bar{q}(x, Q^2)), \quad (2.80)$$

while the first nuclear structure function  $F_1$  is related to  $F_2$  via a longitudinal structure function called  $R_L(x, Q^2)$ :

$$F_2(x, Q^2) = \frac{1 + R_L(x, Q^2)}{1 + 4M^2x^2/Q^2} 2xF_1(x, Q^2). \quad (2.81)$$

### 2.3.3 NEUTRINO EVENT GENERATORS

In the context of neutrino oscillation experiments, it is vital to provide accurate predictions for the cross sections of the different interaction channels alongside a good model for the particles produced in such an interaction. So-called neutrino event generators have been developed as a framework to fulfill this role and provide the necessary information based on theoretical and experimental inputs. Different event generators are currently being developed and used to model neutrino interactions with a variety of target materials. The most popular generators are GENIE [135], NEUT [136], NuWro [137], and GiBUU [138]. While GENIE is developed by a larger group of experimental physicists mainly affiliated with Fermilab-based experiments, NEUT is primarily maintained in the context of the Super-Kamiokande/ Hyper-Kamiokande and T2K experimental efforts. NuWro was created by a smaller team in Wrocław, Poland, and is more oriented towards theory than experimental requirements [128] while GiBUU has the smallest development team and models interactions based on the semi-classical Boltzmann-Uehling-Uhlenbeck transport equation [139].

In general, the generators use a factorized approach for modeling the neutrino interactions with nuclear targets. This is schematically depicted in figure 2.21 in which the individual generator components are highlighted: First of all, the generator needs an initial nuclear model before modeling the primary neutrino interaction. Depending on the encountered interaction, the generator will potentially need to take care of the hadronization process as a next step and then focus on the subsequent hadron transport within the nucleus.

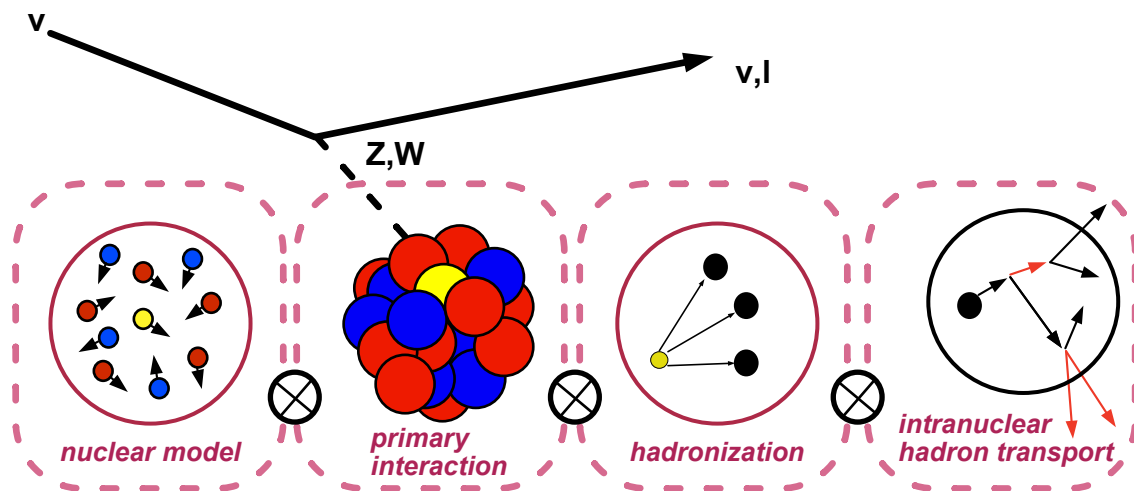


**Figure 2.21:** Schematic representation of the different components in a neutrino event generator. A nuclear model is used to simulate the initial conditions in the nucleus. Afterwards, the primary interaction of the neutrino with one of the nucleons (shown in yellow) is simulated, followed by hadronization effects in the case of quark scattering processes. Eventually, the resulting hadron is propagated through the nucleus to model Final State Interactions, usually in the scope of an intranuclear hadron transport model. Figure taken from [128], with original credit to Costas Andreopoulos (University of Liverpool, Rutherford Appleton Laboratory).

As presented earlier, the initial nuclear configuration is modeled by either a Fermi gas or Spectral Function-related approach while the cross-sections for the different neutrino interactions are implemented based on the considerations and measurements presented in the previous section 2.3.2. The hadronization step is primarily important for Deep

Inelastic Scattering processes which directly interact with individual quarks in the nucleons and require further processes to take place due to the confinement principle of quarks. The hadron transport within the nucleus is usually handled in the scope of so-called intranuclear cascade models which handle Final State Interactions as a series (cascade) of collisions of the involved nucleon.

The input from experiments is vital to verify the accuracy of current neutrino generators and to identify potential flaws in the employed models. In this context, generators can be tuned to match data more reliably by rescaling the weights for different processes and contributions. However, one should be careful to avoid overtuning the models to a specific data set while simultaneously worsening the agreement with another sample. As many measurements as possible are needed to reliably identify weaknesses in the current models and achieve a general improvement of generators for a wide and comprehensive range of physics processes.

### 2.3.4 NEUTRON MULTIPLICITY MEASUREMENTS

The determination of the number of neutrons produced in neutrino interactions is a powerful discriminator between different event topologies: While many interesting physics signals like a potential proton decay mechanism via  $p \rightarrow e + \pi^0$  /  $p \rightarrow K^+ + \nu$  or the Diffuse Supernova Background (DSNB) do not produce any neutrons or exactly one neutron, backgrounds that mimic the expected event signature often produce at least one or even multiple neutrons. The number of neutrons in an event can hence be a powerful discrimination tool to differentiate between a real and a fake signal, if understood properly.

One background source that is of particular interest with respect to the planned future proton decay and DSNB searches are atmospheric neutrinos. In the case of proton decay searches in the  $p \rightarrow e + \pi^0$  mode, high-energetic proton events following atmospheric neutrino interactions can produce pions by scattering in the detector and hence mimic the expected signal event signature. On the other hand, very low-energetic CC interactions or nuclear de-excitation processes in NC processes can imitate the expected event signatures of the Inverse Beta Decay when searching for a potential DSNB signal. While the proton decay modes expect no associated neutron in the majority of cases and the DSNB signal always contains exactly one neutron, atmospheric neutrino interactions generally tend to generate more neutrons. However, the current models and predictions for the neutron multiplicity in such atmospheric background events have large associated uncertainties due to rather poorly understood effects in the neutrino-nucleus interactions. Better understanding the expected number of neutrons in atmospheric neutrino interactions as a function of the lepton kinematics is hence an important aspect to identify and reject this background.

Additional data on the number of neutrons produced in such interactions from different experiments is hence highly valuable in the effort to improve current models and predictions. As an example, the beam neutrinos encountered in the ANNIE experiment (as presented in more detail in chapter 3) possess very similar properties in terms of their energy and the dominant neutrino flavor compared to atmospheric neutrinos. The measurements of ANNIE will hence offer a way for better characterizing this background channel of

atmospheric neutrinos. Due to the rather controlled conditions in an accelerator neutrino environment, the directional and energetic properties are much better known than in the actual atmospheric sample and will reduce the associated systematics and uncertainties in the measurements.

The current section will provide some further information on the proton decay and DSNB detection channels and will highlight the ways in which the background channels can mimic the expected event signatures in both cases. Furthermore, the current status of neutron multiplicity measurements in neutrino interactions will be reviewed by evaluating the atmospheric neutrino analyses of the SNO and Super-Kamiokande experiments before closing with an overview of the impact of neutron measurements on the development of neutrino event generators.

### Relevance in proton decay searches

Proton decay is an exciting phenomenon which is one of the predicted features of Grand Unified Theories (GUTs) [140]. Two main decay modes are generally taken into consideration in experimental searches, namely  $p \rightarrow e^+ \pi^0$  and  $p \rightarrow K^+ + \nu$ . Predecessors of current neutrino experiments, like Kamiokande, were originally designed to search for this elusive channel before being re-purposed as neutrino detectors. However, up until the current day only lower limits on the proton decay lifetimes could be obtained.

In the case of the positron/pion decay channel, typical event selection cuts in Super-Kamiokande involve the requirement of 3 reconstructed Cherenkov rings, an invariant mass in the neutral pion mass range for one pair of rings, and no follow-up Michel electron signature in the detector [141]. Furthermore, additional cuts are applied on the total mass and total momentum variables, as shown in figure 2.22. Atmospheric neutrino interactions can mimic this proton decay event signature, as shown by the few remaining expected background events in the signal region. Currently, the observed events in Super-Kamiokande are compatible with the background expectations, leading to a lower limit on the proton decay lifetime of  $\tau/B(p \rightarrow e^+ \pi^0) > 2.4 \times 10^{34}$  years [141].

In addition to the presented cuts on the reconstructed total mass and total momentum, additional restrictions on the number of neutrons in an event can provide further discrimination possibilities. Since the decay of protons should not be accompanied by the presence of a neutron in the case of free protons and only very rarely include a neutron in the case of bound proton decay within an oxygen nucleus, the fact that atmospheric neutrino interactions will generally produce some neutrons opens up the possibility of further background reduction cuts and better chances of detecting a potential signal [4]. Pure water Cherenkov detectors generally suffer from rather bad neutron detection efficiencies due to the faint signal of the 2.2 MeV gamma produced in a capture reaction on hydrogen. However, the current landscape of water Cherenkov detectors is already taking appropriate measures to mitigate this problem by using Gadolinium-doped water as a target material instead, resulting in a much more easily detectable 8 MeV gamma signal cascade. This renders an additional neutron multiplicity-based event selection cut much more feasible, for instance in the scope of proton decay searches in the current Super-K-Gd detector configuration. More accurate measurements of the neutron multiplicity distribution in

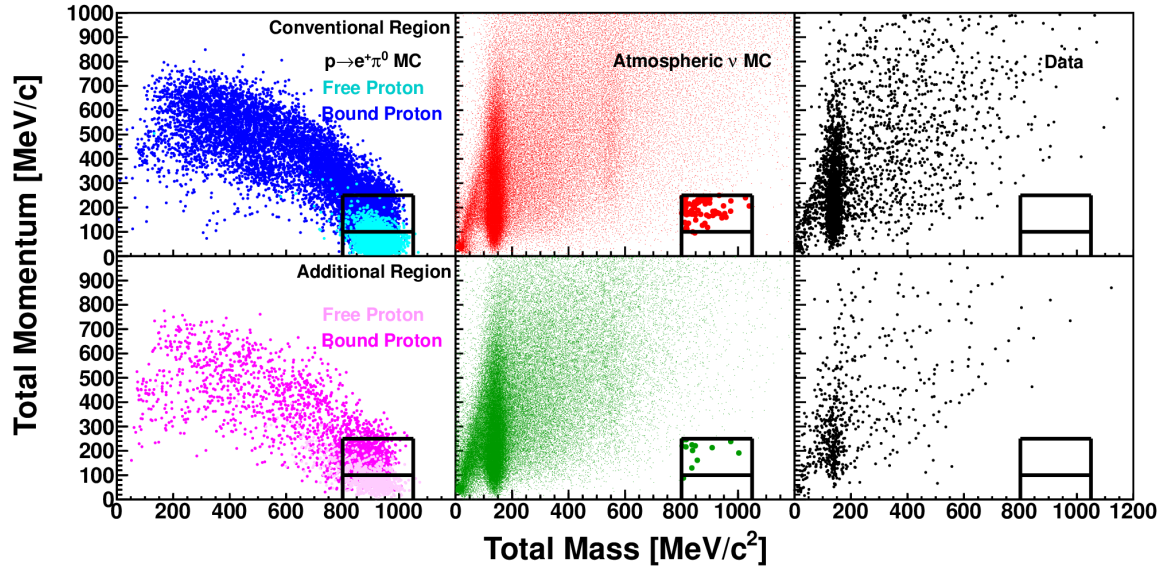


**Figure 2.22:** Signal (*left*) and background (*center*) distributions in the latest proton decay search of the Super-Kamiokande experiment for the decay mode  $p \rightarrow e^+ \pi^0$  in terms of the reconstructed total mass and total momentum parameter space. The two regions of interest are depicted as black boxes in the bottom right corner of the plots. The data distributions (*right*) indicate no candidate events in the parameter space of interest for both the conventional volume (*top row*) and the additional volume (*bottom row*). Figure taken from [141].

atmospheric events will be vital to make the best use of this cut and optimally aid the search for proton decay in future analyses.

### Relevance in DSNB searches

The Diffuse Supernova Background (DSNB) represents the combined signal of all supernovae which happened throughout the observable Universe and subsequently arrived on Earth. Since it is a continuous signal, an integrated measurement over a long period of time becomes feasible without the need for a single supernova to take place in our immediate vicinity. The quest for the detection of the DSNB signal therefore relies less on luck compared to individual supernova neutrino searches which usually cannot predict when the next signal is going to take place. However, the general faintness of the predicted DSNB signal requires measurement times on the order of 10 years and large detector volumes like Super-Kamiokande or even Hyper-Kamiokande to stand a chance at detecting it [142]. The current best upper limit on the DSNB flux for neutrino energies above 17.3 MeV was determined to be  $\phi_{\text{DSNB}} < 2.7 \text{ cm}^{-2} \cdot \text{sec}^{-1}$  by the Super-Kamiokande experiment [143].

The detection channel of choice for the DSNB is the Inverse Beta Decay (IBD) process for which an incoming antineutrino interacts with a proton and simultaneously produces a positron and a neutron. The coincidence between the prompt positron signal and the delayed neutron capture provides a very clean event signature and good background rejection capabilities. As will be pointed out more in detail in chapter 7, backgrounds such as atmospheric NC reactions can mimic the coincidence signature of DSNB events but are often accompanied by more than one neutron, in contrast to IBD interactions which will always produce exactly one neutron. The neutron multiplicity is therefore a vital

additional discrimination variable, similarly to the previously highlighted case of proton decay searches. In order to fully optimize the relevant cuts in terms of achieving the best signal to noise ratio, it would be beneficial to verify the models for neutron production in a dedicated measurement of the neutron yield in the NC channel, highlighting additional needs for more neutron multiplicity measurements.

### Current status of neutron multiplicity measurements - atmospheric neutrinos

The production of neutrons in atmospheric neutrino interactions has so far been studied by two large-scale water Cherenkov detectors, SNO and Super-Kamiokande. Both measurements have been primarily conducted as a function of the visible energy in the detectors.

When investigating the measurement by SNO [6] shown in figure 2.23, a rising slope is observable for the neutron multiplicity for growing visible energy values. This behavior roughly seems to agree with the predicted distribution based on Monte Carlo simulations. Interestingly enough, the observed neutron-energy dependency seems to be primarily caused by secondary neutron production in the medium instead of primary neutron generation in the neutrino interactions themselves: The primary neutron distribution appears flat in visible energy, while the total neutron curve (including primary and secondary neutrons) features the mentioned rising slope. Consequently, a neutron multiplicity measurement simultaneously probes the neutron generation in neutrino event generators in the context of primary neutron generation and the secondary neutron generation in the scope of hadronic models in Geant4. Disentangling the two contributions is not trivial and might require a simultaneous fit or optimized energy windows for each of them.

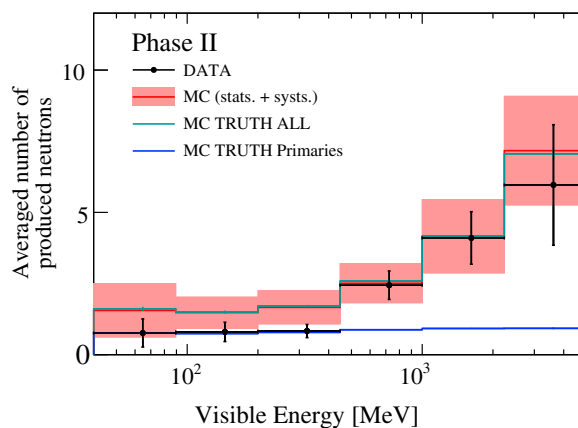


**Figure 2.23:** Measured averaged neutron multiplicity in atmospheric neutrino interactions in the SNO experiment as a function of the visible energy in the detector. The data points are compared to the predicted behavior based on Monte Carlo simulations, separated into primary neutrons from neutrino interactions (*blue*) and all neutrons (*green*), including secondary neutrons from inelastic reactions on other nuclei. Figure taken from [6].

Super-Kamiokande published a similar analysis of the neutron multiplicity in atmospheric neutrino interactions a few years prior to the SNO measurement [7]. As shown in figure 2.24, the Super-Kamiokande data roughly seems to agree with the measurement of SNO after adjusting the latter measurement for the slight difference in target materials ( $D_2O \rightarrow H_2O$ ). While still within the experimental uncertainties, Super-Kamiokande seems

to favor slightly smaller neutron multiplicity values in the visible energy range between 500 MeV and 3 GeV.

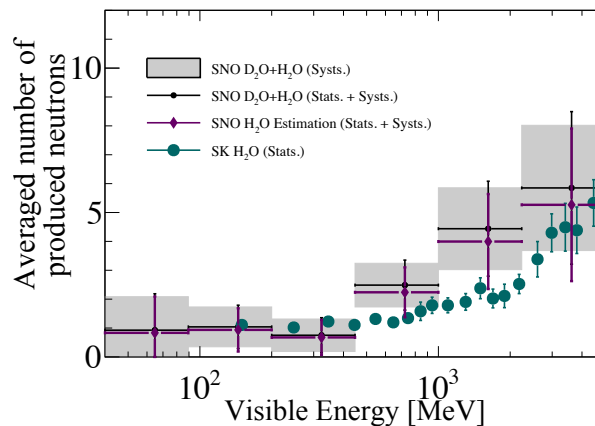


**Figure 2.24:** Measured averaged neutron multiplicities in atmospheric neutrino interactions as a function of the visible energy by the SNO and Super-Kamiokande experiments. The  $D_2O$ -based results of SNO (*black data points*) are converted to expected values in a  $H_2O$ -target medium (*purple data points*) for better comparability with the Super-Kamiokande results. Figure taken from [6].

While these neutron yield measurements for atmospheric neutrino interactions are a good starting point, they are somewhat limited by the fact that the modeling of atmospheric neutrinos requires rather complicated atmospheric simulations in order to conduct a thorough data/simulation comparison, introducing some additional uncertainty. Furthermore, both the initial neutrino direction as well as the neutrino energy are less well known compared to an accelerator neutrino environment. Measurements in an accelerator-based experiment are hence beneficial in terms of gaining additional knowledge on the neutron multiplicity in neutrino interactions, primarily in terms of the neutrino energy but also as a function of the lepton angle with respect to the neutrino direction and the momentum transfer. This is laid out in some more detail in the following paragraph by highlighting a neutron multiplicity measurement conducted on a sample of beam neutrinos in the scope of the T2K experiment.

### Current status of neutron yield measurements - accelerator neutrinos

A first analysis of the neutron yield in accelerator neutrino interactions in the T2K experiment was presented in the PhD thesis *A Study of Neutrons Associated With Neutrino and Antineutrino Interactions on the Water Target at the T2K Far Detector* by Ryosuke Akutsu [144]. The thesis investigated the neutron yield both in neutrino and antineutrino mode and compared the results with expectations based on simulations.

Figure 2.25 shows the resulting neutron multiplicity distribution as a function of the transverse muon momentum both for neutrino mode (*left*) and antineutrino mode (*right*). The particular variable of transverse muon momentum is only accessible in beam neutrino environments since the direction of the neutrino is known in this case, providing a handle on the momentum transfer due to the correlation of the two variables. While the different neutrino generators NEUT, GENIE, and NuWro feature slightly different predictions, all of

them systematically predict higher neutron numbers when compared with the actual measurement.

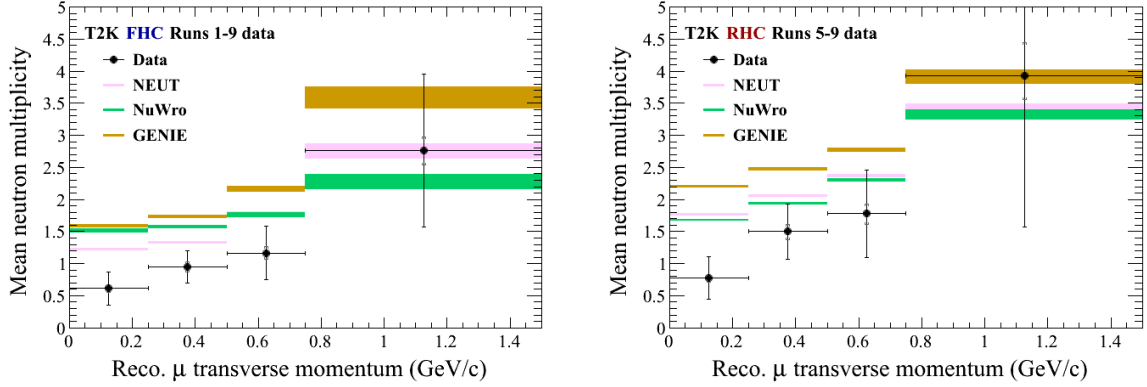


**Figure 2.25:** Average neutron multiplicities as a function of the transverse muon momentum as measured in the T2K experiment for neutrino (*left*) and antineutrino (*right*) mode. In both cases, the models tend to predict too many neutrons. Figure taken from [144].

This is further exemplified when considering the mean neutron multiplicity averaged over the entire transverse muon momentum parameter space, as shown in figure 2.26. For data taking in neutrino mode, an average multiplicity of

$$\bar{n}_{\text{data}} = (1.00 \pm 0.17(\text{stat})_{-0.08}^{+0.07}(\text{syst})) \text{ neutrons}/\nu \text{ interaction}$$

is found, to be compared with an expected value of

$$\bar{n}_{\text{MC}} = (1.50 \pm 0.02(\text{stat})) \text{ neutrons}/\nu \text{ interaction.}$$

Similar neutron yield deficiencies are observed when considering antineutrino mode. This measurement provides an important milestone for the measurement of neutron multiplicities as a function of more restricted variables such as the transverse muon momentum, particularly when considering the benefits for the validation of both neutrino generators and the simulation of inelastic scattering processes.

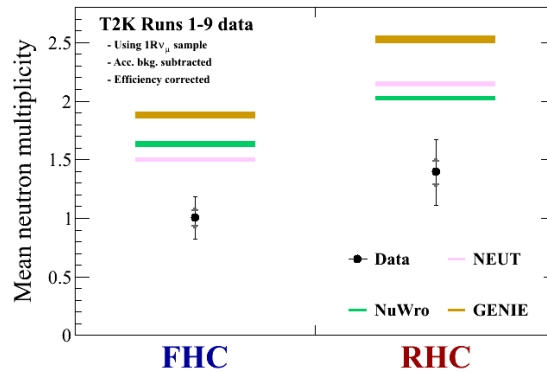


**Figure 2.26:** Mean neutron multiplicity in T2K measured in neutrino mode (labeled as *FHC*) and antineutrino mode (labeled as *RHC*). Figure taken from [144].

### Improving neutrino generators with neutron data

One additional major motivation of measuring the neutron multiplicity in neutrino-nucleus interactions lies within additional tuning information for neutrino generators like GENIE or NEUT. While some amount of data from liquid argon experiments is already available for the proton multiplicity in neutrino interactions, there are much less measurements of the number of neutrons in equivalent reactions. Since the information about the neutron and proton multiplicity are highly complementary to each other, the additional information can only help to make the generators more robust and reliable.

When comparing the nucleon multiplicity between experiments and event generators, a popular measurement scheme is as a function of the muon momentum  $p_\mu$  and the muon angle  $\cos(\theta_\mu)$  with respect to the neutrino beam. Such a measurement makes it possible to identify angular and energetic regions that show discrepancies between the data and the generators. Efforts can then be focused to optimize the utilized models with respect to these problematic regions. While a direct correlation between the multiplicity and the neutrino energy would benefit the generators even more, it is rather problematic for experiments to measure the quantity of the neutrino energy with high accuracy. Due to the difficulty of disentangling different interaction types that produce the same final state particle topology, there is always a risk of introducing a bias into the neutrino energy estimate. Exemplarily, a CC-Resonance reaction with a muon and a pion as intermediate particles might be mis-identified as a CCQE interaction in case the pion is subsequently absorbed in the nucleus. The neutrino energy would be overestimated in such a case.

As a consequence, experiments nowadays tend to measure event topologies instead of interaction types, as highlighted in section 2.3.1. By conducting the theory/experiment comparisons for such an observable-based event topology instead of the true interaction type, systematic uncertainties and biases in the event reconstruction can be minimized. At the same time, the contributions of the different true interaction types still serve as the basis for the predictions on the generator side.

When taking a look at current comparisons of data and generator predictions for the proton multiplicity case, it becomes evident that there is still room for improvement for the current models. Figure 2.27 shows an exemplary comparison of a proton multiplicity measurement by ArgoNEUT (*red*) with the prediction by GENIE (*black*). While the general features of the plot look similar in data and the simulation, it becomes clear that the current models in GENIE tend to over-estimate the number of protons that are produced in such interactions. For instance, there do not seem to be any cases with  $N_p > 4$  in the data, while the simulation predicts non-negligible contributions of proton multiplicities up until  $N_p \approx 9$ . This observation highlights the need for additional measurements by other experiments to better understand the currently observed discrepancies.

Furthermore, complementary information regarding the neutron multiplicity in similar interactions would be highly valuable as a further validation of the current generators. While figure 2.27 also shows a recent measurement of the neutron multiplicity in atmospheric neutrino interactions in the SNO experiment, additional measurements for different event samples are needed in order to get a clearer picture about the accuracy of current models for the primary and secondary neutron production. Currently both the measurements by SNO and by Super-Kamiokande were done on an atmospheric neutrino

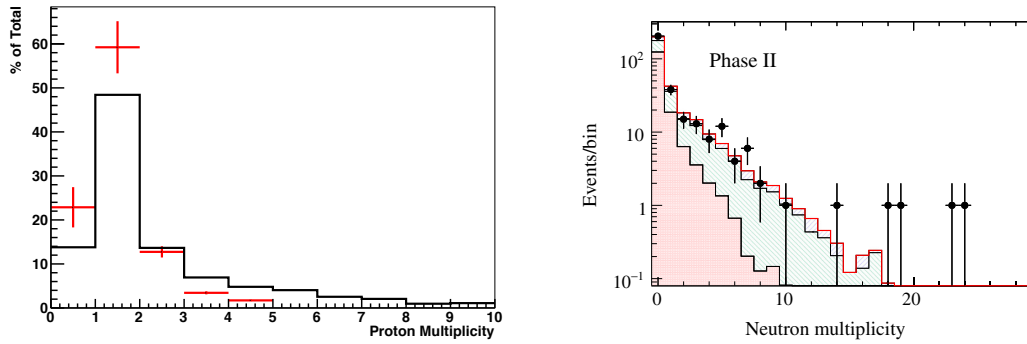


**Figure 2.27:** Left: Comparison of measured proton multiplicity in the ArgoNEUT experiment (*red*) and the predicted proton multiplicity for the same measurement by GENIE (*black*) for data taking in neutrino mode [145]. Right: Comparison of predicted and detected neutron multiplicities in atmospheric neutrino interactions as measured by the SNO experiment [6].

sample, making a similar measurement in a beam environment highly complementary and valuable. The preliminary neutron multiplicity analysis on T2K data, which was mentioned earlier, provides an important first step in this direction. Both the data of T2K and ANNIE will probe the neutron yield in an accelerator neutrino environment with even greater accuracy now that the two experiments are filled with Gadolinium-loaded target materials.



## Part II

# THE ACCELERATOR NEUTRINO NEUTRON INTERACTION EXPERIMENT



# 3

## The Accelerator Neutrino Neutron Interaction Experiment (ANNIE)

---

*“Making an access.  
It’s time to cook Gd.”*

—Vincent Fischer

Interactions of high-energetic neutrinos with nuclei in a target-medium can create a wide range of particles both in Charged Current (CC) and Neutral Current (NC) reactions. Nucleons that are ejected from the nucleus in the process of breakup reactions can provide important insight into the primary event reaction. The number of neutrons and protons that are produced in such reactions are hence a powerful tool to discriminate between different event topologies.

In order to make full use of these nucleon multiplicities in physics analyses, it is important to validate and improve the neutrino interaction generators that predict how many nucleons are produced in the aforementioned neutrino nucleus interactions. Such generators rely on the measurements of neutrino experiments to validate their models and predictions. While liquid argon neutrino experiments are very valuable in characterizing the proton multiplicity, Gadolinium-loaded water Cherenkov detectors are well suited to measure the neutron multiplicity of neutrino-nucleus interactions. Both measurements usually are conducted as a function of event kinematic variables such as the momentum transfer.

The Accelerator Neutrino Neutron Interaction Experiment (ANNIE) is such a water Cherenkov detector that aims to better characterize the neutron multiplicity of neutrino interactions in water. It is located 100 m downstream from the Booster Neutrino Beam target at the Fermi National Accelerator Laboratory and will measure both the neutron multiplicity and the cross-section of neutrino interactions in water. The following chapter will begin with a short introduction about the accelerator and the neutrino beam line in section 3.1, before presenting the ANNIE detector and all its components in more detail in section 3.2. The final sections will then cover the physics analysis goals of ANNIE in section 3.3 and the data taking framework of ANNIE in section 3.4, including the raw data monitoring capabilities, triggering schemes and the event building process.

### 3.1 THE FERMI NATIONAL ACCELERATOR LABORATORY

The **Fermi** National Accelerator **L**aboratory (Fermilab) is a well-known particle physics accelerator complex that is located in the vicinity of Chicago, Illinois in the United States. It was originally primarily known for the proton-antiproton Tevatron collider that facilitated the discovery of the top quark by the experiments  $D\bar{O}$  and the Collider Detector at Fermilab (CDF) in 1995 [146, 147]. In recent years, Fermilab has become the leading facility for accelerator-based neutrino physics experiments. With currently two operating neutrino beams, namely the Neutrinos from the Main Injector beam (NuMI) and Booster Neutrino Beam (BNB), many different experiments are able to study the properties of neutrinos by using the particles in the two beamlines. Experiments located on the BNB beamline focus on properties that can be studied on short distances, such as the cross-sections of the interactions (ANNIE [8], SBND [148], MiniBooNE [149], MicroBooNE [150]) or potential short-distance oscillations mediated by sterile neutrinos within the context of the Short-Baseline Neutrino Program at Fermilab (SBND, MiniBooNE, MicroBooNE, ICARUS [117]). Experiments on the NuMI beamline either focus on cross-sections at higher energies (MINERvA [151]) or serve as the Near Detector for Long Baseline neutrino oscillation experiments (e.g. MINOS [152], No $\nu$ A [153]). While there are currently only two main neutrino beamlines at Fermilab, construction has already begun for a third, even more powerful, neutrino beam that will deliver particles to the next-generation neutrino experiment DUNE [24].

The next section will present the features of the accelerator complex in general before the subsequent part will provide a more detailed description of the Booster Neutrino Beam. The presented information on the accelerator complex closely follows the description given in the *Fermilab Concepts Rookie Book* [154], with any additional information being cited explicitly.

#### 3.1.1 ACCELERATOR COMPLEX OVERVIEW

The Fermilab accelerator complex is schematically shown in the following figure 3.1. The beam line is divided into different sections that each fulfill a separate purpose. The *Proton Source* is shown in red and consists of the Linear Accelerator section and the Booster ring. This section will produce  $E_{\text{kin}} = 8 \text{ GeV}$  protons that are injected into the *MI-8* line that further distributes the beam to the other sections. The *Main Injector* (shown in blue) is currently the largest accelerator ring at Fermilab with a circumference of 3319.4 m and increases the proton kinetic energy from 8 GeV to 120 GeV. The *Recycler* ring (displayed in green) has similar dimensions as the *Main Injector* and is used to increase the intensity before injecting the protons into the *Main Injector*. External beam lines such as the neutrino beams BNB and NuMI are displayed in grey and deliver particles for the neutrino experiments. While the BNB is produced in interactions of 8 GeV protons directly from the *MI-8 Line*, the NuMI beam utilizes much higher-energetic 120 GeV protons from the *Main Injector* ring accelerator. Further areas of interest include the *Muon Campus* (purple) that includes experiments studying the properties of muons and the *Switchyard* that delivers a proton beam to the *Meson* and *Neutrino-Muon* areas.

The following part will mainly focus on the *Proton Source* section because of its high

significance for the Booster Neutrino Beam. Especially the Booster accelerator ring will be covered more in detail to gain a better understanding of the BNB neutrino beam structure.

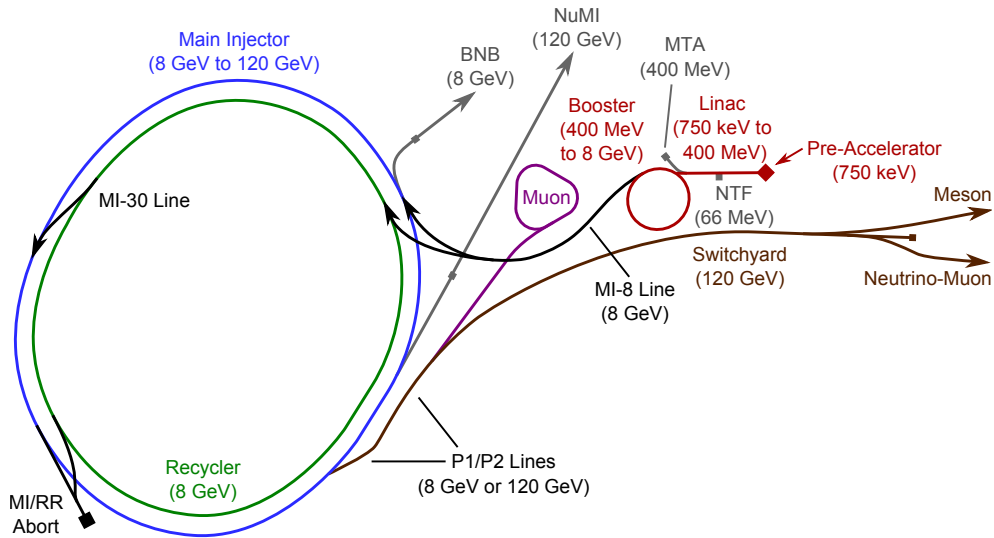


**Figure 3.1:** Overview of the Fermilab accelerator complex [154]. The different components are highlighted in different colors: The proton source that accelerates the protons to an energy of 8 GeV is shown in red, while the Main Injector that further accelerates the protons to an energy of 120 GeV is drawn in blue. The external beamlines such as the two neutrino beams BNB and NuMI are displayed in grey.

### Radio Frequency cavities and magnets

In general, the Fermilab beam complex uses two main types of devices to accelerate, focus and steer the beam. So-called Radio-Frequency cavities (RF cavities) are used to accelerate particles, while magnets are utilized to bend and focus the beam. While dipole magnets bend the beam and can be used to send particles around a corner or to keep them on a circular track, quadrupole magnets are mainly used to focus the beam. Since it is only possible to focus one transverse beam component at the same time while the other transverse component gets defocused, such quadrupole magnets are usually used in a series of focusing (F) and defocusing (D) quadrupoles to focus both transverse beam components. Higher-order magnets like sextupoles and octupoles have more specialized applications and do not play a large role for the particle beamlines at Fermilab.

RF cavities use standing electromagnetic waves with resonantly oscillating electric and magnetic field strengths to boost particles along their way. The through-going particles are accelerated by the electric field component that is present in the cavity. In order to always achieve the desired net positive acceleration, the resonance frequency of the cavity needs to be in phase with the incoming beam particles. While the synchronization of the RF cavity frequency with the beam is not a problem for linear accelerators where each cavity always receives particles of the same energy and the synchronicity can be achieved by varying the distance between the cavities, it is a larger problem for ring accelerators. In such rings, the particle energies increase with every loop and the RF frequency hence also needs to increase over time to stay in phase with the particles. The frequency increase in the cavities is mediated by so-called ferrite-tuners that are attached to the cavities and

change the cavity's inductance based on the current that is applied to them. The resonance frequency of the cavities can therefore be adjusted by changing the current that goes through the ferrite-tuners.

An important concept that is related to RF cavities is the so-called *bucket*, which describes the volume that can be accelerated by the cavity in one oscillation period. The number of particles that can be accelerated within such a bucket is called a *bunch*. Thinking of the beam lines at Fermilab, one should usually consider the particles located in such bunches throughout all beam lines. This beam property necessarily extends from the primary proton beam to the secondary beams such as the neutrino beams, which are also bunched as a consequence. The maximum number of buckets that can be simultaneously accelerated in a ring accelerator setup is the so-called *harmonic number* and will be important for the concept of a *batch* later in the text.

### Proton Source

The Proton Source section consists of the Pre-Accelerator, Linac and Booster areas. The Pre-Accelerator marks the beginning of the acceleration process and provides two  $H^-$  35 keV beam sources at a rate of 15 Hz. These ion beams are accelerated to an energy of 750 keV within the Pre-Accelerator by Radio Frequency (RF) quadrupole magnets before they are forwarded to the Linac section.

After the Pre-Accelerator stage, the 750 keV hydrogen ions are subsequently fed into the linear accelerator complex. The Linac has a length of 150 m and consists of a Low-Energy Linac section and a High-Energy Linac section. The former consists of 5 RF cavities that accelerate the ions to an energy of 116.5 MeV, while the latter consists of 10 RF stations and further accelerates the particles to an energy of 400 MeV. Those 400 MeV ions are then forwarded to the Booster ring with an initial revolution period of 2.2  $\mu\text{s}$  at the time of injection.

### Booster Ring

A stripping foil removes the electrons from the ions such that only protons remain and are accelerated in the Booster ring. The Booster ring has a circumference of 474.2 m and is made up of 19 RF cavity stations. Those stations increase the proton energy from 400 MeV to 8 GeV by adjusting their RF frequencies from 37.8 MHz to 52.8 MHz. At the same time, the revolution time decreases from 2.2  $\mu\text{s}$  at injection to 1.6  $\mu\text{s}$  at extraction. The harmonic number for the Booster accelerator is 84, which means that 84 proton bunches can be accelerated at the same time in the Booster ring. Such a group of 84 bunches is called a *batch*, and those batches are sent to the neighboring MI-8 Line at a rate of 15 Hz.

The MI-8 Line distributes the  $E_{\text{kin}} = 8 \text{ GeV}$  protons to a variety of possible destinations including the Booster Neutrino Beam (BNB), the Booster dump, the Main Injector and the Recycler rings. The BNB beam line is of major interest for ANNIE and will be highlighted and explained in the following subsection.

### 3.1.2 THE BOOSTER NEUTRINO BEAM (BNB)

The Booster Neutrino Beam at Fermilab is produced in interactions of protons with a kinetic energy of 8 GeV (momentum of 8.89 GeV) coming from the MI-8 Line with a stationary Beryllium target located at the MI-12 facility. The beam composition is dominated by muon neutrinos ( $\sim 93\%$ ), followed by muon anti-neutrinos ( $\sim 6\%$ ) and electron (anti) neutrinos ( $\sim 1\%$ ) [155]. This section will describe how the neutrino beam is created and highlight the main features of the different elements of the beam line. It will also give some overview of the expected structure of the beam and highlight the resulting neutrino spectra.

Figure 3.2 provides an overview of the different experiments that are located in the Booster Neutrino Beam line. While both the ANNIE experiment and the SBN Near Detector are located very closely to the BNB target hall ( $\sim 100$  m), the MicroBooNE and SBN Far Detectors are positioned further away. More precisely, MicroBooNE is located at a distance of 470 m and the SBN Far Detector is positioned 600 m away from the Booster Target Hall. In addition to these experiments that are visible in the figure, the ICARUS detector is also present in the Booster Neutrino beam line and is integrated as a part of the Short Neutrino Baseline program.

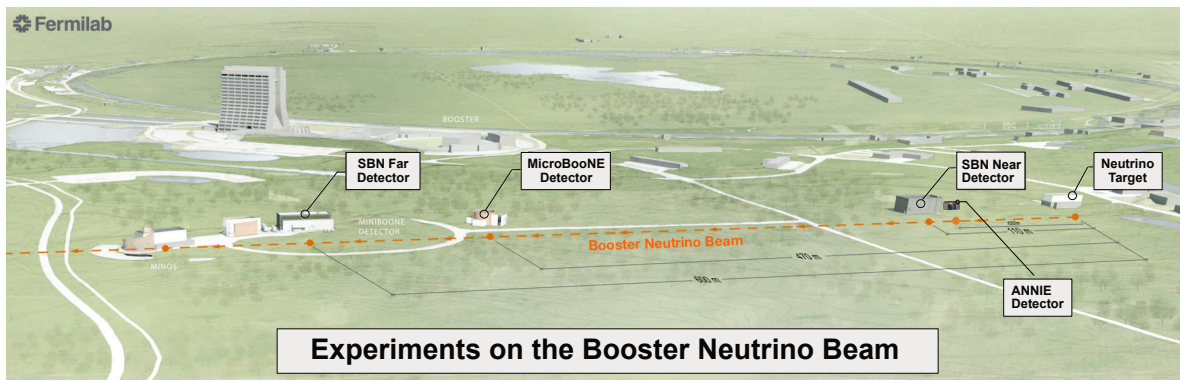


**Figure 3.2:** Overview of the experiments located on the Booster Neutrino Beam. The SBN Near and Far Detectors and MicroBooNE form the Short Baseline Neutrino Program at Fermilab together with the ICARUS experiment. Figure adapted from [117].

#### General overview of the BNB

In order to generate the Booster Neutrino Beam, protons are directed from the Booster synchrotron ring onto a Beryllium target in the MI-12 BNB target hall, as shown schematically in figure 3.3. Secondary particles that are produced in the proton-Beryllium interactions are focused by means of a magnetic focusing horn in downstream direction. The horn will focus either positively or negatively charged particles based on its polarity while simultaneously de-focusing particles of the opposite charge. The polarity of the horn can be changed depending of the needs of the experiments: By switching the polarity, one can select whether a neutrino or antineutrino beam is supposed to be created.

The forward-directed secondary particles enter the 50 m long decay region in which the secondary particles decay into neutrinos, forming the tertiary neutrino beam. While the neutrinos travel unhinged to the experiments along the beam line, other particles that are still present are stopped by an absorber at the end of the decay region.

The Booster Neutrino Beam is primarily composed of muon neutrinos due to the preferred decay of pions into muons alongside the fact that pions are making up the largest fraction of produced secondary particles. The peak of the neutrino energy spectrum is located at an energy of  $E_{\nu, \max} \sim 800 \text{ MeV}$ , where the exact shape of the spectrum will be highlighted in a later paragraph.

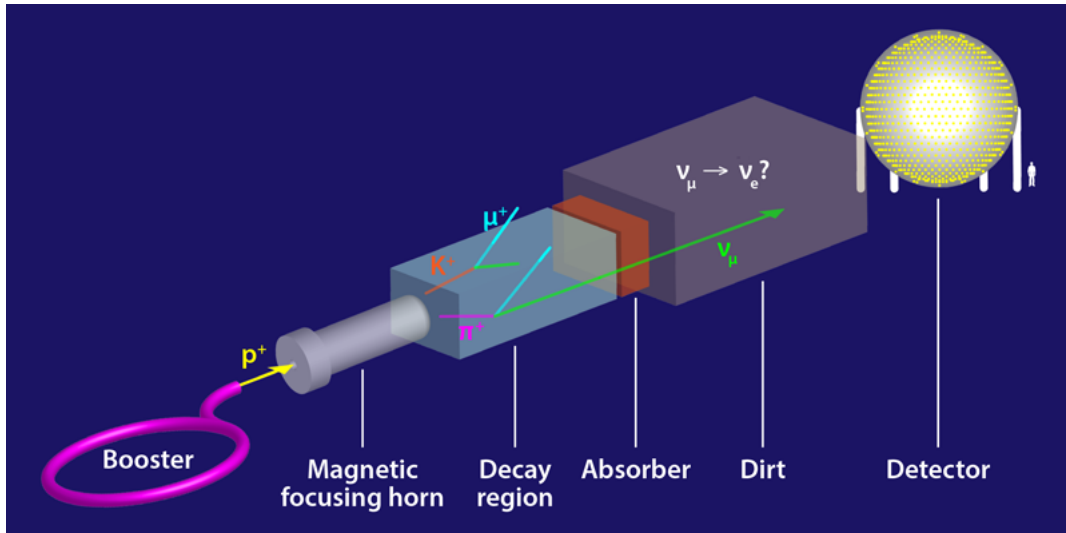


**Figure 3.3:** Overview of the BNB creation process. Protons from the Booster Ring are guided onto a beryllium target. Secondary particles that are created in this interaction are focused by a magnetic focusing horn. The forward-directed secondary particles then decay into neutrinos in the 50 m long decay region before arriving at the neutrino detectors (MiniBooNE exemplarily shown in this figure). Figure taken from [156].

The maximum average repetition rate for the Booster Neutrino Beam is 5 Hz, limited by the design of the magnetic horn and power supply. A maximum of  $5 \cdot 10^{12}$  protons per pulse can be handled. Out of the 84 bunches that can be accelerated simultaneously in the Booster accelerator ring, 81 bunches are filled with protons. The bunches are 2 ns wide and 19 ns apart from each other, resulting in a total width of the beam spill of  $\Delta t_{\text{spill}} = 19 \text{ ns} \cdot 84 = 1596 \text{ ns} \approx 1.6 \mu\text{s}$ .

### Beryllium target & magnetic horn

The BNB target is composed of seven identical cylindrical slugs made of Beryllium with a radius of  $r = 0.51 \text{ cm}$ . The cylinders are lined up in a row, resulting in a total length of  $l = 71.1 \text{ cm}$  [155]. Beryllium as a material was chosen based on two main considerations: In case of a replacement, the residual radioactivity of the Beryllium target would be rather low compared to other possible target materials. In addition, it was deemed more efficient in terms of energy loss considerations in the scope of a cooling system [155].

The magnetic horn is made of an aluminum alloy and creates the necessary magnetic field based on 143  $\mu\text{s}$  long pulses of current flowing through the outer and inner conductors, with current values around 170 kA [155]. The geometric setup of the horn is shown in figure 3.4 and features the inner conductor (green), the outer conductor (grey, transparent) and the elements of the water cooling system. The Beryllium target is included in the inner conductor and was inserted from the left side. The concentric magnetic field is present in the inner conductor and in the cavity region between the inner and outer conductor and

decreases with increasing distance to the central beam axis as  $1/R$ . Cooling is provided by a closed water system that is able to spray water onto the conductors. The polarity of the horn can be reversed by changing the direction of the current: To generate the beam in neutrino mode, the current is sent into the inner conductor from the left and returns alongside the outer conductor.

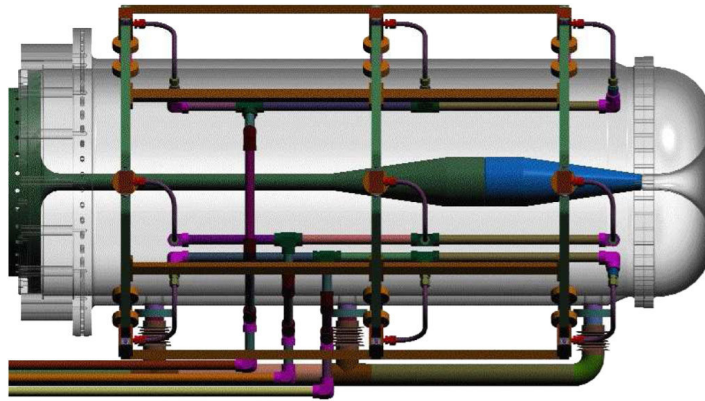


**Figure 3.4:** Schematic drawing of the magnetic horn in use for the Booster Neutrino Beam. The outer conductor is depicted in grey and is made transparent to enable a look at the interior of the horn. The inner conductor is shown in green, while the pipes of the water cooling system can be seen on the top and bottom of the horn. Figure taken from [155].

### Beam monitoring devices

Several beam monitoring systems are in place at multiple positions upstream of the target to ensure stable beam operations as well as minimal losses of the proton bunches. The monitors are designed in such a way that they do not disturb the beam or lower the intensity of the incoming protons. Among these monitoring devices, there are two toroids (TOR875 and TOR860) that measure the intensity of the beam in units of protons per pulse, 22 beam position monitors (BPMs) that check the beam position and width, and a resistive wall monitor (RWM) that records the timing and intensity of single buckets within a beam spill. The following paragraphs will briefly introduce the concepts of the different beam monitoring devices based on information found in reference [154].

Toroids are ring-like objects made out of ferrite material. Proton bunches passing through the toroid can be interpreted as an electric current and are hence accompanied by a surrounding magnetic field according to Ampere's law. The change in the magnetic field strength within the ferrite produced by the passing proton bunch induces an electrical current in a pickup loop wrapped around a section of the ferrite. This current in the pickup loop is then measured by connecting a resistance to the pickup loop and measuring the voltage. Since the strength of the magnetic field is determined by the number of protons within such a bunch, the measured voltage in the pickup loop can then be converted to the absolute number of protons in the bunch, *i.e.* the beam intensity.

Beam Position Monitors (BPMs) use the principle of induction to determine transverse beam deviations. This monitoring device consists of two opposing electromagnetic striplines or plates that experience an induced negative voltage when a positively charged beam is passing through. By comparing the measured voltages on the two plates, one can determine whether the beam passed through the center of the pipe or whether the beam

is shifted by some offset. In the case of a centered beam, both plates will see the same voltage, while a voltage difference will be apparent in case of a non-centered beam. A set of two such plates can measure the displacement either in vertical or in horizontal direction, while a combination of 2 perpendicularly arranged pairs can achieve a combined vertical+horizontal displacement measurement. In the case of the BNB, there are 22 BPMs installed in total. Five of the BPMs measure horizontal displacement only, a set of five different BPMs measure the vertical displacement, and 6 pairs of combined BPMs measure the horizontal and vertical displacement simultaneously [157].

In addition to the vertical displacement being measured by the BPMs, the longitudinal beam profile is supervised by the Resistive Wall-Current Monitor (RWM). This device makes use of negative charges in the wall of the vacuum chamber that are induced by the passing positive beam charges. By measuring the intensity of this induced wall current at a particular position as a function of the time, the longitudinal beam profile can be characterized. By identifying the times of passing protons in that way, individual beam bunches can be identified and cross-referenced with events detected in the neutrino detector.

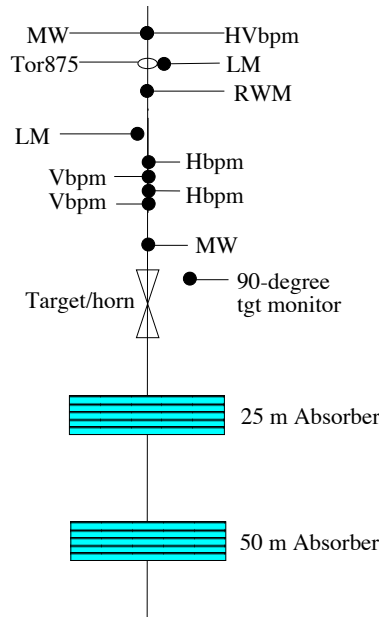
One last important monitoring component are beam loss monitors. They are placed slightly besides the main beam line and monitor the amount of secondary particles that are produced by beam particles that collide with the beam pipe. Most commonly, beam loss monitoring devices are made out of an argon-filled cylinder with two concentric electrodes. Secondary particles that pass through the loss monitor ionize the gas, and the ions are accelerated towards the inner electrode, resulting in a measurable current.

Figure 3.5 shows the last few monitoring elements of the BNB proton beam upstream of the target/horn area. The first element is a combined vertical and horizontal BPM (HVbpm), followed by the second toroid of the BNB (TOR875), the RWM, a beam loss monitor (LM) and a series of single horizontal and vertical BPMs (Hbpm, Vbpm). All these beam quality parameters are supervised around the clock by shifters from the accelerator division. If a problem occurs at some point of the beam line, an expert is notified and takes care of it as soon as possible.

### Neutrino flux predictions

Neutrino flux predictions for the Booster Neutrino Beam were calculated by the MiniBooNE collaboration based on thorough simulations of the proton-Beryllium interactions, followed by propagation of the resulting particles in the scope of a Geant4 simulation [155]. Wherever possible, experimental data was used for the cross-sections of the primary proton interactions, while default models were used for the subsequent propagation of the particles. Custom decay models were then applied to simulate the neutrino decay modes of the secondary pions, kaons and muons that were produced in such interactions. Figure 3.6 shows the resulting neutrino spectra for the simulation in neutrino-mode as well as for the antineutrino-mode.

Muon neutrinos ( $\nu_\mu$ ) are the most dominant neutrino species in neutrino-mode and make up a fraction of 93.6% of all events, followed by muon anti-neutrinos ( $\bar{\nu}_\mu$ ) representing 5.86% of all events. The electron-related fluxes are much smaller, with a fraction of 0.52% being electron neutrinos ( $\nu_e$ ) and 0.05% electron anti-neutrinos ( $\bar{\nu}_e$ ). Both for



**Figure 3.5:** The last beam monitoring elements upstream of the BNB target. The second toroid (TOR875) and the Resistive Wall Monitor (RWM) are located next to each other. In addition, several beam position monitors (BPMs) are visible. Figure adapted from [157].

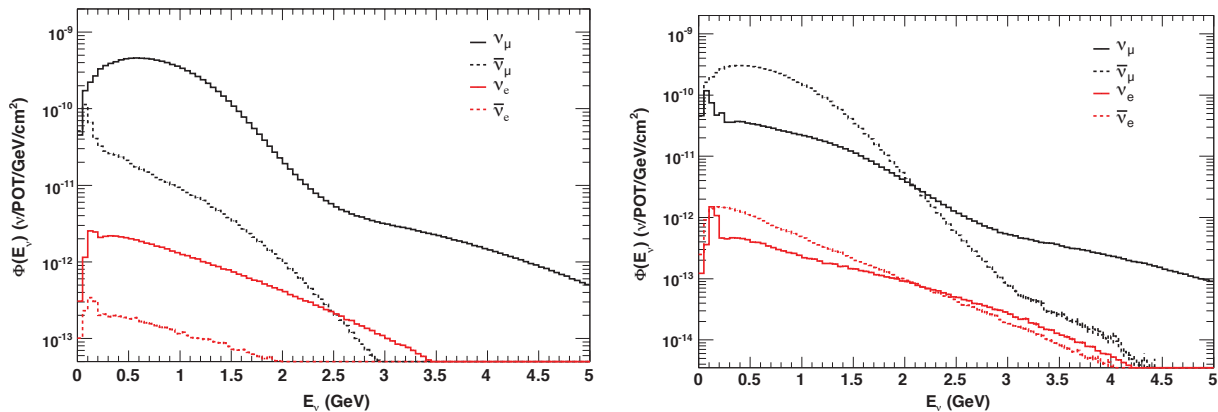


**Figure 3.6:** Neutrino flux prediction for the BNB in neutrino (*left*) and antineutrino (*right*) mode. Muon neutrinos are depicted in black, while electron neutrinos are shown in red. Neutrinos are shown as solid lines, while antineutrinos are given by dashed lines. Figures taken from [155].

electron and muon neutrinos, the contamination of anti-neutrinos in neutrino-mode is rather small at levels of  $\sim 10\%$ . In anti-neutrino-mode, the contamination by neutrinos compared to the main component of anti-neutrinos is a little higher: Muon neutrinos make up 15.71% of the flux in this case, to be compared with a flux fraction of 83.73% for muon anti-neutrinos. When looking at electron neutrinos, the flux of electron neutrinos (0.2%) is even half the flux of electron anti-neutrinos (0.4%).

This effect can be understood better when investigating the decay modes for the different flux components more closely, as shown in table 3.1. Muon neutrinos in neutrino mode are mainly produced by decays of pions, which provide neutrinos in the energy range up until 3 GeV. However, the  $\nu_\mu$  energy spectrum extends to values beyond 3 GeV and shows non-negligible flux contributions up until energies of 5 GeV. This higher-energetic part

of the spectrum is generated by the second most important decay channel  $K^+ \rightarrow \nu_\mu + X$ , which starts to dominate for energies above 2 GeV [155]. The  $\bar{\nu}_\mu$  flux, on the other hand, has a negligible contribution from  $K^-$  decays due to a lower negative kaon production rate in the interactions. The muon antineutrino spectrum hence only extends up until energies of  $\sim 3$  GeV.

Type	Flux ( $\nu/\text{cm}^2/\text{POT}$ )	Flux fraction	Main decay	Second decay
$\nu_\mu$	$5.19 \cdot 10^{-10}$	93.6%	$\pi^+(96.72\%)$	$K^+(2.65\%)$
$\bar{\nu}_\mu$	$3.26 \cdot 10^{-11}$	5.86%	$\pi^-(89.74\%)$	$\pi^+ \rightarrow \mu^+$ (4.54%)
$\nu_e$	$2.87 \cdot 10^{-12}$	0.52%	$\pi^+ \rightarrow \mu^+$ (51.64%)	$K^+(37.28\%)$
$\bar{\nu}_e$	$3.00 \cdot 10^{-13}$	0.05%	$K_L^0(70.65\%)$	$\pi^- \rightarrow \mu^-$ (19.33%)

**Table 3.1:** The table shows the fluxes of the different neutrino components in the BNB in neutrino mode as absolute values and as fractions of the total flux. The main decay mode responsible for creating the respective neutrino species is shown alongside the second most important decay mode. Values are taken from the MiniBooNE flux prediction paper [155].

When contrasting the main decay modes for neutrino and antineutrino beam operation mode (shown in table 3.2), some differences become apparent: In the dominant flux component in antineutrino mode, Kaon decays play a much smaller role than in neutrino mode due to their smaller production rate. In addition, decays from positive kaons become even more significant even though positive particles are effectively defocused by the horn polarity. This effect is due to the positive particles having a harder momentum spectrum because of the leading particle effect, leading to less de-focusing of the positive particles in anti-neutrino mode compared to negatively charged particles in neutrino mode [155]. The combination of less defocusing for positively charged particles alongside a higher production rate of positive kaons and pions leads to the observed asymmetry in the contamination of the neutrino beam in neutrino-mode and antineutrino-mode. Since the first beam data taking campaign of phase II in ANNIE was conducted entirely in neutrino-mode polarity, the presented differences won't affect the current analysis, but might be important for possible future data taking campaigns with BNB in antineutrino mode.

Type	Flux ( $\nu/\text{cm}^2/\text{POT}$ )	Flux fraction	Main decay	Second decay
$\nu_\mu$	$5.42 \cdot 10^{-11}$	15.71%	$\pi^+(88.79\%)$	$K^+(7.53\%)$
$\bar{\nu}_\mu$	$2.93 \cdot 10^{-10}$	83.73%	$\pi^-(98.4\%)$	$K^-$ (0.18%)
$\nu_e$	$6.71 \cdot 10^{-13}$	0.2%	$K^+(51.72\%)$	$K^0(31.56\%)$
$\bar{\nu}_e$	$1.27 \cdot 10^{-12}$	0.4%	$\pi^- \rightarrow \mu^-$ (75.67%)	$K^0(16.51\%)$

**Table 3.2:** The table shows the fluxes of the different neutrino components in the BNB in anti-neutrino mode as absolute values and as fractions of the total flux. The main decay mode responsible for creating the respective neutrino species is shown alongside the second most important decay mode. Values are taken from the MiniBooNE flux prediction paper [155].

While these neutrino flux predictions were made specifically for the MiniBooNE experiment, it is reasonable to apply them also to the case of ANNIE. Besides the absolute flux values, the other properties should be very similar also for different positions along the BNB baseline. We can therefore use the same neutrino flux spectra for simulating neutrino interactions in the ANNIE detector and conducting the data analysis.

### 3.1.3 ACCELERATOR CLOCK SIGNALS

The Fermilab accelerator division provides several beam synchronization signals that facilitate the communication between the different accelerator subsystems. Furthermore, those signals can be used by the beam experiments to synchronize their data acquisition with the beam. The most important clock system at Fermilab is the so-called Tevatron Clock (TCLK) that was established back when the Tevatron experiment went online and can store up to 256 unique clock signals to timestamp events across the whole accelerator complex [158].

Table 3.3 provides a brief overview of six TCLK signals that are related to the Booster acceleration ring and more specifically to the two neutrino beamlines BNB and NuMI. When taking a closer look at the more general Booster-related clock signals, the TCLK \$0C signal represents the 15 Hz Booster repetition rate, which is synchronized to the minimum value of the magnetic field in the Gradient Magnet Power Supplies (GMPS) of the Booster System [159]. For each recurring \$0C signal, there is either a coincident TCLK \$10 or TCLK \$11 signal, with the former indicating upcoming beam in any of the beamlines and the latter representing a so-called *Null Cycle*, i.e. no delivery of protons to any of the beamlines.

The clock signals that are most important for the neutrino beamlines are the TCLK \$15, \$1D, and \$1F signals. The TCLK \$1F signal is called *Booster Extraction Sync* (BES) and provides the reference for when beam is extracted from the Booster Ring and forwarded to one of the other beamlines. This signal is issued independently of the final destination of the beam, i.e. the beam can either be forwarded to the Main Injector ring, the muon campus or to the Booster Neutrino Beam target. In order to determine whether the beam is e.g. expected on the Booster Neutrino Beam line, this signal needs to be evaluated in coincidence with another TCLK clock signal, namely the \$1D signal that indicates that Booster is prepared to send the beam to the BNB line. ANNIE hence uses a coincidence of the \$1D and \$1F signals to trigger on beam events. The TCLK \$15 signal, on the other hand, would indicate that beam is expected to be sent to the NuMI beamline. A coincidence of \$15 and \$1F clock events would thus be used by neutrino events on the NuMI beamline.

ANNIE also makes use of TCLK \$1F signals with no coincident \$1D signal. Since no beam is expected for such cases, ANNIE uses these clock signals to record off-beam data and calibration data in between the neutrino beam triggers. These data samples can then be used to characterize backgrounds and understand the stability and behavior of the detector. The different trigger schemes are presented in more detail in the upcoming chapter 3.4.2.

TCLK Clock Signal	Meaning
\$0C	15 Hz Booster clock
\$10	Booster Reset for Accelerating Beam Cycle
\$11	Booster Reset for Null Cycle (no beam)
\$15	Booster Prepare for NuMI
\$1D	Booster Prepare for BNB
\$1F	Booster Extraction Sync (BES) for Beam cycle

**Table 3.3:** The most important TCLK clock signals in the scope of ANNIE [160]. The trigger for beam events in ANNIE requires a coincidence of the \$1F and \$1D clock signals.

## 3.2 THE ANNIE DETECTOR

The Accelerator Neutrino Neutron Interaction Experiment (ANNIE) is a water-based neutrino experiment in the Booster Neutrino Beam and has two main objectives. On the one hand, the measurements of the neutron multiplicity and the cross-section will be important for a better understanding of the processes governing neutrino interactions in water. On the other hand, the experiment serves as a testbed for new technologies in the field of photosensor technologies and detector target materials. Concerning the first aspect of new photosensor technology, Large Area Picosecond Photodetectors are novel photodetectors that are able to resolve single photon hits with a spatial resolution of  $<1$  cm and timing capabilities of  $\sim 60$  ns, which greatly improves the reconstruction capabilities compared to conventional PMTs. The innovative detector target materials used in ANNIE include Gadolinium-doped water for better neutron detection capabilities in the current phase II and Water-based Liquid Scintillator (WbLS) in a future phase III of the experiment.

The detector is composed of multiple subsystems which are needed to characterize different aspects of the detected events. The center piece of the detector is the water tank filled with Gadolinium-loaded water and instrumented with 132 PMTs and 5 LAPPDs. Interactions of neutrinos are detected within this volume by making use of the Cherenkov light emitted by the corresponding charged lepton in Charged Current interactions. The details of this water tank system segment are highlighted in subsection 3.2.1.

Since the BNB is mainly composed of muon neutrinos, we will predominantly detect muons that are produced in the neutrino interactions. Due to their minimal ionizing nature, they can travel a large distance before being stopped. As such, most of the neutrino-induced muons in ANNIE will leave the water tank and hence not deposit their full kinetic energy into the tank. In order to still get an energy estimate for those particles, the scintillator-steel sandwich detector Muon Range Detector (MRD) is placed downstream of the tank. The main characteristics of this subsystem are highlighted in subsection 3.2.2.

Interactions of neutrinos in the rocks upstream of the water tank can also generate muons that are able to reach the water tank. Such *dirt muons* need to be singled out in order to avoid unwanted backgrounds for our neutrino measurement. They are spotted by the scintillator veto system of ANNIE that is located directly upstream of the water tank. A more detailed description of this Front Muon Veto (FMV) is given in subsection 3.2.3.

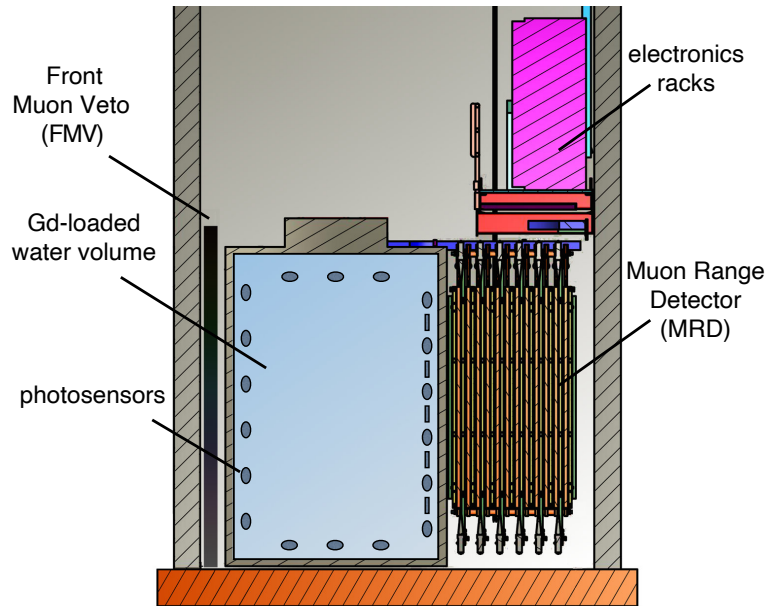


**Figure 3.7:** Schematic view of the ANNIE detector hall with the different components. From left to right, the Front Muon Veto (FMV), water tank, and Muon Range Detector (MRD) are visible. The second floor contains all the electronics racks, while the third floor on the very top stores the DAQ and monitoring computers.

Improved timing resolution of photon detection holds great potential with respect to reconstructing more details of the neutrino interaction. In the case of ANNIE, LAPPDs are used to get such fast timing capabilities. The working principle and calibration results of those photosensors are presented in more detail in subsection 3.2.4.

### 3.2.1 THE WATER TANK

Neutrino interactions in ANNIE are detected via the emission of Cherenkov light in the Gadinated (Gadolinium-loaded) water tank induced by charged particles with energies above their Cherenkov threshold. The tank itself is a steel cylinder with a radius of  $\sim 1.5$  m and a height of  $\sim 4$  m. The photosensors are mounted on a separate octagonal steel structure which is placed inside of the larger water tank. This subsystem is called the *Inner Structure* of ANNIE. The left side of figure 3.8 shows a 3D model view of the water tank and the Inner Structure. The outermost boundaries are defined by the outer water tank, while the Inner Structure containing the PMTs is placed in the center of the tank. Different photomultiplier types are depicted in different colors: The bottom PMTs (*blue*) are 10" Hamamatsu-type PMTs from the LUX experiment, while the twenty top PMTs (*red*) are 11" High-Quantum-Efficiency PMTs from ETEL. Concerning the side walls, there are forty new 8" Hamamatsu PMTs (*red*), while the grey photosensors are 10" PMTs from the WATCHBOY and WATCHMAN experiments. Forty of these 10" PMTs belong to the WATCHBOY experiment, while the 4 HQE PMTs belong to the WATCHMAN collaboration. A picture of the Inner Structure taken during construction and mounting of the PMTs is shown on the right side of figure 3.8.

The top part of the tank is closed off by the circular tank lid, which was also manufactured

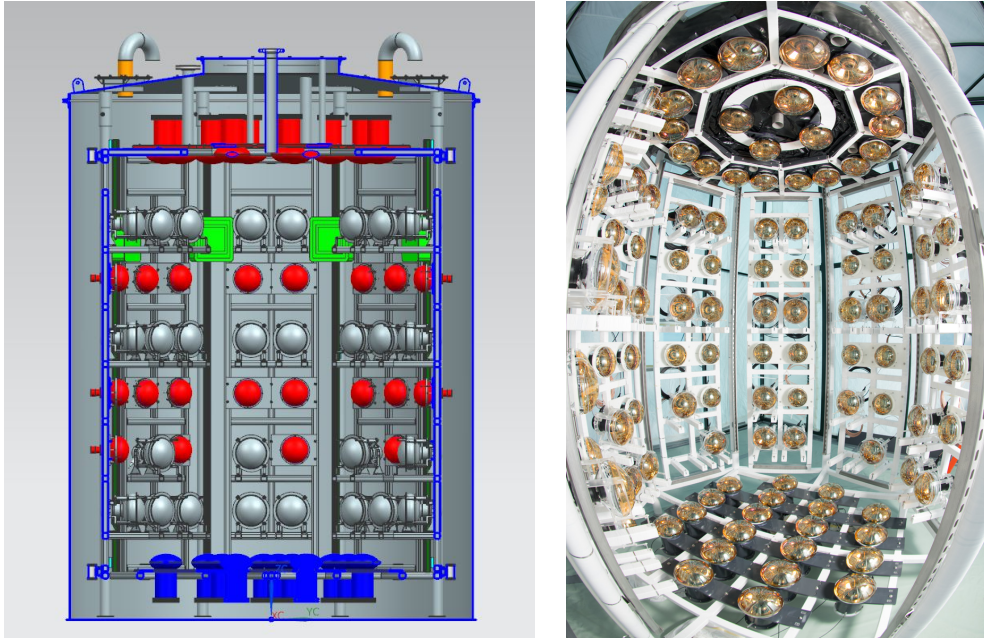


**Figure 3.8:** **Left:** 3D model of the Inner Structure inside of the water tank. Different PMT types are displayed in different colors. The position of the LAPPDs (*green*) is not indicative of their final positioning and only highlights the relative azimuthal  $\varphi$ -position of them in the water tank. **Right:** Picture of the ANNIE Inner Structure with all PMTs mounted before it was inserted into the ANNIE tank.

out of stainless steel. The lid seals off the water tank and contains one larger 1m-wide circular hatch in the middle, and further 5 smaller calibration ports and 8 rectangular LAPPD slot openings. The four innermost top PMTs are actually attached to the hatch and not to the Inner Structure itself. The calibration ports are used to lower radioactive sources into the detector in the scope of dedicated calibration campaigns. The LAPPD "mailbox" slots on the top lid can be utilized to lower the LAPPDs into the water tank via 8 LAPPD columns that extend from the top to the bottom of the tank. Up to 2 LAPPDs can be stored per column and their exact positioning along the column was optimized via simulation studies that assessed the reconstruction performance as a function of the LAPPD positions.

### LAPPD deployment

ANNIE is going to use 5 LAPPDs which are deployed in water-proof housing units to prevent humidity from reaching any of the photosensors. Since their timing is primarily used to improve the vertex reconstruction capabilities of the muon tracks, a positioning in downstream columns was chosen for the greatest benefit.

The design of the LAPPD column structure was chosen to gain flexibility regarding the LAPPD deployment. Since all LAPPDs can be lowered into the water tank after the tank is already filled with water, a variable number of LAPPDs can be inserted whenever they are available. This method allows to take PMT-only data as long as the preparations for the LAPPD deployment are not complete. Furthermore, a potential extension of the detector setup with the deployment of additional LAPPDs (beyond 5) poses no issues at all since

they can simply be inserted via the mailbox slots whenever they become available.

### **Gadolinium compatibility**

Gadolinium-loading of the detector with 0.2%  $\text{Gd}_2(\text{SO}_4)_3$  improves the neutron detection capabilities by a large amount. At the same time, one needs to be rather careful with the compatibility of the detector materials and the Gd-loaded water. Some materials will dissolve into the water and negatively impact the transparency of the detector medium. A dedicated laboratory measurement setup at UC Davis investigated the compatibility of a multitude of materials with Gadolinium-doped water. Stainless Steel 402 was found to be compatible and was therefore used in the construction of the Inner Structure and the water tank. In addition, the whole steel structure was pickle passivated and electro-polished to remove any minor rust spots on the steel structures.

Optical separation of the PMT-enclosed water volume and the outside water segment is achieved via a black plastic liner that is covering the complete Inner Structure. In a similar manner, the inner walls of the tank are separated from the water by a white plastic liner sheet. Care was taken to ensure that both the black and white plastic liner do not contain any UV stabilizers that could dissolve into the water and reduce the transparency. The complete Inner Structure was additionally wrapped in teflon to further improve Gadolinium compatibility. Due to the rather reflective nature of teflon, this wrapping will play a large role for the correct modeling of light propagation in the simulation, as described in chapter 5.

### **Electronics**

The waveforms of all PMTs in the water tank are sampled by 500 MHz FADC cards that are mounted in three VME crates. Trigger signals are forwarded to those 4-channel ADCs via Master Timing (MT) cards that are also located in the same VME crates. Different readout schemes will record different waveform time windows. For example, regular beam triggers will record a waveform buffer of 2  $\mu\text{s}$ , while an extended readout window of 70  $\mu\text{s}$  can also be recorded to search for potential neutron signals.

The required positive High Voltage of  $\sim 2$  kV for the water tank PMTs is provided by CAEN 1734P modules that are stored in a CAEN SY527 HV crate. The HV is forwarded to a pick-off box designed at Iowa State University and sent to the PMTs from there. The same cables are also used to send the waveforms from the PMTs back into the pick-off box and further transmit them to the VME ADC cards from there.

### **3.2.2 THE MUON RANGE DETECTOR (MRD)**

The Muon Range Detector (MRD) is a scintillator-steel sandwich detector that is designed to range out muons that were produced in neutrino interactions in the water tank since the typical muon energies are so high that muons almost always leave the water tank. The steel layers facilitate a characterization of the muon energy since they are capable of stopping the muons pretty effectively. The scintillator layers, on the other hand, consist of multiple paddles per layer and are connected to PMTs at the borders of the paddles.

The scintillation signals are used to record the position and timing of the muon track throughout this subdetector. This information is used to reconstruct the precise muon track and determine the angle at which the muon was propagating. Furthermore, the track information can be used to determine whether the muon track is fully contained and stopped in the MRD. Only for such stopped muon events, we can use the information about the deposited energy to obtain a meaningful handle on the total muon energy - also taking into account the deposited energy in the water tank. Muons that fully traverse the MRD or exit on the side only deposit a part of their energy in the steel layer. For those cases, we can't determine the total energy of the muon and hence can't take them into account for our analysis.

### Geometry and setup

The left side of figure 3.9 shows a picture of the MRD in ANNIE hall. PMTs are visible on all four sides of the detector. The top and bottom PMTs instrument the vertical scintillator paddles of the MRD, while the PMTs on the left and right sides are used to read out the horizontal layers of the MRD. In total, we have 306 paddles that are distributed over 5 horizontal and 6 vertical layers. Each paddle is 15-20 cm wide (depending on the exact paddle type) and 150 cm long, and extends from the location of its PMT up until the center of the respective layer. For each layer, a scintillator strip as defined by two opposing PMTs is realized by a combination of paddles that meet in the center of the layer. Eleven steel layers of 2" ( $\sim 5.1$  cm) width separate the  $\sim 1$  cm wide scintillator layers. The right side of figure 3.9 shows a more schematic view of the detector geometry from a sideways perspective. The different layers and the alternating horizontal and vertical layer structure of the sandwich detector become apparent. Table 3.4 provides an overview of the different layers, their orientation, and the number of paddles for each respective layer.

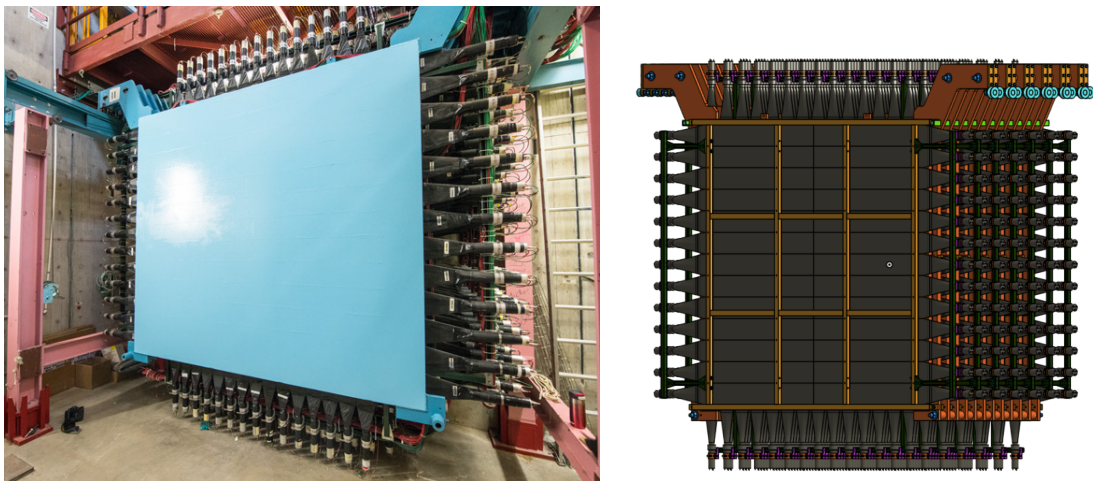


**Figure 3.9:** **Left:** An image of the Muon Range Detector in ANNIE hall. The 2-inch photomultiplier tubes are visible on the sides of the MRD for the horizontal layers and on top and bottom of the MRD for the vertical layers. The photo was taken before the tank was placed in the hall. **Right:** 3D model of the MRD detector setup. This side view provides some more perspective on the depth of the muon detector and the alternating vertical and horizontal layer structure.

While the number of paddles per layer varies from 26 to 34 depending on the respective layer, one further thing to note is that there are two different kinds of scintillator paddles. Most paddles were refurbished from the SciBooNE experiment and are 20 cm wide. However, a couple of paddles were also recycled from the KTeV experiment instead and are only 15 cm wide [161]. These KTeV paddles are only present in the first two vertical layers, while all other layers consist of SciBooNE paddles.

## Electronics

There are different photomultiplier types that come into use in the MRD subdetector. While most PMTs are negative 2" EMI-9954KB or EMI-9839B PMTs and require a high voltage of (2000-2200) V, there are also some negative 2" RC-6342A and HA-2154 PMTs that use negative voltages of 1500 and 1750 V, respectively. One single layer of the MRD is instrumented with 26 EMI-9939B type PMTs that use positive high voltage values in the range (2100-2200) V. The High Voltage is provided by two LeCroy 1440 crates with 28 negative 1443N cards and four positive 1443P cards, providing a total of 448 negative and 64 positive available HV channels.

Layer	Orientation	Number of paddles	Paddle type	PMT type	HV
1	Horizontal	26	SciBooNE	EMI-9954KB / EMI-9839B	-(2100-2200)V
2	Vertical	30	KTeV	EMI-9954KB	-(2000-2200)V
3	Horizontal	26	SciBooNE	EMI-9954KB / EMI-9839B	-(2100-2200)V
4	Vertical	34	KTeV	EMI-9954KB	-(2000-2200)V
5	Horizontal	26	SciBooNE	EMI-9954KB / EMI-9839B	-(2100-2200)V
6	Vertical	26	SciBooNE	RCA-6342A / EMI-9954KB	-(1500/2100)V
7	Horizontal	26	SciBooNE	EMI-9939B	+(2100-2200)V
8	Vertical	30	SciBooNE	RCA-6342A / HA-2154	-(1500/1750)V
9	Horizontal	26	SciBooNE	EMI-9954KB / EMI-9839B	-(2100-2200)V
10	Vertical	30	SciBooNE	RCA-6342A / HA-2154	-(1500/1750)V
11	Horizontal	26	SciBooNE	EMI-9954KB / EMI-9839B	-(2100-2200)V

**Table 3.4:** Characteristics of the different MRD layers and the scintillator paddles that are used within each layer. There are 5 different PMT types in use that all have different set point voltages. Note that the PMTs on layer 7 are the only ones that require a positive HV, while all other PMTs are negative HV channels.

The MRD is externally triggered by signals from the Central Trigger Card that indicate incoming beam neutrinos. Data is taken in COMMON STOP mode, i.e. the trigger signal marks the end of the acquisition window, with MRD acquisition windows being 4  $\mu$ s long. The time information about the scintillator paddle hits is registered by 12 CAMAC LeCroy 3377 32-channel TDC units, after the signal previously passed 24 CAMAC LeCroy 4413 32-channel discriminators. No charge information is recorded since the benefit of this additional information on the muon track reconstruction performance was determined to be negligible. The PMT signals are amplified before passing the discriminators for 90 low-gain 10-stage PMTs in three of the MRD layers, totalling 90 amplified MRD channels.

In addition to the beam trigger acquisition, the MRD can additionally trigger on cosmic muons passing through the detector. This hardware-based trigger evaluates a coincidence of TDC signals in the first and last MRD layer and issues a cosmic trigger signal in case a

coincidence was found. This trigger signal is forwarded to the Central Trigger Card which then evaluates whether there is a conflict of the cosmic trigger with an upcoming neutrino beam trigger. If not, the signal is returned to the MRD and also sent to the VME system to record the cosmic event in both systems.

### 3.2.3 THE FRONT MUON VETO (FMV)

The Front Muon Veto (FMV) is the veto system of the ANNIE detector that is used to identify activity that originated upstream of the hall and can hence not be attributed to a neutrino interaction in the water tank. So-called *dirt muons* originate in neutrino interactions in the rocks upstream of ANNIE hall and can reach the water tank without any problem. The veto will indicate whether any particles passed through and therefore enable a successful tagging of such unwanted events.

#### Geometry and setup

The left side of figure 3.10 shows a picture of the FMV as installed in ANNIE hall. This subsystem consists of two scintillator layers that are each divided into 13 paddles, respectively. The scintillator paddles of dimensions (31.1 cm height, 322.0 cm width) are instrumented with light guides that connect the paddles to 2" PMTs for the signal readout. The paddles originally belonged to the CDF experiment and were refurbished in order to be employed in the scope of ANNIE [162]. The right side of the same figure shows a schematic representation of a dirt muon passing through the FMV, tank and MRD detectors. The scintillation signals from the two layers in the FMV are evaluated in an OR-fashion and would indicate that the muon originated upstream of the tank in such a case.

Since light propagation losses inside the scintillator induce a decreased efficiency at the far end of the paddle with respect to the connected PMT, the light sensors were installed on opposing sides for the two veto layers. This ensures that a low-efficient region of the one layer is compensated with a high-efficient region of the other layer. Dedicated laboratory measurements before phase I of ANNIE determined that the muon tagging efficiency decreases from  $\sim 90\%$  at the near end close to the PMT down to  $\sim 50\%$  at the far end of the paddle. As a consequence, the chance of missing a dirt muon by using the combined information from both layers was determined to be  $< 10\%$ . Updated *in-situ* calibration results of the FMV paddle efficiencies with the current phase II data will be presented in the upcoming chapter 4.

#### Electronics

The readout for the FMV is carried out by the same CAMAC TDC and discriminator setup that is also responsible for the acquisition of the MRD data. In contrast to the MRD channels, all FMV channels are amplified before the signal is evaluated by the discriminators. In a similar fashion to the readout system, the HV system is also shared between the MRD and the FMV. The LeCroy 4410 system also provides HV for the FMV channels, with all of the FMV PMTs requiring negative HV.

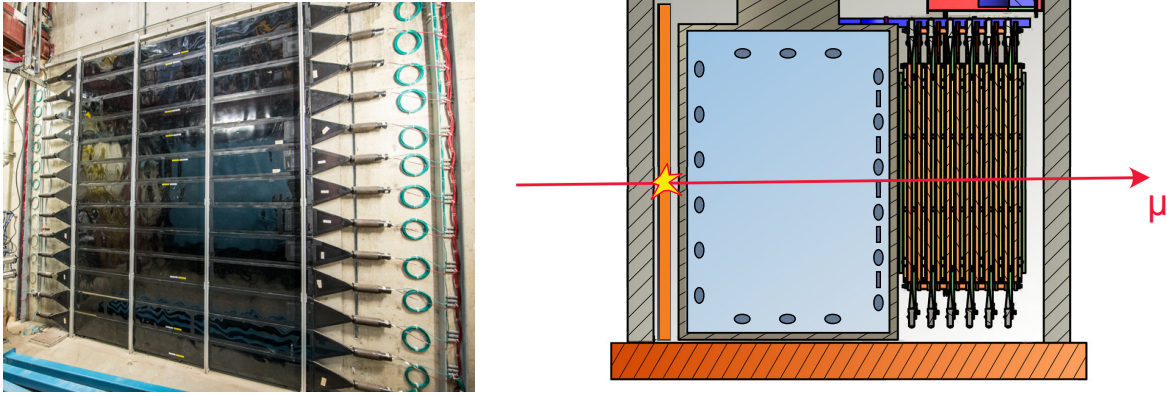


**Figure 3.10:** **Left:** An image of the Front Muon Veto in ANNIE hall. The photomultiplier tubes are visible on the left and right side of the FMV paddles. The PMT mounting location depends on the layer of the respective scintillator paddle. The photo was taken before the water tank was placed in the hall. **Right:** Schematic depiction of a dirt muon inducing a veto signal in the FMV (colored in orange).

### 3.2.4 LARGE AREA PICOSECOND PHOTODETECTORS (LAPPDS)

Large Area Picosecond Photodetectors (LAPPDs) are a pioneering photosensor technology that is utilizing microchannel plate technology for photon detection applications. LAPPDs are manufactured by the company INCOM as tiles with a surface of  $\sim 20 \text{ cm} \times 20 \text{ cm}$  and a thickness of  $< 1 \text{ cm}$  [163]. Their specifications include a very good transit time spread of less than 100 ps and a position resolution of  $< 1 \text{ cm}$  on the tiles, while still achieving gains of  $> 10^7$  [164]. Compared to conventional PMTs with a transit time spread in the order of  $\sim 1 \text{ ns}$  and no position information, this is an extreme improvement both in terms of spatial and timing resolution. This makes the photosensors attractive in a multitude of applications ranging from medical imaging to particle physics, and in particular for neutrino physics.

ANNIE is going to deploy 5 LAPPDs to demonstrate the capabilities of this new photosensor technology in a neutrino beam environment. According to simulations, the use of just such a small number of fast photosensors already improves the event reconstruction capabilities in terms of the vertex and directional reconstruction of the muon in the water tank by a great margin.

The following section will first highlight the general properties of LAPPDs before presenting performance characterization results from a dedicated test stand at Fermilab. At the end of the section, schematic sketches for the deployment and data acquisition in ANNIE will be presented.

#### Geometry and working principle

Each LAPPD consists of a photocathode at the top, anode readout strips at the bottom and two microchannel plates in between as shown schematically in figure 3.11. An incident photon that hits the photocathode will produce a photoelectron that is subsequently accelerated by the potential difference between the cathode and the anode. It will then interact within the microchannel plates operated at  $\sim 1 \text{ kV}$  to produce avalanches of

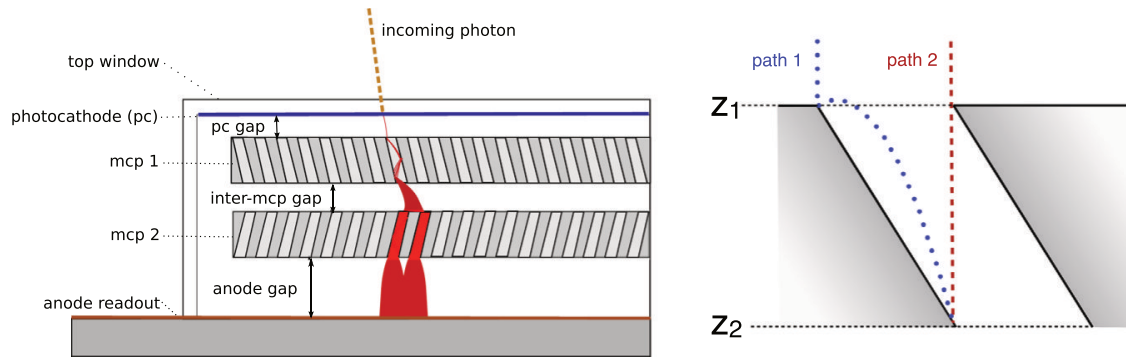


**Figure 3.11:** **Left:** Schematic working principle of an LAPPD: An incoming photon generates a photoelectron at the photocathode, which is subsequently accelerated by the applied electric field between cathode and anode and produces secondary electrons in the coated capillaries of the microchannel plates. The signals are then read out via strips on the anode side. **Right:** Two photons that arrive at the pore surface ( $z_1$ ) at the same time will have slightly different exit times at  $z_2$  depending on their entry position [164].

secondary electrons that are further accelerated and detected at the anode strips. The microchannel plates are borosilicate glass structures that have millions of microcapillaries with diameters on the order of  $20\ \mu\text{s}$  [165]. These pores are coated by means of Atomic Layer Deposition (ALD) [166] with thin-film materials like MgO to provide secondary electron emission capabilities. The pores are oriented in an angle of  $10 - 20^\circ$  to ensure that the photoelectron is colliding with the pore walls and is guaranteed to generate further secondary electrons along the way. The pores in the second microchannel plate are tilted by the same angle in the opposite direction in order to erase any bias in the detected photon position that would otherwise be present due to the angled pathway of the secondary electrons in the first microchannel plate. The tilted microcapillary design has the additional advantage that positive ions that are produced in electron cascades in the bottom microchannel plate are prevented from reaching the photocathode, which could be damaged in such a process [164]. X-shaped spacers separate the two microchannel plates from each other and from the photocathode.

The whole LAPPD structure is vacuum sealed, and different voltages are applied to the photocathode and the two microchannel plates to ensure that the photoelectrons are accelerated throughout the whole construct. Typically, high voltage differences between the different components would be 100V between the photocathode and the first microchannel plate, 875 V per microchannel plate, 200 V between the two microchannel plates, and 200 V between the lower microchannel plate and the anode strips. In order to achieve such a configuration, one could exemplarily set voltage levels of around  $-2200\text{ V}$  for the photocathode,  $-2100\text{ V}$  at the top and  $-1250\text{ V}$  at the bottom of the first microchannel plate and  $-1050\text{ V}$  at the top and  $-200\text{ V}$  at the bottom of the lower microchannel plate, with the anode strips on ground level [167]. For such a configuration with 875 V applied to the microchannel plates, typical dark count rates are below  $1000\text{ Hz/cm}^2$  for gains up to  $6 \cdot 10^6$  [168].

There are a total of 28 anode microstrips with a width of  $\sim 5.2\text{ mm}$  and a separation of  $\sim 1.7\text{ mm}$  at the bottom layer of the LAPPD that are used to detect the avalanches of photoelectrons produced in the layers above. Although the strips are only oriented in one direction, a two-dimensional photon position can be reconstructed based on the dual-side

readout scheme for the LAPPDs. The signal for each strip is read out on both sides of the  $50\ \Omega$  strips, which enables a reconstruction of the photon hit position along the axis of the strip based on the differential timing information between the two sides of the strip. The vertical dimension of the reconstructed position is estimated by constructing a charge barycenter from all adjacent striplines.

Uncertainties on the timing of photon hits arise from two main sources: the first one is displayed on the right side of figure 3.11 and shows the process by which a time jitter is introduced in the scope of the secondary emission process in microchannel plates. Photons that arrive at different angles and positions in the same pore will reach the bottom of the same pore at different times due to the variance in pathlength, with time differences on the order of 10 ps [164]. Further timing uncertainties arise from the noise levels in the recorded signals. When taking both sources of time jitters into account, the variation for the transit time spread (TTS) of single photon-like signals is usually attributed to be on the order of  $\sim (60 - 100)$  ps for LAPPDs.

When evaluating the differential time spread on the LAPPD microstrips, on the other hand, much better time resolutions can be achieved. Since only the difference of the arrival times on the left and right readout side are taken into account, the time resolution for the differential case is on the order of 5 ps and allows to determine the photon position with a resolution of  $<3.5$  mm in the direction of the strip. The vertical position can be inferred from weighting the charge distribution of adjacent strips and allows to determine the vertical position with a resolution of  $\sim 1$  mm.

### Characterization of LAPPDs at the ANNIE test stand

A dedicated LAPPD test stand at Fermilab was designed and realized by the ANNIE collaboration in order to thoroughly calibrate and characterize all five of the LAPPDs to be deployed in ANNIE. Three main observables were of particular interest: the transit time spread for Single Photoelectron (SPE) signals, a gain measurement and a quantum efficiency scan as a function of the position on the LAPPD surface. The test setup that was designed to measure all of these quantities is shown in figure 3.12. It consists of a dark box containing a vertical mounting structure for the LAPPD as well as a movable optical setup that is able to guide both LED and laser light onto different positions on the LAPPD surface. The optical setup is visible on the right side of the figure and is manoeuvrable by a motor. In addition to these main components, a NIST photodiode is mounted on the top left side of the LAPPD and used for reference measurements. Furthermore, all necessary cables for the High Voltages, the power and signal readout are visible on the left and are connected to the outside world via dedicated connectors in the dark box wall. A shutter mechanism automatically turns off the light source as soon as the dark box is opened as a safety precaution.

The LAPPD characteristics are measured in different variations of the LAPPD dark box setup. The Quantum Efficiency scan, for example, uses an LED as the light source. The light is directed onto the surface of the LAPPD and is moved across the whole surface of the LAPPD by the motorized optical arm. For each position, the photocurrent at the first microchannel plate is measured with a pico-ammeter and compared to the photocurrent that is illuminated by the same LED light via a light splitter in the pathway. The ratio of the

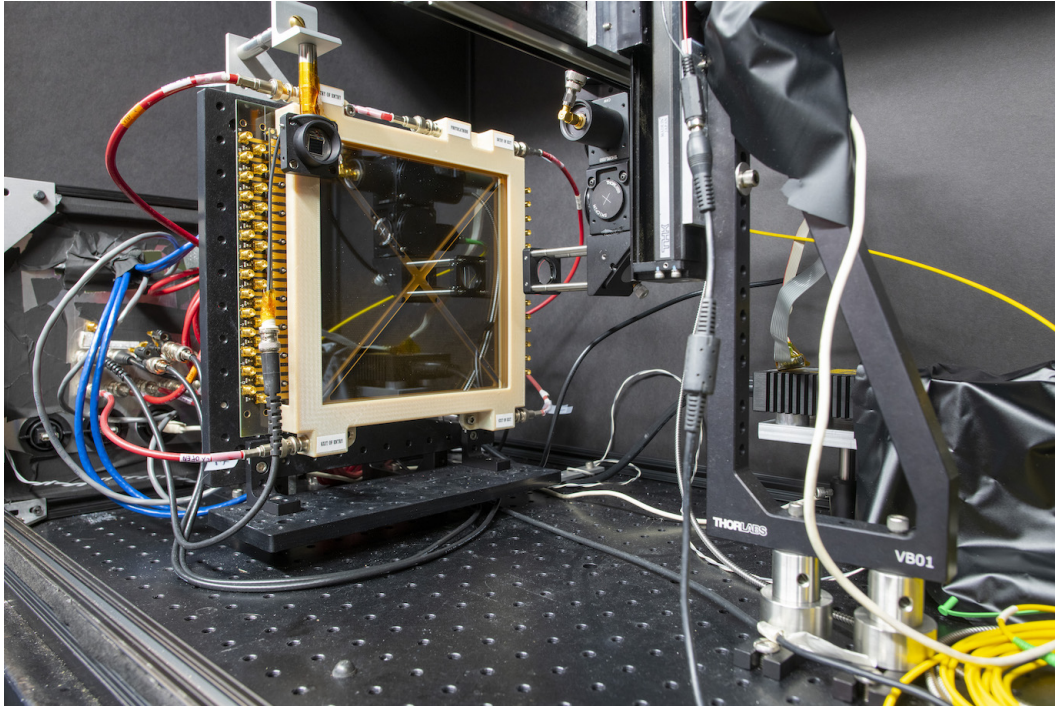


**Figure 3.12:** Picture of a LAPPD being mounted and characterized at the Fermilab-based test stand. The motor-operated movable structure on the right can automatically scan the whole surface of the LAPPD with either LED or laser light. The NIST reference photodiode on the top left provides a reference for the measured photocurrents on the LAPPD.

two measured photocurrents then determines the quantum efficiency at the particular spot of the photocathode. The whole scan across the LAPPD surface is automated in the custom software framework used for the characterization. The calibration of the photodiode current is performed by using a NIST-calibrated photodiode that is mounted on the upper left of the LAPPD. The LED light is steered onto this reference photodiode at the very beginning and end of each run to make sure that the photocurrents measured by the photodiode stay stable.

Figure 3.20 shows the results of such a Q.E. scan for the exemplary LAPPD tile #39. The average measured quantum efficiency across this LAPPD is 23.7%, with the minimum value being 5.8% in the upper left corner and the maximum value being 25.4% in several regions across the photocathode. The Quantum Efficiency scan clearly shows the region of the X-shaped spacer having a low quantum efficiency. Photons that hit the photocathode in this region are basically undetectable by the LAPPD by design since the electrons cannot penetrate the spacers. However, this is not a large issue since the spacers only cover a small fraction of the active area. The histogram of the quantum efficiency values in the upper left corner of the figure further verifies that the photon detection efficiency is very uniform across the surface, which is also visible in the uniform color of the 2D histogram. Overall, the Quantum Efficiency scan for this LAPPD shows very good results and highlights that this tile fulfills the specifications for deployment in ANNIE.

The Transit Time Spread (TTS) describes the variation in the time it takes from the emission of the photoelectron at the photocathode up until the detection of the pulse at the end of the anode strip. The variable is of particular interest since it represents the

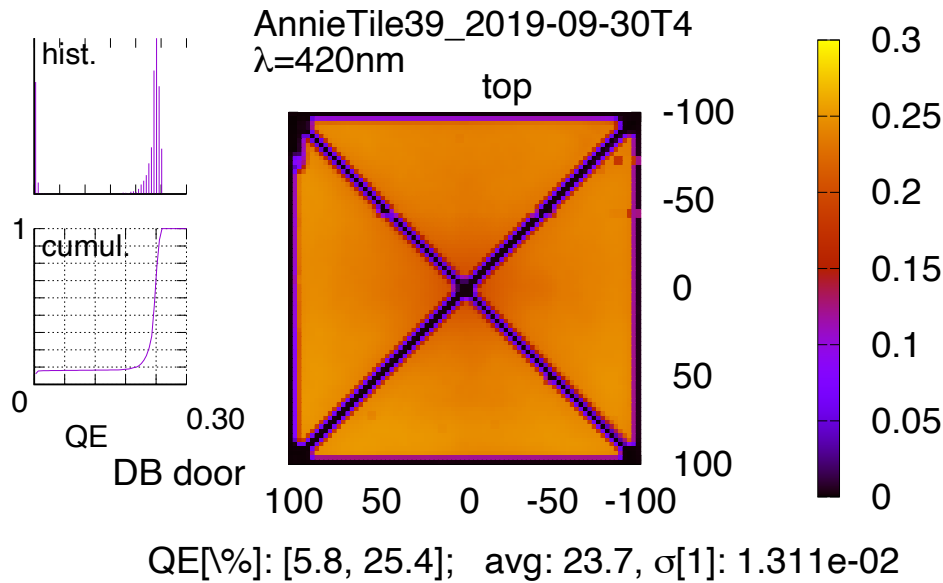


**Figure 3.13:** Results of the Quantum Efficiency scan conducted for LAPPD tile #39 at the Fermilab test stand. The average Q.E. value is 23.7% for this particular tile, with an overall minimum value of 5.8% and a maximum overall observed value of 25.4% across the whole surface.

timing resolution of the LAPPD. It is measured at the LAPPD test stand with a slightly modified version of the setup: While the Q.E. scan only involved the top microchannel plate and neither the lower microchannel plate nor the anode strips, the timing measurement involves all components of the LAPPD. A 405 nm pulsed laser is used as the light source for this characterization in order to achieve a small uncertainty on the light emission time. The photoelectron emission time is then measured with a fast photodiode at the light splitter level and compared to the time at which the pulse is registered at the end of the anode strip. The determined transit times are filled into a histogram and fitted with a Gaussian distribution to determine the spread of the transit time distribution. The left side of figure 3.14 shows the results of such a TTS calibration run for LAPPD #40. The determined TTS of 280 ps is worse than originally expected and currently investigated in more detail within the analysis group. Earlier independent characterizations of LAPPDs have demonstrated timing characteristics on the order of 65 ps [168], indicating that the current measurements still need to improve the test setup in terms of reducing the time jitter induced by the trigger and some small adjustments in the analysis procedure.

The gain is the last important property of the LAPPDs that is characterized at the test stand. As for conventional PMTs, the variable describes by what factor a single photoelectron is amplified in the avalanche processes within the photosensor. For this measurement, the laser light is attenuated by means of a neutral density filter and a polarization filter to achieve a single-photon emission state for which the LAPPD only registers a pulse for a small fraction of the laser pulses. The measured pulse heights are then recorded, converted into gain values and filled into a histogram, as shown on the right side of figure 3.15 for LAPPD #40. The pedestal peak around a gain of 0 is clearly visible, as well as a separated Single-P.E. (SPE) distribution on the right of the pedestal that extends up until gain values of  $1.0 \cdot 10^7$ . The average gain for the SPE distribution of this particular LAPPD was determined to be  $g \sim 1.4 \cdot 10^6$ , which is within the expected specifications for ANNIE.

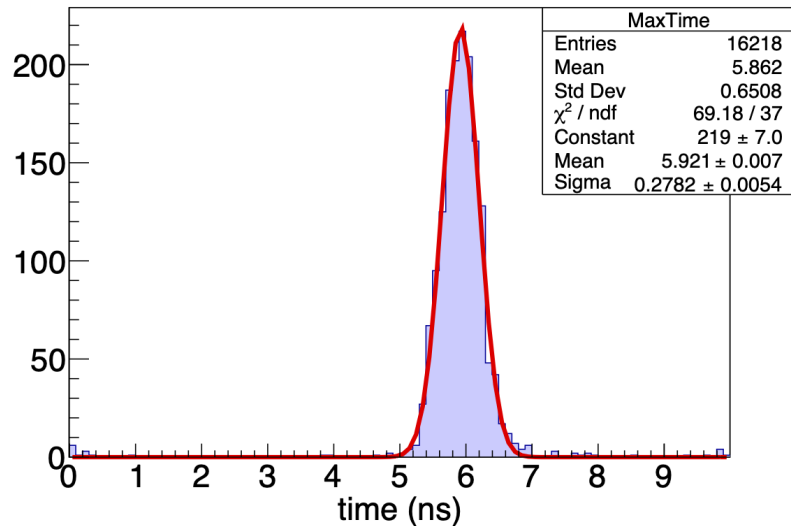


**Figure 3.14:** Transit Time measurement for LAPPD #40 with a measured Transit Time Spread (TTS) of  $\sim 280$  ps.

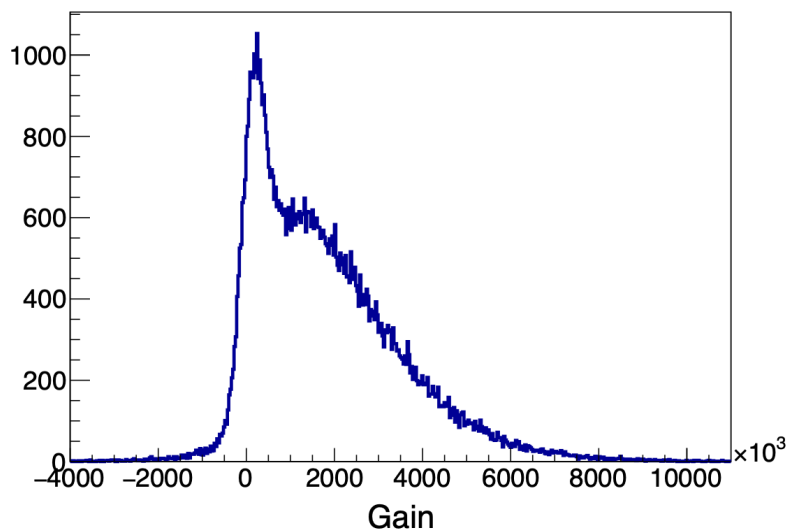


**Figure 3.15:** Measurement of the pulse height distribution for LAPPD #40. The measured gain for this LAPPD is  $\sim 1.4 \cdot 10^6$ .

## Electronics

Sampling very fast waveforms as the ones recorded by LAPPDs requires special hardware and firmware that can deal with the high sampling rate. For this special purpose, switched capacitor array (SCA) analog memory was developed. SCA memory enables to sample waveform at a very high rate, with the caveat of longer readout times [169, 170]. Since beam neutrinos are only expected at a limited rate of up to 5 Hz in ANNIE, this does not introduce any issues, while the fast sampling capabilities provide the necessary foundation for recording the fast LAPPD waveforms.

In order to actually record picosecond-resolved waveforms as necessary for the LAPPDs, the PSEC4 ASIC chip was developed. This chip is based on the SCA technology and is able to record data from 6 channels via SMA or ribbon cable connectors with sampling rates of  $> 10$  GS/s and a bandwidth of 1.5 GHz [171]. Since one LAPPD has around 30 anode strips that are read out separately from both sides, 10 PSEC4 chips are needed to read out the 60 waveform signals. In the case of ANNIE, the chips are mounted on so-called "ACquisition and Digitization with pseC4" (ACDC) front-end boards. One ACDC board can be instrumented with five PSEC4 chips, which in turn requires two ACDC boards to read out one LAPPD.

The information stored in the ACDC cards can be read out via the so-called ANNIE Central Card (ACC). This control card was developed at the University of Chicago and can control up to eight ACDC boards via an ethernet connection. The ACC can communicate with each ACDC card via 8 LVDS lines, of which half are used for sending information and the other half for receiving data from the ACDC card. The data from the ACC can be read out in multiple ways either via USB, dual SFP links, ethernet or a VME interface [172].

Whenever data is available in the PSEC4 chips, it is transferred from the chips to the memory of the FPGA on the ACDC card that is handling the communication with the ACC. Triggers can either be issued externally coming from the ACC or internally via the self-triggering capabilities of the ACDC card. Each PSEC4 chip has a threshold discriminator which can be individually adjusted on a chip-by-chip level. The FPGA combines the discriminator information from all 5 PSEC chips to decide whether a local self-trigger is supposed to be issued. In addition to having either an external or an internal trigger, there is also the option to combine an external trigger with the self-trigger capabilities in a coincidence trigger mode. In the case of ANNIE, such a coincident trigger scheme is used for reading out the LAPPDs: The ACDCs are provided with the external trigger information of incoming beam, and then only record the waveform if the FPGA of the ACDC card detects enough activity within the connected anode strips of the LAPPD.

The discriminator mechanism of the PSEC4 chips uses a comparator to evaluate if the measured waveform signal values crossed a certain *DAC threshold*, indicating that a pulse was observed. In order to enable comparisons between the waveform signal and the threshold, the signals are AC coupled and a DC voltage offset, the so-called pedestal, is added to the signal. Both the pedestal value and the DAC threshold value are programmable and can be set to different values for each individual chip [173].

### **Water-proof housing and deployment in ANNIE**

LAPPDs in ANNIE can be deployed at an individual height in a modular fashion via the mailbox slot system that was presented in section 3.2.1. A waterproof housing with a UVT acrylic front plate and a stainless steel backplate was developed for the LAPPD to prevent humidity from getting in contact with the electronics. Figure 3.16 provides a schematic overview of the components included within this waterproof housing: The LAPPD is directly connected to the Trigger Card and the two ACDC cards via the Analog Pickup Board within the so-called *LAPPD package*. This pickup board is a Passive Bridge Circuit (PBC) that is in contact with the LAPPD anode strips on the one side and contains Samtech connectors on the other side. Signals from the LAPPD anode strips are picked

up and forwarded to the ACDC cards via the Samtech connectors on the other side. In addition to the Passive Bridge Circuit, there is the LAPPD trigger card which is an active bridge circuit with the same dimensions as the PBC. The trigger card evaluates the anode voltages and provide the ACDC cards with a coincidence-based trigger decision for the LAPPD cards.

In addition to the LAPPD package, the waterproof housing contains the LVHV board that provides both the Low Voltage for the ACDC cards as well as the High Voltage that is needed by the LAPPD components. Three low voltage lines of 3.3 V, 2.5 V, and 1.2 V are provided to power the ACDC cards and the trigger card. The High Voltage is produced on the LVHV board and divided down into 5 different HV voltage values for the different stages of the LAPPD, ranging from the photocathode down to the anode. In order to generate both the LV and HV power supply lines, the LVHV board is provided with a 12 V and a ground line via two waterproof cables that connect the waterproof housing box with the outside electronics racks. In addition to powering the electronics and HV components, the LVHV is also responsible for the slow control interface between different sensors such as a temperature and humidity sensor. It communicates with the surface electronics via a CAN-Bus interface. In addition to the LVHV board and the LAPPD package, the waterproof housing contains a further water sensor that is not directly mounted on the LVHV board as an independent safety measure.

The waveforms from the LAPPD strips are recorded by the ACDC cards and transmitted via signal cables to the ANNIE Central Card (ACC) that is located within an electronics rack on the surface. The LAPPD part of the ANNIE DAQ (as described in more detail in chapter 3.4.1) is running on a Raspberry Pi and reads out these waveform signals from the ACC. Whenever files need to be written to disk, the LAPPD data is forwarded from the ACC to the main DAQ computer DAQ-01. In addition to reading out digitized waveforms from the ACDC cards, the ACC also provides the clock reference for the ACDC cards.

So-called breakout boxes supply the waterproof housing boxes with power and serve as an interface between the waterproof cables and more standard cables. There is one breakout box per LAPPD that each contains a Raspberry Pi with two Pi Hat extensions. The first Pi Hat provides a Controller Area Network (CAN) Bus interface that is used to communicate with the modules of the slow-control interface of the LVHV board. The second Pi Hat is a power relay and is able to cut power to the LAPPD in the case of an emergency.

### 3.2.5 GD-LOADING AND WATER FILTRATION

Detecting neutrons in a conventional water Cherenkov detector is a challenge since the neutron capture signals on hydrogen only produce a 2.2 MeV gamma that is difficult to detect. In order to increase the neutron detection efficiency in such detectors, the idea of loading the water with Gadolinium came up in the scope of the GADZOOKS! (**G**adolinium **A**ntineutrino **D**etector **Z**ealously **O**utperforming **O**ld **K**amiokande, **S**uper!) proposal by John Beacom and Mark Vagins in 2004 [175]. Neutron captures on Gadolinium release a 8 MeV gamma cascade that is much easier to detect than the capture signal in pure water. The very large neutron capture cross section of Gadolinium (49 000 barns) compared to free protons (0.3 barns) facilitates the loading of the water: A very small mass fraction

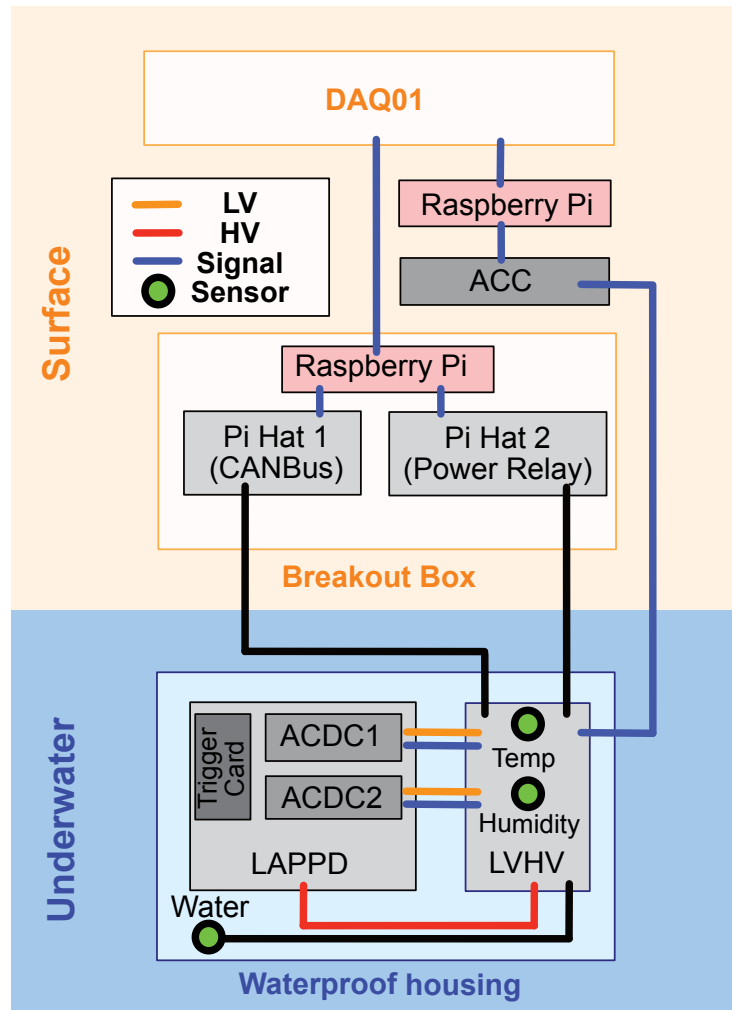


**Figure 3.16:** Simplified schematic of the LAPPD electronics scheme that is used for the deployment within the ANNIE water tank. All components that need to be underwater are protected in a waterproof housing box. The recorded waveform signals are first recorded by the two (ACDC) cards which are directly connected to the LAPPD, and are then forwarded to the ANNIE Central Card (ACC) for further processing. Figure adapted from [174].

of Gadolinium will already cause the majority of captures to occur on Gadolinium [176]. The very efficient capture on Gadolinium is depicted in figure 3.17 as a function of the mass fraction of loaded Gadolinium. A typical mass fraction for Gadolinium in a water Cherenkov detector would be around 0.1% and can be loaded either in form of a chloride ( $\text{GdCl}_3$ ) or sulfate ( $\text{Gd}_2(\text{SO}_4)_3$ ). For such a loading scenario, around 90% of captures will occur on Gadolinium and only 10% on hydrogen, enabling efficient detection of neutrons in the respective water Cherenkov detector. In addition to the larger gamma energy, captures on Gadolinium also reduce the capture time constant from  $\tau_{\text{water}} \sim 200 \mu\text{s}$  to  $\tau_{\text{Gd}} \sim 30 \mu\text{s}$  [177].

### Water filtration in ANNIE

While Gadolinium provides very nice benefits in terms of neutron detection capabilities, some care must be taken to ensure that all detector materials are compatible with Gadolinium and do not dissolve over time, making the water intransparent. Since Gadolinium

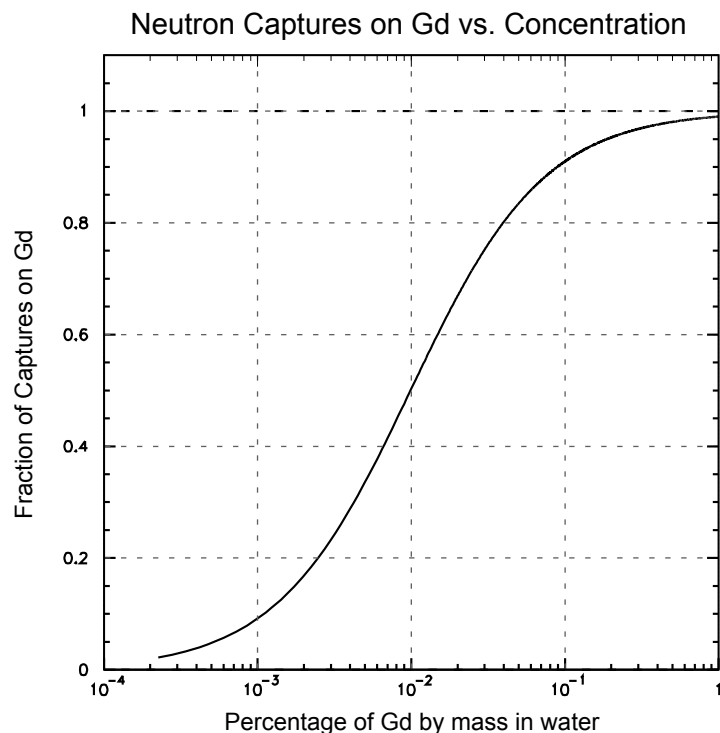


**Figure 3.17:** The fraction of neutron captures on Gadolinium as a function of the Gd mass fraction. A loading of 0.1% already results in capturing 90% of all neutrons on Gadolinium instead of free protons. Figure taken from [178].

sulfate is less reactive than its nitrate counterpart,  $\text{Gd}_2(\text{SO}_4)_3$  was chosen as the Gadolinium salt to be used in ANNIE. Chapter 3.2.1 gives some more details on the compatibility tests that were conducted for all materials used in the ANNIE water tank.

In order to avoid transparency losses in Gd-loaded water Cherenkov detectors over time, the water needs to be filtered with dedicated purification systems. While larger detectors usually make use of novel band-pass molecular filtering techniques to purify their water, a less expensive custom purification system was developed for ANNIE by collaborators at UC Davis [179].

Even in a pure water Cherenkov detector, purification processes are necessary to remove unwanted bacteria, particulates and UV-absorbing ions and molecules from the water in order to keep the transparency levels as high as possible. The purification in normal water is usually achieved by a combination of filters with different pore sizes, ultraviolet lamps and ion exchange resins. Such a conventional purification system would also remove the ionic Gadolinium and hence needs to be modified to be usable in a Gd-loaded environment.

Figure 3.18 provides a schematic overview of the key elements in the water purification setup in ANNIE: Two micro-filters of sizes 0.5  $\mu\text{m}$  and 5  $\mu\text{m}$  are used to filter larger dust particulates out of the water. Subsequently to the first micro-filter, the water passes a UV lamp that removes bacteria from the water. A Total Organic Carbon (TOC) UV lamp is used to get rid of dissolved plastics: Organic bounds of the plastic are broken up by the lamp. However, free radicals are created in the process that can recombine with other molecules and create compounds with non-negligible UV absorption [180]. Usually, such radicals would be filtered out by a mixed-bed anion/cation resin. Since the cation resin would also

remove Gadolinium from the water, only an anion resin is used in the purification system of ANNIE. While the lack of a cation resin leaves some radicals intact, it was shown that this does not affect the water transparency in small scale detectors such as ANNIE and would only have an impact on the observable transparency in larger scale detectors [179].

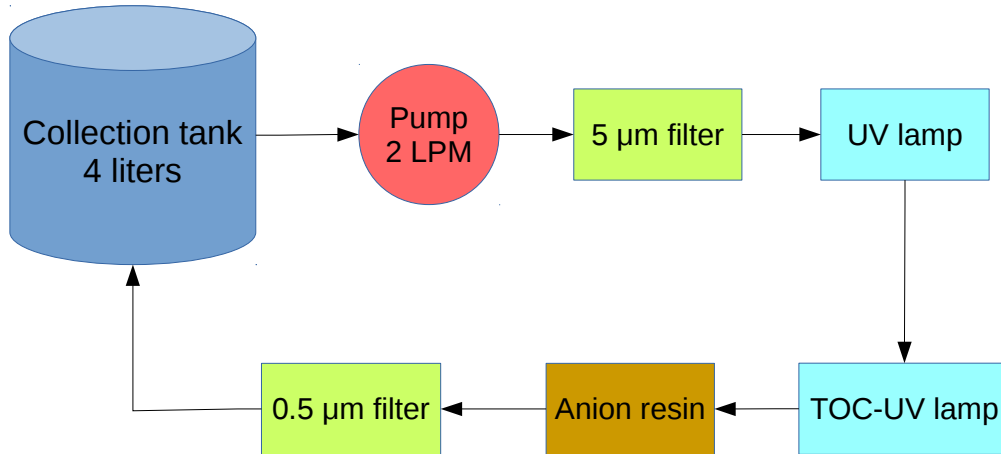


**Figure 3.18:** Schematic overview of the elements of the water purification system that is used in ANNIE [179].

The water purification system is located on the bottom floor of ANNIE hall, in a distance of a few meters to the water tank. Several sensors measure the water conductivity, water flow rate, water temperature and pH value to ensure that the purification system is working as expected. In addition, there is the possibility to extract small water samples from the system and analyze them by a UV Vis spectrometer. The water transparency is monitored regularly by means of six LEDs that emit light in different directions through the detector. No loss of transparency has been observed since the loading in December 2019, indicating that the filtration and purification are working as expected.

### 3.3 PHYSICS ANALYSIS GOALS OF ANNIE

Besides the demonstration of new and pioneering techniques on the detector side, ANNIE is going to provide two interesting physics measurements: the measurement of the neutron multiplicity for muon neutrino interactions on the one hand and on the other hand a cross-section measurement of CC neutrino interactions in water. Both measurements are of particular interest for larger scale future neutrino experiments in the sense that the findings will help to characterize backgrounds and minimize systematic uncertainties in the fields of neutrino oscillation, DSNB and proton decay physics. While the theoretical relevance of both the neutron multiplicity and cross-section measurements in the scope of future physics measurements is studied more in depth in the earlier chapters 2.3.2 and 2.3.4, the following sections will highlight the role of ANNIE for those measurements: The first subsection 3.3.1 will cover the relevance of ANNIE for the neutrino-induced

neutron multiplicity characterization, while the second subsection 3.3.2 will give more insight into the importance of the neutrino cross-section measurement in water. The section will conclude with an overview of the different data taking phases in ANNIE in subsection 3.3.3.

### 3.3.1 NEUTRON MULTIPLICITY MEASUREMENT

While a measurement of the neutron multiplicity in atmospheric neutrino interactions was already carried out by Super-K in 2011 [7] and later also by the SNO experiment [6], there are two main aspects that could potentially be improved in the future. As visible in figure 3.19, the currently available measurements were conducted as a function of the visible energy. Further restricting the results as a function of the muon momentum or even the neutrino energy would provide a more detailed picture and would help to characterize the neutron multiplicity also as a function of the neutrino interaction. This is particularly interesting if one tries to improve current neutrino event generators like GENIE by using the information available in this neutron multiplicity data. Due to the much smaller energy width combined with a much larger homogeneity of the neutrino flavor composition in the Booster Neutrino Beam, ANNIE can provide a more detailed measurement with respect to the muon and neutrino kinematics. Furthermore, the currently available measurement was done with a water target, which has a much smaller neutron detection efficiency compared to Gadolinium-loaded water. Both Super-K-Gd and ANNIE are currently taking data with Gd-loaded water and can use the increased efficiency of their Gadolinium-enriched target material to produce a more precise characterization of the neutron multiplicity.

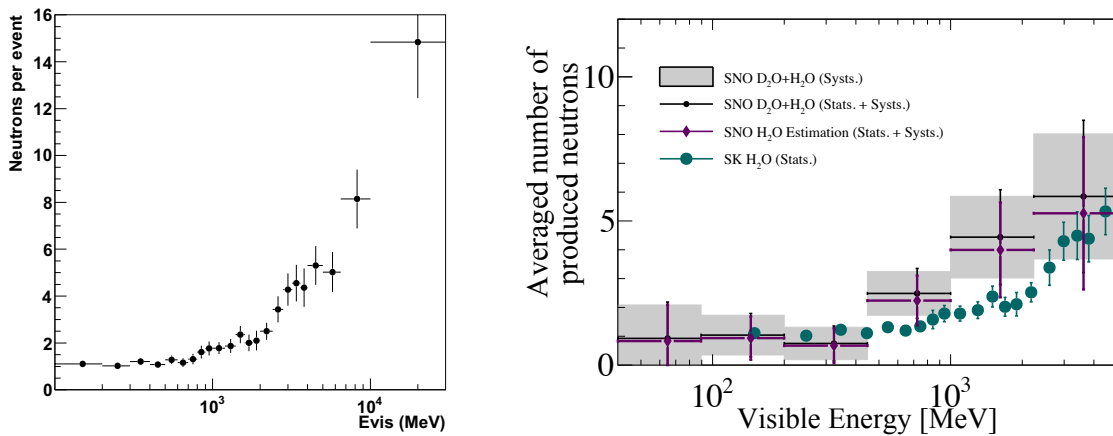


**Figure 3.19:** **Left:** Neutron multiplicity in atmospheric neutrino interactions as a function of the visible energy as measured in Super-Kamiokande in 2011 [7]. **Right:** Neutron multiplicity in atmospheric neutrino interactions as a function of the visible energy as measured by the SNO experiment in 2019 [6].

Since the validation and tuning of neutrino event generators is usually performed as a function of the lepton kinematics and angular distribution, ANNIE aims to measure the neutron multiplicity as a function of both the muon energy and the muon angle with respect to the beam. These distributions can be directly compared to the predictions of different generators and give insight into the aspects of the interaction that show dis-

crepancies. Further measurements could even go beyond the muon kinematics: ideally, they would find a more direct relation between the neutron multiplicity and the neutrino energy or the momentum transfer. Unfortunately, the associated uncertainties would be higher in such a case due to event information that is not accessible in a water Cherenkov detector, e.g. the number of final-state protons below Cherenkov threshold in an event or the energy of associated neutrons. Since all particles will contribute to the understanding of the initial neutrino interaction, missing information about involved particles and particularly regarding their energy will automatically increase the uncertainty with respect to the primary neutrino energy, momentum transfer, as well as the exact interaction type. It is therefore advisable to measure the dependence of the muon kinematics first and potentially carry on with more difficult dependences such as the neutrino energy later.

### Measuring the neutron multiplicity in ANNIE

In order to measure the neutron multiplicity in Charged-Current neutrino interactions with ANNIE, there are several key requirements that need to be met: First of all, the muon produced in the CC interaction needs to be characterized both in terms of energy and direction. Afterwards, the recorded data window is scanned for potential neutron capture signals. The number of neutron capture signals is counted and associated to the lepton kinematic information. Figure 3.20 schematically shows the characteristic event signature of such a CC muon neutrino interaction in ANNIE. After a muon track has been identified to originate in the Fiducial Volume (*first panel*), potentially created neutrons scatter and thermalize in the water material (*second panel*). For an exemplary event with 2 neutrons, the first neutron will capture at a certain time  $t_{\text{neutron},1}$  (*third panel*), while the second neutron will capture at an uncorrelated time  $t_{\text{neutron},2}$  (*fourth panel*). Both neutron capture signals will produce a rather uniform light signal that is then detected by the 132 PMTs employed in ANNIE.

The necessary steps for measuring the neutron multiplicity as a function of the muon energy would then be the following:

1. Firstly, the charged current interaction needs to be identified by tagging the associated muon that is produced in the interaction. A very simple selection of beam-induced muons can be achieved by requiring a coincidence of a reconstructed track in the tank and the MRD.
2. Afterwards, the muon direction and vertex position needs to be reconstructed by making use of the excellent timing resolution of the downstream LAPPDs. Furthermore, the muon momentum is determined by evaluating the track length and angle in the MRD. The track length in the MRD alongside the track length in the tank can then be combined to obtain an energy estimate of the muon.
3. Depending on the exact mode of the measurement, additional cuts like Cherenkov ring counting might be applied to obtain a more restricted event topology like CC- $0\pi$ . A more general CC-inclusive measurement can be achieved without any additional cuts.

4. After the muon kinematics and the event topology have been determined, neutron signals are identified in the subsequent time window. Signals recorded by the PMTs are used and selected for rather uniform light depositions to identify neutron capture signals.
5. The number of detected neutrons is evaluated as a function of the muon kinematics. Correction factors are applied based on the neutron detection efficiencies determined in the AmBe neutron calibration campaign.

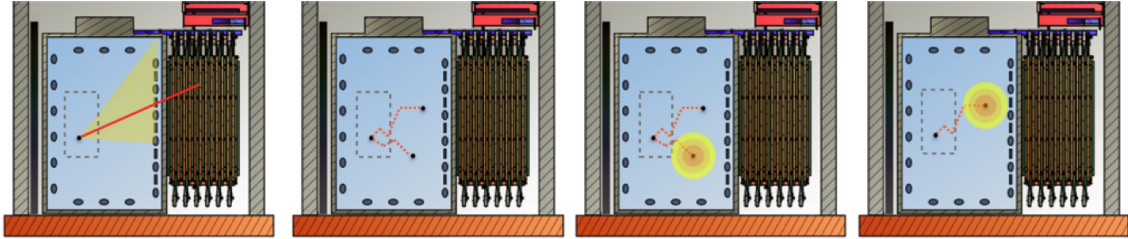


**Figure 3.20:** Schematic depiction of a neutrino interaction in ANNIE. While the muon properties are reconstructed by making use of the LAPPDs and the scintillation paddles in the MRD, the subsequent neutron capture signals are detected by the PMTs [8].

### 3.3.2 NEUTRINO CROSS-SECTION ON WATER

In addition to the neutron multiplicity measurement, ANNIE aims to measure the neutrino cross-section in water as a function of the muon kinematics  $(E_\mu, p_\mu)$  and the muon angle  $\cos(\theta_\mu)$ . The detector position only 100 m away from the BNB beam target provides a rather high flux of neutrinos and hence sufficient statistics for a high-precision cross-section measurement. Understanding the cross-section better will help to minimize systematic uncertainties in neutrino oscillation measurements, particularly for cases in which the target materials in the near and far detectors are different. Experiments like T2K, T2HK, or THEIA that utilize water as the target for their far detector would hence benefit greatly from an improved knowledge of the cross-section in water.

The cross-section will be measured both in an integrated mode averaged over all observed angles and energies and in differential modes as a function of the lepton kinematics. The differential cross-section measurements will include the single-differential cross-sections as a function of the muon momentum  $(\frac{d\sigma}{dp_\mu})$  and as a function of the muon angle  $(\frac{d\sigma}{d\cos(\mu)})$  as well as a double-differential cross-section  $\frac{d^2\sigma}{dp_\mu d\cos(\mu)}$ . The differential modes in particular contain important information that can be used to verify the predictions of neutrino generators.

The primary cross-section measurement will be conducted for a CC-inclusive sample which only requires to have a muon as a final state particle. Some more exclusive channels like CC-0 $\pi$  or CC-1 $\pi$  that have stricter event selection criteria of a muon with no pion or one pion are planned after the CC-inclusive measurement. These more selective event categories are again of particular importance for the validation of event generators, since

differences in more restricted event topologies can be traced down more easily to single interaction types, although each measured event category is still a combination of multiple "true" interaction types.

A measurement of the NC neutrino cross-section is envisioned for the future as soon as the CC-related analyses have been completed. Due to the smaller light output in such events, the NC analysis is a little more challenging and requires more work to successfully identify NC beam signal events against background events. Usual tagging strategies for NCQE events include the use of de-excitation gammas that are emitted from residual nuclei after a nucleon was knocked out from the nucleus by the neutrino. Since this channel plays a huge role in the background modeling for the DSNB signal, it would be interesting to validate the already measured cross-sections for the NCQE channel both by Super-Kamiokande [181] and T2K [182]. Furthermore, the Gd-tagging capabilities open up the possibility to study cross-sections for more exclusive event topologies, such as NCQE events with one detected neutron (NCQE-1n).

### Combined Argon/water cross-section analysis with SBND

Figure 3.21 shows a schematic cross-section view of the Booster Neutrino Beam with the different experiments ANNIE, SBND, MicroBooNE, MiniBooNE and ICARUS and their distance from the beam target schematically shown on the x-axis. The close proximity of the ANNIE detector to the SBND experiment hall provides a unique opportunity to conduct a combined measurement of the neutrino cross-section both on water and on Argon due to the different target materials of the two detectors. Due to having basically the same position in the beam, systematic uncertainties related to the beam flux and the general beam topology would mostly cancel out.

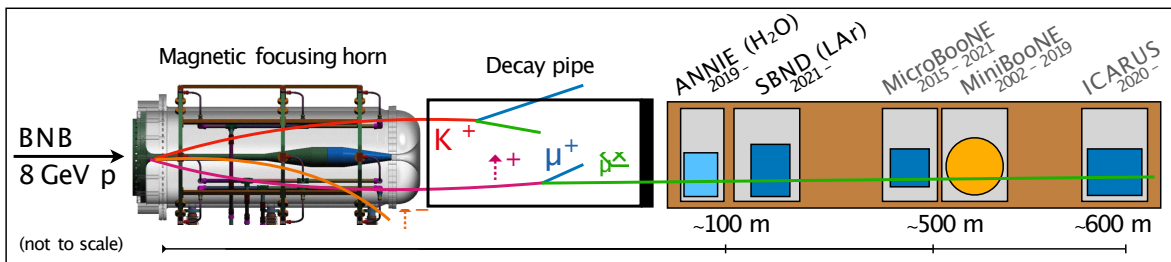


**Figure 3.21:** Experiments on the Booster Neutrino Beam line [183]. ANNIE is directly located next to the SBND detector that uses Liquid Argon (LAr) as target material, which makes a combined Argon/water cross-section measurement possible by combining the data from both experiments.

Particularly interesting measurements would for example include a cross-section ratio for the two materials ( $d\sigma_{\text{H}_2\text{O}}/d\sigma_{\text{Ar}}$ ) that could be of direct use to future neutrino oscillation experiments which use both target materials in their combination of near and far detectors. Furthermore, such a measurement will also help to constrain systematics between experiments with different detector technologies, such as Hyper-K and DUNE. The measured correlated cross-sections for water and Argon would also be an important input for the validation and tuning of neutrino generators, since the two measurements would include the same systematic beam uncertainties. Furthermore, another interesting

opportunity would include a combined neutron and proton multiplicity measurement, with the neutrons being detected in ANNIE and the protons in SBND. Doing such a combined proton and neutron measurement would improve the understanding of both the number of neutrons produced in neutrino interactions in LAr and the number of protons that are produced in water.

### 3.3.3 PHASES OF ANNIE

The data taking in ANNIE is divided into several phases that highlight different geometry configurations and measurement goals.

The first phase of the experiment is labeled *Phase I* and served as a feasibility demonstration of using Gd-loaded water as a medium to measure neutrons in a neutrino beam. The main goal of this phase was to characterize beam-correlated neutron backgrounds and to test the feasibility of a neutrino-induced neutron measurement at the location of the ANNIE detector.

The currently running *Phase II* is designed to measure the neutron multiplicity and neutrino cross-section in different interaction channels in Gadolinium-doped water, as described in the previous subsections.

An upgrade to the detector configuration is planned in the scope of the future *Phase II-Upgrade*, in which a vessel with the novel detection medium Water-based Liquid Scintillator (WbLS) will be placed inside of the Gd-loaded water tank. This phase aims to explore the physics advantages of WbLS in a neutrino beam environment. The following section provides some more details on the characteristics and goals of the past and future phases and will put them into the context of the current phase of the experiment.

#### Detector configurations

As shown in figure 3.22, both Phase I and Phase II-Upgrade use a small vessel for their measurements. The Neutron Capture Volume (NCV) in Phase I was a 50 cm x 50 cm acrylic cylinder filled with EJ-335 Gd-loaded liquid scintillator (0.25% w/w) and was placed at different positions throughout the ANNIE water tank [184]. In total, one central position, 4 vertical positions, and 2 horizontal positions were used for the measurement. For each position, the rate of neutron captures was measured by means of two PMTs that were attached directly to the NCV. An array of 58 photomultipliers at the bottom of the water tank was used to veto coincident cosmic events. Dirt muons were rejected by making use of the scintillating layers of the Front Muon Veto. Furthermore, two out of the eleven MRD layers were instrumented in phase I to veto events with outgoing muons.

Phase II-Upgrade, on the other hand, features the full current Phase II detector configuration described in section 3.2 with 132 PMTs, 5 LAPPDs, a water tank filled with Gadolinium-loaded water and all eleven layers of the MRD operating. Within this detector configuration, the SANDI vessel of dimensions ( $h \sim 0.9$  m,  $d \sim 0.9$  m) will be deployed in the center of the water tank. The SANDI vessel will be filled with Water-based Liquid Scintillator and aims to investigate the benefits of the WbLS medium in a neutrino beam environment.

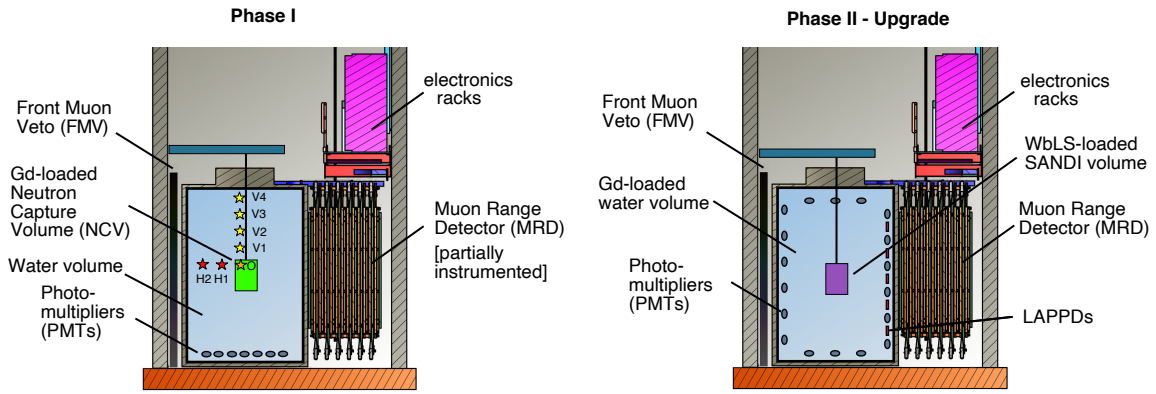


**Figure 3.22:** The ANNIE detector configurations for Phase I (left) and for the planned Phase II-Upgrade (right). While Phase I only had a small vessel filled with Gadolinium-doped water, Phase II-Upgrade has a very similar vessel configuration, in which the vessel is filled with Water-based Liquid Scintillator instead.

### Phase I Results

The beam-correlated neutron background rate is an important quantity that needs to be understood for a successful measurement of the neutrino-induced neutron multiplicity. Such neutron backgrounds can be produced in two main mechanisms, resulting in so-called *dirt neutrons* and *skyshine neutrons*. Dirt neutrons are produced in interactions of neutrinos in the rock upstream of the ANNIE detector and further propagate into the water tank, where they are then detected as neutron capture events. Skyshine neutrons, on the other hand, occur when neutrons are produced in the beam dump and then scatter off molecules in the atmosphere, reaching the water tank after multiple scattering processes [184].

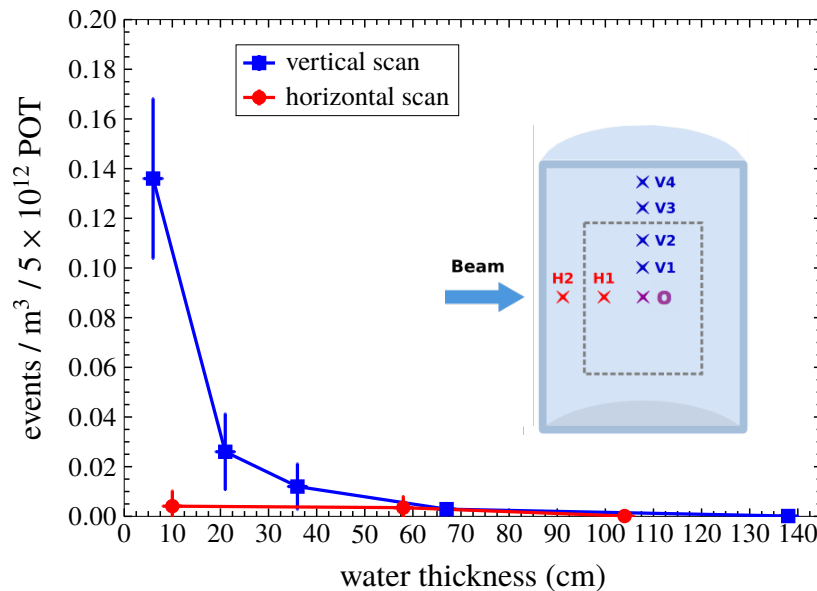


**Figure 3.23:** The results from Phase I of the ANNIE experiment [184]. The beam-correlated neutron background rate is shown as a function of the NCV position within the water tank.

Figure 3.23 shows the results of the measured beam-correlated neutron background rates in Phase I of ANNIE. The blue curve shows the results of the vertical position scan, while

the red curve features the measured rates in the two horizontal positions. It is evident that there is a strong dependence of the beam-correlated background rate with the vertical position in the detector: The position closest to the top of the water tank has a highly elevated neutron background rate of  $R_{\text{top}} \sim (0.14 \pm 0.03) \text{ events/m}^3/10^{12} \text{ POT}$  compared to positions closer to the center of the detector. A vertical shift of 20 cm already results in a reduced skyshine neutron rate of  $R_{\text{n,20cm}} \sim (0.03 \pm 0.015) \text{ events/m}^3/10^{12} \text{ POT}$ . This feature is attributed to be caused by the sky-shine neutron background sample: Since those neutrons are scattered off the atmosphere back into the water tank, their contribution is expected to be highest for the top most position in the detector. Lower water tank positions feature additional shielding from the water overburden and hence have a lower detected skyshine neutron rate.

The three horizontal positions all feature very low neutron background rates  $R_{\text{hor}} < 0.005 \text{ events / m}^3 / 5 \times 10^{12} \text{ POT}$ , which indicates that the dirt neutron contribution to the beam-correlated neutron background is comparatively small.

Since the provisional Fiducial Volume for the Phase II physics analysis of ANNIE features a vertical overburden of  $\sim 100 \text{ cm}$  and a horizontal distance of  $\sim 50 \text{ cm}$  to the water tank walls, the determined beam-correlated neutron background levels are definitely small enough for a successful neutron multiplicity measurement in neutrino interactions on water. The determination of the neutron background levels with Phase I hence paved the way for the currently operating physics phase of the experiment.

### Phase II-Upgrade

One of the limitations of a water Cherenkov detector is the inability to detect neutral particles and charged particles with energies below the Cherenkov threshold. As such, it is very difficult to identify whether e.g. protons were present in any given interaction. This lack of knowledge about the final state particles limits the possibility to reconstruct the exact interaction type of neutrino interactions and, as a consequence, also restricts the accuracy of the neutrino energy reconstruction capabilities.

A novel type of detection material called *Water-based Liquid Scintillator* was first proposed in 2011 and offers the opportunity to improve the proton reconstruction in water-based detectors [185]. Liquid Scintillator droplets are dissolved in water by making use of surfactants that circumvent the fact that organic liquid scintillators are hydrophobic in nature. By having the scintillator droplets in the detector medium, scintillation light will be emitted by particles in addition to their usual Cherenkov light output. In this way, protons become detectable in the WbLS medium via the scintillation light that they emit.

Since the emitted scintillation light follows a slightly delayed emission profile and the Cherenkov light is emitted almost instantaneously, the two light contributions can be separated by making use of time-of-flight corrected photon detection time profiles. Photons that are detected at very early times are more likely to be Cherenkov photons, while photons that are detected slightly later are probably rather scintillation photons. This fact can be used to separate the detected Cherenkov and scintillation light portions and to single out the hadronic light contribution for any given event, which will be mainly composed of scintillation light.

Phase II-Upgrade will investigate how well the separation of Cherenkov and scintillation light works in a larger scale neutrino detector. Of particular interest are the aspects how much the additional scintillation light helps with the neutrino energy reconstruction, and in what sense it improves the neutron detection efficiency in ANNIE. If the tests with the SANDI vessel in Phase II-Upgrade prove to be successful, there are considerations to fill the whole water tank with WbLS in the future. Chapter 8 will highlight some more details on Water-based Liquid Scintillators and their potential benefits on the neutrino energy reconstruction in Phase II-Upgrade based on simulation studies.

### 3.4 DATA TAKING IN ANNIE

In order to achieve the physics analysis goals of ANNIE, the Data Acquisition system needs to be capable of efficiently detecting neutron capture signals. While the photon signal for the gamma cascade following a neutron capture on Gadolinium is sufficiently bright to be detectable in a Water Cherenkov detector, this signal can happen over a large time span. For the nominal loading of a mass fraction of 0.2% Gadolinium sulfate ( $\text{Gd}_2(\text{SO}_4)_3$ ) in ANNIE, the exponential time constant for the capture process is  $\tau \sim 30 \mu\text{s}$  [177]. An extended acquisition window of  $\sim 70 \mu\text{s}$  is therefore able to cover 90% of all neutron capture signals. However, it is not feasible to record such long acquisition windows for every beam trigger due to technical limitations of the VME system. It was therefore decided to implement a charge-current (CC) focused data acquisition system that always records a prompt data acquisition window of  $\Delta t = 2 \mu\text{s}$  for every incoming beam trigger, and only opens up an additional delayed extended acquisition window of  $\Delta t = 68 \mu\text{s}$  in the case that one of the downstream PMTs recorded a charge above 5 p.e. This way, all occurring neutron capture signals can be efficiently detected for CC neutrino interactions. In addition, a forced delayed extended acquisition window is opened up at a low frequency in the absence of a charge current signal. This forced acquisition window enables the detection of neutron capture signals also for NC events, albeit with smaller statistics.

In addition to the acquisition for the tank PMTs, the same beam trigger signals are also sent to the other subdetectors of ANNIE, namely the Muon Range Detector (MRD) and the Large Area Picosecond Photodetectors (LAPPDs). The MRD will always record a  $4 \mu\text{s}$  time window, while the LAPPDs are only able to record a 50 ns window and therefore need to be very accurately aligned with the beam trigger signal. All the data streams from the different subsystems in ANNIE store their data independently from each other. This asynchronous data taking mode enables a greater flexibility for the data taking in ANNIE since the different systems only need to react to the trigger signals from the Central Trigger Card (CTC) and do not need to communicate with each other. On the other hand, this mode of data taking requires an additional post processing step where the different data streams are merged together to form physics events that contain the complete available information from all subsystems.

In addition to the aforementioned beam data acquisition mode, the ANNIE detector also needs to be able to take calibration data. There are hence separate trigger modes for LED, laser, standard candle and Americium-Beryllium (AmBe) calibration runs. The LED calibration runs are used to calibrate the PMT gain and monitor the transparency of the

water in ANNIE, while the laser runs give the opportunity to determine the cable time delays of the PMTs and to efficiently calibrate the timing response of the LAPPDs. The standard candle runs enable to monitor whether the detector response changes significantly over time and the Americium Beryllium runs are used to calibrate the neutron detection efficiency in ANNIE.

The following chapter will provide more details on how the data acquisition system operates in the upcoming subsection 3.4.1, before the utilized triggering schemes are presented in subsection 3.4.2. The subsequent subsection 3.4.3 presents the Event Building process in which the different independent data streams are merged together to form physics events before the last subsection 3.4.4 gives an overview of how the raw data is actively monitored online on shifts.

### 3.4.1 DATA ACQUISITION (DAQ)

The Data Acquisition framework in ANNIE is based on the ToolDAQ environment developed by Ben Richards [186]. ToolDAQ is a modular C++ based framework where single software tasks are implemented in so-called Tools. Multiple tools, each performing a very specialized task, can be put together to form a ToolChain that handles more complex pieces of work. The tools within a ToolChain are always executed sequentially and can communicate with each other by placing information in so-called BoostStores that are accessible by all Tools in a ToolChain. BoostStores are a custom data structure in ToolDAQ that contain (key,value) pairs, similar to the standard C++ map structure. However, there are some differences between the two data formats:

- The keys in a BoostStore will always be of type `string`.
- The values in BoostStores, on the other hand, are much less restricted compared to their C++ map counterparts. Any data structure may be placed as a value inside of a BoostStore. It is even possible to place BoostStores as values in other BoostStores.
- BoostStores have several additional user-friendly features that make them easy to use: They delete stored pointers automatically upon closing, can print a summary of all stored keys and have additional functionality to save information in a separate file such that the information can be accessed again later by reading the files.
- There are different types of BoostStores depending on one's needs: The standard Multi-Event format will save the variables event-by-event in a sequential manner and is particularly useful in a physics context when one wants to save subsequent events happening in the detector. Another important BoostStore format is the Multi-BoostStore one, where multiple BoostStores can be written to the same over-arching main BoostStore output file. The latter format is used in ANNIE to store the raw data. Each subdetector saves its information into a separate BoostStore, and all of these BoostStores are then placed in the overall ANNIE raw data BoostStore.

## ANNIEDAQ

The data acquisition software for ANNIE is called ANNIEDAQ [187] and uses separate ToolChains for the different detectors within ANNIE: The tank PMT data is read out via the VME ToolChain, the MRD and FMV data is accessed by the MRD ToolChain and the LAPPD information is read out via the PSEC ToolChain. This setup is visualized in the following figure 3.24. Several organizational tools that deal with slack communications, the PSQL database connection and the High Voltage system are executed before the three subdetector toolchains come into play. Each of the ToolChains starts with a tool to evaluate the trigger information. If a positive trigger signal is present, the data is read out via the next tool. While the VME ToolChain delegates the readout to separate ToolChains running on the three VME computers, both the MRD and PSEC ToolChain use a single tool for the readout: The PSEC Reader in the case of the LAPPD readout and the Lecroy tool in the case of the MRD readout. In each case, a tool to communicate with the Monitoring systems follows. The last tool in each ToolChain stores the data in output files for the case that new data was present.

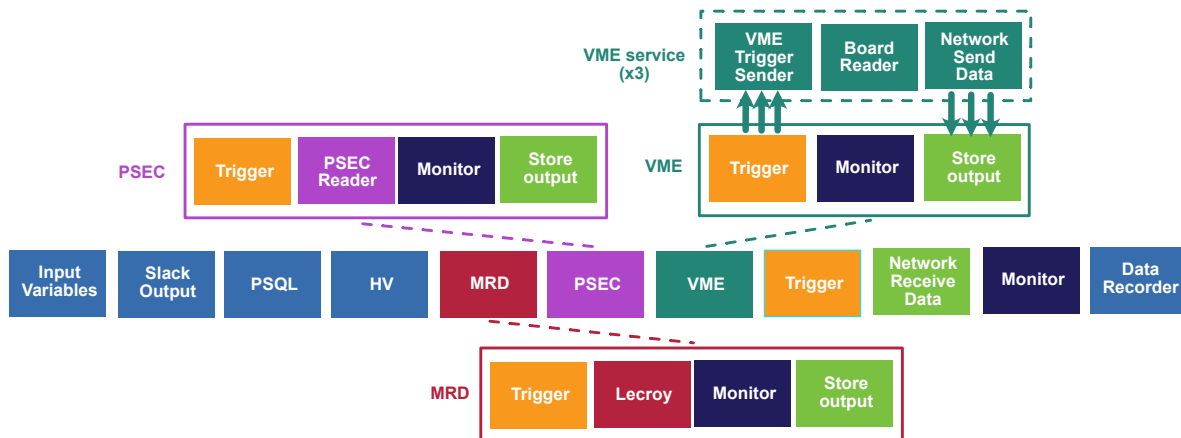


**Figure 3.24:** The main ANNIE DAQ ToolChain with its SubToolChains for the different detector components [188]. Each system evaluates if there is a trigger, reads out the data if a trigger is present, communicates with the Monitoring systems and stores the data in output files.

## Raw data file format

The data for each subsystem is stored in a separate BoostStore, with all of them being stored as separate entries in one overarching binary RawData BoostStore. Each of the subsystem data can be accessed by loading the overall RawData BoostStore and specifying the key for the respective subsystem. Figure 3.25 provides an overview of these subsystem BoostStores and the main variables that are stored within the Stores. The MRD data is saved in a BoostStore with the key "CCData", while the VME data entry has the key "PMTData" and the triggerword data is associated to the "TrigData" key. The data is saved in a different data format for each subsystem, namely in the MRDout class for the MRD data, the CardData class for the VME data and the TriggerData class for the trigger data. While the format of the MRDout class is easily readable, both the VME data and the trigger data need to be decoded first before the recorded data can be used further. Each of the BoostStores contains an additional variable in the header which corresponds to the

number of entries in the respective Store. This variable is used to loop over all available events in each subsystem.

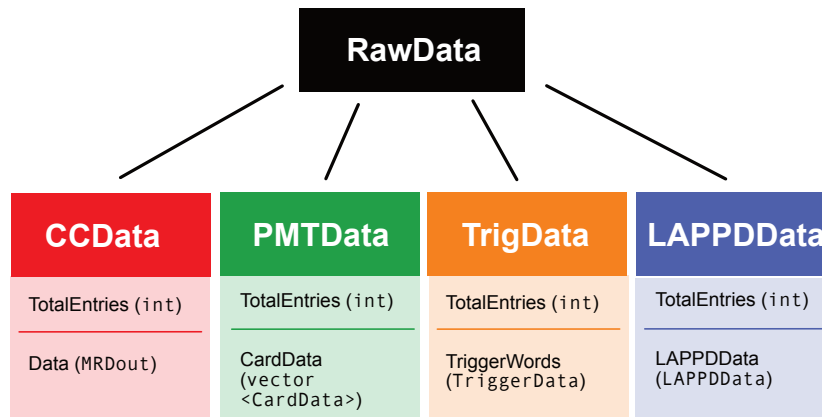


**Figure 3.25:** The different BoostStores that are in use to store the ANNIE raw data. The "CCData" Store contains the MRD data, the "PMTData" Store includes the VME PMT data and the "TrigData" Store comprises the information about all triggerwords and their timestmaps. Each of the BoostStores contains a variable in the header that corresponds to the total number of entries as well as a variable that contains the actual data, stored in different data formats for each system.

The different subsystems store different kinds of information in their data variables depending on the available information within the electronics of the respective subdetector. The MRD data, for example, includes the time information from all the TDC channels that are connected to MRD PMTs. Each entry in the BoostStore contains a timestamp and a list of channels that recorded at least one hit, alongside the TDC value associated to each hit. The TDC channels are identified by their position in the electronic crate, i.e. the crate, slot and channel number that uniquely identifies each TDC channel within the electronic rack setup. The TDCs that are in use for ANNIE are able to register up to 16 hits per channel in each acquisition window, which makes it possible to detect multiple tracks in the MRD that are distributed over the whole acquisition window of  $4\ \mu\text{s}$ . No charge information is saved for the MRD PMTs since there are no ADCs in use for this subsystem. The tracks in the MRD are reconstructed purely based on the time coincidence of the involved scintillator paddles.

The VME system, on the other hand, saves complete waveforms for the water tank PMTs that are recorded by the connected ADCs in the VME crates. Each of the 132 connected PMTs stores their waveform in an encoded form. In addition, also the waveforms for the two input signals of the *Resistive Wall Monitor (RWM)* and the *Booster Radio Frequency (BRF)* are stored in separate ADC channels. These two signals are used to check that the communication signals from the Accelerator Division are stable and that the detector trigger in ANNIE is always aligned with the beam. When using the PMT data for physics analyses, the stored PMT waveforms are scanned for peaks to determine when the respective PMT recorded a signal and how large that signal was. Due to the large amount of information saved in the PMT waveforms, the VME data constitutes a large portion of the disk space that is needed to store the raw data.

The trigger system stores the information about all recorded triggerwords by the Central Trigger Card (CTC) and the timestamps of their occurrence. Each triggerword corresponds to a certain event that was registered by the trigger system. The information about such events can either be sent by external sources (such as information from the Accelerator division about incoming beam spills), or by triggers registered in the hall (for example the SiPM trigger for the AmBe neutron calibration campaign). Further triggerwords document internal communication that is happening within the trigger card. Not all triggerwords are hence associated to real "events" happening in the detector, and only certain triggerwords should be attempted to be matched with the other data streams based on their timestamps. More information about all available triggerwords that are in use for ANNIE will be summarized in the following subsection [3.4.2](#).

Each subsystem records its data independently, which means that not all BoostStores will have the same number of entries and that the data streams will have to be aligned in a post-processing step in order to look at actual physical events. This is achieved by aligning the timestamps from the different data streams and saving events with coincident timestamps in different subdetectors. This EventBuilding process is presented in more detail in section [3.4.3](#).

### Hardware setup and run types

The ANNIE DAQ ToolChain runs on a dedicated computer called `annie-daq01` that is located in ANNIE hall. This DAQ computer can be accessed from the outside world via two gateway machines that are also located in the experiment hall. A so-called *Node Daemon* process is constantly running on the computer and can be used to launch and stop data runs of different data types. Different configuration files and ToolChains are used to launch the different run types, since the runs all have slightly different requirements. While e.g. the Beam run type requires data from all subsystems in order to efficiently characterize the neutrino interactions, some calibration run types like the LED run or the AmBe run type only record the data from the tank PMTs.

The different run types also have different data acquisition time windows depending on their needs: The Beam runs use a combination of prompt and extended delayed readout windows to efficiently detect neutron captures in CC neutrino interactions, while LED and Laser runs only record the prompt time window and AmBe runs always record the extended acquisition window. Once a run of a certain type is started, it will continue running up until it is stopped again. The DAQ framework will periodically save the data to disk after a certain amount of events have been recorded in order to free up the currently used memory. The thresholds for the number of recorded events per file varies between run types and ranges from 1000 events for AmBe runs up to 15000 events for regular Beam runs. Table [3.5](#) summarizes the differences and peculiarities of the different run types and also shows the run type number associated to each run type. This number is used to identify the different run types in the ANNIE PSQL database.

Run type	Run type number	Events/file	Tank	MRD/FMV	LAPPD	Tank Readout window
LED	1	15000	Yes	No	Yes	Prompt
Beam	3	15000	Yes	Yes	Yes	Prompt + Extended
AmBe	4	1000	Yes	No	No	Extended
Cosmic	7	3000	Yes	Yes	Yes	Prompt
Laser	8	15000	Yes	No	Yes	Prompt
MRDRun	9	15000	No	Yes	No	None

**Table 3.5:** The different run types in the ANNIE DAQ alongside the subsystems that are recorded for each type. Different tank readout windows are used for the respective types depending on their needs. Efficient neutron capture detection requires an extended readout window of 70  $\mu$ s, which is enabled for all events in the AmBe neutron calibration run type and for certain events in the Beam run type that exceed a certain charge threshold on any of the downstream PMTs.

### 3.4.2 TRIGGER SCHEMES IN ANNIE

The trigger setup in ANNIE was developed by Jonathan Eisch and is organized by a CAEN V1495 general purpose FPGA VME card, the so-called *Central Trigger Card (CTC)*, and several Master Timing (MT) cards. The CTC is the core piece of the trigger system and decides which triggers are supposed to be issued based on custom firmware. Such trigger signals are then sent to the Master Timing cards that distribute those commands to the ADC cards in the VMEs and the ANNIE Central Cards (ACCs) for the LAPPDs. The type of trigger and its corresponding timestamp are stored within the CTC card. A one-pulse-per-second (PPS) GPS signal is used to calibrate the clock time of the CPUs in the trigger card. The waveform signals that are recorded by the VME system are propagated to an A25 CPU board which can communicate the data with the DAQ system. The general trigger setup is schematically depicted in figure 3.26. When looking at the general setup and features of the trigger schemes in ANNIE, one should keep in mind that complete waveforms are recorded for the tank PMTs, which imposes certain limitations on the maximum possible rate of long readout windows for neutron captures.

There are different trigger mechanisms for different use cases. The most important trigger for the main neutrino analysis is the beam trigger which utilizes signals from the accelerator groups to open an acquisition window in time with the incoming beam. Further triggers include a variety of calibration triggers for the different calibration campaigns, namely the LED, AmBe, laser, and standard candle triggers. The LED and laser triggers record data whenever the respective light source fired. The AmBe trigger, on the other hand, is issued by the signals of two SiPMs crossing a certain threshold. These SiPMs are connected to the AmBe source and are able to identify a gamma that is produced in the same decay mechanism that also produces the neutron, hence flagging the neutron emission. All calibration triggers except for the AmBe trigger record 2  $\mu$ s acquisition windows, while the AmBe trigger issues a 70  $\mu$ s window to efficiently detect neutrons emitted by the AmBe source. One last important trigger is the MRD Cosmic Ray trigger which looks for through-going tracks in the MRD that are not in time with the beam. This cosmic trigger is implemented as a hardware trigger by requiring a coincidence of the first and last MRD layer. The coincidence signal is sent to the Central Trigger Card and

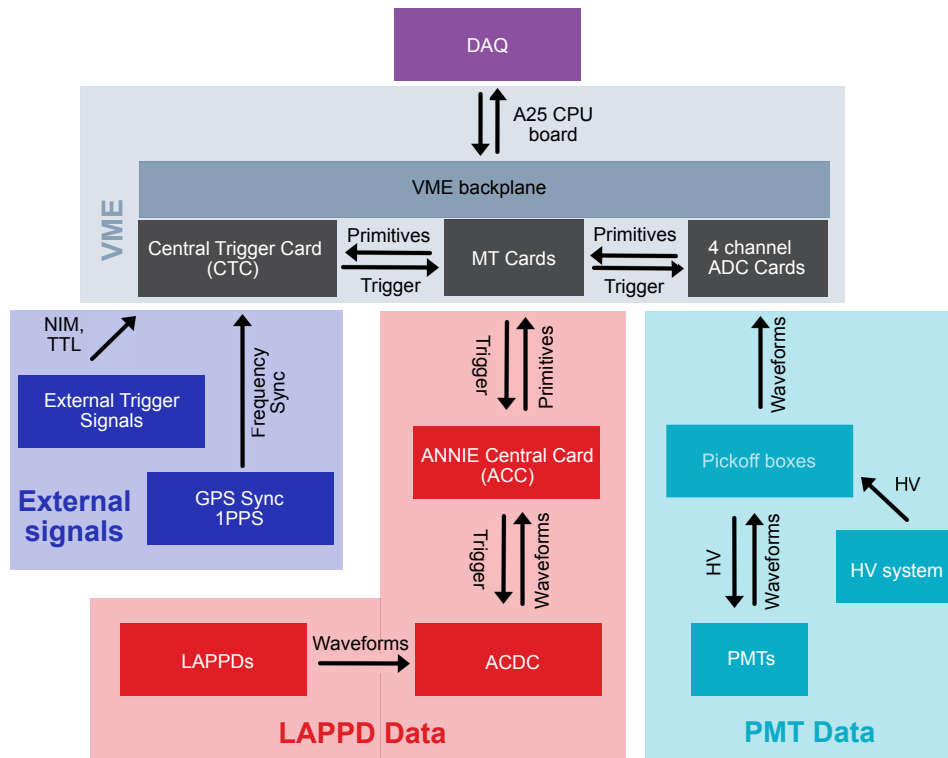


**Figure 3.26:** Overview of the trigger system in ANNIE. The Central Trigger Card is the center piece of the system and is responsible for distributing the trigger signals to the different systems. Main trigger cards (MT cards) that are also mounted in the VME system forward the signals to the ADC cards that record the PMT signals and the ANNIE Central Cards that record the LAPPD waveforms. Schematic based on [189].

sent back to the MRD and the tank PMTs to record the cosmic muon in both systems. An important thing to note is that the Central Trigger Card will always prioritize beam triggers over other triggers and can hence reject MRD Cosmic Ray triggers if they happen to be in time with an incoming accelerator beam signal.

### Charged-Current based extended readout mechanism

The main goal of ANNIE, detecting neutrons via neutron captures on Gadolinium, requires long readout windows of  $\sim 70 \mu\text{s}$  to efficiently detect neutrons. Since the VME system is not capable of reading out such long waveforms for every beam event, a designated CC-focused triggering scheme was developed for ANNIE. A short prompt readout window of  $2 \mu\text{s}$  is recorded for every beam trigger to always record the prompt neutrino interaction. If the prompt event window records a lot of light and hence looks like a Charged Current event, the trigger card will issue an extended readout window. This ensures that neutron captures can efficiently be detected for CC events. The threshold for issuing such an extended window is relatively low and is based on the pulse height of the waveforms. If any of the recorded ADC crosses a certain threshold, the extended readout mechanism is triggered. The relative pulse height above the pedestal value differs slightly for every ADC channel and roughly corresponds to a recorded charge of 5 p.e. This rather low threshold ensures that we record an extended window for almost all CC interactions since the expected charge values per PMT are much higher for those events. At the same

time, the number of extended readouts is reduced enormously due to the large number of low-charge events in the beam data sample. In addition to this CC extended readout, additional forced extended readouts are issued at a certain rate. These Non-CC extended readouts will be used to characterize backgrounds and biases in the main analysis that uses the CC extended readout trigger. Figure 3.27 provides an overview of the discussed trigger mechanisms which are in place during beam runs in form of a flow-chart.

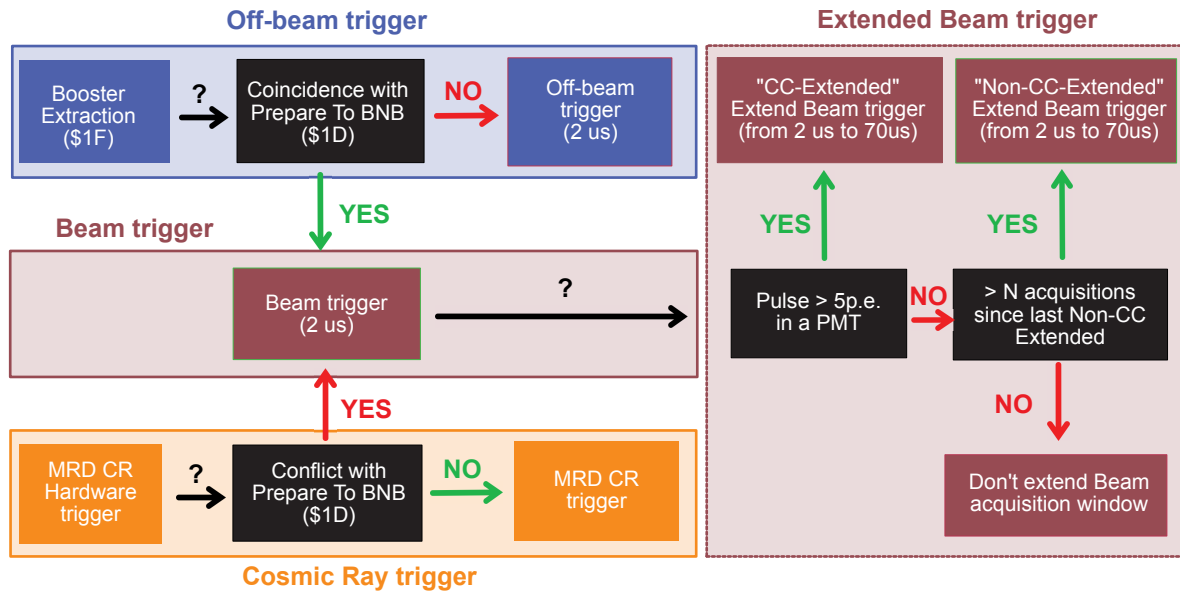


**Figure 3.27:** Overview of the trigger mechanisms present during a conventional Beam run type. A beam-induced 2  $\mu\text{s}$  acquisition window is always recorded if signals from the Booster Neutrino Beam are expected (TCLK \$1D && TCLK \$1F). If one of the PMTs detects increased activity in the tank, the acquisition window is prolonged to 70  $\mu\text{s}$  to efficiently detect neutron capture signals.

### Triggerwords

The information about the trigger process is saved in a dedicated trigger BoostStore in the raw data, which was discussed in some more detail in the previous subsection 3.4.1. Both external events from the accelerator division and internal events happening in ANNIE are assigned dedicated triggerwords that indicate a certain process happening at a given timestamp. These words are used to correlate recorded events to the different trigger types and identify extended readout windows.

The following table 3.6 lists the labels of the most important triggerwords alongside their meaning. The triggerwords 1-4 are used to label the timestamps of the accelerator signals for the Booster Extraction Sync (TCLK \$1F), the RWM, and the TCLK \$1D signals. While the \$1D signal indicates the preparation for the BNB beam delivery, the RWM signal verifies that the protons actually arrived at the BNB site and neutrinos are expected to be produced. The Booster Extraction Sync (\$1F) signal, on the other hand, indicates that protons were extracted from the Booster ring. The extraction process delivers protons either to the Booster Neutrino beam or into the Recycler Ring, such that this triggerword needs to be evaluated in combination with the \$1D signal to make sure the current extraction is scheduled for the BNB.

The other listed words are used to correlate recorded ANNIE data to the different available trigger types. In this context, the `Delay_Beam_Trigger1` triggerword is used to identify beam events, while `LED_start` designates an off-beam LED trigger and the triggerword `MRD_CR` labels MRD cosmic ray triggers. Special triggerwords for the identification of extended readout windows are `BE_status.minbias_start` which identifies a Non-CC extended readout and `BE_status.extend_start` which is issued for CC extended readouts. The triggerword `BE_status.self_trigger_in_window` is assigned when a PMT was detected to have a pulse above its designated CC extended readout threshold. It will hence be present shortly before a `BE_status.extend_start` triggerword. Section 3.4.3 will explain in more detail how the presented triggerwords are used in the event building step. A complete list of all available triggerwords can be found in the appendix in table A.2.

Triggerword	Triggerword label	Detailed description
1	<code>bes_holdoff</code>	Booster Extraction Sync over fiber
2	<code>input_1f</code>	\$1F (Booster Extraction Sync)
3	<code>input_1d</code>	\$1D (Prepare to BNB)
4	<code>input_rwm</code>	RWM input
5	<code>Delay_beam_trigger1</code>	Delayed trigger to ADC system
31	<code>LED_start</code>	Start of LED timer
36	<code>MRD_CR_trigger</code>	MRD Cosmic ray trigger
37	<code>BE_status.activity_window_start</code>	Start of acquisition window
38	<code>BE_status.activity_window_end</code>	End of acquisition window
39	<code>BE_status.self_trigger_in_window</code>	PMT above CC threshold
40	<code>BE_status.minbias_start</code>	Non-CC extended readout
41	<code>BE_status.extend_start</code>	CC-extended readout

**Table 3.6:** The most important triggerwords that are used to identify events in the trigger card within the ANNIE raw data. While the triggerwords 1-4 specify incoming accelerator division signals, the other triggerwords describe ANNIE-internal events and can be correlated to the recorded data. The presented information about the triggerwords was retrieved in personal communication with Jonathan Eisch, who designed the trigger system.

### 3.4.3 EVENT BUILDING

The asynchronous data streams of the ANNIE subsystems require an additional step before the raw data can be used in a physics analysis. In order to obtain events that contain the information from the tank PMTs, MRD, FMV and the CTC, the timestamps of the different systems must be matched. The streams can then be merged into events that contain the full information from all components of the detector. In the process of merging the datastreams, information about the BNB beam status is extracted from the beam database and is also stored for each event. This additional information will be important to select suitable beam spills for the beam neutrino sample. While the general framework for event building already existed, it was extended in the scope of this thesis to include the beam status information and more information on extended acquisition windows.

When matching the timestamps of the subsystems, different time tolerances are allowed depending on the timestamp resolution of the respective system. Since the timestamps of

the MRD system are comparatively imprecise, the timestamps of the MRD and the CTC are allowed to be up to 2 ms apart. On the other hand, the VME timestamps should match the CTC timestamps very closely, which imposes a much smaller allowed tolerance of 300 ns in this case. The merging procedure ideally yields a matched timestamp between all three subsystems. However, it will also match only two of the subsystems (CTC+MRD or CTC+VME) in case no corresponding data is found in the other subdetector. While such events won't be used in the final physics analysis, they are still useful for calibration purposes.

The merged data will be saved in an output BoostStore file that is commonly referred to as a *processed data* file. These processed files are then used as input for the analysis tool chains. All data that could not be matched will be saved in a separate *orphan* output file. The orphan output file is mainly used to evaluate the stability of the event building procedure.

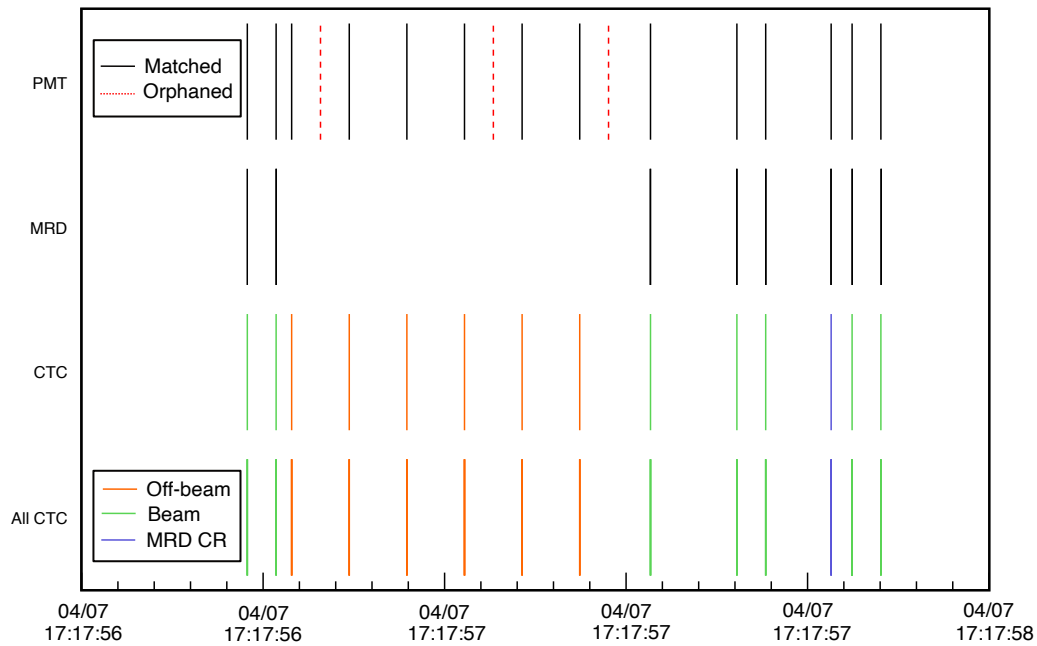
### Exemplary timestamp merging

Figure 3.28 exemplarily shows how the timestamps can be distributed in the different data streams during beam data taking. The CTC data stream contains the information what kind of trigger was encountered, where different triggers are displayed in different colors. The main trigger types that are matched are beam triggers (green), off-beam triggers (orange) and MRD Cosmic Ray triggers (purple). The beam and MRD Cosmic Ray triggers store the data from both the tank PMTs and the MRD, while the off-beam trigger currently only saves the tank PMT information. Consequently, one would usually expect that beam and cosmic ray triggers in the CTC data stream have a coincident timestamp in both the tank PMT data stream and the MRD data stream, while off-beam triggers would only have a coincident tank PMT timestamp. This is clearly visible in the figure and demonstrates that the data taking and event building work as expected. In addition to the matched timestamps, there are several orphaned timestamps in the tank PMT data stream. Those events were most likely triggered by special triggers that are currently not considered in the event building process. All orphaned timestamps are not included in the processed data file and are instead saved in the orphan output file.

When matching beam events, additional information is available in the trigger data stream about whether the tank PMT data recorded an extended time window of 70  $\mu$ s. While the main triggerword for matching beam events (`Delay_beam_trigger1`) is used to identify beam triggers independently of the length of the acquisition windows, there are additional triggerwords in the CTC data stream that can be used in combination with the main triggerword to identify extended readouts based on the trigger information. In this context, the triggerword `BE_status.minbias_start` would identify Non-CC extended readouts, while the triggerword `BE_status.extend_start` would identify CC-induced extended readouts. While the Non-CC extended readouts will occur at a certain pre-defined rate, the CC-induced extended readouts will be triggered by activity detected in the tank PMTs coincident with the beam window, labeled by the triggerword `BE_status.self_trigger_in_window`.

Figure 3.29 shows which triggerwords are present at which times in the case of a CC extended readout. The triggerwords `BE_status.activity_window.start` and `BE_status.`

## Timestamps Event Building



**Figure 3.28:** Exemplary event building picture. Coincident timestamps in the different data streams are merged into ANNIE events that can be used in the analysis. While beam events usually have a match between all three subsystems (CTC + PMT + MRD), off-beam triggers only record data for the tank PMTs and not the MRD.

activity\_window.end (shown in purple) define the time window in which the Central Trigger Card looks for activity in the tank PMTs. The triggerword `BE_status.self_trigger_in_window` (depicted in pink) indicates that at least one of the PMTs detected a pulse above the pre-defined threshold, triggering the extended readout as shown by the presence of the triggerword `BE_status.extend_start` (yellow). The 70  $\mu\text{s}$  acquisition window is then realized in terms of multiple 2  $\mu\text{s}$  readouts one after another due to hardware limitations. The triggerword 46 (`Trigger1_out_reg`, shown in red) indicates the end times of the 35 smaller readout windows that make up the whole 70  $\mu\text{s}$  extended readout. Furthermore, a `Delayed_beam_trigger1` triggerword is also saved for each of the smaller readout windows.

Upon closer inspection, there are two more timestamps present for which activity was detected in one of the tank PMTs. However, the extension of the readout window is only issued in case this activity lies within the specified interval in which the beam is expected to occur. The two additional self trigger timestamps therefore have no influence on the trigger process.

The Non-CC extended readouts are characterized by a similar sequence of triggerwords. In contrast to the CC extended readouts, they feature the triggerword `BE_status.minbias_start` instead of `BE_status.extend_start` and lack the `BE_status.self_trigger_in_window` triggerword. Within the event building process, the extended readouts are identified by looking for `BE_status.minbias_start` and `BE_status.extend_start` in a time frame of 10  $\mu\text{s}$  around the main trigger timestamp that was matched with the other data streams. In case a coincidence is found, an additional extended readout flag is saved for

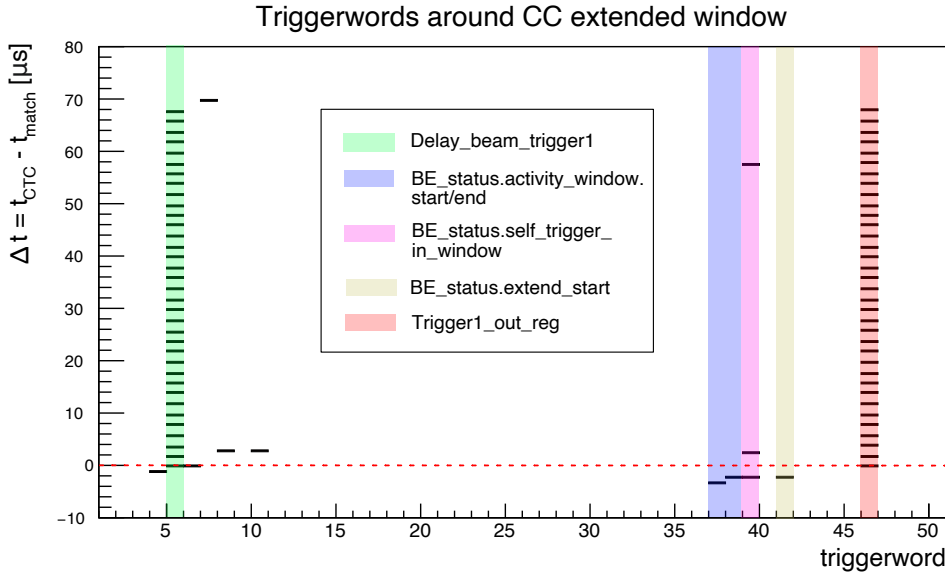


**Figure 3.29:** Timestamp differences of triggerwords in a typical CC-induced extended readout. The presence of the triggerword `BE_status.extend_start` indicates that the event recorded an extended readout due to a large pulse in one of the PMTs, possibly indicating that a Charged Current event took place.

those events.

### Processed data format

The processed data is stored in BoostStore files in the ANNIEEvent format. The key words and data formats for the information from the different subdetectors of ANNIE is predefined such that tools analyzing the processed data files could be tailored to the event structure in place. Regarding the orphaned data files, less data is stored: For each orphaned event, the reason for orphaning alongside the timestamp of the event is saved in the OrphanStore output BoostStore. In addition, the timestamp difference to the closest trigger timestamp is stored for investigation purposes. In the case that a tank event featured an incomplete number of waveforms, the number of waveforms is also stored as an additional variable.

### Data analysis

All data analysis that is presented in the scope of this thesis was conducted using processed data files. Raw data files were only investigated more closely in case the actual waveforms were needed for an aspect of the analysis, for instance when looking for interesting features in pulses of specific PMTs. All good runs that were taken during the first beam year of phase II of ANNIE (January 2021 - June 2021) were hence processed in the way that was presented above before being analyzed.

## 3.4.4 ONLINE MONITORING

The data taking process in ANNIE is constantly supervised by an independent *Monitoring* toolchain that is running on an independent computer in ANNIE hall called `annie-lx02`. This Monitoring framework was developed by me as a general contribution to the experi-

ment in parallel to the rest of the thesis work presented in the later chapters. Raw data files are processed as soon as they are available and diagnostic plots are produced and can be used to quickly identify potential problems in the data taking process. Several diagnostic plots are produced for the different subsystems in ANNIE, and the plots are uploaded to a website that is supervised by shifters around the clock. The website is hosted by a webserver [190] that also runs on `annie-1x02` and is mirrored in order to be accessible outside of the Fermilab network. If any serious error occurs, error messages are additionally sent to slack in order to notify the responsible shifter as quickly as possible.

### Raw data monitoring

The first part of the Monitoring checks general properties of the data acquisition process. For example, interesting file production characteristics that are monitored include the last file size and the time that has passed since the last file was produced. If no new data file has been produced for some amount of time or the file size is unusually small, an error is visible in the main Monitoring status information. Since all beam data files should contain the data from all three subsystems, the last file is also checked for its content. If the information from one of the subsystems is missing, an error is issued. Further things that are logged include the disk space consumption and memory usage on `annie-daq01` and the three VME computers. Unusually high memory usage can hint to a potential problem of backlogging or other issues that should be investigated more closely. Additionally, the presence of three VME processes is always monitored in order to make sure that all three VME computers always run and take data. Figure 3.30 shows a selection of such diagnostic monitoring plots. The top row plots show the general state of the DAQ and the time distribution of hits in the MRD, while the plots in the lower row display the evolution of the raw data file sizes and the recorded waveform for the RWM beam signal. While the general state of the DAQ should always report a "normal" operating mode, the time distribution of MRD hits can be used to check that the beam is still reliably recorded. Since the beam spill is  $1.6 \mu\text{s}$  long, we expect to see an elevated rate with this width in the MRD time distribution plot. The file size, on the other hand, can vary a little depending on the respective BNB beam parameters, but should never drastically rise or decrease without further notice. Very small file sizes below 100 MB would e.g. indicate that we record less than the expected amount of data and something is wrong with the DAQ. Lastly, the RWM waveform should always be located at the same position within the recorded acquisition window to ensure stability of the beam trigger mechanism.

The data of the different subsystems is analyzed individually and checked for general consistency. In particular, the rates of all tank and MRD PMTs are monitored as a function of time to quickly identify problematic channels. Figure 3.31 shows how such a rate time evolution plot exemplarily looks like for one of the TDCs of the MRD system. The various channels display slightly differing rates due to small differences in pulse heights and dark noise levels of the PMTs. However, all channels show a very stable behavior over time in this case. Different problems can occur: A particularly noisy channel will be visible as having a high rate, while an already dead PMT will display a rate of zero. For the tank PMTs, additional current monitoring information is available that is useful to identify particularly high current draws for individual channels, which also indicates problems.

ANNIE DAQ functioning within normal parameters.

VME\_services: 3 / 3

Current time: 2021/4/9-5:2:59

Last File time: 2021/4/9-5:1:52 (1.12 min ago)

Last File name: RAWDataR2633S0p282

Last File size: 515.107 MB

VMEData: True

MRDData: True

TriggerData: True

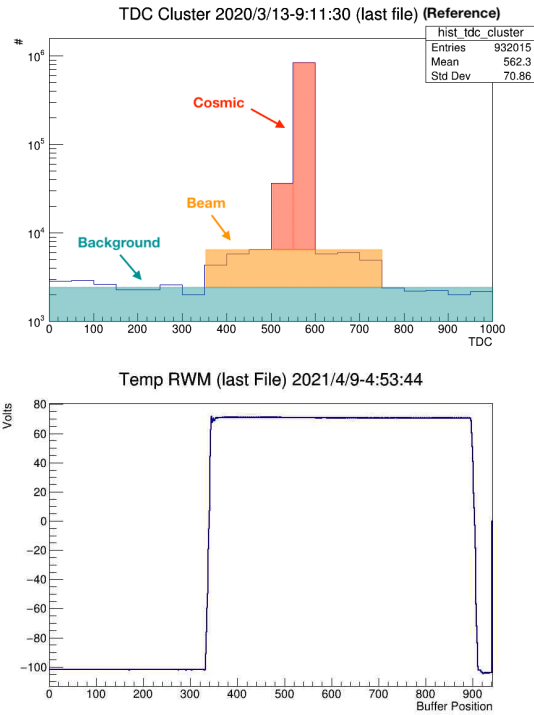


**Figure 3.30:** Several raw data monitoring plots are shown. The top left plot summarizes the status of the DAQ and indicates whether the files contain data from all relevant subdetectors and whether files are produced continuously. The text in the upper row turns red in case something unexpected happens. The histogram shown on the top right indicates whether we still see the beam within the MRD clustered time distribution. Different contributions (background, beam, cosmic) are highlighted in different colors in this plot. The lower left time evolution graph displays the file sizes of the most recent files, while the lower right plot shows the recorded waveform trace for the RWM signal.

This feature is unfortunately not available for the MRD PMTs since the connected LeCroy High Voltage system does not allow to monitor the current draw of individual channels. In their case, we primarily rely on the measured rate to identify potential issues.

We have multiple measures in place to verify that we still reliably record the beam spill. Firstly, the detected time values in the MRD are constantly grouped in time clusters of at least four hits in a time window of 30 ns and plotted in a histogram. Since clustered hits correspond to potential muon tracks in the MRD, this clustering technique makes it possible to visualize the beam spill window in real time for the MRD system. An exemplary version of this plot is shown in figure 3.32 in which the beam spill is clearly visible as an elevated region in the center of the acquisition window for TDC values between 300 and 800. An additional peak around TDC values of 500 can be traced back to cosmic events which are always recorded at the same time in the acquisition window. We therefore verify around the clock that we do see the beam in our muon detector. Since the MRD and the tank PMTs always trigger with the same time delay between them, we can conclude from this check that we also still register the beam spill window with the tank PMTs. Another measure to ensure good beam detection in ANNIE is the RWM signal that indicates incoming beam and is used to trigger on beam events. We constantly observe the trace of the RWM signal to make sure that this signal always arrives at the same time within our acquisition window. This measure ensures that the beam signals are still recorded at the same relative position

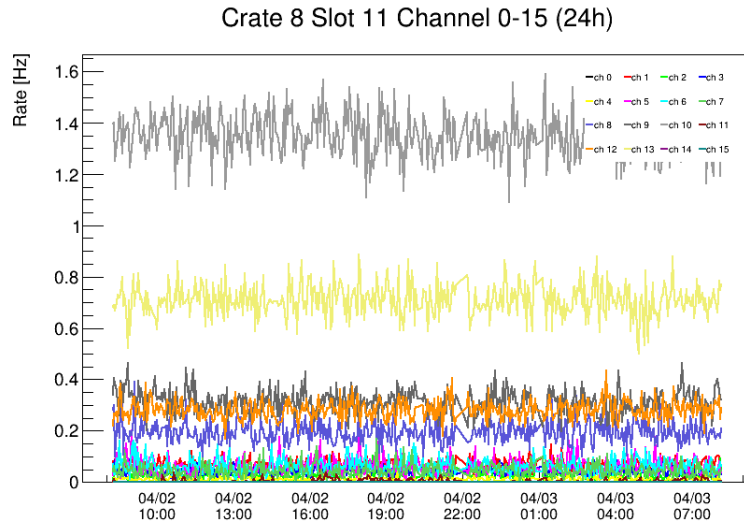


**Figure 3.31:** Exemplary Monitoring rate time evolution plot of MRD PMTs which are recorded by the TDC in crate 8, slot 11 of the MRD data acquisition system. All considered channels display a stable behavior over time in this case.

in our acquisition window and we still capture the whole beam spill at all times.

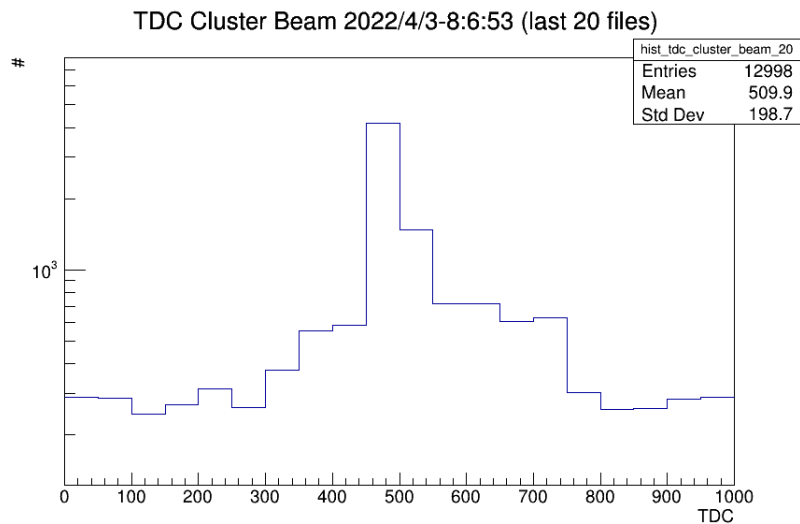


**Figure 3.32:** Exemplary TDC time clustering Monitoring plot. The beam spill window is prominently visible in the center of the acquisition window between TDC values of 300 and 800, verifying that the beam is recorded reliably by the MRD subsystem.

A last important pillar of the Monitoring system is the observation of trigger rates within the recorded trigger data. On the one hand, the trigger rates for the different accelerator division signals provide important information on the current beam repetition rate. We can use this information to verify that our measured rates still agree with the expected beam repetition rates that are provided by the accelerator division. On the other hand, the rates of the different ANNIE-internal triggerwords and their evolution in time are important to verify the stability of the triggering system. The beam, cosmic, and LED trigger rates should be constant in time unless the actual beam rates change. Furthermore, the rates for issuing extended readouts should also not change significantly in a stable

data taking environment.

Figure 3.33 shows a representative Monitoring plot for the time evolution of the trigger rates for the first four triggerwords 1-4 (labeled 0-3 in the plot due to a 0-based counting scheme in the Monitoring). Very stable trigger rates are observed across all triggerwords, with small dips in the plots corresponding to start times of new runs in ANNIE and hence not representative of real losses in the rates.

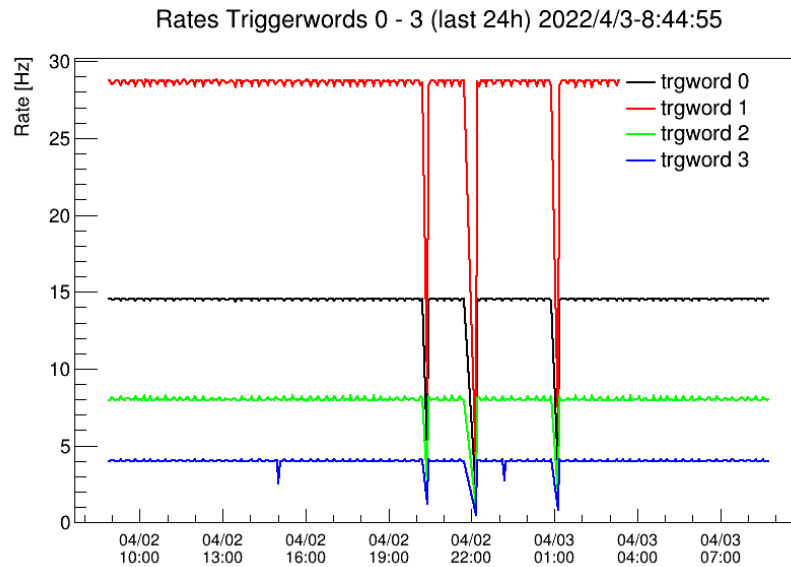


**Figure 3.33:** Exemplary trigger rate time evolution Monitoring plot for the triggerwords 0-3. Very stable rates are observed, with small drops correlated to the start times of new runs in ANNIE.

Some additional things are actively watched by the raw data monitoring. For example, the pedestal values of all tank PMTs are tracked in time to have an additional handle on the stability of those PMTs. An exemplary version of such a plot is shown on the left side of figure 3.34. The pedestal values for all four considered PMTs are very stable across the time window shown in the plot.

In addition to the pedestals, PMT traces are shown for randomly chosen events to verify that the PMT pulses still look reasonable and the PMT baselines are not oscillating. The right side of figure 3.34 shows how this plot typically looks like. In the instance shown in the plot, three of the four channels only recorded baseline values while one channel recorded a pulse for a buffer position around 700 (corresponding to a pulse time of 1.4  $\mu$ s).

### HV and water system monitoring

In addition to the raw data monitoring, several other monitoring systems are in place to ensure smooth and safe detector operations. There are three cameras installed in the hall which constantly take pictures of the water filtration system and the electronics racks. These live images are processed by Raspberry Pis and uploaded to the Monitoring websites. The visual aspect of the images can be used to assess whether anything looks unusual in the hall and whether there are potential problems with either system. Several other diagnostic tools related to the water system are in place for further checks. The most important ones in this regard are the water leak sensors that are placed at four different

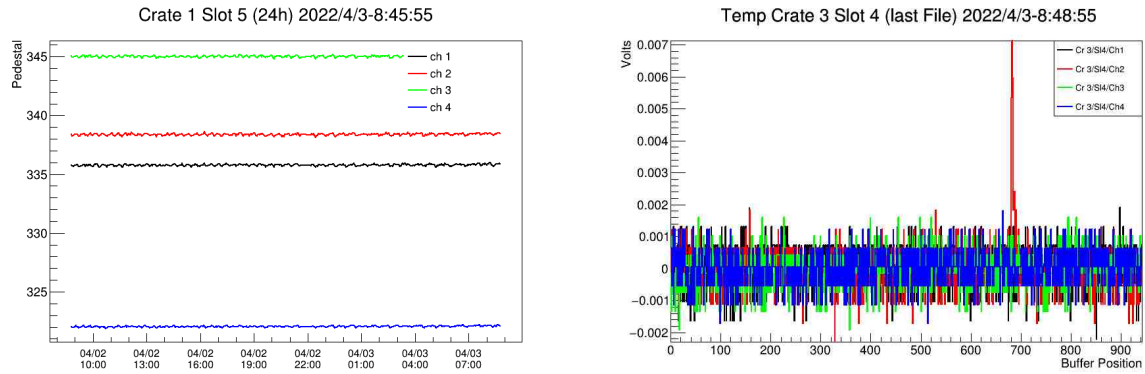
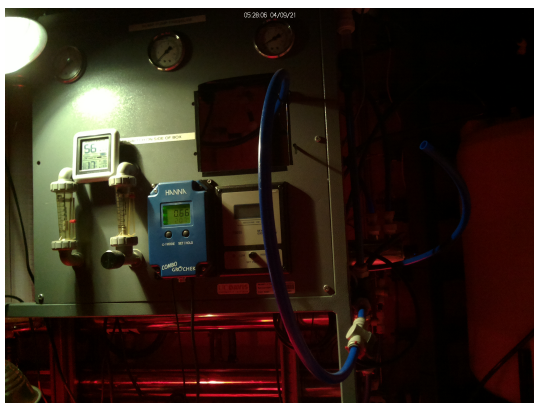


**Figure 3.34:** **Left:** Exemplary pedestal time evolution Monitoring plot for the ADC in slot 5 of the first VME crate. Very stable pedestal values are observed for the four associated PMTs over the considered time frame. **Right:** Exemplary monitored waveforms for the ADC in the fourth slot of the third VME crate. Pedestals (baselines) are observed for three of the four associated PMTs while the second channel (shown in red) features a pulse for a buffer position around 700 (equivalent to a time of 1.4  $\mu$ s).

spots on the floor and which send continuous emergency messages in case of detected humidity. They are of great importance since a potential water leak would have major implications and would need to be fixed immediately. Further sensors include an air temperature and humidity sensor as well as a flowmeter measuring the flow rate of the water through the filters. A decreasing flow rate would be indicative of clogged filters that need to be replaced. The left plot in figure 3.35 shows an exemplary recorded image of the water filtration system. The different sensors that measure the humidity, water flow, temperature and conductivity are visible and monitored regularly to identify potential negative trends in either observable quickly.

The High Voltage system is also monitored independently, with the respective information being available on a separate webpage. The right side of figure 3.35 shows the summary page of the HV monitoring page that provides a general summary and the total monitored currents and voltages for each HV card. The voltage values for all channels are scanned periodically and compared with the expected set values. In case of disagreements between the recorded and set voltages, the shifter is notified immediately via slack and on the webpage. In case of the tank PMTs, the currents for all channels are monitored in addition to their voltages. Any unexpected spikes in the current time evolution plots would hint at a problem with the corresponding PMT and would also trigger an immediate warning in the respective slack channel.



Mirrored at Fri Apr 30 09:08:21 CDT 2021

**Everything is awesome**

Timestamp: 30/04/2021 16:10:32

List of Active Warnings:

Crate Number	Card Number	Total Current Draw	Highest Active I	Lowest Active I	Highest Active V	Lowest Active V
0	0	2.0mA	186.00uA	144.00uA	1748.8V	0.4V
0	1	499.0uA	178.00uA	147.00uA	1659.6V	1379.6V
0	2	2.7mA	240.00uA	127.00uA	1959.8V	1299.0V
0	3	807.0uA	171.00uA	149.00uA	1550.4V	1425.6V
0	4	2.4mA	164.00uA	134.00uA	1989.8V	1633.6V
0	5	2.4mA	157.00uA	138.00uA	1899.8V	1678.6V
0	6	1.8mA	167.00uA	132.00uA	1991.0V	1561.8V
0	7	2.3mA	189.00uA	135.00uA	2198.6V	1418.6V
0	8	2.3mA	189.00uA	3.00uA	1851.2V	4.2V
0	9	2.6mA	190.00uA	137.00uA	1846.4V	1479.6V
Crate Number	Card Number	Total Current Draw	Highest Active I	Lowest Active I	Highest Active V	Lowest Active V
1	0	0.0A	0.00A	0.00A	2202.0V	31.0V
1	1	0.0A	0.00A	0.00A	2112.0V	35.0V
1	4	0.0A	0.00A	0.00A	-1895.0V	-2200.0V
1	5	0.0A	0.00A	0.00A	-1501.0V	-2102.0V
1	6	0.0A	0.00A	0.00A	-1801.0V	-2002.0V

**Figure 3.35:** The most important aspects of the water system and HV monitoring systems are shown. The left plot shows the camera picture of the water filtration system that is regularly inspected with respect to the water flow rate, water temperature and water conductivity. The right plot shows the summary section of the HV monitoring website.

# 4

## Muon Range Detector and Front Muon Veto Efficiencies

---

*“Muons are red, electrons are blue,  
We use both of these particles to find all the nus”*

—NOvA Experiment Twitter account

Both the Muon Range Detector (MRD) and the Front Muon Veto (FMV) are important systems in ANNIE that are used to characterize muons in physics events, as presented in the detector overview in chapters 3.2.2 and 3.2.3. While the scintillator-steel sandwich structure of the MRD is used to range out the energy and direction of muons that were produced in the tank, the FMV uses its scintillator paddles to distinguish background muons that enter the detector from the outside from real neutrino interactions in the tank. In both cases, it is vital to characterize the system’s detection efficiency in order to assess the impact of potential inefficiencies on the final physics measurement: While inefficiencies of the FMV system influence the amount of background in the final physics analysis sample, inefficiencies of the MRD paddles mainly influence the accuracy of the muon fiducialization and of the muon energy reconstruction. The following chapter presents both methods and results for the efficiency determination of the MRD and the FMV system with in-situ calibration data, and closes with an assessment of the impact of the inefficiencies on the track reconstruction performance.

### 4.1 MUON RANGE DETECTOR PADDLE EFFICIENCIES

The Muon Range Detector paddle efficiencies are determined by considering muon events that fully traverse the MRD and by evaluating intersections of the reconstructed muon track with the scintillator paddles. In case a paddle did not register a hit despite intersecting with the muon track, this is considered in the calculation of the inefficiency of the paddle. The following chapter highlights how the efficiencies are obtained in the current phase II data by first presenting the muon track fit procedure developed by Marcus O’Flaherty in 4.1.1 and then covering the general aspects of the determination of the muon paddle efficiencies in chapter 4.1.2. The efficiency determination method is investigated in a

Monte Carlo study presented in chapter 4.1.3 before being applied to the current ANNIE data in chapter 4.1.4.

#### 4.1.1 MUON TRACK FIT PROCEDURE

The muon track fit procedure for tracks in the MRD was developed by Marcus O’Flaherty and will be briefly explained in this section. Since only TDC units are connected to the MRD PMTs, no charge-based information is used in the fit. The time information is used to identify paddle hits that occurred closely distributed in time and form a so-called *MRD cluster*. In this context, the usual condition to form such a MRD cluster requires a minimum of four MRD paddle hits in a time window of 30 ns. In case such a cluster is identified, the geometrical pattern of the hit paddles is investigated for a possible muon track that could explain the observed pattern. A minimum of two hits in vertical paddles and a minimum of two hits in horizontal paddles is required to enable a successful fit. This condition is necessary for the fit to obtain a 2D reference fit both in the vertical and the horizontal plane that can then be merged to get a complete reconstructed track in 3D.

In case a suitable track is found for the MRD cluster, the track reconstruction also determines the energy that is lost by the muon inside of the MRD. Since the deposited energy mainly depends on the amount of steel that the muon had to pass through, the incident angle of the muon w.r.t. the steel layer is very predictive of the amount of energy lost in the MRD. Figure 4.1 shows how the energy loss depends on the incident angle, as predicted by a Monte Carlo simulation. Higher incident angles correspond to larger distances of steel that had to be penetrated by the muon. The highest energy loss rates extend up to 30 MeV/cm for angles around 1.5 rad, while the smallest energy loss rates are  $\approx 5$  MeV/cm for angles directly perpendicular to the steel layers.

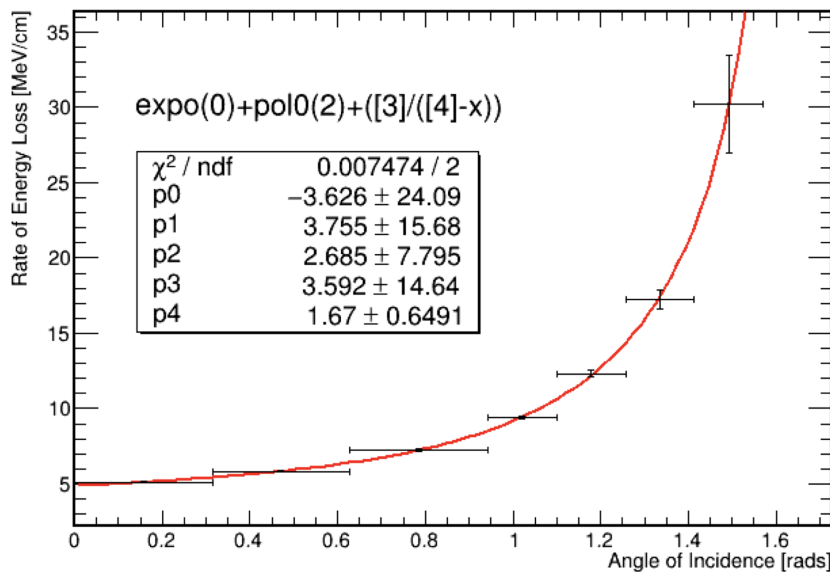


**Figure 4.1:** The energy loss per unit length is shown as a function of the incident angle. The fitted dependency is used to determine the energy deposited in the MRD based on the reconstructed track topology. Figure provided by Marcus O’Flaherty.

The fit formula

$$\exp(a \cdot \theta) + b + \frac{c}{d - \theta} \quad (4.1)$$

was used to describe the observed behavior in the Monte Carlo, with the fit values  $a = (-3.626 \pm 24.09) \ln(\text{MeV}/\text{cm})$ ,  $b = (3.755 \pm 15.68) \text{MeV}/\text{cm}$ ,  $c = (3.592 \pm 14.64) \text{MeV}/\text{cm}$ , and  $d = (1.67 \pm 0.6491)$ . This function is used as a Look-up table in the data to determine the amount of energy deposited by the muon in the MRD based on the reconstructed incident angle.

The energy loss of the muon in the MRD is vital to determine the total energy of the particle, if used in combination with the light emitted in the water tank. It is hence an important variable to determine the dependency of the neutron multiplicity on the muon energy. In terms of the scintillator paddle efficiencies, only the reconstructed start and end positions of the tracks will be used, while the MRD energy loss will not be of particular importance.

#### 4.1.2 EFFICIENCY DETERMINATION METHOD

The efficiencies of the MRD scintillator paddles in all layers are determined by evaluating intersections of MRD tracks with the paddles in all the layers. Fully through-going MRD tracks are selected from a beam data sample by requiring a track with at least one paddle hit in the first and the last layer of the MRD. Since those two border layers are used for selecting the data sample, they are exempt from the determination of the efficiency. As a consequence, the results will only include efficiencies for MRD paddles in layers 2-10.

Based on the track intersection properties, the number of expected hits  $N_{\text{exp},i}$  for each paddle  $i$  can be computed. For each expected hit, we can check if the connected PMT actually registered a pulse, and include this information as the number of observed hits  $N_{\text{obs},i}$ . The efficiency  $\varepsilon_i$  of each paddle is then simply given by

$$\varepsilon_i = \frac{N_{\text{obs},i}}{N_{\text{exp},i}} \quad (4.2)$$

One can go one step further and introduce a position-resolved efficiency  $\varepsilon_i(\vec{x})$  that investigates the dependency of the track intersection position  $\vec{x}$  on the paddle:

$$\varepsilon_i(\vec{x}) = \frac{N_{\text{obs},i}(\vec{x})}{N_{\text{exp},i}(\vec{x})} \quad (4.3)$$

Such a position-resolved efficiency can be useful to investigate the impact of border effects and to study the spatial uniformity of the paddle efficiencies in general.

Figure 4.2 shows an exemplary throughgoing muon event as used in the efficiency calibration campaign, shown in a side view of the MRD on the left and as a top view on the right. Hit times are encoded in a color-scale and show values from 92 ns up to 120 ns. These

paddle hit times are solely used for identifying clusters of paddles with coincident hits, and are not calibrated to sufficient accuracy to determine the relative timing of individual paddle hits within one muon track candidate. As a consequence, the colors cannot be used to infer the direction of the associated muon track, but rather represent that the hits occurred closely in time. The blue arrows highlight helper functions that are used in the course of the fit procedure, while the green dotted line highlights the final muon track fit result. Please note that the larger paddles in the side view show the projections of the vertical paddles and the larger paddles in the top view represent the projections of the horizontal paddles. A hit on any paddle will hence be visible in both projections, while the side view will give more details on the exact horizontal paddle hit topology and the top view is more suited to investigate vertical paddles.

When comparing the fitted muon trajectory with the observed hits, it becomes clear that 2 paddles did not detect a pulse despite crossing paths with the muon track. These paddles are highlighted with red boxes in the figure and would receive a slightly lowered efficiency based on this event. The information about the number of observed and expected events is then combined based on many such events and results in the calculation of the efficiency values for each paddle based on equations (4.2) and (4.3).

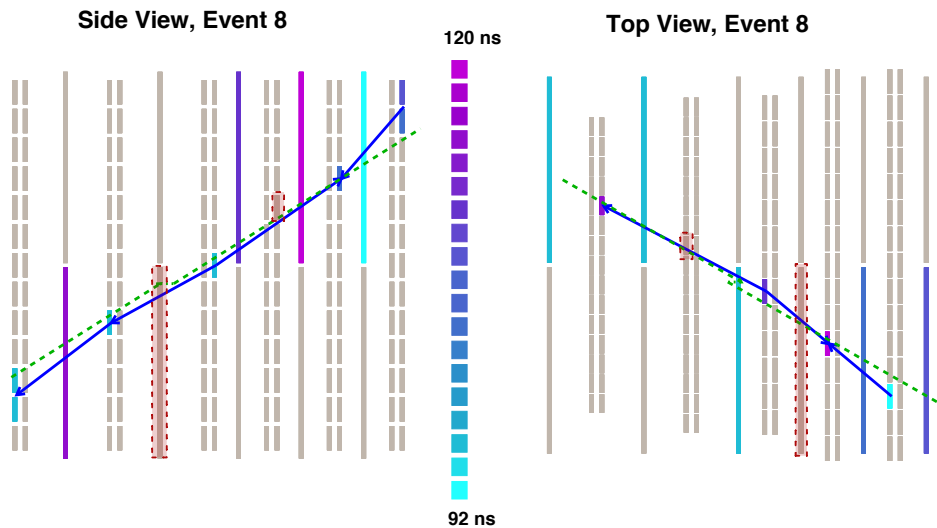


**Figure 4.2:** Exemplary MRD event with paddle hit times encoded in a color scale and the reconstructed muon track shown as a dotted green line. Two paddles (highlighted in red) did not record any hits although they are intersecting with the reconstructed muon track. The information about such missing paddle hits for through-going muon events is evaluated to determine the efficiency for each paddle.

#### 4.1.3 MONTE CARLO EFFICIENCY STUDY

By using a Monte Carlo sample with very similar properties to the real data muon sample, the presented efficiency determination method can be studied in terms of its accuracy and potential biases. For this purpose, a simulation sample was produced in the WCSim simulation framework (highlighted in more detail in chapter 5) in which 2 GeV muons were sampled from a plane directly in front of the MRD in downstream direction. After

running the track reconstruction, the selection cuts of requiring exactly one through-going muon track and a maximum of 50 MRD paddle hits to reject noise clusters were applied to the simulation sample. For the selected events, the intersections of the reconstructed muon tracks with the scintillator paddles were evaluated and efficiencies calculated based on equations (4.2) and (4.3).

Within the Monte Carlo framework, the scintillator paddles are implemented with the expected realistic dimensions and connected to sensitive PMT detectors. The efficiency of transmitting a scintillation pulse through the whole paddle to the PMT detector is implemented based on a very simple threshold mechanism with  $\varepsilon_{\text{MRD,MC}} = 95\%$ , where all energy depositions above 0 MeV are considered to produce a scintillation signal in the paddles. The reconstructed paddle efficiencies are thus expected to be close to this true efficiency value of 95%, and any differences would be indicative of biases in the method.

Figure 4.3 shows the results of the efficiencies obtained in the Monte Carlo study as a function of the MRD channelkey number. The expected true efficiency value in the simulation  $\varepsilon_{\text{MRD,MC}}$  is shown as a red dotted line. It is clearly visible that most channels reproduce the expected true value very well. However, there are some paddles that have significantly lower reconstructed efficiency values, with differences on the order of 10-15%. These paddles will be investigated in more detail in the following.

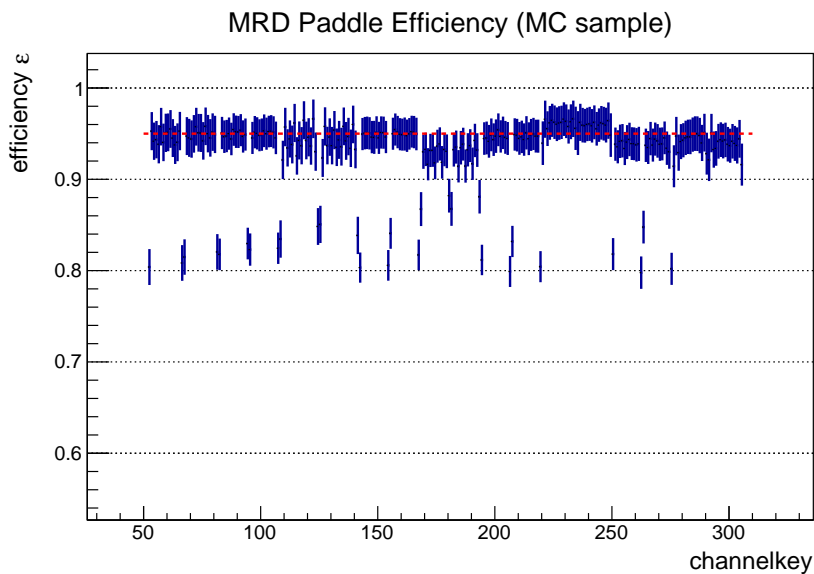


**Figure 4.3:** Determined MRD paddle efficiencies in the simulation sample as a function of the MRD channelkey. All paddles are expected to have an efficiency of 95%, which is depicted as the red dotted line. While the efficiency is reconstructed very closely to the expected value for most paddles, there are some outliers for which the reconstructed efficiency is significantly lower than expected.

When looking at the same efficiency values in a spatial detector view as depicted in figure 4.4, it becomes evident that paddles with systematically lower reconstructed values are clustered at the edges of the horizontal MRD layers L3, L5, L7 and L9. The reconstructed efficiency values for those border paddles are at the level of 80-85% compared to the usual expected level of 95%. The observed decrease in efficiency hence seems to be rooted in edge effects: Paddles that are located at the very ends of horizontal layers are less likely

to be included in the through-going muon event sample since the allowed start and end points for such tracks are very restricted. Additionally, tracks that pass the edge paddles at the very border of the layer are more likely to not deposit any energy in the paddle, even if the reconstructed track would intersect and hence include the paddle in the efficiency calculation.

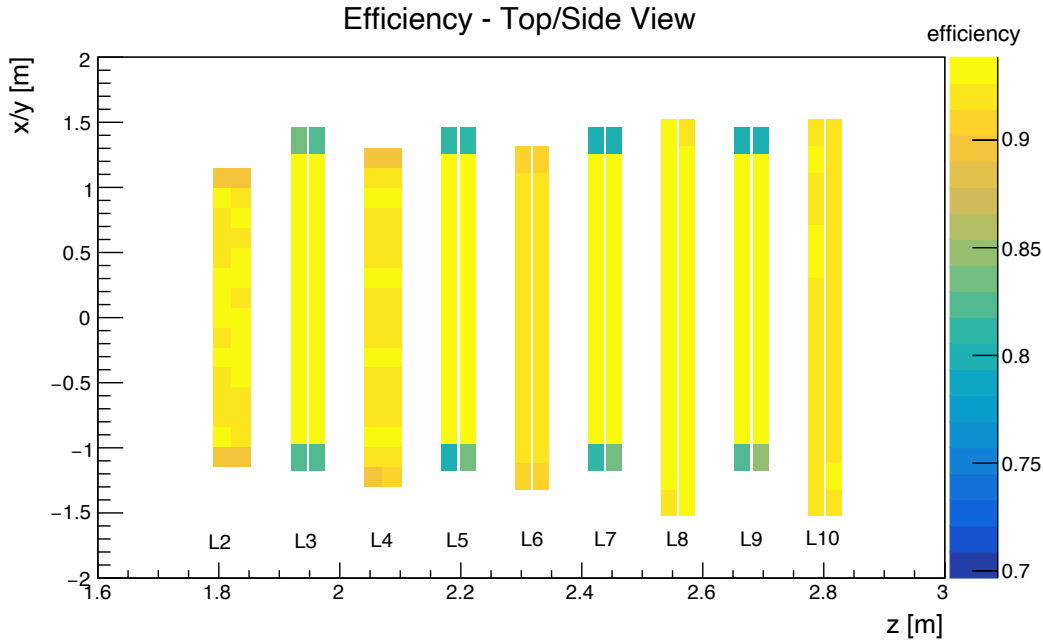


**Figure 4.4:** Reconstructed MRD paddle efficiencies for the simulation sample shown as a function of the spatial position of the MRD paddles. Even-numbered layers correspond to vertical MRD layers, while odd-numbered layers correspond to horizontal layers, with the first and eleventh layer being excluded due to being used in the event selection procedure.

In order to compensate these geometry-driven biases in the efficiency determination, correction factors  $c_{\text{geo},i}$  are calculated for each paddle  $i$  based on the reconstructed efficiency values  $\epsilon_{\text{rec},i}$  in this simulation study:

$$c_{\text{geo},i} = \frac{\epsilon_{\text{MRD,MC}}}{\epsilon_{\text{rec},i}} \quad (4.4)$$

Under the assumption that the MRD scintillator paddles are realistically implemented in the simulation framework, the correction factors can then be applied to the reconstructed MRD paddle efficiencies in data to obtain geometry-corrected MRD paddle efficiencies via

$$\epsilon_{\text{corr},i} = c_{\text{geo},i} \cdot \frac{N_{\text{obs},i}}{N_{\text{exp},i}}. \quad (4.5)$$

To conclude, the presented simulation study shows that MRD paddle efficiencies can be successfully reconstructed based on the presented method of evaluating intersections of reconstructed through-going muon tracks with the MRD paddles. Geometry-driven biases were found in the determination of the efficiencies for paddles located at the edges of the horizontal layers. To compensate for them, correction factors were calculated for all paddles, and will be applied when evaluating the efficiencies on data in the following section 4.1.4.

#### 4.1.4 CURRENT MUON RANGE DETECTOR EFFICIENCIES

When looking at the MRD paddle efficiencies in the data, we consider a sample of through-going muons in BNB beam-triggered events. As for the Monte Carlo case, less than 50 MRD paddle hits are required to avoid particularly noisy and unphysical events. In addition, only events with exactly one reconstructed through-going muon track are selected for this efficiency calibration data sample. Additional tracks in the event might influence or bias the efficiency calculation and are hence excluded.

The resulting MRD paddle efficiencies based on the beam data sample are shown in figure 4.5 in a spatial detector representation for the layers 2-10. Layers 1 and 11 are excluded from the efficiency determination since they define the coincidence condition for selecting through-going events. Paddles which are inoperative due to problems with their respective PMTs are shown in grey and do not collect any data at the moment. Apart from those channels, the detection efficiency seems to be at very high levels around 90% for almost all MRD paddles. Three channels seem to exhibit slightly lower efficiencies around 60% and have been observed to record lower data rates compared to the other channels. They are currently under further investigation and will potentially be amplified in the future to improve their efficiencies.

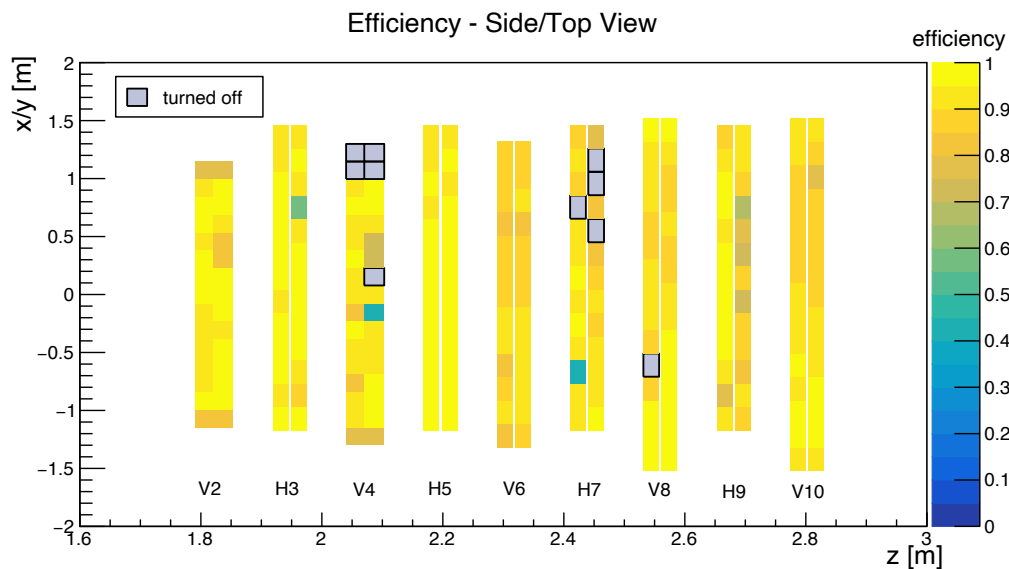


**Figure 4.5:** MRD paddle efficiencies in detector space in a combined side/top view of the subdetector. The two outermost horizontal layers (H1/H11) are excluded from the efficiency determination since they define the coincidence condition for the through-going muon event selection. Tubes that have been turned off due to problems are shown in grey.

When looking at the efficiencies as a function of the channelkey numbers, one obtains the dependency that is shown in figure 4.6. While most channels exhibit very high efficiency values around 95% comparable to the MC study case, there are some instances in which channels seem to have slightly lower efficiencies compared to this almost optimal value. For instance, there are some channels for which the efficiency values are located between 80% and 90%, and even some single channels with efficiencies going down to values around 60% (also visible in the spatial detector view). In addition to those channels, the

figure also shows some very low efficiency values around 0% which can be attributed to channels that have been turned off (marked in grey in the spatial efficiency plot).

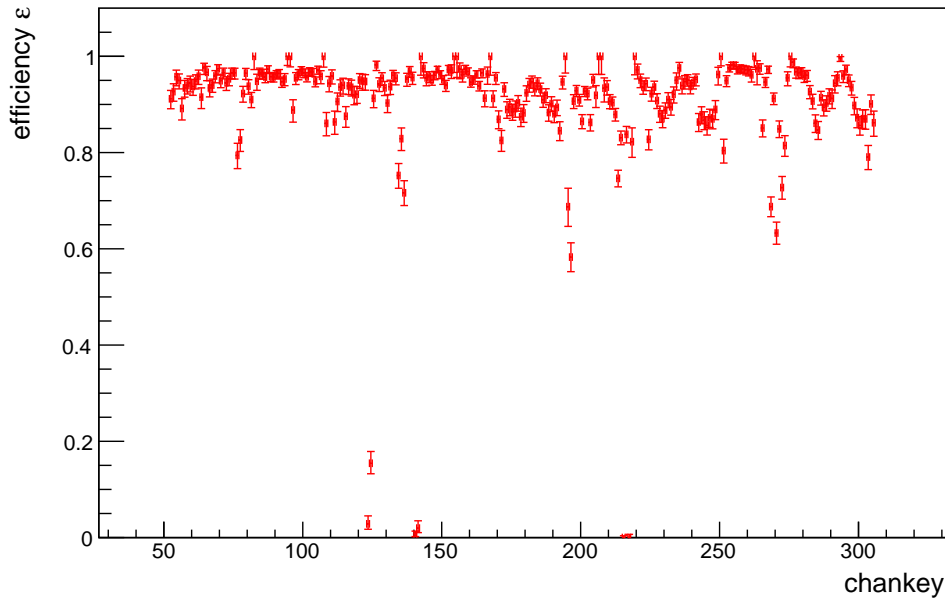


**Figure 4.6:** Corrected MRD paddle efficiencies as a function of the MRD channelkey. Correction factors were calculated based on Monte Carlo studies and were used to remove biases in the efficiency determination for paddles located at the borders of their layer.

Table 4.1 provides an overview of the fraction of MRD paddles in the different efficiency regions from 0 to 100%. 91.3% of all investigated MRD paddles show good efficiency values of at least 80% or higher, with the majority of paddles (77.6%) even displaying an efficiency of at least 90%. 3.1% of MRD paddles show slightly lower efficiency values between 70 and 80%, while 5.1% of MRD paddles populate the efficiency region below 70%. The majority of those paddles (3.9%) are turned off and can be found in the efficiency region between 0 and 10%. Only 3 paddles (1.2%) are turned on but very unreliable: those scintillator paddles exhibit efficiency values between 10% and 70%. In general, the observed MRD paddle efficiency levels are reasonably high with only a small fraction of channels that are either turned off or unreliable. The average efficiency and its associated standard deviation for all MRD scintillator paddles is found to be  $\varepsilon_{\text{MRD}} = (90.3^{+9.7}_{-14.9})\%$ . When only considering channels that are turned on, the average MRD paddle efficiency improves to a value of  $\varepsilon_{\text{MRD}}(\text{active}) = (92.1 \pm 7.9)\%$ .

Efficiency region	0-10%	10-30%	30-70%	70-80%	80-90%	90-100%
Number of paddles	10	2	1	8	35	198
Fraction of paddles	3.9%	0.8%	0.4%	3.1%	13.7%	77.6%

**Table 4.1:** Overview over the number of paddles in the different efficiency regions. Paddles located in the (0-10)% bin had to be powered off due to technical problems. Except for those channels, almost all channels show efficiencies higher than 80%, with only 5% of paddles displaying smaller values.

In addition to the actual efficiency values, it is important to verify that the properties of the scintillator paddles did not change significantly over the course of the data taking

period. In this context, figure 4.7 shows the distribution of the MRD efficiency values as a function of the run number in the form of a candle plot. The data taking period covered by the plot spans from the beginning of run 2285 on the 10th of December, 2020 until the end of run 2873 on 13th of June, 2021. The complete time span is divided into four smaller periods, covering the run numbers (2421-2460), (2506-2630), (2633-2688) and (2767-2873). The candle plot depicts the mean values of the efficiency distributions as circles and the median efficiency values as lines in the center of the boxes. As can be seen from the plot, both the mean and the median MRD paddle efficiency value did stay rather constant over the considered time span.

In addition, single outliers of the efficiency distribution are shown as crosses in the candle plot. The three low-efficient channels mentioned earlier are amongst these outlier points and seem to fluctuate in the range of 20 - 70% between the different run periods, indicating a rather unstable behavior. As mentioned earlier, those channels will potentially be amplified in the future to increase their efficiency and stability. Except for these 3 unstable paddles, the rest of the outliers and high-efficiency paddles seem to remain very stable over time. The MRD efficiency calibration hence demonstrates that the majority of channels of the Muon Range Detector can be considered to detect muons at very high efficiency levels over the whole time period of the ANNIE phase II data taking.

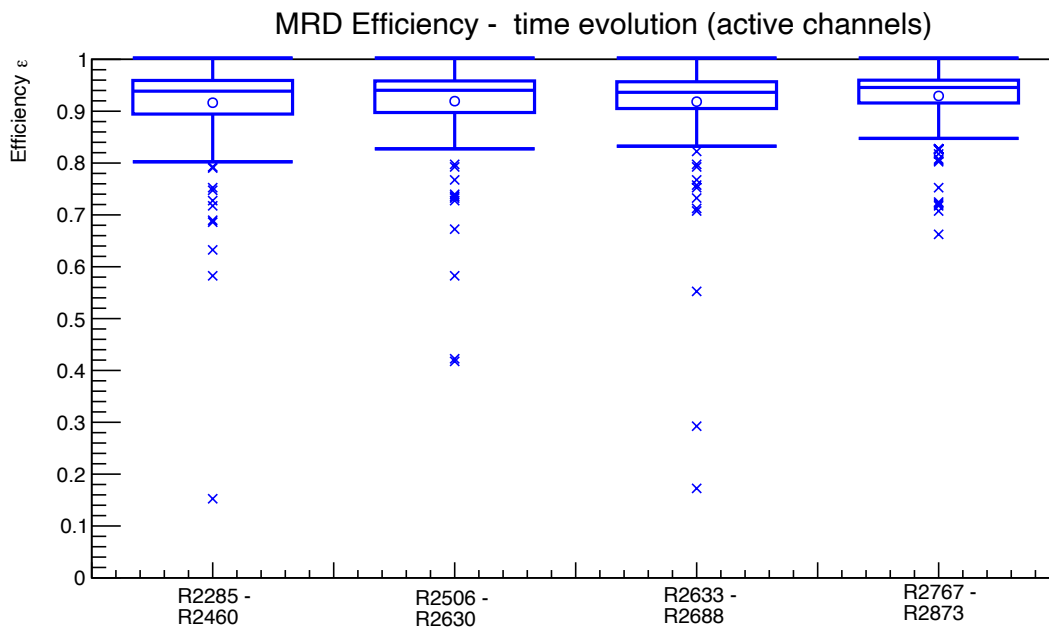


**Figure 4.7:** MRD paddle efficiencies as a function of time. The time axis is labeled in units of run numbers in the phase II data taking period of ANNIE, where run 2285 started recording data on the 10th of December, 2020 and run 2873 was finished by the 13th of June, 2021. The circles represent the mean values of the efficiency distribution at the respective point in time, while the straight line in the middle of the box indicates the median efficiency value. X-shaped markers define outliers of the efficiency distributions.

An additional interesting feature of the paddle efficiencies is their spatial dependency. Based on the intersection properties of the muon with the paddle, one can determine how the detection efficiency varies as a function of the position on the paddle by making use of equation (4.3). Figure 4.8 shows the results of such a position-resolved efficiency scan for

an exemplary MRD layer. The different paddles are highlighted in different colors, and the position  $x_{\text{Layer}}$  denotes the position perpendicular to the paddle orientation. The plot hence shows how the efficiency varies as a function of the position along the width of the paddle. It is evident that the general efficiency levels are very high with values above 90% and that there is uniform behavior across all paddles. Furthermore, there seem to be slight efficiency dips at the borders between paddles. These drops can be attributed to two features: Firstly, the ability to detect muon might be slightly reduced at the edges of the paddles. In addition, the track reconstruction has a certain reconstruction resolution and will in some cases project a track through one of the channels, although the muon actually slightly missed the respective paddle. Such a misreconstruction effect will be most prominent for positions at the edges of the paddles, since a slight shift of the reconstructed track will already make a large difference.

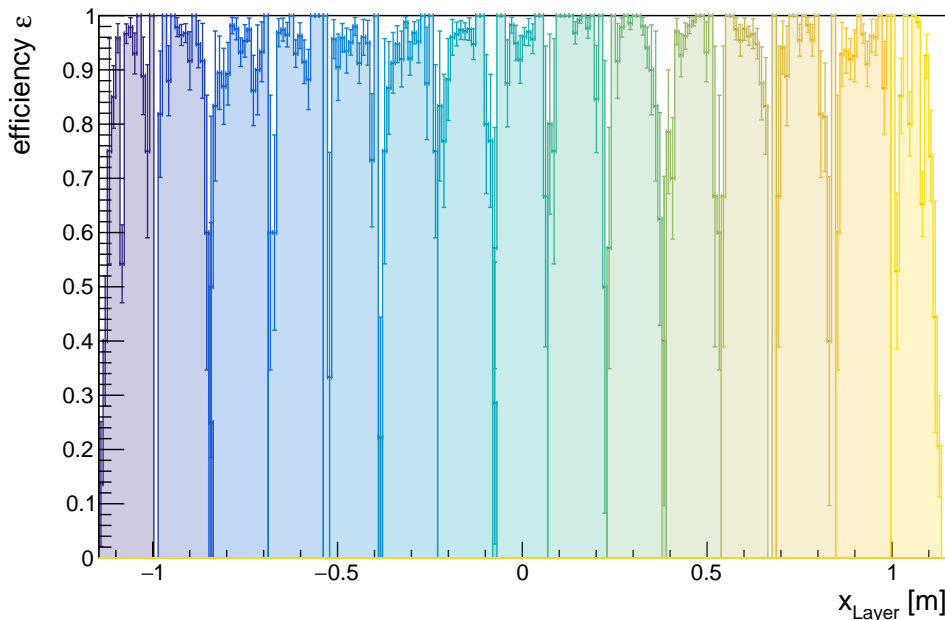


**Figure 4.8:** MRD paddle efficiencies as a function of the perpendicular position for an exemplary MRD layer. Each color represents a different paddle within the MRD layer. The observed efficiencies are very uniform across the layer and only show small dips at the borders between paddles.

Both the averaged and position-resolved MRD paddle efficiencies demonstrate that the MRD operates as expected and is mostly in a good state to take data in the scope of the neutron multiplicity analysis. The upcoming chapter 4.2 will investigate similar efficiency properties in the scope of the Front Muon Veto subdetector.

## 4.2 FRONT MUON VETO PADDLE EFFICIENCIES

The Front Muon Veto (FMV) was designed to single out events for which a muon track originated upstream of the water tank, as described in more detail in chapter 3.2.3. Vetoed events will not be considered as neutrino candidate events but are instead classified as so-called "dirt" muon events. The detection efficiencies of the 26 scintillator paddles that

make up the two layers of the FMV and that were inherited from the CDF experiment therefore directly determine how clean the selected neutrino event sample will be. The subsequent chapter will first present the method of determining the FMV paddle efficiencies in chapter 4.2.1, before evaluating the accuracy of the method in a Monte Carlo study in chapter 4.2.2. In the following, the results of paddle efficiency determinations in a laboratory setup and during ANNIE Phase I are presented in chapter 4.2.3, before concluding with a presentation of the current paddle efficiencies in chapter 4.2.4.

#### 4.2.1 EFFICIENCY DETERMINATION METHOD

The *in-situ* determination of the FMV paddle efficiencies relies on the idea of coincident MRD tracks and FMV hits: In case a muon track is found in the MRD, it is back-propagated to the position of the FMV and checked for a spatial and timely coincidence with a FMV paddle hit in one of the two veto layers. Since the two layers are only separated by a distance of 1-2 cm, a through-going muon should cause a hit in both layers. If a coincidence between a paddle is found for one of the layers, it can be checked whether the adjacent paddle in the other layer also registered a hit. By comparing the number of observed and expected hits, the paddle efficiencies can be determined for each scintillator paddle in an analogous fashion to the MRD case, compare equations (4.2) and (4.3).

Figure 4.9 schematically shows how the muon track (red) is propagated from the MRD back through the entire water tank (dotted black line) up until an intersection is found with the FMV (highlighted in orange), both in a side and top view of the experimental setup. If the intersected paddle registered a hit in one of the two layers, it is checked whether the paddle in the neighboring layer also registered a hit.

Due to aging processes in the scintillator, the used plastic scintillator is not as transparent as it used to be and there are considerable propagation losses of light that is transported inside of the paddle. As a consequence, the particle detection is less efficient for particles crossing the paddle on the far side of the connected PMT: Since the scintillation light will have to travel a larger distance before reaching the PMT, the efficiencies for particle crossings at this so-called far side of the PMT are expected to be rather small, roughly around 50%. This has to be compared to a very good detection efficiency of over 90% at the near side of the paddle, where basically no propagation losses come into play. To compensate for this deficiency in the behavior of the scintillator paddles, the two layers of the FMV are mounted in an opposing fashion. The PMTs are mounted on opposing sides of the paddles for the two layers. In that way, the low-efficient sides of one layer can be compensated by the high-efficient side of the adjacent layer, and vice-versa. In order to make use of the opposing efficiency curves, the veto information will then be evaluated in an OR-fashion between the two layers.

When taking a look at the impact of these inverse efficiency curves on the method, one has to consider their effect on the determined efficiency values. Figure 4.10 schematically shows how two arbitrary efficiency curves for two layers with minimum values of 10% and maximum values of 90% influence the number of detected hits for a uniform track position distribution. Within the first layer, the hits will be detected according to the blue dotted line, assuming that the position along the paddle can be resolved in ten bins. The

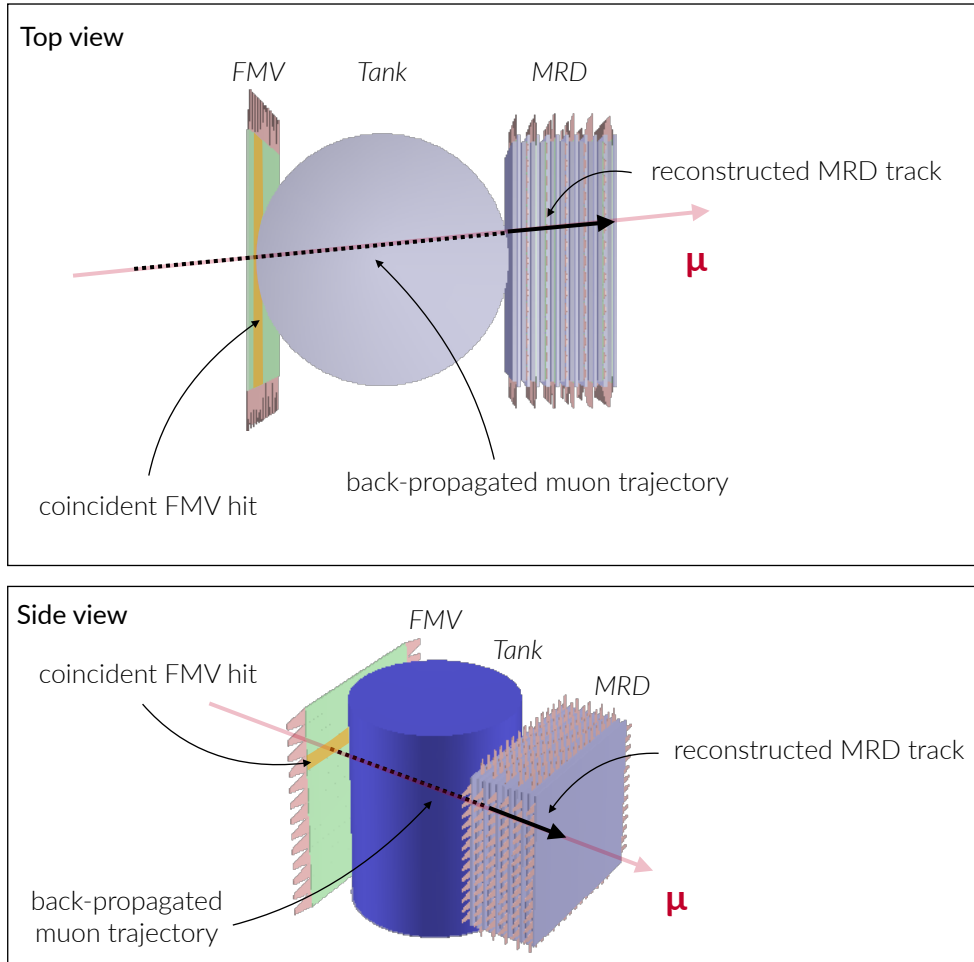


**Figure 4.9:** Schematic depiction of the FMV efficiency determination. Events with a reconstructed MRD track and a coincident FMV hit in one of the layers are selected. The MRD track is propagated back to the position of the FMV and a spatial coincidence of the MRD track and the FMV hit is evaluated. In case a spatial correspondence is found, the paddle in the adjacent FMV layer is considered for the efficiency calculation.

second paddle is subsequently investigated for hits in coincidence with the pulses that were detected in the first layer, resulting in the detection behavior depicted by the red dotted line. If the efficiency of the paddle in the second layer is now approximated by simply integrating the number of coincident events that were found in layer 2 and dividing the number by all events that were in the original layer 1 sample, the efficiency of the specific paddle in layer 2 is systematically underestimated. Position bins that feature a high efficiency in the first layer are given more weight due to making up a larger fraction of the event selection, although the efficiency for the same position will be very low in the second layer. Since higher weights will be given to position bins that feature a lower efficiency in the second layer, the determined efficiencies will be systematically lower if one simply divides the number of observed hits by the number of expected hits. In the exemplary case showcased in the figure, the determined efficiency of layer 2 would be 40%, although the actual true averaged efficiency value is 50%.

If we describe the efficiency curve of layer 1 by  $\epsilon_{L1}(x)$  and the one of layer 2 by  $\epsilon_{L2}(x)$ , the average efficiency  $\bar{\epsilon}_{L2}$  of layer 2 based on counting the number of expected and observed

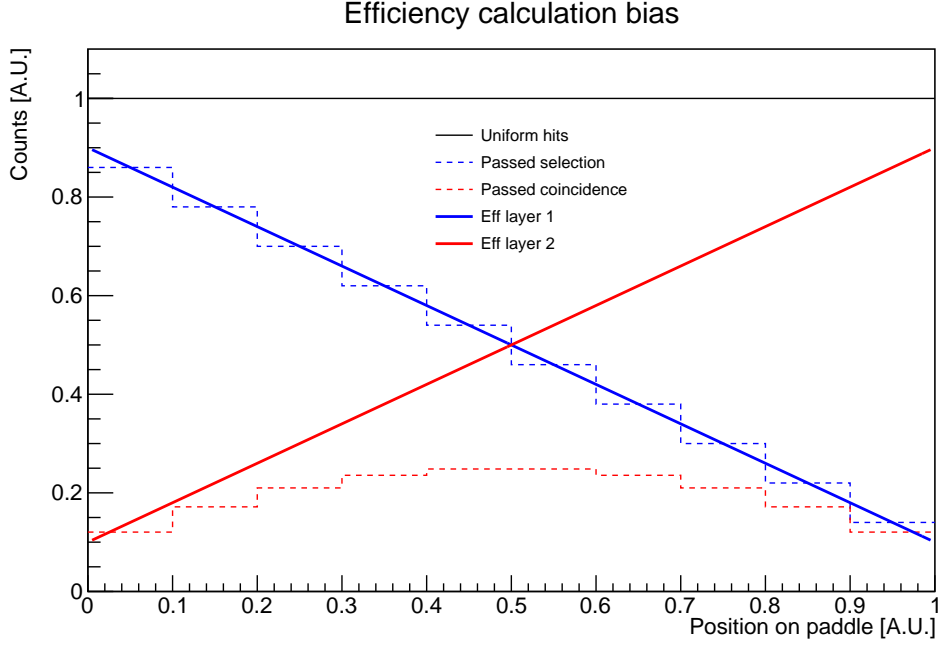


**Figure 4.10:** Effect of opposing efficiency curves on the detected coincidence rates for the FMV. Hits were assumed to be uniformly distributed along the whole length of the paddle (black curve), and efficiency curves with opposing slope were considered for the first and second layer (solid blue and red lines). While the dashed blue line then represents the number of actually detected hits in layer 1, the dashed red line highlights the number of coincident detected hits in the second layer.

hits would be

$$\bar{\varepsilon}_{L2} = \frac{N_{\text{obs}}}{N_{\text{exp}}} = \frac{\int_{x_1}^{x_2} N(x) \varepsilon_{L1}(x) \cdot \varepsilon_{L2}(x)}{\int_{x_1}^{x_2} N(x) \varepsilon_{L1}(x)}, \quad (4.6)$$

where  $N(x)$  denotes the number of true particle tracks as a function  $x$  of the position alongside the paddle, extending from  $x_1$  to  $x_2$ . The fact that the efficiency for the first layer is included in both the integrals in the numerator and denominator results in the systematic underestimation of the determined average efficiency. This has to be seen in contrast to the actual true average efficiency  $\bar{\varepsilon}_{L2,\text{true}}$  that is defined as follows:

$$\bar{\varepsilon}_{L2,\text{true}} = \frac{1}{x_2 - x_1} \int_{x_1}^{x_2} \varepsilon_{L2}(x) = \frac{1}{x_2 - x_1} \int_{x_1}^{x_2} \frac{N_{\text{obs}}(x)}{N_{\text{exp}}(x)} \quad (4.7)$$

In order to get rid of the systematic shift introduced by the convolution with the efficiency of layer 1 as shown in equation (4.6), one can try to get as close as possible to the true average efficiency. This can be achieved by counting the number of expected and observed coincident hits as a function of the position  $x$  in as many bins as possible based on the

available statistics. The true average efficiency is then approximated by

$$\bar{\varepsilon}_{L2} \approx \frac{1}{N_{\text{bins}}} \sum_{i=1}^{N_{\text{bins}}} \frac{N_{\text{obs}}(x_i)}{N_{\text{exp}}(x_i)} \quad (4.8)$$

By calculating the efficiency for each position bin separately and then averaging the information from all bins, the true average efficiency can be approximated much more accurately. As a bonus, the position-dependent efficiency will be available for each FMV paddle when making use of this method.

#### 4.2.2 MONTE CARLO EFFICIENCY STUDY

Before diving into the determination of the FMV paddle efficiencies, it is instrumental to identify selection cuts for choosing coincident MRD tracks and FMV paddle hits based on Monte Carlo simulations. These simulations should feature similar conditions as the real data sample, *i.e.* muon tracks that pass through the FMV, water tank, and MRD and which can be identified by searching for coincidences between all three subdetectors. Such a sample is generated in the simulation framework by sampling muons of  $E_{\mu} = 2 \text{ GeV}$  in a plane upstream of the Front Muon Veto and propagate the muons in downstream direction.

Muon tracks in the MRD are fit based on the usual track finding algorithm presented in section 4.1.1, and the fitted track is extrapolated to the plane of the FMV. In case a scintillator hit is observed in one of the FMV paddles, the spatial distance of the extrapolated MRD track position and the center of the FMV paddle is calculated and plotted in figure 4.11. When looking at this distance plot, a region with increased event rates is visible in the center of the plot for vertical coordinate differences of  $\Delta x = [-1.6\text{m}, 1.6\text{m}]$  and horizontal coordinate differences of  $\Delta y = [-0.4\text{m}, 0.6\text{m}]$ , and is highlighted by a red box in the plot. The observed vertical extent is in agreement with the actual length of the FMV paddles, while the horizontal dimensions of the observed coincidence region is slightly larger than the paddle height. This can be attributed to the larger effect of the MRD track reconstruction uncertainty in the case of the smaller dimension of the paddle height. Hits that are located outside of the box can be mainly attributed to accidental coincidences due to noise hits and are not considered for the event selection procedure for the data.

#### 4.2.3 LABORATORY MEASUREMENTS & PHASE I EFFICIENCIES

Before Phase I of ANNIE started data taking in 2016, the FMV paddles were characterized in a laboratory setup depicted in figure 4.12. By placing one PMT above a specific position on the paddle and one PMT below the same paddle position, cosmic muons that were passing through could be identified. The signals of the top and bottom PMT were fed into an AND electronics unit and forwarded to a scaler to count the number of cosmic muon events. In order to evaluate the efficiency of the FMV paddle, the three-fold coincidence between paddle, top and bottom PMT was evaluated by a second AND unit and counted separately on a scaler. By comparing the scaler numbers of the two-fold PMT coincidence and the three-fold PMT+paddle coincidence, the efficiency of the paddle could be determined for

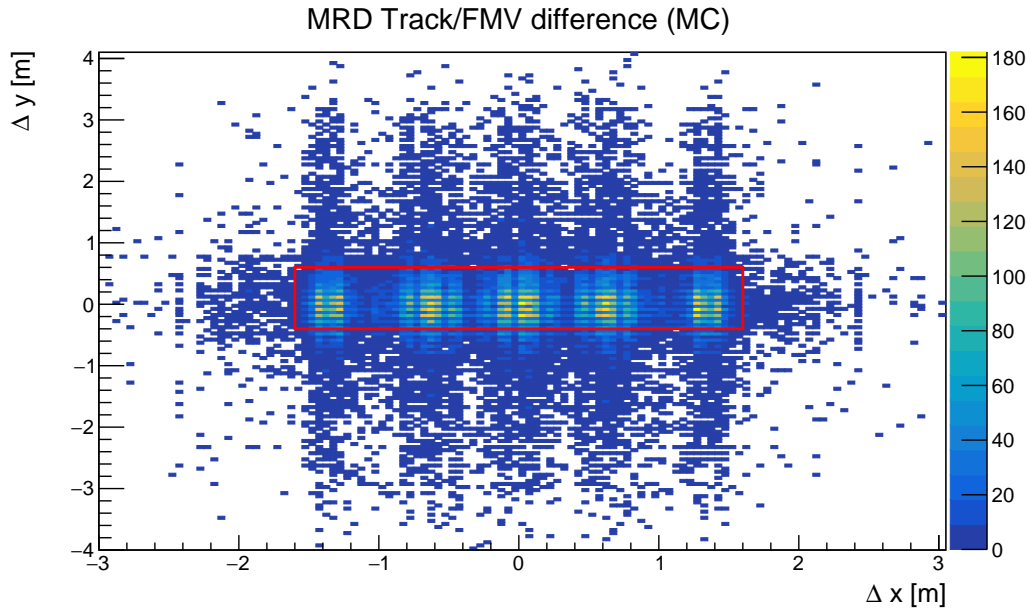


**Figure 4.11:** Spatial difference of extrapolated muon track position and FMV paddle position for coincident FMV hit + MRD track pairs in the Monte Carlo simulation sample. The difference in the  $y$ - (top/bottom) and  $x$ -coordinates (left/right) is calculated with respect to the center of the FMV paddle. The red line indicates a suggested spatial coincidence selection for the MRD tracks and the FMV hits.

the specific paddle position. For each paddle, the efficiency for one near-side and one far-side position was measured. The results indicated that hits at positions close to the PMTs reached efficiencies of 90-100%, while the far-side efficiencies were around 50-60%, as expected due to the aging scintillator properties [191].

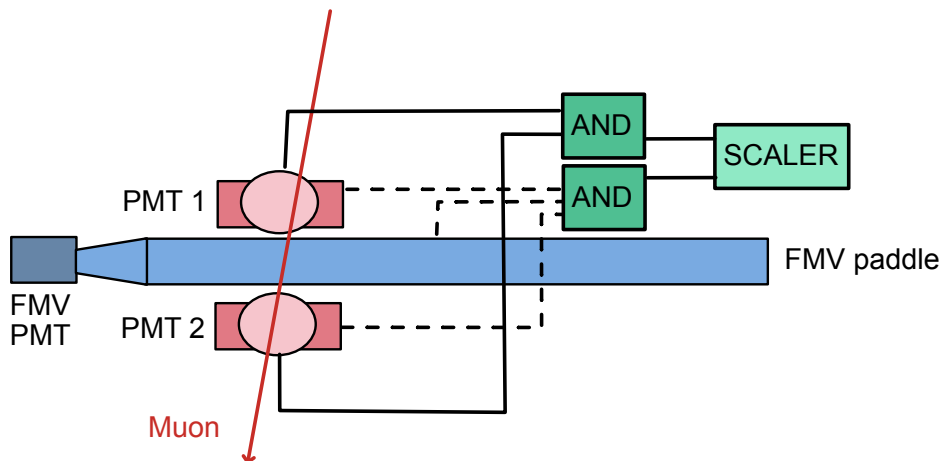


**Figure 4.12:** Setup for the laboratory measurement of the FMV paddle efficiencies conducted before Phase I of the ANNIE experiment. Muons passing through a specific position on the scintillator paddle are identified by a coincident pulse in a PMT above and below the paddle. The paddle efficiency is determined by checking how often the scintillator paddle also recorded a hit for such coincidences. Figure adapted from [191].

In addition to the laboratory measurements conducted before the start of phase I, one can also have a look at the actual data that was taken during phase I to obtain *in-situ*

efficiencies. Coincidences of FMV paddle hits with tank clusters and MRD clusters can be evaluated to obtain simple estimates for the FMV paddle efficiencies during that time. Note that it is not possible to obtain phase I efficiencies of the MRD paddles since only 4 layers of the MRD were instrumented, and it would hence be very difficult to do meaningful track reconstruction and define through-going muon samples.

Regarding the phase I data, runs 798 (April 2017) and 813 (May 2017) were taken into account for the efficiency determination. Figure 4.13 shows the results for the *in-situ* phase I efficiencies (*red*) alongside the results from the laboratory measurement (*black*). Both phase I and laboratory measurements show average paddle efficiency values in the range of 60-80%, which is consistent with the expected behavior based on near side efficiencies of around 90-100% and far-side efficiencies of around 50-60%. While the exact paddle-wise behavior is not exactly matched between the laboratory calibration and the phase I *in-situ* calibration, the general efficiency level observed with both methods matches pretty well. The observed differences can probably be accounted for by taking into account errors of the laboratory measurement (that were unfortunately not documented) and accounting for potential systematic biases in either of the methods. The laboratory measurements confirm the deficiency of detecting hits at the far side of the paddles, while the phase I measurement shows that the efficiencies could also be reconstructed based on recorded data in the hall.

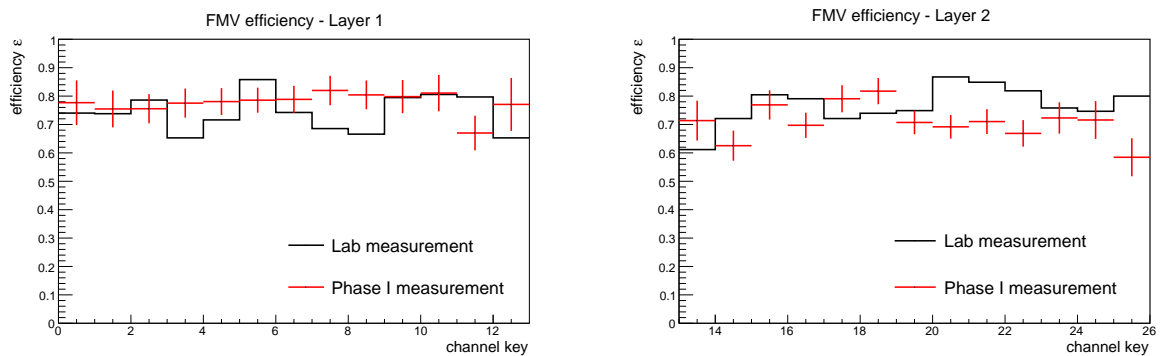


**Figure 4.13:** Comparison of FMV efficiencies determined in lab measurements (*black*) and *in-situ* measurements during ANNIE phase I (*red*) for layer 1 (left) and layer 2 (right). While the laboratory measurements were taken from [192], the phase I efficiencies were determined retrospectively by looking back at the phase I runs 798 and 813 in the scope of this thesis.

#### 4.2.4 CURRENT FRONT MUON VETO EFFICIENCIES

The results for all current phase II FMV paddle efficiencies are shown in figure 4.14 and were obtained by applying the method presented in chapter 4.2.1. Results are shown separately for layer 1 and 2 as a function of the channelkey number. For each of the two layers, increasing channelkey numbers correspond to paddles at increasing heights. All averaged efficiency values are in the range of 65% to 90%, indicating that the paddles generally perform at similar levels compared to the laboratory testing phase and the calibration with phase I data.

In order to obtain the averaged efficiencies for each paddle which are shown in figure 4.14, the efficiency curves for every channel were first determined as a function of the position  $x$

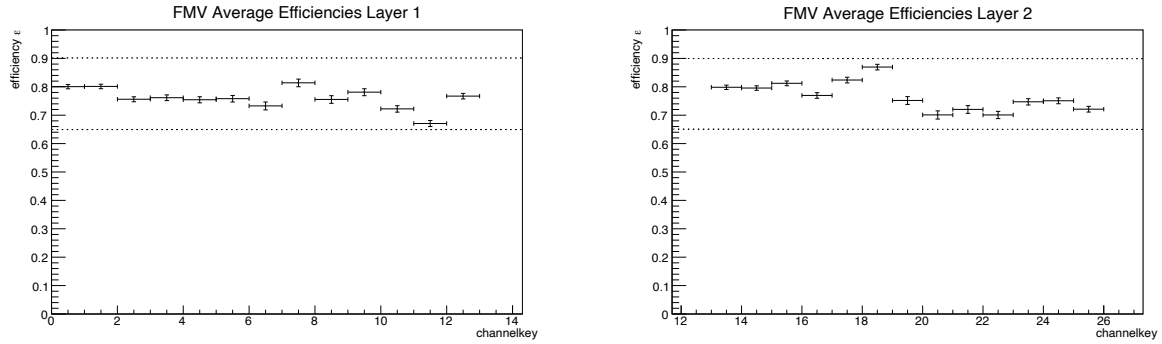


**Figure 4.14:** FMV paddle efficiency as a function of the FMV channelkey for the two FMV layers. The efficiencies for all paddles range from 65% to 90%.

along the paddle. Five position bins covering the whole paddle length range were chosen to evaluate the position-dependency of the efficiency curves. Figure 4.15 shows the averaged position-dependent efficiency results for each layer of the FMV, where the behavior of the first (second) layer is depicted in blue (red). A clear linearly shaped dependency is visible, with efficiencies reaching a level of 90% at the near side of the paddles, and lower efficiency values of  $\approx 60\%$  at the far side of the paddles. The opposing slope of the efficiency curves for the two layers is also visible: While the PMTs are located at the side with negative  $x$  values for layer 1, they are mounted at the side with positive  $x$  values for layer 2. The PMT near-side always exhibits the highest efficiency values, and decreasing efficiencies are observed when moving further away from the PMT. This behavior is expected due to the aging-induced intransparency of the scintillator material, and confirms the findings from previously conducted laboratory measurements, as presented in the earlier chapter 4.2.3. The single position-resolved efficiency curves for all 26 channels of the FMV demonstrate the same behavior and are shown in the appendix in figures B.1 and B.2.

Based on the determined efficiency curves for the paddles in the first and second layer, one can calculate the probability of failing to identify a muon with the FMV. Given the efficiencies  $\epsilon_{L1,i}(x)$  and  $\epsilon_{L2,i}(x)$  of tagging a muon at a certain position  $x$  along paddle number  $i$  in the two layers, the chance of missing a muon at the given position is given by

$$P_{\text{miss},i}(x) = (1 - \epsilon_{L1,i}(x)) \cdot (1 - \epsilon_{L2,i}(x)) \quad (4.9)$$

This probability is calculated for five different positions for each of the 13 paddle pairs. The results are shown in figure 4.16 and indicate that paddles at smaller heights seem to have a lower chance of missing a muon, while paddles mounted at higher positions seem to have a slightly higher risk for missing a muon. Generally speaking, the chance of failing to identify a dirt muon as such is below 10% for all paddles and all positions along those paddles. On average, the average chance of missing a muon is found to be  $\bar{P}_{\text{miss}} = (4.4 \pm 1.6)\%$ , corresponding to an average FMV tagging efficiency of  $\bar{\epsilon}_{\text{FMV}} = (95.6 \pm 1.6)\%$ . This result highlights the fact that the intended specifications of reaching a maximum failure rate of 10% have been met and the FMV system works as intended. However, it also becomes evident that there will be a need for additional software-based selection cuts in order to further reduce the number of dirt muons in the selected neutrino candidate sample. Such

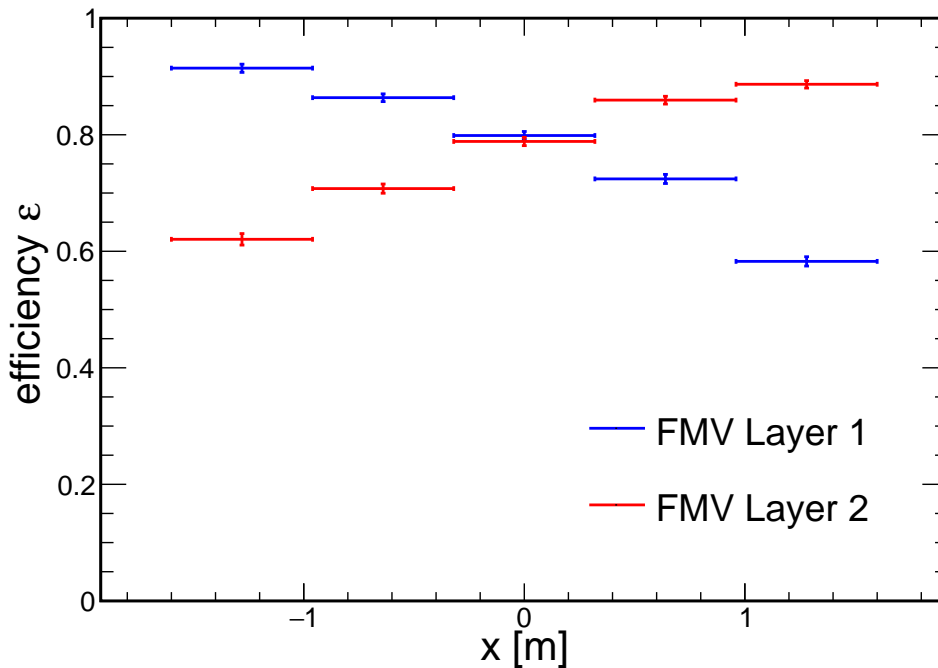


**Figure 4.15:** Averaged FMV efficiencies for the two scintillator layers as a function of the position on the paddle. The opposing efficiency curve is clearly visible. While positions close to the PMT achieve efficiencies of  $\epsilon_{\text{close}} \approx 90\%$ , hits at the far side of the paddle are only detected with an efficiency of  $\epsilon_{\text{far}} \approx 60\%$ .

cuts could make use of the fact that dirt muons will have an entry point in the water tank. PMT tubes located directly next to the entry point will see a large amount of light as a consequence. By looking for these lit PMT tubes opposite of the main detected Cherenkov cone pattern, one can potentially identify additional dirt muons originating from outside of the water tank, compensating the inefficiency of the FMV in some cases.

The evolution of the FMV paddle efficiencies can be investigated over time in a similar fashion to the MRD paddle efficiencies. Figure 4.17 shows a candle plot for the FMV efficiency distribution, for the time period covered by the runs 2421 to 2873. The run period corresponds to the time span from January 20th, 2021 up until June 13th, 2021 and is divided into the segments (R2421-R2460), (R2506-R2630), (R2633-R2688) and (R2767-R2873). Within the plot, the circles indicate the mean of the efficiency distribution, while the line within the box represents the median value of the distribution. Both the mean and median value stay very constant over time with values around 75%. The extent of the distribution, indicated by the hatches, also does not change significantly over time. The FMV efficiency distribution does not contain any outliers, which would be visible in the form of crosses in the plot. All in all, the efficiencies of all FMV paddles seem to be very constant over the entire data taking span of ANNIE phase II. The determined chances of missing a muon with this muon subdetector can hence be considered constant for the whole data taking period.

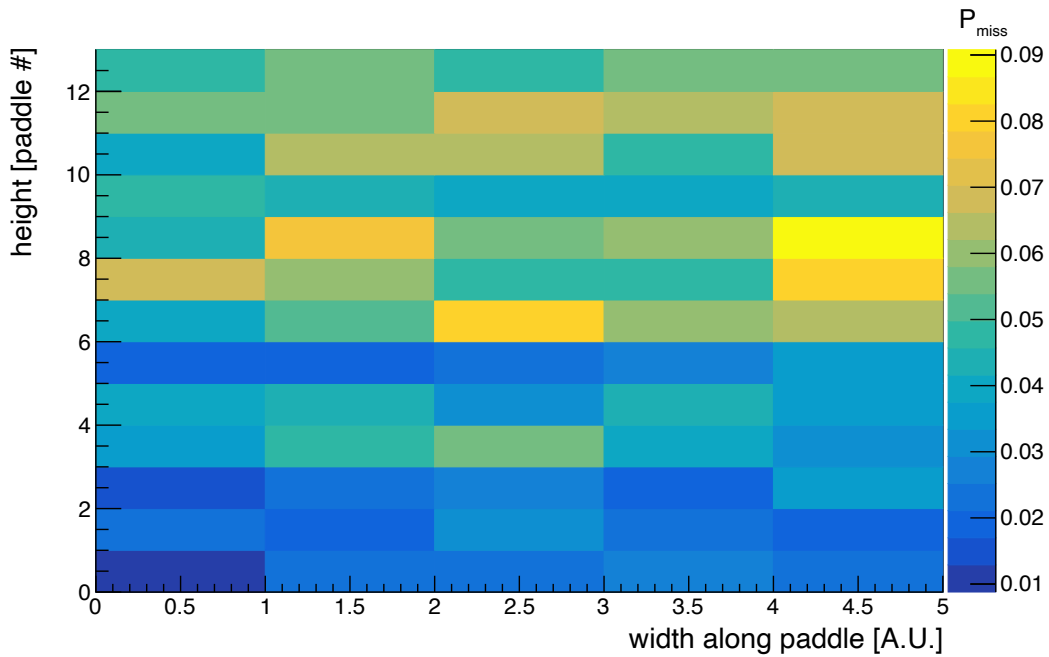


**Figure 4.16:** Probability to miss a muon as a function of the FMV paddle number and position on the paddle. Higher paddle numbers correspond to paddles that are located at greater heights, while the x-coordinate depicts the position alongside the paddles in arbitrary units.

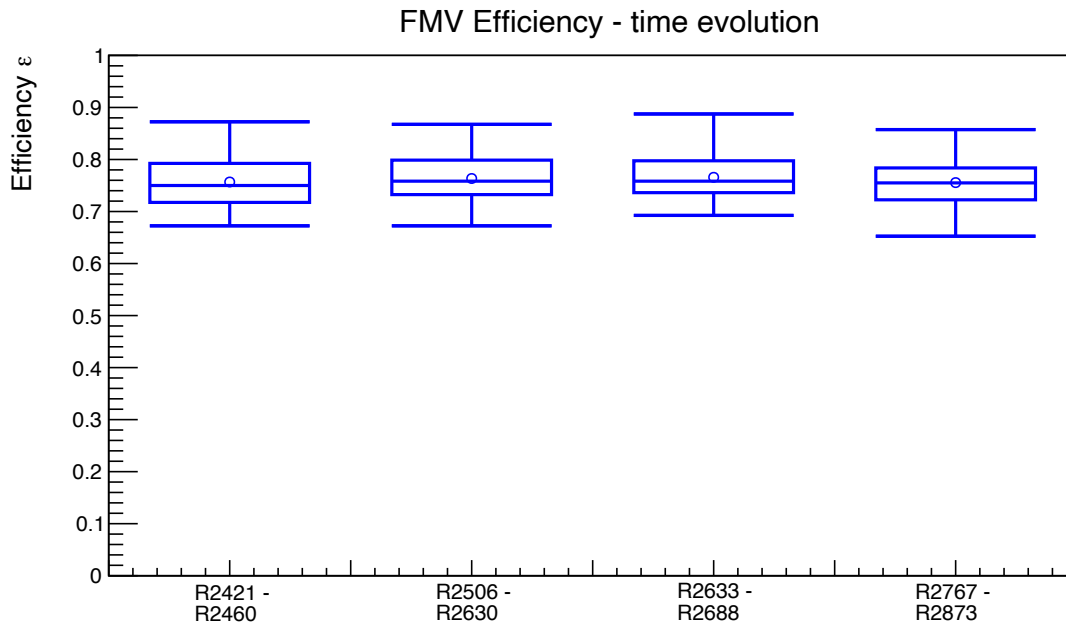


**Figure 4.17:** FMV paddle efficiency distribution as a function of time. The time axis is labeled in units of run numbers in the phase II data taking period of ANNIE, where run 2421 started recording data on the 20th of January, 2021 and run 2873 was finished by the 13th of June, 2021. The circles represent the mean values of the efficiency distribution at the respective point in time, while the straight line in the middle of the box indicates the median efficiency value.

### 4.3 IMPACT OF EFFICIENCIES ON TRACK RECONSTRUCTION PERFORMANCE

After having determined the MRD and FMV scintillator paddle efficiencies as presented in the subsections above, their impact on the neutron multiplicity analysis of ANNIE needs to be evaluated. In this context, inefficiencies in the FMV paddles will lead to a contamination of dirt muon events within the selected beam neutrino sample, while inefficient MRD paddle hits will lead to a distorted muon track reconstruction, associated with increased uncertainties in the reconstruction of the energy and the angular orientation of the primary muon. The impact of both the MRD and FMV paddle inefficiencies will be considered as systematic effects in the preliminary neutron multiplicity analysis in chapter 6, with the details of the systematic analysis presented there. As a preparatory step, the current section will already investigate the direct effect of the paddle inefficiencies on the muon track reconstruction performance in the MRD.

The impact of inefficient channels is studied by creating two simulation samples of beam neutrino interactions in ANNIE: The first sample assumes a standard efficiency of 95% for all paddles, while the second sample assigns individual efficiencies for each paddle based on the characterization results. The track reconstruction algorithm is applied to both samples and evaluated in terms of the reconstruction accuracies. The difference in reconstruction performance is then studied on an overall scope and as a function of the number of missing paddle hits that were caused by inefficiency effects.

Firstly, the impact of the amount of missing channels on the reconstruction performance can be evaluated. Figure 4.18 depicts the fraction of tracks that are still reconstructed successfully even with a certain number of missing paddles as a red line. As expected, the reconstruction efficiency decreases with the number of omitted paddles and goes down to a value of 60% of the nominal efficiency in the case of 6 missing paddle hits. Luckily, this case does not occur very often, as shown by the black line in the same figure which represents the respective frequency for each number of missing paddles. Most frequently, the realistic MRD paddle efficiency values result in no additional missing paddle hits (66%) compared to the nominal simulation, while the cases of 1 missing paddle (25%) and 2 missing paddles (7%) are already much less likely.

When investigating the impact of the realistic MRD paddle efficiency values on the overall reconstruction performance, the distributions of various reconstructed variables can be studied. Figure 4.19 shows the difference of true and reconstructed values for the total track angle (*left*) and the  $x$ -coordinate of the muon track start position. The beam neutrino sample was selected for events that featured a muon originating in the Fiducial Volume of ANNIE and a stopping muon track in the MRD. When comparing the distributions for the realistic MRD paddle efficiencies (*red*) and the nominal MC simulation (*blue*), the lowered track reconstruction efficiency becomes noticeable. A 14% reduction of successfully reconstructed tracks is observed compared to the original simulation. The shapes of the distributions, on the other hand, are very similar: The track angle reconstruction distribution is characterized by a mean value of 0.029 rad (0.032 rad) and a standard deviation of 0.174 rad (0.173 rad) in the case of the nominal MC (realistic MRD paddle efficiencies). On a similar note, the distribution of the  $x$ -coordinate of the start position

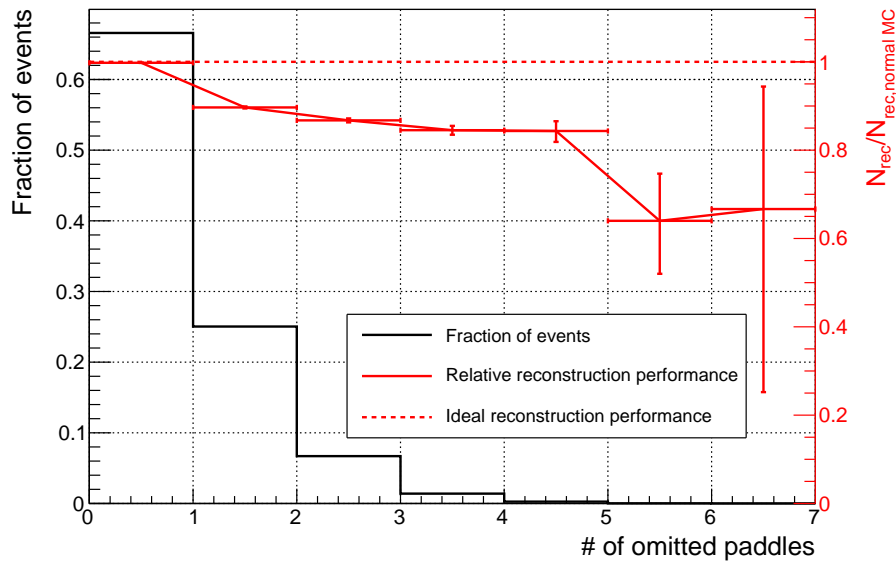


**Figure 4.18:** The fraction of events that featured a certain amount of missing (omitted) paddle hits is shown in black, while the relative reconstruction efficiency with respect to the nominal Monte Carlo simulation is shown in red. The ideal case of identical reconstruction performance is depicted as a red-dashed line.

features very similar standard deviations of 11.56 cm (11.62 cm) for the two cases. The increased number of missing MRD paddle hits hence primarily leads to a decrease in reconstruction efficiency, but does not affect the quality of the track parameters in case a track was successfully reconstructed.

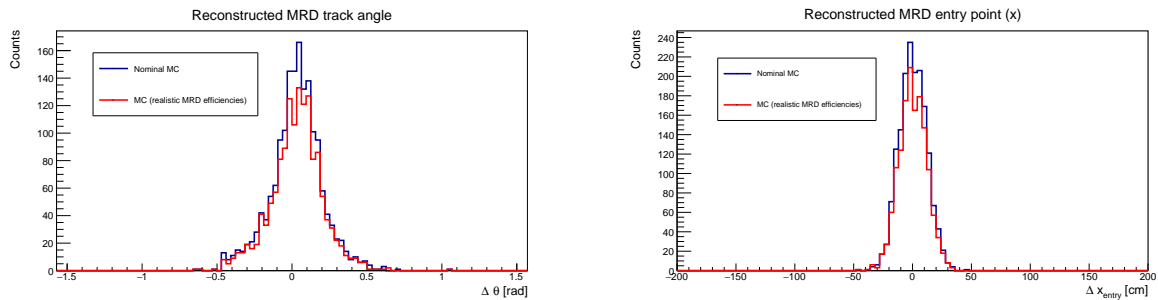


**Figure 4.19:** The MRD track reconstruction accuracy is shown for the case of the nominal Monte Carlo (*blue*) and the realistic paddle efficiency configuration (*red*). The difference of reconstructed and true values are shown for the total track angle (*left*) and the *x*-coordinate of the track start position (*right*).

The decreased MRD track reconstruction efficiency will need to be factored into the CC-related cross-section measurement, but does not affect the neutron multiplicity analysis too strongly. The main impact of the non-perfect paddle efficiencies in the latter case will consist of a reduced number of events in the final data sample and hence an increased statistical uncertainty. This will likely be improved in the future by hardware modifications such as PMT base replacements for channels that exhibit especially bad behavior.



Part III

TOWARDS A NEUTRON MULTIPLICITY MEASUREMENT  
WITH ANNIE



# 5

## Validation & Tuning of the Monte Carlo simulation

---

*“The truth. It is a beautiful and terrible thing, and should therefore be treated with great caution.”*

—Albus Dumbledore

In order to fully understand and characterize the different event signatures that are observed in a particle physics experiment, the detector is usually implemented in the scope of a Monte Carlo-based simulation framework. In such a simulation, random number generators are used to mimic the stochastic nature of physical processes driving the propagation and interactions of particles in matter. Simulating the detector response for well-known physics processes is crucial for developing reconstruction algorithms that can then be used to characterize and understand the real data. This will be highlighted in the subsequent chapter 6 in which simple muon reconstruction techniques will be presented in the scope of a neutron multiplicity analysis, in particular with respect to the vertex and energy reconstruction. In addition, simulated data samples are also very suitable for developing discrimination techniques in terms of Particle Identification (PID) tasks. These classification techniques will be used on the data samples to distinguish electrons and muons as well as single and multi Cherenkov ring events.

In order to make effective use of such a Monte Carlo simulation framework, the simulated detector response needs to match reality as closely as possible. For that reason, the detector geometry should mirror the known geometric features of the detector very accurately. In addition, the photomultiplier tube electronics response should be modeled in a way such that it reproduces the photoelectron charge distribution observed in the data. Furthermore, reflective surfaces within the detector need to be implemented with the right reflectivity in order to reproduce the amount of reflections that are observed. The validation of the Monte Carlo simulation framework is usually performed by making use of calibration samples with known energetic and geometrical features. Such calibration samples should invoke the same detector response in reality and within the simulation. By comparing the detector response of simulation samples for different values of not well-known tuning parameters,

it becomes possible to select the particular tuning parameters that reproduce the data best for a multitude of calibration samples. Since such a validated simulation framework has been proven to reproduce the detector response for the selected calibration samples, it can then be used with reasonable confidence to predict the detector response for other events that are not directly available as a calibration sample, but are then encountered e.g. within the main data sample.

The following chapter will briefly outline the different components of the ANNIE simulation framework in chapter 5.1. Very generally speaking, the simulation is divided into two parts. The interaction of the primary neutrino with the nuclei in the detector medium are simulated in the scope of a so-called neutrino event generator, as presented in chapter 5.1.1. All particles that are produced as a result of the primary neutrino interaction – including optical photons – are then propagated through the detector up until they are absorbed or exit the detector volume in the scope of a separate detector simulation framework that will be highlighted in chapter 5.1.2. In case photons hit the photocathode of the PMT surfaces, the electronics response will be included in the latter framework.

The original unvalidated version of the simulation framework will be investigated briefly in chapter 5.2. In particular, the detector response for neutrino beam events will be compared with commissioning data. In this context, exemplary PMT charge responses will be opposed and compared with each other to gain a first impression of which aspects of the simulation might need to be adjusted.

Modifications and improvements to the original simulation framework are then presented in chapter 5.3. Additions in terms of making both the detector geometry and the PMT charge response more realistic will be highlighted. Response parameters affecting the overall detected light and the amount of reflection will be tuned based on the agreement of Michel electron, through-going muon and neutron calibration samples, as shown in chapter 5.4.

The last section 5.5 of this chapter highlights the agreement of the simulation and the data regarding the MRD detector response. For this purpose, reconstructed muon track parameter distributions are compared for an equivalent beam neutrino data sample.

## 5.1 ANNIE MONTE CARLO SIMULATION

For neutrino experiments that are operating in energy ranges where neutrino-nucleus interactions become the most probable interaction channel, neutrino event generators are usually needed to correctly model the interaction products and their properties. Since neutrino interactions occur only very rarely, the chances for observing a certain interaction are re-weighted such that the relative cross-sections of the respective channels are still correct, but scaled up in a way that every neutrino is guaranteed to interact within the specified detector geometry. The re-weighting process limits the number of unnecessarily generated events that would increase the computation time while still maintaining the correct implementation of the physics processes. When working with such a simulated neutrino sample, the actual expected event rates need to be calculated based on the total

cross-section values and the resulting final state spectra scaled to match the expected rates afterwards.

The neutrino event generator predicts the properties of all particles that are produced in the primary neutrino interaction, including their vertex, direction and energy. All these particles are then placed inside of a Geant4-based [193] simulation framework which further propagates the event topologies within the detector geometry. Ideally, the detector response of those particles predicted by the neutrino beam generators should then match the actually recorded neutrino beam data. Any differences, on the other hand, might hint towards processes that are not reproduced with sufficient accuracy in the simulation so far and could be improved upon in the future.

Figure 5.1 shows the simulation chain that is used in ANNIE and is composed of an event generator and a detector simulation framework. The neutrino interactions are simulated by the event generator GENIE [135], while the subsequent propagation of final state particles in the detector is handled by the Water Cherenkov simulation framework WCSim [194]. In order to accurately model the neutrino interactions, GENIE uses parametrizations of the neutrino beam flux distribution and the geometrical and material properties of the detector to predict the interactions. WCSim uses a much more detailed implementation of the detector geometry and of the electronics response to then predict what is actually recorded by the detector for the given event topology. While the details of the event generation process are highlighted in the first subsection 5.1.1, the detector simulation framework will be presented afterwards in subsection 5.1.2.

### ANNIE Beam simulation

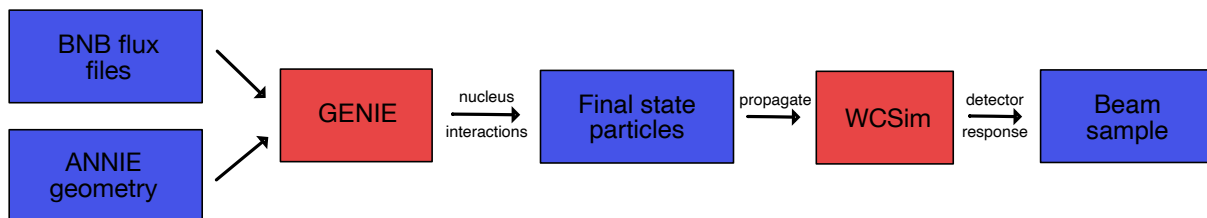


**Figure 5.1:** Overview of the ANNIE simulation chain. Primary neutrino interactions are simulated with the neutrino event generator GENIE. All final state particles are then forwarded to the WCSim framework, where the particles are propagated through the detector geometry and electronics response.

#### 5.1.1 SIMULATION OF NEUTRINO INTERACTIONS

The simulation of the initial neutrino interaction with the nuclei in the detector medium is performed by the GENIE (**Generates Events for Neutrino Interaction Experiments**) event generator framework. GENIE is one of several neutrino event generator frameworks which is based on ROOT [195] and written in C++ and was first developed in the years 2004-2007 [196]. While earlier neutrino event generator installations like NEUT [197] or NUANCE [198] were bound to specific experiments, GENIE is designed to be a universal generator that can be used by many experiments. As a consequence, it is very commonly used in the scope of Fermilab-based beam neutrino experiments. The current chapter will

briefly display the theoretical physical principles that are used to model the interactions, based on the descriptions in the GENIE user manual [196].

The simulation of neutrino interactions very broadly depends on the interplay of three different models: the nuclear structure, correct modeling of cross-sections, and hadronization processes. Regarding the nuclear model, nuclei are approximated by the relativistic Fermi gas approximation in GENIE. Nuclei that are hit are assigned a certain Fermi momentum and an average binding energy, both determined from electron scattering experiments. Short-range nuclear correlations are taken into account by the *Bodek and Ritchie* parametrization [199].

Both total and differential cross-sections are used to model the neutrino interactions. While the former cross-section is important to decide which process occurs for each event, the latter is then used to determine the final state event kinematics for each interaction. There are different models implemented for the various interaction types, based on various theoretical parametrizations: Charged-Current Quasi-Elastic (CCQE) scattering can be modeled by the *Llewellyn-Swift* model [131], the *Smith-Moniz* model [200], or the *Nieves* model [121], while Neutral Current elastic scattering processes are handled by the *Ahrens* model [201]. Baryonic resonances are usually simulated by making use of the *Rein-Sehgal* model [134], while inelastic scattering is implemented in form of the *Bodek-Yang* model [202].

Based on the interaction type and associated event kinematics derived from the cross-section models, the properties of all final state particles are determined in the scope of the so-called *hadronization* or *fragmentation* process. Experimental data for the nature of hadronic states after neutrino interactions are available from several bubble chamber experiments that were performed at CERN, Fermilab and Russia. Models for the hadronization rely on the PYTHIA/JETSET model for high hadronic energies [203] and a model based on Koba-Nielsen-Olesen scaling for lower hadronic energies [204]. The hadronization step includes the process of hadronic cascades in the nucleus within so-called Final State Interactions (FSIs).

Pre-defined generators are available in GENIE for special frequent uses cases, such as simulating atmospheric neutrino interactions with *gevgen\_atmo*, beam neutrinos in the T2K beamline with *gevgen\_t2k* or beam simulations at Fermilab with *gevgen\_fnal*. Since the ANNIE experiment is located at Fermilab, it makes sense to use the special *gevgen\_fnal* generator for simulating neutrino interactions of the Booster Neutrino Beam (BNB) in the detector. The details of the BNB flux are provided to the neutrino generator by means of so-called BNB flux files. The detector geometry of ANNIE is included within a rather simplified *gdml*-representation of the detector, including the whole experimental hall with the water tank and muon detectors, and some rock material around the hall. Interactions can be restricted either to the water volume or the complete volume that is encapsulated in the *gdml* geometry. In the latter case, the simulated sample includes dirt muons and dirt neutrons that are produced from neutrino interactions in the surrounding rock volume. Figure 5.2 shows a picture of the *gdml* geometry representation of ANNIE both with and without the surrounding rock geometry. For each object, the exact material composition is defined such that GENIE can figure out the probability of interacting with any of the nuclei in the material.

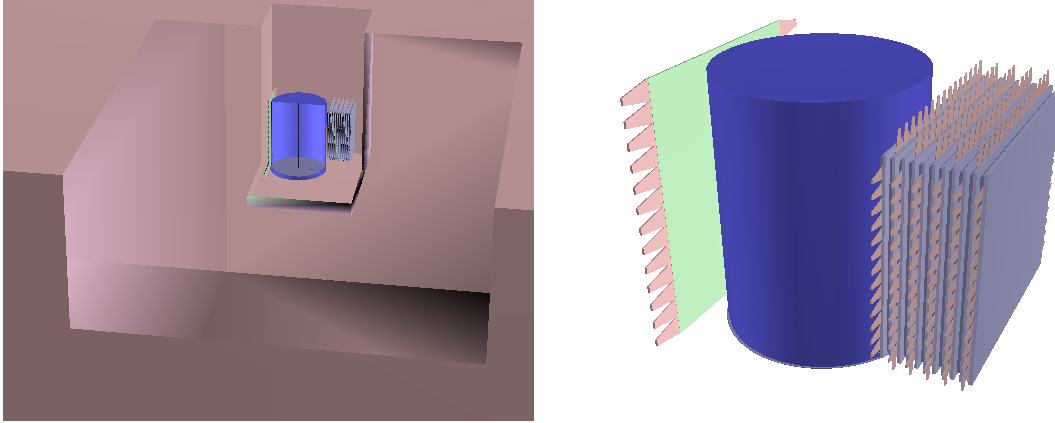


**Figure 5.2:** **Left:** Complete *gdml* geometry including the ANNIE detectors and surrounding rock. Some rock material has been cut out in this particular view for visualization purposes. **Right:** The detector as implemented in the *gdml* geometry, without the surrounding rock material.

### 5.1.2 PHYSICS & DETECTOR SIMULATION

After the primary neutrino interaction in the medium, all final state particles are propagated through the detector geometry in the scope of the Geant4-based [193] simulation framework *WCSim* which was specifically developed for a flexible and easy implementation of different water Cherenkov detector geometries [194]. While the main focus of *WCSim* development lies in developing a simulation environment for the upcoming Hyper-Kamiokande experiment [23] and it was validated to reproduce the properties of the original SKDETSIM Super-Kamiokande simulation [205], the framework can also be used to simulate other detector geometries. In this context, Marcus O’Flaherty implemented the ANNIE experiment in *WCSim*, which is publicly available in the *annie* branch of the *ANNIEsoft* fork of *WCSim* [206].

Different PMT types with different sizes and properties are implemented in the ANNIE version to correctly represent the variety of photomultiplier tubes that are used in the experiment. Furthermore, LAPPDs are implemented as a separate photosensor type that can be placed at 3 different positions for each of the eight LAPPD mailbox slots, totaling a maximum of 24 LAPPDs that can be placed inside of the water tank. In addition to the cylindrical water tank, the ANNIE implementation of *WCSim* additionally features scintillator paddles in the scope of the Front Muon Veto (FMV) and Muon Range Detector (MRD) detectors. Scintillation pulses from the FMV and MRD paddles are configured to be detected with an efficiency of 95%. The Inner Structure is constructed based on a detailed *gdml*-file that contains geometry information from original CAD drawings, providing an accurate representation of the Inner Structure geometry. Figure 5.3 provides an overview of the detector geometry implemented this way. Three LAPPDs are visible in the center of the water tank in the left figure, all placed at different heights within the same mailbox slot. The top view of the geometry on the right side highlights the cylindrical spatial pattern of the top PMTs (*red*) as well as the grid-like structure of the bottom PMTs (*green*). Several small PMTs mounted on the outside of the Inner Structure (*teal*) were originally intended for cosmic veto purposes and were therefore implemented in the simulation environment, but are not a part of the constructed ANNIE detector.

The coordinate system of WCSim is chosen in such a way that its center is located in the center of the FMV, which in turn means that the center of the water tank is located at the coordinates  $\vec{r}_{\text{center,tank}} = (0 \text{ cm}, -14.45 \text{ cm}, 168.1 \text{ cm})$ .

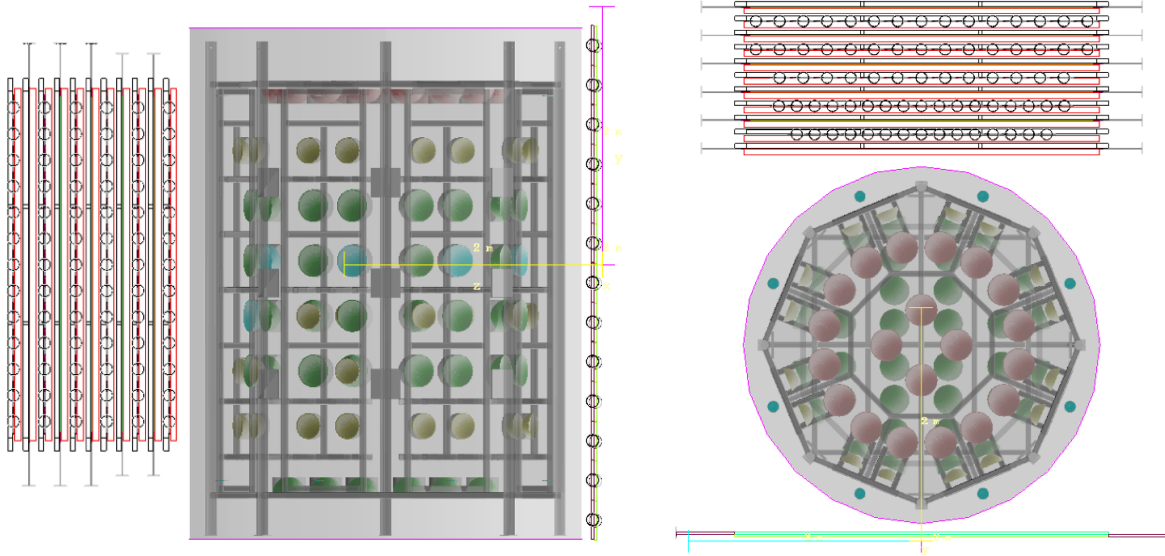


**Figure 5.3:** Original geometry implementation of ANNIE in WCSim. **Left:** Side view of the ANNIE detector: From left to right, the MRD, water tank, and FMV are visible. **Right:** Top view of the ANNIE detector. Figures provided by the courtesy of Marcus O’Flaherty [207].

WCSim uses the comprehensive FTFP\_BERT\_HP physics list recommended for High Energy physics applications to model physics processes. The High Precision (HP) component of the physics list is necessary to model hadronic transport and capture processes more accurately for neutrons in the low-energetic kinetic energy region ( $E_{\text{kin}} < 20 \text{ MeV}$ ). Since neutron captures are of particular importance for ANNIE, additional information such as the capture nucleus and the energy of the gamma cascade is stored in the output file for each neutron capture instance. Optical properties of the water are assumed to be the same as in Super-Kamiokande and will be probed more closely in chapter 5.3 for their suitability in ANNIE. In addition to the WCSim implementation, another independent version of the ANNIE simulation was created by Vincent Fischer in the rat-pac simulation framework [208]. The rat-pac version is mainly used for neutron studies and future WbLS phases of ANNIE, while WCSim is the main simulation environment for the current phase II.

## 5.2 COMMISSIONING DATA: DIFFERENCES BETWEEN DATA & SIMULATION

ANNIE started testing its beam data taking capabilities in the course of several commissioning runs in February and March 2020. This commissioning beam data sample can be used to evaluate the reliability of the simulation by comparing it to a simulated neutrino interaction sample. Charged Current interactions are preferable in this context since they deposit more energy in the detector and are easier to compare. A very simple CC-like

interaction sample can be selected by requiring coincident activity in the water tank and the MRD, while dirt muon events are rejected by selecting only events with no coincident veto paddle hit.

When applying the presented selection procedure to both the data and the simulation sample, the resulting total charge distributions are shown in figure 5.4, with the MC distribution being scaled down to match the statistics of the data sample. While the same spectral features such as a very high event rate in the low charge region ( $q < 500$  p.e.) and a plateau in the higher charge region up until a certain maximum charge value  $q_{\text{max,plateau}}$  are present both in data and in MC, the charge scale seems to be slightly different. Both the start and the end of the plateau region seem to be shifted to higher charge values in the case of data, when comparing it to the simulated shape. This seems to indicate that the detected charge per PMT is under-estimated in the simulation and needs to be scaled up in order to match the observed behavior in the data.

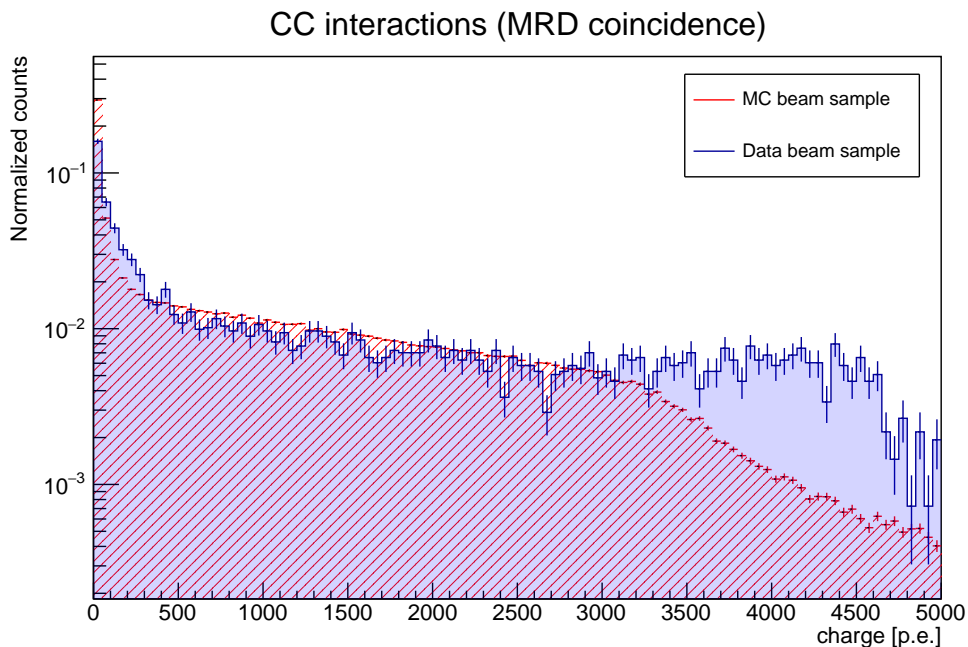


**Figure 5.4:** Charge spectrum of beam neutrino interactions in the data (*blue*) and the simulation (*red*) when selecting events with a coincident cluster in the MRD and the tank. The data spectrum seems to exhibit slightly larger charge values compared to the simulation.

Using this information about the different charge scales, we can utilize the features of the spectrum to apply a simple correction factor and study more aspects of potential discrepancies. The different end points of the plateau region in the data and the MC can be used to calculate a conversion factor for adjusting the charge detected in the simulation to a value in better agreement with the spectrum observed in the data. The flank of the plateau region seems to occur at  $E_{\text{thr,MC}} \sim 3200$  p.e. for the MC sample and at  $E_{\text{thr,data}} \sim 4400$  p.e. for the commissioning data sample, leading to a conversion factor of

$$f_{\text{conv}} = E_{\text{thr,data}}/E_{\text{thr,MC}} \approx 1.375. \quad (5.1)$$

The same conversion factor is applied to all PMTs, independently of the different PMT types that are present in the detector. After scaling the electronics response up that way, we can

check how well the charge distributions match between data and simulation for individual PMTs. Figure 5.5 highlights the agreement for two exemplary PMTs after applying the charge conversion factor  $f_{\text{conv}}$  to the simulation spectrum and scaling both histograms to the same statistics. The charge spectra look generally rather different due to the different positions of the PMT: The tail of the charge distribution extends up until 500 p.e. for the first downstream-located PMT, while it only extends up until 200 p.e. for the second PMT in a more upstream position. While the first PMT exhibits very good agreement between data and Monte Carlo, the second PMT features large differences in the observed spectra. In the latter case, the PMT seems to detect smaller charge values in the simulation case compared to data.

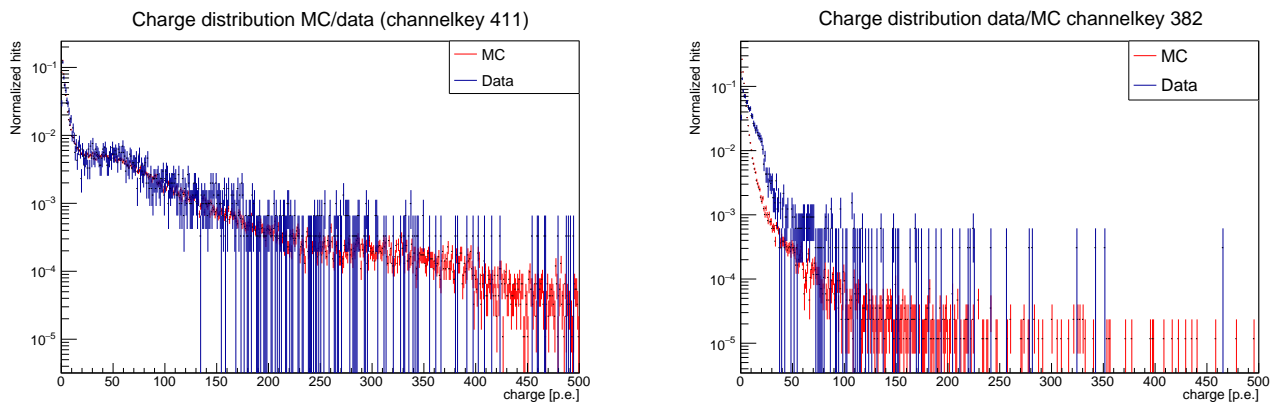


**Figure 5.5:** Charge spectra in the simulation (*red*) and the data (*blue*) for two exemplary PMTs in the beam neutrino sample. While the PMT shown in the left part of the figure shows rather good agreement, the PMT in the right part of the figure displays discrepancies between the data and MC, since higher charge values are present in the data spectrum.

The compatibility of the charge spectra for each PMT can be quantified with a  $\chi^2$ -homogeneity test that is presented in more detail in the upcoming section 5.4. The  $\chi^2$ -compatibility value can be used to look for common properties of PMTs that show good agreement. Figure 5.6 shows how the agreement depends on the PMT location by depicting the  $\chi^2$ -compatibility values for the barrel PMTs in a spatial, "rolled-open" detector view of the cylinder mantle. The azimuthal position of the PMTs is represented by the angular coordinate  $\phi$ , with the downstream (upstream) direction corresponding to a value of  $\phi = 0$  ( $|\phi| = \pi$ ), while the vertical dimensions are represented by the cartesian coordinate  $y$ . When inspecting the spatial dependency of the charge spectrum agreement, it becomes evident that the charge response is represented much better for downstream PMTs with compatibility values close to  $\chi^2/\text{n.d.f} = 1$ , while larger disagreements are observed for the upstream PMTs with  $\chi^2$ -values up until  $\chi^2/\text{n.d.f} \approx 50$ . Since the selected CC beam sample mainly includes muon events in downstream direction, upstream PMTs will mainly see light from reflections, while the downstream PMTs will detect the more direct Cherenkov light. The PMT-by-PMT charge spectrum compatibility study hence seems to indicate that too little reflections are included in the default version of the simulation framework to represent reality accurately.

Summarizing the findings from the presented beam neutrino comparison, there appear to be two major aspects of the simulation that need to be adjusted in order to obtain a more

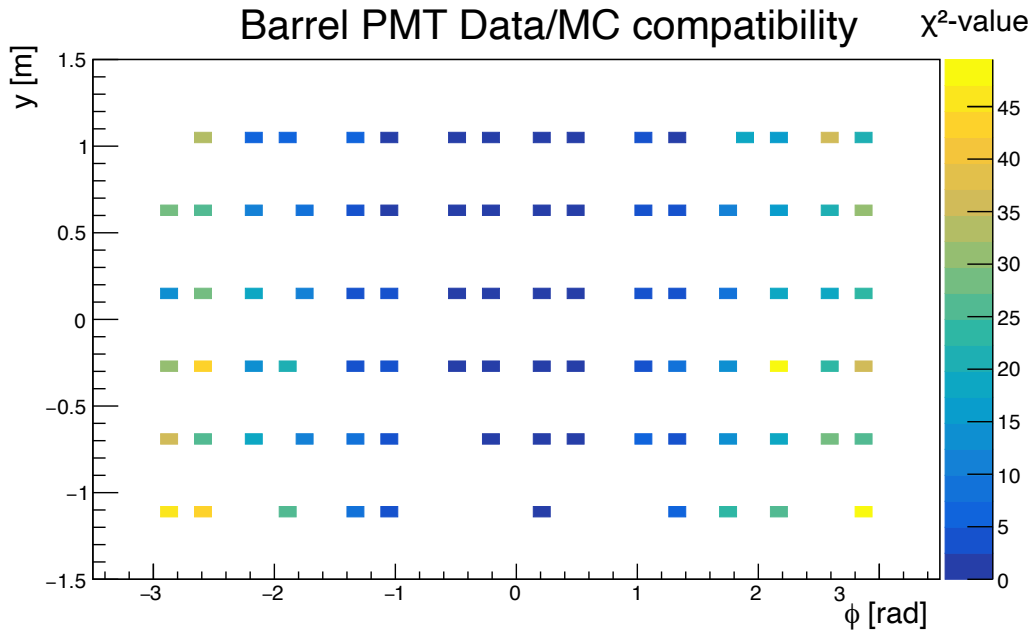


**Figure 5.6:**  $\chi^2$ -compatibility values of charge spectra in the CC beam neutrino sample in a spatial "rolled-open" view of the cylinder mantle.  $\phi$ -values close to 0 correspond to PMTs located in downstream direction, while  $\phi$ -values with  $|\phi| \approx \pi$  correspond to PMTs on the upstream wall of the Inner Structure.

realistic model of the ANNIE detector response: On the one hand, there seems to be the need for a global charge scaling factor to match the amount of charge that is observed in the data. On the other hand, the amount of reflections in the simulation geometry needs to be higher for a better modeling of the reflected light. Both these aspects will be addressed in chapter 5.4 by making use of different calibration samples: A sample of Michel electrons will be used to fine-tune the observed energy scale, while through-going muons will be investigated to adjust the reflectivities of surfaces in the water tank. The resulting parameters will then be validated by testing the agreement for an independent event sample in the form of the AmBe neutron calibration sample. In addition, the simulation framework will be extended by adding holders and precisely derived PMT positions from a laser scan campaign described in the next section 5.3. Moreover, all implemented optical properties will be reviewed and realistic Quantum Efficiency curves and Single PE. charge functions will be introduced in the same section.

### 5.3 MODIFICATIONS TO THE SIMULATION

The general Geant4-based ANNIE simulation setup has been implemented by Marcus O'Flaherty and features the whole detector geometry including the water tank, the Front Muon Veto, the Muon Range Detector, as well as the functionality of PMTs and LAPPDs with variable positioning options, as highlighted in the previous chapter 5.1.2. The following section presents various additions to the simulation framework that were implemented in the scope of this thesis and are aimed to make the simulation more realistic, including the addition of PMT holders, more accurate PMT positions derived from a laser scan

campaign, and calibration-driven charge response functions. General properties of the simulation framework will be highlighted in the first section 5.3.1, before the modifications are presented in the subsequent sections 5.3.2-5.3.4.

### 5.3.1 GENERAL PROPERTIES OF THE SIMULATION

In this section, several general aspects of the simulation like material properties, optical pathlengths, and electronics digitization are investigated. Most of these properties were taken from the original upstream version of the code, which was primarily intended for use in larger kton-scale Water Cherenkov detectors like Super-Kamiokande or future projects like Hyper-Kamiokande. In the following, it is evaluated whether the implementation of each property also makes sense in the case of ANNIE or whether some adjustments are necessary due to slightly different detector conditions.

The implemented optical properties of the Gadolinium-loaded water in terms of the absorption and Rayleigh scattering length are shown in figure 5.7. Both properties were implemented in `WCSim` based on measurements conducted for the Super-Kamiokande experiment. Since the water in Super-K is very transparent due to a sophisticated water filtration system [209], both the absorption and Rayleigh scattering values display very high values. For instance, the maximum absorption length value for optical wavelengths around 350 nm is more than 900 m, while the Rayleigh scattering length reaches values higher than 1000 m for wavelengths above 600 nm. While it is unlikely that ANNIE reaches similar transparency level with its custom water purification setup, the relevant length scales in ANNIE are very short with a maximum path length of  $\approx 5$  m, as indicated by the green region in the plot. Even if the transparency lengths are considerably smaller than the Super-Kamiokande reference values, they will still barely impact photons for path lengths relevant in ANNIE. The implementation of absorption and Rayleigh scattering lengths is hence considered acceptable in the scope of ANNIE.

Figure 5.8 shows the implemented refractive index trend for water in ANNIE as a function of the wavelength. The refractive index is the main quantity that is used by Geant4 to simulate the optical Cherenkov process and should therefore be modeled accurately in a water Cherenkov detector simulation. The distribution used in `WCSim` was adopted from the parametrization used in the Super-Kamiokande simulation. The refractive index of water is, however, well known and does not differ even if the transparency values of two samples are rather different. The implementation is hence expected to be very accurate also in the case of the ANNIE simulation. A cross-check with the independent implementation of the refractive index in the ANNIE `ratpac` simulation framework [208] shows good agreement and further confirms that the implementation is suitable.

There are some peculiarities in the way that Geant4 handles the simulation of Cherenkov photons [210]. For example, the maximum refractive index should occur at the highest optical energies (i.e. the shortest optical wavelengths) in order to guarantee a correct physical simulation. In addition, the refractive index distribution should have no dips. Since both of these criteria are fulfilled in the considered refractive index curve, the modeling of Cherenkov photons should be handled correctly in the case of the ANNIE simulation framework.

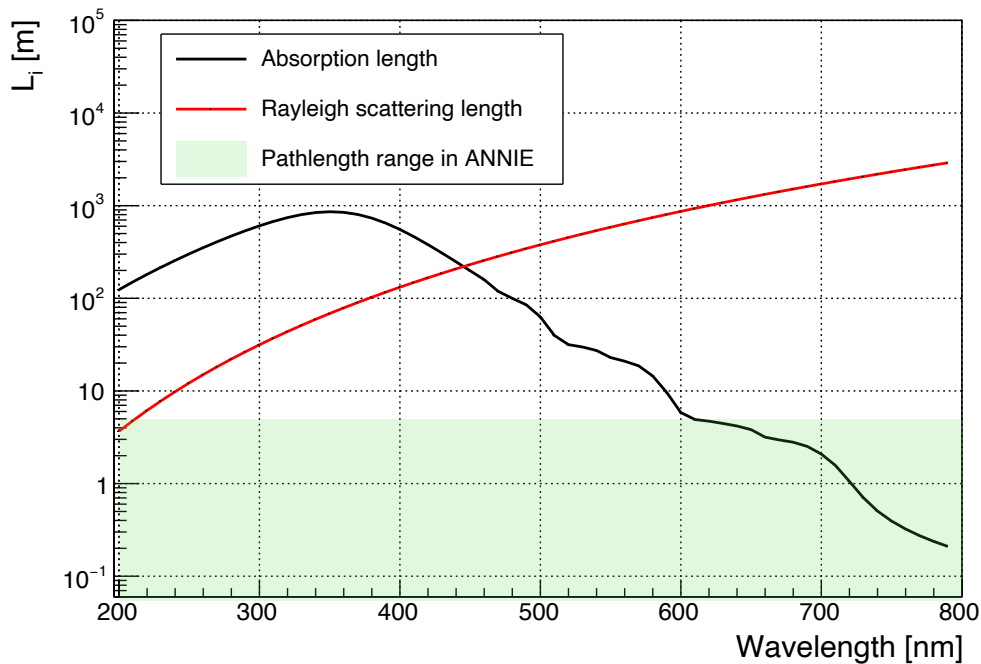


**Figure 5.7:** Absorption length (*red*) and Rayleigh scattering length (*black*) as implemented in the `WCSim` simulation framework in ANNIE. While the Rayleigh scattering length is monotonously increasing as a function of the wavelength, the absorption length shows a peak around 350 nm and decreases for higher wavelengths. The typical range of optical pathlengths in ANNIE is shown in green.

Photomultipliers in `WCSim` are implemented as half-sphere-like objects with a glass surface of thickness  $d_{\text{Glass}} = 0.55$  cm and an inner volume filled with air, as shown in figure 5.9. The half-sphere is constructed by creating a larger half-sphere with a *spherical radius* of  $r_s$ , and then cutting off a part of the volume by imposing a certain height for the PMT, the so-called *expose height*  $d_{\text{expose}}$ . A cylindrical volume filled with water is constructed around the PMT such that the PMT can be inserted without problems into the surrounding water medium. Certain aspects of the PMT implementation are not really conventional compared to the way that such a *sensitive detector* is usually implemented in a Geant4 simulation. While the surface of the PMT usually just activates the electronics response for any photon hit that arrives scaled by the Quantum Efficiency, the `WCSim` version actually requires that the photon deposits energy in the glass surface. If energy is deposited, the Quantum Efficiency curve for the respective PMT type is then used to accept or reject the hit and continue with the digitization process. This implementation may result in fewer photons being accepted at the glass surface, which in turn potentially introduces the need for a scaling factor for the Quantum Efficiency curves.

Another peculiarity of the PMT implementation is the "air" medium filling the inside of the PMT. While in reality there would be a vacuum within the PMT, the special air medium used in `WCSim` features very short absorption lengths on the order of nanometers. Photons within the inner volume of the PMT are therefore simply killed upon entering the volume. Since this effect is also potentially different than in reality, it might introduce additional differences in the photon detection efficiency that will need to be compensated by the

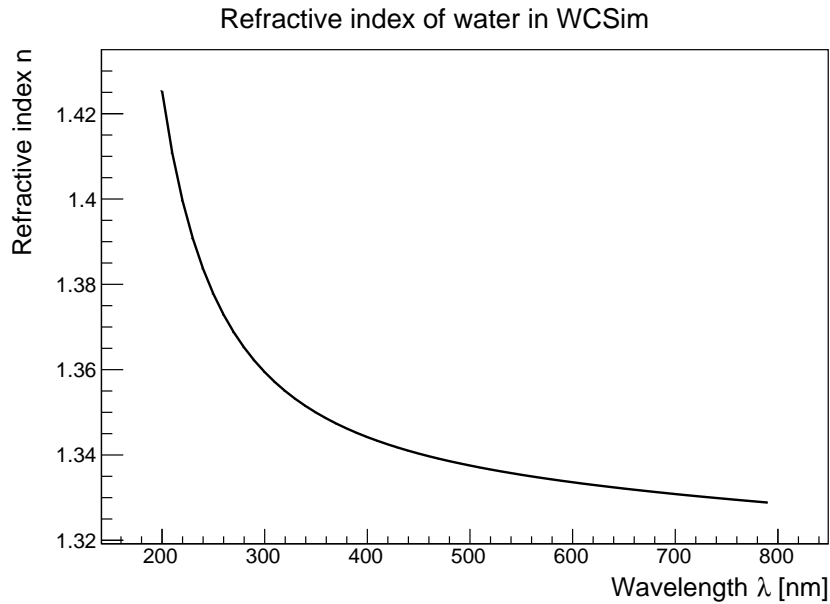


**Figure 5.8:** The refractive index  $n$  of water is shown as a function of the wavelength as implemented in the WCSim simulation framework in ANNIE. An accurate refractive index modeling is essential for a reasonable implementation of the Cherenkov emission process in the detector medium.

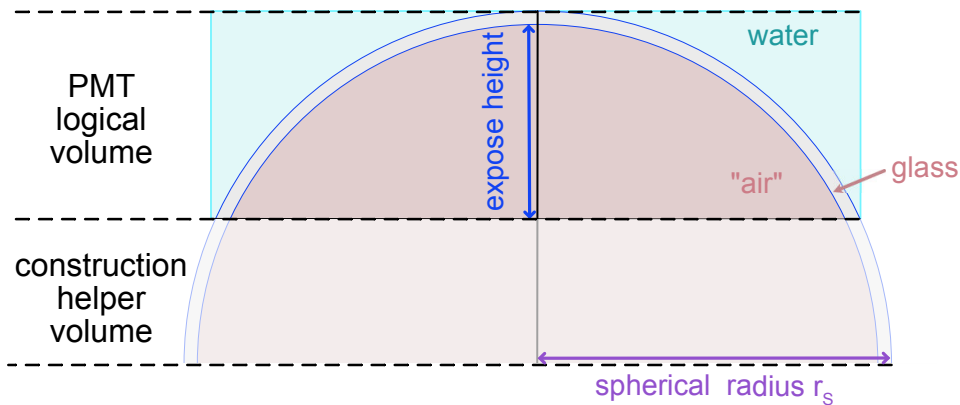


**Figure 5.9:** Schematic overview of the PMT implementation in WCSim. PMTs are constructed by creating a spherical object and subsequently reducing it to a half-spherical-like object of expose height  $d_{\text{expose}}$ . The inner PMT volume is filled with a special opaque "air" material, while the surface is made out of glass.

previously presented tuning factors.

The different PMT types in ANNIE are implemented with different properties based on their geometries and photomultiplier data sheets. Table 5.1 provides an overview of the differences in implementation for the ANNIE, LUX, ETEL, Watchboy, and Watchman tubes which are named either after the original experiments they were used in or based on the manufacturer's name. While different expose heights and radii can be traced back to the differences in the PMT geometry, the transit time spreads and Quantum Efficiency curves were implemented based on the information available in the data sheets [211, 212].

In the context of the PMT type implementation, figure 5.10 provides a visual overview of the different Quantum Efficiency curves that are used in the ANNIE simulation. While

PMT name	PMT type	Size	Expose height	Spherical radius	TTS	Maximum Q.E.
LUX	R7081	10"	117 mm	127.4 mm	3.4 ns	25.15%
ETEL	D784KFLB	11"	118 mm	141.7 mm	1.98 ns	33.96%
ANNIE	R5912HQE	8"	91.6 mm	102.1 mm	2.4 ns	34.50%
Watchboy	R7081	10"	117 mm	127.4 mm	3.4 ns	25.15%
Watchman	R7081HQE	10"	117 mm	127.4 mm	3.4 ns	34.50%

**Table 5.1:** Properties of the different PMT types that are used in ANNIE.

both ANNIE (R5912HQE), Watchman (R7081HQE) and ETEL (D784KFLB) PMT types are High-Q.E. tubes that feature a maximum Q.E. value of  $\approx 35\%$ , the other PMTs (R7081/R5912) are normal Q.E. tubes for which the maximum Q.E. value is around 25%. Note that the PMT types R5912 and R7081 do not differ in terms of their Quantum Efficiency curves, but only regarding their photosensor geometry and transit time spread characteristics. Furthermore, the Quantum Efficiency curve of the LUX PMTs is assumed to be the same as the one of a default 12-inch HQE PMT in WCSim due to the lack of an official data sheet for this PMT type.

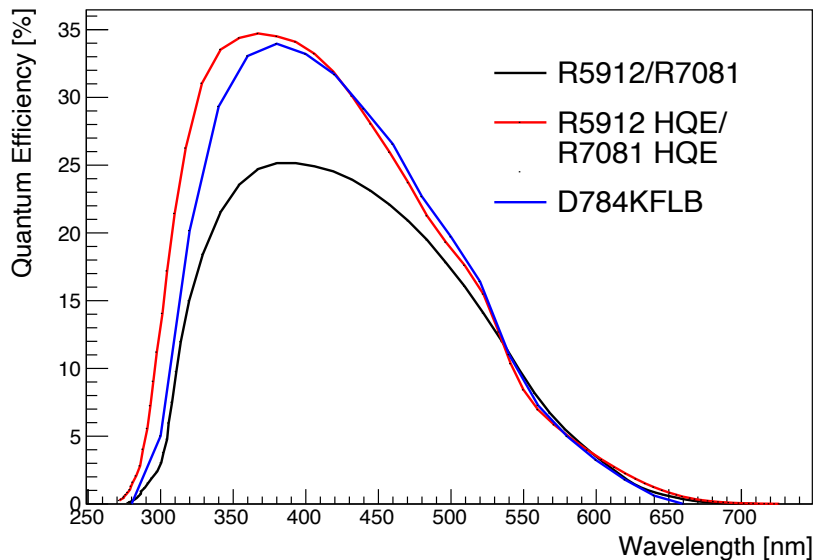


**Figure 5.10:** The Quantum Efficiency (Q.E.) curves used for the different PMTs that are implemented in ANNIE. Both the ETEL (D784KFLB) and ANNIE (R5912 HQE) PMTs are high-Q.E. tubes with maximum values around 35%, while the other PMTs (R5912) are normal-Q.E. photomultiplier with a maximum Q.E. value of around 25%. The curves for R5912 (HQE) are implemented according to their data sheet [211], while the D784KFLB implementation is based on the properties of a default 12-inch HQE PMT in WCSim due to the lack of a data sheet for this particular PMT.

Whenever a photon hits one of the PMTs and is accepted based on the Quantum Efficiency curve, the hit is included in the digitization process that models the electronics response in WCSim. In the case of the original upstream implementation for Super-Kamiokande, hits in a time window of 200 ns are combined into a single electronics signal for each PMT in this step. This so-called *digitized hit* then contains the sum of all photoelectrons produced by all accepted photon hits that were registered in the 200 ns time window. For each photon hit, the registered charge is calculated based on a Single-PE. probability distribution curve,

and a probability threshold is applied depending on the amount of charge that is supposed to be produced. Figure 5.11 demonstrates how this threshold function depends on the charge value  $x$  ( $x = q[\text{p.e.}] + 0.1 \text{ p.e.}$ ). For charges above 0.4 p.e., the probability to actually generate the charge is assigned to be over 80%, while the probability steeply decreases to 0 for charge values smaller than 0.4 p.e. The chance to accept the digitized charge becomes 100% in case of charge values of at least 1 p.e. or bigger.

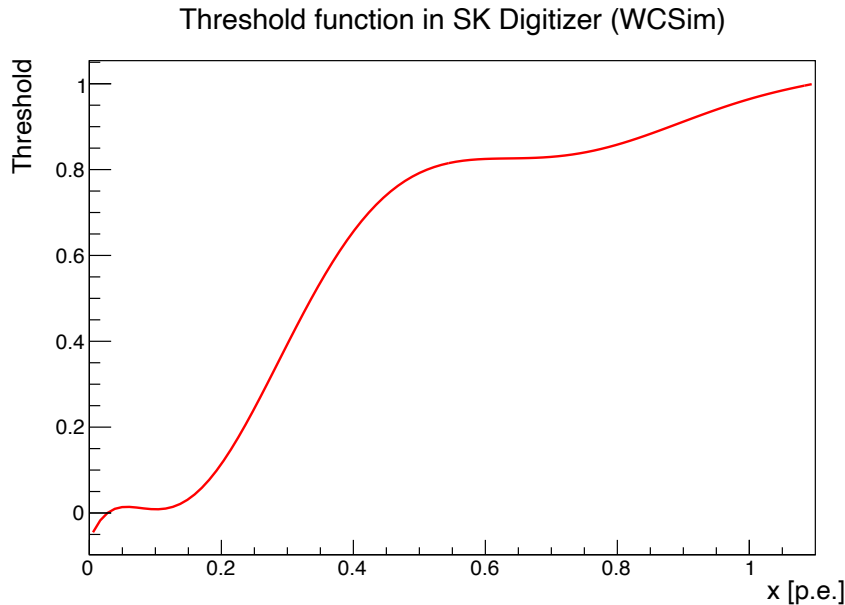


**Figure 5.11:** Threshold function of the original digitization process that is used to digitize photon hits for the Super-Kamiokande PMT implementation within WCSim. The variable  $x$  denotes the digitized charge  $x = Q[\text{p.e.}] + 0.1 \text{ p.e.}$ , while the threshold indicates the probability that the digitized hit is not rejected.

While this digitization procedure might be suitable for describing the electronics response in Super-Kamiokande, it is not applicable in the case of ANNIE. Since complete waveforms are recorded for all PMTs in ANNIE, single PMT hits can be distinguished and shouldn't be integrated over a window of 200 ns. As a consequence, the hits are not integrated in the digitization process in the ANNIE version of the code. Furthermore, there is no indication that smaller charge values are rejected with a higher probability in the pulse finding process. The presented threshold function is therefore not applied in the case of ANNIE, and all charges are accepted equally. The Single-PE. distributions that are used to draw the charge values for each PMT type are extracted from gain measurements in LED calibration data and will be presented in the upcoming section 5.3.4.

### 5.3.2 PMT POSITIONS FROM LASER SCAN FILE

Representing the detector geometry accurately in the simulation is of vital importance to get a realistic representation of the detector response. This is even more important in a small-scale detector like ANNIE, where small misplacements will have a more severe impact on the observed photon hit distributions.

In ANNIE, the two geometrical features with the largest impact on the simulation accuracy are the Inner Structure and precise PMT positions. The former is implemented as accurately as possible by loading a detailed *gdmf*-file version of the Inner Structure steel frame in the WCSim framework and placing it inside of the cylindrical water tank. This *gdmf* parametrization is directly based on the CAD drawings for ANNIE and contains all 8 side panels as well as the top and bottom steel grid. Since almost all aspects of the Inner Structure are located in the innermost part of the water volume which is surrounded by black sheet, photon reflections off the surfaces will potentially be captured by one of the PMTs. The correct geometric modeling of the teflon-wrapped steel surfaces therefore has a direct impact on the charge patterns that are observed and is important for the correct modeling of the detector response. Details of the structure of the outer water tank, on the other hand, are much less important since these outer walls are optically isolated from the innermost volume surrounded by the black sheet.

Besides the Inner Structure, the most important geometric feature in the optically isolated volume are the PMT positions. In order to obtain accurate positions for all PMTs, a 3-dimensional laser scan of the Inner Structure was performed by an external company. Since PMTs would not be visible in such a scan, the very front of the PMT glass surfaces was marked with tape for most PMTs. The positions of the front faces of the PMTs can then be inferred by extracting the positions of those taped crosses.

Figure 5.12 shows the laser scan data for one of the eight side panels, displayed with the open-source mesh processing software MeshLab [213]. The left image shows the panel from some distance and highlights that the scan data includes the geometric information about the general steel surface as well as the PMT holders. The right image, on the other hand, shows a zoomed-in version of the same panel. Two taped crosses are visible, highlighting the front glass positions of two exemplary PMTs.

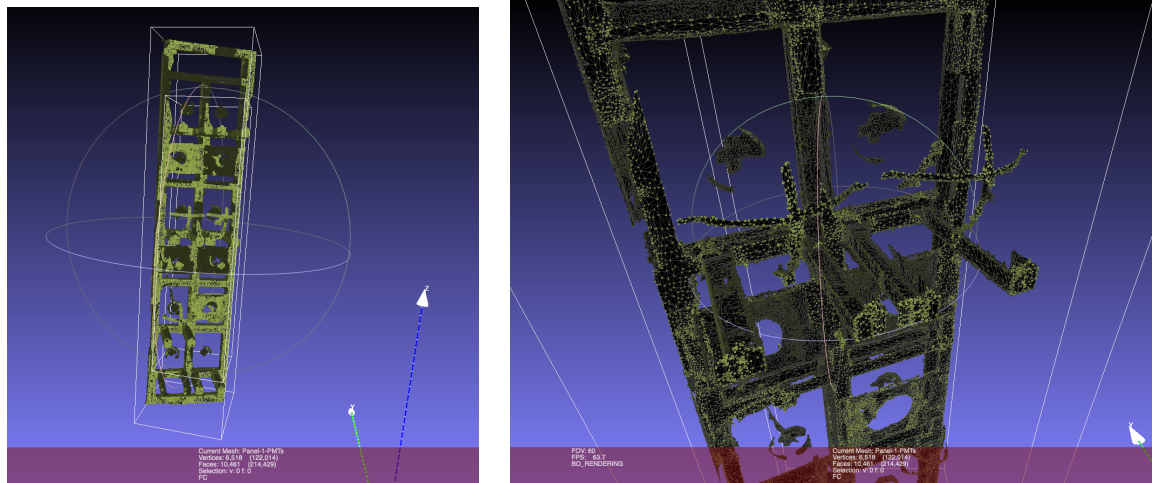


**Figure 5.12:** Laser scan file data for one of the eight panels of the Inner Structure. While the left image shows the complete panel from a larger distance, the right image shows a zoomed version of the same scan data. The front positions of most PMTs can be extracted by making use of the cross-shaped tapes that were placed on the glass surface and which are more clearly visible in the right image.

For each PMT with a taped cross, the PMT front position were extracted by making use of the coordinate extraction utilities for mesh points in MeshLab. The positions of PMTs with

no taped cross were extrapolated based on the positions of the other PMTs on the panel. The radial positions for such PMTs were determined based on the radial position of PMTs of the same type, while the vertical and horizontal positions were extrapolated based on PMTs that were marked in equivalent rows in one of the other panels. Normal vectors for the surfaces were identified by constructing a plane from three points on the steel surface and determining a normal vector representation of that plane. The result was verified by selecting an independent set of three additional points on the steel surface, and repeating the procedure. In addition to the side panels, the same PMT position extraction procedure was performed for the top and bottom panel of the Inner Structure.

Since the scan data was recorded in a different coordinate system than the usual ANNIE simulation coordinate system, there was a need to convert the extracted PMT positions into the ANNIE-specific coordinate system. The *STL*-file representation of the Inner Structure was used to compute the first step of the transformation matrix because of its compatibility with MeshLab and due its coordinate system being already rather similar to the one used in the simulations. The transformation matrix was computed by aligning the panels from the scan file with the Inner Structure from the CAD drawings in MeshLab. The results of this alignment process are shown in figure 5.13, where the Inner Structure is visualized as a grey object, and the different panel mesh objects are shown in different colors. The images show that the alignment worked nicely, indicating that the associated transformation matrix can be used without any problems to convert the PMT coordinates into the STL coordinate system.

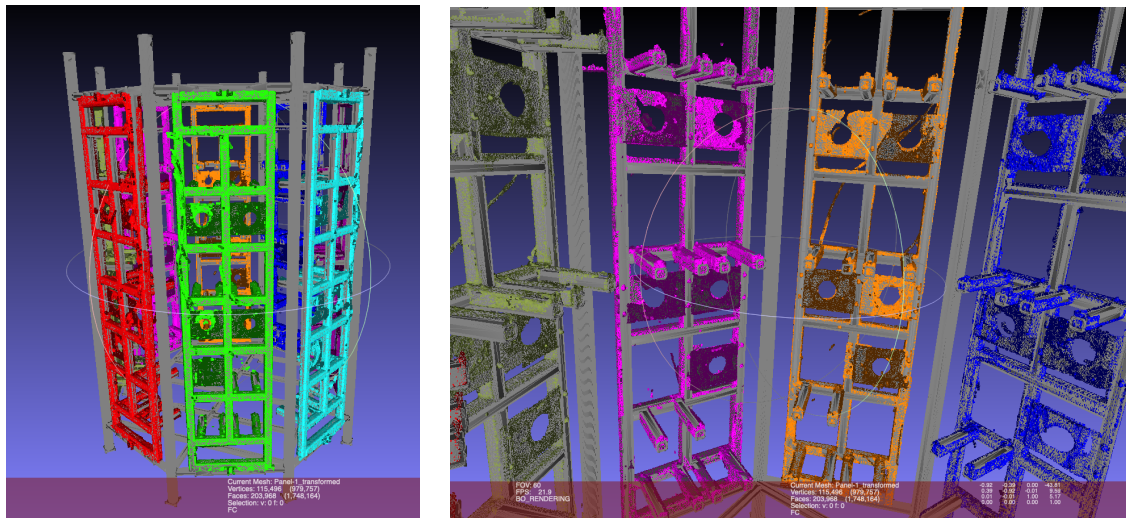


**Figure 5.13:** Pictures of the alignment process of the geometry scan coordinate system and the Inner Structure STL coordinate system. The colored panels were originally in the coordinate system of the laser scan, and were transformed to the STL-based coordinate system by matching them to the Inner Structure (shown in grey).

The extracted coordinate transformation matrix from the laser scan coordinate system to the STL coordinate system (both in units of inches) is then given by

$$\begin{pmatrix} x_i \\ y_i \\ z_i \\ 1 \end{pmatrix}_{STL} = \begin{pmatrix} -0.385 & 0.923 & 0.008 & -9.551 \\ -0.923 & -0.385 & 0.005 & -43.756 \\ 0.007 & 0.005 & 0.999 & 5.298 \\ 0 & 0 & 0 & 1 \end{pmatrix} \cdot \begin{pmatrix} x_i \\ y_i \\ z_i \\ 1 \end{pmatrix}_{scan} \quad (5.2)$$

Compared to the STL coordinate system, the WCSim simulation coordinate system features a rotation of  $\theta = 67.5^\circ$  and different origin coordinates. In addition, the simulation coordinate system uses centimeter as length scale units instead of inches. The transformation from the STL coordinate system is thus given by

$$\begin{pmatrix} x_i \\ y_i \\ z_i \\ 1 \end{pmatrix}_{\text{WCSim}} = \begin{pmatrix} \sin(67.5^\circ) & \cos(67.5^\circ) & 0 & 0 \\ 0 & 0 & 1 & -212.58 \\ \cos(67.5^\circ) & -\sin(67.5^\circ) & 0 & 168.1 \\ 0 & 0 & 0 & 1 \end{pmatrix} \cdot \begin{pmatrix} 2.54 \cdot x_i \\ 2.54 \cdot y_i \\ 2.54 \cdot z_i \\ 1 \end{pmatrix}_{\text{STL}} \quad (5.3)$$

### 5.3.3 ADDITION OF PMT HOLDERS TO THE SIMULATION

Some of the PMTs are mounted on the Inner Structure by means of rectangular wing-like objects, the so-called holders. These PMT holders are located inside the optically isolated volume but are not included in the Inner Structure *gdml* file. They hence need to be implemented separately when constructing the detector geometry in Geant4. Such holders are present for the ANNIE, LUX, and ETEL PMTs, while Watchboy and Watchman tubes, on the other hand, do not feature similar holder objects.

While the ANNIE holders are made of white polyethylene, the LUX and ETEL holders consist of black *Schedule 80 PVC* [214]. Due to the white color, reflections of the ANNIE holders are assumed to play a larger role than reflections of the LUX and ETEL PMT holders, although the latter ones also have a non-negligible reflectivity due to their polished surface. The ANNIE holder are approximated to have a length of  $l_{\text{ANNIE}} \approx 33.5$  cm, a height of  $h_{\text{ANNIE}} \approx 21$  cm, and a thickness of  $d_{\text{ANNIE}} \approx 2$  cm based on information extracted from the laser scan data. Additionally, the hole in the center of the holders is implemented with a radius of  $r_{\text{ANNIE}} \approx 6$  cm in the simulation. The LUX and ETEL holders are modeled to have a length of  $l_{\text{LUX}} \approx 43$  cm, a height of  $h_{\text{LUX}} \approx 15.3$  cm and a thickness of  $d_{\text{LUX}} \approx 2$  cm. Both ETEL and LUX PMTs have cylindrical housings attached to the holders that were also implemented in the scope of adding the holders.

Figure 5.14 shows a visual representation of the implemented ANNIE detector geometry, including the Inner Structure, the black sheet surrounding the inner volume as well as the PMTs and holders. Different PMT types are highlighted in different colors, whereas the black sheet is visualized in green, and the PMT holders and housings are shown in red. While the black sheet completely surrounds the PMT housings on the bottom for the LUX PMTs, the housings of the ETEL PMTs mounted on the top of the Inner Structure extend beyond the volume surrounded by the black sheet. This was implemented according to the real black sheet wrapping situation, in which the bottom side of the Inner Structure is completely enclosed by the black sheet, and holes were inserted into the black sheet on the top to make room for the ETEL housings.

The holders for the top and bottom grid PMTs are visualized in a more vertical perspective in figure 5.15. As in reality, the holders of the LUX PMTs at the bottom can be characterized by a very grid-like rectangular structure, while the holders of the ETEL PMTs at the top rather represent the circular placement of the PMTs. The four ETEL tubes in the center are attached to the removable hatch and can be lifted out of the detector.

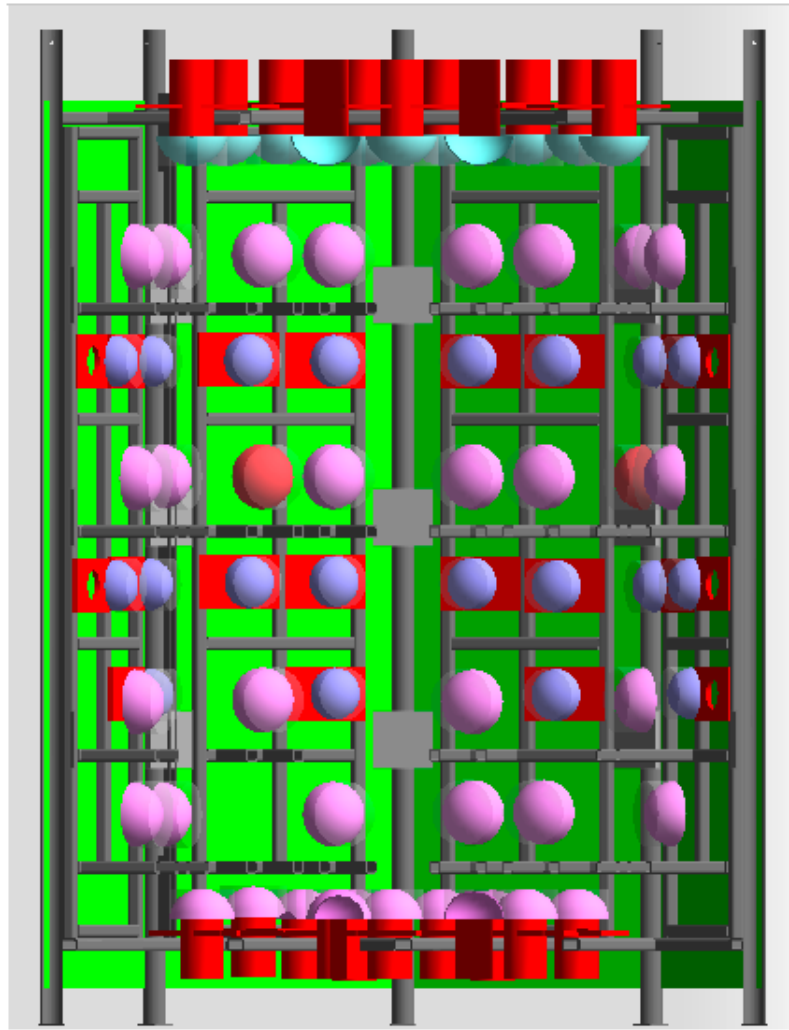


**Figure 5.14:** ANNIE geometry as implemented in the WCSim framework. Different PMT types are depicted in different colors. Holders for the ANNIE Hamamatsu PMTs, the ETEL PMTs and the LUX PMTs are shown in red. In addition, housings for the ETEL and LUX PMTs are also colored in red. The black sheet surrounding the Inner Structure is visible in green.

### 5.3.4 IMPLEMENTATION OF CUSTOM PMT CHARGE RESPONSE FUNCTIONS

Whenever a photon hits a PMT and initiates a photoelectron production cascade, the amplification process in the dynodes of the PMT is characterized by the gain value at the operating voltage of the photomultiplier tube. The gain characterizes how many photoelectrons are typically produced in the avalanche process after a photon was initiating the emission of a photoelectron at the photocathode. Within ANNIE, the PMT gain calibration was conducted by making use of 6 LEDs that are mounted at different positions within the water tank. Due to their spatially uniform placement in the tank, all PMTs can be illuminated by making use of all available LEDs. The charge distributions were plotted

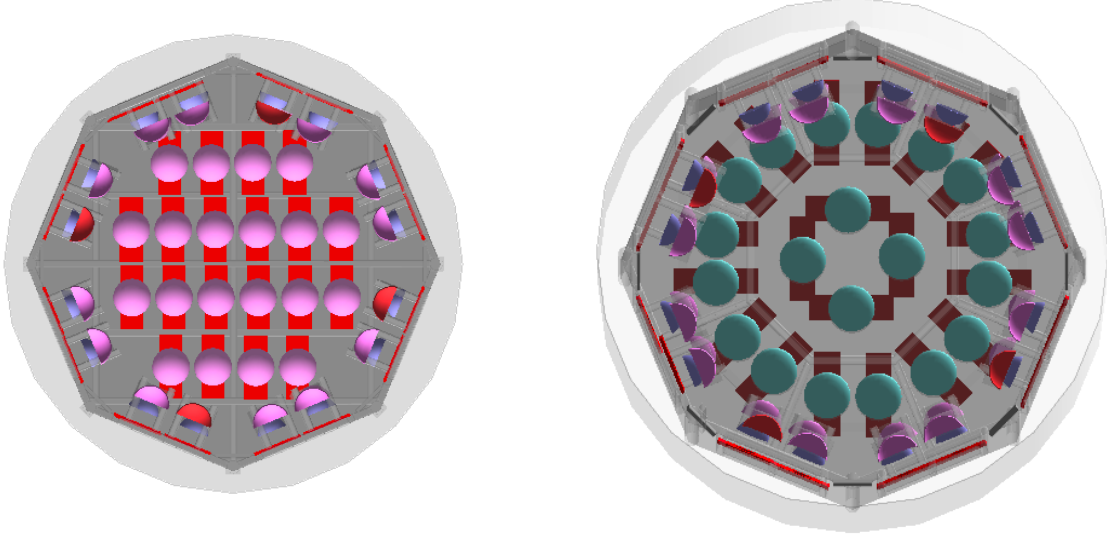


**Figure 5.15:** **Left:** View of the bottom PMT holders in a top-down view of the detector. **Right:** View of the top PMT holders in a bottom-up view of the detector.

for every PMT and fitted with a suitable parametrization containing a pedestal, Single-PE., Multi-PE. and exponential component. The mean value of the Single-PE. component fit was then used to calculate the gain value for each PMT, and High Voltage values were adjusted for every PMT such that similar gains were obtained for all PMTs. This gain calibration campaign was conducted in 2020 in the scope of Teal Pershing's thesis [215] and yielded gain values on the order of  $g_{\text{avg}} \approx 7 \cdot 10^6$  for most PMTs. The fit function that was used was a simplified version of the gain calibration procedure used in the DEAP experiment [216] and follows the subsequent parametrization:

$$\begin{aligned}
 Q(x) = & A_{\text{ped}} \cdot \text{Gauss}(x, \mu_{\text{ped}}, \sigma_{\text{ped}}) + B \cdot e^{-\frac{x-a}{\tau}} \cdot H(Q - \mu_{\text{ped}}) \\
 & + A_{1\text{P.E.}} \cdot (\text{Gauss}(x, \mu, \sigma) + \text{Gauss}(x, f_{\mu} \cdot \mu, f_{\sigma} \cdot \sigma)) \\
 & + A_{2\text{P.E.}} \cdot (\text{Gauss}(x, 2\mu, \sqrt{2}\sigma) + \text{Gauss}(x, (1 + f_{\mu}) \cdot \mu, \sqrt{1 + f_{\sigma}} \cdot \sigma))
 \end{aligned} \tag{5.4}$$

with the usual Gauss-function

$$\text{Gauss}(x, \mu, \sigma) = e^{-\frac{(x-\mu)^2}{2\sigma^2}}. \tag{5.5}$$

While the exponential part of the fit function is used to fine-tune the pedestal aspect of the fit in addition to the  $A_{\text{ped}}$  term, the parameters  $f_{\mu}$  and  $f_{\sigma}$  represent cases of incomplete photoelectron amplification in the tubes. The Heavyside-function  $H$  ensures that the exponential correction for the pedestal is only applied for charge values above the fitted mean pedestal value.

The gain calibration results will be used in the following section to determine an average Single-PE. distribution for every PMT type in ANNIE. These average distributions will be inserted into the WCSim simulation framework to obtain an accurate representation

of the charge response for every PMT. Since the simulation usually records the charge values in units of photo-electrons instead of Coulomb-related units, the gain calibration curves are first converted into units of p.e. by applying the respective gain correction factors. The results are presented in figure 5.16 separately for LUX, ETEL, ANNIE (HM) and Watchboy (WB) PMTs. The distributions for single PMTs are shown in grey, while an average distribution is superimposed in color for every PMT type. While there is quite some spread visible for the gain distributions, the average distributions seem to capture the general features of the charge curve rather well. It seems reasonable to adapt only one average distribution per PMT type instead of using individual gain calibration curves for every PMT.

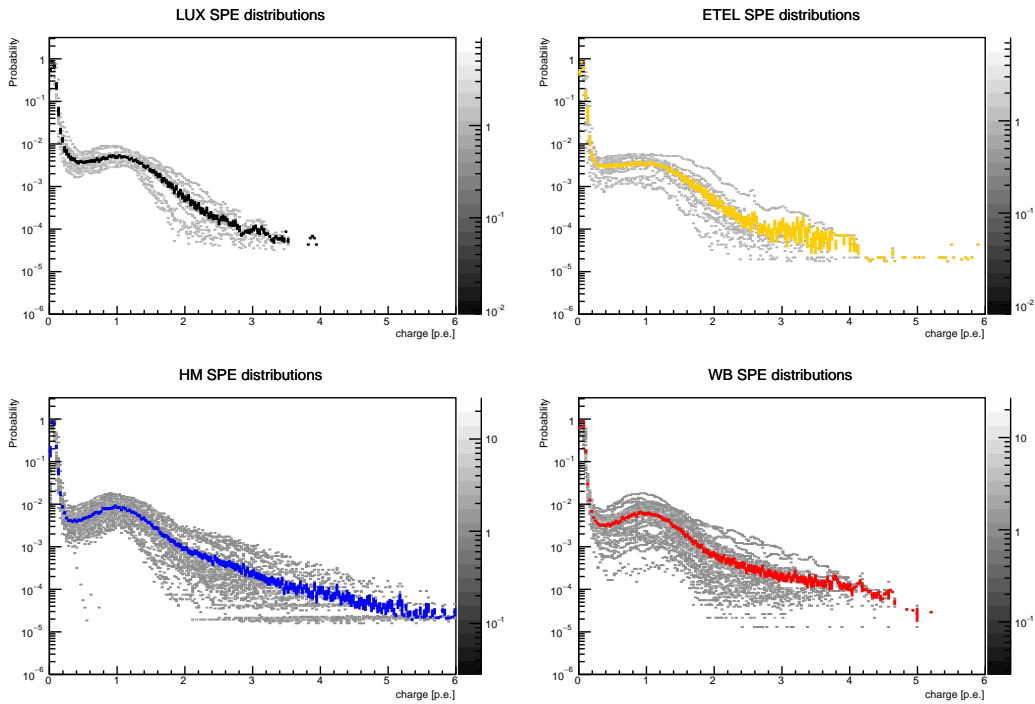


**Figure 5.16:** Gain distributions of the LUX, ETEL, Hamamatsu and Watchboy PMTs that are mounted in ANNIE as determined in the LED calibration campaign. While the single PMT distributions are shown in grey, an average gain distribution was constructed for each PMT type and is superimposed on top of the single distribution in different colors.

Figure 5.17 provides an overview of the average Single-PE. distribution for every PMT type. As expected by construction, the SPE peak is located around 1 p.e., while the pedestal peak is present at a charge value of around 0.1 p.e. Furthermore, the tails of the distributions extend up until charge values of 4-5p.e. with decreasing probability. The SPE peak is more pronounced in the case of the Watchboy and ANNIE PMTs, while it is a little more smeared out for the LUX and ETEL tubes. This already indicates that slightly different distributions will be necessary to model the charge responses of the different PMTs.

For modeling the PMT charge response in the simulation, the implementation of the SPE distribution is of primary importance. In order to extract the SPE component from the average distributions, a fit is conducted according to equation (5.4). Figure 5.18 exemplarily shows how such a fit looks like for investigating the ETEL gain distribution. The different components of the fit are depicted in different colors, with the pedestal being

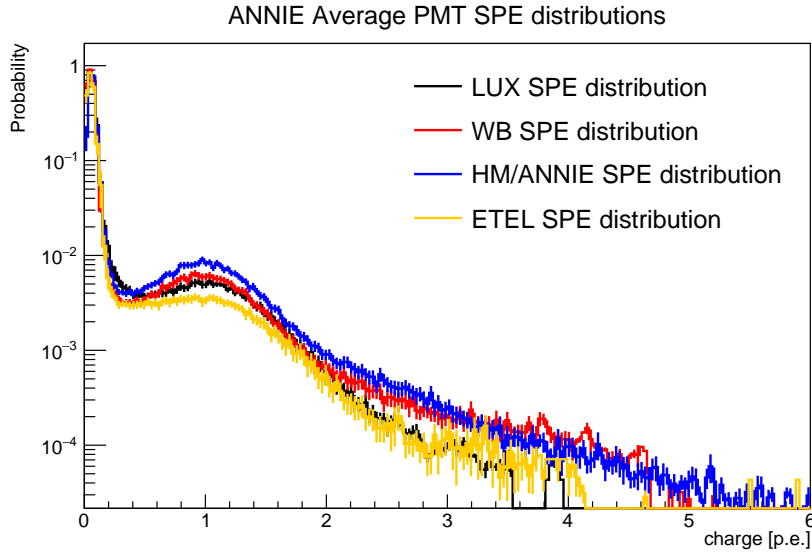


**Figure 5.17:** Average PMT Single PE. distributions for the four different PMT types present in ANNIE, shown in different colors. The pedestal and Single-PE. peak structure is clearly visible.

shown in blue, the SPE fit in green, and the Multi-PE. (MPE) fit in orange. The total fit function is shown in red and seems to fit the observed average charge distribution well. The parameters of the SPE fit function are therefore suitable to model the charge response for a single photon hit and can be used to implement the probability charge distribution in the simulation. Since photons are tracked individually in the simulation, the Single-PE. distribution provides the right model to simulate the charge response for the photon hits on the photocathode surface.

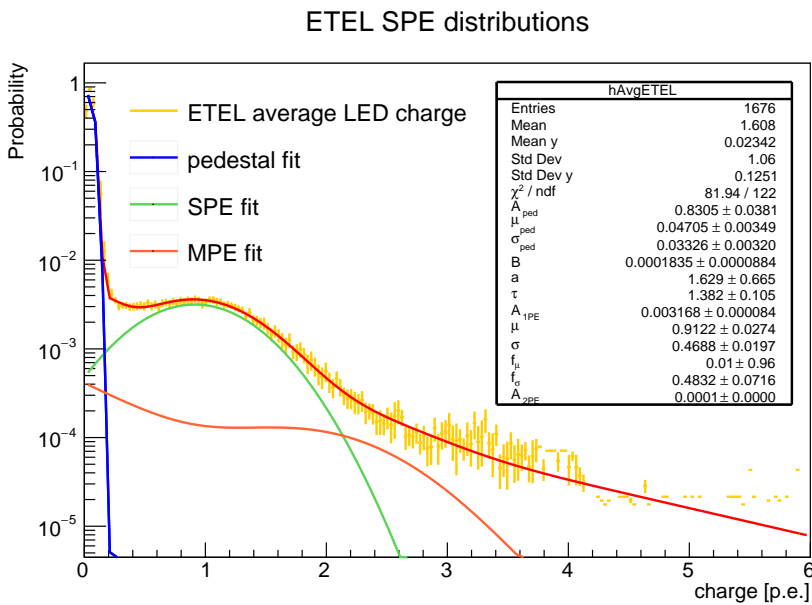


**Figure 5.18:** Combined pedestal, Single-PE. (SPE), and Multi-PE. (MPE) fit of the average ETEL gain distribution obtained from LED calibration data. The Gaussian SPE fit parameters are used in the simulation to model the charge response for all PMTs of ETEL type.

Figure 5.19 shows the results of the SPE distribution fits for the different PMT types. As expected from looking at the gain distributions, the SPE distributions are a little wider for the ETEL and LUX PMTs, while a more narrow peak is observed for the Watchboy and ANNIE PMTs. The SPE distributions feature mean values close to 1 p.e. and standard deviations of  $\sim 0.4$ – $0.5$  p.e. and generally look very reasonable. For comparison purposes, the figure contains a reference SPE curve that is conventionally used in WCSim to model the charge response for Super-Kamiokande PMTs. This charge response was implemented according to gain curves available from calibration data in Super-Kamiokande [217] and is used when performing SK simulations in WCSim or when using the default settings for PMTs. While the inclusion of a pedestal peak in this case is justified based on the validated SK simulation performance, implementing the SPE distribution without a pedestal peak seems to be the more reasonable choice for ANNIE. In this case, the response will still need to be tuned to match the data and the fact that pedestals are a representation of baseline noise rather than actual signals does seem to suggest that they do not need to be included in order to model the photon-induced electronics response. Future improvements to the implementations of the SPE distributions in ANNIE might additionally include a small exponential tail at low charge values to account for photon hits with a smaller amplification factor due to rare occurrences of electrons missing the first dynode.

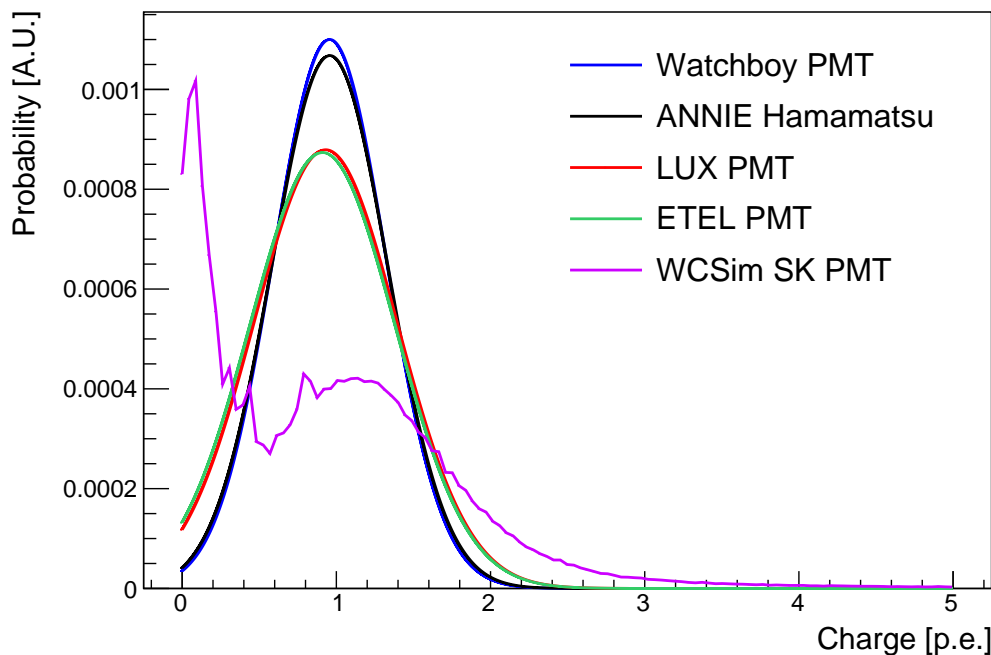


**Figure 5.19:** New SPE implementations for the different PMT types that are present in ANNIE as well as the standard WCSim SK PMT SPE distribution (*purple*). The ETEL and LUX SPE implementations feature a slightly larger spread compared to the Watchboy and Hamamatsu PMTs, as extracted from the gain calibration fits. Future improvements to the implementations of the SPE distributions might include a small exponential tail at low charge values to account for photon hits with a smaller amplification factor due to rare occurrences of missing the first dynode.

## 5.4 TUNING OF PARAMETERS

Now that the general geometrical and electronic properties of the simulation have been set up to represent reality as closely as possible, the detector behavior needs to be validated with respect to real data. Parameters that are of particular interest are reflectivity values of different material surfaces (which were not determined experimentally before) and a general light yield factor to compensate for possible coherent uncertainties in the modeling of the photomultiplier response. Different event samples will be utilized to directly compare the response in Monte Carlo and data: A sample of Michel electrons will be investigated in the first subsection 5.4.1 and will be used to tune the overall light yield detected by the PMTs. In the subsequent section 5.4.2, a sample of through-going muons will be used to verify reflectivity parameters for the most extensive geometric structures, based on the amount of reflections seen in the simulation and the data. The next subsection 5.4.3 investigates the detector response for neutrons detected at different positions within the detector in the scope of the Am-Be neutron calibration campaign. This test will highlight whether the previously tuned parameters yield good agreements also for independent data samples. The tuning concludes in subsection 5.4.4 with an overview of how well the various data samples are reproduced by different configurations of the tuning parameters.

### 5.4.1 TUNING OF OVERALL LIGHT YIELD: MICHEL ELECTRONS

Michel electrons are produced by decaying muons via the exchange of a W-boson, as visualized in figure 5.20 as a Feynman diagram. Electrons produced in such a decay follow a characteristic differential energy spectrum that can be parametrized as follows [218]:

$$\begin{aligned} \frac{d^2\Gamma}{x^2 dx d\cos(\theta)} \propto & (3 - 3x) + \frac{2}{3}\rho \cdot (4x - 3) + 3\eta x_0 \frac{1-x}{x} \\ & + P_\mu \xi \cos(\theta) \left[ (1-x) + \frac{2}{3} \cdot \delta \cdot (4x - 3) \right] \end{aligned} \quad (5.6)$$

with  $x = \frac{E_{\text{elec}}}{E_{\text{max}}}$  being the fractional maximum electron energy,  $E_{\text{max}} = \frac{m_\mu^2 + m_e^2}{2m_\mu} \approx 53 \text{ MeV}$  the maximal possible electron energy in the decay,  $x_0 = \frac{m_e}{E_{\text{max}}}$  the fractional electron mass,  $P_\mu$  the polarization of the muon, and  $\theta$  the angle at which the electron was emitted. According to the V-A theory, the so-called Michel parameters that describe the features of the decay spectrum should have the values  $\rho = \frac{3}{4}$ ,  $\eta = 0$ ,  $\xi = 1$  and  $\delta = \frac{3}{4}$  in the Standard Model [17].

Integrating the Michel energy spectrum over the possible polarizations of the muon and all possible angular emission angles yields a more compact parameterization of the emission spectrum

$$N(E) = \left[ 3 \left( \frac{E}{E_{\text{max}}} \right)^2 - 2 \left( \frac{E}{E_{\text{max}}} \right)^3 \right], \quad (5.7)$$

where the electron energy is still allowed to vary in the range  $E = [0, E_{\text{max}}]$  [6].

In order to select a Michel electron sample from the data, one first needs to identify a muon candidate that stopped in the ANNIE tank, followed by an electron candidate in the

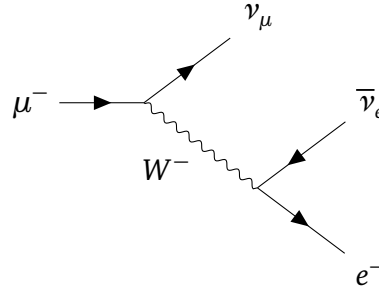


**Figure 5.20:** Feynman diagram for a muon decaying into an electron, alongside associated electron and muon neutrinos. The Feynman graph was created with the tikz-feynman package [25].

time period of a few microseconds later. Activity in the tank is identified by looking for so-called *clusters*, i.e. a minimum of 5 PMT hits registered in a pre-defined time window of 50 ns. A stopping muon candidate is made out by looking for a cluster happening in time with a FMV hit to select muon candidates that enter the water volume from the outside. At the same time, no coincident MRD track should be observed to make sure that the muon did not leave the water tank. Moreover, the charge barycenter of the muon tank cluster is required to be in the downstream region of the tank to exclude upward-going muons originating in the tank. The muon cluster candidate should additionally have the largest total charge of all prompt clusters to ensure there's not a coincident cosmic event that could influence the selection. In case such a muon candidate cluster is found, all subsequent clusters in the time window  $\Delta t_{\text{Michel}} \in [0.1, 6.0] \mu\text{s}$  are investigated for potential electron candidates. An additional cut on the Charge Balance variable is used to filter out any noise clusters that could be misidentified as electron candidates, with the Charge Balance parameter  $q_{\text{CB}}$  defined as

$$q_{\text{CB}} = \sqrt{\frac{\sum Q_i^2}{Q_{\text{sum}}^2} - \frac{1}{N}}. \quad (5.8)$$

In this formula,  $Q_{\text{sum}}$  represents the total charge observed in the cluster,  $Q_i$  references the charge that was observed by PMT  $i$ , and  $N$  is equal to the number of PMTs that were involved in the cluster. Charge Balance values close to 1 indicate that most of the charge was seen by one PMT, implicating that the cluster was probably a noise event. This parameter was previously used in the context of the WATCHBOY experiment [219] and also extensively used in Teal Pershing's thesis [215] to remove background events, particularly in the scope of the neutron calibration campaign of ANNIE.

Figure 5.21 shows the distribution of the Charge Balance variable versus the total recorded charge in electron candidate clusters. When applying a very conservative cut of  $q_{\text{CB}} < 0.2$  which should remove almost all unwanted noise events, the right side of the same figure shows the resulting average charge distribution as a function of the total charge for delayed clusters following a muon candidate. As expected for real Michel electron events, the average charge distribution increases linearly with the total charge, indicating that potential backgrounds have been removed rather successfully. In case noise backgrounds were still present in the data sample, one would expect the presence of a second disjunct

distribution in the average charge representation and potential additional contributions which would not display a linear correlation.

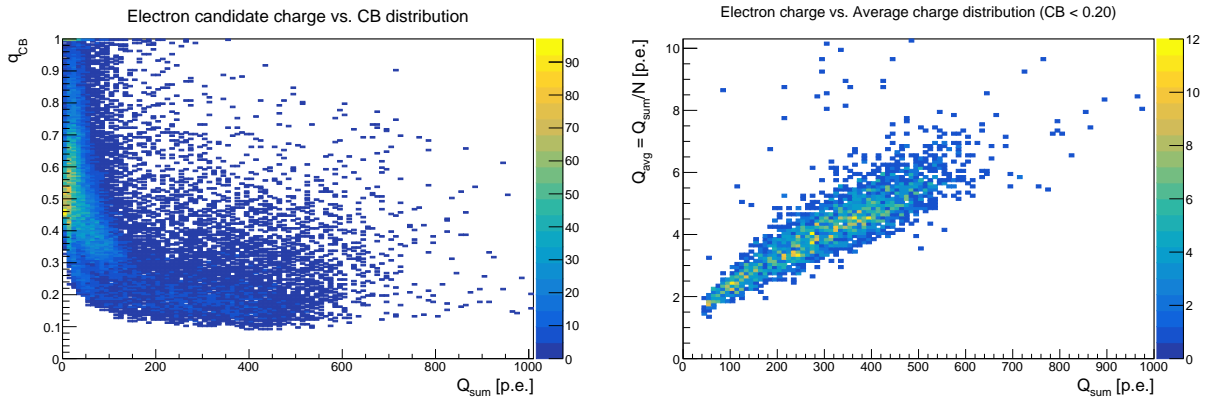


**Figure 5.21:** **Left:** The Charge Balance as a function of the total charge for Michel electron candidate events. While a Charge Balance cut of  $q_{CB} < 0.4$  is usually applied for selecting neutron events, a stricter cut of  $q_{CB} < 0.2$  is applied here to select a very pure electron sample. **Right:** Average charge distribution as a function of the total cluster charge for Michel electron events with  $q_{CB} < 0.2$ .

The time spectrum of electron candidate events that were selected in the outlined selection procedure is shown in figure 5.22. The exponential trend is visible, with an exponential fit yielding a decay time of  $\tau = (2.01 \pm 0.05) \mu\text{s}$  (statistical error only). While this is slightly smaller than the expected value of  $\tau = 2.1 \mu\text{s}$  in water [220], the difference would probably be accounted for when taking into account systematic errors that are introduced by the selection procedure.

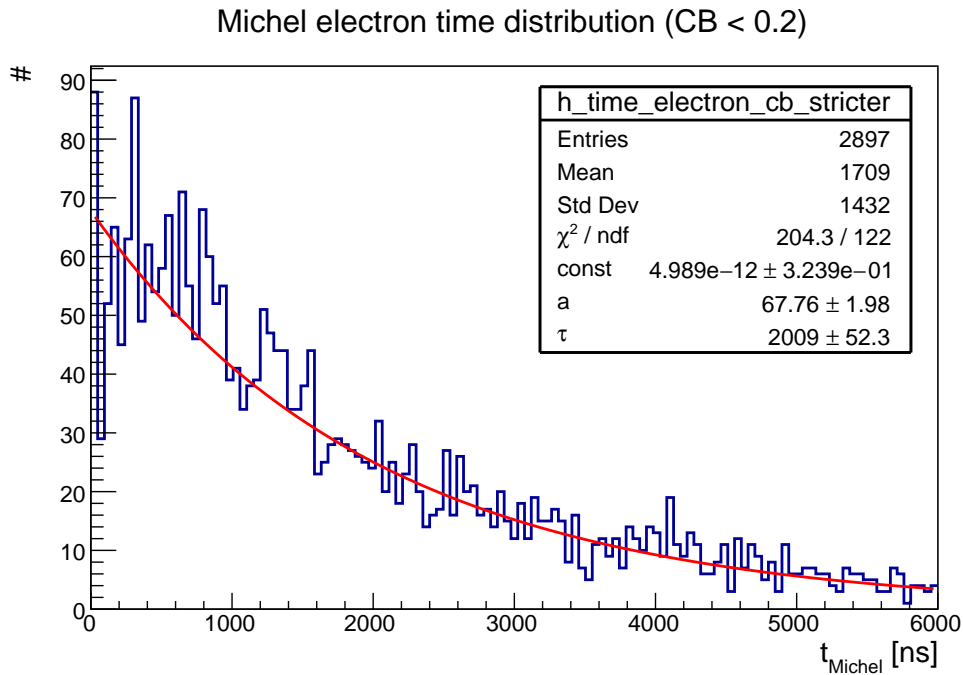


**Figure 5.22:** Time spectrum of Michel electron candidate events in ANNIE beam data. An exponential fit (shown in red) yields a decay time of  $\tau = (2.01 \pm 0.05) \mu\text{s}$ , which is slightly smaller than the expected value  $\tau_{theo} = 2.1 \mu\text{s}$ .

Now that the selection cuts have proven to select a relatively pure Michel electron sample, the energy distributions can be compared between data and MC for different Quantum Efficiency ratio tuning values. Within the simulation, electrons are simulated according to the theoretical Michel electron spectrum (5.7) for uniform vertices and isotropic directions within the water tank. The resulting total charge distributions is contrasted between the simulation and the data to determine the tuning parameter that yields the best agreement. For this purpose, simulations were performed in the Quantum Efficiency tuning factor range  $r_{QE} \in [1.0, 1.6]$  in steps of  $\Delta r_{QE} = 0.05$ . The tuning factor  $r_{QE}$  simply scales the nominal Quantum Efficiency such that the probability to register a hit for an arriving photon is increased independently of its wavelength,  $QE_{scaled}(\lambda) = r_{QE} \cdot QE_{nominal}(\lambda)$ . It will also be referred to as Quantum Efficiency ratio factor in the following.

The figure of merit that is used here for evaluating the agreement of the distributions is a  $\chi^2$ -value based on Pearson's test of homogeneity [221] which is calculated in the scope of the ROOT-function Chi2Test that is included as a part of the TH1 histogram class. In case there are two histograms hData and hMC with the same number of bins  $N_{bins}$ , the  $\chi^2$ -value is computed as

$$\chi^2 = \sum_{i=1}^{N_{bins}} \frac{(n_i - N\hat{p}_i)^2}{N\hat{p}_i} + \sum_{i=1}^{N_{bins}} \frac{(m_i - M\hat{p}_i)^2}{M\hat{p}_i}. \quad (5.9)$$

Within the formula,  $n_i$  denotes the bin contents in the first histogram hData, while  $m_i$  highlights the bin content for the same bin within the other histogram hMC, and  $N$  and  $M$  represent the total number of entries for the two histograms such that e.g.  $N = \sum_{i=1}^{N_{bins}} n_i$ . The maximum likelihood estimator for the probability value  $p_i$  of observing a hit in each bin can be expressed as

$$\hat{p}_i = \frac{n_i + m_i}{N + M}, \quad (5.10)$$

assuming that the homogeneity hypothesis holds true.

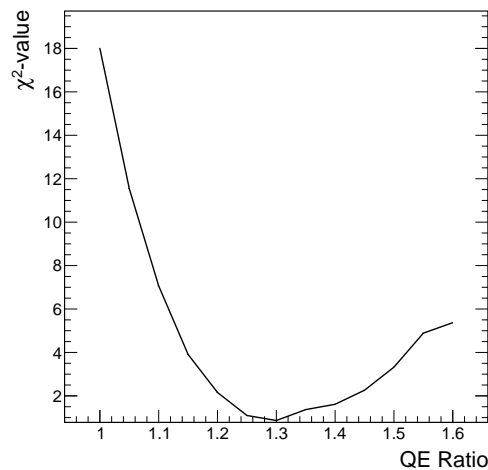


**Figure 5.23:** Scan of the  $\chi^2/n.d.f.$ -value as a function of the Q.E. Ratio tuning parameter  $r_{QE}$ , quantifying the agreement of the Michel electron spectrum between data and MC. The observed minimum at  $r_{QE} \sim 1.30$  indicates the value maximizing the agreement between the two samples.

When using this method to compare the charge spectra obtained for data and simulation, figure 5.23 presents the resulting  $\chi^2$ -distribution as a function of the Quantum Efficiency Ratio tuning factor  $r_{QE}$ . The best agreement is achieved for a Q.E. ratio factor of  $r_{QE,min} = 1.30$ , yielding a  $\chi^2/n.d.f.$ -value of  $\approx 1$ .

The agreement of the Michel electron spectrum in data and the simulation is shown in figure 5.24 for the best fit value of  $r_{QE,min} = 1.30$ . The Charge Balance cut was lowered from the initial threshold of  $q_{CB} < 0.2$  to  $q_{CB} < 0.17$  in order to remove backgrounds at lower charge values even more efficiently. The cut was applied to both the data and the MC sample to obtain samples with equivalent selection steps and similar properties. In addition to the charge balance selection, a charge cut of 2 p.e. was applied to each PMT as an event cleaning cut and to minimize the effects of PMT afterpulsing from the preceding muon cluster. The spectra are shown in red (blue) for the data (simulation) case. Both spectra extend up until charge values of  $q_{max} \approx 500$  p.e. and feature a peak around 300 p.e. When comparing the two distributions, the general features like the right flank for charge values above 300 p.e. and the rising edge below 200 p.e. seem to be well reproduced by the simulation.

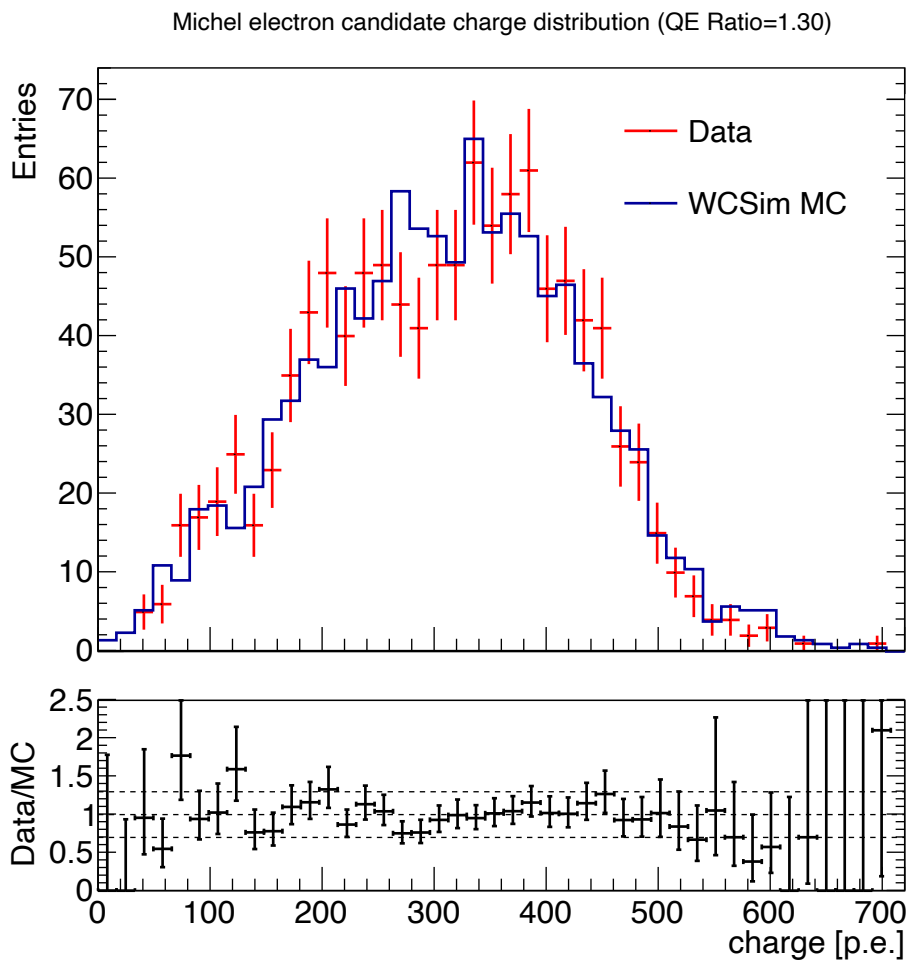


**Figure 5.24:** Michel electron spectrum in data and MC for a Q.E. ratio value of 1.30. The total charge was calculated by summing the contributions of all PMTs that detected at least 2 p.e. for event cleaning purposes.

Generally speaking, the agreement between the data and MC seems to be acceptable for the determined Quantum Efficiency tuning factor of  $r_{QE,min} = 1.30$  in the case of the Michel electron sample. This finding verifies that the particular PMT implementation in WCSim necessitates some form of upscaling for the light collection, which was studied here in the form of a Quantum Efficiency ratio factor. However, there is also the possibility that different material reflectivity values could have an influence on the amount of light that was collected. The interplay of reflectivity and Q.E. tuning factors will be studied in the upcoming subsection 5.4.2, in which both the total detected charge as well as the reflected amount of charge are studied for the case of through-going muons. Since the full directional information is known for those events from the information collected by the MRD, the exact same event topologies can be studied in data and MC and investigated for differences in the general light yield as well as the amount of reflections that are observed.

#### 5.4.2 TUNING OF MATERIAL REFLECTIVITY VALUES: THROUGH-GOING MUONS

There are a couple of surfaces in ANNIE that are potentially highly reflective and could contribute significantly to the amount of light that is backscattered. Introducing the correct reflectivity values for all these surfaces is therefore crucial for a correct representation of reflections in ANNIE. In this context, the following surfaces need to be considered: Firstly, the complete Inner Structure was wrapped in white teflon for Gadolinium material compatibility reasons. Compared to the original Inner Structure steel surface, the white teflon wrapping is very reflective and its surface needs to be implemented as such in the simulation. In addition to the Inner Structure teflon wrapping, the PMT holders are another source of reflections: Particularly the white polyethylene ANNIE holders are potentially very reflective, while the black *Schedule 80 PVC* LUX and ETEL holders feature a smaller, but still non-negligible reflectivity value. In addition to the more reflective surfaces, it is also important to verify that the reflectivity value for the black sheet wrapping is in agreement with the data.

Since none of the reflectivity values are known from an experimental point of view, all these parameters enter the simulation as degrees of freedom. Starting from reasonable initial guesses for all values, the variables can be adjusted to match the data more accurately. Since it's difficult to vary multiple parameters at once, the reflectivity of the largest structure, *i.e.* the Inner Structure, will be adjusted first before potentially going on to vary the parameters for smaller objects such as the PMT holders. The reflectivity value for the black sheet wrapping is assumed to be the same as in Super-Kamiokande at first, but could also be adjusted if the need arises.

In order to compare reflections, events in the data and the MC need to feature the same spatial properties. Both the vertex and the direction of the particle therefore need to be reasonably well known in the data such that the conditions can be replicated in the simulation framework. A relatively simple well-characterized sample is that of through-going muons: This sample includes muons that are produced outside of the water tank, pass through one of the Front Muon Veto scintillator paddles, penetrate the whole water tank and finally also create a track in the MRD. The events can be selected in the data

by requiring a tank cluster in coincidence with a MRD track, as well as a coincident FMV paddle hit. Based on the  $z$ -coordinate of the tank charge barycenter, the direction of the muon can be determined and selected for downstream-directed events. The reconstructed muon track in the MRD can then be extrapolated to a plane in front of the Front Muon Veto. Muons are placed at that particular extrapolated position in the simulation geometry, and are initialized in the direction of the reconstructed MRD track. While the real through-going muon sample will be comprised of a variety of energies, the behavior in the tank will be quite similar for all muons exceeding a certain energy threshold due to the minimum-ionizing-particle (MIP) nature of the muon. The energy of the muons is hence set to a value of  $E_\mu = 2 \text{ GeV}$  to ensure that the muons reliably pass through the entire tank and also produce a track in the MRD. The topology of the reconstructed MRD track in the simulation can then be validated against the original MRD track that was observed in the data to ensure that the same event properties are replicated between data and MC.

The initial tuning with through-going muons will evaluate the agreement of charge observed in different regions of the tank: The charge detected in the downstream region of the detector is evaluated alongside the charge observed in the upstream region and the total charge within the whole water tank. In addition, the fraction of charge that was detected in the upstream region in comparison to the downstream region is used as a separate estimator that was primarily chosen to verify the amount of reflections. Both the Quantum Efficiency ratio  $r_{\text{QE}}$  and the reflectivity of the Inner Structure  $R_{\text{InnerStr}}$  are varied to investigate which parameter combination yields the best agreement. The parameter scans cover the ranges  $r_{\text{QE}} \in [1.20, 1.60]$  and  $R_{\text{InnerStr}} \in [0.65, 1.00]$ , with step sizes of  $\Delta r_{\text{QE}} = \Delta R_{\text{InnerStr}} = 0.05$ . Estimates are used for the reflectivity values of smaller-scale structures like the holders, while the parameterization from Super-Kamiokande is used to characterize the reflectivity of the black sheet. The ANNIE PMT holders are assumed to have a reflectivity of  $R_{\text{ANNIE}} = 0.90$ , while the LUX and ETEL holders are expected to be less reflective and set to a value of  $R_{\text{LUX/ETEL}} = 0.70$ . The initial black sheet reflectivity values are wavelength-dependent and range from  $R_{\text{BS,min}} = 0.11$  to  $R_{\text{BS,max}} = 0.14$ .

### Tuning of the Inner Structure reflectivity

The first parameter of interest is the Inner Structure reflectivity  $R_{\text{InnerStr}}$ . A first constraint on this parameter will be deduced by looking at the fraction of light that was detected in the upstream region of the water tank, compared to the charge observed downstream. Since the event selection already filtered out through-going muons in downstream direction, most of the photons arriving upstream will be caused by reflections inside the water tank, with the Inner Structure responsible for a majority of the them. The distribution of the variable  $f_{\text{upstream}} = Q_{\text{upstream}}/Q_{\text{downstream}}$  is compared between data and simulations with various reflectivity values to determine the value that matches reality most closely. Figure 5.25 highlights the dependence of the data/MC  $\chi^2$ -agreement of the  $f_{\text{upstream}}$ -distribution for a range of  $r_{\text{QE}}$  and  $R_{\text{InnerStr}}$  values. Independently of the Quantum Efficiency scaling factor, the best agreement for the fraction of upstream charge is achieved for the highest possible reflectivity values of  $R_{\text{InnerStr}} = 1.00$ . While the best-fitting QE ratio value will have to be determined by studying different distributions such as the absolute downstream charge values in the following paragraph, the Inner Structure reflectivity value  $R_{\text{InnerStr}}$  will be fixed to a value of 1 by the presented tuning of the  $f_{\text{upstream}}$  value.

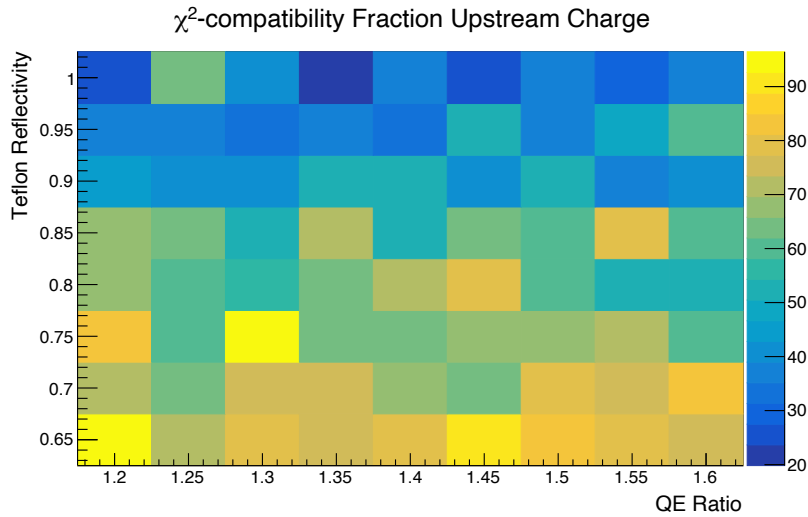


**Figure 5.25:** The  $\chi^2$ -agreement between data and simulation for the distribution of the fraction of charge observed upstream. The agreement is depicted as a function of the Q.E. scaling factor (labeled as QE Ratio) as well as the teflon reflectivity. Rather high reflectivity values around  $R_{\text{InnerStr}} \approx 1.0$  are preferred for a good description of the fraction of charge observed upstream.

The Quantum Efficiency scaling factor will be tuned by comparing the distributions of the charge  $Q_{\text{downstream}}$  that was detected downstream for the selected through-going muon events. Figure 5.26 shows the resulting  $\chi^2$ -agreement of the histograms in the data and the simulations as a function of  $r_{\text{QE}}$  and  $R_{\text{InnerStr}}$ . Keeping in mind the previous results for the Inner Structure reflectivity best fit value of  $R_{\text{InnerStr}} = 1.0$ , the best agreement for the downstream charge distribution is achieved for a Quantum Efficiency scaling factor of 1.20. Although it seems as if lower Q.E. scaling factors might yield an even better agreement, this will not be of major importance once we consider PMT-wise charge comparisons, as described in more detail further below.

One can check the agreement of several charge distributions for the selected values of  $r_{\text{QE}} = 1.20$  and  $R_{\text{InnerStr}} = 1.00$  to verify how well the data is described by this particular set of tuning parameters. In particular, the distributions of the total detected charge  $Q_{\text{total}}$ , the upstream detected charge  $Q_{\text{upstream}}$ , the downstream observed charge  $Q_{\text{downstream}}$ , and the fraction of charge detected upstream  $f_{\text{upstream}}$  will be compared in the following. Figure 5.27 presents the resulting distributions both for the case of data (*blue*) and simulation with the deduced tuning parameters (*red*). In general, good agreement is visible across all four selected variables. Both the downstream and upstream detected charge distributions match pretty well, indicating that both the charge scale and the amount of reflection is roughly modeled correctly. The simulation hence seems to be able to represent reality reasonably well with respect to these four particular observables.

A further interesting comparison includes possible differences in the charge spectra observed by each individual PMT. Rather than on a global level, such an evaluation probes the photodetector implementation within the simulation on a PMT-by-PMT basis. For this purpose, charge histograms are filled individually for all PMTs both in the data and the simulation. Afterwards, the average charge values in the data ( $\bar{q}_{\text{data}}$ ) and the simulation ( $\bar{q}_{\text{MC}}$ ) are extracted as the mean values of the charge distribution histograms and the values

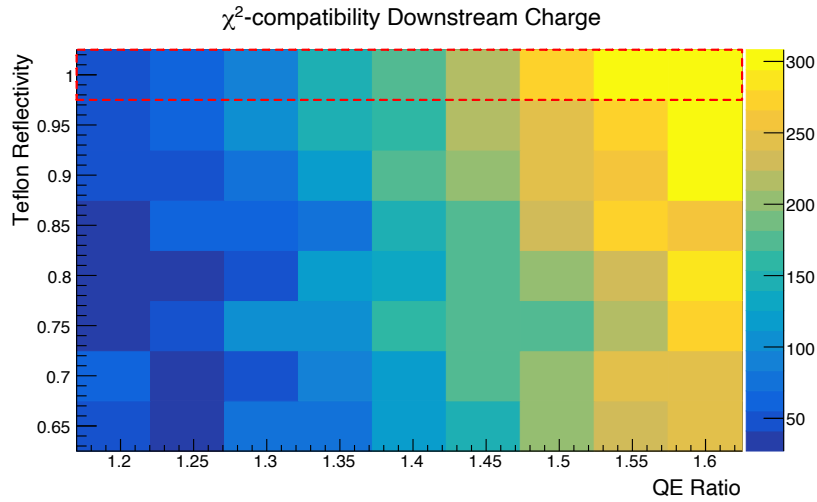


**Figure 5.26:** The  $\chi^2$ -agreement between spectra observed in data and simulation for the distributions of downstream detected charge. The agreement is depicted as a function of the Q.E. scaling factor (labeled as QE Ratio) as well as the teflon reflectivity. The preferred value for the teflon reflectivity has been determined with a different data set and is highlighted by red dashed lines. For this reflectivity, small Q.E. scaling factors of  $r_{QE} = 1.20$  or even smaller seem to be preferred to achieve a good agreement for the charge observed in the downstream region of the detector.

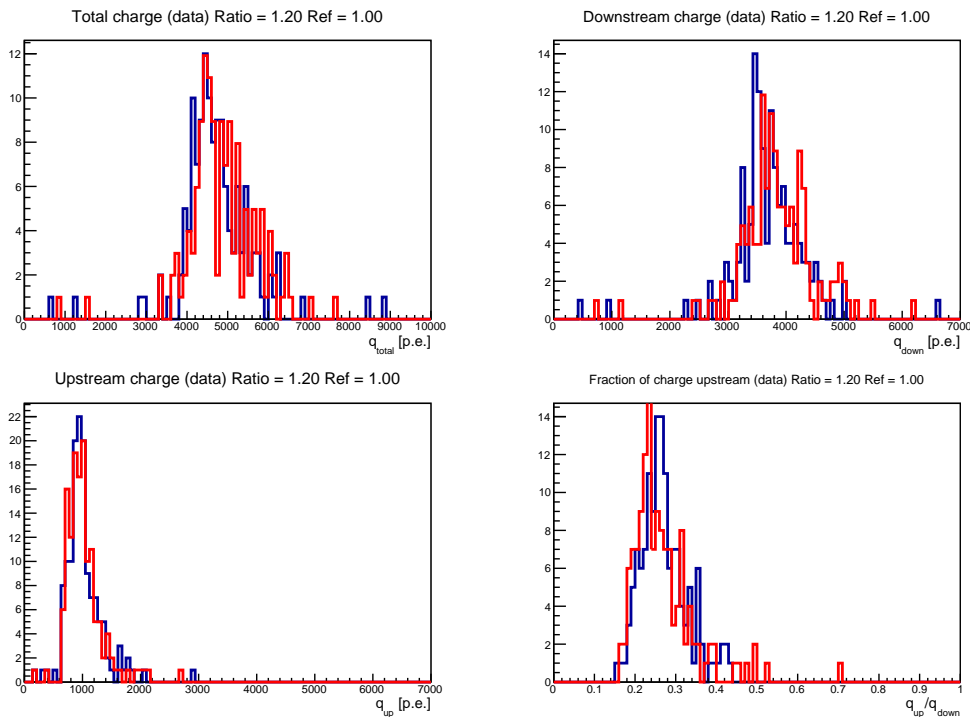


**Figure 5.27:** Different charge distributions are shown for through-going muon data (blue) and simulation (red) samples. Tuning values of  $r_{QE} = 1.20$  and  $R_{InnerStr} = 1.00$  are assumed in this context. The individual histograms depict the total charge (upper left), the charge detected downstream (top right), the upstream charge (bottom left), and the fraction of upstream charge compared to downstream charge (bottom right).

are compared for every phototube. The ratio of the average charge values  $R_{charge} = \frac{\bar{q}_{MC}}{\bar{q}_{data}}$  is calculated for each PMT, as presented in figure 5.28 in the form of an event display-like

representation. While the majority of PMTs is characterized by reasonable charge ratios around 1, some PMTs exhibit considerably worse behavior. Many of them are located in the topmost row of the barrel PMTs, as well as in the third barrel row from the top. Several PMTs in these regions register more charge in the simulation compared to the data, indicating that the Quantum Efficiency scaling factor overestimates the detected charge in these cases. When cross-referencing the affected PMT positions with the PMT type distribution shown in figure A.4 in the appendix, it becomes clear that the PMTs in these rows are Watchboy PMTs. Most of the other barrel PMTs, on the other hand, are Hamamatsu/ANNIE PMTs, and show better agreement. In the case of the ANNIE PMTs, the photosensors actually detect less light in the simulation compared to the light levels observed in data. This seems to indicate that while some PMT types (such as the Watchboy PMTs) are modeled in a way such that they detect too much charge, others (such as the ANNIE PMTs) are modeled with a Quantum Efficiency scaling factor which is slightly too small.

A possible idea for resolving the discrepancy in the charge distributions of the different PMT types and achieving a more uniform charge response relies on the introduction of individual Q.E. scaling factors for different PMT types. The probability of detecting photons arriving at the photocathode of a Watchboy PMT would be scaled to a lesser extent than photons that are registered by ANNIE/Hamamatsu PMTs. Since both the top and bottom PMTs also seem to exhibit too large charge values in the simulation, it would make sense to use the smaller Watchboy-related scaling factor also for the LUX and ETEL tubes located in the top and bottom panels of the detector. The next paragraph will focus on determining the optimal combination of Q.E. scaling factors with respect to the observed charge distributions in the considered through-going muon events.

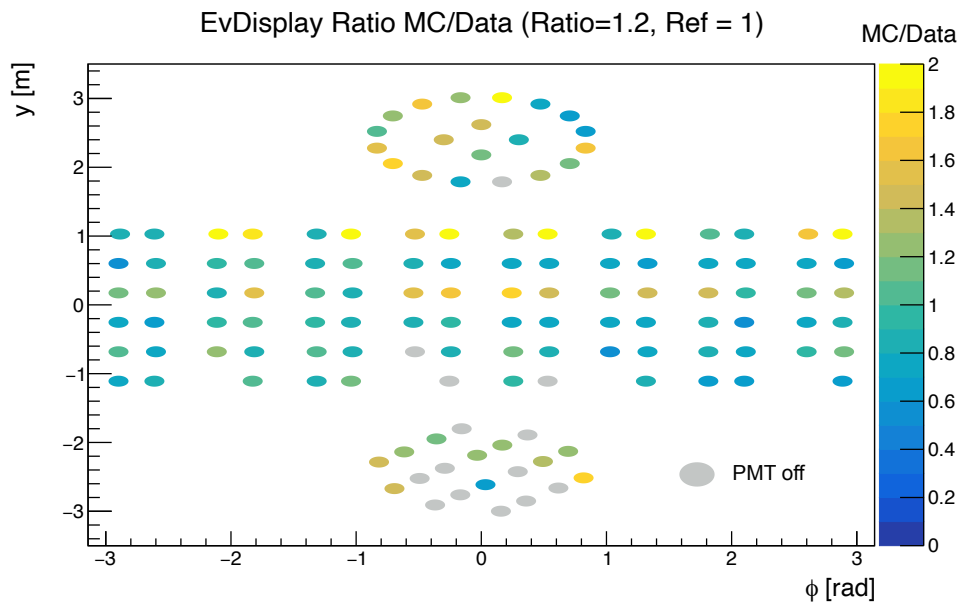


**Figure 5.28:** Ratio values  $R_{\text{charge}} = \frac{\bar{q}_{\text{MC}}}{\bar{q}_{\text{data}}}$  of average detected charges in MC ( $\bar{q}_{\text{MC}}$ ) and data ( $\bar{q}_{\text{data}}$ ), depicted in a rolled-open view of the cylindrical water tank. The largest discrepancies can be seen in the topmost row of barrel PMTs, as well in the third row from the top. In addition, there also seem to exist some deviations in the detected charge distributions for the top and bottom PMTs.

### PMT-type specific Q.E. tuning

Two independent tuning factors  $r_{\text{QE,ANNIE}}$  and  $r_{\text{QE,Other}}$  are introduced to scale the detected light for ANNIE/Hamamatsu PMTs and all other PMTs separately. Since the investigation of the PMT-wise charge distributions revealed that ANNIE PMTs will need a larger scaling factor while the other PMTs can be modeled with a smaller ratio, the parameter ranges are chosen in accordance to this prior knowledge. The parameters will be varied in the ranges  $r_{\text{QE,ANNIE}} \in [1.20, 1.60]$  and  $r_{\text{QE,Other}} \in [0.80, 1.20]$  with step sizes of  $\Delta r_{\text{QE,ANNIE}} = \Delta r_{\text{QE,Other}} = 0.05$ . The resulting  $\chi^2$ -agreement distributions are shown in figure 5.29 for both  $Q_{\text{total}}$  and  $Q_{\text{downstream}}$ . Both variables can be modeled reasonably well by a rather large band of tuning parameter combinations.

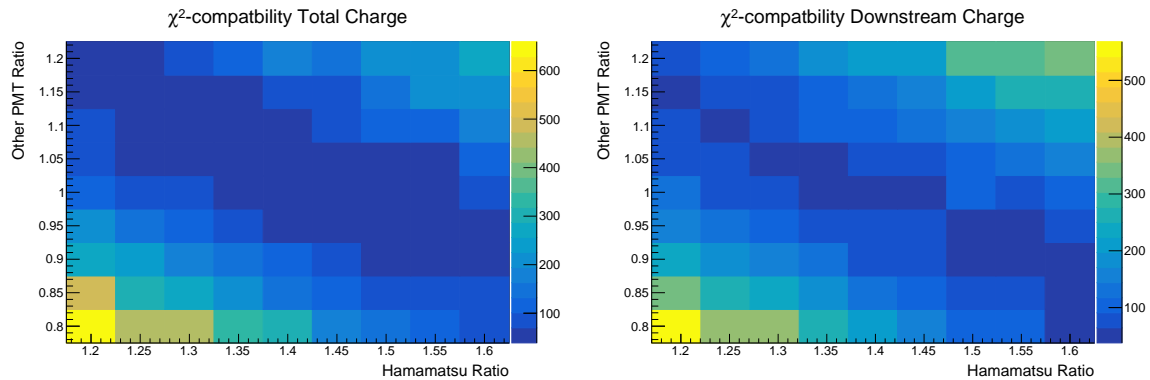


**Figure 5.29:** The  $\chi^2$ -values depicting the agreement of the data and simulation distributions of the total charge  $Q_{\text{total}}$  (left) and the charge  $Q_{\text{downstream}}$  that was detected downstream (right) in the through-going muon sample. The agreement is shown as a function of the Q.E. scaling factor  $r_{\text{ANNIE}}$  for the ANNIE PMTs and the Q.E. scaling factor  $r_{\text{Other}}$  for all other PMTs.

In the following, we will investigate how well a simulation with a parameter combination from the center of the allowed region ( $r_{\text{QE,ANNIE}} = 1.40$ ,  $r_{\text{QE,Other}} = 1.00$ ) is able to model the through-going muon events, particularly with respect to the representation of individual PMTs. In this context, figure 5.30 presents the ratio of average charges in the simulation and the data in a rolled-open view of the cylindrical water tank. In general, the distribution of  $R_{\text{charge}}$  looks much more uniform than in the previous simulation with a global scaling factor which was presented in figure 5.28. Both the PMTs in the top and bottom panel seem to reproduce the charge levels better than before. Similarly, the Watchboy PMTs in the third barrel row from the top also show a slightly better agreement, although some differences are still apparent for a few PMTs. The largest discrepancies are present in the topmost row of the barrel photosensors. The geometric pattern featuring a discrepancy for the right PMT within each panel seems to suggest that there is still some sort of geometrical effect that is currently not well understood. Future studies will hopefully shed some light on the origin of this particular discrepancy. Apart from this, the agreement of the PMT-wise charge patterns looks slightly more uniform with the separate scaling factors  $r_{\text{QE,ANNIE}}$  and  $r_{\text{QE,Other}}$  compared to the case of a global Q.E. scaling factor.

In the scope of the tuning studies with the through-going muon sample, a final Q.E. scaling configuration is explored in the next paragraph. In this tuning version, each PMT is assigned an individual Q.E. scaling factor based on the differences observed in data and MC for every photosensor.

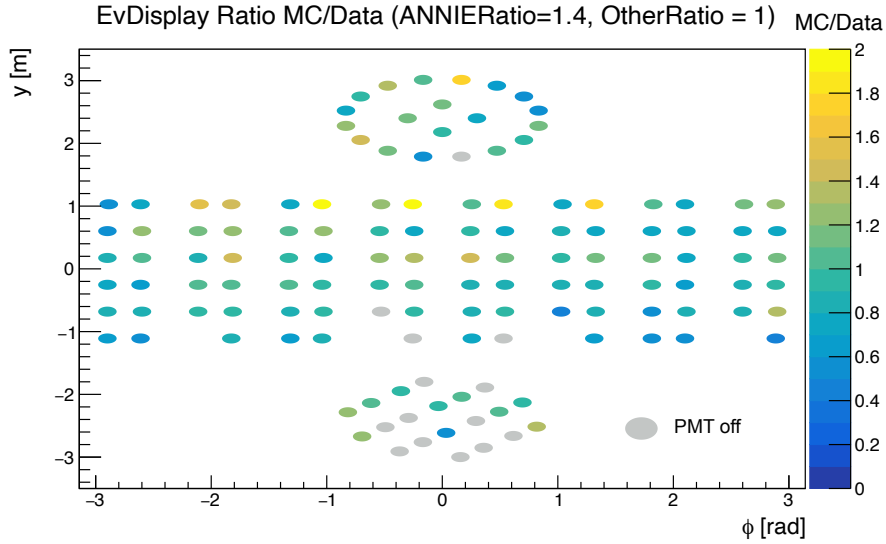


**Figure 5.30:** Ratio values  $R_{\text{charge}} = \frac{\bar{q}_{\text{MC}}}{\bar{q}_{\text{data}}}$  of average detected charges in MC ( $\bar{q}_{\text{MC}}$ ) and data ( $\bar{q}_{\text{data}}$ ), depicted in a rolled-open view of the cylindrical water tank. Simulations were conducted assuming a Q.E. ratio factor of  $r_{\text{QE,ANNIE}} = 1.40$  for the ANNIE PMTs and  $r_{\text{QE,Other}} = 1.00$  for all other PMTs. While there are still some discrepancies visible, the response is much more uniform compared to the case of a single Q.E. scaling factor for all PMTs, as presented in figure 5.28. The largest remaining deviations are visible in the topmost row of barrel PMTs.

### Individual PMT-by-PMT Q.E. tuning

As a final step in tuning the light response of the ANNIE photosensors, individual effective Quantum Efficiency values for each PMT are considered in this paragraph. To first order, these Q.E. values are determined by comparing the mean values of the charge distributions between data and simulation for each PMT from the charge distributions in the through-going muon sample. When simulating the response for a specific photosensor  $i$ , the effective factor  $R_{\text{eff}}(i)$  is multiplied to the nominal Quantum Efficiency value to obtain the probability that a photon invoked a hit on the PMT.

Determining the effective Q.E. values in such a way will inherently result in a very good agreement for the sample that was used to extract the effective tuning parameters. As a consequence, both the individual and total charge responses should match rather closely for the through-going muon sample after implementing such a PMT-by-PMT tuning. As shown in figure 5.31, the overall distributions match really well for the different charge distributions and the fraction of upstream charge.

However, this agreement does not necessarily correspond to a good representation of the detector response in the simulation framework. On the contrary, the deduced individual Q.E. ratio values might include other effects such as reflections or other peculiarities of the through-going muon sample that would artificially boost the agreement of this particular sample. The validity of the individual effective Quantum Efficiency values is hence evaluated in the following by investigating the agreement for independent samples. In this context, the charge response will be compared for neutron events in the following section 5.4.3. In addition, an overview of the simulation agreement for all samples (Michel, Through-going, AmBe) will be provided in section 5.4.4 for the different tuning configurations of a global Q.E. factor, PMT-type dependent factors, and individual factors.

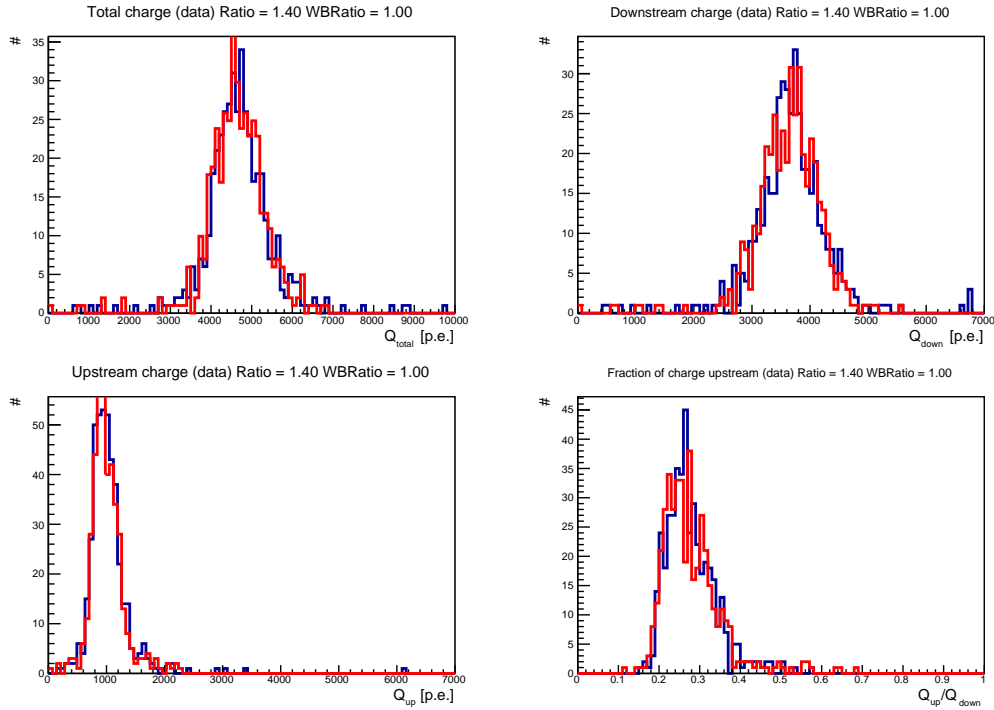
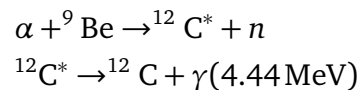


**Figure 5.31:** Different charge distributions are shown for through-going muon data (*blue*) and simulation (*red*) samples. Individual PMT-by-PMT Q.E. ratio factors are assumed in this context. The individual histograms depict the total charge (*upper left*), the charge detected downstream (*top right*), the upstream charge (*bottom left*), and the fraction of upstream charge compared to downstream charge (*bottom right*).

### 5.4.3 AM-BE NEUTRON CALIBRATION

The neutron multiplicity measurement relies on a precise knowledge of the neutron detection efficiency within the ANNIE water tank. For this reason, a dedicated neutron calibration campaign was launched before the beam data taking to characterize how well neutrons are identified in the detector. The neutron source was deployed via the five calibration ports to study the detection efficiency at different positions within the tank. The locations of the calibration ports on the tank lid are shown in figure 5.32 on the left. Four of the calibration ports are located on the central beam axis of the detector, while port 4 is positioned 75 cm to the left off the central beam axis. For each port, the source was deployed at different heights within the tank. Five different heights were chosen for the data acquisition in each calibration port, with one position in the center of the detector and additional vertical variations of 50 cm and 100 cm both above and below the central position. In such a way, a three-dimensional scan of the detection efficiency within the water tank was made possible.

The neutron calibration source relies on a combination of the  $\alpha$ -emitter  $^{241}\text{Am}$  and the Beryllium isotope  $^9\text{Be}$  to generate neutrons. The  $\alpha$ -particle from the Americium is captured by the Beryllium and often generates an excited  $^{12}\text{C}^*$  nucleus in the first excited state, which subsequently decays by emission of a 4.44 MeV gamma to its ground state [223]:



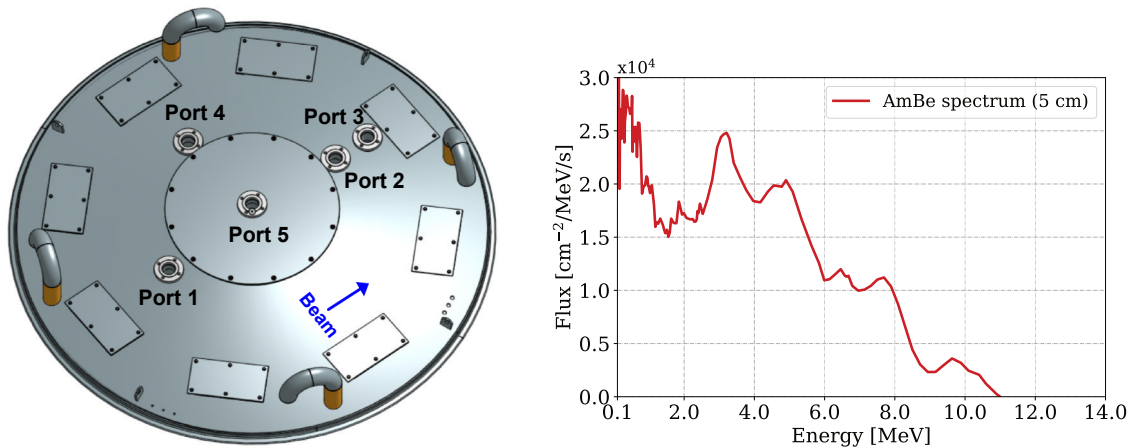


**Figure 5.32:** Left: Positions of the calibration ports on the ANNIE tank lid. Ports 1, 2, 3 and 5 are located on the central beam axis, while port 4 is positioned 75cm to the left of the central beam axis. Right: Exemplary Am-Be neutron energy spectrum for a source in a distance of 5 cm [222].

It is estimated that roughly 60% of all neutrons from an AmBe source will be accompanied by such a gamma, although the exact value varies depending on the exact composition of the radioactive source [224]. The resulting neutron energy spectrum is depicted on the right of figure 5.32. It extends from 0 MeV to roughly 10 MeV and features several peaks primarily around 0.5 MeV, 3 MeV, and 5 MeV. The de-excitation gamma is a useful property of the neutron creation mechanism since it can be used to tag the neutron emission and trigger the data acquisition. As shown in figure 5.33, the AmBe source in ANNIE is deployed in a housing container that contains stainless steel sections for shielding purposes and a BGO crystal in addition to the actual source. When a de-excitation photon occurs in time with the neutron emission, the photon can penetrate the stainless steel section and reach the BGO crystal, where scintillation light is emitted as a consequence of the associated Compton scattering process.

The scintillation light is detected by the two SiPMs which are attached on top of the crystal, triggering the data acquisition in case a coincident signal is observed in both SiPMs. The neutron - which is emitted in time with the gamma - scatters around the detector, thermalizes and is captured on Gadolinium or hydrogen nuclei in the water tank. Since the combination of thermalization and the capture process happens with a time constant of  $\tau_{\text{neutron}} \approx 30 \mu\text{s}$ , the AmBe data acquisition records windows of  $70 \mu\text{s}$  for every SiPM-induced trigger. More detailed information on the DAQ and the triggering can be found in the more detailed general description in chapter 3.4.1.

Since only neutron emissions with an associated gamma will trigger the data acquisition, the available  $Q$ -values for the neutrons are affected by the presence of the 4.44 MeV gamma. Instead of extending to energies around 11 MeV, the neutron energy spectrum only contains energies up to  $\approx 7$  MeV for this particular class of events. Since the exact energy of the neutrons in this energy region is not of particular importance for the scattering behavior, the simulation studies will deploy mono-energetic neutrons of 5 MeV energy at the different calibration locations. The resulting charge spectra will be compared between data and the simulation for each of the positions to validate the neutron response model. In this

### ANNIE AmBe source schematic

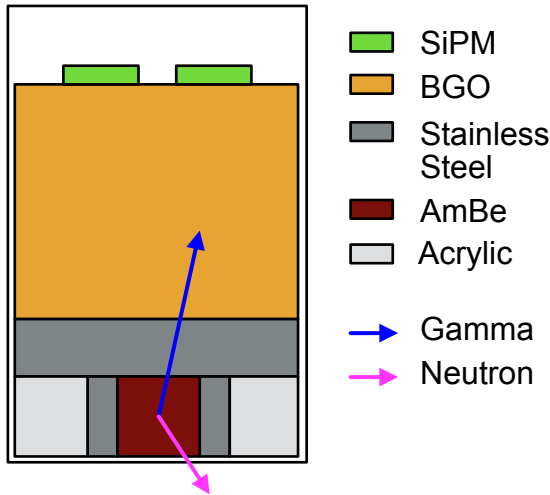
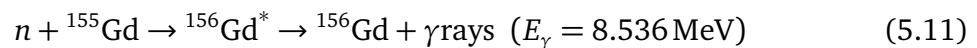


**Figure 5.33:** Left: Schematic cross-section view of the AmBe source. Detection of scintillation light emitted by the gamma in the BGO with the SiPMs provides the tag for the neutron emission. Figure based on [225]. Right: Picture of the AmBe source in the housing.

context, both the total charge spectrum and the individual charge responses of the single PMTs will be compared. Before conducting these comparisons, the model for de-excitation gamma-ray emission in the scope of neutron capture reactions on natural Gadolinium will be discussed. Since the general implementation within the Geant4 simulation is not overly realistic, an updated model based on dedicated measurements at the ANNRI germanium spectrometer located at the J-PARC accelerator facility in Japan will be discussed in the next paragraph.

### ANNRI Gadolinium de-excitation model

Natural Gadolinium is composed of multiple isotopes in the atomic mass range between  $A_{\min, \text{Gd}} = 152$  and  $A_{\max, \text{Gd}} = 160$ . Out of these isotopes, the relevant ones for neutron capture experiments are  $^{155}\text{Gd}$  and  $^{157}\text{Gd}$ , with cross-sections of  $\sigma(^{155}\text{Gd}) = 60.9 \cdot 10^3 \text{b}$  and  $\sigma(^{157}\text{Gd}) = 254 \cdot 10^3 \text{b}$  [226]. After capturing a neutron, the Gadolinium nuclei end up in excited states with subsequent gamma emission [226, 227, 228, 229]:



This de-excitation process can involve either one gamma or multiple gammas, depending on the exact energy levels involved in the de-excitation process. While a detailed model of the gamma multiplicities and individual de-excitation energies is not necessary in the case of Gd-loaded scintillator detectors due to their calorimetric energy detection capabilities, it is much more important in the case of Gd-doped water Cherenkov detectors such as ANNIE or Super-K-Gd. Depending on the exact number of photons and their energies, some of the light is potentially lost if Compton scattered electrons fall below the Cherenkov threshold. Due to the importance of better models, a lot of effort has been concentrated

since then on understanding the emission profile of gamma rays from neutron capture on Gadolinium more in detail. The model discussed in the following was developed based on measurements with the ANNRI germanium detector at J-PARC, using a pulsed neutron beam from the Japan Spallation Neutron Source. After developing a first model for the more dominant component of  $^{157}\text{Gd}$  in 2019 [230], a follow-up model was published one year later for the  $^{155}\text{Gd}$  isotope as well as for natural Gadolinium [231]. In the case of ANNIE, the natural Gadolinium model is of primary relevance and was hence implemented based on the public code provided by the ANNRI-Gd collaboration [232] into the ANNIE branch of WCSim.

The ANNRI-Gd model utilizes a combination of a continuum spectrum and a discrete peak model to describe the spectrum of Gd capture gammas. When considering the example of neutron capture on  $^{157}\text{Gd}$ , the nucleus is typically in a *s*-wave neutron capture resonance state of  $^{158}\text{Gd}$  with a corresponding excitation energy of 7.937 MeV [230]. As highlighted in figure 5.34, there exist multiple discrete lower-lying energy levels as well as a Quasicontinuum region, for which the energy levels are almost indistinguishable due to their high density. Since the direct transition from the neutron capture state ( $2^-$ ) to the ground state ( $0^+$ ) is a M2-transition, it is highly suppressed with respect to other possible de-excitation paths [230]. As a consequence, the most likely scenario is a cascade of multiple gammas with an average number of 4 gammas per neutron capture [233]. The left part of the picture shows an exemplary transition via multiple of the Quasicontinuum intermediate states, while the right side of the figure presents the other possibility of directly transitioning into one of the discrete states. While transitions of the former kind will result in the continuum part of the spectrum, the discrete peaks are a result of transitions of the second kind. Based on the measurements, the continuum part seems to be the dominant distribution of the spectrum, with only small fractions of  $(2.78 \pm 0.02)\%$  and  $(6.94 \pm 0.01)\%$  being caused by discrete peaks for the case of  $^{156}\text{Gd}$  and  $^{158}\text{Gd}$ , respectively.

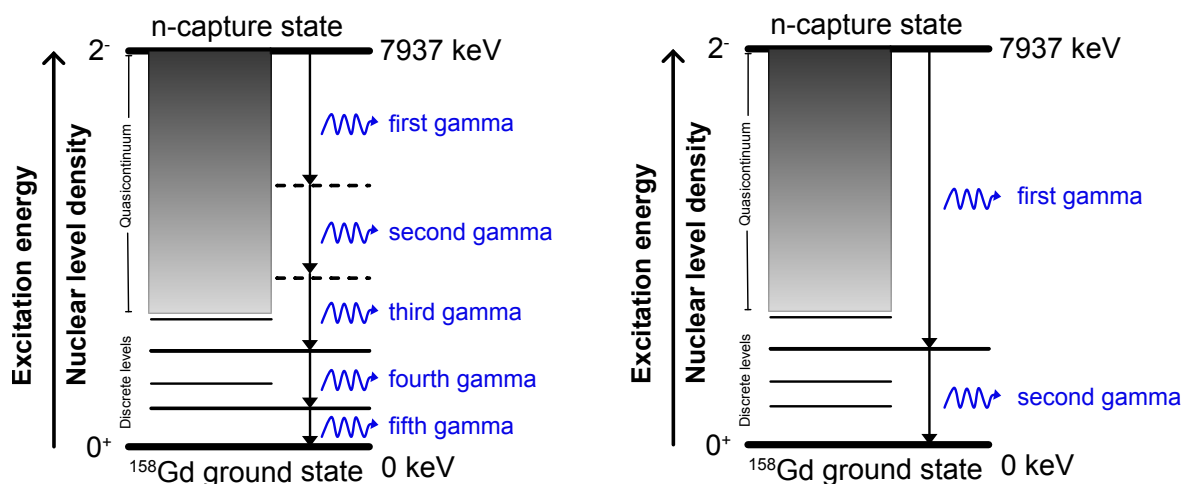


**Figure 5.34:** Possibilities for gamma cascades after neutron captures on  $^{157}\text{Gd}$ . **Left:** Exemplary emission of five gamma rays via multiple intermediate energy levels in the Quasicontinuum spectrum of the gamma emission spectrum. **Right:** Exemplary two-photon emission via a low-lying intermediate state and a very energetic primary gamma-ray. These kind of emissions are responsible for the discrete peaks in the gamma emission spectrum. Figure slightly adapted from [231].

The final performance of the model for natural Gadolinium is evaluated with respect to the agreement of the energy levels between data and the model, as shown in figure 5.35 on the left. While small differences are visible, the developed model seems to represent the data very well. The implementation of the presented model in the scope of ANNIE therefore seems to be well justified in order to achieve a realistic implementation of the Gadolinium capture processes in our simulation. The plot on the right of figure 5.35 provides additional information about the energy spectra of the individual photons, indicating that the earlier photons are more likely to carry more of the accessible energy than later gammas.

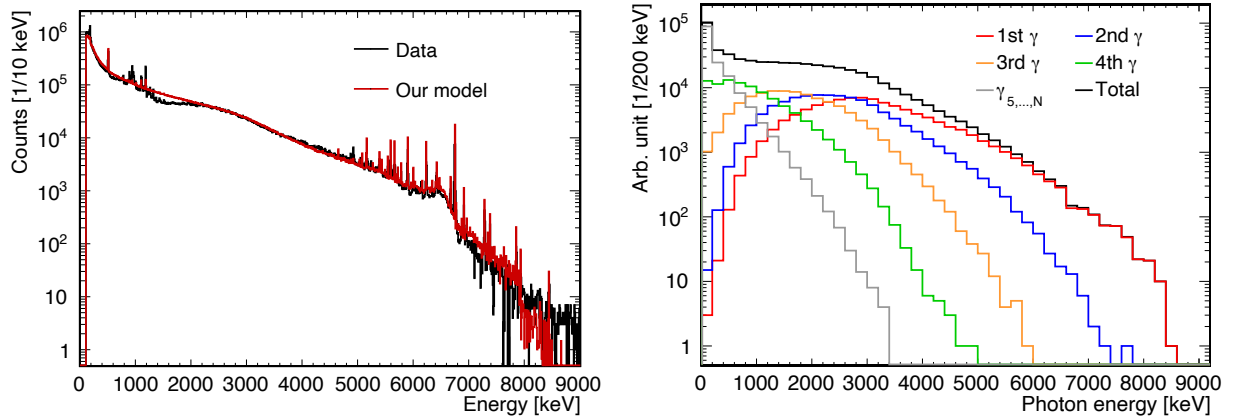


**Figure 5.35:** **Left:** ANNRI-Gd model (*red*) and data (*black*) for natural Gadolinium [231]. Overall, very good agreement is achieved between the data and the ANNRI-Gd model. **Right:** The energy distribution of the first, second, ... ,  $n^{\text{th}}$  emitted photon within the ANNRI-Gd model [231].

## Selection cuts

For achieving a relatively pure selection of neutron capture events within the recorded AmBe calibration data sample, a variety of cuts is used to ensure that an accompanying gamma-ray tag was observed in the attached BGO crystal. A coincident pulse is required in both of the connected SiPMs, with a maximum time difference of 200 ns between the two pulses. The impact of coincident muons on the triggering is minimized by not allowing a cluster to be detected within the prompt event window. In addition, the maximum recorded charge-value within the event is required to be less than 150 p.e., and background events are rejected by selecting events with a Charge Balance value below 0.4.

Since a closer investigation of the Charge Balance distribution in preliminary simulation studies revealed that a charge-dependent Charge Balance cut might be more suitable to reject backgrounds more efficiently for events with higher charges, an additional constraint was deduced for the Charge Balance parameter as a function of the total detected charge within an event. Figure 5.36 shows the Charge Balance value as a function of the total detected charge value for simulated neutron capture events in ANNIE. A clearly pronounced shape is visible that tends to lower Charge Balance values for higher total charge values. A similar main distribution can be observed for the data, shown on the right side of the same figure. In the case of data, a lot more points exist next to this main distribution, extending up to total detected charge values of 500 p.e. or more. A rather clean selection of the main distribution (without any major losses in the simulation case) seems to be

achieved by introducing the charge-dependent Charge Balance cut

$$CB(q) < 0.5 - \frac{q}{300} \quad (5.13)$$

in addition to the overall Charge Balance cut  $CB < 0.4$ . This additional cut is highlighted as a red curve in the figure and will be applied both for data and for the simulation in the scope of the charge spectrum comparisons presented in the next paragraph.

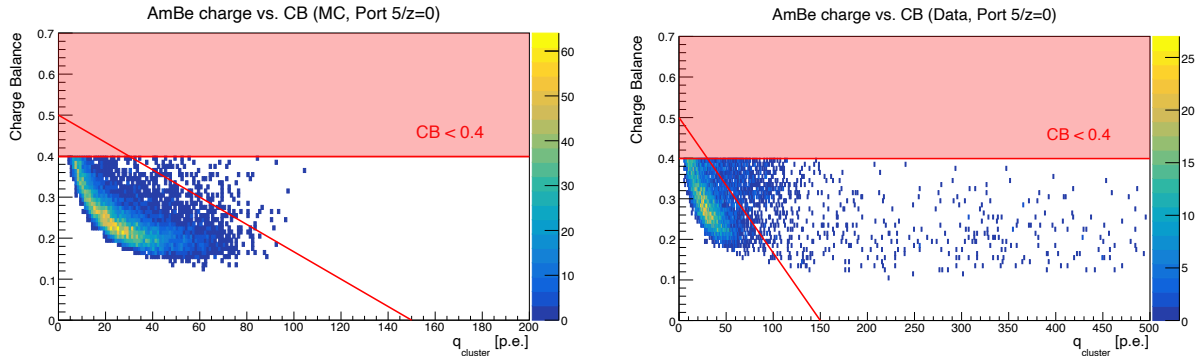


**Figure 5.36:** Charge Balance distributions as a function of the total detected charge within an event. The distribution is shown for the central position (port 5,  $z=0$ ) for the simulation case (*left*) and the data case (*right*). The red line indicates the charge-dependent Charge Balance cut in addition to the more general cut of  $CB < 0.4$ .

### Neutron capture charge spectra agreement

The resulting total charge spectra for the neutron captures are compared between the AmBe calibration data and the simulated neutron capture data with the determined PMT-wise Q.E. ratio factors at the same positions for all five ports. Figure 5.37 exemplarily shows the charge spectra comparison for the five different height positions for port 3. The charge distributions agree quite nicely between the data and simulation in this case for all heights ( $z = -100$  cm,  $z = -50$  cm,  $z = 0$  cm,  $z = 50$  cm and  $z = 100$  cm). Both the peak position and the width of the distribution are represented well within the simulation. While similarly good agreements are observed for ports 1, 2, and 4, port 5 shows slightly worse agreement, as highlighted in figure 5.38. In this case, the width of the simulated distribution is a little smaller than for the charge spectrum from the calibration data. However, the peak position is modeled with sufficient accuracy, and overall the agreement is still acceptable. The neutron capture process is hence well represented in the scope of the ANNRI-Gd model implementation within `WCSim` for neutron captures throughout the whole detector volume of ANNIE.

Verifying the reliability of the implementation for the neutron capture process within the simulation is of utmost importance for obtaining the same conditions as in the real data. After using the same selection cuts, the reconstructed number of neutrons in the simulation sample can directly be compared to the reconstructed number of neutrons in the beam data sample. Selection inefficiencies by the clustering algorithm or low-energetic photons should be fully included in the Monte Carlo simulation in this case. Such a forward-folded analysis approach provides a relatively simple way of validating the neutron production in neutrino event generators and hadronic interaction models by comparing the final number of detected neutrons within the experiment.

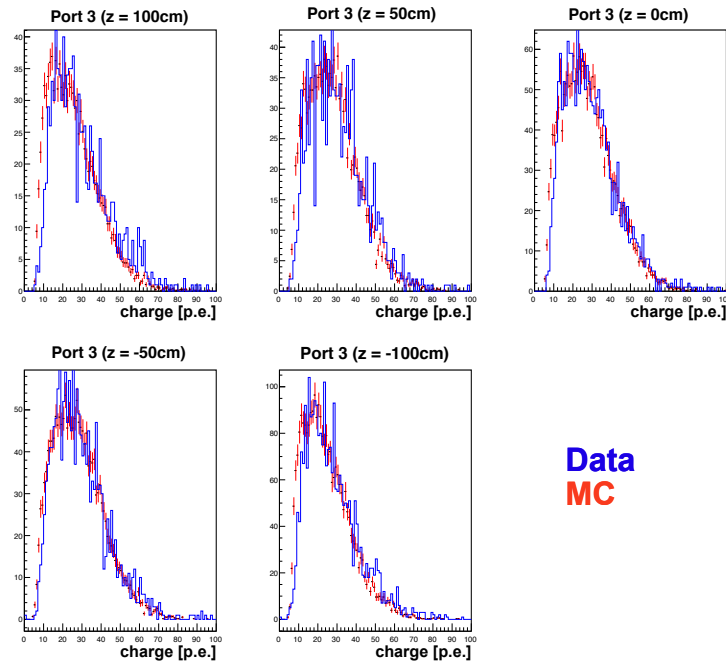


**Figure 5.37:** Charge spectra for neutron captures at the five different positioning heights ( $z = -100$  cm,  $z = -50$  cm,  $z = 0$  cm,  $z = 50$  cm, and  $z = 100$  cm) for port 3. Data spectra are shown in blue, while the simulated distributions are depicted in red. Good agreement is observed for all heights.

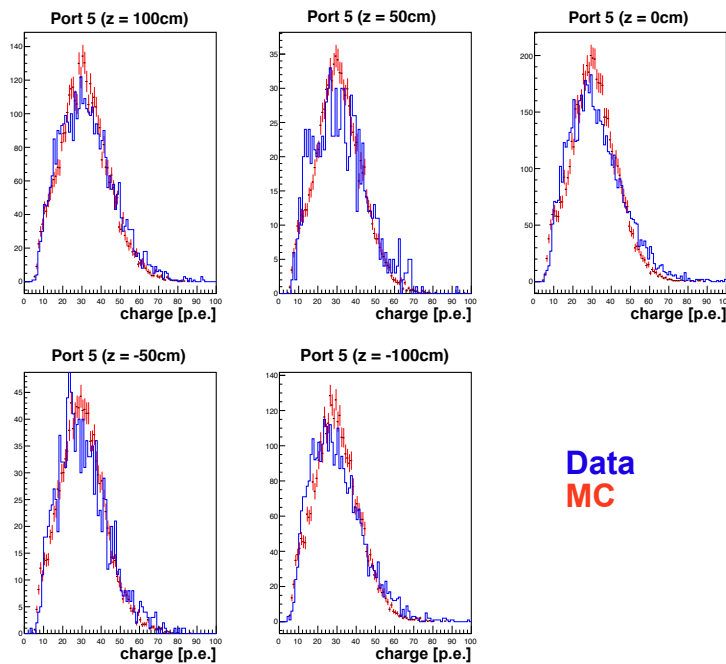


**Figure 5.38:** Charge spectra for neutron captures at the five different positioning heights ( $z = -100$  cm,  $z = -50$  cm,  $z = 0$  cm,  $z = 50$  cm, and  $z = 100$  cm) for port 5. Data spectra are shown in blue, while the simulated distributions are depicted in red. Some discrepancies are visible between the calibration data and the simulated data sample, however the agreement is still reasonable.

#### 5.4.4 VALIDATION OF TUNING CAMPAIGN

The different tuning parameter configurations that were explored in the previous paragraphs are compared in this small summary section with respect to how well they reproduce the different data sample distributions of through-going muons, Michel electrons and AmBe neutrons. Since some of the later tuning configurations were specifically derived from the through-going muon data sample, the two samples of Michel electrons and AmBe neutrons will be the main comparison samples in the context of this validation. The different tuning parameter configurations that are considered are the following:

- *Untuned*: The untuned configuration contains the original WCSim detector geometry with no holders, no Q.E. scaling factor ( $r_{\text{QE}} = 1.00$ ), and a rather low reflectivity of the teflon-wrapped Inner Structure ( $R_{\text{InnerStr}} = 0.55$ ).
- *Global Q.E. ratio*: This tuning parameter configuration contains the updated ANNIE geometry with holders, a global Q.E. scaling factor for all PMTs ( $r_{\text{QE}} = 1.20$ ), and more reasonable reflectivity values ( $R_{\text{OnnerStr}} = 1.00$ ,  $R_{\text{ANNIE-Holder}} = 0.90$ ,  $R_{\text{Other-Holder}} = 0.70$ ).
- *PMT-type Q.E. ratios*: This configuration is very similar to the *Global Q.E. ratio* configuration, but contains separate Q.E. ratio factors for ANNIE-type PMTs and all other PMTs ( $r_{\text{QE,ANNIE}} = 1.40$ ,  $r_{\text{QE,Other}} = 1.00$ ).
- *Individual Q.E. ratios*: Individual Q.E. ratios are assigned to every single PMT in ANNIE based on the observations in the through-going muon sample. The ratio of average charges in the simulation and the data  $R_{\text{average}} = \frac{\bar{q}_{\text{data}}}{\bar{q}_{\text{MC}}}$  is calculated separately for every PMT and used as a correction factor for the simulated Q.E. values of the individual PMTs.

The first metric for evaluating the agreement of the different tuning configurations relies on comparing the total charge spectra observed in the different data sets. While there is only one spectrum in the case of the Michel electron data set, the  $\chi^2$ -value is averaged over the four different spectra (featuring  $Q_{\text{total}}$ ,  $Q_{\text{down}}$ ,  $Q_{\text{up}}$ , and  $Q_{\text{up}}/Q_{\text{down}}$ ) in the case of the through-going muon sample. In a similar fashion, the mean agreement value is calculated for the multitude of spectra (including all the ports and the various source heights within the ports) for the AmBe neutron calibration case. The resulting  $\chi^2/\text{n.d.f.}$ -values are shown in table 5.2.

Tuning configuration	$\frac{\chi^2}{\text{n.d.f.}}$ (Throughgoing)	$\frac{\chi^2}{\text{n.d.f.}}$ (Michel)	$\frac{\chi^2}{\text{n.d.f.}}$ (AmBe)
Untuned	17.97	47.86	23.82
Global Q.E. Ratio	1.62	1.57	2.15
PMT-type Q.E. Ratio	1.11	3.00	3.39
Individual Q.E. Ratio	0.95	1.05	2.12

**Table 5.2:**  $\chi^2$ -values of the data/MC agreement for the different data samples of through-going muons, Michel electrons, and AmBe neutrons. The agreement is depicted for different configurations of the simulation, ranging from an untuned version over a global Q.E. ratio up to individual Q.E. calibration factors.

The general necessity of Q.E. scaling factors for a reasonable depiction of the detector in the simulation framework is exemplified by the very poor  $\chi^2$ -agreement values across all data sets for the untuned simulation framework. All three tuning configurations that were explored in the previous sections show a significant improvement compared to the untuned case. However, there are some differences between the three configurations. While the optimization with two PMT-type dependent scaling factors shows a really good agreement for the through-going muons ( $\chi^2/\text{n.d.f.}=1.11$ ), both the Michel electron and AmBe data sets are modeled worse compared to the configuration with only one global Q.E. ratio factor. Both the global Q.E. and the individual scaling factors show rather good agreements for the Michel and AmBe samples. Between the two configurations, the individual PMT scaling factors seem to result in a slightly better agreement, with  $\chi^2/\text{n.d.f.}$ -values of 1.05 (Michel) and 2.12 (AmBe).

Besides the total charge spectrum agreement, a correct modeling of the photosensor charge response is also vital on a PMT-by-PMT basis. Slightly different properties of the phototubes might not influence the charge values summed over all PMTs, but are indeed important to model the event signatures as closely as possible on an event-by-event basis. This is particularly important if properties like an event display representation of events are used to classify events, for example in the context of a Convolutional Neural Network approach.

The modeling of the individual PMT responses is investigated by comparing the average charge values registered by each photosensor between data and MC. For each PMT, the ratio  $R_{\text{charge}}$  of charge detected in the simulation versus data is computed as  $R_{\text{charge}} = \bar{q}_{\text{MC}}/\bar{q}_{\text{data}}$  and filled into a histogram. The mean and standard deviation values of this charge ratio distribution are then evaluated as an indicator for the correct representation of individual charge responses. Ideally, the mean of the ratio distribution would be at 1.00 and the distribution would feature a very small spread. Table 5.3 provides an overview of these properties for the different tuning configurations and data samples.

Tuning configuration	$\mu(\sigma)$ (Throughgoing)	$\mu(\sigma)$ (Michel)	$\mu(\sigma)$ (AmBe)
Untuned	0.67 (0.28)	0.82 (0.14)	0.72 (0.33)
Global Q.E. Ratio	1.00 (0.28)	0.96 (0.16)	0.99 (0.36)
PMT-type Q.E. Ratio	0.95 (0.25)	0.94 (0.15)	0.93 (0.31)
Individual Q.E. Ratio	0.96 (0.15)	0.96 (0.16)	0.95 (0.26)

**Table 5.3:** Mean values ( $\mu$ ) and standard deviations ( $\sigma$ ) are shown for the distributions of the charge ratio factors  $R_{\text{charge}} = \frac{\bar{q}_{\text{MC}}}{\bar{q}_{\text{data}}}$ . The tuning configuration with individual PMT Q.E. tuning factors features the smallest spread of the charge ratio distribution in the through-going muon and AmBe data samples, while the spread in the Michel sample is also reasonably small.

The untuned tuning configuration again highlights the fact that the PMTs do not register enough light without upscaling the Quantum Efficiency values. All three tuning configurations show reasonable mean values around 1 across all data sets. The standard deviations of the charge ratio distributions stay rather constant for the Michel electron sample, while becoming smallest for the individual Q.E. ratio tuning scenario in the case of the other samples. While this is not surprising for the through-going muon sample, the improvement in the case of the AmBe sample verifies that the determined Q.E. scaling factors are able to

better model the individual PMT response also in an independent data sample. The rather constant standard deviations observed in the case of the Michel electrons can potentially be explained by event topologies of the included events. While data events were selected specifically from decaying muons in downstream direction, the electrons in the simulation were sampled uniformly across the detector volume. The individual PMT charge responses might hence not be reproduced exactly due to slightly different vertex distributions in the two cases.

While both the configuration with a global Q.E. scaling factor and the implementation with individual PMT effective Q.E. values seem to reproduce the data distributions reasonably well, the slightly better  $\chi^2$ -values and individual charge response characteristics favor the implementation with individual charge responses for future simulation studies. This configuration will hence be mainly used for the simulations presented in the upcoming chapters of the thesis.

The agreement of the AmBe spectra for the implementation with this configuration of individual scaling factors was already shown in the preceding section 5.4.3 for the case of the AmBe campaign. Additional figures depicting the agreement for the other ports can be found in the appendix in section C. The resulting spectrum for the Michel electron campaign in the same final tuning configuration is shown in figure 5.39. While some differences are visible between the data and the MC spectrum, the general agreement seems to be reasonably good, as expected from the determined  $\chi^2$ -values earlier.

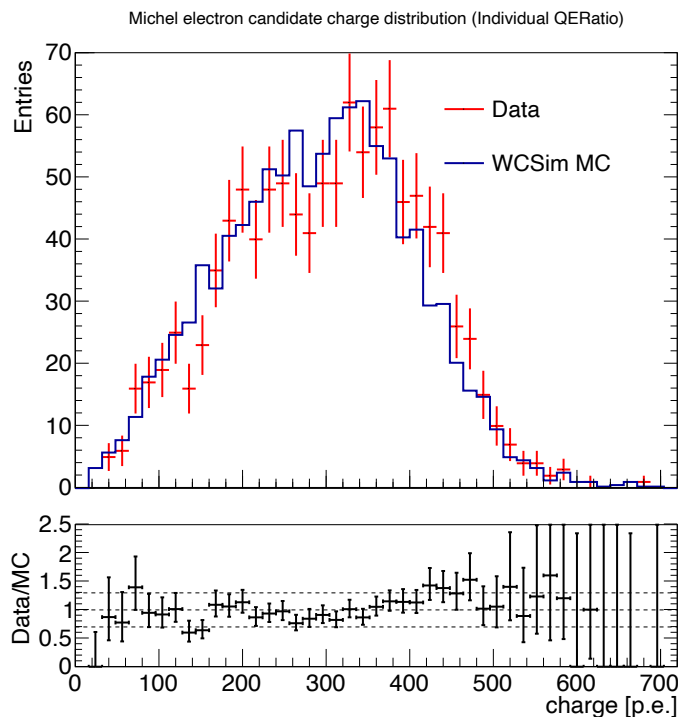


**Figure 5.39:** Michel electron spectrum comparison for the WCSim tuning configuration with individual Q.E. ratio factors. The data spectrum is shown in red, while the Monte Carlo simulation spectrum is depicted in blue.

## 5.5 VALIDATION OF THE MRD IMPLEMENTATION

The detector response of the MRD can be validated in a similar fashion to the tank PMTs by comparing two equivalent data sets in the data and the simulation. For this purpose, a beam neutrino data set is selected in the data by specifically looking for beam triggers that feature a coincident tank and MRD cluster, while requiring that there was no coincident FMV hit. These events are then compared with simulated neutrino interactions in the water (generated with GENIE) that resulted in a charged muon that reached the MRD after being propagated in WCSim.

The MRD track reconstruction algorithm presented in chapter 3.2.2 is used to reconstruct muons in both the data and the simulation neutrino candidate data sample. Among the reconstructed variables, there is the start and end position of each track, the total track length and the energy that was dissipated in the MRD. The more detailed start and end positions can be used to select more specific event topologies, such as muons that exit the MRD on one of the sides, muons that stop in the MRD and muons that go through the entirety of the MRD and leave it again. It should be noted that the reconstruction can not distinguish between muons that are stopped in the last MRD layer and actual through-going muons and will hence label both event categories as through-going muons.

The start and stop positions of the tracks can also be used to define two track angles: A vertical angle representing the track angle in a side view projection, as well as a horizontal angle that describes the angular dependence of muon tracks in a projected top view. Figure 5.40 shows both the vertical and horizontal angle distributions for data and MC for the beam neutrino data sample. The peaks that are visible are artifacts of the reconstruction due to the granularity of the paddles.

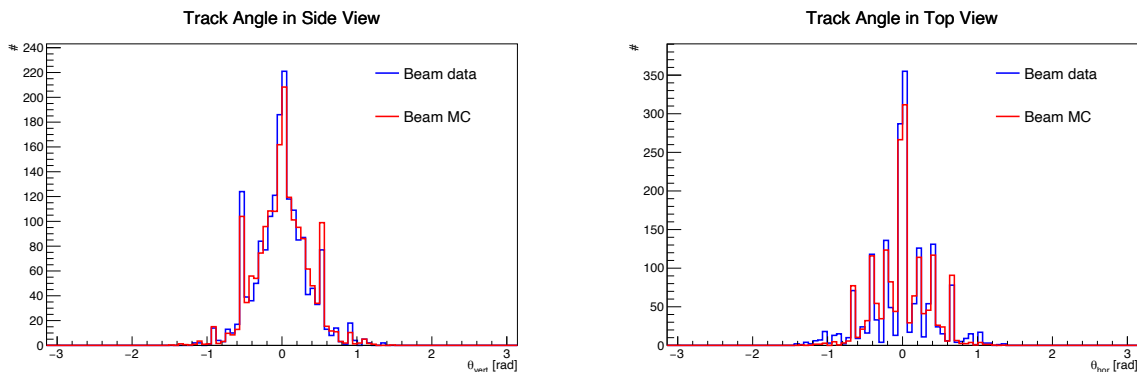


**Figure 5.40:** Reconstructed MRD track parameter distributions for data (*blue*) and MC (*red*) in beam neutrino data samples. The left figure shows the distribution of the side angle, while the right image shows the top angle distribution. The data distribution features more events at larger angles, indicating that some background event have passed the cuts.

The data and the simulation distribution are very much alike for both angles, indicating that similar events were considered in the data and the MC sample. The side angle distribution looks very similar, with the main difference being a slightly smaller amount of horizontal tracks in the case of the data distribution. Concerning the track angle in the top view projection, one can see that the distribution includes higher angles in its tail for

the data case, indicating that the selection process in the data might have included some dirt muons or cosmic muons in addition to the beam neutrino candidates.

Since the MRD is of particular importance for events with a stopped muon, the properties of those events are investigated in more detail in the following. Figure 5.41 shows the reconstructed MRD energy loss distribution for events with a stopping muon. While the general shape of the distributions looks similar in the simulation and the data samples, there are some differences that must be addressed. Larger energy losses seem to be favored in the data compared to MC, with energy losses around 600 MeV being particularly prominent. At the same time, smaller energy losses around 400 MeV seem to be underrepresented in the data.

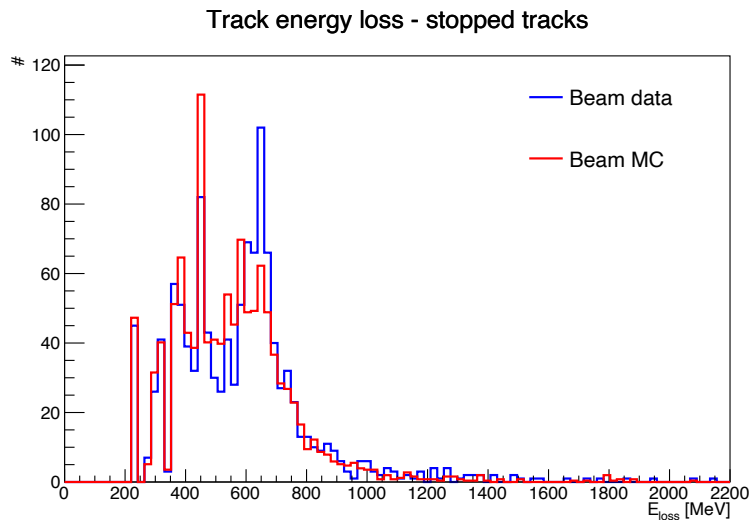


**Figure 5.41:** Reconstructed MRD energy loss distributions for data (*blue*) and MC (*red*) in beam neutrino data samples with a stopping muon track in the MRD.

The observed discrepancies between the reconstructed MRD track distributions in the data and the simulation can most likely be traced back to two main aspects. Firstly, the data might contain some dirt muon events or cosmic muon events that were included due to the small inefficiency of the FMV veto system. Moreover, the dark noise rates in the simulation might have lower rates than in the real data, leading to longer tracks (and consequently larger reconstructed energy losses) induced by additional dark noise hits in the data.

While these differences should be investigated further in the future, the current implementation of the MRD response is deemed acceptable for the moment based on the similarity of the angular distributions and the approximate agreement of the energy loss distribution. Some ongoing studies currently evaluate the potential of additional veto tagging capabilities by making use of more information from the water tank PMTs, especially around the muon entry point in the tank. Employing such an additional software cut to remove additional dirt muon events should reduce the contamination of non-neutrino events in this particular sample. Furthermore, additional studies regarding the dark noise rates will be conducted to evaluate their influence in more detail.

# 6

## ANNIE Phase II neutron multiplicity analysis

---

*“I am afraid neutrons will not be  
of any use to anyone.”*

—Sir James Chadwick

Apart from a measurement of the neutrino cross-section on water, the investigation of the neutron yield in neutrino-nucleus interactions is the main analysis goal of ANNIE in its physics-related data-taking phase II. While the final analysis is envisioned with a detector configuration which includes five deployed LAPPDs, a preliminary analysis with PMT-only data will be presented in the scope of this thesis. This analysis will make use of simplified vertex and energy reconstruction techniques while more sophisticated algorithms are currently being developed [8, 234] and will be applied on the analysis with the final PMT+LAPPD data sample. Furthermore, the current measurement only makes use of a subset of the data acquired during the 2021 beam year.

The chapter will start in section 6.1 with a short overview of the commissioning efforts that were conducted during the 2020 beam year to verify that the ANNIE detector was functioning well and could reliably record beam data. Section 6.2 will provide more details about the considered data taking period for the present analysis, in particular with respect to the covered time frame and the encountered trigger rates and data properties. The subsequent section 6.3 will cover the properties of the leptonic part of the considered beam event in terms of general neutrino selection cuts, muon track reconstruction in the MRD, and associated results of the simplified vertex and energy reconstruction techniques. Section 6.4 will then present the properties of neutron candidates in the same beam events before section 6.5 will eventually highlight the neutron properties as a function of the lepton kinematics, combining the information from the prompt and delayed activity observed in the tank. The last section 6.6 will provide a brief outlook on the various systematic uncertainties of the neutron yield measurement and outline how they will be determined in greater detail in the future.

## 6.1 COMMISSIONING OF THE DETECTOR

Phase II of ANNIE started at the beginning of 2020 in the scope of dedicated commissioning runs which were designed to verify the triggering scheme, beam data taking abilities and general readout capabilities of the detector. A reduced experimental configuration with only PMTs and no LAPPDs in the water tank was used for these runs, with the muon systems MRD and FMV also being operational. After the commissioning was concluded, the subsequent beam year in 2021 was used to acquire more beam neutrino data in the same detector configuration and conduct a preliminary analysis of the neutron multiplicity measurement within this reduced PMT-only detector setup.

The current section will briefly present an overview of the results for the commissioning phase of ANNIE, particularly with respect to the beam data taking abilities of the detector, the timing alignment of the subsystems, and event displays for various event types as a visual check of the detector performance.

### 6.1.1 DETECTING THE BEAM SPILL WINDOW WITH ANNIE

One important aspect of the commissioning phase was the verification of the trigger system's ability to reliably detect beam events that are sent to the detector. Since the beam trigger will be issued based on accelerator signals which arrive directly before the arrival of the respective spill, the beam events should always be present in the same time region within the acquisition window. The  $1.6 \mu\text{s}$  beam spill window composed of 84 individual bunches should hence correspond to a time window in the data with more activity in the tank in case the trigger scheme works reliably.

This was tested by investigating the time distribution of so-called tank PMT clusters, which are defined as coincident activity of multiple PMTs in a short pre-defined time window. Current standard cuts require a minimum of 5 PMT hits in a time window of 50 ns for the formation of a cluster. For each such cluster, the hit time values of the individual involved PMTs were inserted into a timing histogram. Each beam trigger will record an acquisition window of  $2 \mu\text{s}$  – if implemented correctly, the  $1.6 \mu\text{s}$  window should be fully contained and visible within this event window.

As shown in figure 6.1 for the exemplary commissioning run 1634, the obtained cluster time distribution shows a clear elevated structure with a width of  $1.6 \mu\text{s}$  in the center of the acquisition window. This enhanced cluster rate corresponds to the presence of the beam spill in the data, verifying that the trigger scheme works as expected. Additional PMT hits which are present before and after the beam spill region correspond to beam-uncorrelated background events. The fact that the beam spill window is located in the middle of the acquisition window ensures that neither the start nor the end of the beam spill is accidentally missed by the data acquisition. As a consequence, the ANNIE DAQ is able to record the signals from all neutrinos in the BNB, independently of their position within the beam spill.

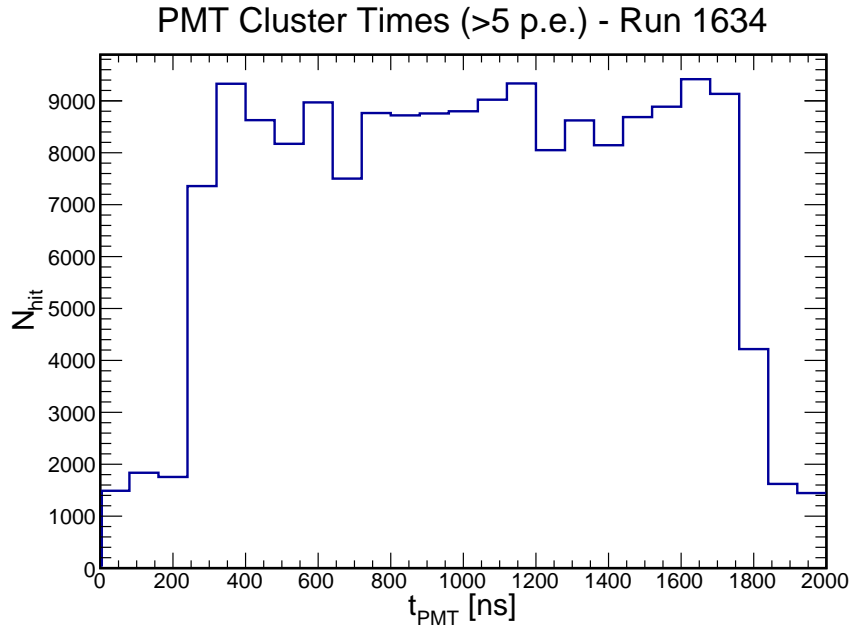


**Figure 6.1:** Time distribution of clustered ANNIE PMT hits for beam run 1634. An elevated region with a width of  $\Delta t \approx 1.6 \mu s$  is clearly apparent in the time window from  $\approx 200$  ns up to  $\approx 1800$  ns, indicating that beam spills are successfully captured in the middle of the  $2 \mu s$  long acquisition windows.

### 6.1.2 SUBSYSTEM TIMING ALIGNMENT

In addition to the verification of the beam taking abilities with the tank PMTs, a further commissioning goal included the timing alignment of the subdetectors which are present in ANNIE. Since every subsystem records its data in an independent data stream (compare chapter 3 for details), this calibration is of vital importance to make sure the same event is actually recorded in all single subdetectors. The timing alignment of the MRD and the tank PMTs was investigated by comparing the cluster hit times in both systems. Similarly to the water PMTs, clusters in the MRD require a certain number of scintillator paddles to fire in a pre-defined time window. Standard cuts for the formation of a MRD cluster impose a minimum of 3 MRD paddle hits in a time frame of 30 ns. The rather low minimum number of hits ensures the possibility to also consider very short tracks that for instance only cover the first two layers of the MRD in case of low-energetic muons.

Figure 6.2 presents the observed relation between cluster times in the water tank PMTs and the MRD paddles for the exemplary commissioning run 1634 both in a two-dimensional view and a one-dimensional time difference distribution. A pronounced distribution of linearly related hit times is visible and indicates the presence of correlated activity in both subsystems which can be traced back to the same physics event. The same behavior can be observed when investigating the hit time differences for tank and MRD clusters: As presented on the right side of the same figure, a clear peak is present at around  $\Delta t = 750$  ns, representative of the timing offset between the two subsystems, induced by trigger settings and cable delays. Events which contain a pair of MRD and PMT clusters and exhibit a time difference around this determined value can be considered to represent the same physics event. In such a case, the event contained a particle that traversed both the water tank and the MRD to some extent and left a detectable signal in both subdetectors. The existence

of such a constant time offset independent of the exact position within the acquisition window indicates that the MRD and tank PMT subsystems are aligned properly and are able to record data from the same physics events reliably.

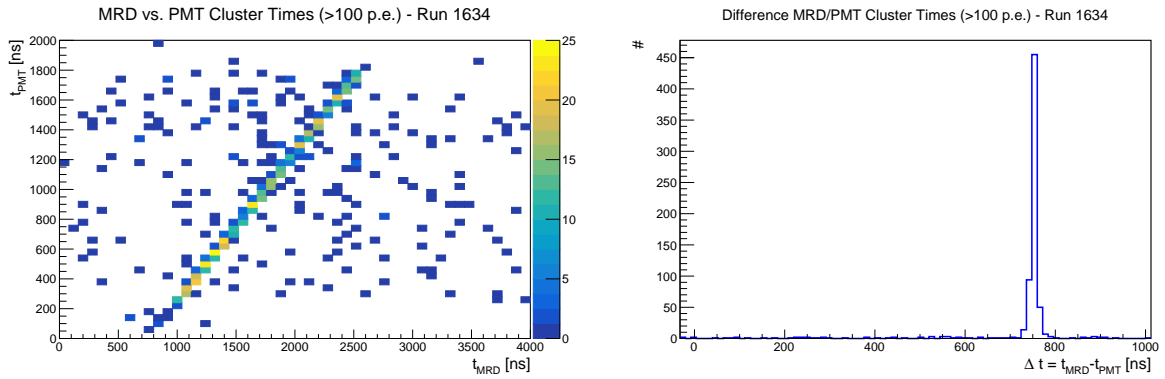


**Figure 6.2:** **Left:** Two-dimensional correlation plot of the tank PMT cluster time versus the MRD cluster time for tank clusters with a minimum charge of 100 photoelectrons. In addition to random associations of noise clusters, a clear linear correlation is visible for actual coincident physics events. **Right:** Time difference distribution of MRD and tank PMT cluster times with a minimum charge of 100 photoelectrons. A clear prominent peak of coincident events is present around  $\Delta t \approx 750$  ns.

The last subsystem of ANNIE is the Front Muon Veto (FMV). Also for this subdetector, the recorded data should be aligned in time with the other systems. Figure 6.3 shows the time difference of the FMV hits with respect to the tank PMT hits and with respect to the MRD cluster hits for the same exemplary commissioning run 1634. In both cases, pronounced peak structures are apparent around  $\Delta t_{FMV,PMT} \approx 800$  ns and  $\Delta t_{MRD,FMV} \approx 50$  ns, indicative of coincident activity in the respectively considered subsystems. The FMV data is hence also correctly aligned with respect to the other subsystems after considering the determined hardware-related timing offsets  $\Delta t_{FMV,PMT}$  and  $\Delta t_{MRD,FMV}$  that were mentioned above. Overall speaking, the verified time alignment of all three detectors (water tank, MRD, FMV) enables the simultaneous detection of physics events across all subsystems and confirms that the trigger signal distribution to all detectors is working as expected.

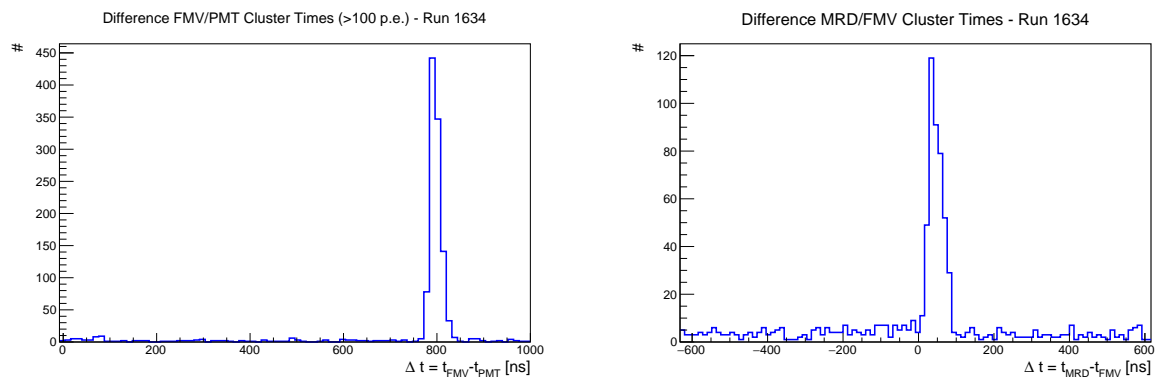


**Figure 6.3:** **Left:** Time difference distribution of hits in the water tank PMTs and the FMV scintillator layers for events with a minimum charge of 100 p.e. in the water tank. A clear peak of coincident activity is visible at  $\Delta t \approx 800$  ns. **Right:** Time difference distribution of MRD and FMV paddle hit times. A clear peak of correlated activity is present for  $\Delta t \approx 50$  ns.

### 6.1.3 EVENT DISPLAYS OF DIFFERENT EVENT TYPES

It is customary to visually represent physics events in Water Cherenkov detectors in the form of so-called *event displays* which typically depict color-encoded charge or timing information of the corresponding photodetectors. The cylindrical detector surface is rolled open to provide a two-dimensional representation in such a way that the mantle is shown in the center of the event display and the top and bottom lids are attached above and below this central region. The Cherenkov light cone emitted during the passage of ultra-relativistic charged particles in the target medium will lead to a detectable Cherenkov ring or disk structure on the inner detector surface which will be visible as a prominent pattern in the event display.

The current section will present exemplary event displays for a variety of physics event categories, particularly neutrino candidates, cosmic events, and neutron candidates. The most interesting neutrino candidates in terms of the analysis will contain a corresponding muon track in the MRD since it is only possible to reliably reconstruct the muon energy for those types of events. As a consequence, only neutrino candidates with such an associated track are shown in the following paragraph. Cosmic events are triggered by a self-trigger mechanism of the MRD and require coincident activity in the first and last layer of this muon detector. They form a background sample which can be used to verify the validity of the detector simulation or to determine the efficiency of the MRD scintillator paddles (compare chapter 4 for details). The event signature of neutron candidates is of primary importance for developing feasible selection cuts for the neutron multiplicity analysis presented later on in this chapter. In contrast to the neutrino candidates and the cosmic particles, the Cherenkov light output in those kinds of events is much smaller and furthermore not characterized by a clean ring or disk pattern but rather a more diffuse photon hit distribution.

#### Neutrino candidates

Event displays of neutrino event candidates provide a visual check of the detector's ability to capture beam events in addition to the tank PMT cluster time distribution presented earlier. Beam neutrino candidate events are expected to traverse the water tank in downstream direction and hence leave a Cherenkov disk imprint on the downstream inner wall of the water tank. In order to only consider likely muon neutrino particles, events with coincident tank and MRD clusters are specifically selected in accordance with the expected hardware-related timing offset between the two systems:

$$700 \text{ ns} < \Delta t_{\text{MRD,PMT}} < 800 \text{ ns}. \quad (6.1)$$

In addition, none of the veto scintillator paddles is allowed to fire within a time offset window of

$$750 \text{ ns} < \Delta t_{\text{FMV,PMT}} < 850 \text{ ns} \quad (6.2)$$

in order to exclude dirt neutrinos from the considered event sample. Figure 6.4 shows a selection of exemplary neutrino candidates after applying the presented event selection cuts. The color-encoded information represents charge values for the tank PMTs (with a lower charge threshold of 30 p.e.) and time values in case of the MRD paddles. In general, the events all feature a very similar event topology with Cherenkov disks detected in the

downstream region of the water tank and aligned tracks in the MRD. However, the sizes and orientations of the Cherenkov disks vary slightly between the events: While both the events on the upper left and the lower right feature a fully through-going muon track in the MRD, the former event passes the detector on the right side compared to a more leftward orientation of the latter one. The events shown on the upper right and the lower left are associated with a stopping muon track in the MRD. In these cases, the muon is only able to pass the first three or four layers of the muon detector. In both instances, the particles are passing the detector pretty centrally but at different heights.

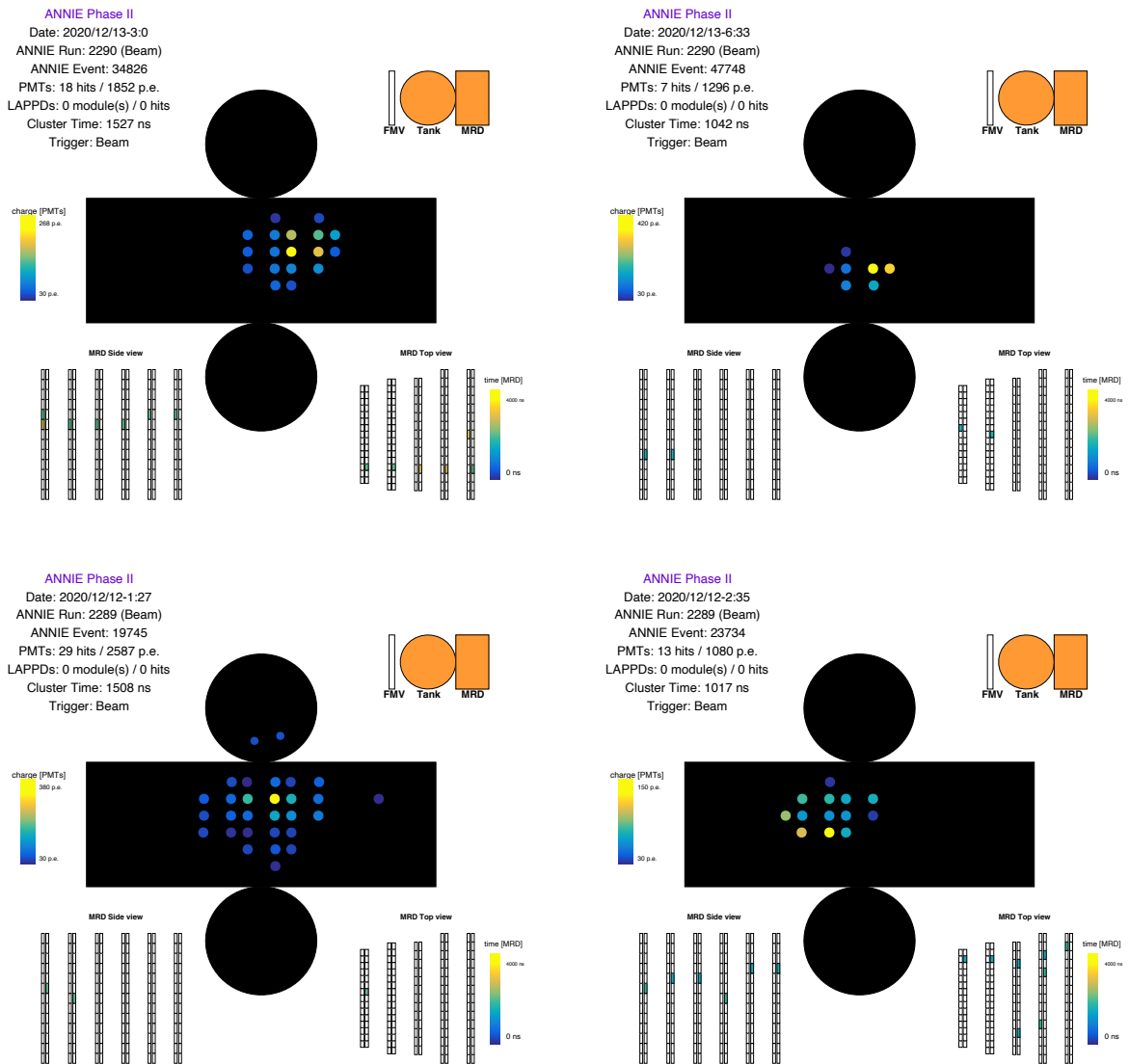


**Figure 6.4:** Event displays for exemplary neutrino event candidates in beam data. **Top left:** Neutrino candidate located on the right side of the tank with a muon track going through the whole MRD. **Top right:** Neutrino candidate oriented in the lower central region of the water tank with a rather short muon track which only passed the first four layers of the MRD. **Bottom left:** Neutrino candidate passing through the top central region of the water tank, with a very short muon track spanning only three layers of the MRD. **Bottom right:** Neutrino candidate located in the top left region of the water tank, featuring a muon track going through the whole MRD.

**Cosmic events**

Atmospheric background particles are constantly produced in shower processes of cosmic radiation in the atmosphere of our Earth. One of the main observable atmospheric backgrounds for neutrino experiments such as ANNIE are cosmic muons since those can travel rather large distances before interacting or decaying due to their minimal ionizing nature and relativistic time dilation effects. ANNIE is able to record samples of cosmic muon candidates with a dedicated hardware-based trigger setup of the MRD: If both the first and last layer of the MRD detect a coincident signal, the cosmic trigger is activated and prompts the data acquisition for both the tank PMT VME system and the MRD CAMAC electronics.

Figure 6.5 depicts an exemplary cosmic event which is characterized by a downward-going track in the MRD passing the experiment in upstream direction. The muon generates a Cherenkov cone which is visible in the bottom mantle and the bottom lid region of the water tank. Only the lowest two PMT rows in the mantle region are illuminated in this case, indicating that the muon was directed at a steep slope and only briefly traversed the water tank.

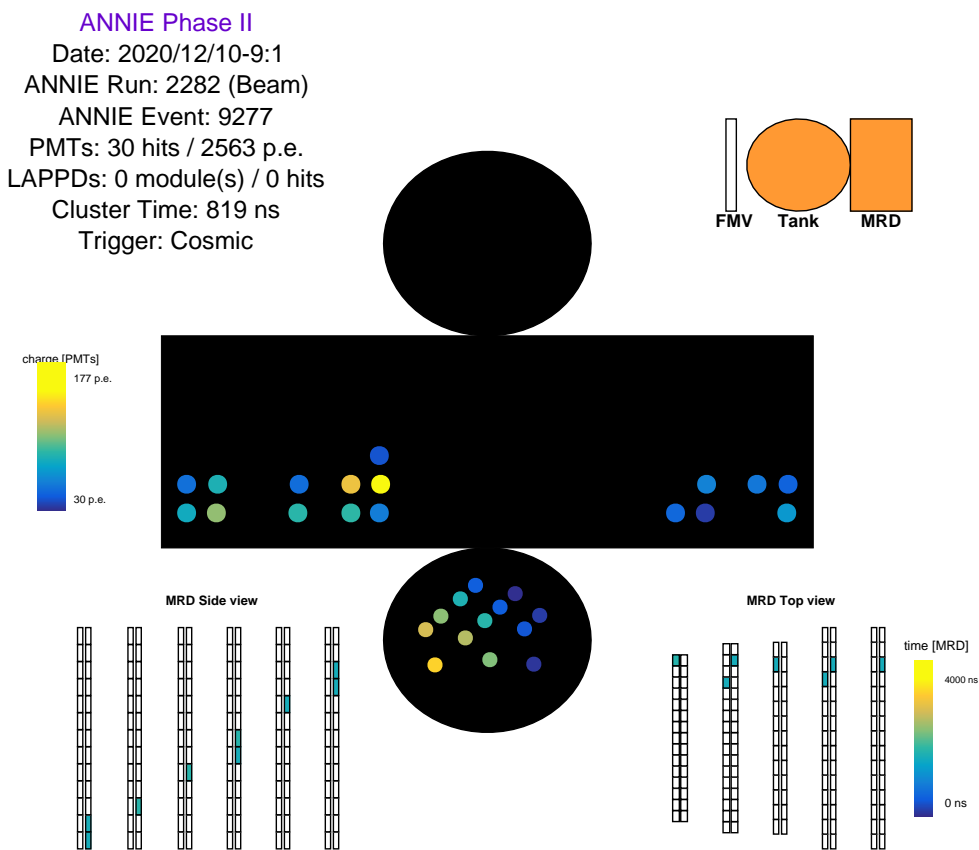


**Figure 6.5:** Event display for an exemplary cosmic event. The muon passes through the MRD from right to left in a downward fashion, illuminating PMTs in the bottom lid region and the lowest two rows of the mantle region in the water tank.

## Neutron candidates

Neutrons will primarily capture on Gadolinium when using a Gd-loaded water target material within the considered experiment, issuing a cascade of typically four to five gammas with a total gamma energy of roughly 8 MeV in the course of the associated de-excitation processes [231]. Only a smaller fraction of events will include captures on hydrogen which are characterized by the emission of a single photon of 2.2 MeV energy that is much more difficult to detect. The Gd-related gammas will be emitted in independent uniformly distributed directions and interact with electrons in the target via Compton scattering. As a consequence, only a fraction of the gamma energy will be visible in the detector. In large water Cherenkov detectors such as Super-Kamiokande-Gd, this typically corresponds to a reduced visible energy value of roughly 5 MeV instead of the 8 MeV of total gamma energy, which was determined in detail by the EGADS experiment [235]. The Cherenkov light emitted by the Compton scattered electrons will thus be very faint and randomly distributed across the whole detector surface.

Figure 6.6 shows two exemplary neutron candidate event displays as observed in a beam neutrino run of ANNIE. In contrast to the previous signatures of neutrino and cosmic events, the event displays feature a much lower charge threshold of 1 p.e. in this case due to the comparatively significantly lower light output in neutron capture events.

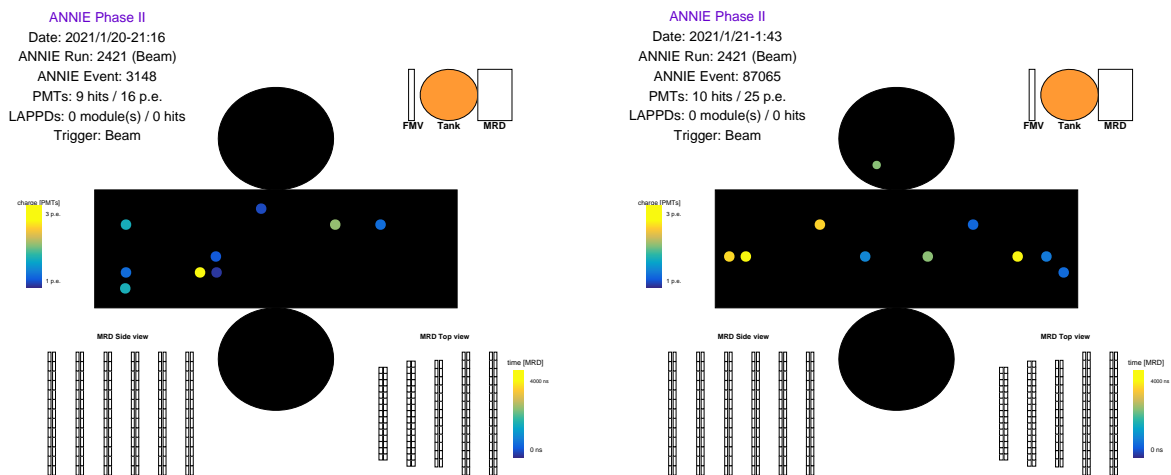


**Figure 6.6:** Event displays for two exemplary neutron candidate events detected in beam interactions. The depicted signatures of very spread out hit distributions with no simultaneous activity in the MRD and the FMV are typical for neutron capture events.

The selection cuts which were used to identify neutron candidates within these data files are presented later in more detail in section 6.4 which covers the analysis of neutron events in delayed windows in beam neutrino data runs. As expected, the patterns observed in the neutron events are rather diffuse and do not feature a single strong Cherenkov pattern as is common for the much more energetic muons and electrons that are produced in beam neutrino interactions. At the same time, the neutrons are contained in the water tank and do not reach neither the FMV nor the MRD.

Based on the shown event signatures alone, one can already conclude that the selection cuts require a combination of a diffuse light pattern and rather low light levels in addition

to no simultaneous activity in one of the muon detectors in order to select neutron capture candidates. While aesthetically less interesting than higher-energetic muons or electrons, the neutron event displays hence also reveal some quite interesting features of the corresponding event signatures.

## 6.2 DATA TAKING OVERVIEW

The data acquisition system of ANNIE is capable of detecting data for a number of different trigger schemes. Most notably and importantly, beam neutrinos will be recorded in dedicated beam runs while other run types are suited to record for instance calibration data in the scope of dedicated LED or AmBe data taking campaigns. While the beam is operating, the majority of the detector uptime is spent acquiring beam runs to fully make use of the available accelerator neutrino statistics. Calibration runs are only performed sparsely in periodic intervals in between other runs to make sure the detector performance did not change over time and the water transparency remained at a high level. The current section will first provide an overview of the different run types that were acquired over the full 2021 beam year and highlight the subset of the data used for the current analysis in subsection 6.2.1 before presenting some general properties of the considered beam runs in terms of trigger rates and the frequency of different event types in subsection 6.2.2.

### 6.2.1 DATA TAKING PERIOD

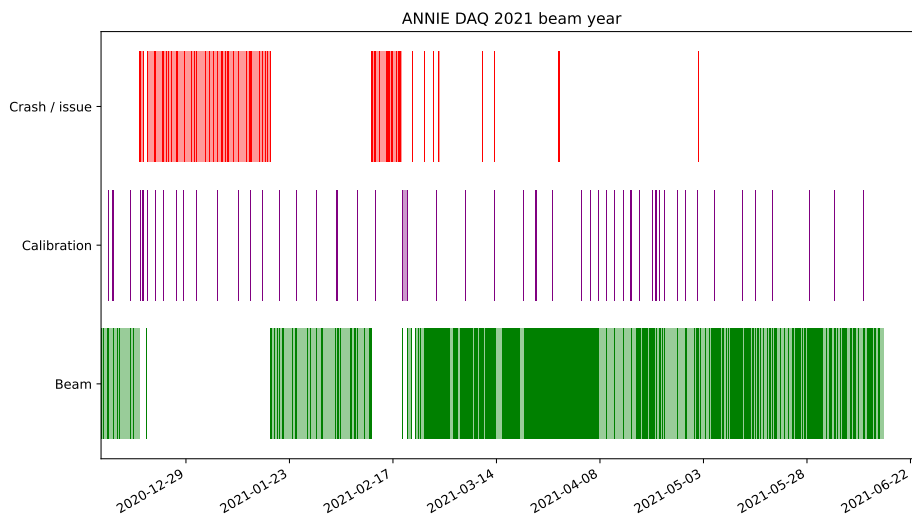


**Figure 6.7:** Overview of the 2021 beam year from in terms of the ANNIE DAQ. The overall time frame is divided into periods of beam (*green*) and calibration (*purple*) runs. A further category is composed of runs that either crashed or featured problems on the hardware side (*red*). Beam runs depicted in a darker shade of green were used in the scope of the presented analysis.

Figure 6.7 presents an overview of all runs acquired by the ANNIE experiment during the 2021 beam year. Beam runs that did not exhibit any issues are shown in green while

beam runs that featured a DAQ-associated crash or hardware-related issues are depicted in red. The latter category of runs are unfortunately not usable for the current analysis: One major common issue that was encountered during those runs were problems with the MRD CAMAC electronics readout which also rendered the veto information from the FMV unreliable and made the identification of dirt events impossible. Most of these problematic runs were recorded before the official start of the data taking campaign during the commissioning phase of ANNIE which lasted until the fourth of February, 2021.

The subsample of all beam runs of the 2021 beam year which were used for the current analysis is shown in a darker shade of green compared to the set of other runs which were not included. In addition to beam runs, calibration runs are shown in purple in the same figure. However, they only correspond to a rather small fraction of the total time of the data taking period in order to maximize the available beam statistics. The largest portion of calibration runs consisted of AmBe neutron calibration runs which were recorded prior to the start of the beam data taking campaign in November 2020. As such, this neutron calibration campaign is not shown in the figure due to its missing interference with the beam data taking operations.

Overall speaking, 21 % of the available events of all adequate beam runs of the 2021 beam year were used in the scope of the analysis which will be presented in the following sections. Further independent checks will be conducted and more sophisticated versions of the reconstruction tools will be finalized before expanding the analysis to the whole available 2021 data sample and reducing the associated statistical errors in the process.

## 6.2.2 TRIGGER RATES & EVENT TYPE FRACTIONS

The overall properties of the considered data runs can be investigated with respect to the encountered trigger rates, the rates of various event topologies, the stability of the subsystem time alignment and the detected charge over the covered time frame. The current section will briefly highlight all of these features and discuss interesting aspects in some more detail.

When investigating the behavior of the trigger rates as shown in figure 6.8, the two most prevalent trigger categories are beam triggers and off-beam triggers which both typically take on values between 3 and 5 Hz. The off-beam trigger rate is correlated to the rate of extractions from the Booster ring which are not sent to the BNB in order to avoid recording off-beam data during actual BNB beam spills. However, since the Booster extraction rate is not directly correlated to the BNB rate, the off-beam trigger rate can vary independently of the actual beam trigger rate. Such autonomous fluctuations are immediately visible in the presented time evolution plot. Furthermore, the off-beam trigger is designed to prevent an overload of the trigger system of ANNIE and limits its acquisition rate in certain scenarios. As a consequence, the corresponding rate is even reduced to a value of 0 Hz in a number of cases such as for runs 2512 and 2578.

When evaluating the behavior of the cosmic trigger in the considered data taking period, a large decrease is visible around run 2570. This decrease can be traced back to deliberate hardware changes in the MRD cosmic trigger setup to reduce the cosmic rate and, in turn, the overall detected rate to improve the stability of the DAQ system. The last category of the

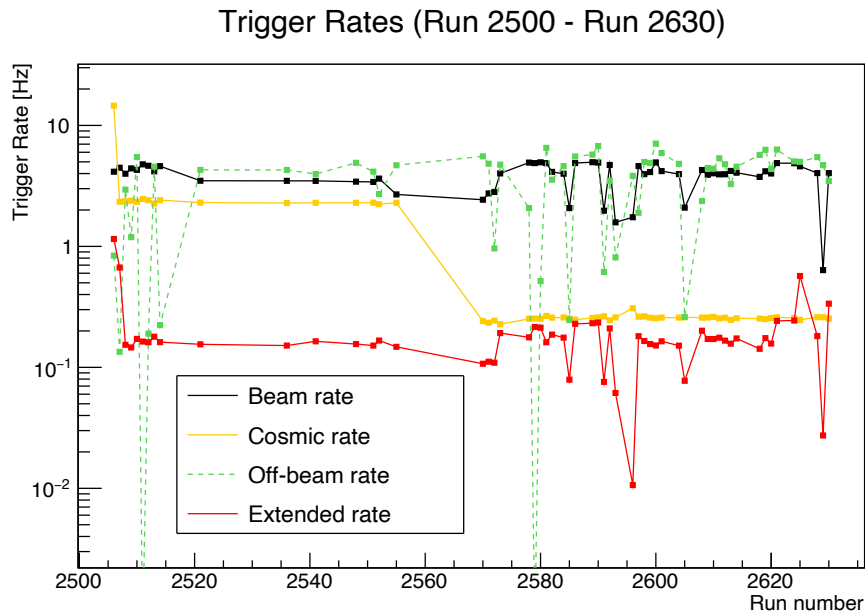


**Figure 6.8:** Trigger rates in ANNIE for the data taking period considered in the analysis, covering the majority of runs between run 2506 and 2630. The rate of beam (*black*), cosmic (*orange*), and off-beam triggers (*green, dashed*) is shown alongside the rate of extended readouts (*red*). The cosmic trigger rate was reduced around run 2570 to stabilize the data taking process. The off-beam trigger is issued depending on the current beam extraction rate. Depending on the exact status of the accelerator signals, it is sometimes set to a value of 0 Hz, as visible for instance in the runs 2512 and 2578.

extended window rate is a subcategory of beam triggers which detected a certain amount of activity in the tank and in turn issued the acquisition of a longer detection window to enable the efficient detection of neutrons for interesting events. These acquisition windows will form the basis for the upcoming neutron multiplicity analysis. Although the rate is much lower, the trend of the extended window trigger rate closely follows the changes in the beam trigger rate.

The rates of events which feature a certain activity in the different subsystems represent another indicator of the stability of the data taking campaign. As presented in figure 6.9, the frequency of events including a PMT cluster is shown alongside the corresponding rates for coincident clusters in the tank and the MRD, or even combined activity in the tank, MRD, and the FMV. Furthermore, coincident tank and MRD clusters without any simultaneous activity in the FMV are shown as a separate category. As expected, reduced rates are observed when requiring more stringent coincidence requirements between different systems. While for instance 0.1 Hz of events feature a tank PMT cluster, the rate of simultaneous tank and MRD clusters will only be around roughly 0.01 Hz. In general, the trends observed in the various cluster categories correspond rather well to the trends in the overall beam trigger rate which is also shown in the same plot, indicating a stable detector performance.

In addition to the beam trigger rate, the PMT cluster rate also depends on the intensity of the beam at any given time. The latter quantity is usually evaluated in units of *protons on target (POT)* describing the number of protons hitting the beam target at any given time. Figure 6.10 shows the trend of the PMT cluster rate in comparison to the POT rate time

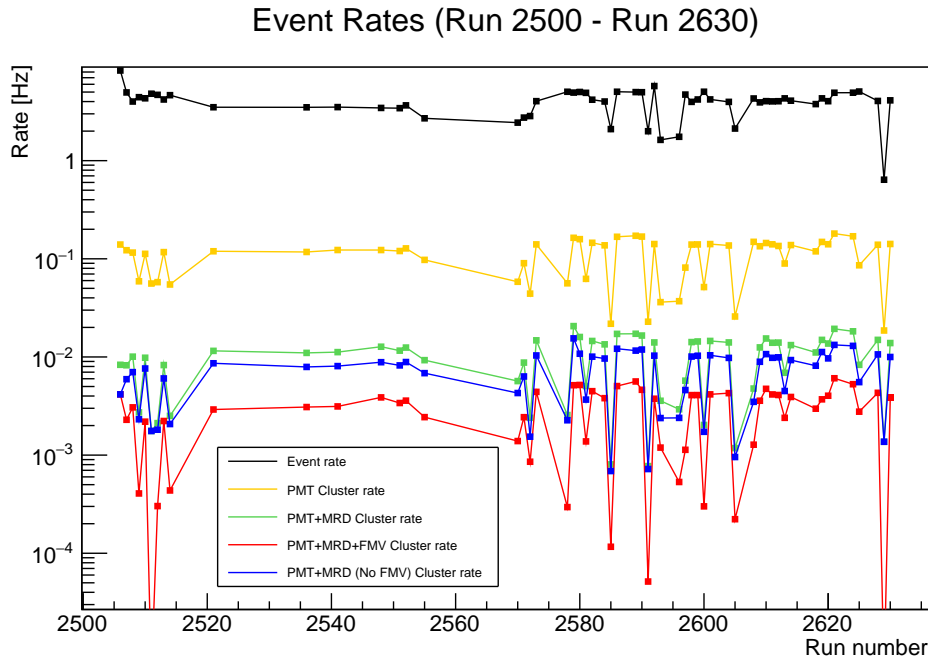


**Figure 6.9:** Event rates in ANNIE for the data taking period considered in the analysis, covering the majority of runs between run 2506 and 2630. The rate of all beam events (*black*), PMT clusters (*orange*), coincident PMT+MRD clusters (*green*), PMT+MRD+FMV coincidences (*blue*), and PMT+MRD+No FMV instances (*red*) is shown.

evolution. As expected, the observed cluster rate in the tank PMT data closely follows the beam intensity values, verifying that the beam is captured reliably by the ANNIE detector.

While the exact beam intensity varies from run to run, all runs are considered for the analysis since the measurement is conducted on an event by event basis and does not require a normalization based on the beam intensity and repetition rate which would be necessary for a cross-section measurement. Therefore, even runs with rather low beam intensity values can be considered in the scope of the upcoming neutron multiplicity analysis under the restriction that the beam parameters (such as the intensity or the horn currents) were reasonable at that particular time. The only requirement to minimize biases involves the presence of an extended window since events without such a longer acquisition window cannot be used to identify neutron candidates.

A further aspect of interest involves the timing alignment between different subsystems within ANNIE. Selection cuts which are designed to identify coincident activity across multiple individual detectors within the experiment depend on a stable timing offset between the systems in the recorded data. Figure 6.11 presents the evolution of this timing alignment between the tank PMTs and the FMV scintillator paddles for the considered run period. The observed offset remains stable over the examined time frame with a mean value of  $\Delta t_{\text{PMT-FMV}} \approx 815$  ns and deviations on the order of  $\pm 10$  ns for individual runs. Such deviations will not affect the selection of coincident events since the selection time window is 100 ns wide and hence basically unaffected by changes of such small magnitudes. Furthermore, the observed fluctuations are likely due to instabilities in the fit procedure for runs with lower statistics rather than actual shifts in the hardware-related timing offsets. The alignment between the tank PMT and the FMV system can hence be

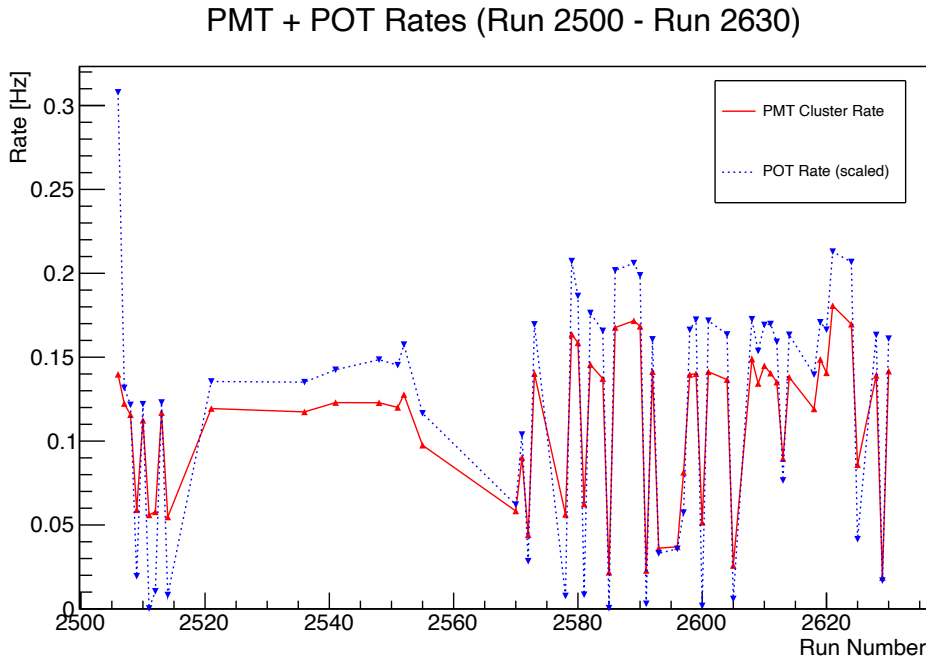


**Figure 6.10:** PMT cluster rates (*red*) and scaled POT rates (*blue*) are shown for the data taking period considered in the analysis, covering the majority of runs between run 2506 and 2630. The PMT cluster rate follows the behavior of the POT rate, indicating that the beam data taking process in the water tank seems to work reliably.

considered stable for the regarded time frame. A similar behavior is found for the timing offset between clusters in the tank and the MRD, indicating that a stable time alignment is found across all three subdetectors for the runs in question. The selection cuts for coincident activity in the various subsystems can hence safely be used in the scope of the presented analysis.

The stability of the PMT responses for the considered time frame is another important factor with regards to the validity of reconstruction algorithms relying on the amount of detected light for correctly inferring properties (such as the energy or the interaction vertex) of the muon and the neutrino. The run-wise charge behavior can be evaluated by investigating the average charge recorded by the PMTs, as shown in figure 6.12 for events featuring coincident activity in the tank and the MRD with no simultaneous hit in the veto detector. In this context, the average charge is assumed to be the mean value  $\mu_{\text{charge}}$  of the histograms filled with the total charge values encountered in the events. The error bars correspond to the uncertainty of this mean value, calculated from the standard deviation  $\sigma_{\text{charge}}$  and the number of events  $N_{\text{charge}}$  of the distributions via  $\sigma_{\text{charge}}/\sqrt{N_{\text{charge}}}$  by assuming a simplified model of Gaussian-distributed charge histograms. The figure shows that the tank PMT response remains stable over the considered run period, indicating that reconstruction algorithms will be valid for the entirety of the examined data set. Small fluctuations of the average charge values are visible for shorter runs with smaller event statistics. However, also these runs are mostly compatible with the expected behavior within their larger uncertainty levels and can therefore also be included in the analysis.

To summarize the findings, the detector performance can be considered stable for the time frame of the analysis based on the investigations presented above. The analysis of the

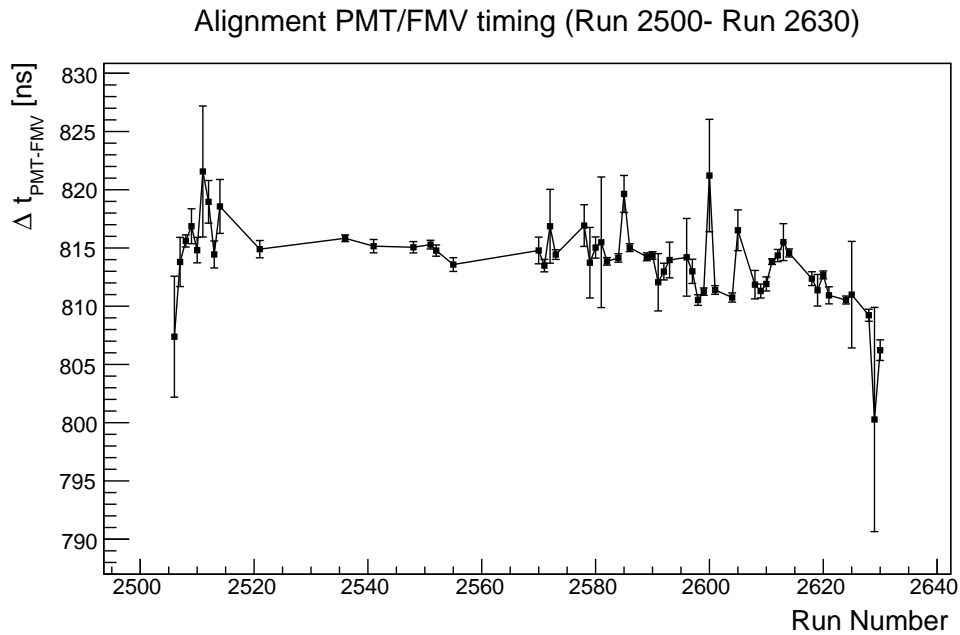


**Figure 6.11:** The time evolution of the timing alignment between the tank PMT and FMV systems is depicted for the data taking period considered in the analysis, covering the majority of runs between run 2506 and 2630. In general, the observed timing alignment shows a stable behavior, with fluctuations on the order of  $\pm 10$  ns which will not affect the selection cuts employed in the analysis.

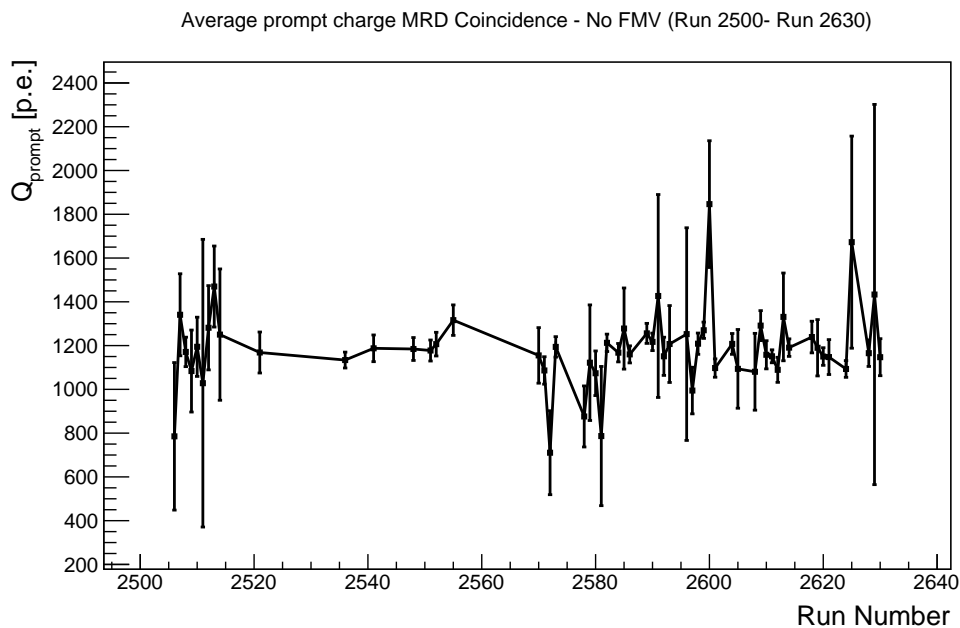


**Figure 6.12:** The time evolution of average tank PMT charge values for events featuring a coincident tank and MRD cluster with no coincident FMV activity is shown for the data taking period considered in the analysis, covering the majority of runs between run 2506 and 2630. The detected charge remains stable over the entire considered time period except for some fluctuations encountered in runs with smaller event statistics.

prompt muon characteristics and the delayed neutron captures presented in the following sections can therefore be conducted on the entire data sample.

## 6.3 PROMPT EVENT ANALYSIS - MUON CLASSIFICATION

The investigation of the neutron yield in neutrino-nucleus interactions requires the identification of neutrino candidates in the acquired data sample before moving on to count neutron candidates. The current section will first highlight how such neutrino interactions are selected from all detected beam triggers in ANNIE in subsection 6.3.1. In this context, the impact of the various selection cuts on the statistics and properties of the data sample will be studied and investigated. Afterwards, the characterization of muon candidates will be presented in subsection 6.3.2 in terms of the reconstructed interaction vertex and the muon energy. These variables will be of major importance for the identification of events within the Fiducial Volume of ANNIE and for the neutron yield measurement as a function of the lepton kinematics which will be presented in the scope of section 6.5.

### 6.3.1 NEUTRINO EVENT CANDIDATE SELECTION

Beam neutrino candidates which are likely associated with a muon as a final state particle are selected by requiring a coincidence between activity in the tank and the MRD while simultaneously requiring no coincident hit in the FMV. The latter cut ensures that the muon candidate which was detected in both the water tank and the MRD could not have entered the tank from the outside and on the contrary must have originated inside the water, rendering a neutrino interaction very likely. Further cuts are more tailored towards the associated neutron multiplicity measurement and involve, on the one hand, certain requirements for beam-related parameters such as horn currents or the beam intensity and, on the other hand, the necessity for events to feature an extended acquisition window of  $70 \mu\text{s}$  in order to reliably detect neutrons. The impact of each of these cuts on the event statistics as well as the tank PMT charge and timing distributions will be highlighted in what follows.

The first cut, which is designed to select coincident activity in the tank and the MRD, is based on the relative timing of the clusters in the tank and the MRD while additionally imposing a lower limit on the detected charge in the water tank to minimize the impact of random coincidences with noise clusters in the tank. The simultaneous veto activity is then excluded by a simple timing-based cut while the beam parameters are compared with the expectations to ensure stable beam operations during the considered event. Both the time window for coincident activity in the MRD and the FMV rely on the time ranges determined during the commissioning phase for which the stability for the considered data taking period was checked as presented in the previous section 6.2.2. The last cut then simply requires an extended acquisition window of  $70 \mu\text{s}$  for the given event. The precise requirements for each of the cuts are the following:

- MRD coincidence: A minimum total charge of 200 p.e. as well as a coincident MRD cluster with  $700 \text{ ns} < \Delta t_{\text{MRD,PMT}} < 800 \text{ ns}$  are required.
- No veto activity: No coincident veto hit is allowed to be recorded within a time window of  $750 \text{ ns} < \Delta t_{\text{FMV,PMT}} < 850 \text{ ns}$ .

- Beam parameters ok: The number of protons on target needs to be in the range  $[5 \cdot 10^{11}, 8 \cdot 10^{12}]$  POT/spill and the peak horn current  $I_{\text{peak,horn}}$  needs to have a value in the range  $[172, 176]$  kA. Furthermore, the intensity in the two relevant toroids E:TOR860 and E:TOR875 need to agree with each other within a tolerance of 5%.
- Extended acquisition window: A full (extended) window of  $70 \mu\text{s}$  must have been recorded for the event in question.

The impact of each cut on the number of events in the data sample is shown in table 6.1. Each successive row also includes all selections of the rows above – the shown numbers hence represent the statistics after the cumulative application of all respective cuts. A large reduction of events is achieved by the first requirement of a coincident MRD cluster since a large number of clusters will not represent muons and only a certain fraction of muons will have the correct geometrical profile allowing an intersection with the MRD. The further restriction of no coincident veto hit further excludes roughly a third of the available events while the requirement of good beam conditions only marginally reduces the number of events by 1.76%. The last cut requiring an extended acquisition window results in an additional 30% drop in the available statistics. While the trigger system should in principle be able to record extended windows for all muon-like event signatures, the deficiency visible in the last cut has been observed across multiple runs in the phase II data and will be addressed in a future upgrade of the trigger system. This upgrade will also include optical readout capabilities for the VME system, enabling a much larger acquisition rate for extended windows in future runs.

Cut	Events	Fraction [%]	Fraction of previous cut [%]
All tank clusters	10693314	100.0	100.0
MRD coincidence	24146	0.23	0.23
No veto	16004	0.15	66.28
Beam ok	15723	0.15	98.24
Extended acquisition	10932	0.10	69.53

**Table 6.1:** Impact of the various selection cuts on the event statistics. Cuts are applied sequentially such that each new row also includes the cuts of the rows above. The largest reduction is prompted by the requirement of a coincident MRD cluster while the additional cuts of no simultaneous veto hit, good beam conditions, and an extended acquisition window further reduce the number of selected events.

The impact of the cuts on the cluster time distribution is shown in figure 6.13. For comparison purposes, the original distribution of all tank clusters in beam triggers is shown in blue. The changes after applying additional cuts of a coincident MRD cluster (*red*), no veto activity (*black*), good beam parameters (*green*), and an extended acquisition window (*purple*) are then superimposed in the same graph in different colors. The  $1.6 \mu\text{s}$ -wide beam spill window in the center of the acquisition window is well visible across all stages of selection cuts, and even before applying any selection at all. While the original tank cluster distribution seems to feature a slightly rising slope as a function of the time, the histograms look much more symmetric after applying the respective cuts. Otherwise, the cuts mainly reduce the available statistics and do not alter the shape of the distribution much.

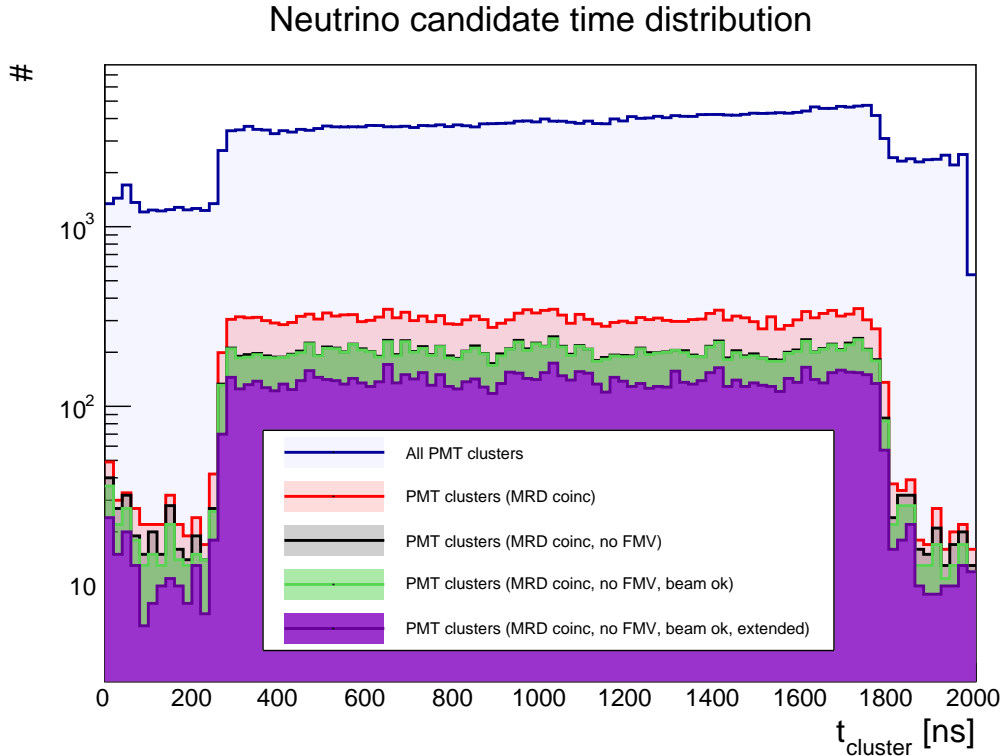


**Figure 6.13:** The effect of the employed selection cuts on the time distribution is shown for tank clusters in beam events. While the requirement of a coincident cluster in the MRD (*red*) significantly reduces the statistics in general, it also renders the beam window in the center of the acquisition window much more prominent. Additional cuts involving no simultaneous veto activity (*black*) and the necessity for an extended acquisition window (*purple*) further reduce the event statistics, while the beam-related selection cuts (*green*) almost have no impact on the number of events.

Regarding the charge distribution, the impact of the selection cuts is shown in figure 6.14. The situation for all tank clusters in beam triggers is depicted as the blue distribution and features a decreasing slope as a function of the detected total charge in the water tank, with a large increase in the number of events for  $q_{\text{cluster}}$ -values below 200 photoelectrons. The MRD-coincidence selection (shown in *red*) significantly reduces the number of events. Furthermore, the additional requirement of a minimal charge of 200 p.e. is also present as a hard cut-off in the distribution. The selection of coincidences with the MRD reveals the presence of a small peak in the charge region between 3000 p.e. and 5000 p.e. which is mainly composed of dirt events originating outside of the water tank. This observation is validated by the impact of the veto cut (shown in *black*) which is able to remove the peak of dirt muons entirely. The fact that the veto cut primarily targets events in that charge region and does not affect the distribution at lower light levels is a good cross-check that the veto system works as expected. The selection of events with good beam parameters (*green*) only slightly reduces the event statistics while the requirement for an extended acquisition window introduces a larger decrease in the number of events. However, the shape of the distribution does not change much as a result of either of the cuts.

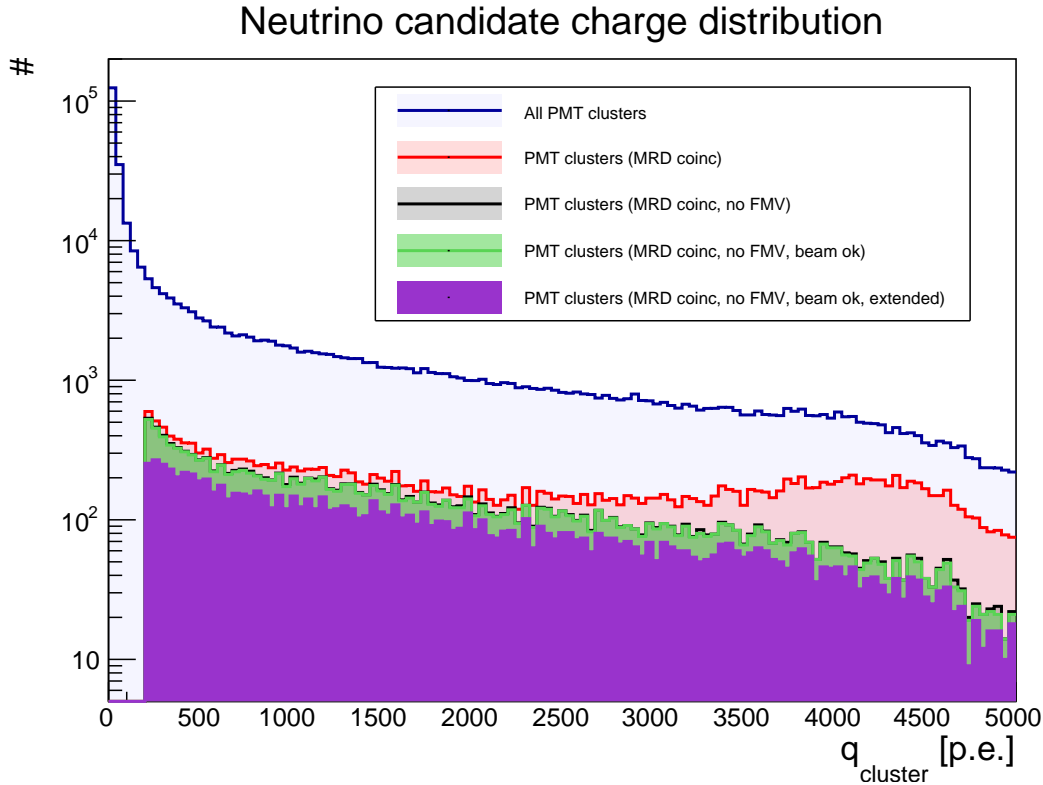


**Figure 6.14:** The effect of the employed selection cuts on the charge distribution is shown for tank clusters in beam events. The requirement of a coincident cluster in the MRD (*red*) significantly reduces the statistics in general and makes a peak-like region around 4500 p.e. more visible. Imposing the additional requirement of no coincident veto hit (*black*) eliminates this peak, rendering through-going muons as the most likely associated event population. Further cuts including good beam conditions (*green*) and the necessity for an extended acquisition window (*purple*) further slightly reduce the event statistics but do not alter the shape of the distribution much.

### 6.3.2 CHARACTERIZATION OF MUON NEUTRINO CANDIDATES IN DATA

After selecting muon neutrino candidates as presented in the previous subsection, the corresponding charged muon particles can be characterized in terms of their energy  $E_\mu$ , interaction vertex  $\vec{r}_{\text{vertex}}$ , and interaction angle  $\cos(\theta_\mu)$ . While more sophisticated reconstruction algorithms are under development both for the energy and the combined vertex and direction reconstruction (compare for instance references [8, 234]), the analysis presented here uses a much simplified technique solely based on the MRD reconstruction presented in chapter 4 and the total charge recorded in the water tank as a first approximation. The following paragraphs will first present the concept of this simplified reconstruction and will showcase the accuracy of the predicted properties based on simulation studies before applying the same algorithms on the data sample.

#### Energy & vertex reconstruction

While propagating in the water, the muon will continuously lose energy via ionization processes which will become visible in the form of Cherenkov light within the detector. Since the muon is a minimum ionizing particle (MIP) in the considered energy range, the

energy loss in a water Cherenkov detector can be assumed to be constant and on the order of  $\frac{dE}{dx} \approx 1.992 \frac{\text{MeV}}{\text{cm}}$  [236]. The total particle energy can therefore be estimated by combining the information about the muon track length in the water and the additional energy loss in the sandwich-structured Muon Range Detector. The latter quantity is derived based on the reconstructed track topology in the MRD, as briefly discussed in chapter 4. The track length in the tank, on the contrary, is estimated based on the amount of charge detected by the PMTs in the tank.

Figure 6.15 schematically displays the event topology of a typical interaction for which an incoming muon neutrino (*dashed, black*) creates a muon (*red*) in a Charged Current interaction which then propagates through the water tank and stops in the MRD. The different stages of energy losses are depicted in various colors: Within the PMT-enclosed volume, the energy  $E_{\mu,\text{tank}}$  (*orange*) is deposited in the water and will be accessible in terms of the total charge  $Q$  detected by the PMTs, connected by a proportionality factor  $\alpha$ :

$$E_{\mu,\text{tank}} = \alpha \cdot Q, \quad (6.3)$$

where  $\alpha$  takes on units of  $\frac{\text{p.e.}}{\text{MeV}}$  and  $Q$  is inserted in units of photo-electrons.

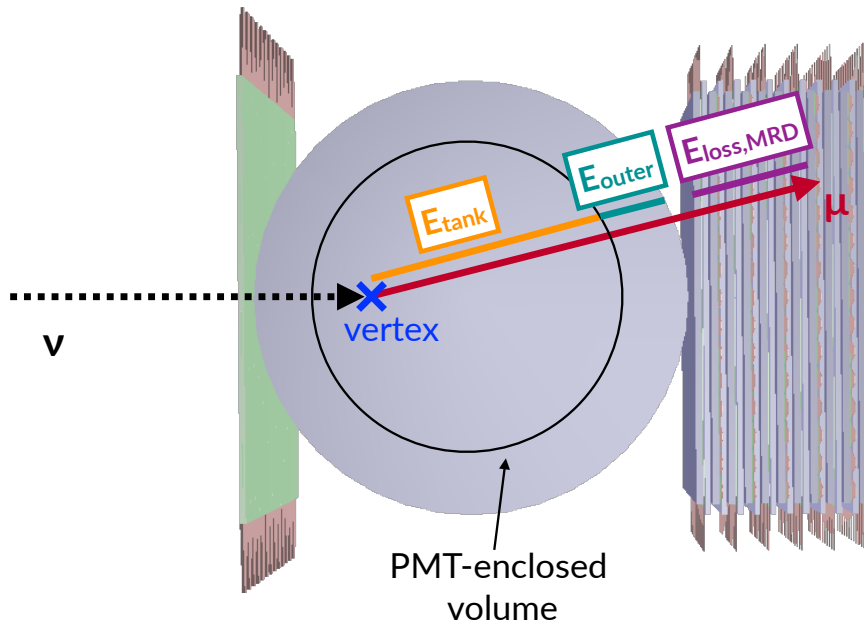


**Figure 6.15:** Principle of the simple energy reconstruction algorithm used to estimate the energies of muons in the presented analysis. The total energy of the considered muons is calculated by combining the energy loss reconstructed in the MRD ( $E_{\text{loss,MRD}}$ ), the light levels observed in the tank ( $E_{\text{tank}}$ ), and the energy lost outside of the PMT-enclosed volume ( $E_{\text{outer}}$ ).

After leaving the PMT-enclosed volume which is separated from the rest of the water tank by a black liner sheet, the muon further traverses more water until it reaches the edge of

the tank, depositing an additional energy of  $E_{\mu,\text{outer}}$  (*green*) in the detector. This energy is not visible in the charge detected by the PMTs due to the optical isolation between the outer and inner volume of the tank. However, the value can be estimated by extrapolating the muon track from the MRD back into the tank and inferring the distance  $d_{\text{outer}}$  travelled in the outer region. The energy loss in the region is then given by

$$E_{\mu,\text{outer}} = \beta \cdot d_{\text{outer}}, \quad (6.4)$$

with  $\beta$  being the proportionality factor described earlier ( $\beta \approx 1.992 \frac{\text{MeV}}{\text{cm}}$ ). The distance  $d_{\text{outer}}$  is calculated based on the extrapolated tank exit position  $\vec{r}_{\text{tank,exit}}$  and the extrapolated PMT-volume exit position  $\vec{r}_{\text{PMT,exit}}$ , both extracted from the reconstructed MRD muon track properties. The distance is simply given by the distance between the two vectors,  $d_{\text{outer}} = \|\vec{r}_{\text{tank,exit}} - \vec{r}_{\text{PMT,exit}}\|$ .

While the muon also propagates through air when transitioning from the water volume to the space occupied by the MRD, the energy loss in this region can be considered negligible due to the much smaller density of air compared to water ( $\rho_{\text{air}}/\rho_{\text{water}} \approx 10^{-3}$  [236]) and the therefore much smaller associated energy losses encountered in that region.

The total muon energy  $E_{\mu,\text{reco}}$  can be estimated by combining all the individual components presented in the paragraphs above, and adding a constant term  $c$  for absorbing potential additional unaccounted effects:

$$E_{\mu,\text{reco}} = E_{\mu,\text{tank}} + E_{\mu,\text{outer}} + E_{\text{loss,MRD}} + c \quad (6.5)$$

$$= \alpha \cdot Q + \beta \cdot d_{\text{outer}} + E_{\text{loss,MRD}} + c. \quad (6.6)$$

The only unknown components in this equation are the conversion factor  $\alpha$  between the observed charge in the tank and the corresponding energy loss in the water tank as well as the constant offset  $c$ . They can be determined based on simulation data in a simple polynomial fit by plotting the estimated deposited energy in the water tank  $E_{\text{tank}}$  versus the observed charge  $Q$ , where  $E_{\text{tank}}$  is given by

$$E_{\text{tank}} = E_{\mu,\text{true}} - \beta \cdot d_{\text{outer}} - E_{\text{loss,MRD}} \quad (6.7)$$

and also includes the constant offset  $c$ . The correlation of  $E_{\text{tank}}$  and the charge  $Q$  is presented in figure 6.16 alongside a linear fit shown in red. The fit results are given by

$$\alpha = (0.08534 \pm 0.00169) \frac{\text{MeV}}{\text{p.e.}},$$

$$c = (87.3 \pm 3.9) \text{ MeV}.$$

The obtained value for  $\alpha$  is in agreement with a similar parameter ( $\alpha' = (0.0833 \pm 0.08) \frac{\text{MeV}}{\text{p.e.}}$ ) discussed in Teal Pershing's thesis [215], obtained with a different data sample of through-going muons, solidifying the reasonability of the presented considerations.

Based on equation (6.6), the muon energy can roughly be reconstructed based on the observed light level in the tank and the MRD muon track reconstruction information.

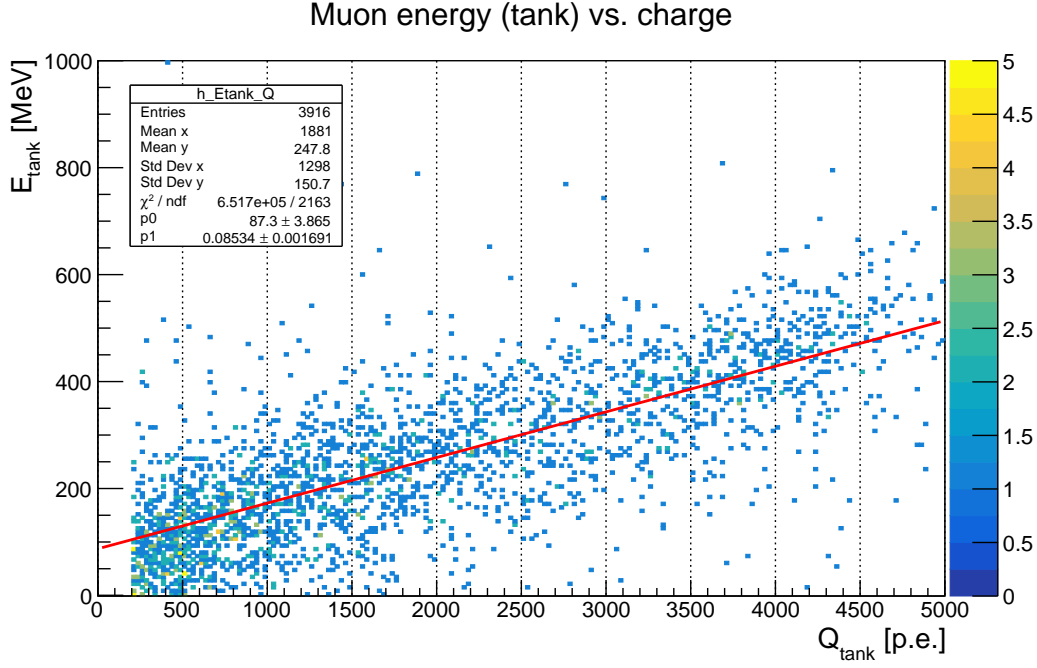


**Figure 6.16:** Correlation of the reconstructed energy deposited in the tank ( $E_{\text{tank}}$ ) and the total charge  $Q$  detected by the PMTs in the water tank. While the linear dependency is not perfect, it provides a sufficiently accurate model for the estimation of the muon energy in the scope of the presented analysis.

The method can further be extended to also infer the property of the interaction vertex by extrapolating the MRD muon track into the region of the water tank. The exact propagation distance is calculated by again making use of the charge detected in the water tank, yielding

$$\vec{r}_{\text{vertex}} = \vec{r}_{\text{PMT,exit}} - \frac{\alpha}{\beta} \cdot Q \cdot \vec{d}_{\text{MRD}}, \quad (6.8)$$

where

$$\vec{d}_{\text{MRD}} = \frac{\vec{r}_{\text{MRD,stop}} - \vec{r}_{\text{MRD,start}}}{\|\vec{r}_{\text{MRD,stop}} - \vec{r}_{\text{MRD,start}}\|} \quad (6.9)$$

is the normalized direction of the reconstructed muon track in the MRD.

The accuracy of the reconstruction is evaluated by comparing the predicted vertex and energy variables with the true values in the scope of a simulation study. The corresponding results are presented in figure 6.17 separately for the muon energy and the three vertex coordinates  $x$ ,  $y$ , and  $z$ . When investigating the reconstruction accuracy for the muon energy, the algorithm generally seems to be able to reconstruct the property rather well, with a Gaussian fit yielding a mean deviation of  $\mu_{\text{energy}} \sim 7 \text{ MeV}$  and standard deviation of  $\sigma_{\text{energy}} \sim 117 \text{ MeV}$ . A tail is visible at the higher end of the  $\Delta E$  distribution – these events very likely contain additional particles such as pions which contribute to the observed light levels in the tank. The contribution of the muon is hence overestimated by the simple algorithm used in this analysis, skewing the reconstruction to higher values.

The position reconstruction in general also delivers quite promising results, with mean  $\Delta x_i$ -values on the order of centimeters and standard deviations on the order of  $\sigma_{x_i} \approx 35 \text{ cm}$ . While the Gaussian fits do not capture the shapes of the distributions perfectly, they do

represent the mean and width values quite well and can hence be considered acceptable for a rough characterization of the reconstruction performance. The largest deviation from the Gaussian shape is observed for the  $\Delta z$ -distribution for which a small population of events seems to be reconstructed too far upstream within the detector, with  $\Delta z$ -values on the order of  $-1$  m. In general, however, the reconstruction seems to work reasonably well both in terms of the energy and the vertex characterization. The charged lepton reconstruction will thus be able to single out events that originated inside of the Fiducial Volume and will further possess the capability to classify them according to their energy.

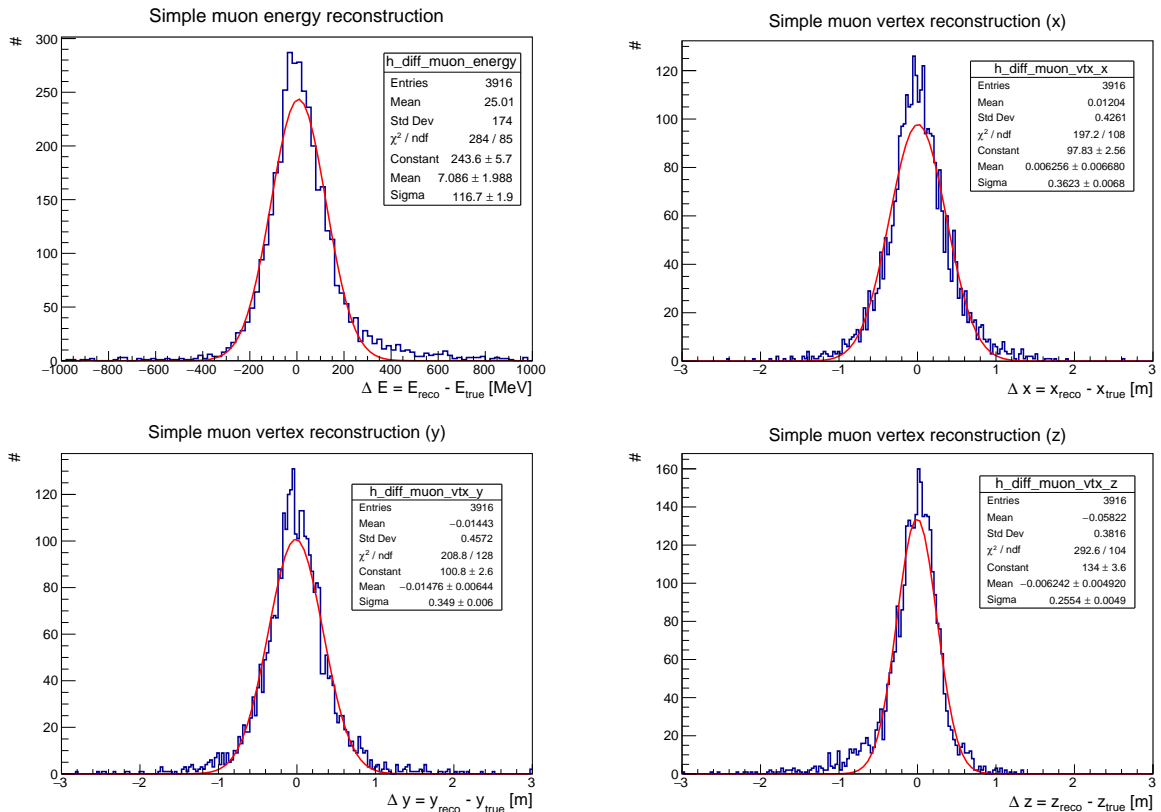


**Figure 6.17:** Reconstruction performance of the simple MRD-based reconstruction technique presented in this section. The muon energy reconstruction (*top left*) shows a tail at higher reconstructed energies due to event topologies that include additional particles such as pions. The vertex reconstruction performance is similar across the three spatial coordinates  $x$  (*top right*),  $y$  (*bottom left*), and  $z$  (*bottom right*) with standard deviations on the order of 36 cm.

### Application of reconstruction algorithms on data

The reconstruction algorithms presented in the previous paragraphs are now applied to the neutrino candidate events which were selected in the data sample based on the criteria highlighted in section 6.3.1. The resulting reconstructed vertex coordinates are presented in figure 6.18 both in a  $y/z$  and a  $x/z$ -view of the ANNIE detector. Some artifacts of the MRD reconstruction technique are visible in terms of lines with increased vertex reconstruction probability due to the finite resolution of the paddle-based MRD reconstruction. The Fiducial Volume selection (shown in *red*) singles out a small zone in

the upstream region of the water tank which is delimited by the following constraints:

$$\begin{aligned}\rho &= \sqrt{x^2 + z^2} < 1.0 \text{ m}, \\ |y| &< 0.5 \text{ m}, \\ z &< 0.0 \text{ m}.\end{aligned}$$

These cuts, on the one hand, ensure that the contamination of so-called *sky-shine* neutrons (consisting of neutrons scattered off molecules in the atmosphere, for more details compare reference [184]) is minimized by selecting a shielding water layer above the selected region. On the other hand, the requirement for vertices to be contained in the upstream region of the tank maximizes the number of neutrons which will actually be captured in the water volume since the beam-associated neutrons will be biased in the forward beam direction.

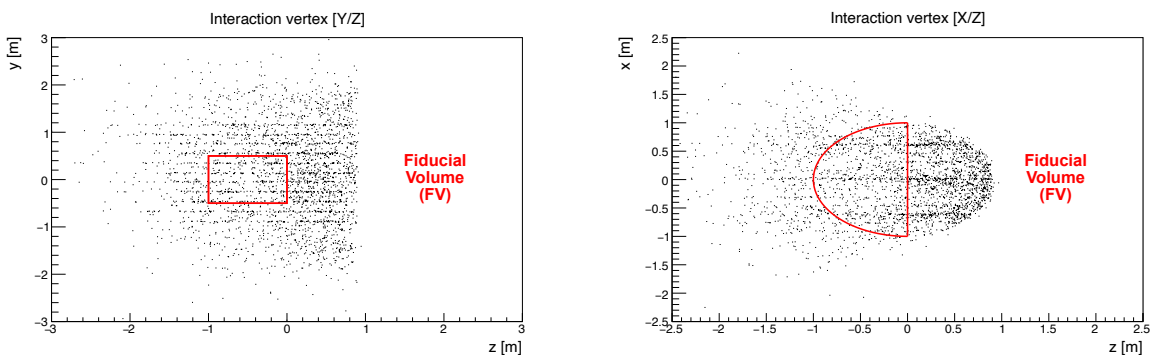


**Figure 6.18:** Reconstructed interaction vertices in the selected neutrino candidate events in the data sample. The vertices are shown both in a  $y/z$  (*left*) and a  $x/z$  (*right*) view of the ANNIE tank. The Fiducial Volume (FV) is depicted in red in both cross-section views.

The reconstructed muon energy values for the selected neutrino candidate events in the data are presented in figure 6.19, both for all events with a stopping muon track in the MRD (*blue*) and for the subset of muons which originated in the Fiducial Volume (*red*). The selection of Fiducial Volume-contained events was conducted based on the reconstructed vertex coordinates as shown in the previous figure 6.18. For comparison purposes, the same reconstruction algorithms were applied to the simulation sample, yielding the solid line distributions in the same figure. The general shapes of the energy distributions in the data and the MC match rather well, indicating that the selection of neutrino candidates worked in the case of the data sample. Furthermore, the agreement can be considered a further proof that the simulation is capable of realistically modeling the interactions, processes and electronics responses within the ANNIE detector.

In a similar manner, the angular distributions of reconstructed muon tracks with respect to the beam direction can be evaluated and compared to the expectations based on simulations. The parameter of interest  $\theta_\mu$  represents the angle between the muon direction  $\vec{d}_\mu$  and the neutrino direction  $\vec{d}_\nu$ :

$$\cos \theta_\mu = \frac{\vec{d}_\mu \cdot \vec{d}_\nu}{|\vec{d}_\mu| \cdot |\vec{d}_\nu|}. \quad (6.10)$$

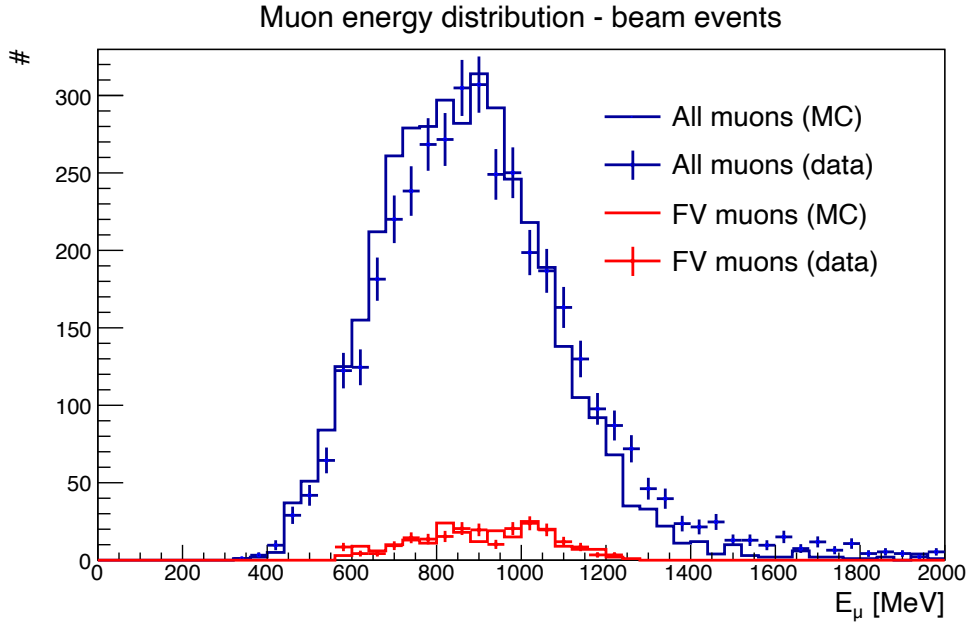


**Figure 6.19:** Muon energy distributions for events with a stopping track in the MRD (*blue*) and events with a muon originating in the Fiducial Volume (*red*). Reconstructed distributions for data (*crosses with error bars*) are contrasted with the expected distributions in the Monte Carlo (*solid lines*).

In our case, the muon direction  $\vec{d}_\mu$  is obtained from the reconstructed track in the MRD and the neutrino direction is inferred to be purely in  $z$ -direction based on the geometry of the beam:

$$\vec{d}_\mu = \vec{r}_{\text{MRD,stop}} - \vec{r}_{\text{MRD,start}} = \begin{pmatrix} d_{\text{MRD},x} \\ d_{\text{MRD},y} \\ d_{\text{MRD},z} \end{pmatrix}, \quad \vec{d}_\nu = \begin{pmatrix} 0 \\ 0 \\ 1 \end{pmatrix}. \quad (6.11)$$

The equation for the calculation of the angle therefore simplifies and takes on the following form:

$$\cos \theta_\mu = \frac{d_{\text{MRD},z}}{\sqrt{d_{\text{MRD},x}^2 + d_{\text{MRD},y}^2 + d_{\text{MRD},z}^2}} \quad (6.12)$$

The resulting distributions for neutrino candidate events with a stopping muon track and with the additional constraint of a reconstructed interaction vertex in the FV of ANNIE are shown in figure 6.20 as blue and red curves, respectively. While the distributions obtained from data are depicted as crosses with error bars, the equivalent MC distributions are shown as solid lines in the plot.

In general, the geometrical setup of ANNIE leads to a selection of primarily downstream-oriented muons, with  $\cos(\theta_\mu) \sim 1$ . More tilted tracks are observed with a decreased probability up until values of  $\cos(\theta_\mu) \sim 0.6$ . Some discrete peaks seem to be present in the angular distribution which are an inherent feature of the MRD track reconstruction technique due to the dimensions of the single scintillator paddles. The comparison of the distributions shows that the selected neutrino candidates in the data and the simulation

seem to exhibit a very similar behavior for both samples, demonstrating that the selected events also match in terms of their angular properties.

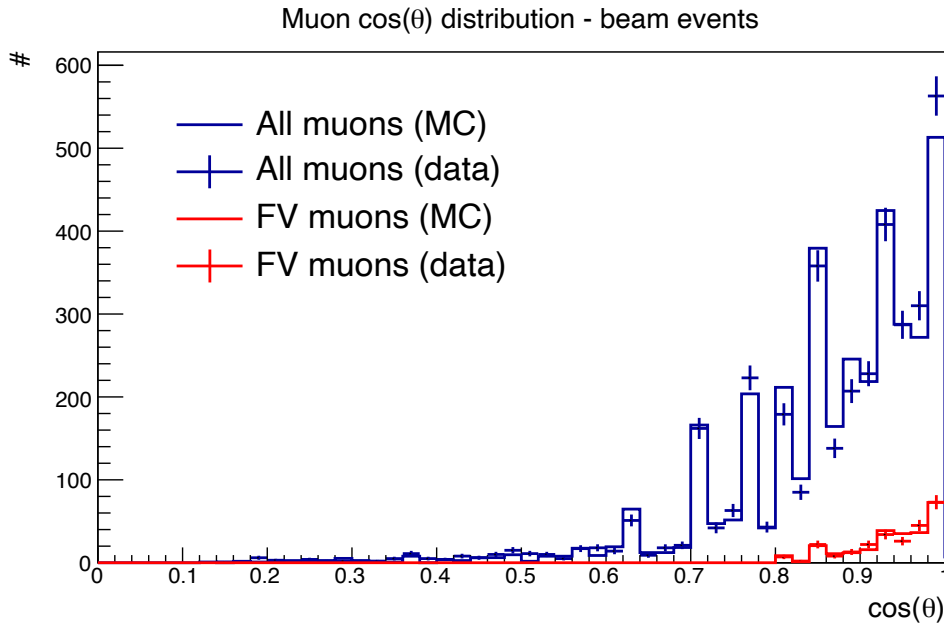


**Figure 6.20:** Muon angular distributions for events with a stopping track in the MRD (*blue*) and events with muons originating in the Fiducial Volume (*red*). Reconstructed distributions for data (*crosses with error bars*) are contrasted with the expected distributions in the Monte Carlo (*solid lines*).

The investigation of the vertex, energy, and angular distributions of associated muons in neutrino candidate events concludes the characterization of the prompt activity in the tank. While it is in principle also possible to extract the neutrino energy for events which were created in a CCQE interaction based on the reconstructed muon energy and the angle between the neutrino and muon directions, this additional step creates further uncertainties and is much more prone to introduce biases, and will hence be included in a future more in-depth analysis.

## 6.4 DELAYED EVENT ANALYSIS - NEUTRON COUNTING

The number of neutrons produced in the neutrino interaction (often referred to as *neutron yield* or *neutron multiplicity*) is a useful indicator for the inelasticity of any given event and can hence be used to reduce biases in the neutrino energy reconstruction. Furthermore, a better understanding of the neutron multiplicity for high-energetic neutrinos will help to constrain backgrounds in DSNB and proton decay searches more efficiently, as presented in subsection 2.3.4 of the theory chapter. The current section will present the prospects of a neutron yield measurement in ANNIE by first highlighting the expected neutron levels based on simulation studies in subsection 6.4.1 before moving on to discuss appropriate selection cuts for neutron candidates based on the calibration campaign in subsection 6.4.2. The properties of selected neutron candidates in the considered data sample will then be shown in subsection 6.4.3 in terms of the associated charge and time spectra. The final subsection 6.4.4 presents the integrated neutron multiplicity results in the data

and contrasts them with the expectations from the theoretical point of view based on simulation data.

#### 6.4.1 EXPECTED NEUTRON YIELD

The expected number of neutrons in ANNIE is estimated based on simulating neutrino interactions in the water tank in the scope of the GENIE event generator before propagating all resulting final state particles in the scope of the Geant4-based WCSim simulation package. The properties of both frameworks are presented in more detail in chapter 5.4 which focuses on the tuning of the Monte Carlo framework.

Neutrons can either be produced directly as a result of the neutrino-nucleus interaction or in the scope of further interactions of final state particles with other oxygen molecules in the water tank, for instance in the scope of inelastic scattering processes. The first category of neutrons is labeled *primary neutrons* and also includes neutrons resulting from Final State Interactions (FSIs) within the nucleus while the latter category of particles is referred to as *secondary neutrons*. ANNIE will observe the total number of neutrons produced in an interaction, including both primary and secondary particles without any possibility to distinguish between the two event categories. Comparisons between data and Monte Carlo are hence not able to directly test the neutrino generator itself in terms of the produced number of primary neutrons but instead probe a combination of the generator and the hadronic models within Geant4 which are responsible for the modeling of the secondary processes and are also known to have some deficiencies [237].

The interaction channel is of primary importance for predicting the number of primary neutrons produced in a neutrino event. In this context, figure 6.21 depicts the primary neutron multiplicity distribution as predicted by GENIE-simulated neutrino interactions in ANNIE, separated into the CC-QE (*green*), CC-RES (*red*), and CC-DIS (*blue*) channels. The Quasi-Elastic interaction very likely does not include any primary neutrons due to the elasticity of the neutrino-nucleon interaction which will instead rather produce a proton. Any neutrons produced in CC-QE interactions are therefore a result of additional FSIs in the nucleus, resulting in a probability of only roughly 34% of observing at least one neutron. The chance of observing more than one neutron is much higher in CC-RES (52%) and CC-DIS (68%) interactions, highlighting the correlation of inelastic processes and the presence of neutrons.

The influence of secondary neutron production on the total observable neutron yield curve is highlighted in figure 6.22: While the neutron multiplicity distribution for primary neutrons (*red*) as predicted by GENIE only extends up to neutron counts of 8, the combined number of primary and secondary neutrons (*blue*) including secondary interactions in Geant4 can extend up to 30 neutrons in very rare cases. In addition, the probabilities for certain event categories change significantly even in the region of low neutron counts. As such, it becomes much less likely to observe events with no neutrons when considering the total sum of primary and secondary neutrons as opposed to counting only primary neutrons. Furthermore, the distribution decreases more uniformly and does not feature a sharp drop for the threshold of two neutrons anymore.

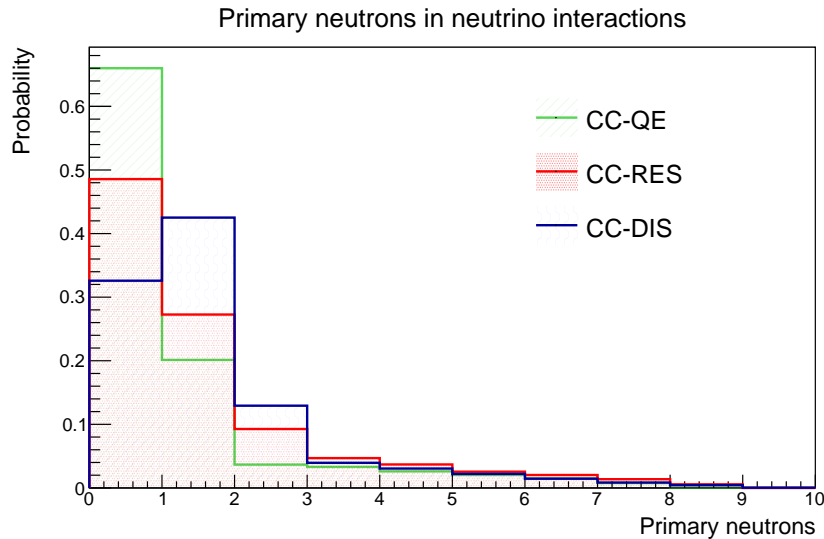


**Figure 6.21:** Predicted number of primary neutrons in Charged Current neutrino-nucleus interactions in water as simulated by GENIE (v2.12.0). The behavior is split into the different channels of CC-QE (*green*), CC-RES (*red*), and CC-DIS (*blue*) interactions. Resonant and Deep Inelastic interactions have a much higher probability of observing at least one neutron compared to the Quasi-Elastic channel.

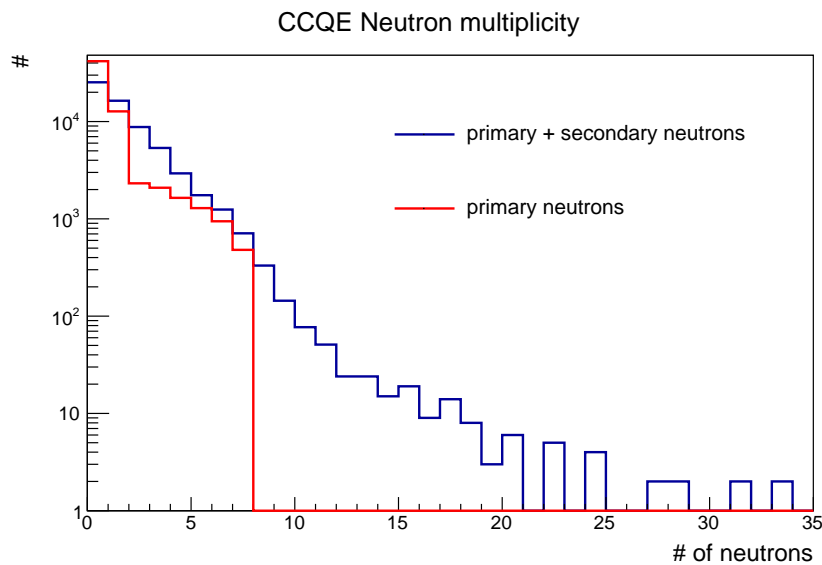


**Figure 6.22:** The neutron multiplicity distribution in CC-QE interactions is shown separately for primary neutrons as predicted by GENIE (*red*) and for all (primary + secondary) neutrons as simulated by a combination of GENIE and WCSim (*blue*). While primary neutrons are the direct product of the neutrino-nucleus interaction, secondary neutrons are produced in further inelastic reactions in the target medium.

## 6.4.2 SELECTION CUTS FOR NEUTRON CANDIDATES

Neutrons in ANNIE in most cases capture on Gadolinium nuclei and subsequently emit a cascade of roughly four to five gammas, as described in more detail in section 5.4.3 highlighting the tuning of the simulation framework in terms of the neutron capture signal. As a consequence, the observed signal across the photomultiplier tubes is rather faint and characterized by a total charge of 10 to 40 p.e. detected by 10 to 20 PMTs. In comparison

to high-energetic muon or electron events, neutron signals are hence much less prominent and need to be distinguished from clusters of afterpulses and dark noise, which both might be able to mimic the event signature. A combination of selection criteria were identified to obtain a relatively pure sample of neutrons while simultaneously rejecting most of the background based on the data acquired in the AmBe neutron calibration campaign. The cuts involve the Charge Balance parameter  $q_{\text{CB}}$  introduced in equation (5.8) and the total charge  $q_{\text{total}}$  such that the following criteria are met:

$$\begin{aligned} q_{\text{total}} &< 120 \text{ p.e.} \\ q_{\text{CB}} &< 0.4 \\ q_{\text{CB}} &< 0.5 - \frac{q_{\text{total}}}{300 \text{ p.e.}} \end{aligned}$$

A visualization of these cuts in a two-dimensional representation is shown in figure 6.23 for data taken during the AmBe calibration campaign. The two main selection criteria are visualized by the red lines, with all events in the bottom left region being selected as neutron candidates. When comparing the distribution with the equivalent distribution of background events (as discussed for example in [215]), it becomes clear that the bent population of events in the lower left region that are being selected this way are primarily neutrons. The selected distribution seems to continue into a population featuring lower charge and higher Charge Balance values: While some clusters in this region will also be neutrons, a significant fraction will also be composed of background events. As a consequence, this region of the selection cut space can only be explored with more sophisticated identification techniques such as neural networks. Work on such more developed event selection criteria is ongoing within the collaboration and will improve the neutron selection efficiency in the future but will not be employed in the present analysis. Besides the main distribution, another population of events is visible for Charge Balance values around 1. These events are characterized by the entire charge being detected by one photomultiplier and can hence safely be considered background events.

Within the beam neutrino analysis, the presented selection cuts need to be applied to the extended acquisition window for events that were identified as muon neutrino candidates. Figure 6.24 exemplarily shows the hit time distribution for a single beam event with an extended acquisition window. The prompt activity of a likely muon candidate is visible as a prominent peak corresponding to almost 130 hit PMTs around a time of 1000 ns. In addition, some increased activity is identifiable in the region between 6 and 10  $\mu\text{s}$  and can most likely be traced back to afterpulsing effects. Some smaller peaks composed of 10 to 20 PMT hits are present in the subsequent time window after 10 microseconds. Such clusters of hits can likely be associated with neutron activity in the tank, given that they pass the relevant cuts presented earlier. Out of the six neutron-like clusters that are visible in the shown time distribution, four pass the selection cuts and are identified as neutron candidates (designated by red arrows in the plot). Besides the muon activity, afterpulsing hits, and the potential neutron candidates, some additional uncorrelated noise hits are present across the full acquisition window of 70  $\mu\text{s}$ . In an attempt to further reduce background from afterpulsing, only the time window after 10  $\mu\text{s}$  is considered for the neutron search in the following analysis in order to exclude the afterpulsing-enriched region between 6 and 10  $\mu\text{s}$ .

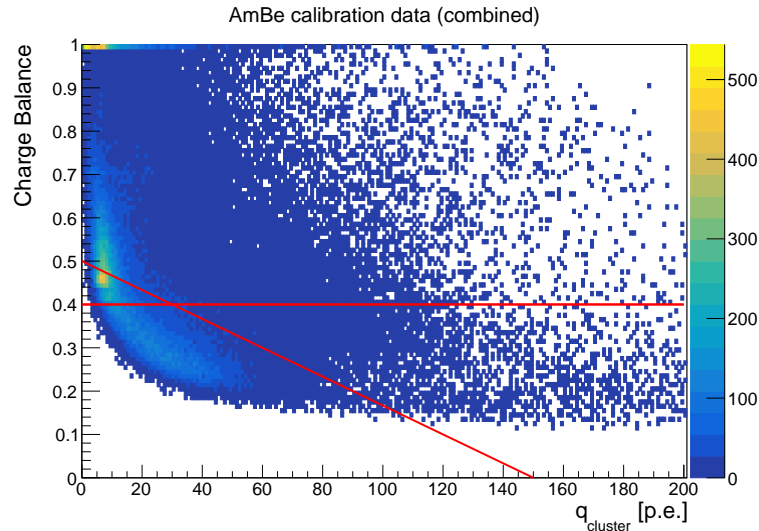


**Figure 6.23:** The visualization of the neutron selection cuts in the *Charge Balance - Total Charge* plane for neutron calibration data. Events located in the lower left region are identified as neutron candidates by the cuts that are employed.

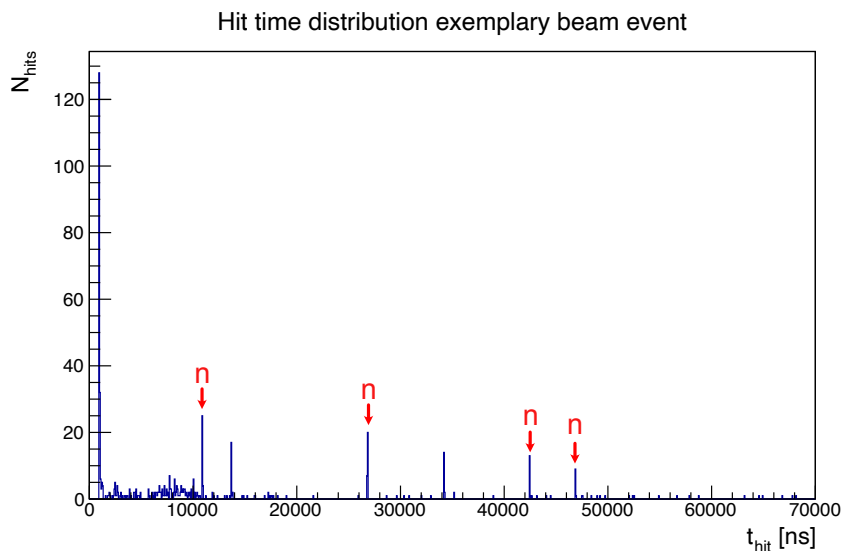


**Figure 6.24:** Time distribution of tank PMT hits detected in an exemplary beam trigger event with an extended acquisition window. The large prompt activity around 1000 ns is indicative of a muon-like event signature while the smaller sharp peaks at later times after 10  $\mu\text{s}$  are potential neutron candidates. Clusters which passed the neutron selection cuts are marked by red arrows. The increased number of hits in the time frame between 6  $\mu\text{s}$  and 10  $\mu\text{s}$  can most likely be traced back to afterpulsing effects. In addition, single uncorrelated noise hits are visible across the entire acquisition window.

### 6.4.3 PROPERTIES OF SELECTED NEUTRON CANDIDATES

The properties of the selected neutron candidates can be evaluated in terms of their charge and time response in order to validate that the employed cuts worked reasonably well to identify neutron-like clusters. In this context, figure 6.25 shows the time distribution of selected neutron candidates in the beam data sample. As expected, a clear exponential shape representative of the neutron capture process is visible. A fit with an exponential

function and a constant term of the form

$$f(t) = c + A \cdot e^{-t/\tau} \quad (6.13)$$

yields the following best fit parameters:

$$c = (14 \pm 12) \frac{\text{counts}}{2400\text{ns}},$$

$$\tau = (29 \pm 7) \mu\text{s}.$$

The constant term  $c$  is included in the fit to account for the amount of beam-uncorrelated background neutrons. The determined decay time constant  $\tau$  is in accordance with the theoretically expected value of  $\tau_{\text{theo}} = 30 \mu\text{s}$  [177] within the determined uncertainties. From the point of view of their timing characteristics, the selected neutron candidates hence behave according to expectations.

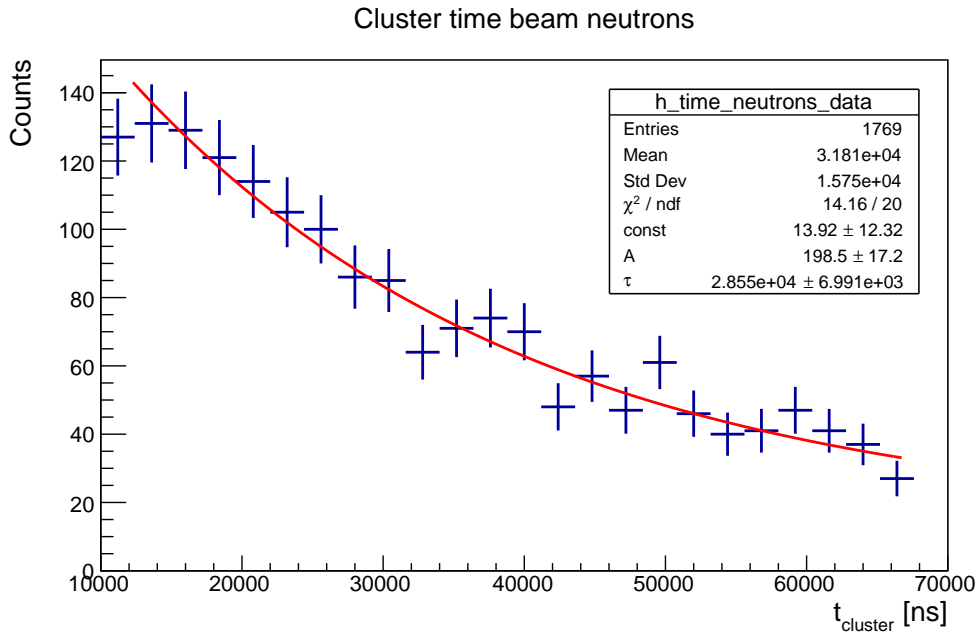


**Figure 6.25:** Time distribution of neutron event candidates from beam neutrino interactions. The distribution was fit with an exponential function including a constant offset. The resulting best fit value for the decay time  $\tau_{\text{decay}} = (29 \pm 7) \mu\text{s}$  is in good agreement with the expected value of  $\tau_{\text{theo}} = 30 \mu\text{s}$ .

Apart from the timing behavior, the other main quantity of interest is the total charge detected by the ensemble of ANNIE PMTs. The charge distribution of the selected neutron candidates in beam events is depicted in figure 6.26. Data events are depicted as red crosses with error bars while the expected behavior based on the Monte Carlo simulation is shown as a shaded blue area. In general, the distributions look rather similar and feature a peak in the charge region between 10 and 30 p.e. followed by a decreasing slope up until a maximum total charge of around 70 photoelectrons. While small differences are visible due to statistical uncertainties and a potential small fraction of remaining background in the selected data sample, the spectra resemble each other closely enough to further confirm the validity of the employed selection approach.

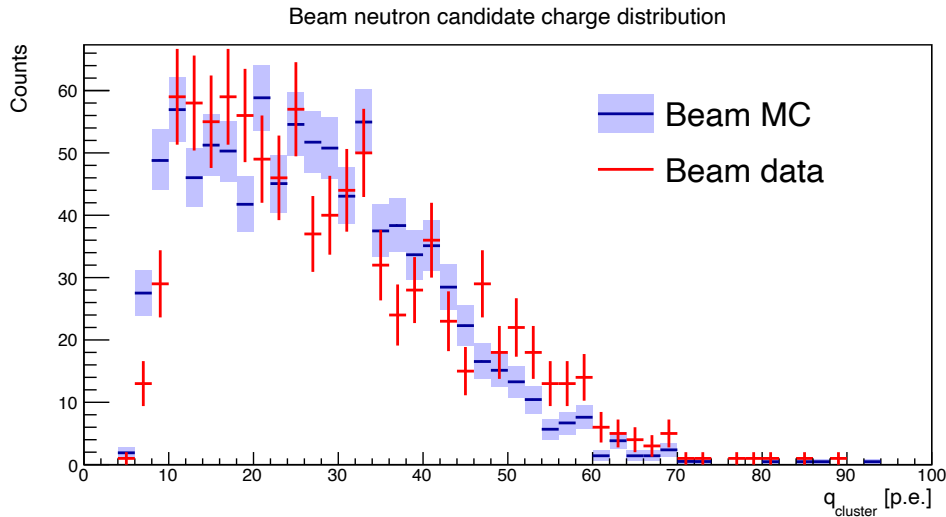


**Figure 6.26:** Charge distribution of neutron candidates from beam neutrino interactions. The spectrum obtained from the beam data is shown in red with the associated statistical uncertainties while the expected spectrum based on Monte Carlo simulations is shown as a shaded blue curve, also indicating the statistical uncertainties.

#### 6.4.4 INTEGRATED NEUTRON MULTIPLICITY

The simplest neutron yield characterization consists of an integrated measurement over the entire parameter space of encountered muon energies and interaction angles. In this context, the number of neutrons is counted for each event and the resulting distribution is compared against the expectations based on Monte Carlo simulations. The current section will present these neutron multiplicity comparisons both for events with a reconstructed stopping track in the MRD and for events that are further restricted to have an interaction vertex inside the Fiducial Volume (FV).

When considering neutrino interactions that generated a stopping muon track in the MRD, the resulting neutron yield distribution is depicted in figure 6.27. The same selection cuts for identifying neutrons presented in section 6.4.2 have been applied to the beam neutrino samples in the case of data and the simulation. The behavior in the data is shown as black crosses in the plot, with the extents of the lines being representative of the statistical uncertainties of the measurement. The expected behavior based on the simulation sample is shown as dotted lines with shaded areas indicating the statistical uncertainties of the prediction. No systematic uncertainties are included in this comparison since the statistical uncertainties are still quite large at the moment and most likely dominate over systematic error sources. Systematic uncertainties are still being studied in more detail at the moment by the collaboration, with an overview of expected error sources and their magnitudes being given in section 6.6. In general, the observed distributions feature a decreasing slope with the most likely case being zero neutrons and much lower probabilities being assigned to higher multiplicities. This is expected based on the dominant interaction channel of CC-QE interactions that will generally produce protons instead of neutrons. Neutron production only happens either in Final State Interactions (FSIs) within the nucleus or in secondary interactions of the produced particles with other oxygen nuclei in the water. Furthermore, neutrons can also result from different interaction channels such as Resonant

Pion production which are more likely to be accompanied by neutron production and which are still included in the current event selection.

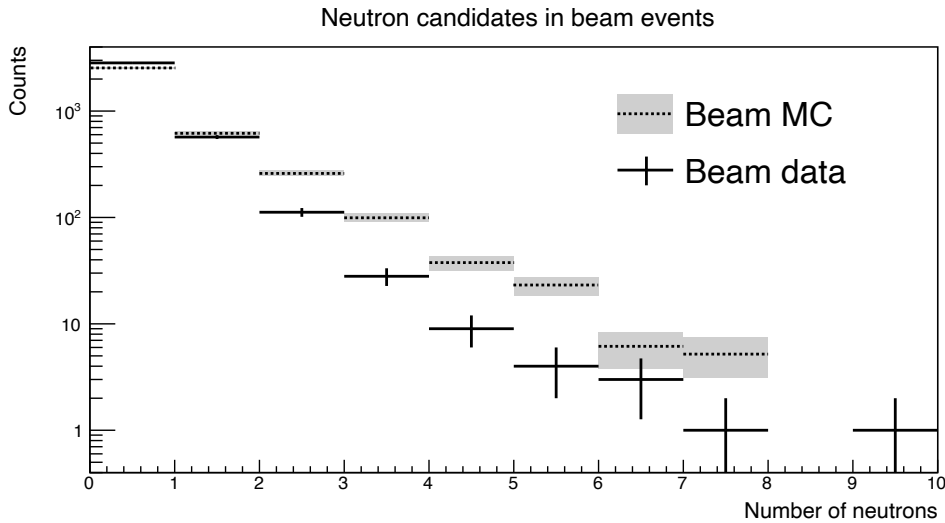


**Figure 6.27:** Neutron multiplicity distribution in data (*points with error bars*) and MC (*shaded areas*) for beam neutrino events featuring a stopping muon track in the MRD. No fiducialization has been applied in this case.

When comparing the measured behavior with the predicted distribution, it becomes clear that less neutrons are observed than expected. Particularly, the occurrence of high-multiplicity events with  $n_{\text{neutron}} \geq 2$  seems to be suppressed greatly with respect to simulations. For instance, the event category of two neutrons is observed more than 2 times less frequently in the measured data sample. Similar observations can be made for even higher multiplicity values. This seems to imply that the models overestimate the number of neutrons which are produced in neutrino interactions and within the subsequent hadronic interactions in the medium. When investigating the compatibility of the data histogram with the expected distribution, the distributions are found to be incompatible at a level of more than  $5\sigma$  ( $\chi^2/\text{n.d.f.} = 254.8/9$ ) and an associated  $p$ -value of  $p < 1 \cdot 10^{-7}$ . While this seems to be a rather significant discrepancy, one should note that this incompatibility will be less severe when including systematic errors in the final analysis.

The event sample can be further restricted by employing the simple interaction vertex reconstruction presented earlier and restricting the muons to originate in a small FV in the upstream region of the water tank. By doing so, the chance of a neutron not being detected is reduced significantly. In addition, the fraction of inelastic events that feature a pion is also diminished since such interactions will likely be characterized by a misreconstruction due to the increased light levels that are observed because of the additional Cherenkov light produced by the pions. The resulting multiplicity distributions for the data sample of muons originating in the FV and featuring a stopping track in the MRD is shown in figure 6.28. Equivalently to the previous figure, the measured distribution is represented as crosses while the simulated (model) prediction is shown as dotted lines with shaded error bar regions.

Similarly to the previous analysis, the models also tend to overpredict the number of produced neutrons for the subsample of events originating in the FV. More events with

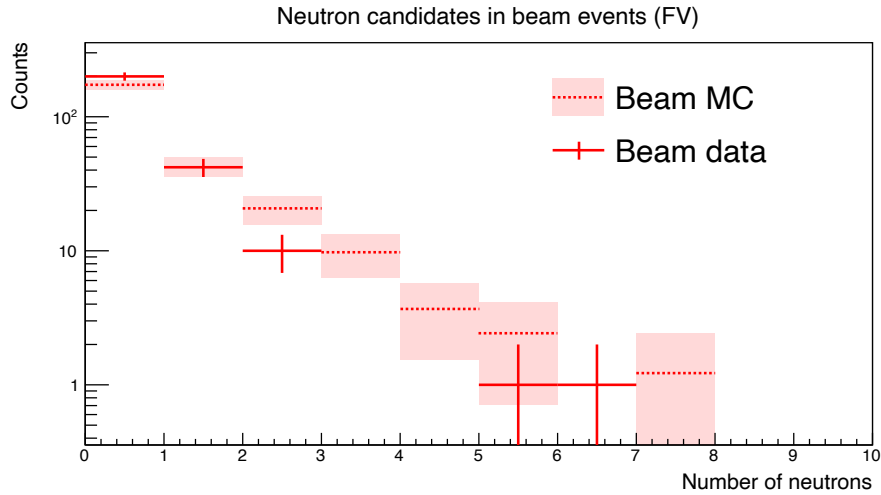


**Figure 6.28:** Neutron multiplicity distribution in data (*points with error bars*) and MC (*shaded areas*) for beam neutrino events featuring a stopping muon track in the MRD. Only events with a reconstructed muon vertex within the Fiducial Volume are selected in this case.

no associated neutrons are observed in the data while the frequency of 1-neutron-events agrees with the predictions. Higher multiplicity events (with  $n_{\text{neutron}} \geq 2$ ) are significantly suppressed in the data, with roughly a factor of two suppression for  $n_{\text{neutron}} = 2$  and no cases of three and four neutrons observed in the data due to limited statistics. The measured distribution is incompatible with expectations on a  $2.33\sigma$ -level ( $\chi^2/\text{n.d.f.} = 20.5/9$ ,  $p = 0.015$ ). It should be noted that also in this case the significance of the discrepancy is overestimated due to the missing systematic error estimation. Compared to the previous sample that only required stopping muon tracks in the MRD, the FV event sample however shows a less significant disagreement with respect to the predicted behavior.

When considering the average neutron yield  $\bar{n}$  per event, the systematically lower measured neutron numbers also become obvious. For the stopping MRD track sample, the predicted average yield of  $\bar{n}_{\text{MC}} = (0.515 \pm 0.007_{\text{stat}})$  needs to be contrasted with the measured multiplicity of  $\bar{n}_{\text{data}} = (0.272 \pm 0.010_{\text{stat}})$ . The average neutron multiplicities for the FV samples show similar discrepancies, with  $\bar{n}_{\text{FV,MC}} = (0.627 \pm 0.031_{\text{stat}})$  compared to  $\bar{n}_{\text{FV,data}} = (0.287 \pm 0.044_{\text{stat}})$ . While it is expected that the FV sample features a higher average neutron yield compared to the stopping muon track sample, this effect is currently only observed in simulations and not the data samples, for which compatible average neutron yields are observed. This behavior is currently not understood and needs to be revisited in future analyses with higher statistics.

## 6.5 COMBINED ANALYSIS - NEUTRON MULTIPLICITY AS A FUNCTION OF MUON KINEMATICS

The last stage of the neutron multiplicity analysis considered in the scope of this work is the evaluation of the neutron yield as a function of the muon kinematics. Such an approach can help to pinpoint which aspects of the theoretical models need to be improved in the future to achieve a better agreement with the observations and – in turn – provide a

more realistic representation of reality. In particular, the dependency of the muon energy and the muon angle with respect to the beam direction is evaluated. The first section 6.5.1 will briefly present the method of combining the data from the prompt and the delayed window and highlight the resulting distributions as a function of the muon energy and the muon angle for the case of data. The second section 6.5.2 will then feature a comparison of these combined distributions with the expected behavior based on simulations. In this context, it will be investigated whether some regions of the event parameter space feature a particularly large disagreement and need to be looked into more closely.

### 6.5.1 COMBINING THE PROMPT AND DELAYED EVENT ANALYSIS

The neutron yield of events can be evaluated in terms of prompt particle properties such as the muon energy  $E_\mu$  or the interaction angle  $\theta_\mu$  to allow an investigation of the multiplicity as a function of the event topology and interaction mechanism. While it would be preferable to obtain these dependencies also for generator-level variables such as the neutrino energy  $E_\nu$  or the momentum transfer  $Q^2$ , the associated errors for estimating said quantities in an unfolding procedure are quite large. It is hence usually considered more robust to determine the dependencies of the neutron multiplicity as a function of detector-accessible quantities such as the muon energy and the interaction angle and perform the comparison with the generators in a *forward-folding* approach, i.e. by inserting the interaction products predicted by the generators in a full simulation of the detector geometry and comparing the resulting distributions.

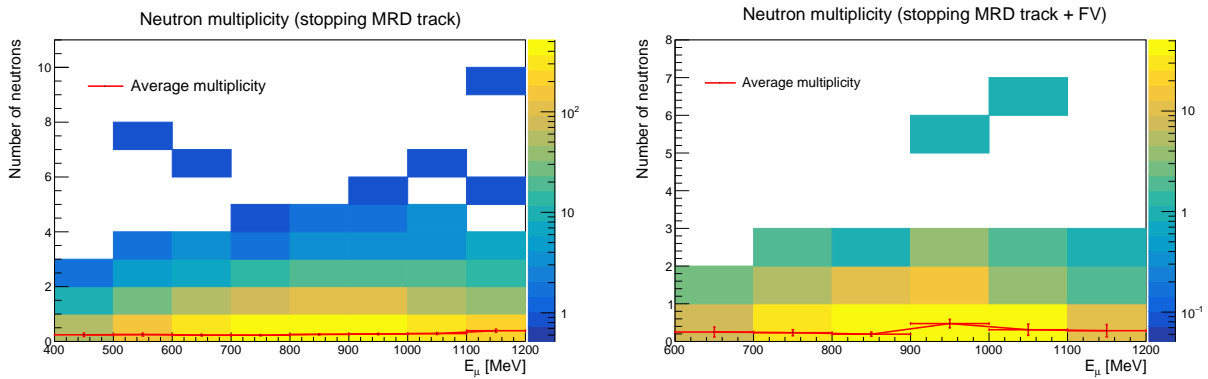
Within the analysis, neutrino candidates with an associated muon track in the MRD are identified in the prompt acquisition window of 2 microseconds according to the selection criteria mentioned previously in section 6.3.1. The muon properties for those events are then reconstructed by utilizing the event reconstruction tools highlighted in subsection 6.3.2. Afterwards, the neutron selection cuts are applied to a subset of the extended acquisition window between 10 and 70 microseconds to minimize the presence of afterpulsing contamination in the selected neutron sample. In the end, the number of identified neutrons  $n$  in the extended window is associated to the reconstructed muon properties  $\cos(\theta_\mu)$  and  $E_\mu$  in the prompt window in the form of two-dimensional correlation plots.

Figure 6.29 shows such a two-dimensional neutron multiplicity plot as a function of the muon energy for neutrino candidates with an associated stopping track in the MRD (*left*) and for events which additionally have a reconstructed interaction vertex inside of the FV of ANNIE (*right*). As expected from the integrated multiplicity distribution, neutron yields of up to 9 (6) neutrons are observed for the stopping MRD track (FV) sample. The majority of events are located in the bins with the lowest neutron multiplicity values while higher multiplicities are suppressed exponentially. Average neutron multiplicities  $\mu_i$  are calculated for each energy bin  $i$  and shown as red points with error bars in the plots. The uncertainty levels represent statistical errors and are estimated as the standard deviations  $\sigma_i$  of the multiplicity distributions for each energy bin. The frequency for observing a certain number of neutrons  $j$  for a given muon energy  $E_i$  will be denoted as  $n_{ij}$  in the

following. The average neutron multiplicities and uncertainty levels are then given by:

$$\mu_i = \frac{1}{N_{\text{total},i}} \sum_j^{N_{\text{bins},y}} j \cdot n_{ij}$$

$$\sigma_i = \sqrt{\frac{1}{N_{\text{total},i} - 1} \sum_j^{N_{\text{bins},y}} (n_{ij} \cdot (j - \mu_i)^2)}$$



**Figure 6.29:** The number of neutron candidates is shown as a function of the reconstructed muon energy for neutrino candidates in the considered data sample with a stopping track in the MRD (*left*) and for events which are additionally restricted to originate in the Fiducial Volume (*right*). Averaged values for the multiplicity are depicted in red for each energy bin .

The average neutron multiplicity distributions obtained this way are presented in figure 6.30 for both event samples as a function of the reconstructed muon energy. While the stopping muon track sample covers the energy region between 400 and 1200 MeV, the FV sample is restricted to energies starting from 600 MeV since the geometrical restriction imposes some boundaries on the minimum possible energy in this case. In both scenarios, average neutron multiplicity values on the order of 0.25 neutrons per neutrino candidate are observed. No strong energetic dependence is found in the considered energy region. Furthermore, no statistically significant deviation is found between the two event samples. One outlier with a higher average neutron yield value of roughly 0.5 neutrons per neutrino event is observed for the FV sample for the muon energy region between 900 and 1000 MeV, most likely due to the limited statistics of the FV sample.

In a similar fashion to the energy-dependent plot, the average neutron multiplicity distribution is shown as a function of the interaction angle in figure 6.31. The stopping MRD track sample covers the angular region described by  $\cos(\theta_\mu) \in [0.7, 1.0]$  while the FV sample is restricted to  $\cos(\theta_\mu)$ -values between 0.8 and 1.0 for geometrical reasons. A rather flat behavior is observed as a function of the interaction angle for the stopping muon track sample, with average neutron multiplicity values on the order of 0.3 neutrons per neutrino interaction across all considered angles. The FV sample displays comparable neutron multiplicities, with an upward fluctuation in the energy bin  $\cos(\theta_\mu) \in [0.8, 0.85]$  which can again most likely be attributed to the limited statistics of this particular data sample.

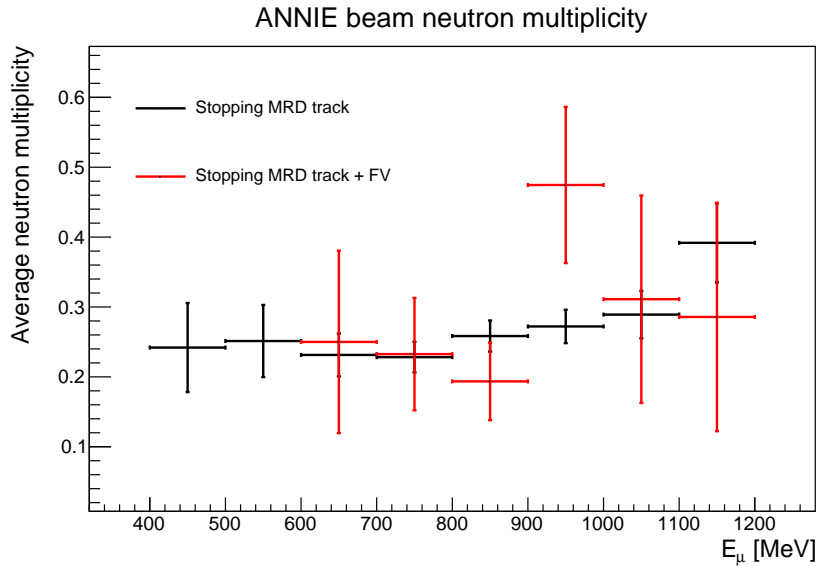


**Figure 6.30:** Average neutron multiplicity for beam neutrino interactions as a function of the reconstructed muon energy  $E_\mu$ . The neutron yield is depicted for two different event samples of interactions with a stopping muon track in the MRD (*black*) and for interactions which additionally originated in the FV (*red*). In general, the observed average neutron multiplicity values range between 0.2 and 0.5 for both samples.

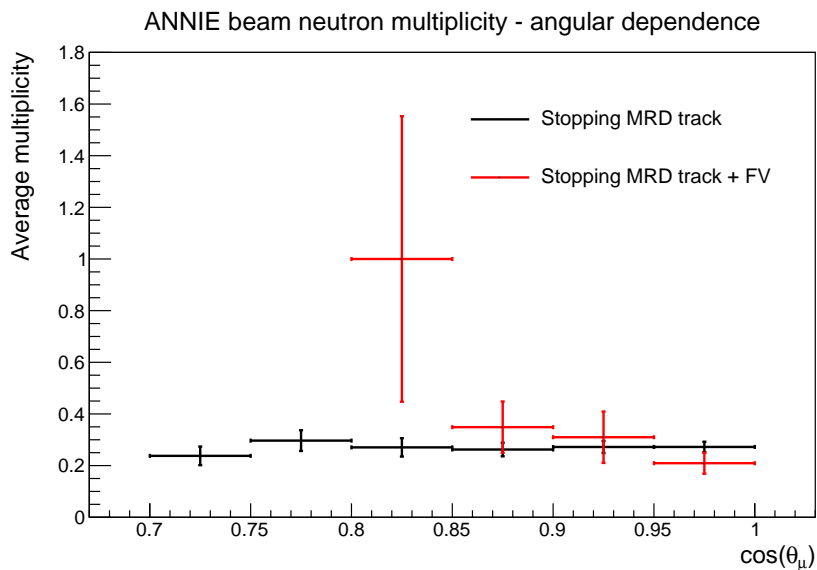


**Figure 6.31:** Average neutron multiplicity for beam neutrino interactions as a function of the reconstructed muon angle  $\cos \theta_\mu$  with respect to the neutrino (beam) direction. The neutron yield is depicted for two different event samples of interactions with a stopping muon track in the MRD (*black*) and for interactions which additionally originated in the FV (*red*).

## 6.5.2 COMPARISON WITH NEUTRON MULTIPLICITY IN SIMULATION

Similarly to the integrated neutron multiplicity distributions, the two-dimensional behavior of the neutron yield as a function of the muon kinematics can also be compared to the model predictions. In order to do so, the same event selection cuts are applied to the simulated beam neutrino sample as in the data case. The resulting distributions are shown in figure 6.32 as a function of the muon energy and in figure 6.33 as a function of the

interaction angle.

When considering the neutron multiplicity as a function of the muon energy, both the stopping MRD track sample (*left*) and the FV sample (*right*) can be considered in the comparison between data and the simulation. In the case of the stopping muon track sample, the model prediction for the neutron yield shows a rather flat behavior with consistently higher average neutron multiplicity values around 0.5 neutrons per neutrino interaction, compared to an average yield of  $\sim 0.25$  neutrons in the measured distribution. The model predictions for the FV sample also feature a rather flat distribution with average yields of roughly 0.6 neutrons per neutrino interaction, compared to approximately 0.3 neutrons in the case of data. The model therefore seems to predict a larger number of neutrons compared to the data for both considered event samples.

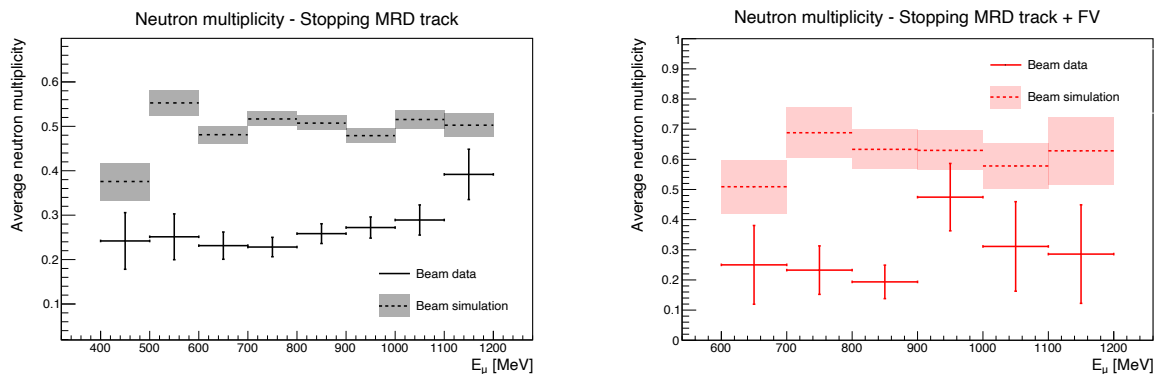


**Figure 6.32:** The average neutron multiplicity is shown as a function of the reconstructed muon energy for beam neutrino candidates with a stopping muon track in the MRD (*left*) and for events which additionally originated in the FV of ANNIE (*right*). The measured behavior is shown as solid lines and is compared to the model prediction (*dashed line*). On average, less neutrons are observed compared to expectations based on MC simulations.

When considering the dependency of the average neutron multiplicity as a function of the interaction angle, the simulations predict a flat behavior for both the stopping MRD track and the FV sample. While in the former case, average neutron multiplicity values of  $\sim 0.5$  are observed, the latter sample features average predictions around 0.6 neutrons per neutrino interaction. The observed measured distributions, on the contrary, are also flat but are characterized by lower average multiplicity values around 0.3 neutrons per neutrino interaction. The model hence also seems to predict a larger number of neutrons when considering the dependency of the interaction angle.

The observed deficit in the measured neutron yield is expected based on the findings from the integrated neutron multiplicity study shown in section 6.4.4. No strong dependency of the neutron yield deficit is found as a function of neither the interaction angle nor the muon energy. The shift to fewer observed neutrons seems to be present across the whole considered parameter space for both variables. The number of neutrons therefore seems to be overestimated in the simulation in general and not just for a particular region of the muon parameter space.

The Fiducial Volume in ANNIE was designed to maximize the acceptance for beam-related neutrons. Since neutrons produced in neutrino-nucleus interactions will be boosted in downstream direction, the neutrino interaction volume is restricted only to the upstream

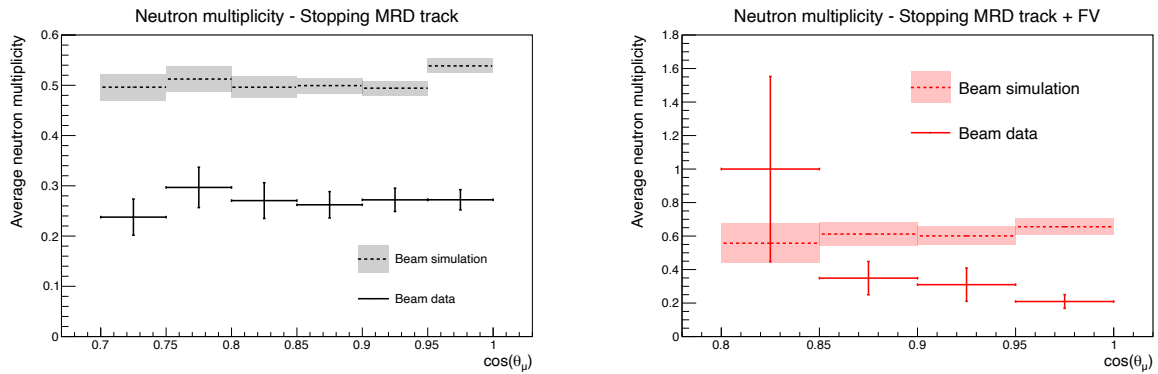


**Figure 6.33:** The average neutron multiplicity is shown as a function of the reconstructed muon angle with respect to the beam direction for beam neutrino candidates with a stopping muon track in the MRD (*left*) and events which additionally originated in the FV of ANNIE (*right*). The measured behavior is shown as solid lines and is compared to the model prediction (*dashed line*). On average, less neutrons are observed compared to expectations based on MC simulations.

region of the tank when applying the FV cut to maximize the available volume for the neutron detection in the Gadolinium-loaded water. This effect is clearly visible in the simulation in the sense that higher average neutron yields are observed in the scope of the Fiducial Volume sample compared to events which only feature a stopping muon in the MRD. However, the same effect is not observed in the data: In this case, the detected neutron multiplicity values are compatible between the two samples. This discrepancy is likely due to the currently rather low statistics of the FV sample in data and will potentially be less severe when moving to larger event statistics.

## 6.6 BRIEF OUTLOOK ON SYSTEMATIC UNCERTAINTIES

The current section will provide a brief consideration of possible systematic uncertainties for the presented neutron multiplicity measurement. While such errors were not studied in further detail in the scope of this thesis, they are currently being investigated by the collaboration and will be included in future analyses. For each systematic error, a possible path for studying the respective uncertainty is outlined in the following paragraphs, alongside some rough estimations for the order of magnitude of the errors.

Systematic uncertainties need to be considered both for the aspects of the kinematics of the prompt muon event and the measurement of the neutron yield itself. The muon reconstruction uncertainty is mostly dominated by the accuracy of the MRD track reconstruction, both with respect to the interaction angle and the muon energy. The neutron yield related systematic uncertainties comprise different factors: First of all, the Fiducial Volume selection introduces a systematic effect due to the resolution of the interaction vertex reconstruction. Furthermore, the slight FMV inefficiency introduces some dirt events into the selected neutrino candidate sample, which will skew the measured neutron multiplicity distribution. Lastly, the neutron detection efficiency might be slightly different in data and the MC, introducing an additional systematic error source to the measurement. Each source of systematic uncertainty will be discussed in more detail in the following.

## Muon reconstruction uncertainty

The muon reconstruction uncertainty of the simple reconstruction technique described in section 6.3.2 affects both the accuracy of the muon energy and the interaction angle estimate regarding events with a stopping track in the MRD, with  $\sigma_E \sim 120$  MeV (compare section 6.3.2) and  $\sigma_\theta \sim 0.17$  rad (compare section 4.3). As such, it introduces a systematic error in the x-axis bins of the two-dimensional neutron yield measurements.

These x-axis shifts can be represented in terms of migration matrices which describe the relation between the true and reconstructed variables in the form of two-dimensional correlation plots. Since the uncertainties of the energy and the interaction angle are assumed to be independent of each other, two separate migration matrices can be constructed for the two variables. Figure 6.34 shows the resulting migration matrices which are characterized by a linear correlation and some less likely occurrences of slightly more misreconstructed variables.

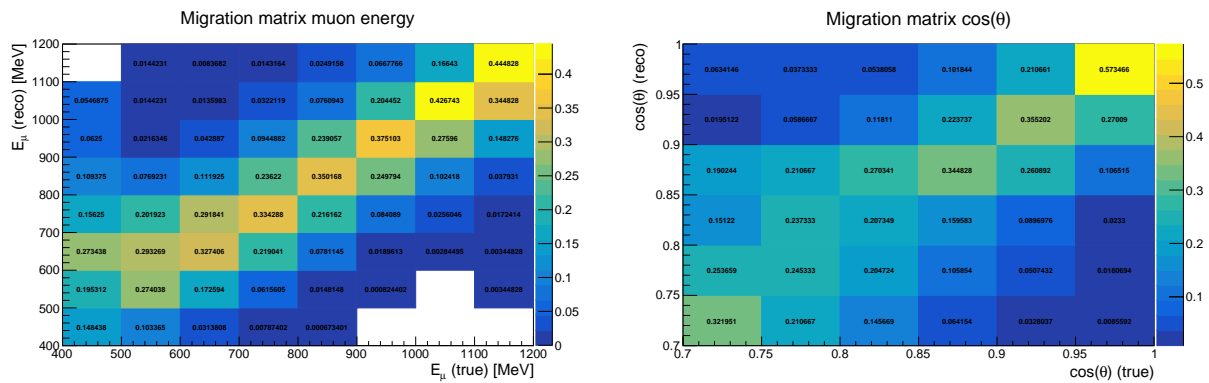


**Figure 6.34:** Migration matrices for the reconstructed muon energy (*left*) and the reconstructed interaction angle (*right*). The entries are normalized in such a way that the sum for each column is equal to 1. A clear linear correlation is visible in both cases.

Since the neutron multiplicity seems to remain rather flat both as a function of the muon energy as well as the interaction angle, the systematic effect related to the presented migration matrices is estimated to be rather small at the moment, but will be studied in greater detail in the future.

## Fiducial Volume selection

The resolution of the simple vertex reconstruction technique described in section 6.3.2 impacts which events are selected for the FV sample. In this context, the uncertainty in the reconstruction can lead to the event sample being contaminated with neutrino events that actually interacted outside of the FV. Similarly, some neutrino events that actually took place inside of the FV can be reconstructed to have originated outside of the volume. The systematic impact of this effect can be investigated by enlarging or shifting the Fiducial Volume within the water tank according to the reconstruction uncertainties. However, since the measured neutron yields of the Fiducial Volume sample are in quite good agreement with the multiplicities measured across the entire water tank, this particular systematic is estimated to be negligible in the scope of the current analysis, and will become more relevant when the statistical uncertainties are reduced in the future.

### FMV inefficiency - dirt muon contamination

As shown in section 4.2, the inefficiency of the FMV scintillator paddles to tag dirt events is less than 10 % when requiring a hit in either of the two veto layers to flag such occurrences. The impact of such a contamination of dirt events can be evaluated by examining the average number of produced neutrons in flagged dirt events ( $\bar{n}_{\text{dirt}}$ ) and considering the change in the average number of detected neutrons  $\bar{n}_{\nu}$ , when combining the neutrino sample with the flagged dirt sample in the corresponding fractions. Assuming a true number of neutrino events ( $N_{\nu}$ ) and a true number of dirt events ( $N_{\text{dirt}}$ ), the detected amounts of neutrino and dirt events are given by

$$\begin{aligned} N_{\nu,\text{det}} &= N_{\nu} + (1 - \varepsilon_{\text{FMV}}) \cdot N_{\text{dirt}} \\ N_{\text{dirt},\text{det}} &= N_{\text{dirt}} \cdot \varepsilon_{\text{FMV}} \end{aligned}$$

with  $\varepsilon_{\text{FMV}}$  corresponding to the efficiency of the FMV to successfully tag dirt events as such. The observed number of neutrons  $\bar{n}_{\nu,\text{det}}$  in neutrino candidate events can be decomposed into the average number of neutrons in true neutrino interactions ( $\bar{n}_{\nu}$ ) and the average neutron yield in dirt events ( $\bar{n}_{\text{dirt}}$ ) as

$$\bar{n}_{\nu,\text{det}} = \frac{N_{\nu} \cdot \bar{n}_{\nu} + (1 - \varepsilon_{\text{FMV}}) \cdot N_{\text{dirt}} \cdot \bar{n}_{\text{dirt}}}{N_{\nu} + (1 - \varepsilon_{\text{FMV}}) \cdot N_{\text{dirt}}}. \quad (6.14)$$

The average neutron yield  $\bar{n}_{\nu}$  for an uncontaminated neutrino sample is hence given by

$$\bar{n}_{\nu} = \frac{\bar{n}_{\nu,\text{det}} \cdot (N_{\nu} + (1 - \varepsilon_{\text{FMV}}) \cdot N_{\text{dirt}}) - \bar{n}_{\text{dirt}} \cdot (1 - \varepsilon_{\text{FMV}}) \cdot N_{\text{dirt}}}{N_{\nu}}. \quad (6.15)$$

The same neutron yield analysis procedure which was presented for the beam neutrino sample was applied to flagged veto events with a stopping track in the MRD, yielding an average neutron multiplicity value of  $\bar{n}_{\text{dirt}} = (0.113 \pm 0.010)$  for a set of  $N_{\text{dirt},\text{det}} = 1715$  veto events. This needs to be contrasted with the average number of neutrons in the neutrino candidate sample, for which  $\bar{n}_{\nu,\text{det}} = (0.272 \pm 0.011)$  and  $N_{\nu,\text{det}} = 3564$ . Assuming an efficiency of  $\varepsilon_{\text{FMV}} \sim 90\%$ , the true numbers of dirt and neutrino events are then given by  $N_{\nu} \sim 3373$  and  $N_{\text{dirt}} \sim 1906$ , resulting in an average neutron yield for the true neutrino sample of

$$\bar{n}_{\nu} = (0.281 \pm 0.012) \quad (6.16)$$

The difference of  $\bar{n}_{\nu}$  with respect to  $\bar{n}_{\nu,\text{det}}$  is representative of the systematic error related to the FMV inefficiency. In the case of the stopping MRD track sample, the neutron yield  $\bar{n}_{\nu}$  is assumed to represent the FMV-corrected neutron multiplicity value, incorporating the systematic difference of  $\sigma_{\text{sys,FMV}} = 0.009$ .

The effect of the dirt muon contamination can be considered to be much lower in the case of the FV sample compared to the stopping MRD track sample since the reconstruction of the event vertex inside of the water tank already poses a strong constraint on the possible points of origin for the muon, making it much less likely to have originated outside of

the water tank. The systematic effect of the FMV inefficiency on the average number of detected neutrons is hence considered to be negligible for the FV sample.

### Neutron detection efficiency

The neutron detection efficiency is a vital input parameter for the determination of the neutron multiplicity and has been mapped out as a function of the position within the water tank in the scope of the AmBe calibration campaign, as discussed in more detail in section 5.4.3. Slight differences in the modeling of the neutron capture and the PMT response might result in systematic differences of the neutron selection cut efficiency and as such influence the resulting neutron yield distributions. The associated systematic shift can be estimated as a function of the vertex within the tank by comparing the neutron detection efficiency for the different positions of the AmBe calibration campaign between data and the simulation. Each position of the AmBe source was simulated in the scope of the Geant4-based WCSim ANNIE simulation framework which was presented in section 5.4.4.

While the efficiency determination requires a rather sophisticated analysis procedure in the case of data to deal with background contamination (as discussed in more detail in reference [215]), the fact that the MC sample is background-free warrants an easier analysis approach in which the efficiency  $\varepsilon(p,z)$  for a given port  $p$  and height  $z$  is simply given by the number of events that pass the selection cuts ( $N_{\text{pass}}$ ) divided by the total number of simulated events ( $N_{\text{events}}$ ):

$$\varepsilon(p,z) = \frac{N_{\text{pass}}(p,z)}{N_{\text{events}}(p,z)}. \quad (6.17)$$

When performing such a simple efficiency estimate for the simulated AmBe samples, the resulting efficiency map for the different positions within the tank is shown in figure 6.35 on the left while the corresponding distribution for the data AmBe campaign is shown on the right side of the same plot. Cluster times in the simulation were restricted to the time window  $t_{\text{cluster}} \in [2, 67] \mu\text{s}$  to be conform with the efficiency calibration performed on the data sample. Both the data and MC efficiency maps are currently still preliminary and subject to changes while the analysis procedures are refined. As a consequence, also the presented considerations related to the associated systematic uncertainty should be considered rather preliminary.

While in general the agreement between the neutron detection efficiencies in the data and the MC is quite reasonable, the simulation seems to feature higher efficiency values for a number of vertices, in particular when considering ports 1 and 5. Looking at the absolute efficiencies, differences on the order of 10% are observed, corresponding to relative differences on the order of 20%. Ports 2, 3 and 4, on the contrary, feature efficiency values which are more compatible between data and the simulation. When considering all positions within the tank, an average relative efficiency difference of  $\sim 9\%$  is present, which can be used to calculate a first estimate of the associated systematic uncertainty. When correcting the observed neutron multiplicity distribution in the MC with this reduction factor, the average neutron yield is reduced from  $\bar{n}_{\text{MC}}(\text{nominal}) = (0.515 \pm 0.007_{\text{stat}})$  to  $\bar{n}_{\text{MC}}(\text{reduced}) = (0.469 \pm 0.007_{\text{stat}})$  for the stopping muon track

sample. This corresponds to a systematic uncertainty of  $\sigma_{\text{sys,eff}} \sim 0.046$  or a relative uncertainty of  $\sigma_{\text{sys,eff}}(\text{rel}) \sim 9\%$ . The fact that the simulation generally features higher efficiency values will result in asymmetric error bars and slightly reduce the tensions between the simulation and the data.

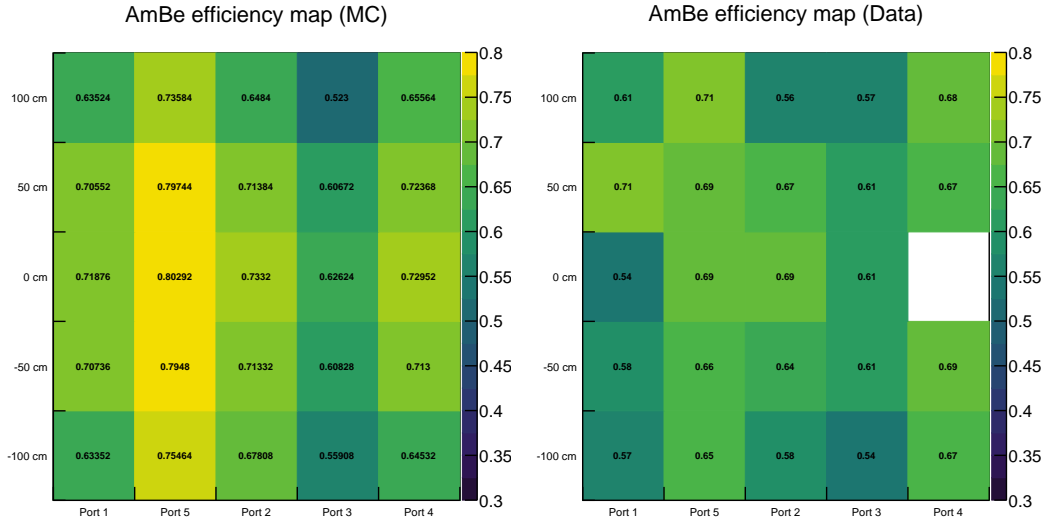


**Figure 6.35:** Neutron detection efficiency as a function of the AmBe source position in the water tank for the simulated case (*left*) and the measured values (*right*) in the time window  $t_{\text{cluster}} \in [2, 67] \mu\text{s}$ . The preliminary data version of the plot was provided as a courtesy of Leon Pickard and the calibration working group. For some ports, the simulation features higher detection efficiencies, with absolute efficiency differences on the order of 10%. Both the data and the MC efficiency maps are currently still preliminary and subject to change in the scope of refined analysis approaches.

Looking ahead, the spatial dependencies of the neutron detection efficiency differences would need to be considered more rigorously by repeating the analysis on the simulated sample a few times and applying position-dependent efficiency correction factors that take into account the slight differences in the neutron detection efficiency. The deviations of these modified analyses from the result on the nominal MC would then serve as an estimate for the systematic uncertainty.

Future analyses of the neutron multiplicity will investigate more restricted event topologies by applying the event classification technique of ring counting in order to obtain a set of events that resembles a pure CC-QE-sample more closely. This CC- $0\pi$  sample will be able to probe Final State interactions more directly without the interference of more inelastic channels such as CC-RES. Furthermore, future analyses will also make use of larger event statistics and better reconstruction techniques and hence reduce the associated uncertainties with respect to these aspects.

## Part IV

### FUTURE APPLICATIONS



# 7

## Detecting the Diffuse Supernova Background in next-generation neutrino experiments

---

*“Remember to look up at the stars  
and not down at your feet.”*

—Stephen Hawking

Core-Collapse Supernovae (CCSN) are very fascinating and violent phenomena that can occur at the end of the lifetimes of larger stars ( $M > 8M_{\text{solar}}$ ) [238]. Within such events, the star collapses under the pressure of its own gravity and subsequently emits a shockwave of star material and particles, leaving only a supernova remnant behind. Depending on the initial size of the star, this remnant can either be a neutron star or a black hole. Due to their small interaction cross-section, neutrinos carry almost all the energy ( $f_\nu \approx 99\%$ ) of the shockwave explosion since they are the only particles capable of early penetration of the surrounding opaque layers of the shockwave. The detection of neutrinos from such a supernova hence provides powerful insights into the details of the supernova explosion mechanism. Moreover, the detection of neutrinos can serve as an early warning system for other types of particle detectors, such as optical telescopes. Since the neutrinos are emitted before all other particles, they will arrive earlier on Earth and their detection hence provides enough time to correctly orient other telescopes in the direction of the neutrino signal. This has led to the formation of the *Supernova Early Warning System (SNEWS)* by multiple neutrino experiments, which combines the information from multiple experiments to issue live alerts based on coincident supernova-like event signatures in multiple detectors [239].

Multiple currently operating neutrino detectors (Borexino, Super-K, SNO+, KamLAND, among others) are capable of detecting such a supernova neutrino signal. The major problem for a detection is the stochastic nature of the supernova occurrence: the experimentalists have to wait patiently for the next one to take place. So far, the neutrino community has not been lucky in this regard: Since the first Galactic supernova was

detected in 1987 by several neutrino detectors (Baksan, Kamiokande II, IMB), no further Galactic supernova has been observed. Similar explosions in neighboring galaxies are very hard to detect due to their fainter signal, although it will be possible to detect supernovae from even further away with next-generation neutrino detectors like Hyper-Kamiokande being able to discriminate different supernova models up to a distance of 100 kpc [240].

Instead of waiting for the next supernova to occur, another interesting signal is the Diffuse Supernova Background (DSNB). It is a continuous signal of all past supernova explosions that occurred throughout the observable universe. In contrast to a single CCSN explosion, this integrated signal should be present at all times and hence detectable without the need for a supernova to take place in the Galactic region. The following chapter will explore the potential to detect this rather faint signal in water Cherenkov detectors with upgrades of current detectors (such as SuperK-Gd) and next-generation neutrino experiments like Hyper-Kamiokande(-Gd). The chapter will start with an overview of the Diffuse Supernova Background in section 7.1 before introducing all relevant backgrounds in the next section 7.2. Among those backgrounds, NCQE reactions of atmospheric neutrinos are the most prominent ones and can potentially be well distinguished from real DSNB interactions. Both the DSNB and atmospheric NCQE events were therefore simulated in a Super-Kamiokande-like detector geometry, with more information provided in section 7.3.2. The classification potential was explored with a Convolutional Neural Network (CNN), as described in more detail in section 7.4. The chapter closes with a short discussion on potential NCQE measurements in the scope of ANNIE in section 7.5. While there are already multiple cross-section measurements on water available from Super-K and T2K [181, 182], it would be beneficial to conduct an additional measurement with an independent detector setup like ANNIE.

The presented study has also been published in the scope of a paper called *CNNs for enhanced background discrimination in DSNB searches in large-scale water-Gd detectors* [241], written in collaboration with David Maksimović and Michael Wurm. The following discussion puts a larger focus on the simulation part and modeling of the interactions which was the main focus of my contribution, while the presented classification results were conducted by David Maksimović and are presented more briefly. The last section of the chapter 7.5 extends beyond the scope of the material presented in the paper and explores the promising role of ANNIE for the future of DSNB measurements by measuring the cross-section and neutron multiplicity of a NCQE sample for an atmospheric-like neutrino sample.

## 7.1 THE DIFFUSE SUPERNOVA BACKGROUND (DSNB)

Due to its rather low flux, the DSNB signal is only detectable by measuring the integrated signal for a rather long time frame of ten years or more. Up until now, there only exists an upper limit for the DSNB flux from Super-Kamiokande. The limit is energy-dependent and varies between

$$\phi_{\text{DSNB}} \leq (1 - 30) \text{ cm}^{-2} \text{ s}^{-1} \text{ MeV}^{-1} (90\% \text{ CL}) \quad (7.1)$$

in the prompt energy window between 14 and 30 MeV [242, 243].

This current upper limit on the flux is roughly a factor of two larger than the predicted flux of the DSNB signal [142]. However, an important reason for the rather high upper bounds of the Super-K limit were created by the very low neutron tagging efficiency in the pure water medium of the experiment. The current data taking phase of Super-Kamiokande with Gadolinium (SuperK-Gd) will be much more sensitive to the DSNB signal due to more efficient background rejection and might hence be able to provide the first detection of the signal. The presented study therefore focuses on such a detector setup due to its potential for a first measurement of the Diffuse Supernova Background. All findings can however also be applied to next generation experiments like Hyper-Kamiokande in case a larger target mass is necessary for a successful detection.

The following section focuses on a mathematical description of the expected DSNB signal, primarily based on the considerations presented in the detailed review by John Beacom in reference [244]. Due to the large cross-section and the excellent tagging capabilities, the following considerations will be applied to the expected antineutrino signal in the context of the Inverse Beta Decay detection mechanism. The expected flux of electron antineutrinos ( $\bar{\nu}_e$ ) is calculated by integrating the expected supernova rate  $R_{\text{SN}}(z)$  over all observable redshifts  $z$ :

$$\frac{d\phi}{dE_{\bar{\nu}_e}}(E_{\bar{\nu}_e}) = \frac{c}{H_0} \int_0^{z_{\text{max}}} R_{\text{SN}}(z) \cdot \varphi(E_{\bar{\nu}_e}(1+z)) \frac{dz}{\sqrt{\Omega_\Lambda + \Omega_M(1+z)^3}}. \quad (7.2)$$

Within the equation, the flux  $\varphi$  of a single supernova explosion is included as a function of the energy of the electron antineutrinos, adjusted by their respective redshift  $z$ . In addition, the cosmological parameters of the Hubble constant ( $H_0$ ), the energy density of dark energy ( $\Omega_\Lambda$ ) and the energy density of matter ( $\Omega_M$ ) are present in the equation.

As a very simple estimate, the neutrino spectra for individual supernovae can be assumed to follow a Fermi-Dirac spectrum with a certain temperature  $T$ . For this study, we will use a more sophisticated prediction of the supernova fluxes as presented in the reference of Kresse *et. al* [245]. In their calculations, the supernova spectra are modeled based on the simulated emission spectra of supernovae of different progenitor stars in the mass range  $M_{\text{progenitor}} = (9-120) \cdot M_{\text{solar}}$ . Within these simulations, so-called "failed supernovae" that result in black hole formation with no light emission are included. The predictions include some variability due to uncertainties in the modeling such that a broad band of fluxes is included. A so-called "fiducial model" serves as the mean prediction between the minimum and maximum allowed flux lines and will be used as the nominal model in our study.

The DSNB flux  $\frac{d\phi}{dE_{\bar{\nu}_e}}$  can be converted into the rate of positron events  $\frac{dN}{dE_{e^+}}$  in a detector by taking into account the number of protons within the whole detector ( $N_p$ , proportional to the target mass) and the cross-section of the Inverse Beta Decay process  $\sigma_{\text{IBD}}$ :

$$\frac{dN}{dE_{e^+}} = \frac{d\phi}{dE_{\bar{\nu}_e}}(E_{\bar{\nu}_e}) \cdot \sigma_{\text{IBD}}(E_{\bar{\nu}_e}) \cdot N_p. \quad (7.3)$$

For the rate calculation, we assume the number of free protons within Super-K-Gd to be  $N_p \approx 1.5 \cdot 10^{33}$  based on the 22.5 kt fiducial target mass. Moreover, the Inverse Beta Decay

cross-section was implemented based on value used in Beacom’s review [244]. Figure 7.1 shows the resulting rates of positrons in a Super-K-like detector geometry for the fiducial model of the previously presented DSNB prediction (*black line*). The upper and lower bounds of the predicted rates (*dashed grey lines*) result from the variability of the DSNB flux models, indicating how the event rates differ for the most extreme cases of the lowest and highest DSNB flux prediction limits.

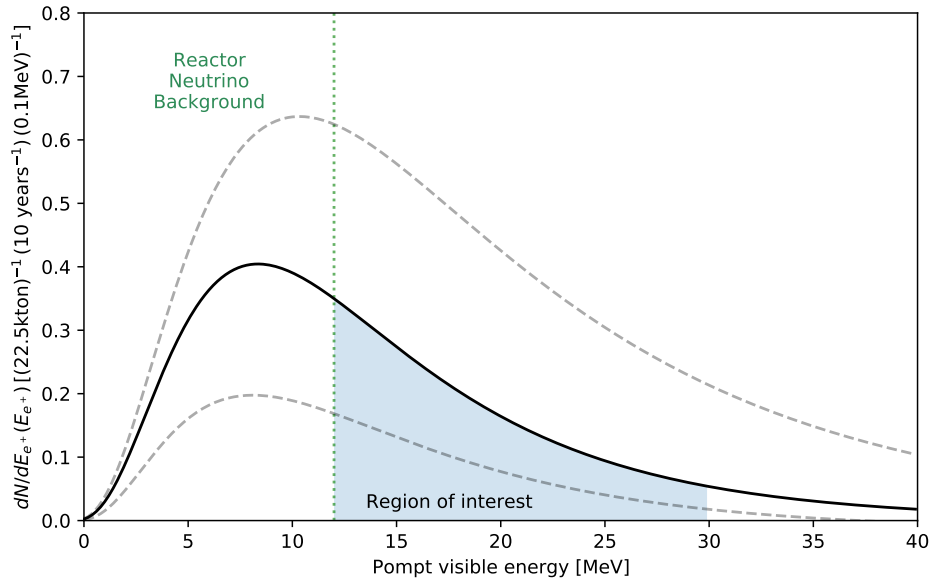


**Figure 7.1:** Prompt visible energy spectrum of the DSNB signal as predicted by *Kresse et al* [245]. The solid black line shows the predicted event rate for the mean flux model, while the dotted grey lines highlight the upper and lower event rate boundaries, defined by the upper and lower bounds on the DSNB flux model. The region of interest for the DSNB measurement between 12 MeV and 30 MeV is highlighted in blue.

The region of interest for a DSNB search (indicated as the blue region in the plot) is limited to a small visible energy region between  $E_{\min} \approx 12$  MeV and  $E_{\max} \approx 30$  MeV due to overwhelming backgrounds in other regions. Below the minimum visible energy of 12 MeV, reactor antineutrino reactions dominate over the DSNB signal. Due to the exact same interaction channel and consequently identical event signature, those events are indistinguishable from DSNB neutrino reactions and hence pose an irreducible background. For the energy region above 30 MeV, the electron antineutrino component of the atmospheric flux starts to prevail over the DSNB signal, leaving only the window between 12 and 30 MeV for a DSNB search.

Within the region of interest, a total of 2 IBD events per year are expected for the considered detector volume of 22.5 kt in the case of the fiducial DSNB model, while only 0.9 events are expected for the lowest flux prediction and 4.9 events per year would be achieved for the upper bound of the flux prediction. All the presented event rates already incorporate a neutron tagging efficiency of 67% for selecting events with exactly one neutron, which is expected for a loading of 0.1% mass fraction of Gadolinium [246]. The exact tagging fraction depends on the final loading of Super-K-Gd and might be slightly lower in case that less Gadolinium is mixed into the water.

The much improved neutron detection efficiency in a Gd-loaded detector environment is key for a successful DSNB search since it significantly reduces backgrounds which are more likely to either include no neutron at all or multiple neutrons. However, there are still some backgrounds that need to be taken into account which will be presented in the following section 7.2, namely the Neutral Current component of the atmospheric neutrino flux as well as invisible muons created in spallation reactions.

## 7.2 BACKGROUNDS FOR THE DSNB SEARCH

The region of interest for the DSNB search was selected in a way to minimize the presence of the irreducible backgrounds of reactor neutrinos in the region below 12 MeV and Charged Current reactions of atmospheric electron antineutrinos in the visible energy region above 30 MeV. However, there are still important backgrounds within this specific energy window. First of all, atmospheric neutrinos reacting via NC interactions can mimic the IBD event signature by knocking out neutrons in combination with de-excitation processes of oxygen nuclei. The discrimination between this event signature and actual DSNB events is the main focus of this study and will be investigated in terms of the classification power of a Convolutional Neural Network in the later sections. A more detailed description about these atmospheric NC interactions is given in this chapter, with atmospheric neutrinos being highlighted in section 7.2.1 before introducing the Quasi-Elastic component of the NC background in section 7.2.2 and the pion-related NC background in section 7.2.3. Besides the atmospheric NC background, another background source is introduced by so-called "invisible muons", which are presented in more detail in section 7.2.4. While this background component is also highly relevant for the DSNB search, a differentiation between this component and actual DSNB events is not really possible based on the observed event hit patterns and therefore not included in the presented classification study.

### 7.2.1 ATMOSPHERIC NEUTRINOS

Atmospheric neutrinos are a continuous source of neutrinos produced by interactions of cosmic ray particles in the atmosphere. From the variety of particles produced in the showering process of these cosmic rays, pions and muons are the most important components for the production of neutrinos. Since muon neutrinos are generated both in decays of pions as well as in muon decays while electron neutrinos are only produced in the latter process, the final flavor ratio of atmospheric neutrinos roughly corresponds to  $\nu_e : \nu_\mu : \nu_\tau \sim 1 : 2 : 0$ .

The exact energy-dependent flux spectra of the different neutrino flavors are predicted based on simulations with the FLUKA Monte Carlo code [247]. Based on models of the primary cosmic ray composition, three-dimensional simulations of the particle interactions within the atmosphere were carried out in reference [248]. After simulating the hadronic interactions and subsequent secondary processes, predictions for the absolute atmospheric neutrino fluxes are obtained. The resulting spectra for electron and muon (anti)-neutrinos are depicted in figure 7.2 on the left. The muon component dominates the electron

component by roughly a factor of two, as pointed out above. The anti-neutrino components behave similarly to their neutrino counterparts, and exhibit only slightly lower fluxes. These flux predictions are used as direct input parameters for the GENIE event generation process, which will be presented in some more detail in section 7.3.2. The detector medium is assumed to be water and interactions are restricted to Neutral Current Quasi-Elastic (NCQE) ones, resulting in the interaction rates which are shown on the right of figure 7.2. Due to the larger cross-section of NCQE interactions of neutrinos compared to anti-neutrinos [249], the interaction rates are significantly lower for the antineutrino case. This goes as far as pushing the interaction rates of the muon anti-neutrino component below the curve of electron neutrinos for the majority of the spectrum. The step-like structure of the interaction rate spectrum is introduced by the binning of the FLUKA input fluxes, and is not expected to influence the results significantly.

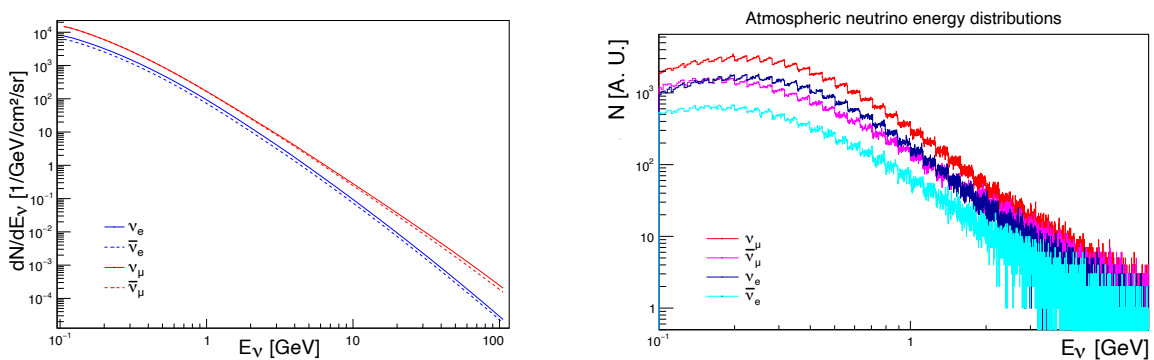


**Figure 7.2:** Left: Atmospheric neutrino fluxes, with values taken from FLUKA atmospheric flux calculations [248]. Right: Interaction rates of different neutrino flavors after propagating neutrinos according to the FLUKA flux files through GENIE.

## 7.2.2 ATMOSPHERIC NCQE BACKGROUND

The coincidence signal of the Inverse Beta Decay in the case of real DSNB event can be imitated by a Neutral Current reaction of atmospheric neutrinos by a combination of knock-out nucleons and de-excitation gammas. De-excitation gammas are emitted from excited states of nuclei either produced in the primary neutrino-nucleus interaction of the atmospheric neutrino or in ensuing secondary reactions of the nucleons in the surrounding detector medium. These gammas can produce similar levels of visible light as the positron produced in the IBD reaction of a DSNB anti-neutrino. They can therefore mimic the prompt event signature of the DSNB event. At the same time, the delayed neutron capture signal can be imitated in case the knocked out nucleon in the NCQE reaction was a neutron. Furthermore, inelastic scattering processes of nucleons with other oxygen nuclei in the medium can also produce neutrons. Although the rather large energies of the atmospheric neutrinos lead to rather violent processes with often many neutrons, it still happens quite often that only one neutron is detected, providing the same coincidence signature as a real DSNB event. This chapter provides some more details about the employed modeling of de-excitation gammas and knock-out nucleons, which are vital for obtaining the final simulation sample.

## Nuclear shell approximation of oxygen nuclei

In the rather simple *nuclear shell* approximation of an oxygen nuclei, the different nucleons in the nucleus are located on different shells in the nucleus which correspond to different energy levels, similarly to the case of the atomic shell model. The main energy levels in the case of oxygen are the ( $1p_{1/2}$ ), ( $1p_{3/2}$ ), and ( $1s_{1/2}$ ) levels, occupying 2, 4, and 2 neutrons and protons respectively. In the case that a neutrino interacts with a nucleon  $N$  and knocks it out, the residual nucleus  $X_\alpha$  is potentially in an excited state and in turn decays via the emission of a photon:



Assuming  $X_\alpha$  denotes an excited state of the nucleus  $X$ , the cross-section for associated decay into a final nucleus  $Y$  alongside the emission of gammas needs to take into account the Branching ratio  $\text{BR}(X_\alpha \rightarrow \gamma + Y)$  for gamma-accompanied decays [249]:

$$\sigma_\gamma = \sigma(\nu + {}^{16}\text{O} \rightarrow \nu + Y + \gamma + N) \quad (7.5)$$

$$= \sum_\alpha \sigma(\nu + {}^{16}\text{O} \rightarrow \nu + X_\alpha + N) \text{BR}(X_\alpha \rightarrow \gamma + Y) \quad (7.6)$$

The nucleons in the oxygen nucleus have different removal energies depending on the shell they are located on. For protons, those energies roughly correspond to 12.1 MeV ( $1p_{1/2}$ ), 18.4 MeV ( $1p_{3/2}$ ), and a more diffuse region between 20 and 60 MeV with a peak around 40 MeV for the ( $1s_{1/2}$ ) shell [250]. For neutrons, the removal energies are shifted to slightly higher values by 3.54 MeV [251]. Figure 7.3 illustrates the distribution of the removal energies for both neutrons and protons, where the peaks of the  $p$ -related shells as well as the more diffuse distribution of the  $s$ -shell are immediately apparent. On the right side of the same figure, the different energy levels and occupations are illustrated in a schematic potential well representation, with neutrons depicted in blue and protons shown in red.

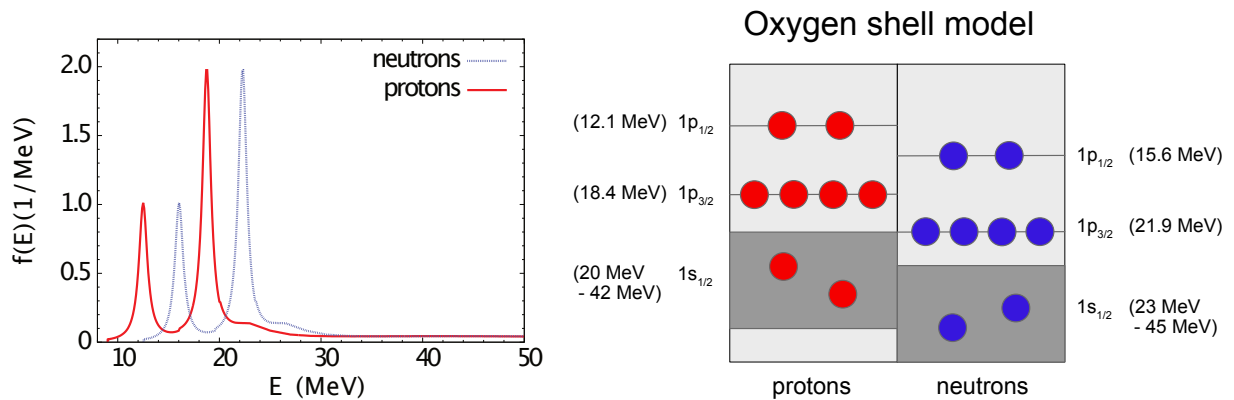


**Figure 7.3:** Left: Removal energy distribution for protons (red) and neutrons (blue) in a  ${}^{16}\text{O}$  nucleus [249]. The two large peaks correspond to the ( $1p_{1/2}$ ) and ( $1p_{3/2}$ ) shells, while the washed out distribution for higher energies is associated to the ( $1s_{1/2}$ ) shell. Right: Schematic depiction of the energy levels of an oxygen nucleus in the nuclear shell model.

The probability to knock out a nucleon of a specific shell  $\alpha$  can be expressed in terms of so-called spectroscopic strength functions  $S_\alpha$ . These spectroscopic factors were summarized

first in the work by Ejiri in 1993 [252] based on proton pickup reactions on deuterium and proton knock-out reactions on oxygen nuclei. The determined factors were  $S(1p_{1/2}) = 2$  for the ground state,  $S(1p_{3/2}) = 3.83$  for the first excited state, and  $S(1s_{1/2}) = 2$  for the continuous  $s$ -shell excitation states. Based on a total number of 8 nucleons of each type, these factors correspond to branching ratios of  $BR(1p_{1/2}) = 0.25$ ,  $BR(1p_{3/2}) = 0.47$ , and  $BR(1s_{1/2}) = 0.25$ , respectively for the different shells. While the knock-out from a ground state is not associated with any de-excitation gammas, the  $1p_{3/2}$  state can result in excited energy levels of 6.32 MeV, 9.93 MeV, and 10.7 MeV, of which the first two are accompanied by de-excitation gammas. Knock-outs from the  $s$ -shell result in excitation energies between roughly 20 and 40 MeV, enabling emissions of nucleons and alpha-particles in addition to gamma de-excitation. Only a small percentage of  $s_{1/2}$ -holes are accompanied by de-excitation gammas, especially when considering the particularly interesting more high-energetic gammas above 3-4 MeV.

After the initial considerations by Ejiri, further measurements were conducted by Leuschner *et. al* in the scope of an electron-oxygen scattering experiment at NIKHEF-K which revealed that the spectroscopic strengths were actually smaller than previously expected [253]. These new findings indicated that the factors were rather around 63% (68%) of the previous estimate for the case of the  $1p_{1/2}$  ( $1p_{3/2}$ ) state, as highlighted in table 7.1. Similar results are obtained when integrating the excitation energy curves from the paper by Ankowski *et. al* that were presented earlier in figure 7.3, resulting in reduction factors of 63%, 70%, and 44% for the spectroscopic strengths of the ( $1p_{1/2}$ ), ( $1p_{3/2}$ ), and ( $1s_{1/2}$ ) shells. The discrepancy between the original factors obtained with ( $d, ^3\text{He}$ ) and the subsequent measurements with ( $e, e'p$ ) reactions can be traced back to problems in the original theoretical modeling of the deuterium pickup reactions. When including non-locality and finite-range corrections in the original Distorted Wave Born approximation calculations alongside a more realistic model of the bound-state wave function, a consistent reduction of the spectroscopic factor is also observed for the original ( $d, ^3\text{He}$ ) measurements [254]. For our atmospheric neutrino background sample, the smaller spectroscopic strengths simply result in a smaller absolute rate of background events. In the following subsection, a more detailed emphasis will be put on the particular modes containing an associated de-excitation gamma, alongside the exact energy values and branching ratios for the various gamma rays.

Nuclear Shell	Ejiri	Leuschner et.al	Ankowski et.al
$1p_{1/2}$	0.25	0.16	0.16
$1p_{3/2}$	0.47	0.31	0.33
$1s_{1/2}$	0.25	-	0.11

**Table 7.1:** Branching ratios of knock-out states for proton holes in  $^{16}\text{O}$ , as predicted by Ejiri [252], Leuschner *et. al* [253] and Ankowski *et. al* [249]. The branching ratios represent the spectroscopic factor  $S_\alpha$  divided by the total number of each nucleon (8) within an oxygen nucleus,  $BR(\alpha) = S_\alpha/8$ .

### Measurements of de-excitation gammas in oxygen scattering experiments

Although a large variety of de-excitation channels exists, only the ones with associated gamma rays are of particular importance in the scope of modeling the background for a

DSNB search. The following section will provide an overview of the most important decay modes, their branching ratios and energy levels.

In the case that a nucleon is knocked out of the ground state shell ( $1p_{1/2}$ ), no de-excitation gamma is emitted. A ( $1p_{3/2}$ ) hole, on the other hand, leads to a de-excitation gamma of 6.32 MeV in 87.2% of cases, and to a 9.93 MeV photon with a probability of 6.4%. In the remaining instances (6.4%), the resulting residual nucleus  $^{15}\text{N}$  resides in an excited state of 10.7 MeV with no gamma emission, and rather emits a nucleon instead.

When considering the  $s$ -hole state, more variations are possible in the de-excitation of the residual nucleus, with excitation energies of up to 60 MeV being accessible. Since these excitation energies are above the particle emission threshold, the emission of nucleons and nucleon-compound particles such as deuterons and tritons becomes possible. In the context of such nucleon emission processes, the residual nucleus can end up in an excited state, giving rise to de-excitation gamma emissions. Such excited energy levels of residual nuclei are depicted schematically in figure 7.4 on the right. Starting from an  $s$ -hole state in  $^{15}\text{N}$ , the particle emission of a neutron, proton, deuteron or triton leads to the residual nuclei  $^{14}\text{N}$ ,  $^{14}\text{C}$ ,  $^{13}\text{C}$ , and  $^{12}\text{C}$ . For each of the residual nuclei, possible states with photon de-excitation are shown as solid lines, while the dotted lines depict the thresholds for particle emission in the respective residual nucleus (above which no gammas will be emitted).

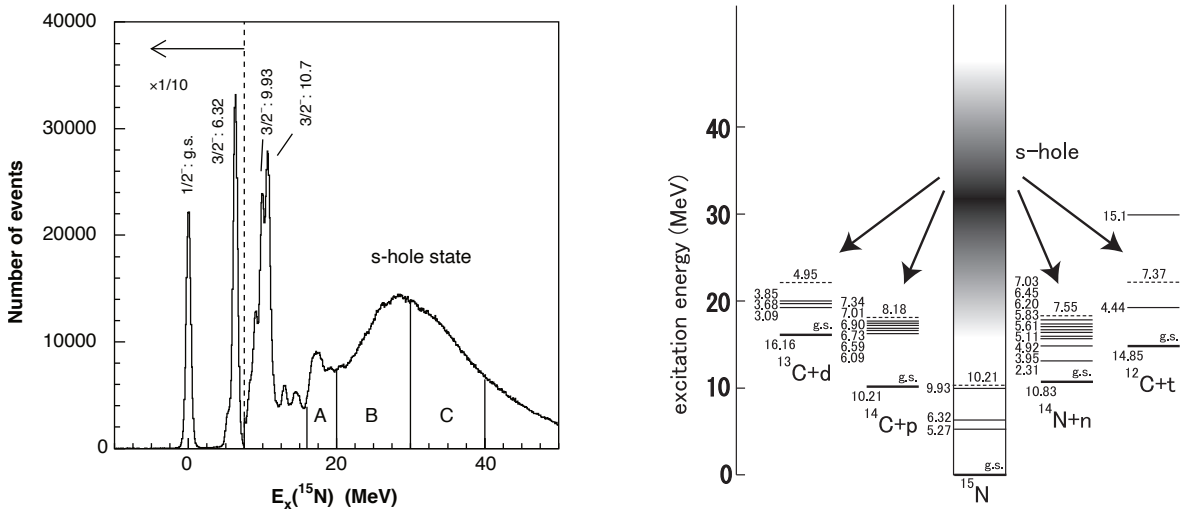


**Figure 7.4:** Left: Excitation energy levels of  $^{15}\text{N}$  after proton knock-out within an oxygen nucleus [255]. Discrete peaks are visible for the  $p$ -holes, while a continuous de-excitation spectrum is apparent for the  $s$ -hole state. Right: Different de-excitation modes for proton-knockouts of the ( $1s_{1/2}$ ) shell. Figure taken from [255], with energy level information from [256].

The branching ratios for the various de-excitation gammas and decay modes of the  $s$ -hole state were measured in the scope of the  $^{16}\text{O}(p,p)^{15}\text{N}$  scattering experiment RCNP-E148 in 2005 [257] and updated in 2006 [255]. The measured de-excitation energy spectrum of the proton-knockout-induced nucleus  $^{15}\text{N}$  is shown on the left of figure 7.4 for the updated measurement from 2006. The peaks for the  $p$ -holes are clearly visible on the left side of the spectrum, with the statistics being downscaled by a factor of 10 below 8 MeV. The region of the  $s$ -hole state is visible in the excitation region between 15 MeV

and 50 MeV as a very broad distribution without any particularly sharp and narrow peaks. For excitation energies in this region, the final state particle composition was determined for the different decay modes  $k$  and the branching ratio of associated gamma decays was determined for each mode. In total, only a branching ratio of  $(27.9 \pm 1.5_{-2.6}^{+3.4})\%$  of  $s$ -hole decay modes are associated with a gamma between 3 MeV and 6 MeV [255]. This ratio is even lower if one only considers decay modes with gammas above 6 MeV. In this case, the branching ratio reduces to  $(15.6 \pm 1.3_{-1.0}^{+0.6})\%$  of all  $s$ -hole processes.

Table 7.2 provides a comprehensive overview of the different photon de-excitation modes for all three shells of  $^{15}\text{N}$ . For each decay mode, the energy level within the shell as well as the energy of associated gamma ray emissions are given, alongside the branching ratio of the particular mode  $k$  as a function of all processes  $N_{\text{tot},\alpha}$  within one shell  $\alpha$  ( $N(k)/N_{\text{tot},\alpha}$ ). Taking into account the spectroscopic factors of each nuclear shell  $\alpha$  (as presented previously in table 7.1), the overall probability  $P(k)$  for observing a certain decay mode  $k$  is given by

$$P(k) = \frac{N(k)}{N_{\text{tot},\alpha}} \cdot \frac{S_\alpha}{8} \quad (7.7)$$

The spectroscopic factors in the table are modeled according to the calculations by Ankowski *et.al* [249]. It is important to consider that this introduces a discrepancy for the probabilities of the decay modes of the  $1s_{1/2}$  state with respect to the estimates of the RCNP-E148 experiment. While the model of Ankowski *et.al* predicts a spectroscopic factor of  $S(1s_{1/2}) = 0.9$  (44% of the naïve prediction of  $S = 2$ ), the RCNP experiment uses a factor of  $S(1s_{1/2}) = 1.6$  based on calculations with the distorted wave impulse approximation (DWIA) [258], resulting in significantly higher decay mode probabilities for the  $s$ -hole state, denoted by  $P_{\text{DWIA}}$  within the table.

The de-excitation model that is employed in the course of this study is the one implemented in GENIE, which uses the original predictions by Ejiri for the  $p$ -hole knockout states, and the measurements of the RCNP-E148 experiment from 2005 for the predictions of the  $s$ -hole proton knockout state. The implementation of the  $s$ -hole-related de-excitation gammas based on the original measurements in 2005 lacks some of the modes which were discovered with more statistics in the updated measurement from 2006. However, the most important modes are already present with similar branching ratios, rendering the modeling of the  $s$ -hole-related gamma de-excitations sensible enough for our purposes. Due to the lack of data for neutron knock-out reactions, very conservative estimates based on the original predictions by Ejiri are used for the  $(1s_{1/2})$  state in the GENIE implementation. While these predictions for the neutron-knockout mainly include higher-energetic gammas, the impact of potentially missing lower-energetic gamma rays is estimated to be low due to the low probability of ending up in the selected visible energy window of the DSNB search. In addition, the low branching ratios of the  $s$ -hole related de-excitation modes with associated gamma production results in a lower mismodeling impact compared to the dominant  $(1p_{3/2})$  contribution. A further difference of the GENIE implementation with respect to the current state of knowledge are the spectroscopic factors, which are modeled according to the original naïve assumptions based on the  $(d, ^3\text{He})$  pickup reactions. However, the absolute rate normalization as presented in the later section 7.3.2 will introduce a data-driven normalization of the rate of atmospheric NCQE background

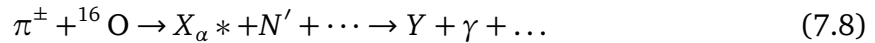
events. As a consequence, only the relative fractions of the different event classes are deemed important, and higher absolute event class fractions are allowed during the process of simulating the events.

Shell	Decay	Energy level ( $J^\pi$ )	$\gamma$ -ray energy	$N(k)/N_{\text{tot}}$	$P(k)$	$P_{\text{DWIA}}$	Model
$1p_{1/2}$	$^{15}\text{N}$	0.00 MeV ( $1/2^-$ )	no gamma	100%	16%	16%	I, II, III
$1p_{3/2}$	$^{15}\text{N}$	6.32 MeV ( $3/2^-$ )	6.32 MeV	87.2%	28.8%	28.8%	I, II, III
	$^{15}\text{N}$	9.93 MeV ( $3/2^-$ )	9.93 MeV	6.4%	2.1%	2.1%	I, II, III
	$^{15}\text{N}$	10.7 MeV ( $3/2^-$ )	no gamma	6.4%	2.1%	2.1%	I, II, III
$1s_{1/2}$	$^{13}\text{C}+d$	3.09 MeV ( $1/2^+$ )	3.09 MeV	3.0%	0.33%	0.60%	I, II, III
	$^{13}\text{C}+d$	3.68 MeV ( $3/2^+$ )	3.68 MeV	4.2%	0.46%	0.84%	I, II, III
	$^{13}\text{C}+d$	3.85 MeV ( $5/2^+$ )	3.09 MeV (1.20%) 3.68 MeV (36.3%) 3.85 MeV (62.5%)	4.6%	0.51%	0.93%	I, II, III
	$^{12}\text{C}+t$	4.44 MeV ( $2^+$ )	4.44 MeV	5.8%	0.64%	1.16%	I, II, III
	$^{14}\text{N}+n$	4.92 MeV ( $0^-$ )	4.92 MeV	5.2%	0.57%	1.04%	I, II, III
	$^{14}\text{N}+n$	5.11 MeV ( $2^-$ )	5.11 MeV	0.0%	0.00%	0.00%	I, II, III
	$^{14}\text{N}+n$	5.69 MeV ( $1^-$ )	3.38 MeV (63.9%) 5.69 MeV (36.1%)	4.5%	0.50%	0.91%	III
	$^{14}\text{N}+n$	5.83 MeV ( $3^-$ )	5.11 MeV (62.9%) 5.83 MeV (21.3%)	0.54%	0.06%	0.11%	III
	$^{14}\text{N}+n$	6.20 MeV ( $1^+$ )	3.89 MeV (76.9%) 6.20 MeV (23.1%)	0.0%	0.00%	0.00%	III
	$^{14}\text{N}+n$	6.45 MeV ( $3^+$ )	5.11 MeV (8.1%) 6.44 MeV (70.1%)	2.8%	0.31%	0.56%	III
	$^{14}\text{N}+n$	7.03 MeV ( $2^+$ )	7.03 MeV	[6.7%]	[0.74%]	[1.35%]	I, II, III
	$^{14}\text{C}+p$	6.09 MeV ( $1^-$ )	6.09 MeV	[0.0%]	[0.00%]	[0.00%]	I, II, III
	$^{14}\text{C}+p$	6.59 MeV ( $0^+$ )	6.09 MeV	[0.0%]	[0.00%]	[0.00%]	I, II, III
	$^{14}\text{C}+p$	6.73 MeV ( $3^-$ )	6.09 MeV (3.6%) 6.73 MeV (96.4%)	0.43%	0.05%	0.09%	I, II, III
	$^{14}\text{C}+p$	6.90 MeV ( $0^-$ )	6.09 MeV	[0.0%]	[0.00%]	[0.00%]	III
	$^{14}\text{C}+p$	7.01 MeV ( $2^+$ )	6.09 MeV (1.4%) 7.01 MeV (98.6%)	[0.0%] [6.7%]	[0.00%] [0.74%]	[0.00%] [1.35%]	I, II, III
	$^{14}\text{C}+p$	7.34 MeV ( $2^-$ )	6.09 MeV (49.0%) 6.73 MeV (34.3%) 7.32 MeV (16.7%)	5.7%	0.63%	1.15%	I, II, III

**Table 7.2:** De-excitation channels of  $^{16}\text{O}$  after proton knock-out reactions. Branching ratios are taken from Ejiri's predictions in the case of the  $p$ -hole states [252], and from the RCNP-E148 experiment in the case of the  $s$ -hole states [255]. The total probabilities for the various modes  $P(k)$  are calculated by combining the branching ratios with the spectroscopic factors  $S_\alpha$  for each shell, as predicted by Ankowski *et al* [249]. Alternative total probabilities  $P_{\text{DWIA}}$  are calculated based on an alternative spectroscopic factor value obtained with the distorted wave impulse approximation [258]. Branching ratios denoted by squared brackets show the combined measured branching ratio in cases where multiple decay modes result in the same or very similar de-excitation energy. The *Model* column indicates whether the respective decay mode is implemented in the GENIE model (I), the RCNP-E348 measurement from 2005 (II), and the updated measurement from 2006 (III).

### 7.2.3 ATMOSPHERIC NC- $N\pi$ BACKGROUND

In addition to the NCQE channel, de-excitation gammas can additionally be produced in the scope of so-called NC- $n\pi$  reactions, involving a number of  $n$  pions. One typical primary interaction type in this context would be NC-Resonant (NCRES) interactions, which typically involve a  $\Delta$ -baryon resonance that subsequently decays into a pion. Other interaction types that potentially create a pion comprise the coherent interaction of the neutrino with the whole nucleus, although those contribute to a much smaller extent. Additional pions can be created in intranuclear cascades during Final State interactions (FSIs) within a nucleus. The resulting pions can then be absorbed by oxygen nuclei and in turn produce excited nuclei states  $X_\alpha^*$  that can convert into their ground states  $Y$  via emission of de-excitation gammas:



Such pion absorption processes emit an associated  $\gamma$ -ray with a branching ratio of less than 6.1% [246], based on experimental data from pion absorption in water conducted at CERN [259]. While the NC- $n\pi$  reactions will not be simulated explicitly for the extent of this particular study, they can be included via simple upscaling of the NCQE event rates due to their almost identical event signature. The exact scaling factor will be based on experimental data of atmospheric neutrino interactions within the Super-Kamiokande experiment and will be discussed in more detail in the subsequent chapter 7.3.2.

### 7.2.4 INVISIBLE MUONS

In the case of lower-energetic Charged Current interactions of atmospheric neutrinos in water, the resulting muon can feature an energy below the Cherenkov threshold and traverse the water undetected. In the case of such an "invisible muon", the only light output that is accessible is the Cherenkov light of the Michel electron produced in the decay of the muon. Since the energy region of such Michel electrons has a maximum energy of  $\approx 50$  MeV and hence overlaps with the energy region of DSNB events, the electrons can be mis-identified easily as DSNB-induced positrons. The delayed neutron tag is provided by nucleon knock-out in the initial neutrino interaction with the nucleus. While Gadolinium loading and the requirement of exactly one neutron significantly reduces the statistics of this invisible muon background, even the residual background with  $n_{\text{det}} = 1$  is non-negligible and dominates the DSNB signal for visible energies above  $\approx 20$  MeV. However, the differences of event signatures of positrons and electrons in a water Cherenkov detector are very subtle and not expected to be identifiable by an image-based feature recognition technique such as Convolutional Neural Network. Invisible muons will hence not be included in the presented discrimination study, and the corresponding spectrum will be considered irreducible in the scope of our CNN method.

## 7.3 SIMULATION OF THE DSNB AND ATMOSPHERIC NCQE BACKGROUND SIGNALS

Both the DSNB antineutrino events and the atmospheric NCQE background signals were modeled in the scope of a Monte Carlo simulation of a Super-K-Gd-like detector configuration. The following chapter briefly outlines the properties of the simulation framework and detector parameters in section 7.3.1, before more aspects are provided for the simulation of the DSNB signal sample in section 7.3.2 and the atmospheric NCQE sample in section 7.3.3. The last section 7.3.4 provides an overview of the event selection cuts and normalizations that were applied to the data samples before the classification process.

### 7.3.1 DETECTOR CONFIGURATION AND SIMULATION FRAMEWORK

All simulations were conducted in the frame of the open-source simulation framework WCSim [194], which is based on Geant4 [193] (version 4.10.1 with FTFP\_BERT\_HP physics list) and which was specifically designed for modeling particle interactions in water Cherenkov detectors. The physics list FTFP\_BERT\_HP was selected to provide a reasonable representation of neutron-related processes such as neutron captures and inelastic scattering processes. A cylindrical Super-K like detector geometry with dimensions ( $r \sim 17$  m,  $h \sim 36$  m,  $\sim 11150$  PMTs) was chosen for this study to investigate the potential application of the classification technique in a current-generation neutrino experiment environment. In this context, Gadolinium-loaded water with a mass fraction of  $f_{\text{Gd}} = 0.1\%$  was selected as the detector medium to represent the current SuperK-Gd phase of the experiment. Detector parameters such as dark noise rates, Quantum Efficiency values and water transparency values are assumed to be identical to the configuration in the original SKDETSIM detector simulation framework. WCSim has been validated to reproduce the detector response of SKDETSIM and should therefore provide a realistic representation of the detector response [205]. The trigger threshold was set to 25 PMTs within a time window of 200 ns, equivalent to around 3-4 MeV of minimum energy for triggered events. Both signal and background samples were simulated across a Fiducial Volume of dimensions ( $r \sim 15$  m,  $h \sim 32$  m), corresponding to a minimum distance of 2 m to the cylindrical detector walls. The Fiducial Volume contains a fiducial mass of 22.5 kt and was chosen following reference [260]. While the Fiducial Volume selection relies on the true vertex information within this study, well-probed time-of-flight based vertex reconstruction techniques can be used for selecting events in the final experiment.

### 7.3.2 SIMULATION OF DSNB SAMPLE

For the simulation of the DSNB antineutrino event reactions, only the end products of the Inverse Beta Decay (IBD) reaction are simulated:

$$\bar{\nu}_e + p \rightarrow n + e^+ \quad (E_{\text{thr}} = 1.8 \text{ MeV}) \quad (7.9)$$

For each event, both the positron and the neutron are placed at the same vertex, with vertices distributed uniformly across the whole detector volume. The positron energy is

modeled according to the predicted antineutrino energy distribution by *Kresse et. al* [245], as presented in chapter 7.1.

### 7.3.3 SIMULATION OF ATMOSPHERIC NCQE SAMPLE

The atmospheric NC reactions are caused by very energetic atmospheric neutrino interactions with the nuclei in the water volume. As a consequence, the final state particles cannot be as easily determined as in the case of the DSNB signal. Both a detailed model of the atmospheric event reactions and the neutrino-nucleus interactions become necessary to predict which particles are produced in the reaction. While the former is provided by the FLUKA atmospheric event spectra [248], the latter is simulated with the atmospheric neutrino event generator *gevgen\_atmo* in GENIE (v3.0.6) [135, 196]. Nucleons within the nuclei are approximated with the Relativistic Fermi Gas model in GENIE, and the interactions of neutrinos with individual nucleons as well as subsequent Final State Interactions are included. De-excitations of nuclei are implemented only for oxygen nuclei, which is sufficient for our case where only oxygen de-excitations are relevant. The primary particles that are generated in GENIE are propagated alongside their properties (momentum, direction) to the WCSim framework, in which the interactions of the primary particles with the detection medium as well as the detector response are evaluated.

While the aforementioned de-excitation of excited oxygen nuclei provides one source of gammas, there is another photon creation mechanism that can mimic the prompt positron signal of the IBD signal. Inelastic reactions of neutrons and protons with neighboring nuclei produce additional *secondary* gammas that can be misidentified as positrons. In addition to secondary gammas, these inelastic reactions can also produce further neutrons from break-up reactions of oxygen nuclei [237]. These interactions hence both influence the prompt gamma signal as well as the number of neutrons that are produced within an event.

### 7.3.4 EVENT SELECTION & NORMALIZATION

In both event categories, events with a prompt visible energy  $E_{\text{vis}}$  between 12 and 30 MeV and one detected neutron are selected. The prompt energy window is mainly defined by other backgrounds that prevent the detection for smaller and lower energy values, as presented in more detail in section 7.1. The neutron criterion, on the other hand, makes sure that the selected event signatures are IBD-like. The visible energy value is proportional to the number of observed photoelectrons and is normalized in a way to represent the equivalent positron energy for a given number of photoelectrons. The conversion factor was deduced based on positron simulation data in WCSim and contains a constant offset to account for the dark noise, alongside a proportionality factor of roughly 9 p.e./MeV. While the prompt signal is composed of a single positron in the case of a real DSNB event, multiple gammas are usually involved in the composition of the prompt light output in the case of an atmospheric NCQE background event. As described above, such additional gammas are usually created in the scope of inelastic nucleon scattering reactions off oxygen nuclei in the water medium. Regarding the delayed event, the number of

detected neutrons is estimated based on the true number of total neutrons within an event, corrected by the nominal tagging fraction of 67% in SK-Gd after all necessary cuts [246].

While the neutron tagging efficiency simply results in a downscaling of the event rate in the case of DSNB events (since they always contain exactly one true neutron), the selected atmospheric NCQE signal is composed of multiple true neutron classes. The probability to detect a certain number of neutrons  $n_{\text{det}}$  is related to the true number of neutrons  $n_{\text{true}}$  ( $n_{\text{true}} \geq n_{\text{det}}$ ) in an event as follows:

$$P(n_{\text{det}}|n_{\text{true}}) = \binom{n_{\text{true}}}{n_{\text{rec}}} \cdot \epsilon^{n_{\text{det}}} \cdot (1 - \epsilon)^{n_{\text{true}} - n_{\text{det}}}. \quad (7.10)$$

As a consequence, we can describe the signal of detecting exactly one neutron ( $n_{\text{det}} = 1$ ) as a combination of multiple true event classes ( $n_{\text{true}} = 1, 2, 3, \dots$ ). Assuming that each true event class registers a certain amount of events  $N(n_{\text{true}})$ , the detected number of events  $N(n_{\text{det}})$  can be written as:

$$N(n_{\text{det}} = 1) = \sum_{n_{\text{true}} \geq 1} P(1|n_{\text{true}}) \cdot N(n_{\text{true}}) = \sum_{n_{\text{true}} \geq 1} \binom{n_{\text{true}}}{1} \cdot \epsilon \cdot (1 - \epsilon)^{n_{\text{true}} - 1} \cdot N(n_{\text{true}}) \quad (7.11)$$

The coefficients before  $N(n_{\text{true}})$  can be used as scaling factors for the simulated true event classes. These considerations can now be applied to obtaining the expected energy distribution of atmospheric neutrino interactions with exactly one detected neutron. Figure 7.5 shows the visible energy spectra for different amounts of true neutrons for the atmospheric NCQE sample, before applying any scaling factors. While the lower-energy part below 10 MeV is heavily dominated by the  $n_{\text{true}} = 1$  component, events with higher visible energies ( $E_{\text{vis}} > 15$  MeV) are more likely to result from interactions with more than one true neutron. Each component can now be scaled by its corresponding coefficient according to equation (7.10) to obtain the expected spectrum of NCQE events with one detected neutron, assuming a neutron detection efficiency of  $\epsilon$ . It should be noted that the true number of neutrons is composed of the sum of primary and secondary neutrons. Therefore both neutrons from the primary neutrino-nucleus interactions as well as neutrons from inelastic interactions in the detector medium are considered.

The absolute rate normalization was done relative to the recent atmospheric NC neutrino spectrum measured by Super-Kamiokande in 2019 [181]. Their measured NC spectrum consists of two primary components, the NCQE component as well as a NC- $n\pi$  component. Since we only simulated the NCQE component in our study, we will obtain the rate normalization solely based on this component. The detected spectrum includes a minimum number of one neutron, and features an energy-dependent neutron efficiency distribution that is also given in the reference. For the rate normalization, we hence correct the detected spectrum of Super-K by their efficiency curve and scale our equivalent distribution of events with at least one true neutron to match the observed rate in the reference spectrum.

The comparison of the reference distribution and our scaled distribution is shown in figure 7.6 as solid and dashed black lines, respectively. The agreement of the two spectra confirms that the simulation of the atmospheric NCQE interactions represents reality

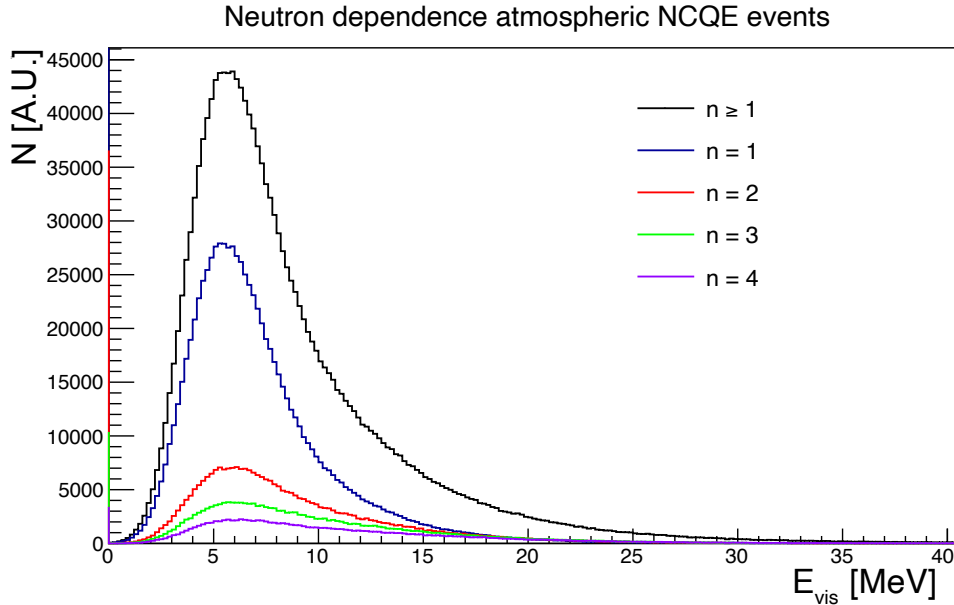


**Figure 7.5:** Visible energy spectra of atmospheric NCQE events with different amounts of true neutrons. The total spectrum consisting of the sum of all components ( $n_{\text{true}} \in [1, 4]$ ) is depicted in black.

reasonably well. The same graph additionally shows the atmospheric spectrum for the case that we require only one detected neutron, which already reduces the number of background events quite significantly. Before the classification process, the NCQE background with  $n_{\text{det}} = 1$  exceeds the DSNB signal statistics by a factor of 7:1. This already represents a serious background reduction compared to the original case of  $n_{\text{true}} \geq 1$  with a Signal-to-Background ratio of  $\sim 1 : 24$ , highlighting the vast benefits of Gadolinium loading with respect to a potential DSNB detection.

When comparing the distributions of DSNB signal events (*blue*) to the spectrum of atmospheric NCQE background events (*red*) in figure 7.6, it becomes apparent that the background domination is most prominent for lower visible energy values, while the statistics of the two samples becomes rather similar at the higher end of the energy spectrum. The network will hence need to perform particularly well especially for events in the lower energy part of the spectrum in order to reduce the background levels below the signal distribution.

Since the NC- $n\pi$  is the second most prominent component in the atmospheric NC background distribution, it needs to be considered when evaluating the classification potential in the context of a DSNB detection study. While this background component was not simulated explicitly in the scope of this classification study, the event signatures of de-excitation gammas should be almost identical to the NCQE event topology. We can hence take the NC- $n\pi$  component into account by scaling up the rate of our NCQE spectrum. Figure 7.7 shows the reference spectra on the left, and the resulting  $n_{\text{det}} = 1$  distributions on the right. The spectral shape of the NC- $n\pi$  distribution was determined by combining the single-pion and multi-pion contributions given in the reference, and the absolute rate normalization was applied according to the relative fractions of NCQE and NC- $n\pi$  events. The addition of the NC- $n\pi$  component elevates the background levels from the red to the

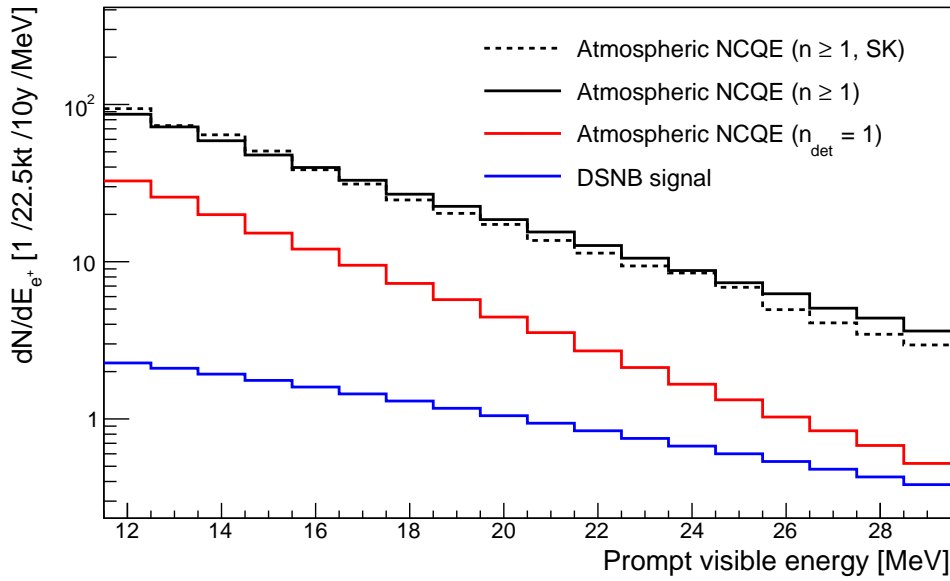


**Figure 7.6:** Event rates for the DSNB signal (*blue*) and simulated atmospheric NCQE interactions are presented as a function of the prompt visible energy. The event rate for the NCQE signal with  $n \geq 1$  (*black, solid*) was normalized to the measured rate of an equivalent data sample measured by Super-Kamiokande (*black, dashed*) [181]. The relevant atmospheric NCQE spectrum with 1 detected neutron ( $n_{\text{det}} = 1$ ) is shown in red.

black curve, increasing the background-to-signal ratio from 7:1 to roughly 11:1.

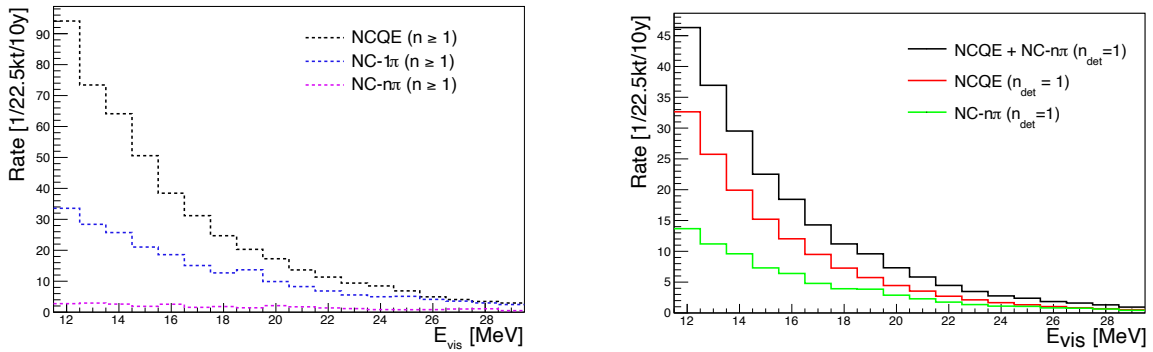


**Figure 7.7:** **Left:** NCQE (*black*), NC- $1\pi$  (*blue*) and NC-multi $\pi$  (*red*) spectra extracted from the Super-Kamiokande reference and corrected for the neutron detection inefficiency [181]. **Right:** NCQE (*red*), NC- $n\pi$  (*green*) and total NCQE+NC $n\pi$  spectra (*black*) for our simulation sample when assuming the same event category fractions as in the reference and selecting for one detected neutron.

## 7.4 DSNB/NCQE EVENT DISCRIMINATION WITH CONVOLUTIONAL NEURAL NETWORKS

The following chapter will describe the general layout of the Convolutional Neural Network as well as discussing the resulting event spectra after the classification process. The idea

of using pattern recognition for this discrimination task is based on the differences in the expected event topologies. While positrons from real DSNB events are expected to produce a clear Cherenkov ring, atmospheric NCQE events are more likely to produce multiple gamma-rays and hence a more scattered event display with several fainter ring-like structures. Convolutional Neural Networks are ideally suited to detect such differences in images like the investigated event displays. The first section 7.4.1 will present the general layout and features of the network, while the next section 7.4.2 will evaluate the resulting energy spectra after applying the CNN to a simulation sample with realistic fractions of signal and background events.

### 7.4.1 NETWORK ARCHITECTURE & PERFORMANCE

It is very common for water Cherenkov detectors to visualize individual events in terms of a so-called *event display*, i.e. a rolled-open two-dimensional projection of the cylindrical mantle that depicts the recorded charge and time values of the PMTs in a color scale. These event images are an ideal candidate to be classified by a Convolutional Neural Network, since specific features of the classes can be recognized and identified by the network. We produced event displays for both signal and background event classes, and provided them as an input for our CNN, without any additional information about the vertex, energy or direction of the particle. The CNN in the following is trained via *supervised learning*, i.e. knowing the event labels for each training event. After the training phase, the network is applied to and evaluated on an independent test data set. Before inspecting the details of the network architecture, more details are provided about the input data format of the event displays. After the general architecture has been presented, the network will be further analyzed in terms of its Receiver Operating Characteristic (ROC) as well as potential systematic effects.

#### Input data format

In order to create the two-dimensional event display input images, the three-dimensional spatial coordinates of the PMTs ( $x_{\text{PMT}}, y_{\text{PMT}}, z_{\text{PMT}}$ ) have to be converted into their equivalent projected coordinates ( $\phi_{\text{proj}}, z_{\text{proj}}$ ) that represent their position on the rolled-open cylinder plane. For PMTs which are mounted on the detector mantle and not the top or bottom caps, this conversion is pretty straightforward: The vertical coordinate  $z_{\text{PMT}}$  is chosen to be the new  $z_{\text{proj}}$  variable, and the angle  $\phi_{\text{proj}}$  is calculated between the other two coordinates  $x_{\text{PMT}}$  and  $y_{\text{PMT}}$  via simple trigonometric relations. The units of the projected coordinates are chosen such that every PMT in the barrel region is represented by a unique pixel. For the top and bottom planes, phototubes are organized in terms of their radial position. Since the largest circle of PMTs is closest to the last row of barrel photomultipliers, the pixels for these sensors are placed in the next closest row in the projected view. PMTs that are located in the region of the second largest radius within the top and bottom planes are then placed in the next row, and so on. The horizontal position  $\phi_{\text{proj}}$  within the projected image is calculated based on the azimuthal position of the PMT within the top or bottom plane. This leads to some empty pixels for the projected areas of the top and bottom plane photosensors, since the inner regions with the lowest radius values are populated by the least amount of PMTs. However, the empty pixels are not a problem since they will be zero for each event and hence be recognized as not significant by the network. In a

similar fashion, the discontinuity of the event display on the left and right edge of the projection (at  $\phi_{\text{proj}} = 0, 2\pi$ ) is also recognized by the network during the training process. Cherenkov rings that are registered across both the left and right edges should therefore still be recognized and classified correctly.

For each simulated DSNB and atmospheric NCQE event, the detected charge values and first hit time values are evaluated for every PMT in a time window of 270 ns around the trigger time, with a pre-trigger window of 20 ns and a post-trigger window of 250 ns. Both the time and charge values are then converted to a range of  $[0,1]$ , normalized to the minimum and maximum observed values. These normed values are then assigned to the corresponding projected pixel of the respective photosensor, resulting in a separate charge and time event display. The normalization procedure was designed to minimize potential biases with respect to the visible energy of the events, as well as with respect to extremely early and late dark noise hits.

Figure 7.8 shows exemplary event displays for an atmospheric (*top*) and DSNB event (*bottom*) of similar visible energies of  $E_{\text{vis,NCQE}} \approx 19 \text{ MeV}$  and  $E_{\text{vis,DSNB}} \approx 22 \text{ MeV}$ . From left to right, the event displays are depicted in their charge, time and saliency representation. The saliency map highlights the areas of the image that were of major importance for the classification decision of the network. The difference in the two event topologies is even visible to the naked eye: While the DSNB event features a strong Cherenkov ring pattern, the event display is much more diffuse in the case of an atmospheric NCQE event. This is also mirrored in the saliency map distributions, where the ring pattern is identified in the case of the DSNB event, and parts of the diffuse structure are deemed important by the network in the case of the background event. The criteria for event classification by the CNN hence seem plausible from a physics perspective.

### Network architecture

The layout of the used Convolutional Neural Network is shown in a schematic representation in figure 7.9. The features of the event display input images are extracted by making use of six consecutive double-convolutional "packages", each consisting of two convolutional layers, one additional 2x2 Max-Pooling Layer, a Batch normalization layer and a 20% dropout layer. Each convolutional layer consists of 64 kernels and is capable of detecting geometric features and shapes in the input layer by scanning the image with the help of so-called filters or kernels. The images that are produced during the application of the kernels across the image are called feature maps and are investigated further by the subsequent layers. The kernels themselves are optimized during the training process. The subsequent Max-Pooling layers always select the highest values in small subsections of the image (e.g. in our case 2x2 pixel areas) and hence reduce the size and dimension of the images. They are primarily used to lower the size of images while simultaneously achieving location-independence for the detected features. The Batch Normalization layer is inserted for stabilization of the training process and in turn lowering the necessary amount of training epochs. The dropout layers are important for achieving a high generalization of the network and are present for four of the six double-convolutional packages. Dimension-wise, the convolutional packages feature (7,7), (5,5), (3,3), and (2,2)-dimension kernels for the first, second, third & fourth and the two last double-convolutional packages, respectively.

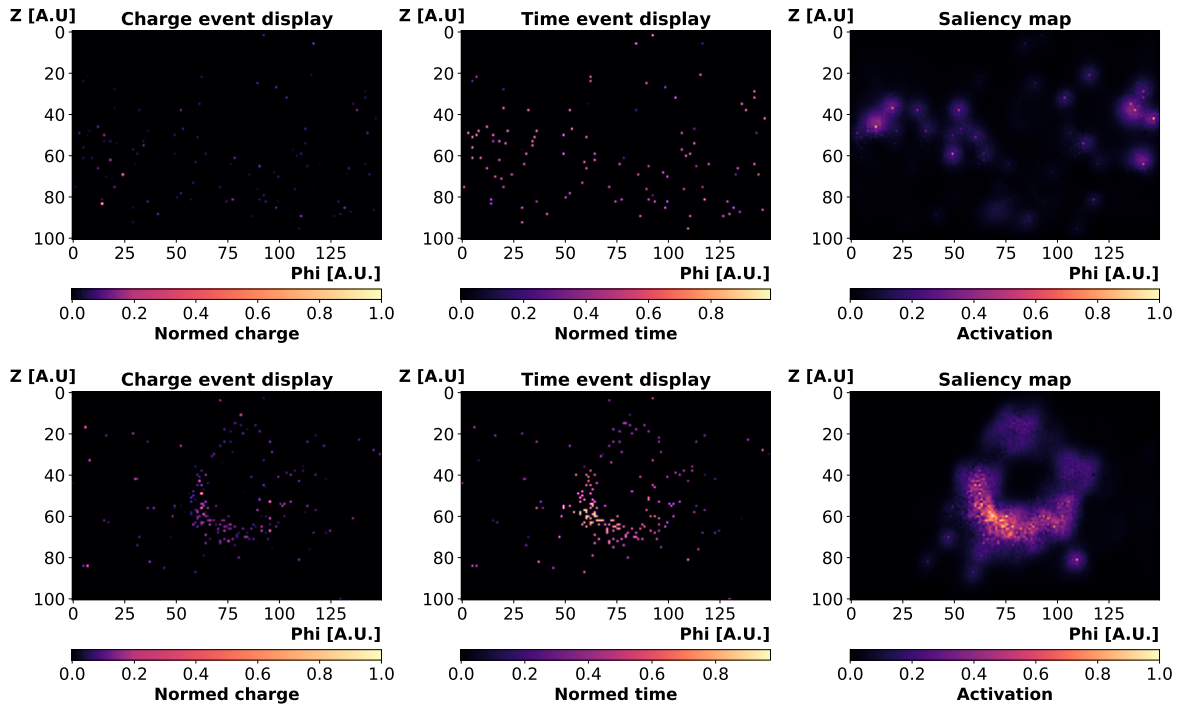


**Figure 7.8:** Charge and time event displays as well as saliency maps for exemplary DSNB (bottom row) and atmospheric NCQE events (top row) of similar visible energy ( $E_{\text{vis,NCQE}} \approx 19 \text{ MeV}$ ,  $E_{\text{vis,DSNB}} \approx 22 \text{ MeV}$ ). While a nice Cherenkov ring is visible in the case of a DSNB event, the pattern for the NCQE event is more scattered due to multiple gammas being present.

After this main component of the network, there are a few additional layers that lead to the final prediction. A flattening layer of 384 nodes produces an array with 384 entries based on the final output of the convolutional packages. This flattened vector is fed into a dense layer with 256 nodes before the result is processed by another batch normalization and Dropout layer. The final output is a two-dimensional output vector containing the predicted probabilities that the event is DSNB-like or NCQE-like, where  $P_{\text{DSNB}} = 1 - P_{\text{NCQE}}$ . The two-dimensional final output vector could hence also be described by a single value and is arbitrarily chosen to be represented in this specific two-dimensional fashion.

The Convolutional Neural Network was implemented in python 3.7 [261], making extensive use of the Keras library [262] as well as the TensorFlow framework [263]. The presented network architecture includes a total of 726k trainable and 1200 non-trainable parameters. Since we apply the network to a binary classification problem, the binary cross-entropy function was selected as a suitable loss function for the training. *Rectified Linear Units (ReLU)*s are used as activation function for most convolutional layers, while a *softmax* activation function was used for the final output layer. The *adam* optimizer [264] was chosen to handle the necessary back-propagation via stochastic gradient descent methods.

### CNN training

The supervised training mode of the Convolutional Neural Network is conducted on a dedicated training sample of 185,000 events, equally balanced as 92,500 DSNB and 92,500 NCQE background events. In addition to the training sample, a validation sample of 15,000

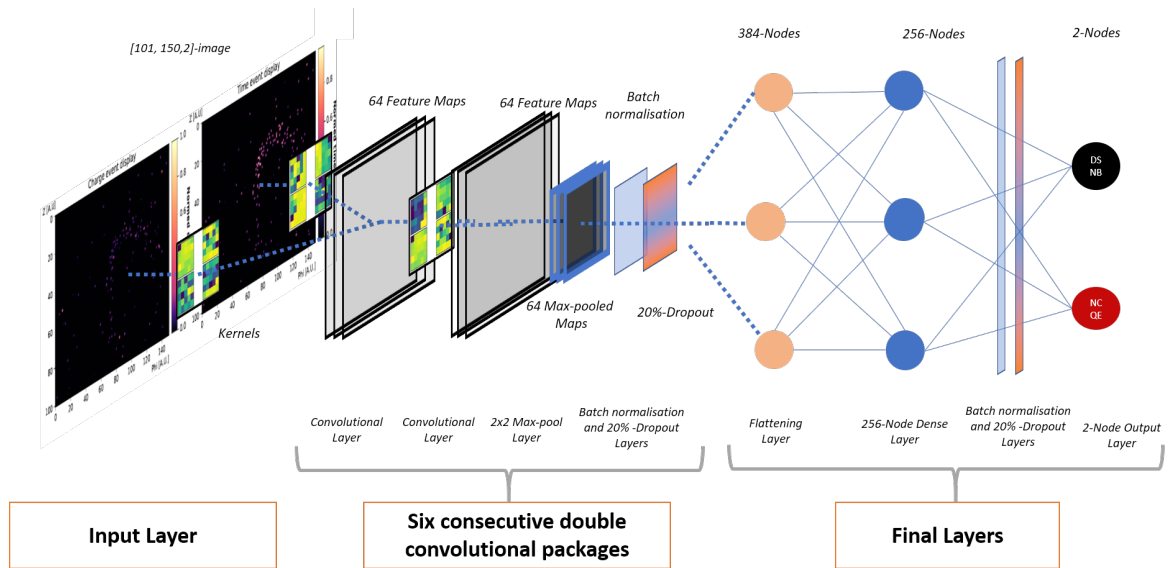


**Figure 7.9:** Architecture of the Convolutional Neural Network (CNN) employed for event classification between DSNB and atmospheric NCQE events. Six double-convolutional layer packages are used to extract the features of the event displays.

events is employed as a regular cross-check of the progression of the training after each epoch. It is also used to infer possible adjustments for the utilized hyperparameters. To prevent overtraining, tensorflow-specific callbacks are employed and the performance on the validation set is closely supervised. After the training is completed, the final evaluation of the performance takes place on the test sample, composed of 20,000 events between 10 MeV and 30 MeV (14,000 events between 12 and 30 MeV). This test data sample is only used once and is meant to represent the real data sample which was never encountered during the training process. The network classification accuracy on the test sample can hence be used to estimate the expected performance on an unknown data sample.

### Network performance

The Convolutional Neural Network provides a continuous output parameter  $r \in [0, 1]$  that can be interpreted as the confidence of the network that a signal event was observed. A simple threshold cut on  $r$  is usually used to determine which class is predicted by the network, with the default cut value being  $r_{\text{default}} = 0.5$ . All events with  $r \geq 0.5$  are then classified as DSNB events, while detector signatures with  $r < 0.5$  are labeled as NCQE background events. The performance of the network is evaluated on the test sample for various cut parameters. The resulting Receiving Operating Characteristic (ROC) curve depicts which combinations of signal efficiency and residual background levels can be achieved for different such threshold values  $r_{\text{thr}}$ . The ROC curve is shown in figure 7.10 and makes clear that the overall classification performance is high, with an area of 0.995 covered by the curve. Two different threshold values are highlighted in the plot,  $r_{\text{default}} = 0.5$  and  $r_{\text{optimized}} = 0.965$ . When looking at the associated classification parameters, the default cut value achieves a signal efficiency of 98.0% alongside a residual background fraction of 4.1%. While this is already quite good, the high background levels give room for adapted cut values that better reject background events. The optimized cut value  $r_{\text{optimized}} = 0.965$ , for instance, reduces the residual background contamination by

half to a fraction of only 2.0%, while the signal efficiency is lowered only slightly to a value of 96.2%.

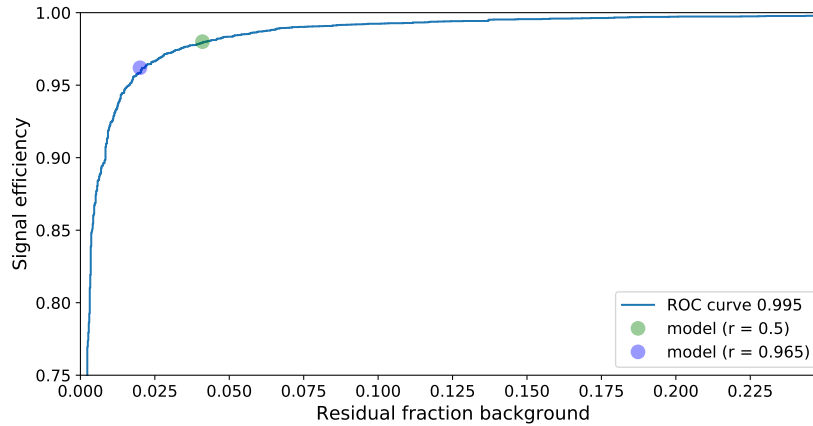


**Figure 7.10:** Receiver Operating Characteristic (ROC) curve of the classification performance of the Convolutional Neural Network. Two different threshold values are highlighted in the plot,  $r_{\text{default}} = 0.5$  and  $r_{\text{optimized}} = 0.965$ .

### Systematic effects and potential biases

The network performance was evaluated and analyzed systematically with respect to its properties and potential biases. The following subsection will present the findings with respect to the classification dependence on visible energy and the number of neutrons, as well as additional checks conducted with the help of saliency maps.

Figure 7.11 depicts the classification accuracy as a function of the visible energy (*left*) and the neutron number (*right*). When considering the visible energy, a slight spectral dependence is visible: In the region with visible energies below 15 MeV, atmospheric NCQE events are classified more accurately than DSNB events. On the other hand, DSNB events are identified more accurately in the upper visible energy window above 15 MeV. In this regime, additional particles can contribute to the NCQE gamma signal that can be conceived more easily as a positron-like event signature. For instance, protons above the Cherenkov threshold can be produced in the initial neutrino-nucleus scattering reaction if the neutrino energy was high enough. Such event signatures make a distinction from the DSNB positron signals very challenging and explain the decreased classification accuracy in this energy regime. No evidence was found indicating that the network uses any further information beyond the image features (such as the total visible energy) to make its decision. The spectral dependency is rather believed to come into place because the observed patterns look more similar between the two event classes for this higher energy region.

The investigation of the accuracy as a function of the neutron number was carried out to explore whether events with various amounts of neutrons are classified differently. While the final data sample only consists of events with one detected neutron, it also includes entries with multiple true neutrons due to the non-perfect neutron detection efficiency  $\epsilon$ . The figure shows that no dependence on the true neutron number is observed, meaning that the network does not classify events differently based on the number of neutrons.

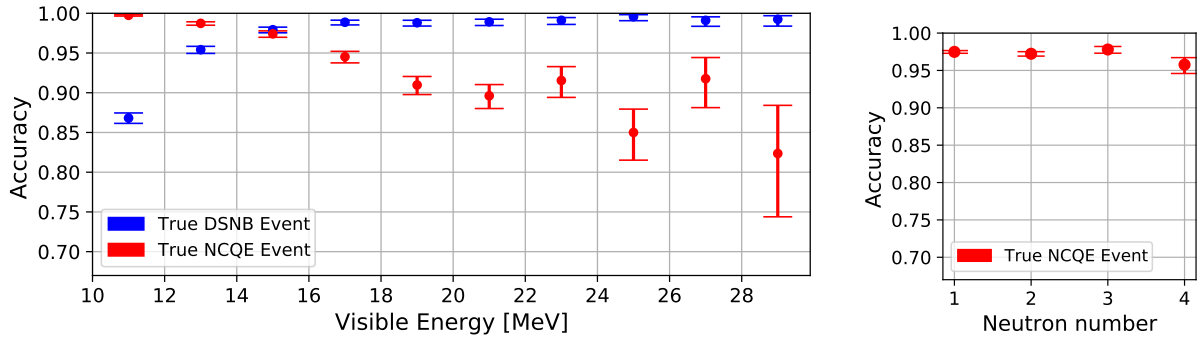


**Figure 7.11:** Classification accuracy as a function of the visible energy (*left*) and the neutron number (*right*). While the accuracy is generally very high, a slight spectral dependence is visible. Events with higher visible energy are more likely to be identified as DSNB events, while events with lower visible energy  $E_{\text{vis}} < 14$  MeV are more prone to be identified as atmospheric NCQE events. No strong dependence of the neutron number is observed.

Figure 7.12 presents an exemplary event display for an NCQE event of visible energy  $E_{\text{vis}} \approx 26$  MeV which is classified incorrectly as a DSNB event. A clear Cherenkov ring pattern is visible, explaining why the network assumed that this signature would belong to a DSNB event with relatively high confidence. The saliency map on the very right further highlights that the ring pattern was used as the main indicator for the decision of the network. In this specific case, a high-energetic proton above the Cherenkov threshold was present in the event, leading to the observed clear ring pattern. Such events are very hard to distinguish due to the almost identical topological features that are present. However, the frequency of NCQE events in this higher visible energy region is very small, forgiving a higher misidentification rate.

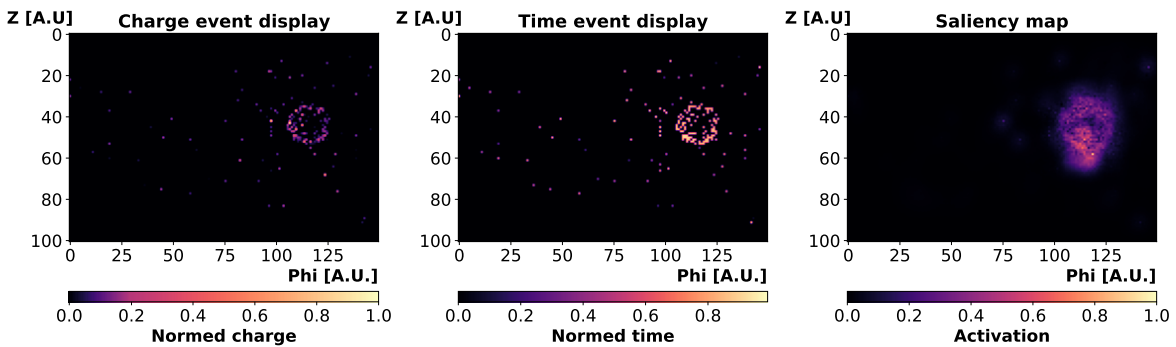


**Figure 7.12:** Event display of a mis-identified atmospheric NCQE event with a visible energy of  $E_{\text{vis}} \approx 26$  MeV. A clear Cherenkov ring is visible, produced by a proton above the Cherenkov threshold which was present in the event. The saliency map verifies that the Cherenkov ring pattern is of major importance for the decision of the network.

The saliency maps presented earlier in this section are extremely useful tools to identify areas of particular importance for the network, and hence provide an idea what information is used by the network to make its decision. They utilize back-propagation methods to track only positive gradient contributions from the output layer to the corresponding sections of the input layer. For each pixel in the input layer, the combined positive gradient contribution is represented by a certain metric related to the classification decision of the network [265]. By looking through exemplary saliency maps for each event class, we have

verified that the attention of the network is indeed focused on the stronger single-ring structures and the more diffuse multi-ring topologies. The CNN hence uses expected characteristics and differences of the DSNB and NCQE events to come to its decision, proving the classification mechanism to be sensible from a physics-driven perspective.

In addition to the aforementioned investigations, the input images were analyzed with respect to their uniformity. The network could in principle pick up on the fact that the average hit patterns for each class look different, e.g. for the case that positrons in DSNB events were preferentially emitted in one direction of the detector. In order to investigate such a possible effect, the vertex and directional distributions were compared for DSNB and atmospheric events. In addition, average hit frequency maps were created for both classes, representing the mean charge value detected in each pixel. No difference was identified in the vertex and directional distributions. Furthermore, the average hit patterns were found to be identical. We hence ruled out a topological bias in the input event classes, rendering the geometric conditions in the event generation identical for signal and background samples.

A last sanity check investigated the influence of having a two-channel input image, featuring both charge and timing information. The influence of both the charge and the time information were evaluated individually by setting the input from the other channel to zero, and then applying this modified network to the test sample. While the time-only network performed reasonably well and similar to the original two-channel network, the charge-only version of the CNN achieved significantly worse classification accuracies. While this implies that the charge information is not prioritized in our fully trained two-channel-based network, it does not mean that the charge information itself is flawed. We trained two additional one-channel networks with only charge and only time information in the input images, and compared the classification accuracies. Both networks performed equally well in this case, and not significantly worse than our two-channel network. We hence conclude that the CNN mainly focuses on the topological features of the event, and in our case decides to mainly use the time input maps to look for these shapes. The additional information from the charge input maps is then of importance in the case of ambiguous geometric shapes, and hence improves the accuracy slightly with respect to the one-dimensional network counterparts. We will hence use the CNN with the two-dimensional input image for evaluating the effect of the network on the test sample. At the same time, the main focus on the topological features indicates that similarly structured networks can be applied to other water Cherenkov geometries, with the accuracy mainly depending on the pixelization or granularity of the photosensor coverage.

## 7.4.2 RESULTS OF DSNB/NCQE CLASSIFICATION

The final classification performance of the network is evaluated by applying the fully trained CNN to the test sample and scaling the associated energy spectra to the expected exposure of  $225 \text{ kt} \cdot \text{y}$  within 10 years in a Super-K-Gd-like detector geometry. This results in an initial sample of  $\approx 20$  DSNB events and  $\approx 221$  atmospheric NC events, composed of 148 NCQE events and 73 NC- $n\pi$  events. The initial spectra alongside the spectra after classification are shown in figure 7.13 for the more stringent threshold value  $r = 0.965$ , with the initial atmospheric NC (DSNB) spectrum shown in orange (black) and the spectra

after classification depicted in red (blue). The atmospheric NC spectrum is reduced below the level of the DSNB spectrum, achieving a signal-to-background ratio of 4:1. This provides a significant improvement from the initial situation, for which the signal-to-background ratio was 1:11. For a default threshold of  $r = 0.5$ , the background reduction is slightly less effective, but still results in a signal-to-background ratio of 2:1. Due to their similar event topology, invisible muons (*green* in the figure) are assumed to be irreducible in the context of DSNB searches and slightly limit the detection capabilities. Overall, the presented classification based on Convolutional Neural Network seems to be a very promising technique to reduce background levels in current-generation detectors like Super-K-Gd, but also future water Cherenkov detectors like Hyper-Kamiokande. The CNN provides a completely independent approach for reducing the background levels in DSNB searches compared to more traditional approaches which are rather based on Ring Counting and Likelihood-driven classification techniques. This also explains the rather different shape of the initial NCQE+NC- $n\pi$  distribution in our case compared to references like [142], which already include some additional cuts for the NCQE background sample. While the actual event classification procedure does not require any of the traditional classification cuts, common event selection cuts like a Fiducial Volume cut, a spallation rejection cut and Michel electron discrimination cut will still be required before the classification is attempted.

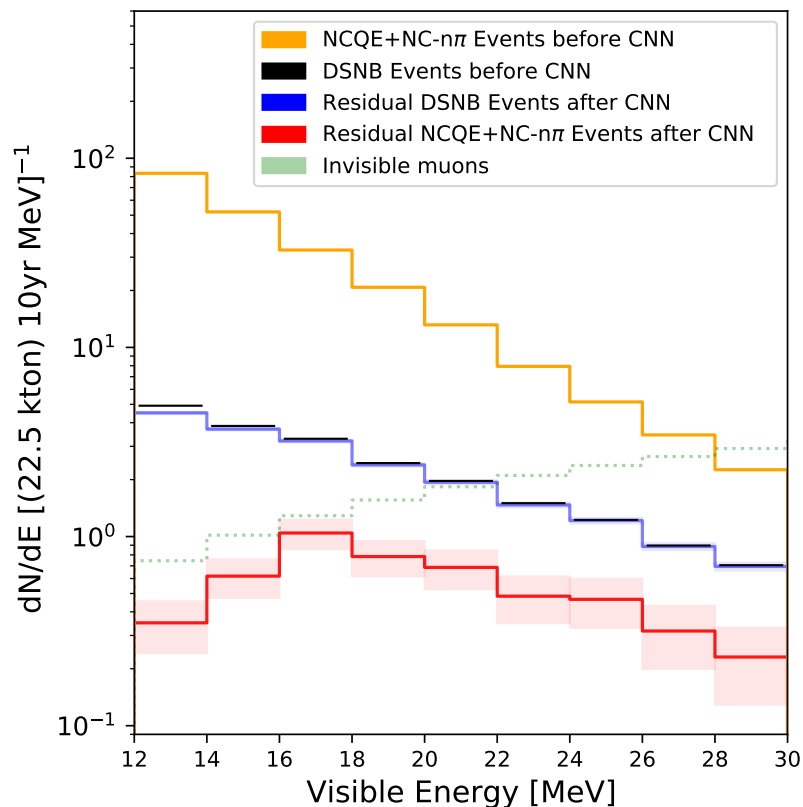


**Figure 7.13:** Spectra of DSNB signal and atmospheric NC background events before and after application of the neural network with a threshold of  $r = 0.965$ . While almost all DSNB events are classified correctly (*black*  $\rightarrow$  *blue*), the atmospheric NC background is reduced significantly by the network (*orange*  $\rightarrow$  *red*), resulting in a final Signal-to-Background ratio of 4:1.

## 7.5 FUTURE NCQE MEASUREMENT WITH ANNIE

While the current trigger setup and analysis goals of ANNIE are fully dedicated to measurements related to Charged Current (CC) neutrino interactions, both a cross-section measurement as well as a neutron multiplicity measurement would also be very interesting for the case of NCQE interactions. The cross-section measurement would provide an important cross-check of measurements conducted by other experiments (Super-K, T2K), whereas the neutron multiplicity measurement could serve as an important validation of neutron production in current neutrino generators and hadronic physics models. Moreover, the neutron multiplicity measurement could be used as a direct input for modeling the atmospheric neutrino background in DSNB searches. The chapter will briefly summarize necessary changes to the trigger setup in section 7.5.1, primarily with respect to the neutron multiplicity measurement. The chapter then closes in section 7.5.2 with highlighting possible selection cuts for obtaining the NC-associated spectrum from the whole beam data sample.

### 7.5.1 NEUTRAL CURRENT TRIGGER SETUP

The phase II triggering scheme is focused on the neutron search in CC interactions. As such, usually only events containing at least one PMT with a charge larger than  $\approx 5$  p.e. induce the acquisition of an extended readout window of  $70 \mu\text{s}$ . Such an extended window is required to efficiently detect neutrons within an acquisition. In addition, only a certain fraction of events triggers an extended window independently of the charge within the event. This independent acquisition of extended readouts is key for a detection of neutrons in NC-related events. While this particular trigger mode is currently set to very infrequent intervals of once every 200 events, its frequency would need to be set to a much higher value to gain feasible statistics for a NCQE-related neutron multiplicity measurement.

Regarding the cross-section measurement of NCQE interactions, the extension of the trigger window is of much smaller importance. In this case, only the information from the prompt acquisition time region of  $2 \mu\text{s}$  is sufficient to do a measurement. Since such a prompt window is recorded for all incoming beam signals, the NCQE cross-section can already be determined with the current trigger configuration. The main task here will be to efficiently select such NCQE interactions by a suite of feasible selection cuts. The next section will briefly cover which cuts could be used to achieve such an event selection.

### 7.5.2 NC EVENT SELECTION STEPS

As discussed earlier for the NCQE/DSNB classification study, the most promising strategy to detect NCQE events within a water Cherenkov detector relies on tagging de-excitation gamma rays from excited nuclei created in nucleon knock-out reactions and secondary hadronic inelastic interactions. In order to select such events with associated gamma-ray emissions, some basic event cleaning cuts can be envisioned. First of all, only beam triggered events will be considered, and restricted to have a certain minimum number of hit PMTs to guarantee that some light was detected. The total detected charge will be restricted to the visible energy window expected for the de-excitation gamma-rays,

for instance below 30 MeV. In addition, no coincident veto and MRD activity should be recorded for the NCQE candidate cluster within the prompt event window. Following the cuts applied for the measurement of the NCQE cross-section in T2K [182], one could further use a low-energy vertex reconstruction technique to verify that the event took place within the water tank and to check the goodness of fit for successful vertex reconstruction. Moreover, some radioactive background and afterpulsing rejection cuts are necessary to distinguish real physics events from noise and background events. In this context, the charge balance cut could be applied for discriminating de-excitation gammas from background, similarly to its use in the neutron candidate selection. In case the simulation is capable of simulating backgrounds realistically, the use of a neural network to reject background events provides another exciting opportunity to conduct the event selection of the NCQE sample, paving the way for a successful NCQE cross-section measurement in ANNIE.



# 8

## Future endeavors: Water-based Liquid Scintillators

---

*“Any sufficiently advanced technology is indistinguishable from magic.”*

—Arthur C. Clarke

The experimental landscape of neutrino detectors has long been dominated by scintillator and water Cherenkov detectors, while nowadays liquid argon detectors also begin to play a more dominant role in the scope of the current Short-Baseline Neutrino Program at Fermilab [117] or the next-generation accelerator neutrino experiment DUNE [24]. Both the detection of neutrinos with scintillation light as well as with Cherenkov light is coupled to a few advantages and disadvantages: Scintillation light, on the one hand, provides a very detailed calorimetric energy reconstruction of particles including hadronic particles such as protons, combined with a very low energy threshold for detection, e.g. 50 keV in the case of solar neutrino detection with Borexino [33]. On the flip side, scintillators emit light isotropically in all directions and hence don't allow for a directional reconstruction of the incoming particle. Cherenkov light, on the other hand, is emitted in a cone-like structure along the particle track and hence enables the reconstruction of the particle direction based on the observed photon topology. However, the threshold for detection is coupled to the energy (and hence also the mass) of the particle. This imposes a harder boundary on the detection energy range of neutrinos compared to liquid scintillator detectors, preventing e.g. the detection of low-energetic solar neutrino detection such as  ${}^7\text{Be}$ -neutrinos in water. In addition, it is not possible to detect lower-energetic protons with Cherenkov light due to their very large mass and hence very high Cherenkov energy threshold.

Usually, experiments focus on one of the two technologies to detect neutrinos, realized as pure water Cherenkov detectors and liquid scintillator detectors. While technically liquid scintillator detectors also feature Cherenkov light emission, the small attenuation length and the small fraction of Cherenkov photons compared to scintillation photons usually prevent a successful detection in this case. However, it has recently been demonstrated that the detection of Cherenkov photons is indeed possible on a statistical basis in the

scope of the liquid scintillator detector Borexino [266, 267] but not on an event-by-event basis.

Since pure water Cherenkov detectors and liquid scintillator detectors have proven to be very successful in the past, a lot of thought has been put into developing a novel detection medium that could potentially combine the advantages of both scintillation and Cherenkov light, while simultaneously getting rid of the disadvantages. These efforts recently succeeded in the synthesis of Water-based Liquid Scintillators (WbLS), a compound of mainly water combined with small liquid scintillator droplets. This medium combines the large transparency and directionality advantages of water Cherenkov detectors with the calorimetric information of liquid scintillator detectors.

The following chapter will explore this novel detection medium in more depth, and particularly applied to the case of ANNIE. In the first section 8.1, general properties and the production mechanism of WbLS are presented in some detail. Afterwards, section 8.2 presents simulation studies of using a small WbLS volume in ANNIE, showcasing the improvement in neutrino energy reconstruction in a beam neutrino environment. The presented simulation study was conducted in collaboration with Daniele Guffanti, who helped with extensions of the simulation framework, and David Maksimović, who implemented the random forest regressor for the neutrino energy reconstruction task. The last section 8.3 briefly highlights future experiment setups that will potentially use WbLS as their detection medium and demonstrates the expected benefits of doing so.

## 8.1 THE NOVEL DETECTION MEDIUM WATER-BASED LIQUID SCINTILLATOR (WBLS)

The concept of a Water-based Liquid Scintillator (WbLS) material was first proposed by a group of people at Brookhaven in 2011 as a potentially suitable material for future proton decay and neutrino precision measurements [185]. The basic idea of creating WbLS consists of mixing a small amount of scintillator into a water medium by adding surfactants to the scintillator and as a consequence providing a hydrophilic component that is capable of dissolving in water. The benefits of creating such a medium can be traced back to keeping the high transparency of water while simultaneously improving the energy reconstruction by the additional scintillation light and enabling the detection of lower-energetic particles below the Cherenkov threshold. In addition, the aqueous component of WbLS makes it easier to dissolve metallic ions, which is potentially beneficial for instance for loading a variety of materials in the scope of neutrinoless double beta decay searches [268].

The first subsection 8.1.1 will emphasize the benefits of combining the information from scintillation and Cherenkov light in the same detector medium and will outline what requirements need to be met for an efficient separation of the two light components. The subsequent subsection 8.1.2 will present the chemical structure of the WbLS material and the general production process, before the last subsection 8.1.3 will delve into the latest characterization results from dedicated material calibration measurements. This concluding subsection will additionally include an overview of currently not well-known

properties of the WbLS medium, such as quenching effects and the details of the re-emission process.

### 8.1.1 THE BEST OF BOTH WORLDS: SCINTILLATION & CHERENKOV LIGHT

In order to gain simultaneous access to the directional information from the Cherenkov light and the calorimetric information from the scintillation light, the two light populations need to be separated in the recorded data. As shown in figure 8.1, there are several ways how such a separation can be achieved. First of all, the emission time profile structure is different: While Cherenkov light is emitted basically instantaneously, scintillation light follows a slightly slower emission curve that is caused by energy transfer processes and slight delays in the de-excitation of the liquid scintillator molecules. Depending on the exact properties of the scintillator, the decay constants can be very different. Slower decay constants are preferable to achieve a relatively pure selection of fast Cherenkov photons, leading to efforts of developing slow scintillator mixtures [269]. In general, very fast photosensors like Large Area Picosecond Photodetectors or arrays of SiPMs are advantageous for an efficient distinction of Cherenkov and scintillation light based on their emission time profile.

Another separation method relies on the chromatographic properties of the emitted light. While typical scintillator mixtures produce photons in the wavelength range between 300 nm and 550 nm, the Cherenkov effect results in photons that follow a  $1/\lambda^2$ -distribution. Cherenkov photons can hence also have wavelengths which are above or below the typical scintillator range. Experimental efforts have revolved around using dichroic filters to filter out Cherenkov light based on its wavelength, for example in preparation of Hyper-Kamiokande [270], in form of the ARAPUCA device developed for DUNE [271], or in combination with a Winston cone design in the case of the so-called dichroicon [272].

The last separation method relies on the differences in spatial hit patterns. Cherenkov light is emitted in form of a cone around the particle direction and thus only produces hits in a very small angular region, while scintillation light is emitted isotropically with a uniform angular emission profile. Cherenkov photons can be specifically selected by counting only photons that arrive in the projected Cherenkov ring area. This has been demonstrated for instance in the scope of the CHerenkov/Scintillation Separation (CHESS) experiment [273], where PMTs located on the projected Cherenkov ring could be correlated to the earliest photons.

In the case of ANNIE, the main strategy for separating the WbLS component relies on using the excellent timing properties of the LAPPDs to identify early photon hits. In addition, Cherenkov photons will preferably be detected in the downstream region of the tank due to the geometric topology of beam events, which makes an additional geometric selection possible. Supplementary geometric information can be extracted from the detected muon tracks in the MRD to refine the predictions of the expected Cherenkov light pattern based on the event vertex and direction of the muon.

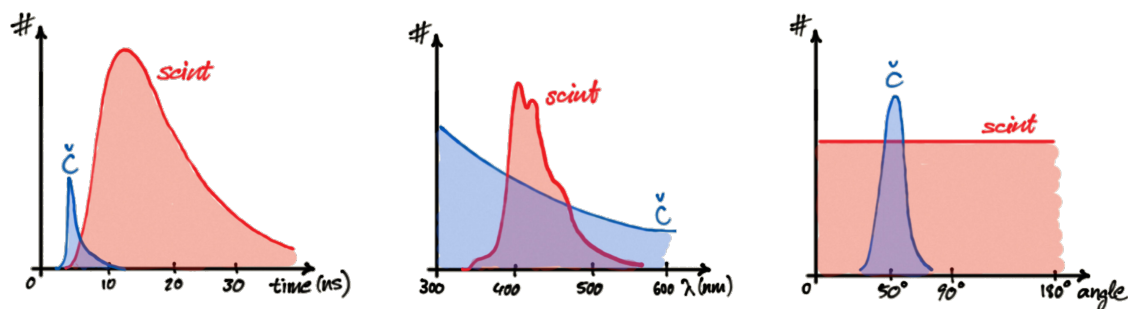


**Figure 8.1:** Different approaches are presented for the separation of scintillation and Cherenkov light. The two light emission mechanisms can be distinguished based on their timing (*left*), their wavelength (*center*), or their geometric angular properties (*right*). Figure taken from [274].

### 8.1.2 CHEMICAL STRUCTURE AND PRODUCTION OF WbLS

The chemical properties of water and liquid scintillators generally prevent them from mixing due to their different polarities. It is hence necessary to introduce an additional supplementary component into the detector medium besides water and the scintillator in order to create a WbLS. This role is fulfilled by so-called surfactants which are composed of hydrophilic heads and hydrophobic tails. A micelle-structure of liquid scintillator droplets surrounded by surfactant molecules enables the mixing process: The heads of the surfactant are in contact with the water while the tails bridge the connection to the liquid scintillator droplet, as shown in figure 8.2. As a consequence, it becomes possible to dissolve scintillators in water.

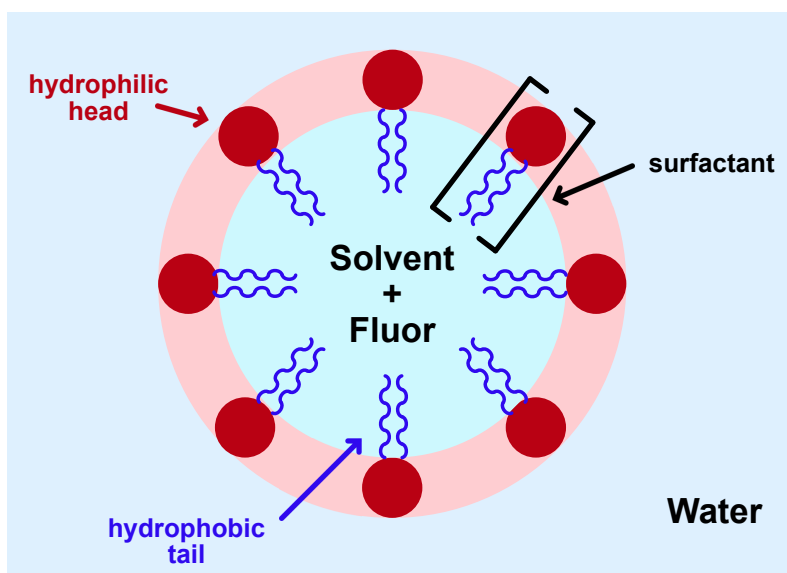


**Figure 8.2:** Schematic depiction of the micelle structure of WbLS. The scintillator mixture consisting of a solvent and a fluor is mixed into the water by making use of surfactant molecules containing hydrophilic heads and hydrophobic tails. Figure based on [275], originally found in references [276, 277].

The general production process of WbLS is presented schematically in figure 8.3. First of all, the surfactant is mixed into the water by making use of an impeller. As a next step, a

so-called "master solution" is created out of the solvent, fluor, and potential wavelength-shifters. This master solution is subsequently dissolved into the water/surfactant medium by using the impeller at moderate speeds [278].

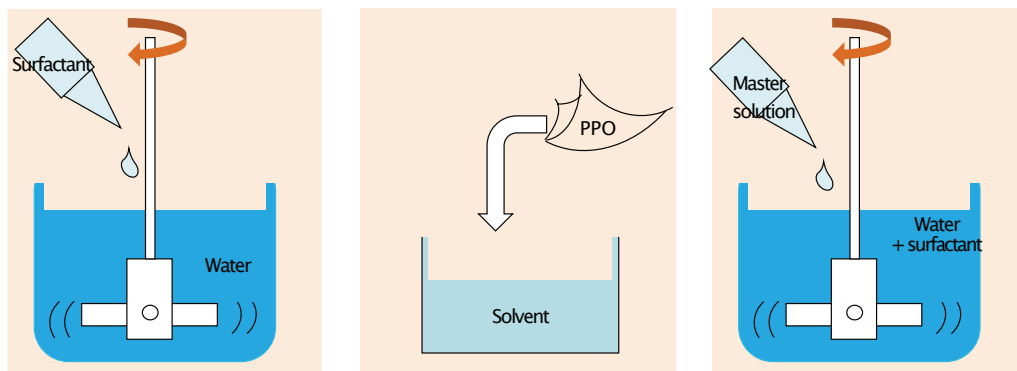


**Figure 8.3:** Procedure for producing a WbLS solution with wavelength shifter material (PPO). The surfactant is first dissolved in the water (*left*), before the master solution is created by mixing the solvent with the fluor PPO and potential additional wavelength shifters (*center*). At the end, the master solution is given to the water/surfactant solution (*right*). Figure taken from [278].

A variety of surfactant materials are in principle available for the production process of WbLS. Several surfactants have been investigated for their suitability in terms of WbLS production in reference [278]. Three main candidates were identified that remained transparent over time, namely Triton X-100, NP 10, and LAS. Out of them, Triton X-100 showed the highest light yield and was identified as a good candidate for a WbLS mixture. LAS, however, showed some unstable behavior in the past and has a dark brown color, which would need to be removed before its use.

### 8.1.3 CHARACTERIZATION OF WbLS

While some expectations for the properties of the Water-based Liquid Scintillator can be roughly extrapolated based on the attributes of its single components under consideration of their relative concentrations, experimental measurements are needed to determine the real behavior of this new detection medium. This section will highlight the current knowledge of different properties of WbLS, such as its light yield, emission time profile, absorption and re-emission behavior, and quenching. Current gaps in our knowledge will be highlighted and plans for further experimental characterization efforts will be unveiled.

#### Light Yield

The light yield of WbLS samples with different concentrations was recently evaluated in an experimental setup at the University of Berkeley consisting of a radioactive source, a vial with the WbLS solution and a photomultiplier [279]. Within this setup, the light yield of the WbLS probes was determined by replicating the experimental apparatus in the scope of a Monte Carlo simulation and comparing the observed charge spectra between data and the simulation. The best-fit value was determined by varying the light yield parameter in the MC and identifying which configuration yielded the best agreement with the data. Figure 8.4 presents the results of this measurement. The light yield is

shown as a function of the WbLS concentration, including a reference measurement of pure liquid scintillator at the corresponding concentration of 100%. A linear fit with a floating intercept value at vanishing concentration of liquid scintillator is found to provide the best agreement (*orange line*), with a slope of  $127.9 \pm 17.0$  photons/MeV/%LS [279]. The non-zero intercept value hints at a non-linear light output behavior at concentrations below 1%. Furthermore, it is interesting to note that the measured light yield values for the WbLS samples are higher than one would assume based on a linear extrapolation of the pure LS light yield scaled to the relative concentrations of the samples (indicated by the grey curve).

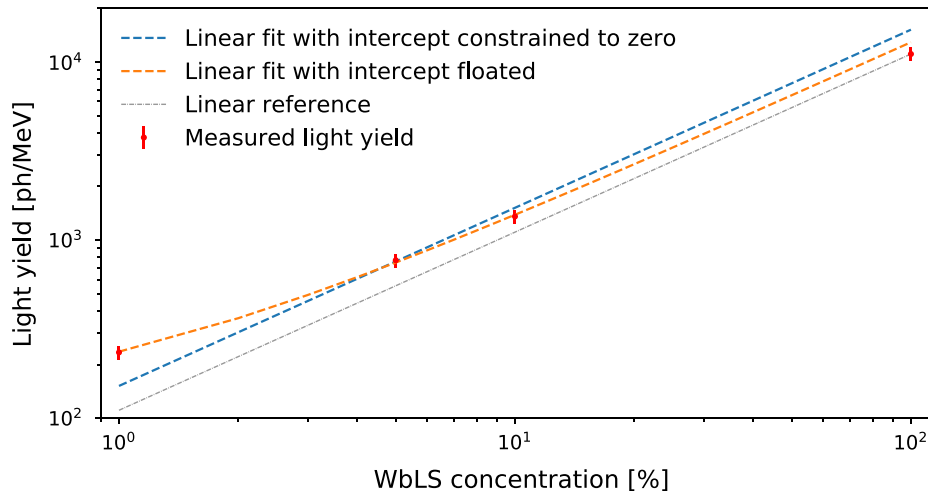


**Figure 8.4:** Measured light yield in photons/MeV as a function of the WbLS concentration. For a WbLS mixture with a concentration of 1%, the light output is slightly higher than 200 photons per MeV. Figure taken from [279].

### Emission time profile

The emission time profile  $f_{\text{emission}}(t)$  of liquid scintillators can be parameterized by a combination of exponential decays with different decay constants  $\tau_i$  and associated weights  $w_i$  alongside a rise time constant  $\tau_r$  as follows:

$$f_{\text{emission}}(t) = \sum_i w_i \cdot \frac{e^{-t/\tau_i} - e^{-t/\tau_r}}{\tau_i - \tau_r} \quad (8.1)$$

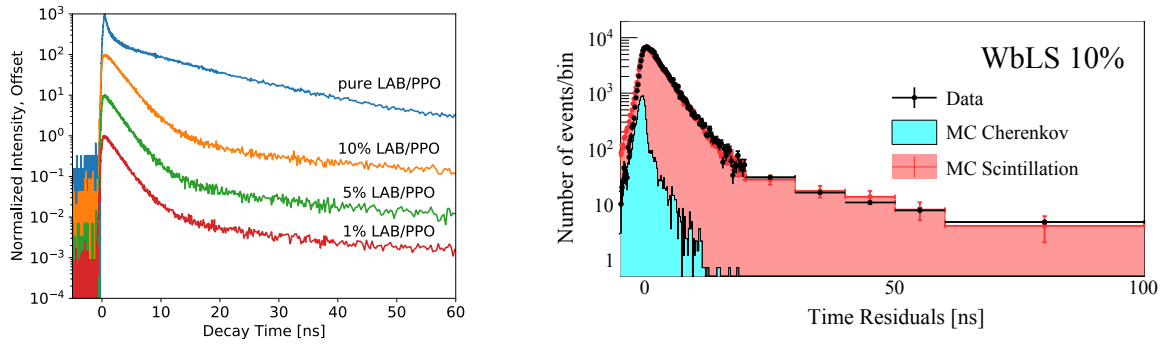
While the rise time only affects the very early region of the time profile, the time constants  $\tau_i$  influence both the width of the distribution and also the behavior at later times. The parameters of this emission time profile were extracted by two independent measurements that were using X-ray excitation and a  $\beta$ -source, with the results depicted in table 8.1 for a 1% WbLS probe. Rather small primary decay times in the range  $\tau_1 \in [2.00, 2.25]$  ns and a small rise time  $\tau_r \in [0.00, 0.23]$  ns were obtained in those experiments. Such a fast scintillator response provides a challenge for the separation of Cherenkov photons and scintillation photons based on timing alone.

Figure 8.5 shows the measured time profiles that were used to extract the parameters presented in table 8.1. The left part of the figure highlights how the time response differs

Measurement	$\tau_r$ [ns]	$\tau_1$ [ns]	$w_1$	$\tau_2$ [ns]	$w_2$	$\tau_3$ [ns]	$w_3$
X-ray excitation [280]	$0.23 \pm 0.06$	$2.00 \pm 0.03$	87%	$12 \pm 1$	6.8%	$110 \pm 10$	6.2%
$^{90}\text{Sr}$ $\beta$ -source [279]	$0.00 \pm 0.06$	$2.25 \pm 0.15$	96%	$15.10 \pm 7.47$	4%	-	-

**Table 8.1:** Comparison of the extracted emission time profile parameters for a 1%-WbLS probe for measurements conducted with a X-ray source and a  $^{90}\text{Sr}$   $\beta$ -emitter source. The results show good agreement (within  $1\sigma$ ) for the prompt time window of 5 ns while there are some discrepancies at later times due to the limited sensitivity of the measurement with the beta-emitter in this late time window [279].

for different concentrations of WbLS and pure liquid scintillator samples. While the overall normalization changes drastically based on the concentration of the WbLS sample due to the change in light yield, the decay time profile is consistent between the different samples. The right side of the figure highlights the contributions of the fast Cherenkov component (*blue*) and the slower scintillation component (*red*) to the overall observed spectrum for a sample of 10% WbLS. The simulated spectra seem to match the recorded data well for the best-fit emission parameters that were shown in the table above. Samples with smaller concentrations will feature a smaller relative contribution of scintillation light to the overall time spectrum but can be parameterized by similar timing parameters.



**Figure 8.5:** Left: Measured time profiles of different WbLS samples and a reference liquid scintillator sample that were acquired by making use of X-ray excitations of the media. Figure taken from [280]. Right: Measured time profile of a 10% WbLS sample (*black points*) alongside the simulated contributions of Cherenkov (*blue*) and scintillation (*red*) light for the best-fit configuration. Measurements were conducted with a  $^{90}\text{Sr}$   $\beta$ -source in this case. Figure taken from [279].

### Absorption spectra & Re-emission

The attenuation coefficient  $a_{\text{WbLS}}$  of WbLS can be determined to first order using the Beer-Lambert law based on the attenuation coefficients of its components (water, LAB, PPO) as follows:

$$a_{\text{WbLS}} = \sum_i a_i = \sum_i \epsilon_i \cdot \eta_i \quad (8.2)$$

with the molar attenuation coefficients  $\epsilon_i$ , the molar concentrations  $\eta_i$ , and the index  $i$  looping over all constituents (water, LAB, PPO).

The resulting expected absorption length spectrum of the WbLS mixture was calculated by Daniele Guffanti in the context of simulation studies for the planned WbLS test cell

in Mainz and is shown in figure 8.6. The individual absorption spectra of the single constituents are depicted as dashed lines and rely on data from the JUNO MC optical model (LAB) [281], the OSIRIS MC package (water) [282], and the PhotochemCAD absorption database (PPO) [283]. Furthermore, the total expected absorption and re-emission spectra for WbLS are shown as solid lines. While water constitutes the dominant contribution for photon wavelengths above 350 nm, the absorption process for shorter wavelengths is dominated by the absorption on PPO, and to some extent also by the absorption on LAB.

This model should be well suited for preliminary simulation studies, but it will be vital to validate this expectation by dedicated measurements of the absorption length for a realistic WbLS sample. This also applies in particular to the mechanism of re-emission in WbLS. Based on experience from conventional liquid scintillator detectors, one would expect that photons absorbed by LAB will be able to transfer their excitation energy with an efficiency of 80% to PPO, which would in turn release a re-emission photon. In the case that photons are directly absorbed by PPO, the re-emission takes place with an efficiency of 100%. It is, however, not entirely clear whether the same efficiencies can be assumed for the case that the LAB/PPO mixture is bound in the form of micelles in a larger water volume. Dedicated absorption length measurements in the form of a UV-Vis spectrometer are needed in the future to verify the expectations for the absorption curves in the case of WbLS samples.

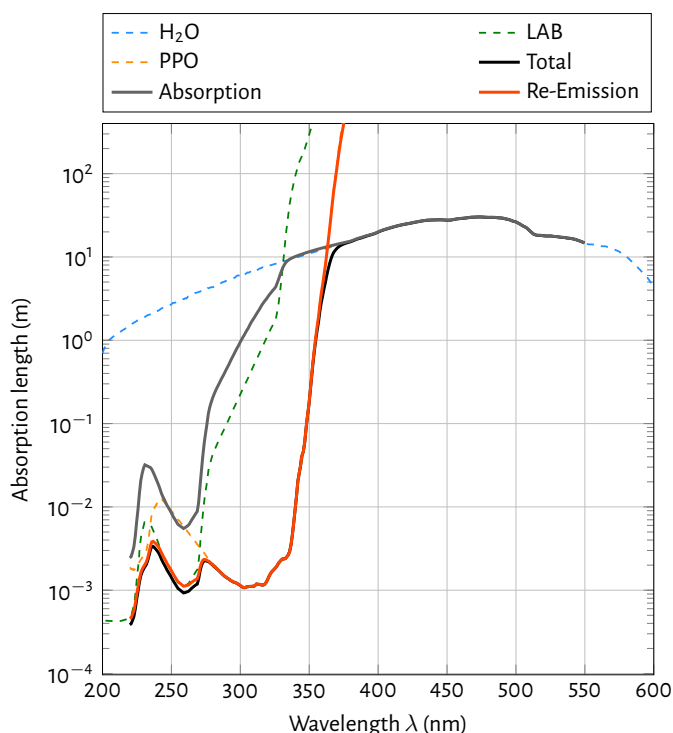


**Figure 8.6:** Extrapolated absorption length spectrum for a 1% WbLS solution (*black*), separated into a re-emission (*orange*) and absorption component (*grey*). The single constituents of the WbLS spectrum (water, LAB, PPO) are depicted in addition. Figure provided as a courtesy by Daniele Guffanti.

## Quenching

The amount of scintillation light per unit length  $dL/dx$  within liquid scintillators can

be characterized as a function of the particle energy  $E$  by the modified Birks formula as follows [34]

$$\frac{dL}{dx} = \frac{S \cdot \frac{dE}{dx}}{1 + kB \frac{dE}{dx}}, \quad (8.3)$$

with the absolute scintillation yield  $S$ , the Birks' constant  $kB$  and the energy loss per unit length  $\frac{dE}{dx}$ , which behaves differently for different particle types. Following reference [284], the total amount of scintillation light can be computed as

$$L(E) = \int_0^E dL = \int_0^E \frac{S dE}{1 + kB \frac{dE}{dx}}. \quad (8.4)$$

Particles such as electrons that generally feature a rather low stopping power  $\frac{dE}{dx}$  end up to produce amounts of scintillation  $L_{\text{electron}}(E)$  light that exploit the full scintillation light yield of the detector medium. Ions and other heavier particles, however, are characterized by a high stopping power and observe a reduced light yield  $L_{\text{ion}}(E)$ :

$$L_{\text{electron}}(E) = S \cdot E$$

$$L_{\text{ion}}(E) = \frac{S \cdot E}{kB}$$

The factor  $kB$  will be labeled the *quenching factor* in what follows, since it describes the decrease in light yield observed for ion-like particles.

Due to the complex chemical structure of WbLS, the amount of quenching is difficult to predict just based on the known values for pure liquid scintillator samples. It is therefore crucial to measure the quenching behavior in an experimental setting. So far, only one measurement of quenching effects in WbLS exists, which was conducted at Brookhaven National Lab utilizing high-energetic proton beams. Two different samples of WbLS were investigated for their scintillation light yield, with concentrations of 0.4% (1.0%) for the first (second) sample. Quenching parameters of  $kB = (0.70 \pm 0.12 \pm 0.07)$  mm/MeV and  $kB = (0.44 \pm 0.01 \pm 0.04)$  mm/MeV were found for the samples of 0.4% and 1.0% concentration [268], respectively. Contrary to expectations, these values are higher than those measured for conventional liquid scintillators, which typically range from  $kB = 0.07$  mm/MeV to  $kB = 0.2$  mm/MeV [285, 286, 287, 288]. Further independent measurements are hence needed to provide clarification on this matter in the future.

## 8.2 WBLS IN ANNIE

Besides the first demonstration of the usability of LAPPDs in a neutrino beam environment and the utilization of Gadolinium-doped water as the main target material, the exploration of WbLS forms another important pillar of the R&D segment of ANNIE. While dedicated small-scale experiments like CHESS [273] already exist and are in the process of characterizing the properties of this new medium, ANNIE will play a leading role in determining the material's potential in a beam neutrino environment. In this context, a first data taking campaign labeled *Phase II-Upgrade* will be launched by placing an acrylic vessel filled with WbLS inside the current ANNIE water tank configuration. The

first subsection 8.2.1 will present the characteristic aspects of this phase, before subsection 8.2.2 highlights how the modified detector setup is implemented in the simulation. The subsequent subsection 8.2.3 presents the features of neutrino interactions within ANNIE based on simulation studies and outlines the plans how to exploit the additional scintillation light to improve the neutrino energy reconstruction capabilities. Related to these ideas, subsection 8.2.4 details how the muon and hadronic light contributions could be separated, before the final subsection 8.2.5 delves into the expected improvements of the neutrino energy reconstruction compared to the case of water as the target material.

### 8.2.1 PHASE II UPGRADE: DEPLOYING THE SANDI VOLUME

The benefits of using WbLS in a neutrino beam environment are going to be investigated in the scope of ANNIE in the upcoming Phase II-Upgrade, in which a vessel filled with WbLS will be placed within the existing Phase II detector infrastructure. The vessel is named SANDI, inspired by an older proposal called the **S**mall **A**NNIE **N**eutrino **D**etector at **I**SU that was considered as a test environment for LAPPDs during ANNIE phase I [289].

Figure 8.7 provides a sketch of the vessel on the left side and a schematic representation of the placement of the vessel within the overall ANNIE experiment on the right side. Dimension-wise, the cylindrical vessel features an inner diameter of 72 cm and an outer diameter of 76 cm. The top and bottom lid extend even further with a diameter of 92 cm, with the top part incorporating an additional structural hanger construction. This hanger construction will be used to lower the vessel into the detector, with the other side of the rope being connected to a support beam above the water tank which is connected to the side wall of the experimental hall (shown in *green* on the right side of the figure). The main cylinder has a height of 90 cm while the top and bottom lids both add an additional height of 10.5 cm, respectively.

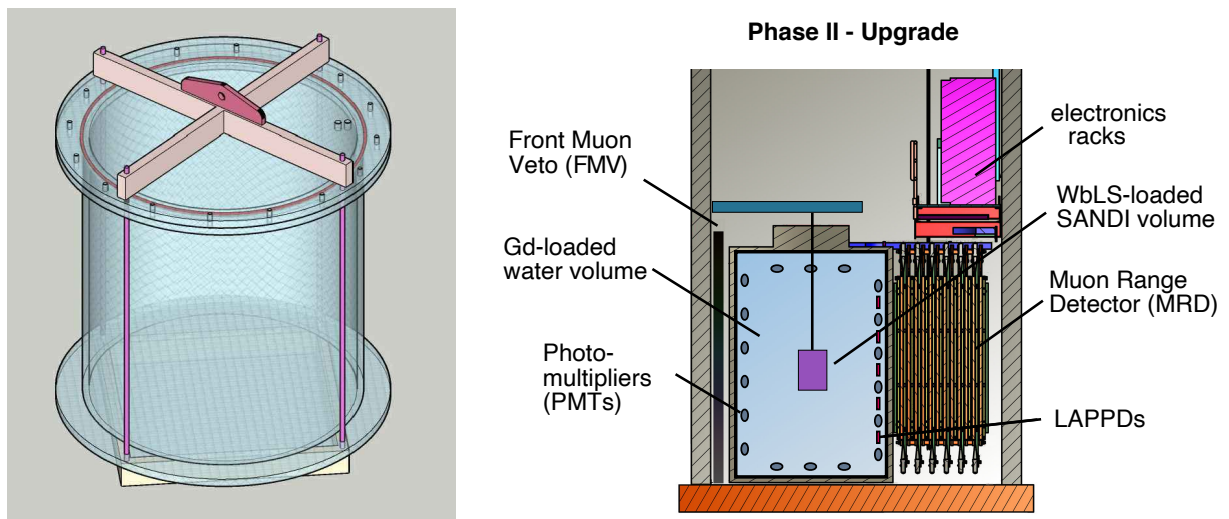


**Figure 8.7:** **Left:** 3D-Sketch of the SANDI vessel before production. **Right:** Schematic of the planned detector geometry for ANNIE Phase II-Upgrade, with the WbLS-filled SANDI volume depicted in purple.

The method of deploying a WbLS-filled vessel in the existing ANNIE detector framework provides a non-invasive way of evaluating the performance of the detector material in a

beam environment. In case promising results are achieved with the small WbLS vessel, a further upgrade with the complete cylindrical tank being filled with WbLS could be envisioned for future phases of ANNIE.

### 8.2.2 SIMULATION OF SANDI IN ANNIE

The SANDI vessel needs to be incorporated in two places within the simulation chain: Firstly, the *gdml*-file used in the GENIE event generator step needs to be updated to include such a smaller volume within the main water tank. In addition, also the Geant4-based simulation geometry needs to include an additional WbLS volume. Contrary to the Monte Carlo environment for the current phase II, the framework *ratpac* will be used to carry out the detector simulation instead of *WCSim*. Since many other experiments (like WATCHMAN or THEIA) tend to use *ratpac* for their studies, a lot of effort has been put into the implementation of a realistic WbLS model and the framework is hence deemed to be better suited to model the upcoming Phase II-Upgrade of ANNIE. A specific ANNIE-oriented version of *ratpac* [208] that incorporates the correct geometry will be used.

Regarding the simulation of interactions in GENIE, the neutrinos will interact differently with the scintillator within the vessel compared to the surrounding water. Although the fraction of scintillator will just be 1% in the case of ANNIE, it is still important to model the vessel with the correct material composition. Figure 8.8 provides an overview of the updated *gdml*-geometry with the SANDI vessel placed in the center of the water tank. This geometry was used to simulate the neutrino interactions for the Phase II-Upgrade phase. While the exact location of the SANDI volume is not determined yet and could also be slightly off-centered, the findings from the following study using a central WbLS volume should be easily transferrable to a slightly modified geometric setup.

The neutrino interactions are restricted to the WbLS SANDI volume in GENIE such that no interactions in the water are modeled. Vertex reconstruction methods will need to be employed to select a similar WbLS-restricted sample in the case of real data. Figure 8.9 shows the interaction frequency as a function of the vertex position in a side and top view of the detector. Both the side and top view show very uniform interaction vertex distributions for a very small coordinate ranges corresponding to the SANDI vessel dimensions. The fact that the side view shows slight decreases at the upstream and downstream edges of the vessel simply can be traced back to projection effects of the cylindrical volume onto a plane.

Within *ratpac*, the properties of the WbLS are incorporated for the planned mixture of 1%-WbLS, with LAB as the solvent, PPO as the primary fluor and LAS as the surfactant. In addition, it is planned to dope the WbLS mixture with Gadolinium to obtain a uniform neutron capture probability across the normal water volume of ANNIE and the SANDI volume within. The emission time profiles of the scintillation and re-emission light are modeled according to the time profile parameters  $\tau_{\text{rise}} = 0.25 \text{ ns}$ ,  $\tau_1 = 2.01 \text{ ns}$  ( $w_1 = 98.7\%$ ),  $\tau_2 = 12.73 \text{ ns}$  ( $w_2 = 1.02\%$ ), and  $\tau_3 = 116.86 \text{ ns}$  ( $w_3 = 0.1\%$ ) according to recent measurements conducted at the University of Berkeley [290]. The light yield of the WbLS is modeled to be 234 photons per MeV.

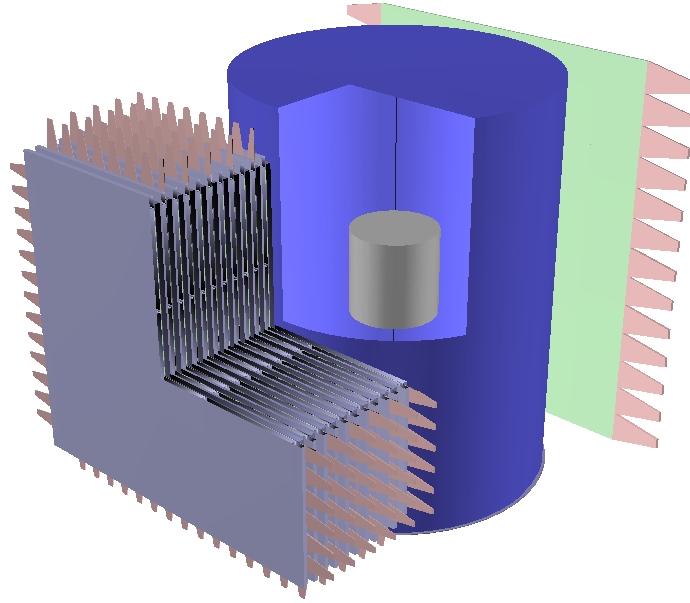


**Figure 8.8:** *GDML* geometry of the ANNIE experiment for the planned PhaseII-Upgrade. The SANDI volume (grey) is positioned in the center of the larger conventional ANNIE water tank (blue).

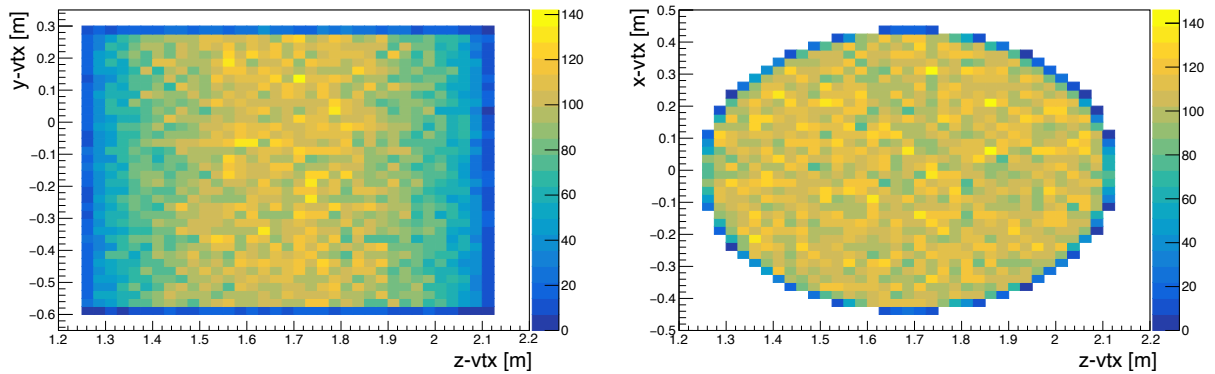


**Figure 8.9:** Interaction frequency of neutrino interactions in the cylindrical SANDI volume within ANNIE, shown in both a side view (*left*) and a top view (*right*) of the SANDI cylinder.

The fast scintillation emission times make it harder to separate the slightly faster Cherenkov photons from the scintillation light. Figure 8.10 emphasizes this difficulty: It shows the time-of-flight corrected arrival times of Cherenkov photons, scintillation photons, and re-emission photons for simulated events within the SANDI volume. As expected, the peak position of the Cherenkov time distribution is located around  $t_{\text{tof}} = 0$  ns, indicating that the photons were emitted instantaneously in this case and the only time delay was caused by photon propagation. For the scintillation and re-emission photons, the peak positions are shifted to slightly higher values of 2 ns due to their delayed emission profiles. However, the small difference of  $\Delta t_{\text{tof}} = 2$  ns makes it challenging to separate out the Cherenkov

contribution and imposes hard constraints on the PMT-by-PMT cable delay calibration procedure. A precision of 1 ns or less is required for the timing calibration campaign to provide feasible conditions for the usage of WbLS in ANNIE. Such levels of precision will be achieved in the upcoming laser calibration campaign utilizing a picosecond pulsed laser source.

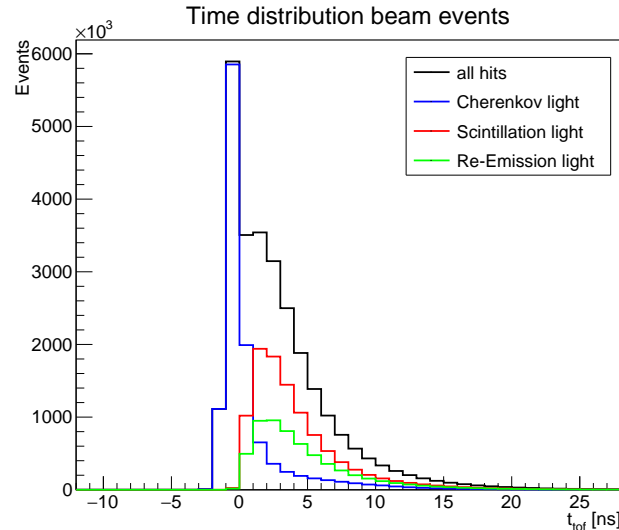


**Figure 8.10:** Time-of-flight corrected timing distribution of photons emitted within the WbLS SANDI volume in ANNIE, separated into the contributions from the different emission processes of Cherenkov light (*blue*), scintillation light (*red*) and re-emitted light (*green*).

### 8.2.3 INVESTIGATION OF NEUTRINO INTERACTIONS IN SANDI

The application of WbLS in a neutrino beam environment is expected to be beneficial in the identification of more complex event topologies and in terms of the calorimetric energy reconstruction capabilities. Combining these two aspects, one main goal is to minimize biases in the energy reconstruction of neutrinos. This subsection will highlight basic properties of simulated beam neutrino interactions such as the amount of Cherenkov and scintillation light observed for different particle types. It will furthermore point out which aspects of this additional information will be used to improve the neutrino energy reconstruction capabilities in the scope of this study.

Neutrino interactions are modeled according to the BNB flux files and restricted to interact within the SANDI volume within GENIE. All final state particles are then propagated through ratpac according to their specified properties (vertices, directions, energies). Photons are tracked throughout the whole detector and the resulting PMT charge and time distributions are stored for analysis.

Figure 8.11 shows the resulting total charge distributions (summed over all PMTs), separated into different photon types (*left*) and different particle types (*right*). The photon-type separated distributions highlight that Cherenkov light is the most dominant contribution in terms of its total light output, with a mean value of around 2000 p.e. per event. Scintillation light is almost as dominant but has a slightly lower mean value than the Cherenkov

photons. Re-emission photons contribute least to the total amount of observed charge, with the peak value of the distribution being located below 1000 p.e. In the scope of this comparison, it is important to consider that the Cherenkov light distribution also includes light that was emitted in the water region outside of the SANDI volume, while both the scintillation and re-emission components are solely emitted in the WbLS volume. When evaluating the charge response by particle type, it becomes evident that muons produce the dominant fraction of light observed in the beam neutrino interactions. Their charge distribution features a peak around 3000 p.e. and extends up to charge values of 8000 photoelectrons. The second most dominant contribution is caused by pions, with a peak charge value around 1500 photoelectrons. Both protons and neutrons are characterized by less light output with steeply declining distributions. In a direct comparison, protons deposit more light in the detector than neutrons by roughly a factor of two.

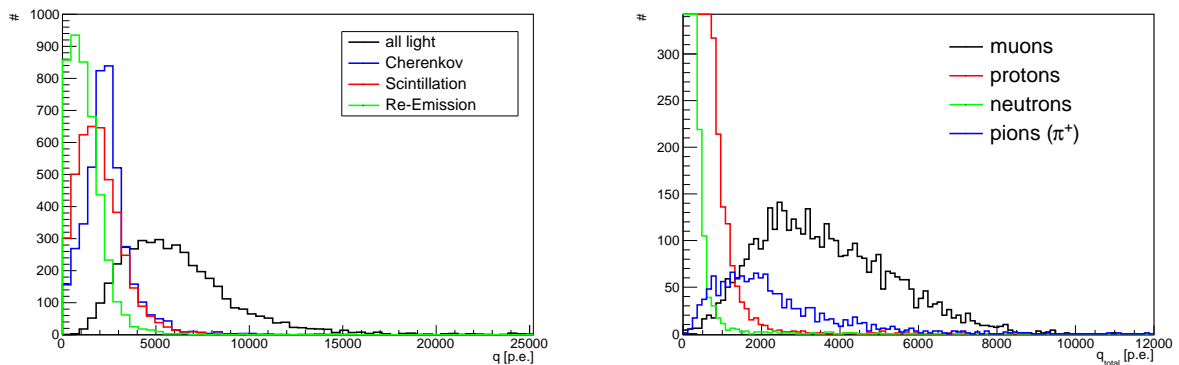


**Figure 8.11:** Left: Charge distributions of beam neutrino interactions in SANDI, separated in contributions from Cherenkov (blue), scintillation (red), and re-emission (green) processes. Right: Charge contributions of different particle types in beam neutrino interactions within SANDI. Muons feature the largest charge contribution (black), followed by pions (blue), protons (red), and neutrons (green).

In terms of the calorimetric energy reconstruction capabilities, one key aspect of the scintillation light output is its proportionality to the initial particle energy. If such a correlation is found, the observed scintillation light can be used to infer the kinetic energy of the respective particle by making use of a simple conversion factor. As a means of investigating whether such a proportionality exists within the simulation sample, the total PMT charge induced by a particle ( $Q_{\text{particle}}$ ) was evaluated as a function of its kinetic energy  $E_{\text{kin}}$  in term of a so-called particle light yield parameter  $L_{\text{particle}} = Q_{\text{particle}}/E_{\text{kin}}$ . Since multiple particles are usually present in beam neutrino interactions, the particle-induced charge  $Q_{\text{particle}}$  is obtained by looping over all photon hits for each PMT and selecting only those which were created in interactions of a certain primary particle. Photon emissions of secondary particles that were created in interactions of the primary particles are included in this photon selection since the emission of such photons can ultimately be traced back to the presence of the respective primary particle.

Figure 3.1.3 depicts the resulting light yield distributions for muons, protons, pions, and neutrons. The distributions of muons, pions, and neutrons is rather diffuse and features no clear peak. In the case of the muon, this can be explained rather easily by the minimum-ionizing nature of the energy loss process in this case. Muons deposit a

certain amount of ionization energy per unit length, rather independently of their kinetic energy. As a consequence, the amount of scintillation light will on the contrary depend on the path length that was traversed by the muon instead of its associated energy. Similar arguments can be used to explain the observed distribution of pions. In the case of neutrons, the missing peak structure in the distribution is expected from their behavior within conventional liquid scintillators. Since neutrons will primarily interact via elastic scattering in the scope of their thermalization process, the amount of scintillation light is generated by the recoil particles such as protons or oxygen nuclei. The scintillation light generated by those particles will not correspond linearly to the neutron kinetic energy due to the stochastic nature of the elastic scattering process [291, 292]. Furthermore, neutrons might leave the SANDI volume during thermalization, and in turn making parts of their kinetic energy inaccessible.

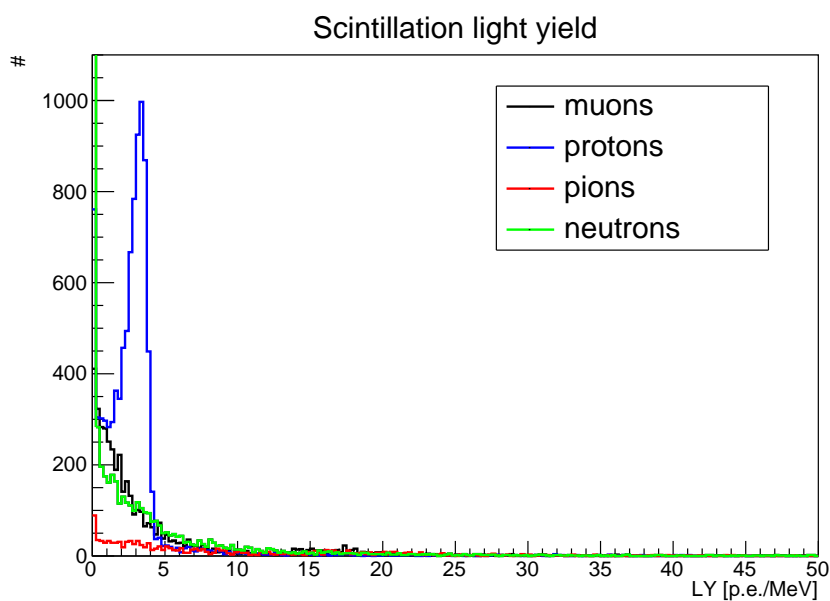


**Figure 8.12:** Scintillation light yield of different particles in the 1% WbLS SANDI volume within ANNIE. Protons are the only particle species showing a clear peak structure, indicating that protons are usually contained in the SANDI volume and emit an amount of light proportional to their energy. The scintillation light of muons, on the contrary, is independent of their energy due to the minimal ionizing nature and most muons not being contained in the SANDI volume.

The only particles that feature a clear pronounced peak in the light yield distribution are protons. Due to their large energy loss values, they are typically very contained and deposit their whole kinetic energy within the SANDI volume in form of ionization processes. This provides the exciting opportunity to detect protons in the first place, and additionally makes it possible to also infer their energy based on the amount of observed light. Compared to water as a detection medium, this represents a large improvement since protons are usually not observable in water Cherenkov detectors at all. The information about the deposited energy of protons is very helpful for improving the performance of the neutrino energy reconstruction since it represents one part of the total energy that is deposited by all primary particles created in the neutrino interaction.

Within beam interactions, the main challenge in identifying this proton energy will lie in

the isolation of the signal from the light contributions of other particles. In this context, it will be vital to subtract contributions from particles above the Cherenkov threshold based on the observed Cherenkov light signal from the overall detected charge distribution. This strategy will be thematized in more detail in the following paragraph, in which the necessary steps for such a reconstruction procedure will be outlined one by one.

### Neutrino energy reconstruction

Separating out the muon light contribution from the overall detected charge distribution requires some knowledge about the general geometric properties of the involved muon. Based on the vertex and the direction of the muon, the path length of its particle track in the water and WbLS volume can be calculated and associated with the corresponding Cherenkov, scintillation and re-emission photon light outputs. These can then be subtracted from the total observed charge to obtain the light levels that were induced by other particles such as protons, neutrons, or pions.

Figure 8.13 schematically depicts this procedure. An incoming beam neutrino interacts in the SANDI WbLS volume within ANNIE and produces a muon in the process. The muon emits Cherenkov light (*red*) within the whole water tank and scintillation light (*green*) only within the SANDI vessel. The first step revolves around the reconstruction of the muon track parameters, *i.e.* the vertex  $\vec{r}_{\text{vertex}}$  and direction  $\vec{d}_{\text{track}}$  of the particle. Based on these parameters, the track length in SANDI  $l_{\text{SANDI}}$  and in water  $l_{\text{water}}$  can be calculated based on geometric considerations. In the following, we will assume that the track parameters can be reconstructed with a certain accuracy since the necessary reconstruction tools are still under development for the case of muon tracks in WbLS.

Once the track lengths have been determined for the WbLS and water sections, the corresponding light contributions are calculated for the different photon emission types. Proportionality factors of detected charge as a function of the travelled distance are determined for Cherenkov, scintillation and re-emission photons based on information from simulations. The factors are used in combination with the total track length (SANDI track length) to determine the amount of Cherenkov (scintillation/re-emission) light emitted by the muon.

As a final step, the determined muon light levels are subtracted from the overall observed total charge to obtain the light emitted by residual other particles, such as protons, neutrons, or pions. Events featuring pions can be filtered out by making use of ring counting techniques which evaluate the number of observed Cherenkov patterns. For such selected single-ring events, the residual particle contribution will be mainly composed of protons and neutrons. As a consequence, the charge levels obtained after the subtraction of the muon contribution will be mainly composed of scintillation light. In this way, the total detected charge is separated into the two distinct contributions from muons and hadronic "recoil" particles. These properties will serve as additional input parameters for the random forest regressor which is reconstructing the neutrino energy based on observables in ANNIE, which is presented in more detail in the subsection 8.2.5 below.

While the presented method will have the potential to separate the muon-induced from the hadronic-related light output, it will be challenging to separate more similar contributions like the ones of protons and neutrons. The main accessible observable in that case is the

## WbLS neutrino energy reconstruction

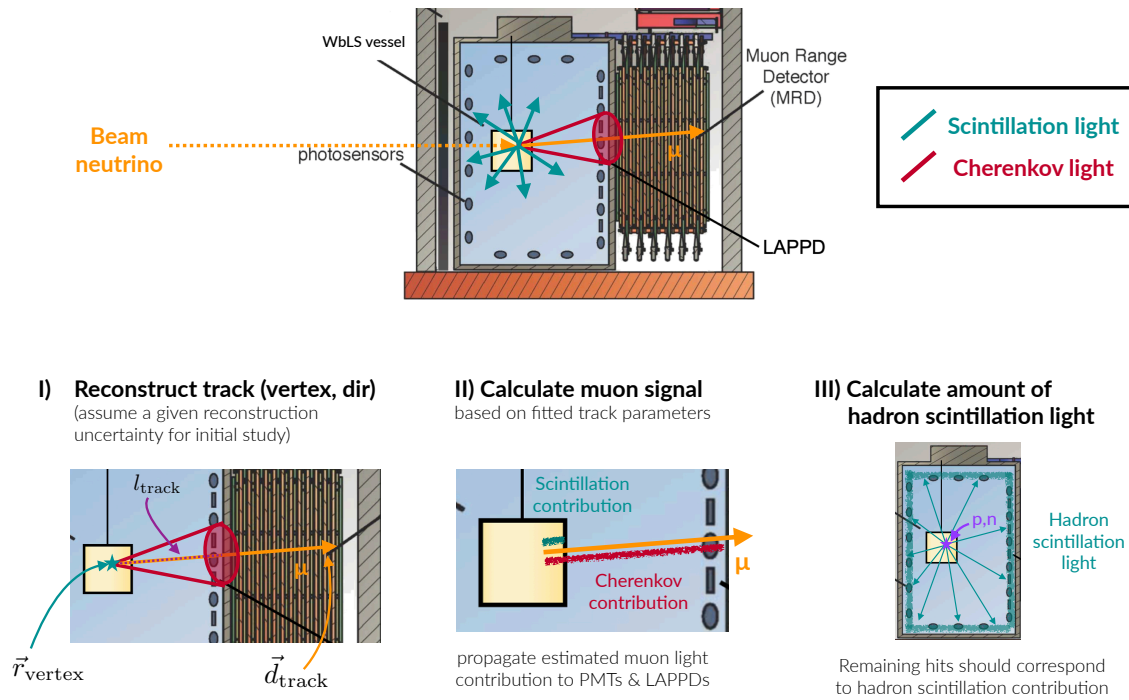


**Figure 8.13:** Neutrino energy reconstruction scheme for the WbLS volume in ANNIE. Based on the muon track parameters obtained from a reconstruction algorithm (*panel 1*), the Cherenkov and scintillation contributions of the muon light signal are calculated (*panel 2*). The residual light contribution from hadrons and other involved particles can subsequently be estimated using the total amount of detected light and the calculated muon contribution (*panel 3*). The determined muon and residual light signals can then be employed as additional inputs to achieve more accurate estimates for the neutrino energy.

number of neutrons, which can be obtained by counting the number of delayed neutron capture signals in the data. However, it will not be possible to predict the light output of those neutrons to great detail based on the neutron multiplicity, which will result in an enlarged uncertainty on the determined proton and neutron charge contributions and as a consequence also on the neutrino energy.

### 8.2.4 MUON & RECOIL LIGHT CONTRIBUTIONS

Reconstructing the muon and recoil charge contributions ( $Q_{\text{muon}}$ ,  $Q_{\text{recoil}}$ ) based on the corresponding track length values  $l_{\text{track}}$  requires the determination of the proportionality factors for the light output in Cherenkov, scintillation and re-emission photons. Those factors can be computed by evaluating the individual light outputs as a function of the path lengths, as shown in figure 8.14 in a 2-dimensional representation (*left*) and as a ratio of the two variables  $r = Q_i/l_{\text{track}}$  (*right*). The total track length across the water and WbLS volume was used to compute  $l_{\text{track}}$  in the case of the Cherenkov light while only the path length in the SANDI vessel was assumed in case of the scintillation and re-emission

photons. A clear peak structure is visible in the distribution of the ratio  $r$  for all three photon emission types, indicating that the use of a single conversion factor is roughly suitable for reconstructing the amount of charge that was observed in each case. A small tail is visible for the scintillation ratio distribution which will slightly skew the reconstructed light values in this case. The determined conversion factors are  $r_{\text{Cherenkov}} = (1.40 \pm 0.26)$  p.e./mm,  $r_{\text{scintillation}} = (2.70 \pm 0.33)$  p.e./mm, and  $r_{\text{reemission}} = (2.55 \pm 0.32)$  p.e./mm.

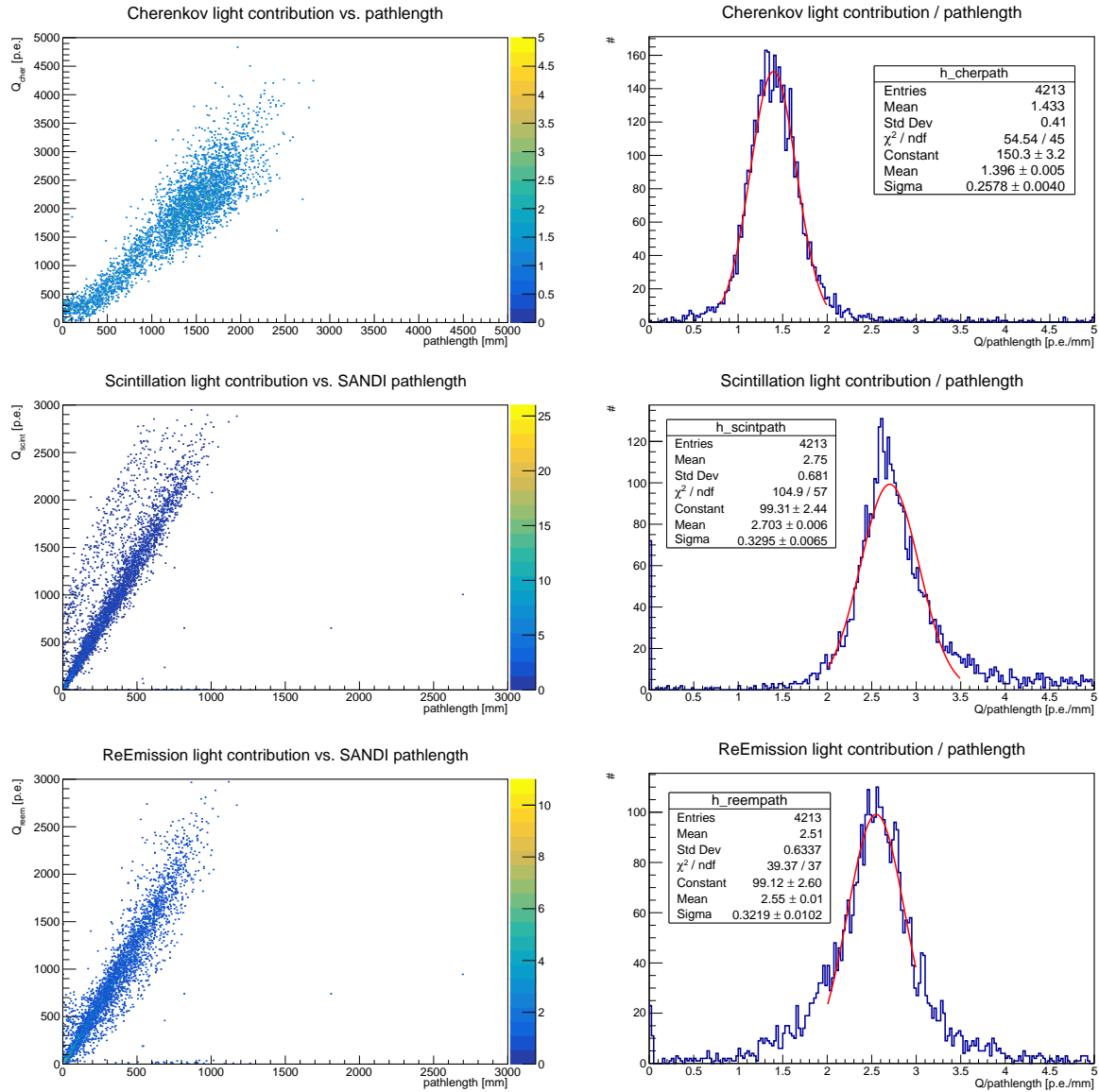
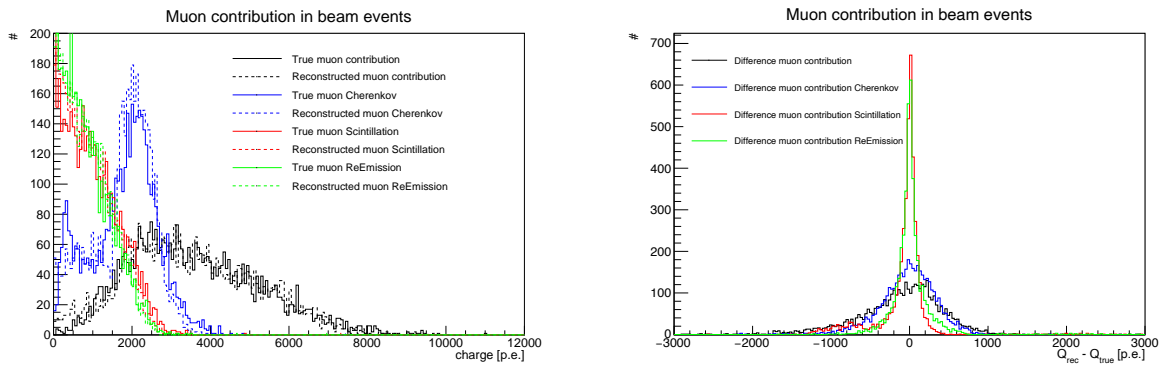


**Figure 8.14:** Total charge detected for Cherenkov (*top*), scintillation (*center*), and re-emission (*bottom*) processes. The left column shows the charge as a function of the muon path length while the right column depicts the distribution of the total charge values divided by the path length, including Gaussian fits for the peaks.

The conversion factors  $r_i$  for each photon type  $i \in \{\text{Cherenkov, scintillation, reemission}\}$  will be used to calculate the expected corresponding charge distributions  $Q_i$  as follows:

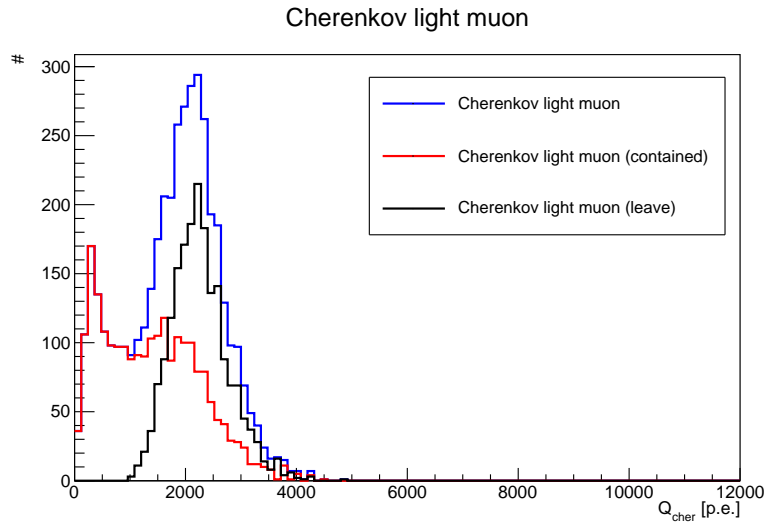
$$Q_i = r_i \cdot l_{\text{track}} \quad (8.5)$$

Figure 8.15 shows the resulting reconstructed muon charge distributions for the different photon contributions (*left*) and the difference between true and reconstructed values (*right*) for beam neutrino events with associated muons. When considering the muon charge distributions on the left, the reconstructed values are depicted as histograms with dashed lines while the true distributions are shown as solid lines. The overall shapes of the spectra are well reproduced in the reconstruction. When looking at the charge difference distributions  $\Delta Q = Q_{\text{rec}} - Q_{\text{true}}$  on the right, the mean value is close to zero in all cases, with  $\mu_{\text{Cherenkov}} = -20$  p.e.,  $\mu_{\text{scintillation}} = -84$  p.e., and  $\mu_{\text{reemission}} = 14$  photoelectrons. The widths of the spectra are very similar for the scintillation and reemission case while larger spreads are observed for Cherenkov light. This can likely be traced back to the fact that Cherenkov photons are emitted in the whole ANNIE tank, which in turn results in larger absolute charge values and therefore also larger absolute deviations from the true values. The standard deviations of the distributions have the values  $\sigma_{\text{Cherenkov}} = 357$  p.e.,  $\sigma_{\text{scintillation}} = 341$  p.e., and  $\sigma_{\text{reemission}} = 259$  photoelectrons. The relatively large spread for the scintillation light is caused by a cluster of events from the tail of the ratio distribution that are not very well reconstructed. When considering the total amount of light from all photon types, a mean value of  $\mu_{\text{total}} = -111$  p.e. and a standard deviation of  $\sigma_{\text{total}} = 545$  p.e. are observed.



**Figure 8.15:** **Left:** Reconstructed (*dashed line*) and true (*solid line*) charge contributions for muon particles in SANDI, separated into Cherenkov (*blue*), scintillation (*red*), and re-emission (*green*) components. **Right:** Difference of true and reconstructed charge contributions for muons in SANDI, split into the same emission components.

The Cherenkov charge distribution shown in the previous figure 8.15 is characterized by a two-peak structure, with the larger peak centered around a charge value of 2000 p.e. and the smaller peak located at 500 photoelectrons. When investigating the geometric properties of the corresponding muon tracks, it becomes clear that the two peaks belong to different kinds of muon event topologies, as highlighted in figure 8.16. While particles that are contained in the water tank deposit charge values in the region of the lower peak, higher charge values around the more dominant peak are primarily associated with muons that leave the water tank. Since those particles will generally have a larger path length in the water than the contained events, the observed larger charge values make sense. Regarding the neutrino energy reconstruction capabilities, only muons from the larger primary peak will be present due to selecting events with a coincident MRD track, and therefore requiring the muons to leave the tank.



**Figure 8.16:** Cherenkov light contributions of muons in the ANNIE phase II Upgrade configuration, depicted separately for contained events (*red*) and muons that leave the water tank (*black*). Events with charge values below 1000 p.e. are basically entirely composed of contained muons while the leaking muons constitute the majority of the peak at around 2000 photoelectrons.

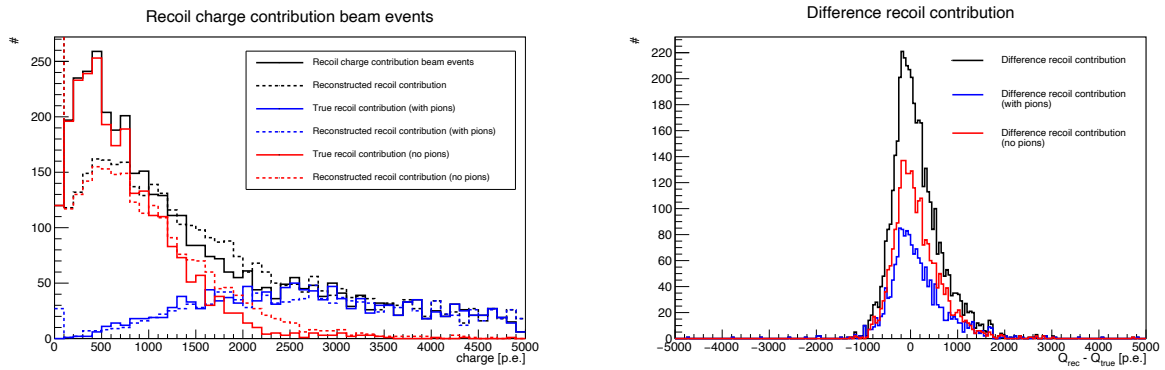
After having determined the muon-related charge contributions, the light emitted by other recoil particles can be inferred by subtracting the muon charge from the overall detected light level:

$$Q_{\text{recoil}} = Q_{\text{total}} - Q_{\text{muon}}. \quad (8.6)$$

Figure 8.17 shows the resulting reconstructed recoil charge distributions, separated into events with pions (*blue*) and without pions (*red*). While the spectral shapes are generally reproduced quite well by the reconstruction, really low charge values are underrepresented in the calculated recoil charge values. This effect can be traced back to the uncertainty of the muon charge reconstruction, which directly translates into a corresponding uncertainty in the recoil charge determination. Since the width of the total muon  $\Delta Q$ -distribution is around 500 p.e., it becomes challenging to detect recoil charge values below this value. This becomes directly noticeable as a reduction of reconstructed events in this energy region, which are then rather shifted to higher reconstructed charges. The effect of shifts to higher reconstructed values is also apparent in the  $\Delta Q_{\text{recoil}}$  spectrum, which features a mean value of 128 p.e. and a standard deviation of 555 photoelectrons. The right-hand tail of the distribution is more populated compared to the left side due to the aforementioned effect. Except for the misreconstruction in the low charge regime, the recoil light levels seem to be estimated reasonably well.

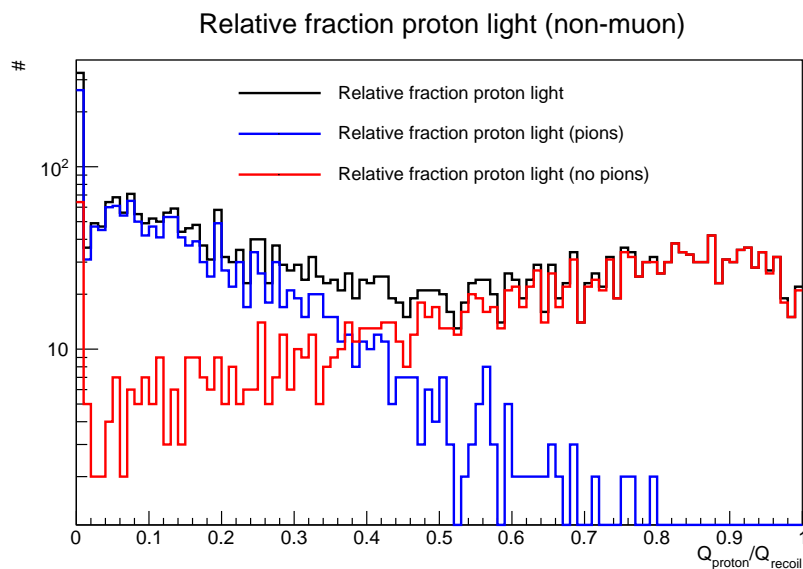
As a final step, we can evaluate the difference between the combined recoil charge distribution and the charge contribution that is specifically associated to protons as primary particles. This is interesting since the light levels induced by protons can be directly associated to their kinetic energy. In case the proton charge contributions can be isolated, one could hence get direct access to the energies of those particles as inputs for the neutrino energy reconstruction.

Figure 8.18 highlights the relative fraction of the proton-induced charge in comparison to



**Figure 8.17:** Left: Energy distributions for recoil particles, separated into events with pions (*blue*) and events without pions (*red*). Reconstructed charge distributions are depicted as dashed lines while the true distributions are shown as solid lines. Right: Difference of reconstructed and true recoil charge contributions for events with pions (*blue*) and events without pions (*red*).

the total recoil charge level ( $f_{\text{proton}} = Q_{\text{proton}}/Q_{\text{recoil}}$ ). Two separate distributions of  $f_{\text{proton}}$  are shown for the case of events including pions (*blue*) and for events without pions (*red*). Given that pions are present, they will contribute the largest fraction to the observed recoil charge value. As a consequence, the proton contribution to the overall recoil charge will be rather low, showing a most likely fraction around 10%. Events that do not involve any pions feature a rather high proton contribution, with the most dominant fraction being 90%. However, the tail of the proton fraction distribution further extends down to very low values with decreasing frequency in this case. While it is likely that protons are responsible for a large amount of the recoil charge, there will be a considerable fraction of events where other particles feature a larger contribution also in the case that no pions are present.



**Figure 8.18:** Relative fraction of the proton light of the non-muon *recoil* charge distribution for beam neutrino interactions in SANDI. The distributions are split into events with pions (*blue*) and events without pions (*red*).

The validity of the assumption that the entirety of the recoil charge is created by protons for different event categories can be easily probed by calculating the difference of the true proton-induced charge and the reconstructed recoil charge, as shown in figure 8.19. As expected, events that include a pion will be characterized by a severe misreconstruction of the proton-related charge value, since all photons generated by the pions will also be attributed to the proton. The proton charge reconstruction works considerably better in the case that no pions are present. However, the estimated proton charge in this case still includes light which was produced by other particles. As a consequence, the mean of the the  $\Delta Q_{\text{proton}}$  distribution is shifted to slightly higher values, with  $\mu_{\text{proton}} = 303$  p.e. and  $\sigma_{\text{proton}} = 562$  photoelectrons. The approximation of estimating the proton light contribution by the total amount of reconstructed recoil charge is therefore always overestimating the proton contribution due to other particles being present. A direct determination of the energies of involved protons is hence challenging even in the case that no pions are present. However, the total non-muon charge can still provide a useful handle on improving the neutrino energy reconstruction, which will be explored in the next subsection.

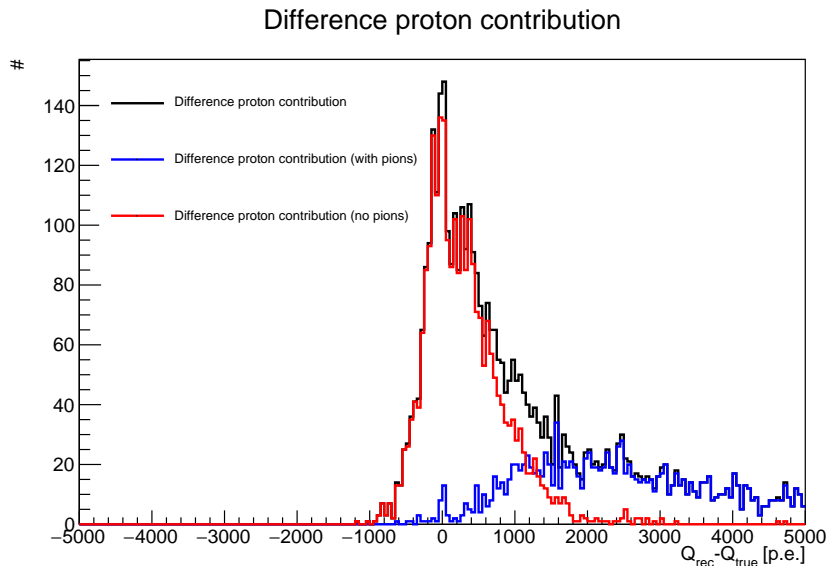


**Figure 8.19:** Difference of true and reconstructed charge contributions for protons in SANDI, split into events that feature pions and such that do not include any pions. The reconstructed proton charge is assumed to be identical to the total reconstructed recoil charge value in this case.

### 8.2.5 IMPROVED NEUTRINO ENERGY RECONSTRUCTION

Beam-related neutrino energy reconstruction in water Cherenkov detectors usually focuses around selecting a sample of CCQE-like interactions, since a relatively simple energy reconstruction formula exists for this case that solely depends on the primary lepton energy and angle with respect to the beam direction. Other interaction channels like the resonance channel or Deep Inelastic Scattering pose larger challenges in terms of estimating the corresponding neutrino energy since many other particles are typically present and some processes become inelastic. The variety of typical interaction channels in

beam neutrino interactions and their properties are presented in more detail in section 2.3.1 within the neutrino theory chapter.

The current section will investigate whether the neutrino energy reconstruction can be improved also for the more challenging interaction types based on the additional calorimetric information which is present in WbLS. The potential improvements will be investigated first by extending the formula for the neutrino energy reconstruction in subsection 8.2.5.1 by adding correction factors based on the amount of observed non-muon related charge, before the impact of the additional information will be probed in the scope of a random forest regressor in the subsequent subsection 8.2.5.2.

### 8.2.5.1 SIMPLE FORMULA-BASED RECONSTRUCTION

Charged-Current Quasielastic (CCQE) interactions are characterized by a relatively simple event topology in which the muon neutrino interacts with a neutron within the nucleus to form a muon and a proton:



Due to the limited amount of involved particles, the neutrino energy can be reconstructed simply by making use of energy and momentum conservation considerations, as presented for example in reference [293]. Under the assumption that the nucleon is at rest in the nucleus, the formula for the neutrino energy then only depends on the muon energy  $E_{\mu}$  and its direction with respect to the beam  $\theta_{\mu}$  and some constant parameters like the proton and neutron masses  $m_p$  and  $m_n$  and their binding energy  $E_b$ :

$$E_{\nu} = \frac{m_p^2 - (m_n - E_b)^2 - m_{\mu}^2 + 2(m_n - E_b)E_{\mu}}{2(m_n - E_b - E_{\mu} + p_{\mu} \cos \theta_{\mu})} \quad (8.8)$$

When applying this formula to our data sample of Charged-Current neutrino interactions in the SANDI volume within ANNIE, the resulting energy reconstruction performance is shown in figure 8.20 in form of the deviation from the true energy value. While quasi-elastic interactions are reconstructed reasonably well with the peak of the distribution around  $\Delta E \approx 0$  GeV, the other interaction types of Meson Exchange Current and Resonance interactions show much larger deviations. The neutrino energy is underestimated in these cases, with peak values of  $\Delta E_{\text{MEC}} \approx -200$  MeV and  $\Delta E_{\text{RES}} \approx -300$  MeV. Deep Inelastic Scattering processes play a subdominant role in the energy region of the Booster Neutrino beam and are hence not visible in the graph.

In order to achieve better energy reconstruction capabilities particularly for the interaction types of MEC and RES interactions, the CCQE-based formula (8.8) needs to be modified. The fact that the reconstructed values for the neutrino energy are underestimated seems to signal that the information from the muon itself is not sufficient for an accurate estimate of the neutrino energy in these cases. It might hence be useful to consider the amount of energy that is present in other primary particles besides the muon as additional input parameters.

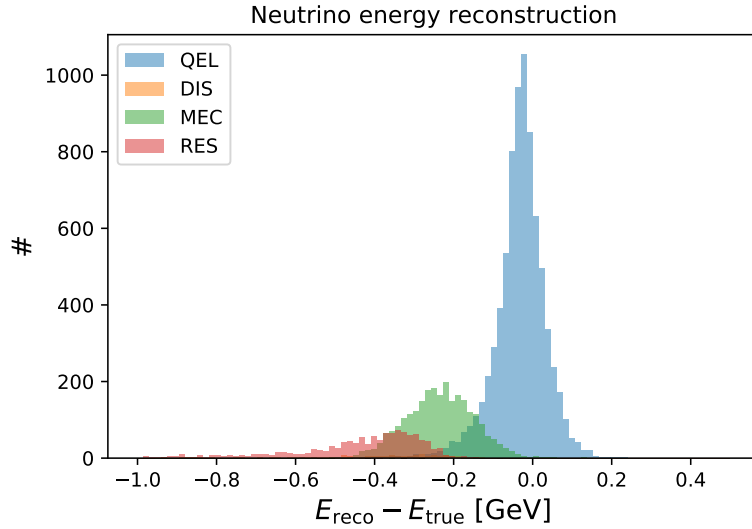


**Figure 8.20:** Neutrino energy reconstruction performance in terms of deviations from the true energy value when using the CCQE-based formula. Distributions are separated for the different interaction types of Quasi-Elastic events (QEL), Deep Inelastic Scattering (DIS), Meson Exchange Current (MEC), and Resonance interactions (RES).

As shown in the previous sections, the amount of charge deposited by the muon can be estimated based on its vertex and track parameters. The residual light not associated with the muon therefore provides an interesting candidate for a supplementary parameter in the reconstruction formula. Figure 8.21 evaluates how the non-muon charge contribution is related to the energy misreconstruction  $\Delta E = E_{\text{reco}} - E_{\text{true}}$  for the case of the true (reconstructed) non-muon charge on the left (right) side of the figure. A clear anti-correlation is visible between the two variables, indicating that the non-muon related charge could indeed be used to optimize the neutrino energy reconstruction. When comparing the two distributions, the spread in reconstructed non-muon charge values becomes apparent in comparison to the true charge equivalent, and could be slightly optimized by a more sophisticated charge reconstruction technique in the future.

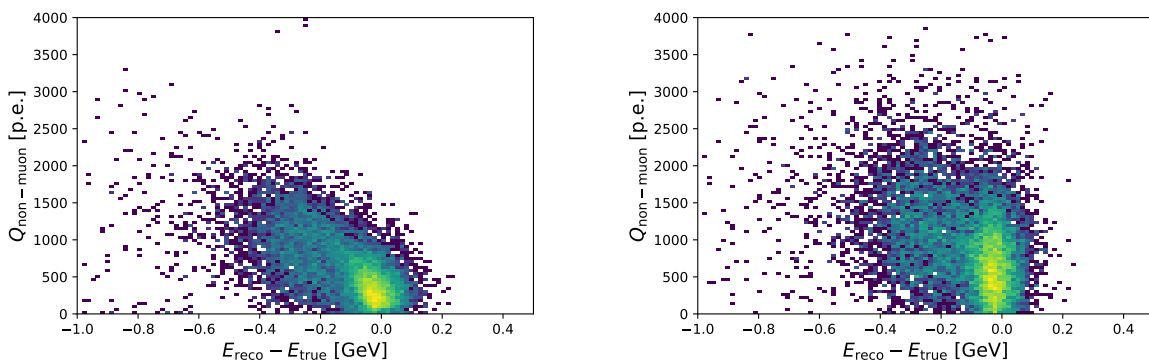


**Figure 8.21:** The non-muon charge contribution is depicted as a function of the neutrino energy misreconstruction  $\Delta E = E_{\text{reco}} - E_{\text{true}}$  for the case of the true (*left*) and reconstructed (*right*) non-muon charge value. A clear anti-correlation is visible between the two variables.

The anti-correlation between the non-muon related charge contribution and the energy

misreconstruction provides an opportunity for calculating a correction factor for the energy reconstruction procedure based on the observed muon track topology. However, such a correction should ideally only be applied in case of the interaction type being RES or MEC. As a consequence, it is vital to identify a selection mechanism for separating CCQE events from CC-RES and CC-MEC interactions. When considering a muon-neutrino beam, CCQE interactions will generally be accompanied by a proton. Neutrons will be produced rather rarely, for instance in the scope of Final State Interactions in the nucleus. Detecting at least one neutron capture could thus be a reasonable approach to primarily select non-CCQE interactions. The left part of figure 8.22 depicts the neutron capture distribution for the different interaction types, highlighting that CCQE interactions only marginally contribute to events that include at least one neutron capture.

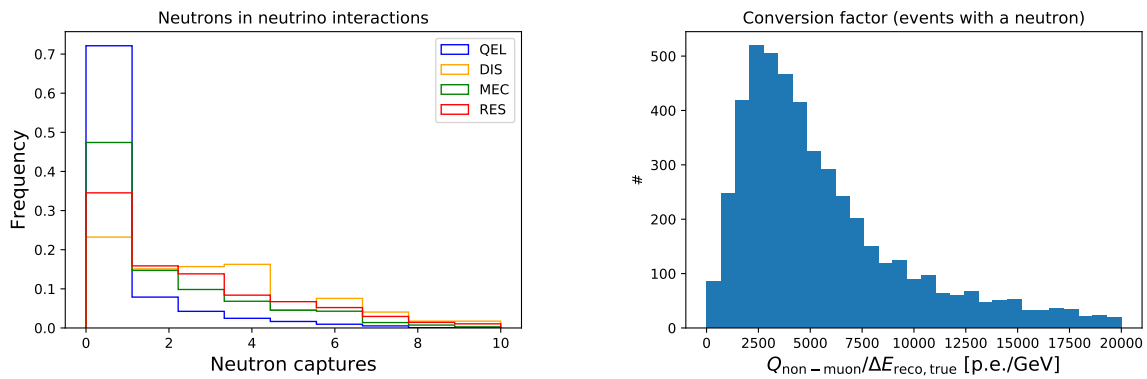


**Figure 8.22:** **Left:** The number of neutron captures is shown as a function of the neutrino interaction types as predicted by GENIE (v3.0.6). **Right:** The distribution of a correction factor constructed based on the ratio of the non-muon charge and the amount of neutrino energy misreconstruction for events featuring at least one neutron capture.

After having selected non-CCQE event topologies, a correction factor  $f_{\text{corr}}$  needs to be applied to the reconstructed neutrino energy based on the charge not associated with the muon:

$$E_{\nu} = E_{\nu}(\text{CCQE}) + f_{\text{corr}} \cdot Q_{\text{non-muon}} \quad (8.9)$$

The distribution of the ratio of non-muon-related charge and the energy misreconstruction is shown on the right side of figure 8.22. Since the distribution looks rather broad and has a large tail, the most probable ratio is chosen to be slightly larger than the peak position, corresponding to a correction factor of  $f_{\text{corr}} = 1/4000 \text{ GeV/photoelectrons}$ .

The resulting corrected neutrino energy values are shown in figure 8.23 for the case of using the true (reconstructed) value for the non-muon charge on the left (right). The blue distribution depicts the reconstruction performance in case no correction is applied while the orange histogram highlights the behavior assuming that the correction is applied for all events, and the green distribution shows the performance provided that the correction is only applied to events with at least one neutron capture. As expected, the correction overcompensates when being applied to all events, since especially CCQE events will be attributed an energy which is too large. However, an improvement is visible when applying the correction only for events that feature at least one neutron capture: A more symmetric distribution is achieved around the correct energy value. When using the reconstructed

$Q_{\text{non-muon}}$ -value, the neutrino energy reconstruction performance is characterized by a larger spread around the true energy value. However, the results still represent a large improvement with respect to the unmodified formula.

Overall, the application of a correction factor based on the energy deposited by non-muonic particles seems to be a promising technique for improving the neutrino energy reconstruction performance in WbLS detectors. Further additions in the future could encompass a more accurate muon charge estimation method and a more sophisticated correction factor that could take into account more features of the event topology.

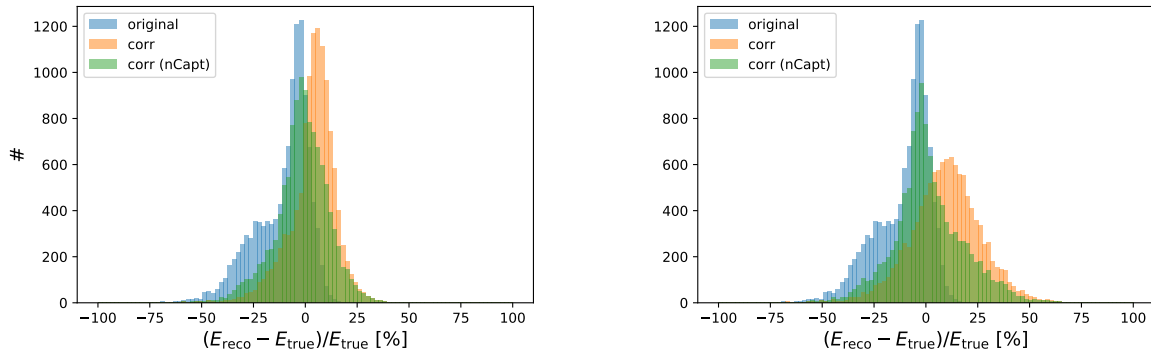


**Figure 8.23:** The neutrino energy misreconstruction  $\Delta E = \frac{E_{\text{reco}} - E_{\text{true}}}{E_{\text{true}}}$  is shown for the case of the CCQE neutrino reconstruction formula (*blue*) and in case corrections are applied based on the non-muon-related charge contribution for all events (*orange*) and restricted to events with a neutron (*green*). The spectra on the left are corrected based on the true non-muon charge while the ones on the right utilize the reconstructed non-muon charge values.

### 8.2.5.2 RANDOM FOREST

As an alternative approach to using a formula as described in the previous section, the neutrino energy can also be estimated by making use of a random forest regressor. Random forests provide ensemble-based regression and classification utilities and are constructed out of a multitude of decision trees. The approach of using such a Random Forest-based regression technique will be explored in this subsection, particularly with respect to the largest possible improvements which can be achieved by adding observables that can only be accessed in WbLS and not in conventional water Cherenkov detectors.

The reconstruction of the neutrino energy will be a two-fold process, in which the muon energy is estimated first by one regressor, and the neutrino energy is reconstructed afterwards by a second regressor. This approach is closely following the work done by E. Drakopoulou who developed energy reconstruction techniques for the current water phase of ANNIE [234]. The regressors were implemented by David Maksimović and are set up to be composed of 1000 trees with a maximal depth of 50. Furthermore, the bootstrapping technique is enabled during training. Initial tests with a Multi-Layer Perceptron showed worse classification performances compared to the Random Forest regressor and the MLP classifier was hence disregarded as an alternative option.

Different parameter sets were probed in terms of their energy reconstruction performance. Some global parameters describing the general properties of the encountered events are

common to all parameter sets. Those global variables include for instance the muon track length, the interaction vertex coordinates, the direction of the muon, the distance of the vertex from the detector walls, and the number of hit PMTs and LAPPDs. In addition, they contain WbLS-specific variables like the muon-related charge, the charge detected at early and late times for separating Cherenkov and scintillation contributions, and the upstream detected charge as an additional estimate of the total scintillation light. In addition to those common variables, the different parameter sets were set up to represent the achievable neutrino energy reconstruction performance in different scenarios:

- The *standard* parameter set was designed to include variables that are realistically accessible as a part of typical reconstruction tools. They consist of all variables that are present in the global parameter set.
- The *extended standard* parameter set represents the potential of the reconstruction technique for the case that the muon-associated charge could be reconstructed more accurately. It contains the true values for the muon and non-muon related charge values.
- The *ideal set* contains the true information about the event topology, such as the interaction type, the number of protons and neutrons alongside their energies. The set illustrates how well the neutrino energy could be estimated in case that all the information about the primary particles were accessible. It hence represents a best-case scenario that will most certainly not be achieved when looking at real data.
- The *reduced ideal set* represents a slightly more realistic version of the *ideal set*. Since both the energy of the neutron and the interaction type will most likely not be accessible in the reconstruction, those variables are left out of the set in this case.

A complete overview of the different variables and their presence in the various parameter sets is given in table 8.2. The reconstruction performance for the presented sets is then shown in table 8.3 in form of the mean and standard deviations of the distributions for the energy misreconstruction variable  $\Delta E = E_{\text{reco}} - E_{\text{true}}$ .

The distribution of the ideal set is characterized by a standard deviation of 4.6% and a mean value of 0.1%. When leaving out the interaction type and the neutron energy, the reconstruction gets considerably worse and features a standard deviation of 7.8%. The (extended) standard set achieves a width of 12.3% (10.6%) for the  $\Delta E$ -distribution. This decrease in reconstruction performance for the standard sets highlights the importance of the exact information about the proton and neutron energies in comparison to a combined charge value that encompasses both light generated by neutrons and by protons. The difference between the standard set and the extended standard set additionally exemplifies the possible improvement under the assumption that a more accurate muon charge estimate can be achieved.

The direct comparison with the reconstruction performance in water is of primary importance for evaluating the benefits of the additional scintillation information which is accessible in the WbLS volume. When using the standard parameter set within an identical

Random Forest regressor architecture in beam neutrino interactions in water, a standard deviation of 14.4% is achieved for the  $\Delta E$ -distribution. This implies that the random forest regressor already compensates for some of the inaccuracies of the formula-based reconstruction, even in the case of water. An improvement of 2.1% is visible for the equivalent parameter configuration in WbLS, indicating that the additional information slightly helps with the reconstruction. As indicated by the ideal parameter sets, the potential improvement is even larger in case a separation of the neutron and proton charge and energy contributions can be achieved by more sophisticated reconstruction techniques in the future.

Variable	Short description	$E_\mu$	$E_\nu$ (I)	$E_\nu$ (II)	$E_\nu$ (III)	$E_\nu$ (IV)
nPrimProt	Number of protons	no	yes	yes	no	no
nPrimNeut	Number of neutrons	no	yes	yes	no	no
nNeutCapt	Number of neutron captures	yes	yes	yes	yes	yes
Eprot	Energy of protons	no	yes	yes	no	no
Eneut	Energy of neutrons	no	yes	no	no	no
Qprot	Proton-induced charge	no	yes	yes	no	no
Qneut	Neutron-induced charge	no	yes	yes	no	no
InteractType	Interaction type	no	yes	no	no	no
TrueEmuon	Muon energy	no	yes	yes	no	no
RecoEmuon	Reconstructed muon energy	no	yes	yes	yes	yes
d	Track length	yes	yes	yes	yes	yes
$d_{\text{SANDI}}$	SANDI track length	yes	yes	yes	yes	yes
$d_{\text{MRD}}$	MRD track length	yes	yes	yes	yes	yes
$\theta$	Angle w.r.t. beam	yes	yes	yes	yes	yes
nPMT	Number of hit PMTs	yes	yes	yes	yes	yes
nLAPPD	Number of LAPPD hits	yes	yes	yes	yes	yes
vtxx	x-coordinate of vertex	yes	yes	yes	yes	yes
vtxy	y-coordinate of vertex	yes	yes	yes	yes	yes
vtxz	z-coordinate of vertex	yes	yes	yes	yes	yes
dirx	x-coordinate of muon direction	yes	yes	yes	yes	yes
diry	y-coordinate of muon direction	yes	yes	yes	yes	yes
dirz	z-coordinate of muon direction	yes	yes	yes	yes	yes
dR	distance tank side wall	yes	yes	yes	yes	yes
dY	distance tank lid	yes	yes	yes	yes	yes
qMu	Muon-induced charge	yes	yes	yes	yes	yes
qNonMu	Non muon-induced charge	yes	yes	yes	yes	yes
qEarly	Early charge	yes	yes	yes	yes	yes
qLate	Late charge	yes	yes	yes	yes	yes
qUpStream	Upstream detected charge	yes	yes	yes	yes	yes
qDownStreamEarly	Early downstream detected charge	yes	yes	yes	yes	yes
qDownStreamLate	Late downstream detected charge	yes	yes	yes	yes	yes

**Table 8.2:** Overview of the variety of variables used in the random forest approach for neutrino energy reconstruction. For each variable, it is indicated whether the parameter is used in the scope of the muon energy reconstruction and in the different parameter sets for the neutrino energy reconstruction. The latter are labeled in roman numerals, representing the *ideal set (I)*, the *reduced ideal set (II)*, the *extended standard set (III)*, and the *standard set (IV)*.

Variable set	$\mu_{\text{WbLS}}$	$\sigma_{\text{WbLS}}$	$\mu_{\text{water}}$	$\sigma_{\text{water}}$
Ideal set	0.001	0.046	0.001	0.046
Reduced ideal set	-0.008	0.078	-0.008	0.078
Extended standard set	-0.016	0.106	-	-
Standard set	0.022	0.123	-0.029	0.144

**Table 8.3:** Means and widths of the relative energy difference  $\Delta E_{\text{rel}} = \frac{E_{\text{rec}} - E_{\text{true}}}{E_{\text{true}}}$  distributions in water and WbLS. The influence of the parameter configuration is highlighted by displaying sets of parameters, with the standard set being mostly composed of reconstructed quantities and the ideal set offering the full truth-based information for the events. The ideal sets perform the same in water and WbLS since they mostly rely on MC truth information, which is identical in both cases.

The spreads of the reconstructed neutrino energy distributions are visualized in figure 5.7 for different parameter sets. The left part of the figure highlights the difference in the energy reconstruction performance between the reduced ideal and the standard parameter set. The histograms on the right side of the figure represent the reconstruction performances in water and WbLS for the extended standard parameter set. The direct comparisons visualize the improvements in the energy reconstruction accuracy, both when comparing the ideal set to the standard set and when comparing the reconstruction in WbLS with the one in water.

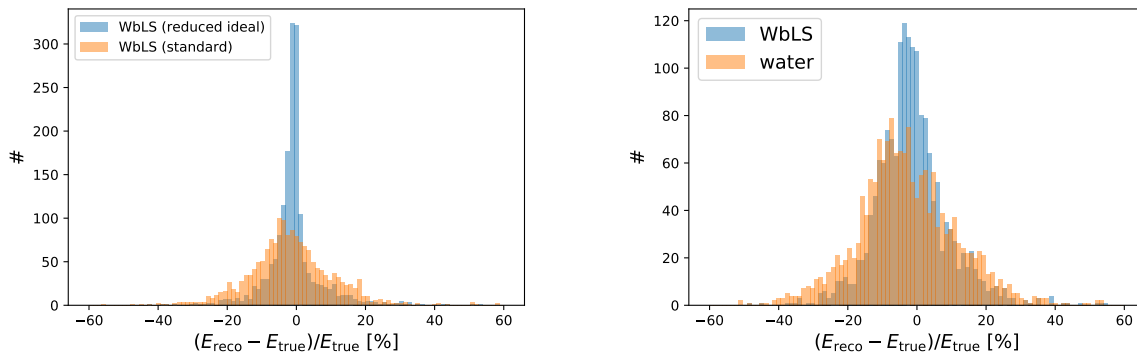


**Figure 8.24:** **Left:** Energy reconstruction performance for the reduced ideal (*blue*) and standard (*orange*) parameter set in the scope of the random forest regressor approach. A smaller standard deviation of  $\sigma = 7.8\%$  is observed for the case of the reduced ideal set, in comparison to  $\sigma = 12.3\%$  for the standard parameter set. **Right:** Comparison of the neutrino energy reconstruction performance in WbLS (*blue*) and water (*orange*) for the extended standard parameter set. A reduction of 3.8% is observed for the standard deviation in the WbLS case in comparison to the reconstruction in water.

The importances of the variables with respect to the Gini score of the random forest regressor were extracted and are shown in table 8.4 for the standard and reduced ideal parameter set. In both cases, the information about the muon energy is the most important variable for the prediction of the neutrino energy with similar importance values of 52% and 53%. The second most important variable is the non-muon related charge in the case of the standard set with an importance of 15% and the proton energy in case of the reduced ideal parameter set with an importance of 22%. These variables are also closely related since the non-muon-associated charge is connected very directly to the

proton energy. The other parameters differ between the two sets and comprise the early downstream charge, the z-direction, and the angle  $\theta$  for the case of the standard set and the non-muon related charge and the neutron charge for reduced ideal set.

The regressors develop very similar criteria for the regression task in the different parameter sets. Once again, it becomes clear that the information about the true proton energy is favorable over the combined neutron+proton charge information. Assuming that both the proton energy and the non-muon associated charge are available as input parameters such as in the case of the reduced ideal set, the random forest regressor tends to favor the proton energy (22%) over the non-muon charge (7%). Overall, the additional information provided by WbLS seems to provide exciting opportunities to improve the energy reconstruction in neutrino interactions.

Standard set		Reduced ideal set	
Variable	Importance (%)	Variable	Importance (%)
$E_{\mu,\text{pred}}$	53	$E_{\mu,\text{true}}$	52
qNonMu	15	Eprot	22
qDownStreamEarly	2.5	QNonMuTrue	7
dirz	2.4	qNonMu	2
theta	2.4	Qneut	2

**Table 8.4:** The most important parameters for the neutrino energy random forest regressor are shown for the case of the standard and reduced ideal parameter sets. The most important variable is in both cases related to the muon energy while the second most important variable is associated with the scintillation light deposited by non-muonic particles.

### 8.3 WBLS IN FUTURE NEUTRINO EXPERIMENTS

WbLS is considered to be a very suitable target material also in the scope of future larger-scale experiments. The following section will briefly highlight the plans for using WbLS in non-proliferation applications like the Advanced Instrumentation Testbed and in neutrino physics-driven applications such as the proposed large-scale THEIA detector.

#### Advanced Instrumentation Testbed – WATCHMAN

The Advanced Instrumentation Testbed (AIT) program aims to explore the potential of non-proliferation applications of neutrino detectors in the scope of monitoring nuclear reactors [294]. Observing the antineutrino flux as a function of time is expected to provide some insight into the operating scheme of a nuclear power plant, and could help to distinguish whether the nuclear material is used for non-peaceful applications. The first detector that is going to be operational within the frame of the testbed is the WATER Cherenkov Monitor for ANTineutrinos (WATCHMAN) [295]. This experiment is schematically depicted in figure 8.25 and encompasses a 6 kt volume of Gadolinium-loaded water with a mass fraction of 0.1% Gd and around 4,000 PMTs in total [294]. The detector will be located at the Boulby mine in the United Kingdom and will primarily detect the reactor neutrinos from the Hartlepool Reactor Complex situated 26 kilometers away. It is expected to detect around 1000 Inverse Beta Decay interactions during its operational time of 2 years. While the first phase of the experiment will only use Gd-doped water,

WbLS is considered as a detection medium for a future phase of the experiment. Due to the additional scintillation light, the antineutrino detection efficiency is expected to increase in this case, enabling an even better measurement of reactor neutrinos and possibly even geoneutrinos.

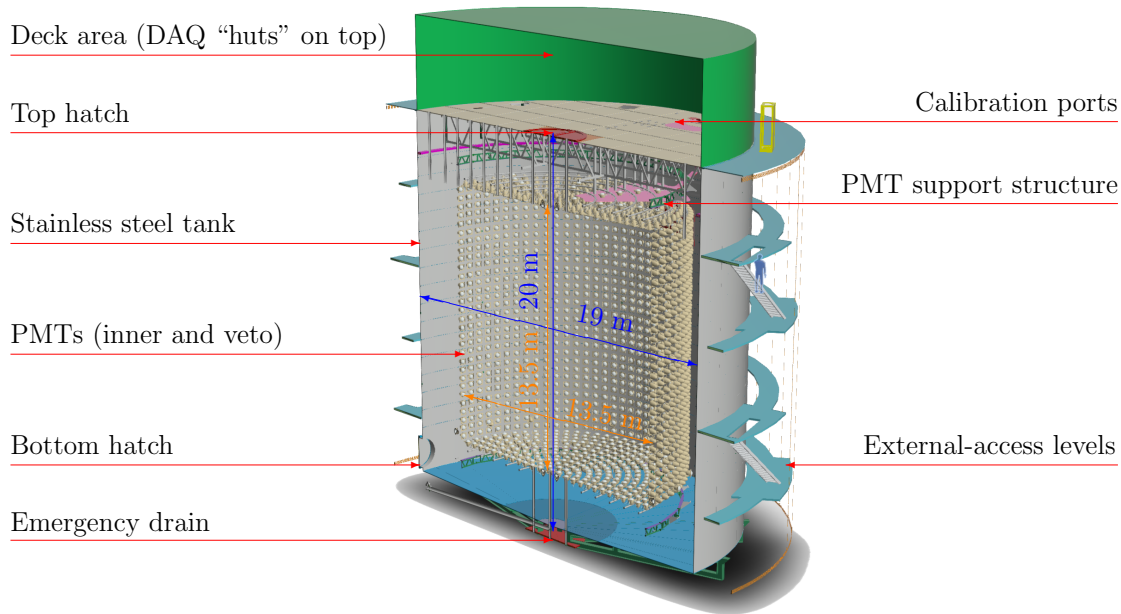


**Figure 8.25:** Schematic view of the planned detector layout for WATCHMAN. In its first operational phase, the detector will be filled with  $\sim 6,000$  tons of Gadolinium-loaded water. Figure taken from [294].

## THEIA

THEIA is a proposed next-generation neutrino experiment aiming to measure the CP violating phase  $\delta_{CP}$  in the context of a long baseline neutrino beam environment. In addition, many other neutrino-physics related goals are included in the design: Measurements of solar neutrinos (including CNO neutrinos), geoneutrinos, supernova bursts, the Diffuse Supernova Background, neutrinoless double beta decay and nucleon decay are envisioned as physics goals of the experiment [296]. The main candidate detection medium is WbLS, however other options such as slow scintillators or normal scintillator in combination with dichroicon-based photon chromatography are also considered. The common feature of all detector configurations is the goal of achieving a separation of Cherenkov and scintillation light in order to gain sensitivity on the signals and reduce backgrounds as much as possible.

Two main geometry designs are considered as shown in figure 8.26, namely THEIA-25 and THEIA-100. The first option envisions a 25kt detector configuration in one of the DUNE caverns, which would provide complementary information to the liquid argon technology used in the other DUNE far detector caverns. The second option features a 100 kt volume in a cylindrical shape, with multiple possible locations.

The Cherenkov/scintillation separation aspect of the experiment can be of vital importance for the detection of rare signals, such as the Diffuse Supernova Background (DSNB). In a dedicated study of the DSNB detection potential in THEIA, it was determined that a

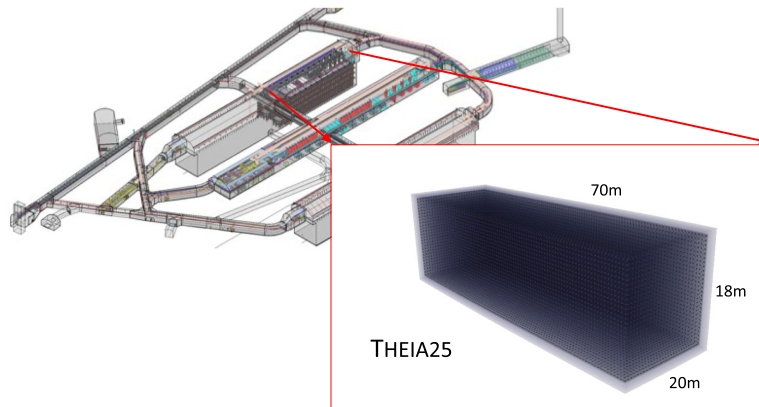


**Figure 8.26:** Schematic depictions of the suggested THEIA detector geometry options. The location of THEIA-25 in one of the DUNE caverns is shown in the top row while the bottom row shows the modeled geometries of THEIA-25 (*left*) and THEIA-100 (*center, right*). Figures taken from [296].

DSNB discovery would be possible for moderate exposures of 190 kt-yrs when assuming conventional DSNB model predictions [297]. Compared to other detection media, WbLS offers a very high Signal-to-Background ratio and signal efficiency. It will therefore provide exciting detection opportunities in the case of its use in next-generation neutrino experiments.

# 9

## Conclusion & Outlook

---

*“End? No, the journey doesn’t end here.”*

—J.R.R. Tolkien

There are still a lot of mysteries surrounding the elusive nature of neutrinos: Many of their features like the mass ordering or the value of the CP-phase  $\delta_{\text{CP}}$  are currently still unknown and will be probed by future large-scale neutrino experiments. Within such experiments, the reconstruction of the neutrino energy is vital to correctly measure the neutrino oscillation signatures. However, inelastic events often introduce a bias into the neutrino energy estimate and contribute substantially to systematic uncertainties for this kind of measurements. Tagging neutrons is a promising strategy to identify such inelastic events and reduce the associated systematic errors, especially when considering lower-energetic beam neutrino energies in the Charged Current (CC) Quasi-Elastic (QE) interaction regime. However, the complexity of neutrino-nucleus interactions poses a challenge in terms of modeling the expected neutron production yield correctly.

As laid out in this thesis, the Accelerator Neutrino Neutron Interaction Experiment (ANNIE) aims to improve the understanding of neutrino-nucleus interactions by measuring the amount of neutrons produced in such collisions, the so-called *neutron yield* or *neutron multiplicity*. Located in the Booster Neutrino Beam (BNB) at Fermilab, ANNIE uses a Gadolinium (Gd)-loaded water target to efficiently detect neutron captures in Charged Current neutrino interactions. At the same time, the muons produced in the CC neutrino-interactions are characterized in terms of their energy and direction by a sandwich-structured Muon Range Detector (MRD) while unwanted *dirt* neutrino interactions taking place in the rocks surrounding the detector hall are flagged by a Front Veto wall composed of scintillator paddles. The close proximity of the detector to the beam target enables a high statistics measurement of the neutron multiplicity, with the possibility to map out the neutron yield as a function of the muon kinematics and hence test the current state-of-the-art models and generators in a multi-dimensional parameter space. While the event characterization in ANNIE will be substantially better in the future by employing new photosensors called Large Area Picosecond Detectors (LAPPDs), this thesis presents a preliminary neutron multiplicity analysis with PMT-only data and hence highlights the potential of the experiment for such a measurement.

In order to conduct a successful measurement of the neutron multiplicity in ANNIE, the efficiency of the various subsystems needs to be known with sufficient accuracy for a reasonable estimation of systematic uncertainties. In this context, the scintillator paddles used in the Front Muon Veto (FMV) and the Muon Range Detector (MRD) were investigated in the scope of this thesis. An average efficiency of  $\bar{\epsilon}_{\text{MRD}} = 92.1\%$  with a standard deviation of 7.9% was found when investigating the active MRD scintillator paddles, while the Front Muon Veto was found to successfully flag veto events with an efficiency of  $\bar{\epsilon}_{\text{FMV}} = (95.6 \pm 1.6)\%$ . The inefficiency of the MRD paddles mainly influences the number of successfully reconstructed muon tracks but does not affect the reconstruction performance itself. Consequently, the consideration of the MRD efficiencies reduces the available event statistics but does not have any other impacts on the neutron multiplicity measurement. The slight FMV inefficiency, on the contrary, introduces dirt neutrino events into the beam neutrino sample and hence directly influences the neutron yield measurement, which will need to be considered as a systematic uncertainty.

The successful development of reconstruction and classification tools for the characterization of events in the scope of the neutron multiplicity analysis in ANNIE requires a realistic simulation of the experimental apparatus, including the correct modeling of physics processes and the electronics response. In addition, a validation of the simulation framework is also necessary to conduct the same neutron multiplicity analysis both on the measured and the simulated data sample, allowing for an evaluation of the employed physics models. A Geant4-based implementation of ANNIE was adapted and tuned in the scope of this thesis to represent reality as closely as possible. In this context, the detector response was validated for three different samples of Michel electrons, through-going muons, and Americium Beryllium (AmBe) calibration neutrons. The geometry of the detector was optimized by including PMT holder objects and more precise PMT positions derived from a laser scan campaign. In addition, reflectivity values of several surfaces were increased, effective Quantum Efficiency correction factors introduced, and data-driven Single-PE. distributions implemented to achieve a better agreement with the measured data samples and, in turn, a more realistic representation of the detector response. The final adapted simulation framework is able to reproduce the charge spectra for the three validation samples reasonably well, with  $\chi^2/\text{n.d.f.}$ -compatibility values of 0.95 (throughgoing sample), 1.05 (Michel electron sample), and 2.12 (AmBe neutron calibration sample). The validation of the simulation conducted in the scope of this thesis hence enabled the development of reconstruction algorithms as well as opening up the possibility to conduct an equivalent neutron multiplicity analysis on the simulated beam neutrino sample. This will also be very important in the future, since the validated framework will be a vital tool for more sophisticated energy and vertex reconstruction algorithms and classification tools which can be employed to characterize the data.

The neutron multiplicity in neutrino interactions was investigated on a small subset of ANNIE 2021 beam data covering the time frame between the end of February and the beginning of April as a part of this work. Charged Current muon neutrino interactions were identified by selecting muon events which produced a coincident signal in the water tank and the MRD with no simultaneous detected activity in the Front Muon Veto. Simplified MRD-based energy and vertex reconstruction algorithms were used to characterize the charged lepton response of the neutrino interaction while neutron candidates were selected

based on cuts developed during a dedicated AmBe neutron calibration campaign. Average neutron yields of  $\bar{n}_{\text{data}}(\text{beam}) = (0.272 \pm 0.010_{\text{stat}})$  and  $\bar{n}_{\text{data}}(\text{beam, FV}) = (0.287 \pm 0.044_{\text{stat}})$  are found for the beam neutrino sample when considering all neutrino candidates with a stopping muon track in the MRD and when additionally requiring a reconstructed vertex inside of the Fiducial Volume of ANNIE, which was optimized to maximize the neutron acceptance. These measured values are substantially lower than the ones predicted by an equivalent Monte Carlo study, which finds average neutron yields of  $\bar{n}_{\text{MC}}(\text{beam}) = (0.515 \pm 0.007_{\text{stat}})$  and  $\bar{n}_{\text{MC}}(\text{beam, FV}) = (0.627 \pm 0.031_{\text{stat}})$ . No strong dependency of the neutron multiplicity is found as a function of neither the muon energy nor the muon angle both in the data and the simulation sample. The findings suggest that neutron production yields are overestimated either on the neutrino generator level or within secondary interactions modeled by Geant4 (or both), but a more detailed evaluation will only be possible once the investigation of systematic errors has concluded and when including a larger event sample. A first assessment of relevant systematics identified the Fiducial Volume selection, the muon reconstruction uncertainty, the FMV inefficiency, and the neutron detection efficiency as possible contributors. For the investigated data set, we find that the neutron detection efficiency and the FMV inefficiency are the most important, amounting to an overall systematic uncertainty of 0.05 neutrons per neutrino interaction and a shift in mean value by 0.01 neutrons per neutrino interaction. While these studies will have to be refined in future analyses, even after including the systematic effects there remains a significant difference between experimental data and generator expectations, hinting towards potential deficiencies in the employed models.

The correct modeling of neutron yields in neutrino interactions will also be very important in the scope of future searches for interesting physics signatures like the Diffuse Supernova Background (DSNB). Since the signal in this case will always produce one neutron via the Inverse Beta Decay reaction, backgrounds like Neutral Current Quasi-Elastic (NCQE) neutrino interactions – which generally tend to produce more neutrons – can be suppressed by making use of neutron tagging techniques. This is especially true for detectors with high neutron capture cross-sections like Gd-loaded water Cherenkov experiments. In this thesis, additional background discrimination methods were explored for the DSNB search in the form of Convolutional Neural Networks. For a Super-Kamiokande-like detector geometry filled with Gd-loaded water, it was shown that the NCQE background can be suppressed below the signal levels by making use of combined information from neutron captures and a Convolutional Neural Network, achieving a Signal-to-Background ratio of 4:1. This provides the exciting prospect of detecting the DSNB signal in the near future with current-generation experiments like Super-K-Gd, given a large enough DSNB flux holds true. Such a detection would provide important insights into the mechanisms behind Core-Collapse Supernova explosions and would be an exciting milestone in the detection of low-energy astrophysical neutrino sources.

Looking ahead, neutron tagging will also play an important role in future experiments using the novel detection medium of Water-based Liquid Scintillators (WbLS). This target material is composed of small liquid scintillator droplets dissolved in water and aims to allow an efficient detection of both Cherenkov and scintillation light within the corresponding experiment. The simultaneous detection of scintillation and Cherenkov light can have substantial benefits on the neutrino energy reconstruction: While the simple CCQE-based

formula which is typically used in water Cherenkov experiments tends to underestimate the neutrino energy for inelastic interaction topologies, the scintillation light of hadronic particles like protons can be used to correct such biases when using WbLS as a target medium. The work presented in this thesis shows that the neutrino energy reconstruction performance can be improved by identifying inelastic events through neutron tagging and subsequently applying a correction factor based on the observed hadronic scintillation light levels. Similarly, the additional scintillation light information can also be used in the scope of a Random Forest regressor, improving the energy resolution  $\sigma(E_\nu)$  by 2% (from 14% in water to 12% in WbLS) when using the hadron-related scintillation light as an additional variable. In the case that more detailed information like the proton energy can be reconstructed in the scope of more sophisticated algorithms in the future, even larger neutrino energy reconstruction improvements of  $\sim 6\%$  can be expected, resulting in a final resolution of around 8%. The work presented in the thesis hence highlights interesting concepts on how the neutrino energy reconstruction performance can be optimized in WbLS targets, which can be built upon in the future. Such improved energy resolution levels with decreased biases will be of vital importance for next-generation neutrino oscillation experiments like THEIA which aim to measure neutrino properties with a much higher level of accuracy.

With the deployment of the first LAPPD at the end of March 2022 and the imminent deployment of a Water-based Liquid scintillator vessel during the summer period of the same year, ANNIE is further ramping up its role as a test bed for next-generation detection capabilities in neutrino experiments. Successful demonstrations for the use of both technologies of LAPPDs and WbLS in the scope of the neutron multiplicity measurement will pave the way for these technologies to become available also in other experiments, enabling much faster timing and Cherenkov/scintillation separation capabilities. The resulting improved background rejection capabilities will be of vital importance for entering the precision era of neutrino physics and uncovering the last secrets of this elusive particle.

# Bibliography

---

- [1] W. Pauli. *Letter to Tübingen conference participants*. 1930 (cit. on pp. 3, 7, 16).
- [2] B. Pontecorvo. “Mesonium and Antimesonium”. In: *Soviet Journal of Experimental and Theoretical Physics* 6 (Jan. 1958) (cit. on p. 3).
- [3] B. Abi et al. “Long-baseline neutrino oscillation physics potential of the DUNE experiment”. In: *Eur. Phys. J. C* 80.10, 978 (2020). DOI: [10.1140/epjc/s10052-020-08456-z](https://doi.org/10.1140/epjc/s10052-020-08456-z). arXiv: [2006.16043](https://arxiv.org/abs/2006.16043) [hep-ex] (cit. on pp. 3, 39).
- [4] I. Anghel et al. “Letter of Intent: The Accelerator Neutrino Neutron Interaction Experiment (ANNIE)”. In: *arXiv Preprints* (Apr. 2015). arXiv: [1504.01480](https://arxiv.org/abs/1504.01480) [physics.ins-det] (cit. on pp. 3, 53).
- [5] L. Alvarez-Ruso et al. “NuSTEC White Paper: Status and challenges of neutrino–nucleus scattering”. In: *Prog. Part. Nucl. Phys.* 100 (2018), pp. 1–68. DOI: [10.1016/j.ppnp.2018.01.006](https://doi.org/10.1016/j.ppnp.2018.01.006). arXiv: [1706.03621](https://arxiv.org/abs/1706.03621) [hep-ph] (cit. on pp. 3, 46).
- [6] B. Aharmim, S.N. Ahmed, A.E. Anthony, N. Barros, E.W. Beier, A. Bellerive, B. Beltran, M. Bergevin, S.D. Biller, R. Bonventre, et al. “Measurement of neutron production in atmospheric neutrino interactions at the Sudbury Neutrino Observatory”. In: *Physical Review D* 99.11 (2019). ISSN: 2470-0029. DOI: [10.1103/physrevd.99.112007](https://doi.org/10.1103/physrevd.99.112007) (cit. on pp. 3, 55, 56, 59, 92, 163).
- [7] H. Zhang. “Neutron tagging and its application to physics in Super-Kamiokande IV”. In: *32nd International Cosmic Ray Conference*. 2011. DOI: [10.7529/ICRC2011/V04/0353](https://doi.org/10.7529/ICRC2011/V04/0353) (cit. on pp. 3, 55, 92).
- [8] A. R. Back et al. “Accelerator Neutrino Neutron Interaction Experiment (ANNIE): Preliminary Results and Physics Phase Proposal”. In: *arXiv Preprints* (2017). arXiv: [1707.08222](https://arxiv.org/abs/1707.08222) [physics.ins-det] (cit. on pp. 4, 7, 64, 94, 187, 204).
- [9] E. Fermi. “Versuch einer Theorie der  $\beta$ -Strahlen. I”. In: *Zeitschrift für Physik* 88.3 (1934), pp. 161–177. DOI: [10.1007/BF01351864](https://doi.org/10.1007/BF01351864) (cit. on p. 7).
- [10] Jr. Cowan C. L., F. Reines, F. B. Harrison, H. W. Kruse, and A. D. McGuire. “Detection of the Free Neutrino: A Confirmation”. In: *Science* 124.3212 (July 1956), pp. 103–104. DOI: [10.1126/science.124.3212.103](https://doi.org/10.1126/science.124.3212.103) (cit. on pp. 7, 16).
- [11] G. Aad et al. “Observation of a new particle in the search for the Standard Model Higgs boson with the ATLAS detector at the LHC”. In: *Phys. Lett. B* 716 (2012), pp. 1–29. DOI: [10.1016/j.physletb.2012.08.020](https://doi.org/10.1016/j.physletb.2012.08.020). arXiv: [1207.7214](https://arxiv.org/abs/1207.7214) [hep-ex] (cit. on p. 8).
- [12] S. Chatrchyan et al. “Observation of a new boson at a mass of 125 GeV with the CMS Experiment at the LHC”. In: *Phys. Lett. B* 716 (2012), pp. 30–61. DOI: [10.1016/j.physletb.2012.08.021](https://doi.org/10.1016/j.physletb.2012.08.021). arXiv: [1207.7235](https://arxiv.org/abs/1207.7235) [hep-ex] (cit. on p. 8).
- [13] M. Ruhdorfer, J. Serra, and A. Weiler. “Effective field theory of gravity to all orders”. In: *Journal of High Energy Physics* 05.083 (2020). DOI: [10.1007/JHEP05\(2020\)083](https://doi.org/10.1007/JHEP05(2020)083). arXiv: [1908.08050](https://arxiv.org/abs/1908.08050) [hep-ph] (cit. on p. 8).
- [14] S. Weinberg. “On the development of effective field theory”. In: *Eur. Phys. J. H* 46.6 (2021). DOI: [10.1140/epjh/s13129-021-00004-x](https://doi.org/10.1140/epjh/s13129-021-00004-x). arXiv: [2101.04241](https://arxiv.org/abs/2101.04241) [hep-th] (cit. on p. 8).

- [15] C. Giunti and C. W. Kim. *Fundamentals of Neutrino Physics and Astrophysics*. Oxford: Oxford Univ., 2007. DOI: [10.1093/acprof:oso/9780198508717.001.0001](https://doi.org/10.1093/acprof:oso/9780198508717.001.0001). URL: <https://cds.cern.ch/record/1053706> (cit. on pp. 8, 10, 11, 25).
- [16] M. Thomson. *Modern Particle Physics*. Cambridge University Press, 2013. DOI: [10.1017/CB09781139525367](https://doi.org/10.1017/CB09781139525367) (cit. on pp. 8, 12, 13, 26).
- [17] P. A. Zyla et al. “Review of Particle Physics”. In: *Progress of Theoretical and Experimental Physics* 2020.8, 083C01 (2020). ISSN: 2050-3911. DOI: [10.1093/ptep/ptaa104](https://doi.org/10.1093/ptep/ptaa104). eprint: <https://academic.oup.com/ptep/article-pdf/2020/8/083C01/34673722/ptaa104.pdf> (cit. on pp. 9, 24, 27, 33–35, 163).
- [18] Cush and MissMJ. *Standard Model of Elementary Particles*. 2019. URL: [https://commons.wikimedia.org/wiki/File:Standard\\_Model\\_of\\_Elementary\\_Particles.svg](https://commons.wikimedia.org/wiki/File:Standard_Model_of_Elementary_Particles.svg) (cit. on p. 9).
- [19] E. C. G. Sudarshan and R. E. Marshak. “Chirality Invariance and the Universal Fermi Interaction”. In: *Phys. Rev.* 109.5 (1958), pp. 1860–1862. DOI: [10.1103/PhysRev.109.1860](https://doi.org/10.1103/PhysRev.109.1860).2 (cit. on p. 10).
- [20] C. S. Wu, E. Ambler, R. W. Hayward, D. D. Hoppes, and R. P. Hudson. “Experimental Test of Parity Conservation in Beta Decay”. In: *Phys. Rev.* 105.4 (1957), pp. 1413–1415. DOI: [10.1103/PhysRev.105.1413](https://doi.org/10.1103/PhysRev.105.1413) (cit. on p. 10).
- [21] T. Nakano and K. Nishijima. “Charge Independence for V-particles\*”. In: *Progress of Theoretical Physics* 10.5 (Nov. 1953), pp. 581–582. ISSN: 0033-068X. DOI: [10.1143/PTP.10.581](https://doi.org/10.1143/PTP.10.581). eprint: <https://academic.oup.com/ptp/article-pdf/10/5/581/5364926/10-5-581.pdf> (cit. on p. 10).
- [22] M. Gell-Mann. “The interpretation of the new particles as displaced charge multiplets”. In: *Il Nuovo Cimento (1955-1965)* 4.2 (1956), pp. 848–866. DOI: [10.1007/BF02748000](https://doi.org/10.1007/BF02748000) (cit. on p. 10).
- [23] K. Abe et al. *Hyper-Kamiokande Design Report*. 2018. arXiv: [1805.04163](https://arxiv.org/abs/1805.04163) [[physics.ins-det](https://arxiv.org/abs/1805.04163)] (cit. on pp. 11, 36, 39, 145).
- [24] B. Abi et al. “Volume I. Introduction to DUNE”. In: *Journal of Instrumentation* 15.08, T08008 (2020). DOI: [10.1088/1748-0221/15/08/T08008](https://doi.org/10.1088/1748-0221/15/08/T08008). arXiv: [2002.02967](https://arxiv.org/abs/2002.02967) [[physics.ins-det](https://arxiv.org/abs/2002.02967)] (cit. on pp. 11, 36, 64, 259).
- [25] J. P. Ellis. “TikZ-Feynman: Feynman diagrams with TikZ”. In: *Computer Physics Communications* 210 (2017), pp. 103–123. ISSN: 0010-4655. DOI: [10.1016/j.cpc.2016.08.019](https://doi.org/10.1016/j.cpc.2016.08.019) (cit. on pp. 12, 164).
- [26] P. A. Čerenkov. “Visible Emission of Clean Liquids by Action of  $\gamma$  Radiation”. In: *Doklady Akad. Nauk SSSR* 2 (1934), pp. 451–453 (cit. on p. 13).
- [27] A. D. Buckingham. “A theory of the dielectric polarization of polar substances”. In: *Proceedings of the Royal Society of London Series A* 238.1213 (1956), pp. 235–244. DOI: [10.1098/rspa.1956.0216](https://doi.org/10.1098/rspa.1956.0216) (cit. on p. 13).
- [28] A. Horvath. *The geometry of the Cherenkov radiation shown for the ideal case of no dispersion*. 2006. URL: [https://en.wikipedia.org/wiki/Cherenkov\\_radiation#/media/File:Cherenkov.svg](https://en.wikipedia.org/wiki/Cherenkov_radiation#/media/File:Cherenkov.svg) (cit. on p. 14).
- [29] I. M. Frank and I. Tamm. “Coherent visible radiation of fast electrons passing through matter”. In: *Physics-Uspekhi* 93 (1937), pp. 388–393 (cit. on p. 14).

- [30] K. A. Olive. “Review of Particle Physics”. In: *Chinese Physics C* 38.9 (2014). DOI: [10.1088/1674-1137/38/9/090001](https://doi.org/10.1088/1674-1137/38/9/090001) (cit. on p. 14).
- [31] C. Buck and M. Yeh. “Metal-loaded organic scintillators for neutrino physics”. In: *J. Phys. G* 43.9 (2016). DOI: [10.1088/0954-3899/43/9/093001](https://doi.org/10.1088/0954-3899/43/9/093001). arXiv: [1608.04897](https://arxiv.org/abs/1608.04897) [physics.ins-det] (cit. on p. 15).
- [32] M. J. Sauer and J. Enderlein. “Handbook of Fluorescence Spectroscopy and Imaging: From ensemble to single molecules”. In: John Wiley & Sons, Ltd, 2011. ISBN: 9783527633500. DOI: [10.1002/9783527633500](https://doi.org/10.1002/9783527633500) (cit. on p. 15).
- [33] M. Pallavicini et al. “Scintillator purification, detector performance and first results from Borexino”. In: *J. Phys. Conf. Ser.* 120 (2008). DOI: [10.1088/1742-6596/120/5/052017](https://doi.org/10.1088/1742-6596/120/5/052017) (cit. on pp. 15, 259).
- [34] J. B. Birks. *The Theory and Practice of Scintillation Counting*. Oxford, UK: Pergamon, 1964. ISBN: 9781483156064 (cit. on pp. 15, 267).
- [35] W. Pauli. “Discussion of paper by M. Heisenberg on “La Structure du Noyau””. In: *Rapp. Septieme Conseil Phys. Solvay* (1934), pp. 324–325 (cit. on p. 16).
- [36] J. N. Bahcall. “Solar models: An Historical overview”. In: *AAPPS Bull.* 12.4 (2002), pp. 12–19. DOI: [10.1016/S0920-5632\(03\)01306-9](https://doi.org/10.1016/S0920-5632(03)01306-9). arXiv: [astro-ph/0209080](https://arxiv.org/abs/astro-ph/0209080) (cit. on p. 16).
- [37] Ilídio Lopes. “New neutrino physics and the altered shapes of solar neutrino spectra”. In: *Phys. Rev. D* 95.1 (2017). DOI: [10.1103/PhysRevD.95.015023](https://doi.org/10.1103/PhysRevD.95.015023). arXiv: [1702.00447](https://arxiv.org/abs/1702.00447) [astro-ph.SR] (cit. on p. 17).
- [38] M. Agostini et al. “Comprehensive measurement of pp-chain solar neutrinos”. In: *Nature* 562 (2018), pp. 505–510. DOI: [10.1038/s41586-018-0624-y](https://doi.org/10.1038/s41586-018-0624-y) (cit. on pp. 17, 33).
- [39] M. Agostini et al. “Experimental evidence of neutrinos produced in the CNO fusion cycle in the Sun”. In: *Nature* 587 (2020), pp. 577–582. DOI: [10.1038/s41586-020-2934-0](https://doi.org/10.1038/s41586-020-2934-0) (cit. on p. 17).
- [40] N. Vinyoles et al. “A New Generation of Standard Solar Models”. In: *The Astrophysical Journal* 835.2 (2017). DOI: [10.3847/1538-4357/835/2/202](https://doi.org/10.3847/1538-4357/835/2/202) (cit. on p. 17).
- [41] Raymond Davis. “A review of the Homestake solar neutrino experiment”. In: *Progress in Particle and Nuclear Physics* 32 (1994), pp. 13–32. ISSN: 0146-6410. DOI: [https://doi.org/10.1016/0146-6410\(94\)90004-3](https://doi.org/10.1016/0146-6410(94)90004-3). URL: <https://www.sciencedirect.com/science/article/pii/0146641094900043> (cit. on p. 18).
- [42] B. T. Cleveland et al. “Measurement of the Solar Electron Neutrino Flux with the Homestake Chlorine Detector”. In: *The Astrophysical Journal* 496.1 (1998), pp. 505–526. DOI: [10.1086/305343](https://doi.org/10.1086/305343) (cit. on p. 18).
- [43] J. N. Bahcall, M. H. Pinsonneault, and S. Basu. “Solar Models: Current Epoch and Time Dependences, Neutrinos, and Helioseismological Properties”. In: *The Astrophysical Journal* 555.2 (2001), pp. 990–1012. ISSN: 1538-4357. DOI: [10.1086/321493](https://doi.org/10.1086/321493). URL: <http://dx.doi.org/10.1086/321493> (cit. on pp. 18, 19).
- [44] P. Anselmann et al. “Solar neutrinos observed by GALLEX at Gran Sasso”. In: *Physics Letters B* 285.4 (1992), pp. 376–389. ISSN: 0370-2693. DOI: [10.1016/0370-2693\(92\)91521-A](https://doi.org/10.1016/0370-2693(92)91521-A) (cit. on p. 18).
- [45] M. Altmann et al. “GNO solar neutrino observations: results for GNO I”. In: *Physics Letters B* 490.1 (2000), pp. 16–26. ISSN: 0370-2693. DOI: [https://doi.org/10.1016/S0370-2693\(00\)00915-1](https://doi.org/10.1016/S0370-2693(00)00915-1). URL: <https://www.sciencedirect.com/science/article/pii/S0370269300009151> (cit. on p. 18).

- [46] M. Altmann et al. “Complete results for five years of GNO solar neutrino observations”. In: *Physics Letters B* 616.3 (2005), pp. 174–190. ISSN: 0370-2693. DOI: [10.1016/j.physletb.2005.04.068](https://doi.org/10.1016/j.physletb.2005.04.068). URL: <https://www.sciencedirect.com/science/article/pii/S0370269305005149> (cit. on p. 18).
- [47] A. I. Abazov et al. “Search for neutrinos from the Sun using the reaction  ${}^{71}\text{Ga}(\nu_e, e^-){}^{71}\text{Ge}$ ”. In: *Phys. Rev. Lett.* 67.24 (1991), pp. 3332–3335. DOI: [10.1103/PhysRevLett.67.3332](https://doi.org/10.1103/PhysRevLett.67.3332) (cit. on p. 18).
- [48] J. N. Abdurashitov et al. “Measurement of the solar neutrino capture rate with gallium metal. III: Results for the 2002–2007 data-taking period”. In: *Phys. Rev. C* 80 (2009). DOI: [10.1103/PhysRevC.80.015807](https://doi.org/10.1103/PhysRevC.80.015807). arXiv: [0901.2200](https://arxiv.org/abs/0901.2200) [nucl-ex] (cit. on p. 18).
- [49] K. S. Hirata, T. Kajita, et al. “Observation of  ${}^8\text{B}$  solar neutrinos in the Kamiokande-II detector”. In: *Phys. Rev. Lett.* 63.1 (1989), pp. 16–19. DOI: [10.1103/PhysRevLett.63.16](https://doi.org/10.1103/PhysRevLett.63.16) (cit. on p. 18).
- [50] Y. Fukuda et al. “Measurements of the Solar Neutrino Flux from Super-Kamiokande’s First 300 Days”. In: *Phys. Rev. Lett.* 81.6 (1998), pp. 1158–1162. DOI: [10.1103/PhysRevLett.81.1158](https://doi.org/10.1103/PhysRevLett.81.1158) (cit. on p. 18).
- [51] Y. Fukuda et al. “Solar Neutrino Data Covering Solar Cycle 22”. In: *Phys. Rev. Lett.* 77.9 (1996), pp. 1683–1686. DOI: [10.1103/PhysRevLett.77.1683](https://doi.org/10.1103/PhysRevLett.77.1683) (cit. on p. 19).
- [52] J. Hosaka et al. “Solar neutrino measurements in Super-Kamiokande-I”. In: *Phys. Rev. D* 73.11 (2006). DOI: [10.1103/PhysRevD.73.112001](https://doi.org/10.1103/PhysRevD.73.112001) (cit. on p. 19).
- [53] A. Dar. *Standard physics solution to the solar neutrino problem?* Singapore: World Scientific Publishing Co Pte Ltd, 1997. ISBN: 981-02-3177-6. URL: [http://inis.iaea.org/search/search.aspx?orig\\_q=RN:30013144](http://inis.iaea.org/search/search.aspx?orig_q=RN:30013144) (cit. on p. 19).
- [54] B. Pontecorvo. “Neutrino Experiments and the Problem of Conservation of Leptonic Charge”. In: *Soviet Journal of Experimental and Theoretical Physics* 26 (May 1968), pp. 984–988 (cit. on p. 19).
- [55] V. Gribov and B. Pontecorvo. “Neutrino astronomy and lepton charge”. In: *Physics Letters B* 28.7 (Jan. 1969), pp. 493–496. DOI: [10.1016/0370-2693\(69\)90525-5](https://doi.org/10.1016/0370-2693(69)90525-5) (cit. on p. 19).
- [56] S. P. Mikheyev and A. Yu. Smirnov. “Resonant amplification of  $\nu$  oscillations in matter and solar-neutrino spectroscopy”. In: *Il Nuovo Cimento C* 9.1 (1986), pp. 17–26. DOI: [10.1007/BF02508049](https://doi.org/10.1007/BF02508049) (cit. on pp. 19, 29).
- [57] J. Boger et al. “The Sudbury Neutrino Observatory”. In: *Nuclear Instruments and Methods in Physics Research Section A: Accelerators, Spectrometers, Detectors and Associated Equipment* 449.1 (2000), pp. 172–207. ISSN: 0168-9002. DOI: [10.1016/S0168-9002\(99\)01469-2](https://doi.org/10.1016/S0168-9002(99)01469-2). URL: <https://www.sciencedirect.com/science/article/pii/S0168900299014692> (cit. on p. 19).
- [58] B. Aharmim et al. “Electron energy spectra, fluxes, and day-night asymmetries of  ${}^8\text{B}$  solar neutrinos from measurements with NaCl dissolved in the heavy-water detector at the Sudbury Neutrino Observatory”. In: *Phys. Rev. C* 72.5 (2005). DOI: [10.1103/PhysRevC.72.055502](https://doi.org/10.1103/PhysRevC.72.055502) (cit. on p. 19).
- [59] Y. Fukuda et al. “Evidence for Oscillation of Atmospheric Neutrinos”. In: *Phys. Rev. Lett.* 81.8 (1998), pp. 1562–1567. DOI: [10.1103/PhysRevLett.81.1562](https://doi.org/10.1103/PhysRevLett.81.1562) (cit. on p. 20).
- [60] Daya Bay Collaboration. “A Precision Measurement of the Neutrino Mixing Angle  $\theta_{13}$  using Reactor Antineutrinos at Daya Bay”. In: *arXiv Preprint* (2007). URL: <https://arxiv.org/abs/hep-ex/0701029> (cit. on p. 26).

- [61] S. Kim. “RENO: Reactor Experiment for Neutrino Oscillation at Yonggwang”. In: *AIP Conference Proceedings* 981.1 (2008), pp. 205–207. DOI: [10.1063/1.2898934](https://doi.org/10.1063/1.2898934). eprint: <https://aip.scitation.org/doi/pdf/10.1063/1.2898934> (cit. on p. 26).
- [62] F. Ardellier et al. “Double Chooz: A Search for the neutrino mixing angle  $\theta_{13}$ ”. In: *arXiv Preprint* (2006). arXiv: [hep-ex/0606025](https://arxiv.org/abs/hep-ex/0606025) (cit. on p. 26).
- [63] F. Suekane, T. Iwamoto, H. Ogawa, O. Tajima, and H. Watanabe. “An overview of the KamLAND 1-kiloton liquid scintillator”. In: *arXiv Preprint* (2004) (cit. on p. 26).
- [64] N. Okamura. “Effect of the smaller mass-squared difference for the long base-line neutrino experiments”. In: *Prog. Theor. Phys.* 114.4 (2006), pp. 1045–1056. DOI: [10.1143/PTP.114.1045](https://doi.org/10.1143/PTP.114.1045). arXiv: [hep-ph/0411388](https://arxiv.org/abs/hep-ph/0411388) (cit. on p. 27).
- [65] H. Nunokawa, S. J. Parke, and R. Z. Funchal. “Another possible way to determine the Neutrino Mass Hierarchy”. In: *Phys. Rev. D* 72 (2005). DOI: [10.1103/PhysRevD.72.013009](https://doi.org/10.1103/PhysRevD.72.013009). arXiv: [hep-ph/0503283](https://arxiv.org/abs/hep-ph/0503283) (cit. on p. 27).
- [66] A. Cervera et al. “Golden measurements at a neutrino factory”. In: *Nuclear Physics B* 579.1-2 (2000), pp. 17–55. ISSN: 0550-3213. DOI: [10.1016/S0550-3213\(00\)00221-2](https://doi.org/10.1016/S0550-3213(00)00221-2) (cit. on p. 27).
- [67] N. Freund. “Analytic approximations for three neutrino oscillation parameters and probabilities in matter”. In: *Physical Review D* 64.5 (2001). ISSN: 1089-4918. DOI: [10.1103/physrevd.64.053003](https://doi.org/10.1103/physrevd.64.053003) (cit. on p. 27).
- [68] E. K. Akhmedov, R. Johansson, M. Lindner, T. Ohlsson, and T. Schwetz. “Series expansions for three-flavor neutrino oscillation probabilities in matter”. In: *Journal of High Energy Physics* 2004.04 (2004). ISSN: 1029-8479. DOI: [10.1088/1126-6708/2004/04/078](https://doi.org/10.1088/1126-6708/2004/04/078) (cit. on p. 27).
- [69] S. P. Mikheev and A. Y. Smirnov. “Resonance enhancement of oscillations in matter and solar neutrino spectroscopy”. In: *Sov. J. Nucl. Phys. (Engl. Transl.); (United States)* 42.6 (Dec. 1985). URL: <https://www.osti.gov/biblio/5714592> (cit. on p. 29).
- [70] S. J. Parke. “Nonadiabatic Level Crossing in Resonant Neutrino Oscillations”. In: *Phys. Rev. Lett.* 57.10 (1986), pp. 1275–1278. DOI: [10.1103/PhysRevLett.57.1275](https://doi.org/10.1103/PhysRevLett.57.1275) (cit. on p. 31).
- [71] NobelPrize.org. *The Nobel Prize in Physics 2015*. URL: <https://www.nobelprize.org/prizes/physics/2015/summary/> (cit. on p. 32).
- [72] V. Berezinsky and M. Lissia. “Electron-neutrino survival probability from solar-neutrino data”. In: *Physics Letters B* 521.3 (2001), pp. 287–290. ISSN: 0370-2693. DOI: [10.1016/S0370-2693\(01\)01212-6](https://doi.org/10.1016/S0370-2693(01)01212-6). URL: <https://www.sciencedirect.com/science/article/pii/S0370269301012126> (cit. on p. 33).
- [73] M. C. Gonzalez-Garcia, M. Maltoni, and T. Schwetz. “NuFIT: Three-Flavour Global Analyses of Neutrino Oscillation Experiments”. In: *Universe* 7.11 (Nov. 2021). arXiv: [2111.03086](https://arxiv.org/abs/2111.03086) [hep-ph] (cit. on p. 33).
- [74] K. Abe et al. “Measurements of neutrino oscillation in appearance and disappearance channels by the T2K experiment with  $6.6 \times 10^{20}$  protons on target”. In: *Phys. Rev. D* 91.7 (2015). DOI: [10.1103/PhysRevD.91.072010](https://doi.org/10.1103/PhysRevD.91.072010). arXiv: [1502.01550](https://arxiv.org/abs/1502.01550) [hep-ex] (cit. on p. 33).
- [75] P. Adamson et al. “Measurement of the neutrino mixing angle  $\theta_{23}$  in NOvA”. In: *Phys. Rev. Lett.* 118.15 (2017). DOI: [10.1103/PhysRevLett.118.151802](https://doi.org/10.1103/PhysRevLett.118.151802). arXiv: [1701.05891](https://arxiv.org/abs/1701.05891) [hep-ex] (cit. on p. 33).

- [76] K. Abe et al. “T2K measurements of muon neutrino and antineutrino disappearance using  $3.13 \times 10^{21}$  protons on target”. In: *Phys. Rev. D* 103.1 (2021). DOI: [10.1103/PhysRevD.103.L011101](https://doi.org/10.1103/PhysRevD.103.L011101) (cit. on p. 33).
- [77] M. A. Acero et al. “An Improved Measurement of Neutrino Oscillation Parameters by the NOvA Experiment”. In: *arXiv Preprint* (Aug. 2021). arXiv: [2108.08219 \[hep-ex\]](https://arxiv.org/abs/2108.08219) (cit. on pp. 33, 34).
- [78] K. Abe et al. “Constraint on the matter–antimatter symmetry-violating phase in neutrino oscillations”. In: *Nature* 580 (2020). [Erratum: *Nature* 583, E16 (2020)], pp. 339–344. DOI: [10.1038/s41586-020-2177-0](https://doi.org/10.1038/s41586-020-2177-0). arXiv: [1910.03887 \[hep-ex\]](https://arxiv.org/abs/1910.03887) (cit. on p. 33).
- [79] K. Abe et al. “Physics potential of a long-baseline neutrino oscillation experiment using a J-PARC neutrino beam and Hyper-Kamiokande”. In: *PTEP* 2015.5 (2015). DOI: [10.1093/ptep/ptv061](https://doi.org/10.1093/ptep/ptv061). arXiv: [1502.05199 \[hep-ex\]](https://arxiv.org/abs/1502.05199) (cit. on p. 36).
- [80] S. Adrian-Martinez et al. “Letter of intent for KM3NeT 2.0”. In: *J. Phys. G* 43.8, 084001 (2016). DOI: [10.1088/0954-3899/43/8/084001](https://doi.org/10.1088/0954-3899/43/8/084001). arXiv: [1601.07459 \[astro-ph.IM\]](https://arxiv.org/abs/1601.07459) (cit. on p. 36).
- [81] M. G. Aartsen et al. “Letter of Intent: The Precision IceCube Next Generation Upgrade (PINGU)”. In: *arXiv Preprints* (Jan. 2014). arXiv: [1401.2046 \[physics.ins-det\]](https://arxiv.org/abs/1401.2046) (cit. on p. 36).
- [82] F. An et al. “Neutrino Physics with JUNO”. In: *J. Phys. G* 43.3, 030401 (2016). DOI: [10.1088/0954-3899/43/3/030401](https://doi.org/10.1088/0954-3899/43/3/030401). arXiv: [1507.05613 \[physics.ins-det\]](https://arxiv.org/abs/1507.05613) (cit. on p. 36).
- [83] M. G. Aartsen et al. “Combined sensitivity to the neutrino mass ordering with JUNO, the IceCube Upgrade, and PINGU”. In: *Phys. Rev. D* 101.3, 032006 (2020). DOI: [10.1103/PhysRevD.101.032006](https://doi.org/10.1103/PhysRevD.101.032006). arXiv: [1911.06745 \[hep-ex\]](https://arxiv.org/abs/1911.06745) (cit. on p. 36).
- [84] P. F. De Salas, S. Gariazzo, O. Mena, C. A. Ternes, and M. Tortola. “Neutrino Mass Ordering from Oscillations and Beyond: 2018 Status and Future Prospects”. In: *Front. Astron. Space Sci.* 5 (2018), p. 36. DOI: [10.3389/fspas.2018.00036](https://doi.org/10.3389/fspas.2018.00036). arXiv: [1806.11051 \[hep-ph\]](https://arxiv.org/abs/1806.11051) (cit. on p. 36).
- [85] A. de Gouvêa. “Neutrino Mass Models”. In: *Ann. Rev. Nucl. Part. Sci.* 66 (2016), pp. 197–217. DOI: [10.1146/annurev-nucl-102115-044600](https://doi.org/10.1146/annurev-nucl-102115-044600) (cit. on p. 36).
- [86] F. Maltoni, J. M. Niczyporuk, and S. Willenbrock. “Upper Bound on the Scale of Majorana-Neutrino Mass Generation”. In: *Phys. Rev. Lett.* 86.2 (2001), pp. 212–215. DOI: [10.1103/PhysRevLett.86.212](https://doi.org/10.1103/PhysRevLett.86.212) (cit. on p. 37).
- [87] Z. Z. Xing and S. Zhou. “Neutrinos in Particle Physics, Astronomy and Cosmology”. In: *Springer* (2011). DOI: [10.1007/978-3-642-17560-2\\_11](https://doi.org/10.1007/978-3-642-17560-2_11) (cit. on p. 37).
- [88] A. de Gouvêa, W. Huang, and J. Jenkins. “Pseudo-Dirac neutrinos in the new standard model”. In: *Phys. Rev. D* 80.7, 073007 (2009). DOI: [10.1103/PhysRevD.80.073007](https://doi.org/10.1103/PhysRevD.80.073007) (cit. on p. 37).
- [89] N. Sahu and U. Sarkar. “Leptogenesis bound on neutrino masses in left-right symmetric models with spontaneous D-parity violation”. In: *Phys. Rev. D* 74, 093002 (2006). DOI: [10.1103/PhysRevD.74.093002](https://doi.org/10.1103/PhysRevD.74.093002). arXiv: [hep-ph/0605007](https://arxiv.org/abs/hep-ph/0605007) (cit. on p. 37).
- [90] M. Agostini et al. “Improved Limit on Neutrinoless Double- $\beta$  Decay of  $^{76}\text{Ge}$  from GERDA Phase II”. In: *Phys. Rev. Lett.* 120.13, 132503 (2018). DOI: [10.1103/PhysRevLett.120.132503](https://doi.org/10.1103/PhysRevLett.120.132503) (cit. on p. 38).

- [91] C. Alduino et al. “First Results from CUORE: A Search for Lepton Number Violation via  $0\nu\beta\beta$  Decay of  $^{130}\text{Te}$ ”. In: *Phys. Rev. Lett.* 120.13, 132501 (2018). DOI: [10.1103/PhysRevLett.120.132501](https://doi.org/10.1103/PhysRevLett.120.132501) (cit. on p. 38).
- [92] A. Gando et al. “Search for Majorana Neutrinos Near the Inverted Mass Hierarchy Region with KamLAND-Zen”. In: *Phys. Rev. Lett.* 117.8, 082503 (2016). DOI: [10.1103/PhysRevLett.117.082503](https://doi.org/10.1103/PhysRevLett.117.082503) (cit. on p. 38).
- [93] M. J. Dolinski, A. W. P. Poon, and W. Rodejohann. “Neutrinoless Double-Beta Decay: Status and Prospects”. In: *Ann. Rev. Nucl. Part. Sci.* 69 (2019), pp. 219–251. DOI: [10.1146/annurev-nucl-101918-023407](https://doi.org/10.1146/annurev-nucl-101918-023407). arXiv: [1902.04097](https://arxiv.org/abs/1902.04097) [[nucl-ex](#)] (cit. on pp. 38, 39).
- [94] N. Abgrall et al. “The Large Enriched Germanium Experiment for Neutrinoless Double Beta Decay (LEGEND)”. In: *AIP Conf. Proc.* 1894.1 (2017). DOI: [10.1063/1.5007652](https://doi.org/10.1063/1.5007652). arXiv: [1709.01980](https://arxiv.org/abs/1709.01980) [[physics.ins-det](#)] (cit. on p. 38).
- [95] M. Aker et al. “Direct neutrino-mass measurement with sub-electronvolt sensitivity”. In: *Nature Physics* 2 (2022), pp. 160–166. DOI: [10.1038/s41567-021-01463-1](https://doi.org/10.1038/s41567-021-01463-1) (cit. on p. 38).
- [96] N. Aghanim et al. “Planck 2018 results. VI. Cosmological parameters”. In: *Astron. Astrophys.* 641 (2020). [Erratum: *Astron. Astrophys.* 652, C4 (2021)], A6. DOI: [10.1051/0004-6361/201833910](https://doi.org/10.1051/0004-6361/201833910). arXiv: [1807.06209](https://arxiv.org/abs/1807.06209) [[astro-ph.CO](#)] (cit. on p. 38).
- [97] A. D. Sakharov. “Violation of CP Invariance, C asymmetry, and baryon asymmetry of the universe”. In: *Pisma Zh. Eksp. Teor. Fiz.* 5 (1967). DOI: [10.1070/PU1991v034n05ABEH002497](https://doi.org/10.1070/PU1991v034n05ABEH002497) (cit. on p. 39).
- [98] J. H. Christenson, J. W. Cronin, V. L. Fitch, and R. Turlay. “Evidence for the  $2\pi$  Decay of the  $K_2^0$  Meson”. In: *Phys. Rev. Lett.* 13.4 (1964), pp. 138–140. DOI: [10.1103/PhysRevLett.13.138](https://doi.org/10.1103/PhysRevLett.13.138) (cit. on p. 39).
- [99] H. Albrecht et al. “Observation of B0-B0 mixing”. In: *Physics Letters B* 192.1 (1987), pp. 245–252. ISSN: 0370-2693. DOI: [10.1016/0370-2693\(87\)91177-4](https://doi.org/10.1016/0370-2693(87)91177-4). URL: <https://www.sciencedirect.com/science/article/pii/0370269387911774> (cit. on p. 39).
- [100] S. Schael et al. “Precision electroweak measurements on the Z resonance”. In: *Phys. Rept.* 427 (2006), pp. 257–454. DOI: [10.1016/j.physrep.2005.12.006](https://doi.org/10.1016/j.physrep.2005.12.006). arXiv: [hep-ex/0509008](https://arxiv.org/abs/hep-ex/0509008) (cit. on p. 39).
- [101] P. A. R. Ade et al. “Planck 2015 results - XIII. Cosmological parameters”. In: *Astron. Astrophys.* 594 (2016), A13. DOI: [10.1051/0004-6361/201525830](https://doi.org/10.1051/0004-6361/201525830) (cit. on p. 39).
- [102] C. Athanassopoulos et al. “Results on  $\nu_\mu \rightarrow \nu_e$  Neutrino Oscillations from the LSND Experiment”. In: *Phys. Rev. Lett.* 81.9 (1998), pp. 1774–1777. DOI: [10.1103/PhysRevLett.81.1774](https://doi.org/10.1103/PhysRevLett.81.1774) (cit. on p. 39).
- [103] A. A. Aguilar-Arevalo et al. “Updated MiniBooNE neutrino oscillation results with increased data and new background studies”. In: *Phys. Rev. D* 103.5, 052002 (2021). DOI: [10.1103/PhysRevD.103.052002](https://doi.org/10.1103/PhysRevD.103.052002). arXiv: [2006.16883](https://arxiv.org/abs/2006.16883) [[hep-ex](#)] (cit. on p. 39).
- [104] G. Mention, M. Fechner, Th. Lasserre, Th. A. Mueller, D. Lhuillier, M. Cribier, and A. Le-tourneau. “The Reactor Antineutrino Anomaly”. In: *Phys. Rev. D* 83 (2011), p. 073006. DOI: [10.1103/PhysRevD.83.073006](https://doi.org/10.1103/PhysRevD.83.073006). arXiv: [1101.2755](https://arxiv.org/abs/1101.2755) [[hep-ex](#)] (cit. on p. 40).
- [105] D. Frekers et al. “The  $^{71}\text{Ga}(^3\text{He},t)$  reaction and the low-energy neutrino response”. In: *Physics Letters B* 706.2 (2011), pp. 134–138. ISSN: 0370-2693. DOI: [10.1016/j.physletb.2011.10.061](https://doi.org/10.1016/j.physletb.2011.10.061) (cit. on p. 40).

- [106] J. Ashenfelter et al. “The PROSPECT Reactor Antineutrino Experiment”. In: *Nuclear Instruments and Methods in Physics Research Section A: Accelerators, Spectrometers, Detectors and Associated Equipment* 922 (2019), pp. 287–309. DOI: [10.1016/j.nima.2018.12.079](https://doi.org/10.1016/j.nima.2018.12.079). arXiv: [1808.00097](https://arxiv.org/abs/1808.00097) [physics.ins-det] (cit. on p. 40).
- [107] N. Allemandou et al. “The STEREO experiment”. In: *Journal of Instrumentation* 13.7, P07009 (2018). DOI: [10.1088/1748-0221/13/07/p07009](https://doi.org/10.1088/1748-0221/13/07/p07009) (cit. on p. 40).
- [108] I. Alekseev et al. “DANSS: Detector of the reactor AntiNeutrino based on Solid Scintillator”. In: *Journal of Instrumentation* 11.11, P11011 (2016). DOI: [10.1088/1748-0221/11/11/p11011](https://doi.org/10.1088/1748-0221/11/11/p11011) (cit. on p. 40).
- [109] Y. J. Ko et al. “Sterile Neutrino Search at the NEOS Experiment”. In: *Phys. Rev. Lett.* 118.12, 121802 (2017). DOI: [10.1103/PhysRevLett.118.121802](https://doi.org/10.1103/PhysRevLett.118.121802). arXiv: [1610.05134](https://arxiv.org/abs/1610.05134) [hep-ex] (cit. on p. 40).
- [110] A. P. Serebrov et al. “Neutrino-4 experiment on the search for a sterile neutrino at the SM-3 reactor”. In: *Journal of Experimental and Theoretical Physics* 121.4 (2015), pp. 578–586. DOI: [10.1134/S1063776115100209](https://doi.org/10.1134/S1063776115100209) (cit. on p. 40).
- [111] M. Andriamirado et al. “Improved short-baseline neutrino oscillation search and energy spectrum measurement with the PROSPECT experiment at HFIR”. In: *Phys. Rev. D* 103.3, 032001 (2021). DOI: [10.1103/PhysRevD.103.032001](https://doi.org/10.1103/PhysRevD.103.032001). arXiv: [2006.11210](https://arxiv.org/abs/2006.11210) [hep-ex] (cit. on p. 40).
- [112] H. Almazán et al. “Improved sterile neutrino constraints from the STEREO experiment with 179 days of reactor-on data”. In: *Phys. Rev. D* 102.5, 052002 (2020). DOI: [10.1103/PhysRevD.102.052002](https://doi.org/10.1103/PhysRevD.102.052002). arXiv: [1912.06582](https://arxiv.org/abs/1912.06582) [hep-ex] (cit. on p. 40).
- [113] M. Danilov. “New results from the DANSS experiment”. In: *PoS ICHEP2020* (2021). DOI: [10.22323/1.390.0121](https://doi.org/10.22323/1.390.0121). arXiv: [2012.10255](https://arxiv.org/abs/2012.10255) [hep-ex] (cit. on p. 40).
- [114] Z. Atif et al. “Search for sterile neutrino oscillation using RENO and NEOS data”. In: *arXiv Preprints* (Nov. 2020). arXiv: [2011.00896](https://arxiv.org/abs/2011.00896) [hep-ex] (cit. on p. 40).
- [115] A. P. Serebrov et al. “Search for sterile neutrinos with the Neutrino-4 experiment and measurement results”. In: *Phys. Rev. D* 104.3, 032003 (2021). DOI: [10.1103/PhysRevD.104.032003](https://doi.org/10.1103/PhysRevD.104.032003) (cit. on p. 40).
- [116] V. Kopeikin, M. Skorokhvatov, and O. Titov. “Reevaluating reactor antineutrino spectra with new measurements of the ratio between U235 and Pu239  $\beta$  spectra”. In: *Phys. Rev. D* 104.7, L071301 (2021). DOI: [10.1103/PhysRevD.104.L071301](https://doi.org/10.1103/PhysRevD.104.L071301). arXiv: [2103.01684](https://arxiv.org/abs/2103.01684) [nucl-ex] (cit. on p. 40).
- [117] P. A. N. Machado, O. Palamara, and D. W. Schmitz. “The Short-Baseline Neutrino Program at Fermilab”. In: *Annual Review of Nuclear and Particle Science* 69.1 (2019), pp. 363–387. ISSN: 1545-4134. DOI: [10.1146/annurev-nucl-101917-020949](https://doi.org/10.1146/annurev-nucl-101917-020949) (cit. on pp. 40, 64, 67, 259).
- [118] P. Abratenko et al. “Search for an Excess of Electron Neutrino Interactions in MicroBooNE Using Multiple Final State Topologies”. In: *arXiv Preprints* (Oct. 2021). arXiv: [2110.14054](https://arxiv.org/abs/2110.14054) [hep-ex] (cit. on p. 40).
- [119] C. A. Argüelles, I. Esteban, M. Hostert, K. J. Kelly, J. Kopp, P. A. N. Machado, I. Martinez-Soler, and Y. F. Perez-Gonzalez. “MicroBooNE and the  $\nu_e$  Interpretation of the MiniBooNE Low-Energy Excess”. In: *arXiv Preprints* (Nov. 2021). arXiv: [2111.10359](https://arxiv.org/abs/2111.10359) [hep-ph] (cit. on p. 40).

- [120] E. J. Moniz, I. Sick, R. R. Whitney, J. R. Ficenece, R. D. Kephart, and W. P. Trower. “Nuclear Fermi Momenta from Quasielastic Electron Scattering”. In: *Phys. Rev. Lett.* 26.8 (1971), pp. 445–448. DOI: [10.1103/PhysRevLett.26.445](https://doi.org/10.1103/PhysRevLett.26.445) (cit. on p. 43).
- [121] J. Nieves, J. E. Amaro, and M. Valverde. “Inclusive quasielastic charged-current neutrino-nucleus reactions”. In: *Phys. Rev. C* 70 (5 2004), p. 055503. DOI: [10.1103/PhysRevC.70.055503](https://doi.org/10.1103/PhysRevC.70.055503). URL: <https://link.aps.org/doi/10.1103/PhysRevC.70.055503> (cit. on pp. 43, 144).
- [122] Y. Hayato and L. Pickering. “The NEUT neutrino interaction simulation program library”. In: *The Eur. Phys. J. Special Topics* (2021). DOI: [10.1140/epjs/s11734-021-00287-7](https://doi.org/10.1140/epjs/s11734-021-00287-7). URL: <https://doi.org/10.1140/epjs/s11734-021-00287-7> (cit. on p. 43).
- [123] A. Bodek and T. Cai. “Removal Energies and Final State Interaction in Lepton Nucleus Scattering”. In: *Eur. Phys. J. C* 79.4, 293 (2019). DOI: [10.1140/epjc/s10052-019-6750-3](https://doi.org/10.1140/epjc/s10052-019-6750-3). arXiv: [1801.07975 \[nucl-th\]](https://arxiv.org/abs/1801.07975) (cit. on p. 43).
- [124] O. Benhar, N. Farina, H. Nakamura, M. Sakuda, and R. Seki. “Electron- and neutrino-nucleus scattering in the impulse approximation regime”. In: *Phys. Rev. D* 72.5, 053005 (2005). DOI: [10.1103/PhysRevD.72.053005](https://doi.org/10.1103/PhysRevD.72.053005) (cit. on p. 44).
- [125] O. Benhar, P. Huber, C. Mariani, and D. Meloni. “Neutrino–nucleus interactions and the determination of oscillation parameters”. In: *Phys. Rept.* 700 (2017), pp. 1–47. DOI: [10.1016/j.physrep.2017.07.004](https://doi.org/10.1016/j.physrep.2017.07.004). arXiv: [1501.06448 \[nucl-th\]](https://arxiv.org/abs/1501.06448) (cit. on p. 44).
- [126] A. M. Ankowski, O. Benhar, and M. Sakuda. “Improving the accuracy of neutrino energy reconstruction in charged-current quasielastic scattering off nuclear targets”. In: *Phys. Rev. D* 91.3, 033005 (2015). DOI: [10.1103/PhysRevD.91.033005](https://doi.org/10.1103/PhysRevD.91.033005) (cit. on p. 44).
- [127] J. Nieves, I. Ruiz Simo, F. Sánchez, and M. J. Vicente Vacas. “CCQE, 2p2h excitations and  $\nu$ -energy reconstruction”. In: *AIP Conf. Proc.* 1663.1, 050005 (2015). DOI: [10.1063/1.4919493](https://doi.org/10.1063/1.4919493). arXiv: [1304.1032 \[hep-ph\]](https://arxiv.org/abs/1304.1032) (cit. on p. 44).
- [128] S. Dolan. “Neutrino Interactions”. In: *International Neutrino Summer School 2021* (Aug. 2021). URL: [https://indico.cern.ch/event/1011452/contributions/4448411/attachments/2291131/3895428/sDolanNuXSec\\_part2.pdf](https://indico.cern.ch/event/1011452/contributions/4448411/attachments/2291131/3895428/sDolanNuXSec_part2.pdf) (cit. on pp. 44, 47, 51).
- [129] J. E. Sobczyk and J. Nieves. “Tensions in neutrino-nucleus modeling”. In: *PoS NuFact2019* (2020). DOI: [10.22323/1.369.0009](https://doi.org/10.22323/1.369.0009) (cit. on p. 45).
- [130] J. A. Formaggio and G. P. Zeller. “From eV to EeV: Neutrino Cross Sections Across Energy Scales”. In: *Rev. Mod. Phys.* 84 (2012), pp. 1307–1341. DOI: [10.1103/RevModPhys.84.1307](https://doi.org/10.1103/RevModPhys.84.1307). arXiv: [1305.7513 \[hep-ex\]](https://arxiv.org/abs/1305.7513) (cit. on pp. 48–50).
- [131] C. H. Llewellyn Smith. “Neutrino reactions at accelerator energies”. In: *Physics Reports* 3.5 (1972), pp. 261–379. DOI: [10.1016/0370-1573\(72\)90010-5](https://doi.org/10.1016/0370-1573(72)90010-5). URL: <https://www.sciencedirect.com/science/article/pii/0370157372900105> (cit. on pp. 49, 144).
- [132] K. Nakamura et al. “Review of Particle Physics”. In: *Journal of Physics G: Nuclear and Particle Physics* 37.7A, 075021 (2010). DOI: [10.1088/0954-3899/37/7a/075021](https://doi.org/10.1088/0954-3899/37/7a/075021) (cit. on p. 50).
- [133] A. Gazizov, M. Kowalski, K. S. Kuzmin, V. A. Naumov, and Ch. Spiering. “Neutrino-nucleon cross sections at energies of Megaton-scale detectors”. In: *EPJ Web of Conferences* 116, 08003 (2016). DOI: [10.1051/epjconf/201611608003](https://doi.org/10.1051/epjconf/201611608003) (cit. on p. 50).
- [134] D. Rein and L. M. Sehgal. “Neutrino-excitation of baryon resonances and single pion production”. In: *Annals of Physics* 133.1 (1981), pp. 79–153. ISSN: 0003-4916. DOI: [https://doi.org/10.1016/0003-4916\(81\)90242-6](https://doi.org/10.1016/0003-4916(81)90242-6). URL: <https://www.sciencedirect.com/science/article/pii/0003491681902426> (cit. on pp. 50, 144).

- [135] C. Andreopoulos et al. “The GENIE Neutrino Monte Carlo Generator”. In: *Nucl. Instrum. Meth. A* 614.1 (2010), pp. 87–104. DOI: [10.1016/j.nima.2009.12.009](https://doi.org/10.1016/j.nima.2009.12.009). arXiv: [0905.2517](https://arxiv.org/abs/0905.2517) [hep-ph] (cit. on pp. 51, 143, 244).
- [136] Y. Hayato. “A neutrino interaction simulation program library NEUT”. In: *Acta Phys. Polon. B* 40 (2009), pp. 2477–2489 (cit. on p. 51).
- [137] J. Żmuda, K. M. Graczyk, C. Juszczak, and J. T. Sobczyk. “NuWro Monte Carlo generator of neutrino interactions - first electron scattering results”. In: *Acta Phys. Polon. B* 46.11 (2015). DOI: [10.5506/APhysPolB.46.2329](https://doi.org/10.5506/APhysPolB.46.2329). arXiv: [1510.03268](https://arxiv.org/abs/1510.03268) [hep-ph] (cit. on p. 51).
- [138] O. Buss, T. Gaitanos, K. Gallmeister, H. van Hees, M. Kaskulov, O. Lalakulich, A. B. Larionov, T. Leitner, J. Weil, and U. Mosel. “Transport-theoretical Description of Nuclear Reactions”. In: *Phys. Rept.* 512 (2012), pp. 1–124. DOI: [10.1016/j.physrep.2011.12.001](https://doi.org/10.1016/j.physrep.2011.12.001). arXiv: [1106.1344](https://arxiv.org/abs/1106.1344) [hep-ph] (cit. on p. 51).
- [139] H. R. Gallagher. “Neutrino Event Generators: A Review”. In: *AIP Conference Proceedings* 1189.1 (2009), pp. 35–42. DOI: [10.1063/1.3274187](https://doi.org/10.1063/1.3274187) (cit. on p. 51).
- [140] P. Langacker. “Grand unified theories and proton decay”. In: *Physics Reports* 72.4 (1981), pp. 185–385. ISSN: 0370-1573. DOI: [10.1016/0370-1573\(81\)90059-4](https://doi.org/10.1016/0370-1573(81)90059-4). URL: <https://www.sciencedirect.com/science/article/pii/0370157381900594> (cit. on p. 53).
- [141] A. Takenaka et al. “Search for proton decay via  $p \rightarrow e^+ \pi^0$  and  $p \rightarrow \mu^+ \pi^0$  with an enlarged fiducial volume in Super-Kamiokande I-IV”. In: *Phys. Rev. D* 102.11, 112011 (2020). DOI: [10.1103/PhysRevD.102.112011](https://doi.org/10.1103/PhysRevD.102.112011). arXiv: [2010.16098](https://arxiv.org/abs/2010.16098) [hep-ex] (cit. on pp. 53, 54).
- [142] K. Møller, A. M. Suliga, I. Tamborra, and P. B. Denton. “Measuring the supernova unknowns at the next-generation neutrino telescopes through the diffuse neutrino background”. In: *Journal of Cosmology and Astroparticle Physics* 1805.5, 066 (2018) (cit. on pp. 54, 233, 255).
- [143] K. Abe et al. “Diffuse supernova neutrino background search at Super-Kamiokande”. In: *Phys. Rev. D* 104.12, 122002 (2021). DOI: [10.1103/PhysRevD.104.122002](https://doi.org/10.1103/PhysRevD.104.122002). arXiv: [2109.11174](https://arxiv.org/abs/2109.11174) [astro-ph.HE] (cit. on p. 54).
- [144] R. Akutsu. “A Study of Neutrons Associated with Neutrino and Antineutrino Interactions on the Water Target at the T2K Far Detector”. PhD thesis. University of Tokyo, 2019 (cit. on pp. 56, 57).
- [145] O. Palamara. “Hints on nuclear effects from ArgoNeuT data”. In: *AIP Conf. Proc.* 1663.1 (2015), p. 090003. DOI: [10.1063/1.4919498](https://doi.org/10.1063/1.4919498) (cit. on p. 59).
- [146] S. Abachi et al. “Observation of the Top Quark”. In: *Phys. Rev. Lett.* 74.14 (1995), pp. 2632–2637. DOI: [10.1103/PhysRevLett.74.2632](https://doi.org/10.1103/PhysRevLett.74.2632). arXiv: [hep-ex/9503003](https://arxiv.org/abs/hep-ex/9503003) (cit. on p. 64).
- [147] F. Abe et al. “Observation of Top Quark Production in  $\bar{p}p$  Collisions with the Collider Detector at Fermilab”. In: *Phys. Rev. Lett.* 74.14 (1995), pp. 2626–2631. DOI: [10.1103/PhysRevLett.74.2626](https://doi.org/10.1103/PhysRevLett.74.2626) (cit. on p. 64).
- [148] S. Tufanli. “The SBND experiment”. In: *PoS HQL2016* (2017). DOI: [10.22323/1.274.0070](https://doi.org/10.22323/1.274.0070) (cit. on p. 64).
- [149] I. Stancu et al. “The MiniBooNE detector technical design report”. In: *Fermilab Technical Design Reports* (May 2001). DOI: [10.2172/809967](https://doi.org/10.2172/809967) (cit. on p. 64).
- [150] B. Fleming. “The MicroBooNE Technical Design Report”. In: *Fermilab Technical Design Reports* (Feb. 2012). DOI: [10.2172/1333130](https://doi.org/10.2172/1333130) (cit. on p. 64).
- [151] “MINERvA Technical Design Report”. In: *Fermilab Technical Design Reports* (2006) (cit. on p. 64).

- [152] I. Ambats et al. “The MINOS Detectors Technical Design Report”. In: *Fermilab Technical Design Reports* (Oct. 1998) (cit. on p. 64).
- [153] D. S. Ayres et al. “The NOvA Technical Design Report”. In: *Fermilab Technical Design Reports* (Oct. 2007). DOI: [10.2172/935497](https://doi.org/10.2172/935497) (cit. on p. 64).
- [154] Accelerator Division Operations Department. “Fermilab - Concepts Rookie Book”. In: *Fermilab Internal Document* (2020). URL: [https://operations.fnal.gov/rookie\\_books/concepts.pdf](https://operations.fnal.gov/rookie_books/concepts.pdf) (cit. on pp. 64, 65, 69).
- [155] A. A. Aguilar-Arevalo et al. “The Neutrino Flux prediction at MiniBooNE”. In: *Phys. Rev. D* 79, 072002 (2009). DOI: [10.1103/PhysRevD.79.072002](https://doi.org/10.1103/PhysRevD.79.072002). arXiv: [0806.1449](https://arxiv.org/abs/0806.1449) [hep-ex] (cit. on pp. 67–72).
- [156] J. Kopp. “The Plot Thickens For a Fourth Neutrino”. In: *APS Physics* (May 2018). eprint: <https://physics.aps.org/articles/v11/122> (cit. on p. 68).
- [157] I. Stancu et al. “Technical Design Report for the 8 GeV Beam”. In: *Fermilab Technical Design Reports* (May 2001). DOI: [10.2172/1212167](https://doi.org/10.2172/1212167) (cit. on pp. 70, 71).
- [158] D. Beechy and R. Ducar. “Time And Data Distribution Systems At The Fermilab Accelerator”. In: *Nuclear Instruments and Methods in Physics Research A* 247 (1986) (cit. on p. 73).
- [159] Fermilab Accelerator Division. *Booster Rookie Book*. 2009. URL: [https://operations.fnal.gov/rookie\\_books/Booster\\_V4.1.pdf](https://operations.fnal.gov/rookie_books/Booster_V4.1.pdf) (cit. on p. 73).
- [160] G. Vogel. *TCLK Event Definitions 13-Jan-2021*. 2021. URL: [https://www-bd.fnal.gov/controls/hardware\\_vogel/tclk.htm](https://www-bd.fnal.gov/controls/hardware_vogel/tclk.htm) (cit. on p. 74).
- [161] K. Arisaka et al. “KTeV design report: Physics goals, technical components, and detector costs”. In: *Fermilab Technical Design Reports* (1992) (cit. on p. 79).
- [162] G. Pauletta. “Scintillation Counters for the CDF Muon Upgrade”. In: *International Journal of Modern Physics A* 16.suppl1c (2001), pp. 1139–1142. DOI: [10.1142/S0217751X01009132](https://doi.org/10.1142/S0217751X01009132) (cit. on p. 80).
- [163] Incom. *Large Area Picosecond Photodetector*. 2021. URL: <https://incomusa.com/lappd/> (cit. on p. 81).
- [164] B.W. Adams, A. Elagin, H.J. Frisch, R. Obaid, E. Oberla, A. Vostrikov, R.G. Wagner, J. Wang, and M. Wetstein. “Timing characteristics of Large Area Picosecond Photodetectors”. In: *Nuclear Instruments and Methods in Physics Research Section A: Accelerators, Spectrometers, Detectors and Associated Equipment* 795 (2015), pp. 1–11. ISSN: 0168-9002. DOI: [10.1016/j.nima.2015.05.027](https://doi.org/10.1016/j.nima.2015.05.027). URL: <https://www.sciencedirect.com/science/article/pii/S0168900215006592> (cit. on pp. 81–83).
- [165] B. W. Adams et al. *A Brief Technical History of the Large-Area Picosecond Photodetector (LAPPD) Collaboration*. 2016. arXiv: [1603.01843](https://arxiv.org/abs/1603.01843) [physics.ins-det] (cit. on p. 82).
- [166] S. M. George. “Atomic Layer Deposition: An Overview”. In: *Chemical Reviews* 110.1 (2010), pp. 111–131. DOI: [10.1021/cr900056b](https://doi.org/10.1021/cr900056b) (cit. on p. 82).
- [167] Incom. *Measurement & Test Report for LAPPD* 39. 2019 (cit. on p. 82).

- [168] A.V. Lyashenko, B.W. Adams, M. Aviles, T. Cremer, C.D. Ertley, M.R. Foley, M.J. Minot, M.A. Popecki, M.E. Stochaj, W.A. Worstell, J.W. Elam, A.U. Mane, O.H. W. Siegmund, H.J. Frisch, A.L. Elagin, E. Angelico, and E. Spiegman. “Performance of Large Area Picosecond Photo-Detectors (LAPPD)”. In: *Nuclear Instruments and Methods in Physics Research Section A: Accelerators, Spectrometers, Detectors and Associated Equipment* 958, 162834 (2020). Proceedings of the Vienna Conference on Instrumentation 2019. ISSN: 0168-9002. DOI: [10.1016/j.nima.2019.162834](https://doi.org/10.1016/j.nima.2019.162834). URL: <https://www.sciencedirect.com/science/article/pii/S0168900219312690> (cit. on pp. 82, 85).
- [169] G. Haller and B. Wooley. “A 700 MHz Switched Capacitor Analog Waveform Sampling Circuit”. In: *SLAC-PUB-6414* (1993). URL: <http://citeseerx.ist.psu.edu/viewdoc/download?doi=10.1.1.433.9386&rep=rep1&type=pdf> (cit. on p. 86).
- [170] S.A. Kleinfelder. “Development of a switched capacitor based multi-channel transient waveform recording integrated circuit”. In: *IEEE Transactions on Nuclear Science* 35.1 (1988), pp. 151–154. DOI: [10.1109/23.12695](https://doi.org/10.1109/23.12695) (cit. on p. 86).
- [171] E. Oberla, J.-F. Genat, H. Grabas H. and Frisch, K. Nishimura, and G. Varner. “A 15GSa/s, 1.5GHz bandwidth waveform digitizing ASIC”. In: *Nuclear Instruments and Methods in Physics Research Section A: Accelerators, Spectrometers, Detectors and Associated Equipment* 735 (2014), pp. 452–461. ISSN: 0168-9002. DOI: [10.1016/j.nima.2013.09.042](https://doi.org/10.1016/j.nima.2013.09.042) (cit. on p. 87).
- [172] M. Bogdan, E. Oberla, H. J. Frisch, and M. Wetstein. “A modular data acquisition system using the 10 GSa/s PSEC4 waveform recording chip”. In: *2016 IEEE-NPSS Real Time Conference (RT)*. 2016, pp. 1–3. DOI: [10.1109/RTC.2016.7543167](https://doi.org/10.1109/RTC.2016.7543167) (cit. on p. 87).
- [173] J. Podczerwinski. *Characterization of Self-Trigging on the PSEC4 Waveform Digitizing ASIC*. ANNIE Internal Database document (cit. on p. 87).
- [174] A. Weinstein and M. Wetstein. *LAPPD Module Deployment: Status, Progress and Schedule*. Internal ANNIE database document. 2021. URL: <https://annie-docdb.fnal.gov/cgi-bin/private/ShowDocument?docid=4370> (cit. on p. 89).
- [175] J. F. Beacom and M. R. Vagins. “Antineutrino Spectroscopy with Large Water Čerenkov Detectors”. In: *Physical Review Letters* 93.17 (2004). ISSN: 1079-7114. DOI: [10.1103/physrevlett.93.171101](https://doi.org/10.1103/physrevlett.93.171101) (cit. on p. 88).
- [176] R. B. Firestone and V. S. Shirley. *Table of Isotopes*. John Wiley, New York, 1996 (cit. on p. 89).
- [177] S. Dazeley, A. Bernstein, N.S. Bowden, and R. Svoboda. “Observation of neutrons with a Gadolinium doped water Cherenkov detector”. In: *Nuclear Instruments and Methods in Physics Research Section A: Accelerators, Spectrometers, Detectors and Associated Equipment* 607.3 (2009), pp. 616–619. ISSN: 0168-9002. DOI: [10.1016/j.nima.2009.03.256](https://doi.org/10.1016/j.nima.2009.03.256). URL: <https://www.sciencedirect.com/science/article/pii/S0168900209007475> (cit. on pp. 89, 99, 216).
- [178] M. Vagins. *Large-Scale Testing and Development of Gadolinium Trichloride for Use in Neutron Detection in Large Water Cherenkov Detectors*. A Scientific/Technical Report for the Advanced Detector Research Program. 2006. URL: <https://www.osti.gov/servlets/purl/915115> (cit. on p. 90).
- [179] V. Fischer, J. He, M. Irving, and R. Svoboda. “Development of an ion exchange resin for gadolinium-loaded water”. In: *Journal of Instrumentation* 15.07 (2020). DOI: [10.1088/1748-0221/15/07/p07004](https://doi.org/10.1088/1748-0221/15/07/p07004) (cit. on pp. 90, 91).

- [180] I. Kano, D. Darbouret, and S. Mabic. “UV technologies in water purification systems”. In: *Merck Millipore Publication* (2012) (cit. on p. 90).
- [181] L. Wan et al. “Measurement of the neutrino-oxygen neutral-current quasielastic cross section using atmospheric neutrinos at Super-Kamiokande”. In: *Phys. Rev. D* 99.3, 032005 (2019). DOI: [10.1103/PhysRevD.99.032005](https://doi.org/10.1103/PhysRevD.99.032005). arXiv: [1901.05281 \[hep-ex\]](https://arxiv.org/abs/1901.05281) (cit. on pp. 95, 232, 245, 247).
- [182] K. Abe et al. “Measurement of neutrino and antineutrino neutral-current quasielasticlike interactions on oxygen by detecting nuclear deexcitation  $\gamma$  rays”. In: *Phys. Rev. D* 100.11 (2019), p. 112009. DOI: [10.1103/PhysRevD.100.112009](https://doi.org/10.1103/PhysRevD.100.112009). arXiv: [1910.09439 \[hep-ex\]](https://arxiv.org/abs/1910.09439) (cit. on pp. 95, 232, 257).
- [183] A. Mastbaum. “ANNIE - Future Physics Opportunities”. In: *New Directions in Neutrino Nucleus Scattering (NDNN) workshop* (2021) (cit. on p. 95).
- [184] A. R. Back et al. “Measurement of beam-correlated background neutrons from the Fermilab Booster Neutrino Beam in ANNIE Phase-I”. In: *Journal of Instrumentation* 15.03 (2020). ISSN: 1748-0221. DOI: [10.1088/1748-0221/15/03/p03011](https://doi.org/10.1088/1748-0221/15/03/p03011) (cit. on pp. 96, 97, 209).
- [185] M. Yeh, S. Hans, W. Beriguete, R. Rosero, L. Hu, R. L. Hahn, M. V. Diwan, D. E. Jaffe, S. H. Kettell, and L. Littenberg. “A new water-based liquid scintillator and potential applications”. In: *Nucl. Instrum. Meth. A* 660 (2011), pp. 51–56. DOI: [10.1016/j.nima.2011.08.040](https://doi.org/10.1016/j.nima.2011.08.040) (cit. on pp. 98, 260).
- [186] B. Richards. *ToolDAQ/ToolDAQFramework: ToolDAQ Framework v2.2.1*. Version v2.2.1. May 2019. DOI: [10.5281/zenodo.3229251](https://doi.org/10.5281/zenodo.3229251). URL: <https://doi.org/10.5281/zenodo.3229251> (cit. on p. 100).
- [187] B. Richards and J. Eisch. *ANNIEDAQ Phase 1 (Version V1.0.0)*. Version v1.0.0. 2018. DOI: [10.5281/zenodo.1489338](https://doi.org/10.5281/zenodo.1489338) (cit. on p. 101).
- [188] B. Richards. *Software Status*. Internal ANNIE database document. 2020. URL: <https://annie-docdb.fnal.gov/cgi-bin/private/ShowDocument?docid=4439> (cit. on p. 101).
- [189] J. Eisch. *ANNIE DAQ Electronics Overview*. Internal ANNIE database document. 2020. URL: <https://annie-docdb.fnal.gov/cgi-bin/private/ShowDocument?docid=3642> (cit. on p. 105).
- [190] B. Richards. *WebServer*. <https://github.com/ANNIEsoft/WebServer>. 2021 (cit. on p. 111).
- [191] M. Chen. “The Accelerator Neutrino Neutron Interaction Experiment(ANNIE) Front Anti-Coincidence Counter (FACC) Testing”. M.Sc. Thesis, University of California Davis. 2016 (cit. on p. 131).
- [192] J. Podczerwinski. *Calibration and Testing of Muon Detectors for ANNIE*. SULI report. 2016. URL: <https://annie-docdb.fnal.gov/cgi-bin/sso/ShowDocument?docid=274> (cit. on p. 132).
- [193] S. Agostinelli et al. “Geant4 - a simulation toolkit”. In: *Nuclear Instruments and Methods in Physics Research Section A: Accelerators, Spectrometers, Detectors and Associated Equipment* 506.3 (2003), pp. 250–303. ISSN: 0168-9002. DOI: [10.1016/S0168-9002\(03\)01368-8](https://doi.org/10.1016/S0168-9002(03)01368-8). URL: <https://www.sciencedirect.com/science/article/pii/S0168900203013688> (cit. on pp. 143, 145, 243).
- [194] A. Himmel, E. O’Sullivan, B. Richards, B. Viren, and C. Walter. *The Water Cherenkov Simulator (WCSim)*. <https://github.com/WCSim/WCSim>. 2020 (cit. on pp. 143, 145, 243).

- [195] R. Brun and F. Rademakers. “ROOT: An object oriented data analysis framework”. In: *Nucl. Instrum. Meth. A* 389 (1997), pp. 81–86. DOI: [10.1016/S0168-9002\(97\)00048-X](https://doi.org/10.1016/S0168-9002(97)00048-X) (cit. on p. 143).
- [196] C. Andreopoulos, C. Barry, S. Dytman, H. Gallagher, T. Golan, R. Hatcher, G. Perdue, and J. Yarba. “The GENIE Neutrino Monte Carlo Generator: Physics and User Manual”. In: *arXiv Preprints* (Oct. 2015). arXiv: [1510.05494 \[hep-ph\]](https://arxiv.org/abs/1510.05494) (cit. on pp. 143, 144, 244).
- [197] Y. Hayato. “Neut”. In: *Nuclear Physics B - Proceedings Supplements* 112.1 (2002), pp. 171–176. ISSN: 0920-5632. DOI: [10.1016/S0920-5632\(02\)01759-0](https://doi.org/10.1016/S0920-5632(02)01759-0). URL: <https://www.sciencedirect.com/science/article/pii/S0920563202017590> (cit. on p. 143).
- [198] D. Casper. “The nuance neutrino physics simulation, and the future”. In: *Nuclear Physics B - Proceedings Supplements* 112.1 (2002), pp. 161–170. ISSN: 0920-5632. DOI: [10.1016/S0920-5632\(02\)01756-5](https://doi.org/10.1016/S0920-5632(02)01756-5). URL: <https://www.sciencedirect.com/science/article/pii/S0920563202017565> (cit. on p. 143).
- [199] A. Bodek and J. L. Ritchie. “Further studies of Fermi-motion effects in lepton scattering from nuclear targets”. In: *Phys. Rev. D* 24.5 (1981), pp. 1400–1402. DOI: [10.1103/PhysRevD.24.1400](https://doi.org/10.1103/PhysRevD.24.1400) (cit. on p. 144).
- [200] R.A. Smith and E.J. Moniz. “Neutrino reactions on nuclear targets”. In: *Nuclear Physics B* 43 (1972), pp. 605–622. ISSN: 0550-3213. DOI: [10.1016/0550-3213\(72\)90040-5](https://doi.org/10.1016/0550-3213(72)90040-5). URL: <https://www.sciencedirect.com/science/article/pii/0550321372900405> (cit. on p. 144).
- [201] L. A. Ahrens et al. “Measurement of Neutrino - Proton and anti-neutrino - Proton Elastic Scattering”. In: *Phys. Rev. D* 35.3 (1987). DOI: [10.1103/PhysRevD.35.785](https://doi.org/10.1103/PhysRevD.35.785) (cit. on p. 144).
- [202] A. Bodek and U. K. Yang. “Higher twist, xi(omega) scaling, and effective LO PDFs for lepton scattering in the few GeV region”. In: *J. Phys. G* 29.8 (2003), pp. 1899–1906. DOI: [10.1088/0954-3899/29/8/369](https://doi.org/10.1088/0954-3899/29/8/369). arXiv: [hep-ex/0210024](https://arxiv.org/abs/hep-ex/0210024) (cit. on p. 144).
- [203] T. Sjöstrand, S. Mrenna, and P. Skands. “PYTHIA 6.4 physics and manual”. In: *Journal of High Energy Physics* 2006.05 (2006). The code and further information may be found on the Pythia web page: <http://www.thep.lu.se/~torbjorn/Pythia.html>. DOI: [10.1088/1126-6708/2006/05/026](https://doi.org/10.1088/1126-6708/2006/05/026) (cit. on p. 144).
- [204] Z. Koba, H. B. Nielsen, and P. Olesen. “Scaling of multiplicity distributions in high-energy hadron collisions”. In: *Nucl. Phys. B* 40 (1972), pp. 317–334. DOI: [10.1016/0550-3213\(72\)90551-2](https://doi.org/10.1016/0550-3213(72)90551-2) (cit. on p. 144).
- [205] Y. Nishimura. “Development of the Hyper-Kamiokande Detector”. In: *Proceedings of the 2nd International Symposium on Science at J-PARC - Unlocking the Mysteries of Life, Matter and the Universe*. DOI: [10.7566/JPSCP.8.023009](https://doi.org/10.7566/JPSCP.8.023009). eprint: <https://journals.jps.jp/doi/pdf/10.7566/JPSCP.8.023009> (cit. on pp. 145, 243).
- [206] A. Himmel, M. O’Flaherty, E. O’Sullivan, B. Richards, B. Viren, and C. Walter. *The Water Cherenkov Simulator (WCSim) [ANNIE version]*. <https://github.com/ANNIEsoft/WCSim/tree/annie>. 2021 (cit. on p. 145).
- [207] M. O’Flaherty. *March Collaboration WCSim Updates*. Internal ANNIE database document. 2019. URL: <https://annie-docdb.fnal.gov/cgi-bin/sso/ShowDocument?docid=2666> (cit. on p. 146).
- [208] B. Land, A. Mastbaum, and V. Fischer. *RAT (is an Analysis Tool), Public Edition [ANNIE version]*. <https://github.com/vfischer/ANNIEratpac>. 2021 (cit. on pp. 146, 150, 269).

- [209] S. Fukuda et al. “The Super-Kamiokande detector”. In: *Nucl. Instrum. Meth. A* 501 (2003), pp. 418–462. DOI: [10.1016/S0168-9002\(03\)00425-X](https://doi.org/10.1016/S0168-9002(03)00425-X) (cit. on p. 150).
- [210] E. Dietz-Laursonn. “Peculiarities in the Simulation of Optical Physics with Geant4”. In: *arXiv Preprints* (2016). arXiv: [1612.05162](https://arxiv.org/abs/1612.05162) [[physics.ins-det](https://arxiv.org/abs/1612.05162)] (cit. on p. 150).
- [211] Hamamatsu. *Combined Hamamatsu Data Sheet for R5912, R7081, and R12860*. [https://www.hamamatsu.com/resources/pdf/etd/LARGE\\_AREA\\_PMT\\_TPMH1376E.pdf](https://www.hamamatsu.com/resources/pdf/etd/LARGE_AREA_PMT_TPMH1376E.pdf). 2019 (cit. on pp. 152, 153).
- [212] N. Barros, T. Kaptanoglu, B. Kimelman, J. R. Klein, E. Moore, J. Nguyen, K. Stavreva, and R. Svoboda. “Characterization of the ETEL D784UKFLB 11 in. photomultiplier tube”. In: *Nucl. Instrum. Meth. A* 852 (2017), pp. 15–19. DOI: [10.1016/j.nima.2017.01.067](https://doi.org/10.1016/j.nima.2017.01.067). arXiv: [1512.06916](https://arxiv.org/abs/1512.06916) [[physics.ins-det](https://arxiv.org/abs/1512.06916)] (cit. on p. 152).
- [213] P. Cignoni, M. Callieri, M. Corsini, M. Dellepiane, F. Ganovelli, and G. Ranzuglia. “MeshLab: an Open-Source Mesh Processing Tool”. In: *Eurographics Italian Chapter Conference*. The Eurographics Association, 2008. ISBN: 978-3-905673-68-5. DOI: [10.2312/LocalChapterEvents/ItalChap/ItalianChapConf2008/129-136](https://doi.org/10.2312/LocalChapterEvents/ItalChap/ItalianChapConf2008/129-136) (cit. on p. 155).
- [214] V. Fischer. *Private communication*. 2021 (cit. on p. 157).
- [215] T. J. Pershing. “The Accelerator Neutrino-Neutron Interaction Experiment”. PhD thesis. UC, Davis, 2020. DOI: [10.2172/1638651](https://doi.org/10.2172/1638651) (cit. on pp. 159, 164, 206, 214, 227).
- [216] P. A. Amaudruz et al. “In-situ characterization of the Hamamatsu R5912-HQE photomultiplier tubes used in the DEAP-3600 experiment”. In: *Nucl. Instrum. Meth. A* 922 (2019), pp. 373–384. DOI: [10.1016/j.nima.2018.12.058](https://doi.org/10.1016/j.nima.2018.12.058). arXiv: [1705.10183](https://arxiv.org/abs/1705.10183) [[physics.ins-det](https://arxiv.org/abs/1705.10183)] (cit. on p. 159).
- [217] K. Abe et al. “Calibration of the Super-Kamiokande Detector”. In: *Nucl. Instrum. Meth. A* 737 (2014), pp. 253–272. DOI: [10.1016/j.nima.2013.11.081](https://doi.org/10.1016/j.nima.2013.11.081). arXiv: [1307.0162](https://arxiv.org/abs/1307.0162) [[physics.ins-det](https://arxiv.org/abs/1307.0162)] (cit. on p. 162).
- [218] R. Bayes et al. “Experimental Constraints on Left-Right Symmetric Models from Muon Decay”. In: *Phys. Rev. Lett.* 106 (2011). DOI: [10.1103/PhysRevLett.106.041804](https://doi.org/10.1103/PhysRevLett.106.041804) (cit. on p. 163).
- [219] S. Dazeley et al. “A search for cosmogenic production of neutron emitting radionuclides in water”. In: *Nuclear Instruments and Methods in Physics Research. Section A, Accelerators, Spectrometers, Detectors and Associated Equipment* (Mar. 2016), pp. 151–159. DOI: [10.1016/j.nima.2016.03.014](https://doi.org/10.1016/j.nima.2016.03.014) (cit. on p. 164).
- [220] P. Allison et al. “Observing muon decays in water Cherenkov detectors at the Pierre Auger Observatory”. In: *29th International Cosmic Ray Conference*. Aug. 2005. arXiv: [astro-ph/0509238](https://arxiv.org/abs/astro-ph/0509238) (cit. on p. 165).
- [221] K. Pearson, J. A. Harris, A. E. Treloar, and M. Wilder. “On the Theory of Contingency”. In: *Journal of the American Statistical Association* 25.171 (1930), pp. 320–327. ISSN: 01621459. URL: <http://www.jstor.org/stable/2278196> (cit. on p. 166).
- [222] M. Cecchetto et al. “0.1-10 MeV Neutron Soft Error Rate in Accelerator and Atmospheric Environments”. In: *IEEE Transactions on Nuclear Science* 68.5 (2021), pp. 873–883. DOI: [10.1109/TNS.2021.3064666](https://doi.org/10.1109/TNS.2021.3064666) (cit. on p. 176).
- [223] R. J. Holmes. *Gamma ray and neutron sources*. Tech. rep. Australia, 1982, pp. 123–136. URL: [http://inis.iaea.org/search/search.aspx?orig\\_q=RN:14792880](http://inis.iaea.org/search/search.aspx?orig_q=RN:14792880) (cit. on p. 175).

- [224] J. Scherzinger et al. “Tagging fast neutrons from an  $^{241}\text{Am}/^{9}\text{Be}$  source”. In: *Applied Radiation and Isotopes* 98 (2015), pp. 74–79. ISSN: 0969-8043. DOI: [10.1016/j.apradiso.2015.01.003](https://doi.org/10.1016/j.apradiso.2015.01.003) (cit. on p. 176).
- [225] L. Pickard. *Neutron capture calibration using AmBe source*. Internal ANNIE database document (DocDB ID 3239). 2019. URL: <https://annie-docdb.fnal.gov/cgi-bin/sso/ShowDocument?docid=3239> (cit. on p. 177).
- [226] S. F. Mughabghab. *Atlas of Neutron Resonances, Fifth Edition: Resonance Parameters and Thermal Cross Sections, Z = 1 – 100*. Amsterdam: Elsevier, 2006 (cit. on p. 177).
- [227] G. Leinweber et al. “Neutron Capture and Total Cross-Section Measurements and Resonance Parameters of Gadolinium”. In: *Nuclear Science and Engineering* 154.3 (2006), pp. 261–279. DOI: [10.13182/NSE05-64](https://doi.org/10.13182/NSE05-64) (cit. on p. 177).
- [228] H. D. Choi et al. “Radiative Capture Cross Sections of  $^{155,157}\text{Gd}$  for Thermal Neutrons”. In: *Nuclear Science and Engineering* 177.2 (2014), pp. 219–232. DOI: [10.13182/NSE13-49](https://doi.org/10.13182/NSE13-49) (cit. on p. 177).
- [229] M. Mastromarco et al. “Cross section measurements of  $^{155,157}\text{Gd}(n,\gamma)$  induced by thermal and epithermal neutrons.” In: *Eur. Phys. J. A* 55.9 (2019). DOI: [10.1140/epja/i2019-12692-7](https://doi.org/10.1140/epja/i2019-12692-7) (cit. on p. 177).
- [230] K. Hagiwara et al. “Gamma-ray spectrum from thermal neutron capture on gadolinium-157”. In: *Progress of Theoretical and Experimental Physics* 2019.2, 023D01 (Feb. 2019). ISSN: 2050-3911. DOI: [10.1093/ptep/ptz002](https://doi.org/10.1093/ptep/ptz002). eprint: <https://academic.oup.com/ptep/article-pdf/2019/2/023D01/27970473/ptz002.pdf> (cit. on p. 178).
- [231] T. Tanaka et al. “Gamma-ray spectra from thermal neutron capture on gadolinium-155 and natural gadolinium”. In: *Progress of Theoretical and Experimental Physics* 2020.4, 043D02 (Apr. 2020). ISSN: 2050-3911. DOI: [10.1093/ptep/ptaa015](https://doi.org/10.1093/ptep/ptaa015). eprint: <https://academic.oup.com/ptep/article-pdf/2020/4/043D02/33040537/ptaa015.pdf> (cit. on pp. 178, 179, 194).
- [232] M. Reen, T. Sudo, A. Ali, E. Gazzola, and M. Sakuda. *Website of the ANNRI-Gd model*. 2020. URL: [http://www.physics.okayama-u.ac.jp/~sakuda/ANNRI-Gd\\_ver1.html](http://www.physics.okayama-u.ac.jp/~sakuda/ANNRI-Gd_ver1.html) (cit. on p. 178).
- [233] A. Chyzh et al. “Measurement of the  $^{157}\text{Gd}(n,\gamma)$  reaction with the DANCE  $\gamma$  calorimeter array”. In: *Phys. Rev. C* 84.1, 014306 (2011). DOI: [10.1103/PhysRevC.84.014306](https://doi.org/10.1103/PhysRevC.84.014306) (cit. on p. 178).
- [234] E. Drakopoulou. “ANNIE Phase II Reconstruction Techniques”. In: *arXiv Preprints* (2018). arXiv: [1803.10624](https://arxiv.org/abs/1803.10624) [physics.ins-det] (cit. on pp. 187, 204, 284).
- [235] Ll. Marti et al. “Evaluation of gadolinium’s action on water Cherenkov detector systems with EGADS”. In: *Nuclear Instruments and Methods in Physics Research Section A: Accelerators, Spectrometers, Detectors and Associated Equipment* 959 (2020). ISSN: 0168-9002. DOI: [10.1016/j.nima.2020.163549](https://doi.org/10.1016/j.nima.2020.163549). URL: <https://www.sciencedirect.com/science/article/pii/S0168900220301315> (cit. on p. 194).
- [236] D. E. Groom, N. V. Mokhov, and S. I. Striganov. “Muon stopping power and range tables 10 MeV-100 TeV”. In: *Atomic Data and Nuclear Data Tables* 78.2 (2001), pp. 183–356. ISSN: 0092-640X. DOI: <https://doi.org/10.1006/adnd.2001.0861>. URL: <https://www.sciencedirect.com/science/article/pii/S0092640X01908617> (cit. on pp. 205, 206).

- [237] Y. Ashida et al. “Measurement of  $\gamma$ -ray production via neutron- $^{16}\text{O}$  reaction using a 77 MeV quasi-monoenergetic neutron beam”. In: *arXiv Preprints* (Feb. 2019). arXiv: [1902.08964](https://arxiv.org/abs/1902.08964) [[nucl-ex](#)] (cit. on pp. 212, 244).
- [238] H. A. Bethe. “Supernova mechanisms”. In: *Rev. Mod. Phys.* 62.4 (1990), pp. 801–866. DOI: [10.1103/RevModPhys.62.801](https://doi.org/10.1103/RevModPhys.62.801) (cit. on p. 231).
- [239] S. Al Kharusi et al. “SNEWS 2.0: a next-generation supernova early warning system for multi-messenger astronomy”. In: *New Journal of Physics* 23.3, 031201 (2021). DOI: [10.1088/1367-2630/abde33](https://doi.org/10.1088/1367-2630/abde33) (cit. on p. 231).
- [240] K. Abe et al. “Supernova Model Discrimination with Hyper-Kamiokande”. In: *The Astrophysical Journal* 916.1, 15 (2021). ISSN: 1538-4357. DOI: [10.3847/1538-4357/abf7c4](https://doi.org/10.3847/1538-4357/abf7c4) (cit. on p. 232).
- [241] D. Maksimović, M. Nieslony, and M. Wurm. “CNNs for enhanced background discrimination in DSNB searches in large-scale water-Gd detectors”. In: *Journal of Cosmology and Astroparticle Physics* 2021.11, 051 (2021). DOI: [10.1088/1475-7516/2021/11/051](https://doi.org/10.1088/1475-7516/2021/11/051) (cit. on p. 232).
- [242] H. Zhang et al. “Supernova Relic Neutrino search with neutron tagging at Super-Kamiokande-IV”. In: *Astroparticle Physics* 60 (2015), pp. 41–46. ISSN: 0927-6505. DOI: [10.1016/j.astropartphys.2014.05.004](https://doi.org/10.1016/j.astropartphys.2014.05.004). URL: <https://www.sciencedirect.com/science/article/pii/S0927650514000681> (cit. on p. 232).
- [243] Y. Zhang. “Search for Supernova Relic Neutrinos with 2.2 MeV Gamma Tagging at Super-Kamiokande-IV”. In: *Physics Procedia* 61 (2015), pp. 384–391. ISSN: 1875-3892. DOI: [10.1016/j.phpro.2014.12.079](https://doi.org/10.1016/j.phpro.2014.12.079). URL: <https://www.sciencedirect.com/science/article/pii/S1875389214006920> (cit. on p. 232).
- [244] J. F. Beacom. “The Diffuse Supernova Neutrino Background”. In: *Annual Review of Nuclear and Particle Science* 60.1 (2010), pp. 439–462. DOI: [10.1146/annurev.nucl.010909.083331](https://doi.org/10.1146/annurev.nucl.010909.083331) (cit. on pp. 233, 234).
- [245] D. Kresse, T. Ertl, and H.-T. Janka. “Stellar Collapse Diversity and the Diffuse Supernova Neutrino Background”. In: *The Astrophysical Journal* 909.2, 169 (2021). ISSN: 1538-4357. DOI: [10.3847/1538-4357/abd54e](https://doi.org/10.3847/1538-4357/abd54e) (cit. on pp. 233, 234, 244).
- [246] K. Huang. “Measurement of the neutrino-oxygen neutral current quasi-elastic interaction cross-section by observing nuclear de-excitation  $\gamma$ -rays in the T2K experiment”. PhD thesis. Kyoto U., 2015 (cit. on pp. 234, 242, 245).
- [247] A. Ferrari, P. R. Sala, A. Fasso, and J. Ranft. “FLUKA: A multi-particle transport code (Program version 2005)”. In: *CERN Yellow Reports: Monographs* (Oct. 2005). DOI: [10.2172/877507](https://doi.org/10.2172/877507) (cit. on p. 235).
- [248] G. Battistoni, A. Ferrari, T. Montaruli, and P. R. Sala. “The FLUKA atmospheric neutrino flux calculation”. In: *Astropart. Phys.* 19.2 (2003), pp. 269–290. DOI: [10.1016/S0927-6505\(02\)00246-3](https://doi.org/10.1016/S0927-6505(02)00246-3). arXiv: [hep-ph/0207035](https://arxiv.org/abs/hep-ph/0207035) (cit. on pp. 235, 236, 244).
- [249] A. M. Ankowski, O. Benhar, T. Mori, R. Yamaguchi, and M. Sakuda. “Analysis of  $\gamma$ -ray production in neutral-current neutrino-oxygen interactions at energies above 200 MeV”. In: *Phys. Rev. Lett.* 108.5, 052505 (2012). DOI: [10.1103/PhysRevLett.108.052505](https://doi.org/10.1103/PhysRevLett.108.052505). arXiv: [1110.0679](https://arxiv.org/abs/1110.0679) [[nucl-th](#)] (cit. on pp. 236–238, 240, 241).
- [250] K. G. Fissum et al. “Dynamics of the quasielastic  $^{16}\text{O}(e, e'p)$  reaction at  $Q^2 \approx 0.8$  (GeV/c) $^2$ ”. In: *Phys. Rev. C* 70.3, 034606 (2004). DOI: [10.1103/PhysRevC.70.034606](https://doi.org/10.1103/PhysRevC.70.034606) (cit. on p. 237).

- [251] R. B. Firestone et al. *The 8th edition of the Table of Isotopes*. John Wiley, New York, 1997 (cit. on p. 237).
- [252] H. Ejiri. “Nuclear deexcitations of nucleon holes associated with nucleon decays in nuclei”. In: *Phys. Rev. C* 48.3 (1993), pp. 1442–1444. DOI: [10.1103/PhysRevC.48.1442](https://doi.org/10.1103/PhysRevC.48.1442) (cit. on pp. 238, 241).
- [253] M. Leuschner et al. “Quasielastic proton knockout from  $^{16}\text{O}$ ”. In: *Phys. Rev. C* 49.2 (1994), pp. 955–967. DOI: [10.1103/PhysRevC.49.955](https://doi.org/10.1103/PhysRevC.49.955) (cit. on p. 238).
- [254] G. J. Kramer, H. P. Blok, and L. Lapikás. “A consistent analysis of (e,e’p) and (d,3He) experiments”. In: *Nuclear Physics A* 679.3-4 (2001), pp. 267–286. ISSN: 0375-9474. DOI: [10.1016/s0375-9474\(00\)00379-1](https://doi.org/10.1016/s0375-9474(00)00379-1) (cit. on p. 238).
- [255] K. Kobayashi et al. “De-excitation gamma-rays from the s-hole state in N-15 associated with proton decay in O-16”. In: *arXiv Preprints* (Apr. 2006). arXiv: [nucl-ex/0604006](https://arxiv.org/abs/nucl-ex/0604006) (cit. on pp. 239–241).
- [256] F. Ajzenberg-Selove. “Energy levels of light nuclei A = 13 & 15”. In: *Nuclear Physics A* 523.1 (1991), pp. 1–196. ISSN: 0375-9474. DOI: [10.1016/0375-9474\(91\)90446-D](https://doi.org/10.1016/0375-9474(91)90446-D). URL: <https://www.sciencedirect.com/science/article/pii/037594749190446D> (cit. on p. 239).
- [257] K. Kobayashi et al. “Detection of nuclear de-excitation gamma-rays in water Cherenkov detector”. In: *Nucl. Phys. B Proc. Suppl.* 139 (2005), pp. 72–76. DOI: [10.1016/j.nuclphysbps.2004.11.206](https://doi.org/10.1016/j.nuclphysbps.2004.11.206) (cit. on p. 239).
- [258] M. Yosoi et al. “Structures and decay of deep-hole states in light nuclei populated by the (p, 2p 2p) reactions”. In: *Physics of Atomic Nuclei* 67.10 (2004), pp. 1810–1817. DOI: [10.1134/1.1811183](https://doi.org/10.1134/1.1811183) (cit. on pp. 240, 241).
- [259] H. D. Engelhardt, C. W. Lewis, and H. Ullrich. “The Absorption of pi- at Rest on Complex Nuclei”. In: *Nucl. Phys. A* 258.3 (1976), pp. 480–512. DOI: [10.1016/0375-9474\(76\)90486-3](https://doi.org/10.1016/0375-9474(76)90486-3) (cit. on p. 242).
- [260] K. Bays et al. “Supernova Relic Neutrino Search at Super-Kamiokande”. In: *Phys. Rev. D* 85.5, 052007 (2012). DOI: [10.1103/PhysRevD.85.052007](https://doi.org/10.1103/PhysRevD.85.052007). arXiv: [1111.5031](https://arxiv.org/abs/1111.5031) [hep-ex] (cit. on p. 243).
- [261] G. Van Rossum and F. L. Drake. *Python 3 Reference Manual*. Scotts Valley, CA: CreateSpace, 2009. ISBN: 1441412697 (cit. on p. 250).
- [262] F. Chollet et al. *Keras*. <https://keras.io>. 2015 (cit. on p. 250).
- [263] M. Abadi et al. *TensorFlow: Large-Scale Machine Learning on Heterogeneous Systems*. 2015. URL: <https://www.tensorflow.org/> (cit. on p. 250).
- [264] Keras. *Adam*. <https://keras.io/api/optimizers/adam/>. 2021. (Visited on 02/13/2021) (cit. on p. 250).
- [265] S.-A. Rebuffi, R. Fong, X. Ji, and A. Vedaldi. *There and Back Again: Revisiting Backpropagation Saliency Methods*. 2020. arXiv: [2004.02866](https://arxiv.org/abs/2004.02866) [cs.CV] (cit. on p. 253).
- [266] M. Agostini et al. “First Directional Measurement of Sub-MeV Solar Neutrinos with Borexino”. In: *Phys. Rev. Lett.* 128.9, 091803 (2022). DOI: [10.1103/PhysRevLett.128.091803](https://doi.org/10.1103/PhysRevLett.128.091803) (cit. on p. 260).
- [267] M. Agostini et al. “Correlated and integrated directionality for sub-MeV solar neutrinos in Borexino”. In: *Phys. Rev. D* 105.5, 052002 (2022). DOI: [10.1103/PhysRevD.105.052002](https://doi.org/10.1103/PhysRevD.105.052002) (cit. on p. 260).

- [268] L. J. Bignell et al. “Characterization and Modeling of a Water-based Liquid Scintillator”. In: *Journal of Instrumentation* 10.12, P12009 (2015). DOI: [10.1088/1748-0221/10/12/P12009](https://doi.org/10.1088/1748-0221/10/12/P12009). arXiv: [1508.07029](https://arxiv.org/abs/1508.07029) [physics.ins-det] (cit. on pp. 260, 267).
- [269] Z. Guo, M. Yeh, R. Zhang, D.-W. Cao, M. Qi, Z. Wang, and S. Chen. “Slow liquid scintillator candidates for MeV-scale neutrino experiments”. In: *Astroparticle Physics* (2019) (cit. on p. 261).
- [270] C. Rott, S. In, F. Retière, and P. Gumplinger. “Enhanced photon traps for Hyper-Kamiokande”. In: *Journal of Instrumentation* 12.11, P11021 (2017). DOI: [10.1088/1748-0221/12/11/p11021](https://doi.org/10.1088/1748-0221/12/11/p11021) (cit. on p. 261).
- [271] E. Segreto et al. “Liquid argon test of the ARAPUCA device”. In: *Journal of Instrumentation* 13.08, P08021 (2018). DOI: [10.1088/1748-0221/13/08/p08021](https://doi.org/10.1088/1748-0221/13/08/p08021) (cit. on p. 261).
- [272] T. Kaptanoglu, M. Luo, B. Land, A. Bacon, and J. R. Klein. “Spectral photon sorting for large-scale Cherenkov and scintillation detectors”. In: *Phys. Rev. D* 101.7, 072002 (2020). DOI: [10.1103/PhysRevD.101.072002](https://doi.org/10.1103/PhysRevD.101.072002) (cit. on p. 261).
- [273] J. Caravaca, F. B. Descamps, B. J. Land, J. Wallig, M. Yeh, and G. D. Orebi Gann. “Experiment to demonstrate separation of Cherenkov and scintillation signals”. In: *Phys. Rev. C* 95.5, 055801 (2017). DOI: [10.1103/PhysRevC.95.055801](https://doi.org/10.1103/PhysRevC.95.055801). arXiv: [1610.02029](https://arxiv.org/abs/1610.02029) [physics.ins-det] (cit. on pp. 261, 267).
- [274] M. Wurm. *New Detection Techniques - Advanced Scintillator Detectors*. 2018. DOI: [10.5281/zenodo.1286782](https://doi.org/10.5281/zenodo.1286782) (cit. on p. 262).
- [275] “Long-Baseline Neutrinos at THEIA”. In: *Snowmass2021 - Letter of Interest* (2021). URL: <https://www.snowmass21.org/docs/files/summaries/NF/SNOWMASS21-NF1-NF10-178.pdf> (cit. on p. 262).
- [276] R. Fichter. *Back to Basics: What Is Soap and How Does It Work?* URL: <https://www.themacbeth.com/blog/tag/soap+chemistry> (cit. on p. 262).
- [277] Wikimedia Commons. *File: A lipid micelle.png*. [Online; accessed 15-October-2021]. 2020. URL: [https://commons.wikimedia.org/w/index.php?title=File:A\\_lipid\\_micelle.png&oldid=457822711](https://commons.wikimedia.org/w/index.php?title=File:A_lipid_micelle.png&oldid=457822711) (cit. on p. 262).
- [278] A. Chilingarian, S. H. So, K. K. Joo, B. R. Kim, B. K. Kim, S. C. Kim, C. D. Shin, and I. S. Yeo. “Development of a Liquid Scintillator Using Water for a Next Generation Neutrino Experiment”. In: *Advances in High Energy Physics* 2014, 327184 (2014). DOI: [10.1155/2014/327184](https://doi.org/10.1155/2014/327184) (cit. on p. 263).
- [279] J. Caravaca, B. J. Land, M. Yeh, and G. D. Orebi Gann. “Characterization of water-based liquid scintillator for Cherenkov and scintillation separation”. In: *The European Physical Journal C* 80.9, 867 (2020). DOI: [10.1140/epjc/s10052-020-8418-4](https://doi.org/10.1140/epjc/s10052-020-8418-4) (cit. on pp. 263–265).
- [280] D. R. Onken, F. Moretti, J. Caravaca, M. Yeh, G. D. Orebi Gann, and E. D. Bourret. “Time response of water-based liquid scintillator from X-ray excitation”. In: *Mater. Adv.* 1.1 (2020), pp. 71–76. DOI: [10.1039/D0MA00055H](https://doi.org/10.1039/D0MA00055H) (cit. on p. 265).
- [281] A. Abusleme et al. “JUNO Physics and Detector”. In: *arXiv Preprints* (2021). arXiv: [2104.02565](https://arxiv.org/abs/2104.02565) [hep-ex] (cit. on p. 266).
- [282] A. Abusleme et al. *The Design and Sensitivity of JUNO’s scintillator radiopurity pre-detector OSIRIS*. 2021. arXiv: [2103.16900](https://arxiv.org/abs/2103.16900) [physics.ins-det] (cit. on p. 266).

- [283] M. Taniguchi and J. S. Lindsey. “Database of Absorption and Fluorescence Spectra of >300 Common Compounds for use in PhotochemCAD”. In: *Photochemistry and Photobiology* 94.2 (2018), pp. 290–327. DOI: [10.1111/php.12860](https://doi.org/10.1111/php.12860). eprint: <https://onlinelibrary.wiley.com/doi/pdf/10.1111/php.12860> (cit. on p. 266).
- [284] V. I. Tretyak. “Semi-empirical calculation of quenching factors for ions in scintillators”. In: *Astroparticle Physics* 33.1 (2010), pp. 40–53. ISSN: 0927-6505. DOI: [10.1016/j.astropartphys.2009.11.002](https://doi.org/10.1016/j.astropartphys.2009.11.002). URL: <https://www.sciencedirect.com/science/article/pii/S0927650509001650> (cit. on p. 267).
- [285] M. N. Peron and P. Cassette. “A Compton coincidence study of liquid scintillator response to low-energy electrons”. In: *Nuclear Instruments and Methods in Physics Research Section A: Accelerators, Spectrometers, Detectors and Associated Equipment* 369.2 (1996), pp. 344–347. ISSN: 0168-9002. DOI: [10.1016/S0168-9002\(96\)80006-4](https://doi.org/10.1016/S0168-9002(96)80006-4). URL: <https://www.sciencedirect.com/science/article/pii/S0168900296800064> (cit. on p. 267).
- [286] L. Torrisi. “Plastic scintillator investigations for relative dosimetry in proton-therapy”. In: *Nuclear Instruments and Methods in Physics Research Section B: Beam Interactions with Materials and Atoms* 170.3 (2000), pp. 523–530. ISSN: 0168-583X. DOI: [10.1016/S0168-583X\(00\)00237-8](https://doi.org/10.1016/S0168-583X(00)00237-8). URL: <https://www.sciencedirect.com/science/article/pii/S0168583X00002378> (cit. on p. 267).
- [287] R. Broda, K. Małetka, T. Terlikowska, and P. Cassette. “Study of the influence of the LS-cocktail composition for the standardisation of radionuclides using the TDCR model”. In: *Applied Radiation and Isotopes* 56.1 (2002). Proceedings of the Conference on Radionuclide Metrology and its Applications, ICRM’01, pp. 285–289. ISSN: 0969-8043. DOI: [10.1016/S0969-8043\(01\)00202-0](https://doi.org/10.1016/S0969-8043(01)00202-0). URL: <https://www.sciencedirect.com/science/article/pii/S0969804301002020> (cit. on p. 267).
- [288] B. von Krosigk, L. Neumann, R. Nolte, S. Röttger, and K. Zuber. “Measurement of the proton light response of various LAB based scintillators and its implication for supernova neutrino detection via neutrino–proton scattering”. In: *The European Physical Journal C* 73.4, 2390 (2013). DOI: [10.1140/epjc/s10052-013-2390-1](https://doi.org/10.1140/epjc/s10052-013-2390-1) (cit. on p. 267).
- [289] J. Eisch. *SANDI: The Small ANNIE Neutron Detector at ISU*. Internal ANNIE database document (DocDB ID 263). 2016. URL: <https://annie-docdb.fnal.gov/cgi-bin/sso/ShowDocument?docid=263> (cit. on p. 268).
- [290] Z. Bagdasarian and G. Orebi Gann. *Private communication*. 2021 (cit. on p. 269).
- [291] M. Cecconello. “Liquid Scintillators Neutron Response Function: A Tutorial”. In: *Journal of Fusion Energy* 38.3 (2019), pp. 356–375. DOI: [10.1007/s10894-019-00212-w](https://doi.org/10.1007/s10894-019-00212-w) (cit. on p. 273).
- [292] V. V. Verbinski, W. R. Burrus, T. A. Love, W. Zobel, N. W. Hill, and R. Textor. “Calibration of an organic scintillator for neutron spectrometry”. In: *Nuclear Instruments and Methods* 65.1 (1968), pp. 8–25. ISSN: 0029-554X. DOI: [10.1016/0029-554X\(68\)90003-7](https://doi.org/10.1016/0029-554X(68)90003-7). URL: <https://www.sciencedirect.com/science/article/pii/0029554X68900037> (cit. on p. 273).
- [293] J. Nieves, F. Sánchez, I. Ruiz Simo, and M. J. Vicente Vacas. “Neutrino energy reconstruction and the shape of the charged current quasielastic-like total cross section”. In: *Phys. Rev. D* 85.11, 113008 (2012). DOI: [10.1103/PhysRevD.85.113008](https://doi.org/10.1103/PhysRevD.85.113008) (cit. on p. 281).
- [294] V. A. Li. “Far-Field Monitoring of Reactor Antineutrinos for Nonproliferation”. In: *arXiv Preprints* (2019). arXiv: [1907.08891](https://arxiv.org/abs/1907.08891) [physics.ins-det] (cit. on pp. 288, 289).

- [295] M. Askins et al. “The Physics and Nuclear Nonproliferation Goals of WATCHMAN: A WATER CHerenkov Monitor for ANTineutrinos”. In: *arXiv Preprints* (2015). arXiv: [1502.01132](https://arxiv.org/abs/1502.01132) [[physics.ins-det](#)] (cit. on p. 288).
- [296] M. Askins et al. “THEIA: an advanced optical neutrino detector”. In: *Eur. Phys. J. C* 80.5, 416 (2020). DOI: [10.1140/epjc/s10052-020-7977-8](https://doi.org/10.1140/epjc/s10052-020-7977-8). arXiv: [1911.03501](https://arxiv.org/abs/1911.03501) [[physics.ins-det](#)] (cit. on pp. 289, 290).
- [297] J. Sawatzki, M. Wurm, and D. Kresse. “Detecting the diffuse supernova neutrino background in the future water-based liquid scintillator detector Theia”. In: *Phys. Rev. D* 103.2, 023021 (2021). DOI: [10.1103/PhysRevD.103.023021](https://doi.org/10.1103/PhysRevD.103.023021). URL: <https://link.aps.org/doi/10.1103/PhysRevD.103.023021> (cit. on p. 290).



# Appendix

---

## A DATA STRUCTURES IN ANNIE

The following section provides some useful auxiliary information on the nomenclature of different data structures and labels in the scope of ANNIE. The first subsection will focus on the unique labels of electronic channels within ANNIE, the so-called channelkeys. Spatial distributions of channelkeys are presented for all subdetectors and can be used as a quick look-up guide to cross-correlate channelkey numbers with their location in the detector. The second subsection will provide a more complete overview of all the triggerwords used to label different triggers by the Central Trigger Card, expanded from the short introduction given in section 3.4.2.

### CHANNELKEY LABELING

The introduction of the term *channelkey* in ANNIE is based on the idea of associating a unique identifier with each electronic channel in the detector. The properties of each electronic channel (such as its geometric location, its gain, its location in the electronic rack, etc.) can then be stored in a database-like structure and accessed whenever needed. At the same time, the channel information can be reduced to this one variable in the processed output data files.

Conventional PMTs record the cumulative signal from all photons interacting with their photocathode surface such that we can identify each photomultiplier by a single channelkey number. On the other hand, LAPPDs can actually distinguish electronic signals between their different strips, meaning that we need multiple channelkeys to represent each LAPPD. As every LAPPD contains a total of 28 anode strip lines with double-sided readout mechanics, 56 channelkeys are required to describe signals acquired by a single LAPPD. Table A.1 provides an overview of the specific channelkey numbers that are in use for the different subdetectors in ANNIE. In terms of the absolute channelkey assignments, the 26 FMV paddles are assigned the first channelkeys [0,25], the 306 MRD channels populate the channelkey region [26,331], and the 132 water tank PMTs take up the subsequent channelkey numbers [332,464]. Channelkeys larger than 465 are reserved for the LAPPD anode strips. While the assignments for all channelkeys up to 464 are already set, the exact location channelkey mapping is outstanding for the case of the LAPPDs and might be introduced dynamically depending on the final deployment strategy.

The spatial distribution of channelkeys in ANNIE is shown in figure A.1 for the FMV paddles, in figure A.2 for the MRD and in figure A.3 for the water tank PMTs.

Subdetector	Channelkeys/sensor	Sensors	Channelkey range
FMV	1	26	0-25
MRD	1	306	26-331
Tank PMTs	1	132	332-464
Tank LAPPDs	60	5	465-765

**Table A.1:** Overview of the channelkey characteristics for the photosensors in the different subdetectors in ANNIE. While one channelkey per sensor is satisfactory to describe the conventional PMTs used in the FMV, MRD, and the water tank, multiple channelkeys are needed to describe each LAPPD.

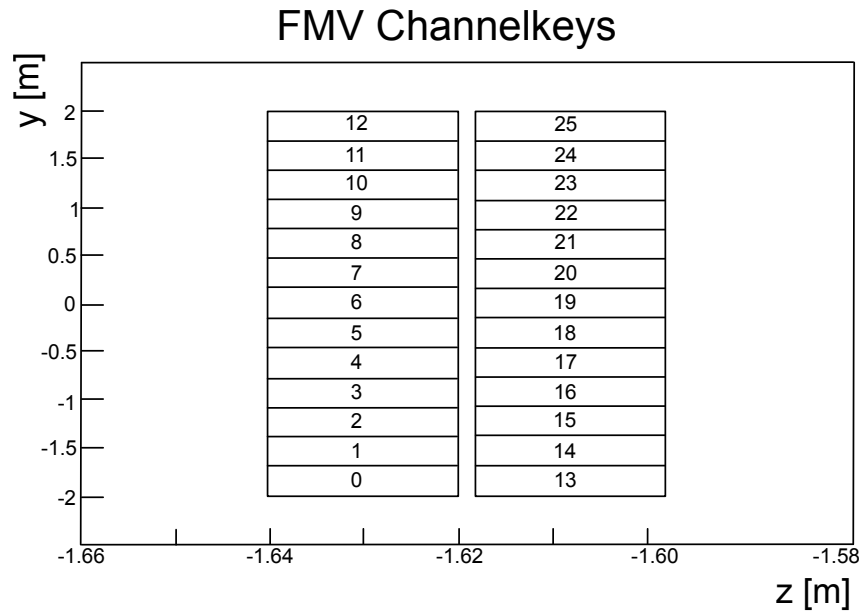


**Figure A.1:** Distribution of FMV channelkeys in a side view of the veto detector. Each of the two layers is comprised of 13 channels, covering the channelkey range from 0 up to 25. The PMTs are mounted on opposing sides for the two layers.

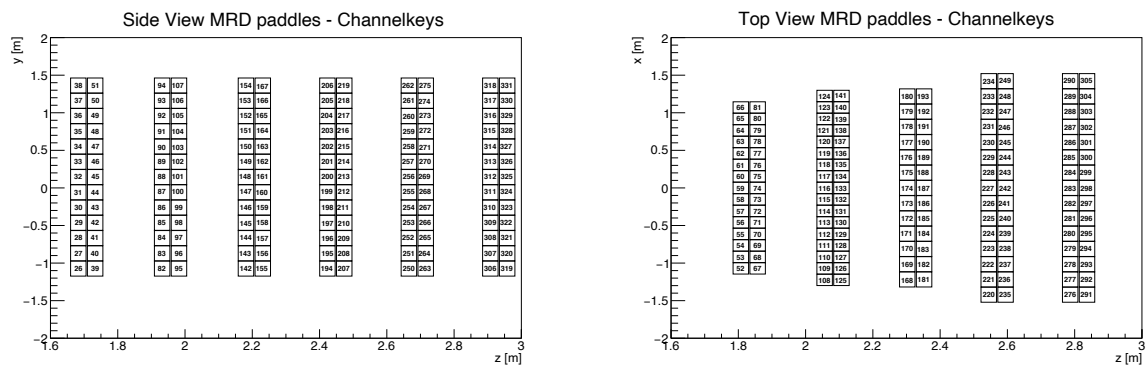


**Figure A.2:** Distribution of channelkeys for the channels associated to the different MRD scintillator paddles, ranging from 26 to 305. The image shows the indices of paddles in horizontal layers in a side view (left), while the numbers of vertical channels are displayed in a top view of the detector (right).

## TRIGGERWORD OVERVIEW

Table A.2 provides a comprehensive overview of the different triggerwords in use by the Central Trigger Card in ANNIE.

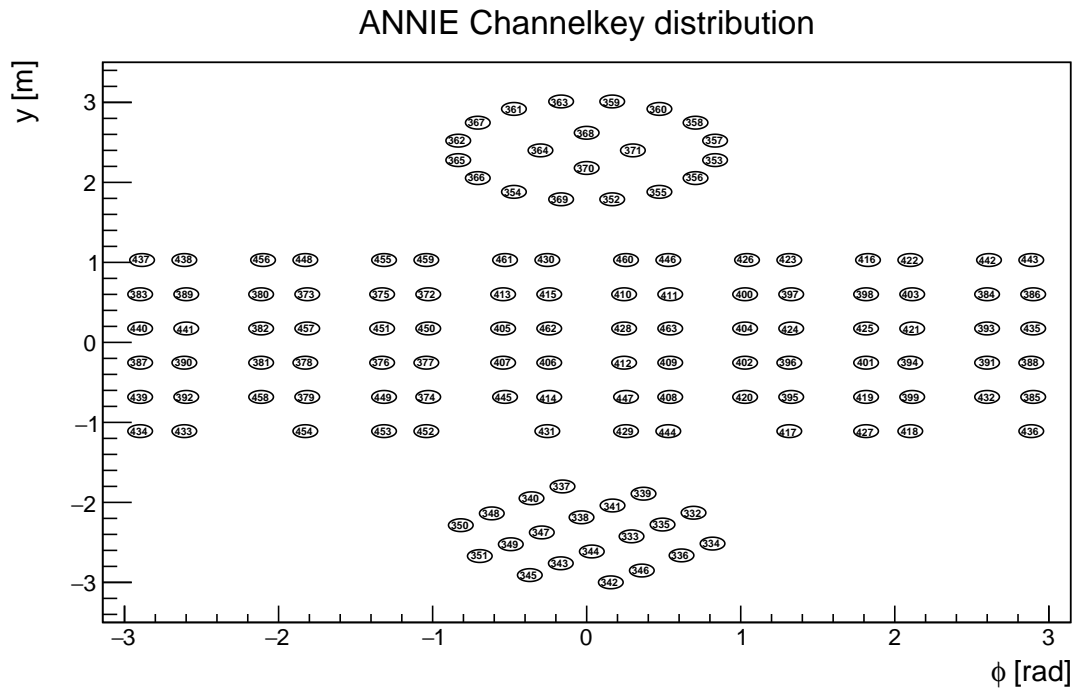


**Figure A.3:** Distribution of channelkeys in the ANNIE detector in a rolled-open representation of the water tank. The water tank PMTs occupy the channelkey numbers in the range of 332 to 464, while the FMV PMTs are represented by channelkeys 0-25 and the MRD channels are labeled by channelkeys 26-305.

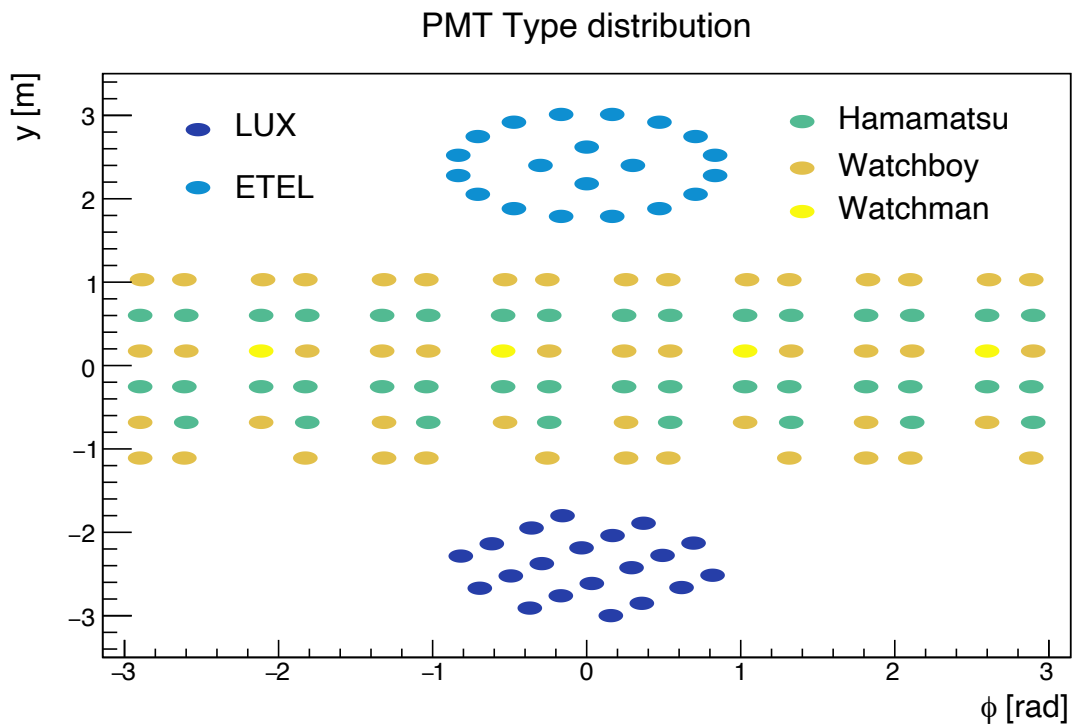


**Figure A.4:** Distribution of PMT types in the ANNIE detector in a rolled-open representation of the water tank. In total, there are 20 LUX PMTs, 20 ETEL PMTs, 40 Hamamatsu/ANNIE PMTs, 48 Watchboy PMTs, and 4 Watchman PMTs present in the ANNIE water tank.

Triggerword	Triggerword label	Detailed description
1	bes_holdoff	Booster Extraction Sync over fiber
2	input_1f	\$1F (Booster Extraction Sync)
3	input_1d	\$1D (Prepare to BNB)
4	input_rwm	RWM input
5	Delay_beam_trigger1	Delayed trigger to ADC system
6	Beam_veto1	Beam1 veto high
7	NOT Beam_veto1	Beam1 veto low
8	Delay_beam_trigger2	Delayed trigger to MRD system
9	Beam_veto2	Beam2 veto high
10	NOT Beam_veto2	Beam2 veto low
11	Delay_ext_trigger	Delayed external trigger
12	Ext_veto	External veto high
13	NOT Ext_veto	External veto low
14	Beam_trigger	Undelayed Beam Trigger
15	Ext_trigger	Undelayed external trigger
16	SoftTrigger_out	Software trigger
17	TimeLatch_in	Timelatch (not a trigger, used to sync with CPU)
18	Self_ADC_Window	Selftrigger back from ADC system AND Window_true
19	input_trigger	External Trigger Input
20	input_calsource	Calibration Source Trigger Input
21	Cal_Trigger	Undelayed Calibration Trigger
22	Periodic_trigger	Constant period Trigger
23	Window_true	Window open
24	NOT Window_true	Window close
25	Window_trigger	Window trigger
26	MinRate_trigger	Minimum Rate Trigger
27 - 30	CosmicTriggers	Cosmic-ray muon trigger outputs
31	LED_start	Start of LED timer
32	input_sync	GPS 1PPS Sync signal
33	LED_adc_trigger	Trigger to ADC after LED delay
34	input_8f	TCLK \$8F 1PPS Signal
35	Self_ADC	SelfTrigger if used to trigger the ADCs
36	MRD_CR_trigger	MRD Cosmic ray trigger
37	BE_status.activity_window_start	Start of acquisition window
38	BE_status.activity_window_end	End of acquisition window
39	BE_status.self_trigger_in_window	PMT above CC threshold
40	BE_status.minbias_start	Non-CC extended readout
41	BE_status.extend_start	CC-extended readout
42	input_numi	NuMI beam input
43	offbeam_led_trigger	Offbeam LED
44	offbeam_nextcosmic_start	Off-beam Next Cosmic (Start)
45	offbeam_nextcosmic_trigger	Off-beam Next Cosmic (Trigger)
46	Trigger1_out_reg	Regular trigger output
47 - 64	Other	Unused triggerwords

**Table A.2:** The different triggerwords that are used to identify events in the trigger card within the ANNIE raw data. The presented information about the triggerwords was retrieved in personal communication with Jonathan Eisch who designed the trigger system.

## B ADDITIONAL INFORMATION ON FMV EFFICIENCIES

The following chapter provides some additional information on the channel-wise FMV efficiencies. Figure B.1 presents the spatial dependence of the efficiency for all paddles in the first FMV layer. Increasing channelkey numbers correspond to moving upwards within the layer (compare the channelkey maps in the previous chapter A). The linearly decreasing trend is visible across all paddles, with near-edge efficiencies around 90% and far-edge efficiencies of around 60%.

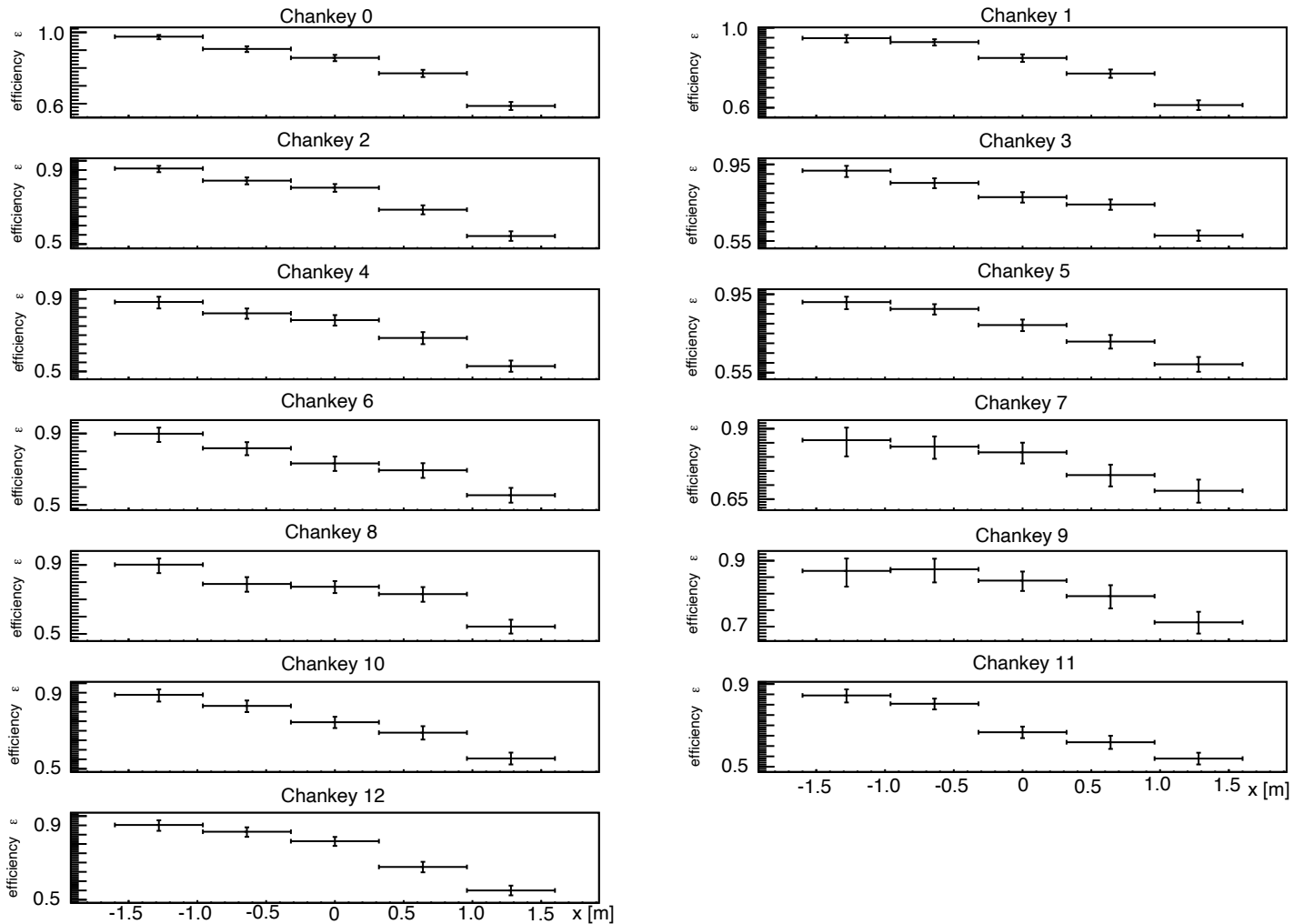


**Figure B.1:** Position-resolved FMV paddle efficiencies for the 13 scintillator paddles of the first layer of the FMV. Hits on the near end of the PMTs at negative  $x$  values display very high efficiencies around 90%, while the far ends of the paddles show lower efficiencies around 60%.

In a similar manner, the channel-wise efficiency dependencies are shown in figure B.2 for the second layer of the FMV. The smallest channelkey number corresponds to the scintillator paddle at the bottom of the layer, with increasing channelkeys being associated to going upward within the layer. As expected, the observed spatial dependence is reversed compared to the first layer. All channels seem to exhibit a similar behavior, and the spatial dependence is clearly visible equally across all channels.

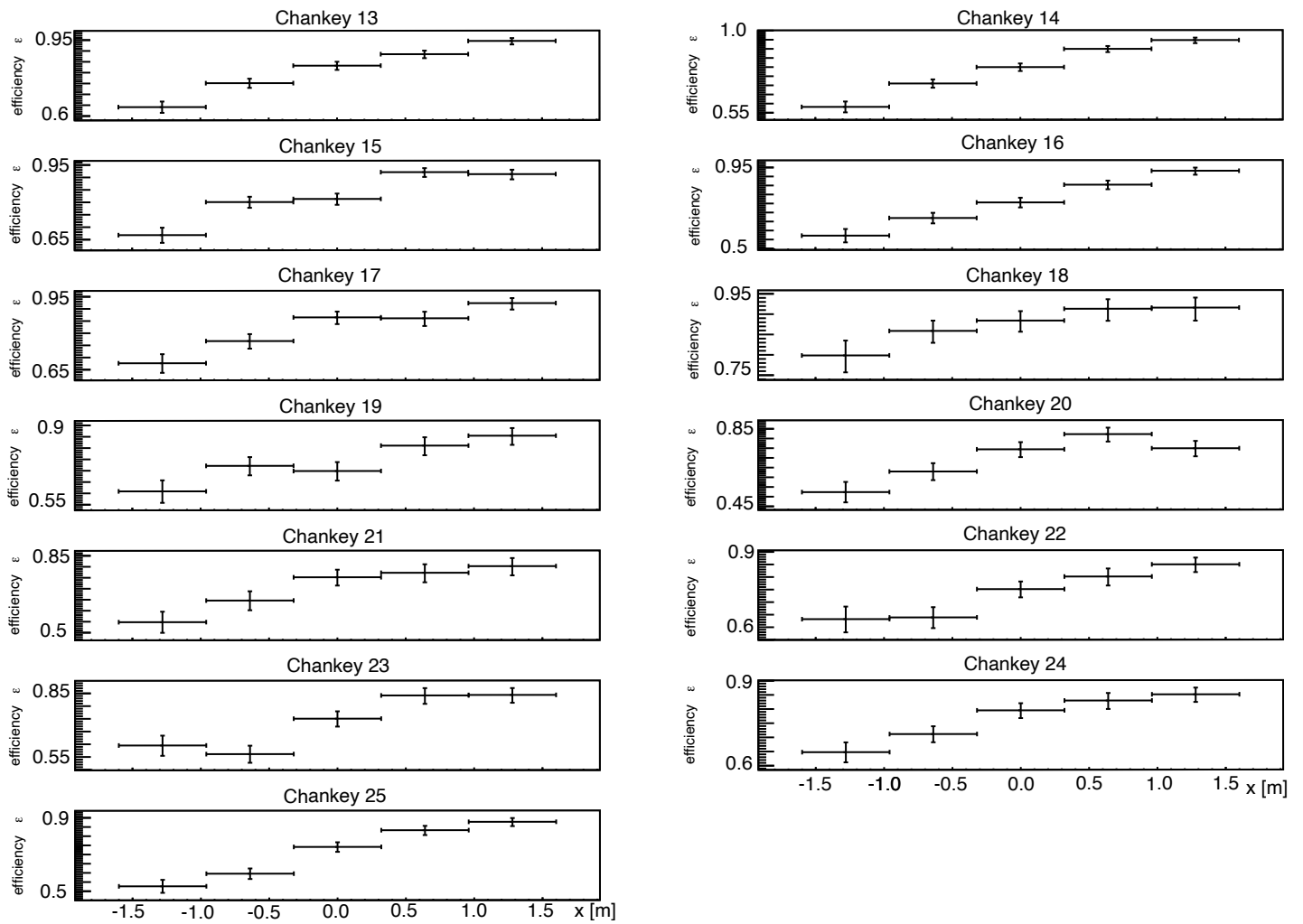


**Figure B.2:** Position-resolved FMV paddle efficiencies for the 13 scintillator paddles of the second layer of the FMV. Hits on the near end of the PMTs at positive  $x$  values display very high efficiencies around 90%, while the far ends of the paddles show lower efficiencies around 60%.

## c COMPLEMENTARY AMBE CALIBRATION PLOTS

Additional AmBe neutron calibration charge spectra comparisons between data and simulation are shown for the calibration ports 1, 2, and 4 in the following figures C.1 - C.3. Simulations were conducted with the tuned version of the WCSim framework with individual effective Q.E. values. Equivalent plots for the ports 3 and 5 have been shown in section 5.4.3 in the main part of the thesis.

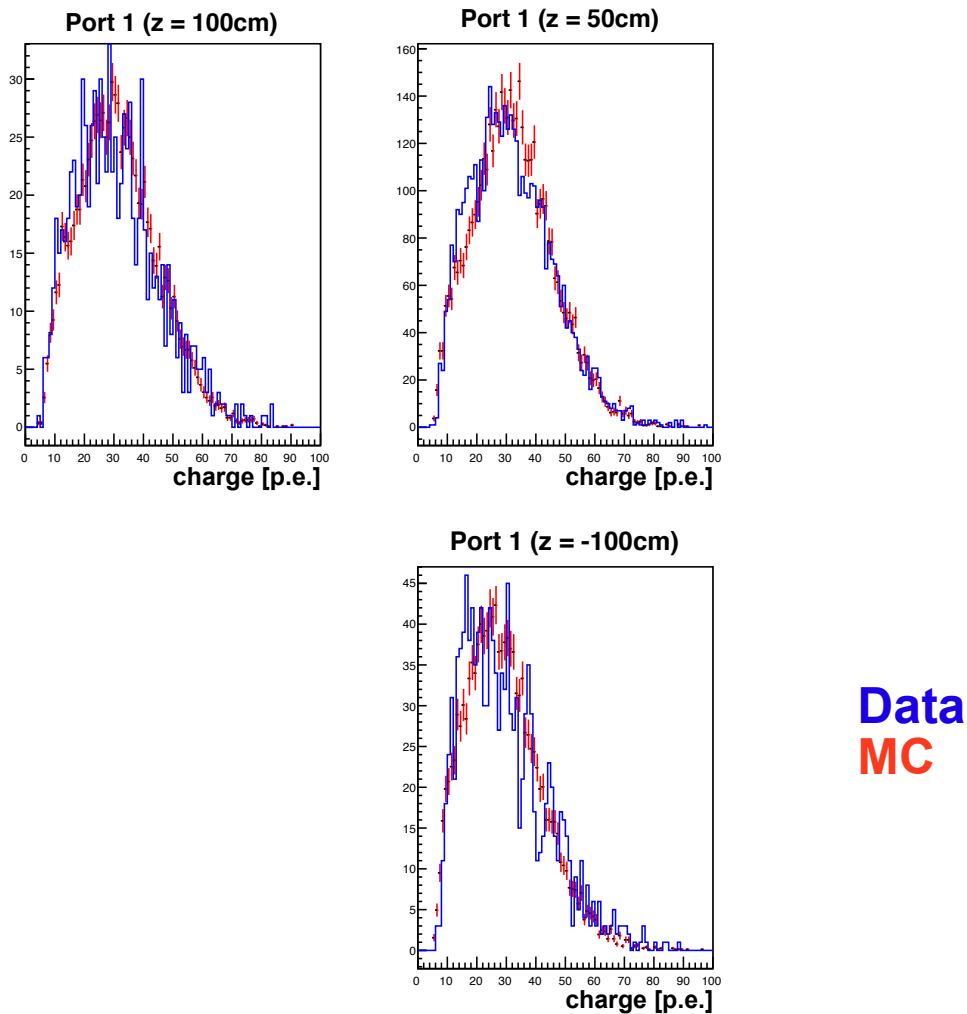


**Figure C.1:** Charge spectra for neutron captures at the three different source heights ( $z = -100\text{ cm}$ ,  $z = 50\text{ cm}$ , and  $z = 100\text{ cm}$ ) within port 1. Data spectra are shown in blue, while the simulated distributions are depicted in red. Good agreement is observed for all heights.

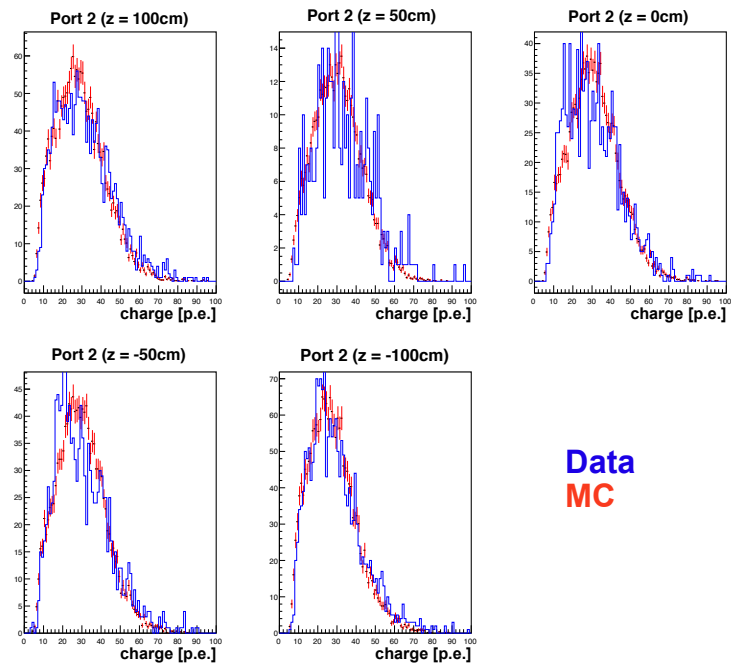


**Figure C.2:** Charge spectra for neutron captures at the five different source heights ( $z = -100\text{ cm}$ ,  $z = -50\text{ cm}$ ,  $z = 0\text{ cm}$ ,  $z = 50\text{ cm}$ , and  $z = 100\text{ cm}$ ) within port 2. Data spectra are shown in blue, while the simulated distributions are depicted in red. Good agreement is observed for all heights, with the worst agreement visible for the central position ( $z = 0$ ).

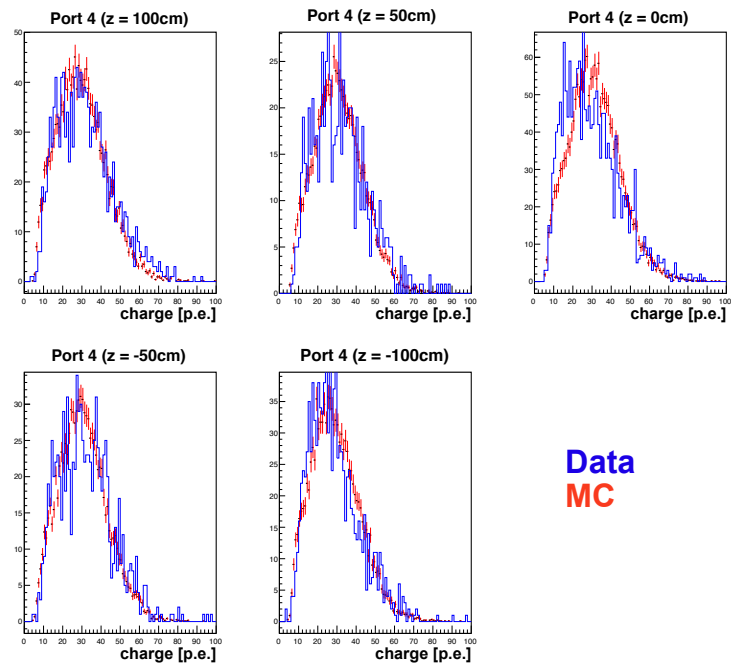


**Figure C.3:** Charge spectra for neutron captures at the five different source heights ( $z = -100\text{ cm}$ ,  $z = -50\text{ cm}$ ,  $z = 0\text{ cm}$ ,  $z = 50\text{ cm}$ , and  $z = 100\text{ cm}$ ) within port 4. Data spectra are shown in blue, while the simulated distributions are depicted in red. Good agreement is observed for all heights, with the worst agreement visible for the central position ( $z = 0$ ).

# Acknowledgements

---

This thesis owes its existence to the help of a lot of people, without which the work presented in the previous chapters would have never been possible. If you are wondering why you spent a considerable fraction of your lifetime reading this work, this section is dedicated to you. While I tried my best to include everyone, I am very sorry if I forgot someone and already apologize in advance.

First of all, I would like to express my sincerest gratitude to my advisor Michael Wurm, who enabled me to work on this interesting topic in the first place. I am thankful for the faith in my capabilities, the freedom to explore my own ideas, flexibility in thesis topics when the original thesis-related experiment ceased to exist for unforeseen reasons, quick responses and always very helpful ideas and discussions whenever I got stuck somewhere. Furthermore, I am glad for the opportunities to work on the experiment on-site and to present the progress of the experiment at conferences, which both helped to put the software and analysis work into some perspective.

Secondly, I would like to thank Martin Fertl for his willingness to co-supervise this thesis as the second reviewer – thanks a lot for that.

Furthermore, I would like to thank the whole ANNIE crew for a very warm and productive work environment. The donut-rich collaboration meetings and the good atmosphere while working on the experiment on-site will always be remembered very fondly by me. In particular, I would like to thank Marcus O’Flaherty for his immense help: the very detailed and always helpful discussions on the simulation framework, the analysis and reconstruction in general, and the possibility to rant about debugging issues in R00T, Geant, and ToolAnalysis were always very valuable to me. Similarly, I want to thank Ben Richards for answering all sorts of software-related questions with great patience and for his help with setting up the Monitoring environment for the experiment. Thanks a lot also to Evangelia Drakopoulou, who helped me with getting more familiar with machine learning techniques and Ashley Back for making git a little more understandable. At the same time, I want to thank Steven Gardiner for taking the time to help me with some GENIE-related questions. I would also like to thank Teal Pershing for the collaborative look at the first beam data and the first neutrinos recorded by ANNIE in 2020, which proved to be a very exciting task. In addition, I am very fond of having worked with Emrah Tiras at Fermilab, who always took good care of us *part-time visitors* at the lab and made sure we felt like at home. In this context, I am also glad that I was able to meet and work with a lot of people at the lab: starting with the Sheffield crew in 2018 including my flatmates Tom Shaw, Max Callé, Abishek Upreti, as well as Marcus O’Flaherty who all made the work at DAB and the PMT test stand a lot more fun. While not directly ANNIE-related, I am also glad to have met Pratyush (Reik) Das at the lab, who never failed to promote his amazing work surrounding the uproot project (sorry that I failed so long to install it) and always was a secret supporter and fan of ANNIE. I will also always fondly remember the time in the summer of 2019 where I was able to witness the transport and lowering of the Inner

Structure into the ANNIE hall and later was able to help with connecting the PMT HV and signal cables together with Julie He, Lena Korkeila, and David Maksimović. While I learned a lot about all the ways that cables can end tangled up, I also very much enjoyed the time outside of the lab where we managed to fail spectacularly at an escape room and explored Chicago together. Later that summer, I am also glad to have worked with Byron Peralta and Liang Li during the water fill of ANNIE. Thanks a lot also to Vincent Fischer, who spent a good amount of time at the lab chasing problematic MRD channels and helping me debug my ratpac-related issues – sorry for putting you through all of that. A big thanks also to Malte Stender for always fun book discussions, his help on the Monitoring system for the LAPPDs, and enduring my poor flying skills at the flight simulator. I further want to thank Jonathan Eisch, Frank Krennrich, and Navaneeth Poonthottathil for their help in understanding the trigger system a little better and Marc Breisch for his help in understanding the LAPPD data structure and slow control monitoring data. I would also like to thank Emily Pottebaum for high-quality meme content on the ANNIE slack and Carrie McGivern for brightening pandemic zoom calls with the presence of her child. Lastly, I would also like to thank Matt Wetstein just for being his optimistic self and making ANNIE possible in the first place.

Of course there are also a lot of people in Mainz which I grew very fond of during this time of my PhD. A large thank you to Wilfried Depnering for being a great friend, his endless support, fun piano/Cello jam sessions, (unsuccessfully) trying to bring Star Trek closer to me and taking great care of my plants time after time. Similarly, I want to thank David Maksimović for a lot of walks along the Rhein during the pandemic, his large passion for astrophysics and Star Wars, a great time in the States, and many fascinating collaborative projects. Many thanks to Annika Hollnagel for a lot of fun board game nights, hat-building evenings, and always delicious Kimchi. Thanks a lot to Paul Hackspacher for fun Singstar evenings, movie nights, and his always great costumes during Halloween and carnival. Furthermore, I also want to thank Joakim Sandroos and Peter Peiffer for some fun board game evenings (both off- and online). Thanks a lot also to Johann Martyn and Stefan Weinz for fun trips to Gran Sasso, joint complaints about our favorite computing farm *cnaffe* and in general for making the office life much more enjoyable. In this context, I also want to thank some Borexino collaborators for their help and collaborative work over the years, in particular Alessio Caminata, Chiara Ghiano, Birgit Neumair, Lea Di Noto and Koun Choi. A large thank you also to Daniele Guffanti for being a great office mate, a steady supply of Italian cookies and home-made tiramisu, and very helpful brainstorming sessions about physics- and simulation-related issues. Thanks also to Seva Orekhov for being fun around the office despite his tireless efforts to get me to play chess or attend dancing lessons, and to George Parker for bringing his British charm to the office. Thanks also to Heike Enzmann for very enjoyable (and delicious) annual *Plätzchen* baking events. Many thanks also to Jan Weldert for exploring the Rheinsteig together, and enduring my canoeing "skills". A big thanks also to Alexander Fritz for many cokes at the 3sein, pizza at Milano, and breaks at university whenever one of us did not want to work (and for dragging me to the gym for my own good). Of course also a big thanks to Thomas Ehrhardt for fun football discussions and his always very insightful physics explanations. I'm also glad to have met Elisa Lohfink, David Stipp, David Kappesser, Kai Loo, Oliver Pilarczyk, Patrick Deucher, Nils Brast, Sebastian Lorenz, and Dorina Zundel over the years.

A big thanks also to all the proof readers of this thesis for their valuable input. In this context, I want to thank Daniele Guffanti, Wilfried Depnering, Paul Hackspacher, David Maksimović, Johann Martyn, Kai Loo, Julia Nieslony, and George Parker for their time and comments on the manuscript.

In addition, there are several people that helped but do not fall in any of the other categories. In this context, I want to thank Julia Sawatzki for her insight into the simulation of NCQE neutrino reactions and associated de-excitation channels and Mark Vagins and Koun Choi for their help in reading the first draft of the related paper. I further want to thank Zara Bagdasarian and Gabriel Orebi Gann for discussions and access to their custom WbLS model.

This thesis would also not have been possible without the support of my friends over the years – a particular thank you to Heiko Gerstmayr, Sven Claßen, Moritz Schuck, Tim Wolz, Timothy Gebhard, Woo-Jeong Baek, Carl Degitz, Lukas Diewald, and Marleen Braun.

I would also like to thank the coffee machine on the fifth floor for a steady (and much needed) supply of coffee and Konya Döner for always providing delicious food and keeping me from starving.

Finally, I would like to thank my girlfriend Anna for her endless support during the last couple of months – thank you for keeping me sane, always being your cute self, and showing me the importance of gourmet food. I am also extremely thankful for the continuous support of my parents Beate and Marian and my sisters Laura and Julia over this whole period of my life, particularly during very stressful times. Thank you for always being there for me and believing in me, this thesis would not have been possible without you.

